

AWARD NUMBER: W81XWH-07-1-0306

TITLE: PROSPECT: Profiling of Resistance Patterns & Oncogenic Signaling
Pathways in Evaluation of Cancers of the Thorax and Therapeutic Target
Identification

PRINCIPAL INVESTIGATOR: Waun Ki Hong, M.D.

CONTRACTING ORGANIZATION: University of Texas, M.D. Anderson Cancer
Center
Houston, TX 77030

REPORT DATE: June 2009

TYPE OF REPORT: Annual

PREPARED FOR: U.S. Army Medical Research and Materiel Command
Fort Detrick, Maryland 21702-5012

DISTRIBUTION STATEMENT: Approved for Public Release;
Distribution Unlimited

The views, opinions and/or findings contained in this report are those of the author(s) and should not be construed as an official Department of the Army position, policy or decision unless so designated by other documentation.

REPORT DOCUMENTATION PAGE

Form Approved
OMB No. 0704-0188

Public reporting burden for this collection of information is estimated to average 1 hour per response, including the time for reviewing instructions, searching existing data sources, gathering and maintaining the data needed, and completing and reviewing this collection of information. Send comments regarding this burden estimate or any other aspect of this collection of information, including suggestions for reducing this burden to Department of Defense, Washington Headquarters Services, Directorate for Information Operations and Reports (0704-0188), 1215 Jefferson Davis Highway, Suite 1204, Arlington, VA 22202-4302. Respondents should be aware that notwithstanding any other provision of law, no person shall be subject to any penalty for failing to comply with a collection of information if it does not display a currently valid OMB control number. **PLEASE DO NOT RETURN YOUR FORM TO THE ABOVE ADDRESS.**

1. REPORT DATE 1 June 2009		2. REPORT TYPE Annual		3. DATES COVERED 1 June 2008 – 31 May 2009	
4. TITLE AND SUBTITLE PROSPECT (Profiling of Resistance Patterns & Oncogenic Signaling Pathways in Evaluation of Cancers of the Thorax and Therapeutic Target Identification)				5a. CONTRACT NUMBER	
				5b. GRANT NUMBER W81XWH-07-1-0306	
				5c. PROGRAM ELEMENT NUMBER	
6. AUTHOR(S) Waun Ki Hong, M.D. E-Mail: whong@mdanderson.org				5d. PROJECT NUMBER	
				5e. TASK NUMBER	
				5f. WORK UNIT NUMBER	
7. PERFORMING ORGANIZATION NAME(S) AND ADDRESS(ES) University of Texas, M.D. Anderson Cancer Center Houston, TX 77030				8. PERFORMING ORGANIZATION REPORT NUMBER	
9. SPONSORING / MONITORING AGENCY NAME(S) AND ADDRESS(ES) U.S. Army Medical Research and Materiel Command Fort Detrick, Maryland 21702-5012				10. SPONSOR/MONITOR'S ACRONYM(S)	
				11. SPONSOR/MONITOR'S REPORT NUMBER(S)	
12. DISTRIBUTION / AVAILABILITY STATEMENT Approved for Public Release; Distribution Unlimited					
13. SUPPLEMENTARY NOTES					
14. ABSTRACT We will develop a high throughput therapeutic-target focused (TTF) profiling platform and will combine this with tumor genome wide mRNA profiling and with serum or plasma profiling of phosphopeptides and DNA. We will use these molecular profiles to help define how various molecular factors alone and in combination relate to resistance to therapy, to prognosis, and to metastatic patterns at relapse. Using tumor and blood samples from non-small cell lung cancer (NSCLC) patients as well as NSCLC cell lines with defined chemotherapy resistance patterns, we will examine how molecular profiles may confer resistance and will identify new, potential therapeutic targets. The PROSPECT approach will be novel in that we will assess tumors from NSCLC patients undergoing surgical resection after having received neoadjuvant therapy as a model of resistance. Tumor surviving neoadjuvant therapy would be expected to be enriched for resistant cells. We will define what combinations of targeted therapies are most effective against resistant cell lines with similar molecular profiles, and this will drive later clinical trials (beyond the scope of this Program). Similar studies will be conducted in patients with mesotheliomas undergoing surgical resection of tumor after neoadjuvant therapy with the new Src inhibitor dasatinib.					
15. SUBJECT TERMS Lung cancer, mesothelioma, target-focused profiling, resistance					
16. SECURITY CLASSIFICATION OF:			17. LIMITATION OF ABSTRACT	18. NUMBER OF PAGES	19a. NAME OF RESPONSIBLE PERSON USAMRMC
a. REPORT U	b. ABSTRACT U	c. THIS PAGE U			19b. TELEPHONE NUMBER (include area code)
			UU	427	

TABLE OF CONTENTS

INTRODUCTION	4
PROGRESS REPORT (BODY).....	4
<i>Project 1.....</i>	<i>5</i>
<i>Project 2.....</i>	<i>10</i>
<i>Project 3.....</i>	<i>13</i>
<i>Project 4.....</i>	<i>26</i>
<i>Project 5.....</i>	<i>28</i>
<i>Pathology Core</i>	<i>33</i>
<i>Biostatistics Core</i>	<i>38</i>
KEY RESEARCH ACCOMPLISHMENTS.....	41
REPORTABLE OUTCOMES	44
CONCLUSIONS	49
APPENDICES.....	51
Appendix A - Abstracts and Publications	
Appendix B - Biostatistics Database Screenshots	
Appendix C - New Investigator Biosketches	

INTRODUCTION

Lung cancer is the leading cause of cancer death in the world. Non-small cell lung cancer (NSCLC) accounts for 85% of all lung cancer cases. Only 15% of patients diagnosed with lung cancer survive five years from diagnosis. Therapy for advanced disease increases average life expectancy by only a few months, and slightly improves quality of life. Similarly, adjuvant chemotherapy for resected disease has only a modest impact on survival rates. More effective therapy is needed. We believe that applying state-of-the-art molecular tools to carefully conducted clinical trials will lead to the identification of molecular mechanisms that contribute to lung cancer therapeutic resistance and that drive prognosis, and that this in turn will lead to the development of drugs with novel biological and therapeutic functions. Therefore, we have undertaken a translational research program named **PROSPECT: Profiling of Resistance Patterns & Oncogenic Signaling Pathways in Evaluation of Cancers of the Thorax and Therapeutic Target Identification**. The goal of PROSPECT is to use therapeutic target-focused (TTF) profiling along with genome-wide mRNA and serum phosphopeptide profiling to identify and evaluate molecular targets and pathways that contribute to therapeutic sensitivity or resistance, prognosis, and recurrence patterns, and to use this information to guide formulation of new rational therapeutic strategies for NSCLC and mesotheliomas. In the Program, we have 5 research projects and 3 Cores to address 3 central issues: therapeutic resistance, prognosis and new therapeutic targets and strategies.

PROGRESS REPORT (BODY):

Project 1: Therapeutic target-focused (TTF) profiling for the identification of molecular targets and pathways that contribute to drug sensitivity or resistance *in vitro* and the development of rational treatment strategies for NSCLC.

(Leader: Dr. John Heymach; Co-Leader: Dr. John Minna)

Hypotheses:

We hypothesize that a broad, systematic molecular profiling of NSCLC cell lines, using both TTF and global approaches, will lead to the following results:

1. The identification of new potential therapeutic targets for NSCLC
2. The development of predictive markers for *in vitro* sensitivity to targeted agents, which will form the starting point for the development of a predictive model of *in vivo* sensitivity using clinical specimens as described in Aim 3.
3. Insights into the molecular mechanism underlying therapeutic resistance and into the relationship of resistance mechanisms to factors innately affecting tumor growth rate and prognosis
4. Identification of readily translatable therapeutic strategies to combat these resistance mechanisms.

Specific Aims:

In this project, we will develop and validate a novel therapeutic target-focused (TTF) profiling platform at M.D. Anderson Cancer Center. The platform will provide a high throughput, quantitative, scalable, and highly sensitive set of assays to assess activation of key signaling pathways (e.g., PI3K/AKT, STAT, RAS-RAF-ERK) as well as other potential therapeutic targets such as receptor tyrosine kinases (RTKs). It will be coupled with global profiling of gene expression using Affymetrix 2.0 array. These molecular profiles will then be coupled with information from a broad drug and therapeutic target siRNA (DATS) screen to develop markers for predicting drug sensitivity *in vitro* based on molecular profiles, elucidate the molecular determinants of sensitivity or resistance to a given therapeutic agent, and identify potential

therapeutic targets for tumor cells resistant to a given agent. This project lays the foundation for Project 3, where the same TTF and global profiling approaches will be used to characterize clinical tumor specimens and investigate molecular markers identified in this project, for Project 4, in which the profiles and therapeutic targets for mesothelioma will be explored, and for Project 2, in which the profiles will be correlated with patient prognosis and metastatic patterns. The specific aims of this project are as follows:

Specific Aim 1: To develop a TTF profile for assessing critical signaling pathways and potential therapeutic targets, and to apply TTF and gene expression profiling to NSCLC and mesothelioma cell lines.

- 1.1. Development and technical validation of a TTF profile using reverse phase lysate arrays (RPPA) and multiplexed bead array technology.
- 1.2. Application of TTF profiling to a cell line panel representing malignant (NSCLC and mesothelioma) and non-malignant (endothelial and stromal cells, normal bronchial epithelium) cell types.
- 1.3. Gene expression profiling of the cell line panel using Affymetrix microarrays.
- 1.4. Correlation of TTF and gene expression profiles from the cell line panel to determine gene expression signatures that correlate with activation of individual proteins (e.g., EGFR activation) and critical signaling pathways (e.g., RAS pathway activation).

Specific Aim 2: To determine the sensitivity of the cell line panel to the selected drug and therapeutic target siRNA (DATS) screen.

- 2.1. Screening of the cell line panel for sensitivity to a panel of 20-25 targeted agents and standard chemotherapy agents.
- 2.2. Screening of the cell line panel using siRNA representing potential therapeutic targets, including molecules targeted by specific agents in Aim 2.1 (e.g., EGFR, IGFR-1, etc.) and potential therapeutic targets for which drugs are not currently available (e.g., RTKs for which drugs are currently in development).
- 2.3. Comparison of *in vitro* and *in vivo* profiles (TTF and global) and drug sensitivity in selected NSCLC cell lines and xenografts grown from the same lines.

Specific Aim 3: Development of markers for predicting drug and targeted siRNA sensitivity *in vitro* based on TTF and molecular profiles, and identification of candidate therapeutic targets in chemotherapy-resistant lines.

Summary of Research Findings

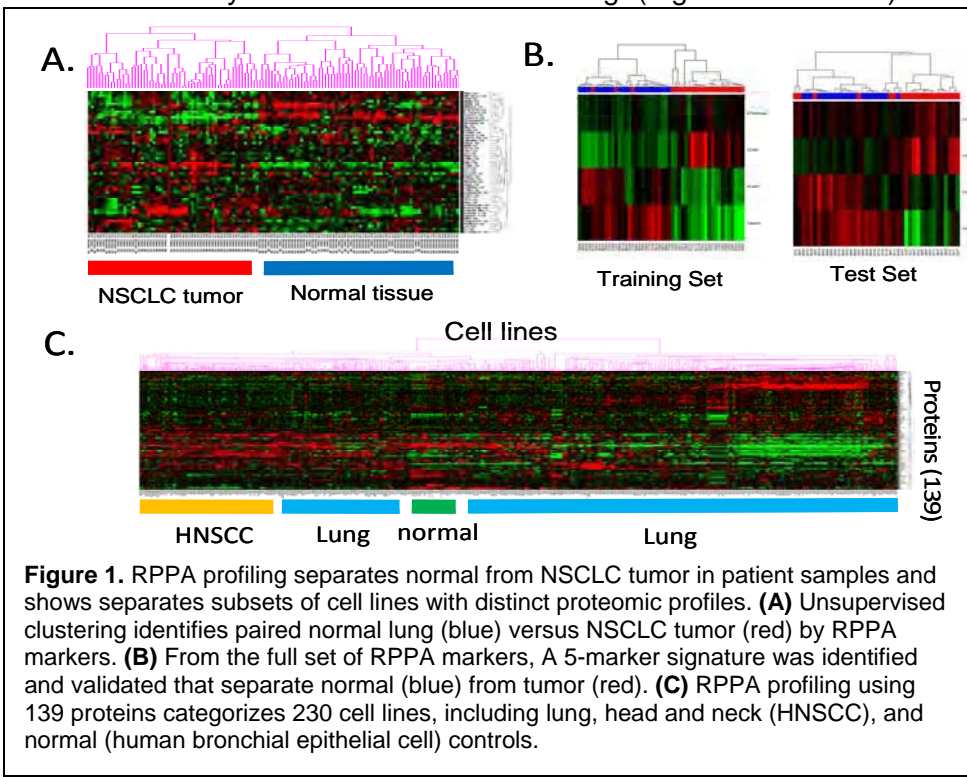
In March 2009, Dr. Li Mao (former Co-Leader) left the institution to accept a position at the University of Maryland at Baltimore; therefore, Dr. Heymach has assumed responsibility for completion of Dr. Mao's proposed studies.

Over the past year, we have expanded our set of NSCLC cell lines and have completed gene expression and protein profiling on all of these cell lines. The mRNA expression data from each of 50 NSCLC lines correlated with various drug response phenotypes and we identified signatures predictive of response. Likewise, proteomic profiles correlated with *in vitro* drug response data for a variety of drugs. We are in the process of validating these findings in xenografts and in clinical samples from patients treated with these drugs.

Database of preclinical molecular profiles including mRNA gene expression and proteomic profiles of NSCLC cell lines, tumor specimens, and xenografts; mRNA profiling of NSCLC cell lines and tumors. We have already performed genome-wide mRNA expression profiling using Affymetrix HGU133A, B, or Plus2 or Illumina WG6-v2 gene chips for more than 50 NSCLC and 30 SCLC lung cancer lines, 5 immortalized human bronchial epithelial cell strains (HBECS), and more than 40 NSCLC xenografts. This activity will be extended to include the full set of ~70 NSCLC lines in the bank. We will also assess the molecular profiles of 40 heterotransplants for validation of predictive signatures. It is worth noting that we found few differences in the gene expression profiles between NSCLC cell lines grown *in vitro* or *in vivo* (either subcutaneously or orthotopically in the lung); in an unsupervised clustering analysis, each tumor line grouped with itself (tissue culture, subcutaneous, or orthotopic xenograft) rather than other tumor lines, illustrating that a cell line can be linked to an *in vivo* profile.

Proteomic profiling of NSCLC cell lines and tumors. We have already conducted an RPPA analysis from a set of NSCLC tumors (Figure 1). Using a panel of 59 proteomic markers, unsupervised clustering sorted primary lung cancer from normal lung tissue specimens. A five-marker signature was able to identify tumor versus normal lung (Figure 1A and B) and

squamous versus adenocarcinoma histology. We also assessed a panel of 75 NSCLC cell lines grown under three media conditions and analyzed for ~150 proteins and phosphoproteins. RPPA profiling was able to separate distinct subsets of cell lines, normal lung tissue, and lung and HNSCC by clustering analysis. Interestingly, a group of lung cell lines was identified that was characteristically similar to the HNSCC (Figure 1C). This



panel of cell lines was also correlated with *in vitro* drug response, which identified predictive signatures of response (Figure 3). In the next grant period, the proteomic profiles will be extended to include those of the heterotransplant models, including post-treatment samples.

Database of molecular profiles from clinical NSCLC specimens, including tumors from the BATTLE-1 trial. To validate the signatures derived from the cell line panel, we will leverage the currently available molecular profiles, and additional ones that will be available over the next 6 months, from the BATTLE-1 clinical trial as well as the more than 100 NSCLC tumors profiled from our tumor archives. We currently have global gene expression profiling data in tumor specimens from 70 patients, and it is anticipated that data from at least 70 more will become

available by late 2009. Among these tumors, *EGFR* mutations were observed in 13 patients, and *KRAS* mutations were detected in 11 patients.

Baseline gene expression drug response signatures.

The mRNA profiles for 50 NSCLC lines were correlated with the various drug response phenotypes to derive signatures predictive of response to various drugs including erlotinib and the MEK inhibitor AZD6244 (Figure 2). As shown in the figure, the drugs also clustered by their general mechanism of action (e.g., EGFR inhibitors gefitinib, erlotinib, and cetuximab together), with AZD6244 having a distinct profile.

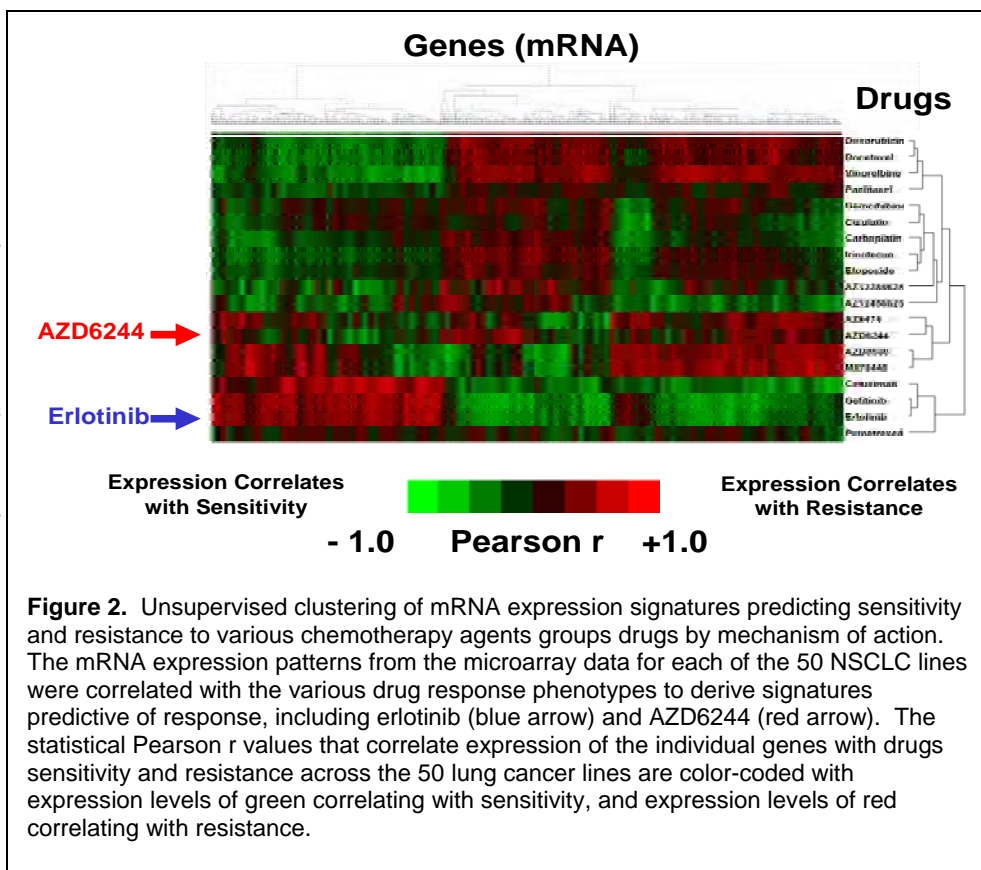


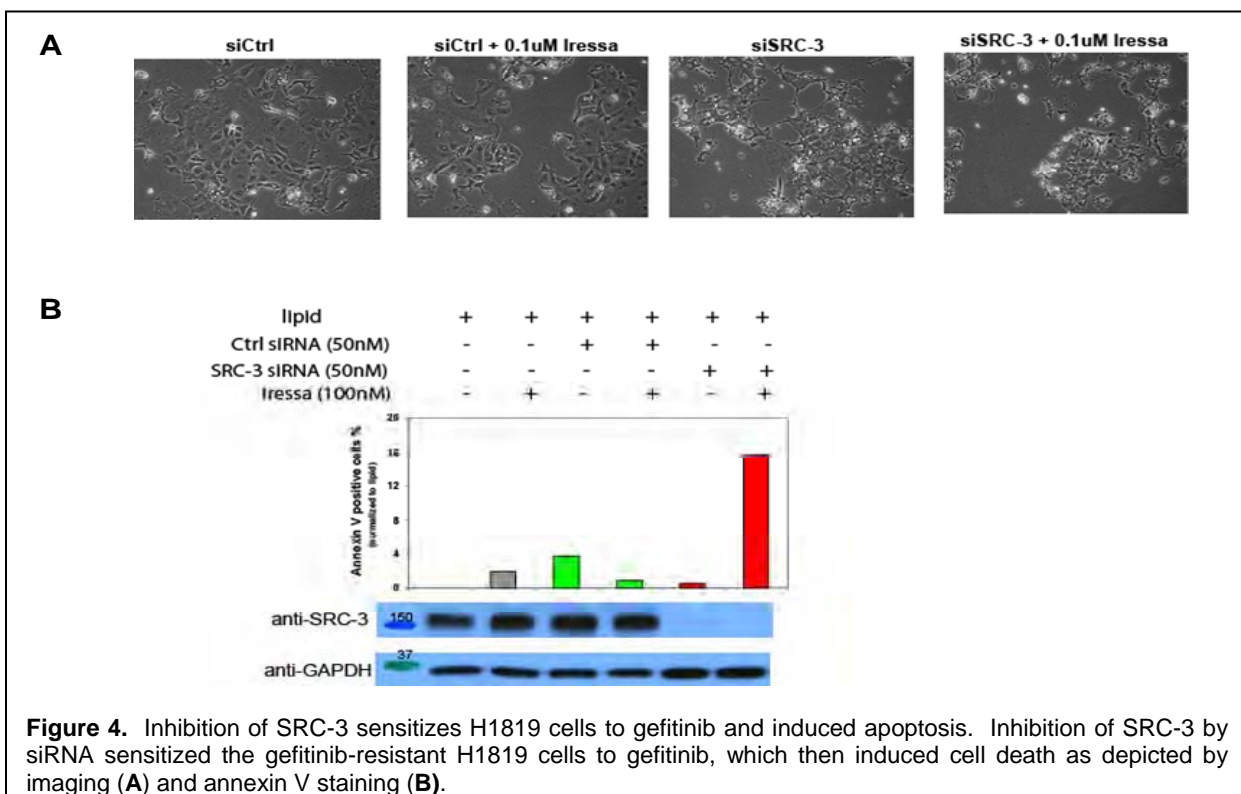
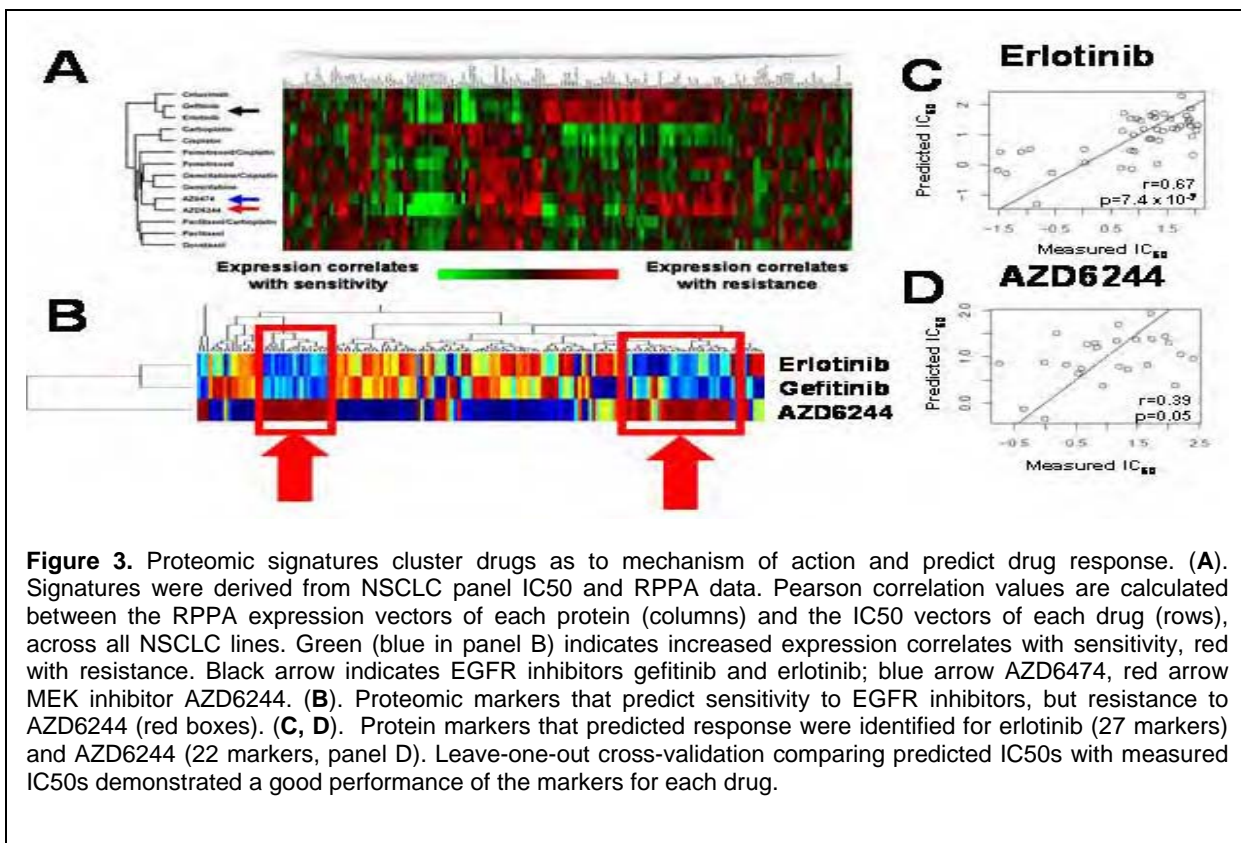
Figure 2. Unsupervised clustering of mRNA expression signatures predicting sensitivity and resistance to various chemotherapy agents groups drugs by mechanism of action. The mRNA expression patterns from the microarray data for each of the 50 NSCLC lines were correlated with the various drug response phenotypes to derive signatures predictive of response, including erlotinib (blue arrow) and AZD6244 (red arrow). The statistical Pearson *r* values that correlate expression of the individual genes with drugs sensitivity and resistance across the 50 lung cancer lines are color-coded with expression levels of green correlating with sensitivity, and expression levels of red correlating with resistance.

Proteomic drug response signatures.

We correlated the proteomic profiles with *in vitro* drug response data for a variety of drugs (Figure 3). Sixty cell lines were tested for sensitivity to the EGFR inhibitor erlotinib, and 30 to AZD6244. The cell lines were then classified into "sensitive," "intermediate sensitivity," and "resistant" classes based on IC₅₀ values, and were correlated with baseline expression of ~150 proteins measured by RPPA. Proteomic signatures of *in vitro* response to EGFR inhibition by erlotinib or gefitinib, or to MEK inhibition using AZD6244, were derived and retested, showing a significant correlation with drug response. For erlotinib, markers of sensitivity included EGFR itself, HER-2, p16, pSTAT3, and ERK1, several of which had been previously identified; markers associated with resistance included IGF-1R, FOXO3, and EMT marker N-cadherin. The MEK inhibitor AZD6244 had a distinct profile, with pSTAT3 and pSRC associated with sensitivity, and p16, p85 subunit of PI3K, MEK2, and phosphoAMPK associated with resistance. These data illustrate that this approach can be used to derive predictive proteomic signatures.

High SRC-3 expression correlates with EGFR-TKI resistance.

The Steroid Receptor Co-activator 3 (SRC-3) overexpression was correlated with resistance to the EGFR tyrosine kinase inhibitors cetuximab, gefitinib, and erlotinib by proteomic profiling of NSCLC cell lines. Subsequent downregulation of SRC-3 by siRNA in a gefitinib-resistant NSCLC cell line (H1819) restored sensitivity to gefitinib, which then induced cell death (Figure 4).



Key Research Accomplishments

- Completed protein profiling and gene expression profiling for 50 NSCLC cell lines.
- Derived baseline gene expression signatures predictive of response by correlating mRNA expression with drug response.
- Derived proteomic drug response signatures by correlating proteomic profiles with drug response data for a variety of drugs.
- Using baseline proteomic profiles, markers of radiation sensitivity and resistance were identified in lung cancer cell lines (Yordy et al., ASTRO 2008; Yordy et al., ASCO 2008).
- Identified factors associated with age and sex differences in NSCLC (Herynk et al., Proceeding of the Flight Attendants Medical Research Institute, 2009; Herynk et al., Proceedings of the International Association for the Study of Lung Cancer, 2009).
- Identified SRC-3 as a potential biomarker of response to the EGFR inhibitor.

Conclusions

RPPA proteomic profiling and gene expression profiling for a large number of cell lines was performed and has provided the basis for identifying intracellular signaling pathways and proteins associated with sensitivity and resistance to chemotherapies and targeted agents in NSCLC cell lines and tumor samples. These profiles will allow multiple biomarker analyses. One of the identified markers, SRC-3, was found to be correlated with resistance to EGFR inhibitors. Inhibition of SRC-3 in a gefitinib-resistant cell line was able to reverse resistance to the inhibitor. These results show that the model is successful at identifying relevant biological targets that, when inhibited, are able to reverse resistance to a targeted agent. Our findings will be further investigated by correlating RPPA of tumor samples with clinical outcomes in samples from the BATTLE-1 trial and other clinical samples with the goal of developing predictive markers that can guide treatment selection and identify new targets in NSCLC.

Project 2: Tumor molecular profiles in patients with operable non-small cell lung cancer (NSCLC): impact on stage, prognosis, and relapse pattern.

(Leaders: Drs. David Stewart, Jack Roth; Co-Leaders: Drs. Roy Herbst, Edward Kim, Katherine Pisters, Stephen Swisher)

Hypotheses:

We hypothesize that:

1. In tumors from patients with NSCLC, patterns of co-expression of molecules that modulate cell proliferation, survival, angiogenesis, invasion, metastasis and apoptosis will substantially influence tumor stage and size at the time of diagnosis, and will largely define patient prognosis.
2. Impact of adjuvant and neoadjuvant therapies on disease-free, progression-free, and overall survival will vary across prognostically distinct groups.
3. Specific molecular signatures in primary tumors will predict both metastatic patterns at relapse and molecular profiles of recurrent tumors, and this could help guide adjuvant strategies and therapeutic strategies at relapse.

Specific Aims:

Aim 1: To define characteristic TTF/gene expression profiles of prognostically distinct subpopulations of patients with resectable NSCLC, and to assess the extent to which these molecular profiles correlate with tumor stage and/or size.

The main goal of this aim is to use 150 archival NSCLC tumor samples from our tissue bank (with corresponding clinical data) and to prospectively collect tumor samples, blood samples, and clinical data from 300 additional patients undergoing surgical resection of NSCLC. The tissue and blood samples will be used by Project 3 and the Pathology Core to generate comprehensive TTF/gene expression molecular profiles using methods developed in Project 1. We will construct Kaplan-Meier estimated survival curves for disease-free survival, progression-free-survival, and overall survival, and will use Cox proportional hazards models and recursive partitioning methods to identify important biomarkers and prognostically distinct subpopulations. We will also correlate TTF/gene expression molecular profiles with initial tumor size and stage. In addition, we will explore the feasibility of using nonlinear regression analyses of semilog plots of % disease-free survival, % progression-free survival, and % overall survival vs time to facilitate identification of prognostically distinct subpopulations with characteristic TTF/gene expression molecular profiles.

Aim 2: To assess the impact of adjuvant and neoadjuvant chemotherapy on disease-free survival, progression-free survival, and overall survival in prognostically distinct subgroups, and to provide tumor, blood and clinical data to Project 3 for an assessment of factors contributing to resistance to chemotherapy and to Project 5 for assessment of profiling of EGFR and related molecules by new quantum dot technologies.

Of the 450 patients included in the project, we will assess 100 new prospectively recruited patients who will receive neoadjuvant therapy, 100 patients who will receive postoperative adjuvant therapy (including approximately 20 tumor bank patients and 80 new patients), and 250 patients who did not receive adjuvant or neoadjuvant therapy (including approximately 130 tumor bank patients and 120 new patients). We will collect patient clinical data on all 450 patients and will collect blood samples on the 300 new, prospectively recruited patients. Tumor and blood samples and clinical data will be provided to Project 3 for studies of therapeutic resistance and to Project 5 for assessment of profiling of epidermal growth factor receptor (EGFR) and related molecules by new quantum dot technologies, while in Project 2 we will assess impact of adjuvant and neoadjuvant therapy on outcome in each prognostic group.

Aim 3: To correlate TTF/gene expression molecular profiles in the primary tumor with metastatic patterns and with tumor molecular profiles at relapse.

For patients who relapse, we will define metastatic sites at relapse, obtain tumor tissues from selected patients who undergo biopsies to confirm relapse, and define TTF/gene expression molecular profiles in the patients' original primary tumor specimens that predict sites of later relapse (and in particular that predict relapse in brain). We will also assess whether tumor at relapse is enriched for particular molecular characteristics that may promote metastasis when compared to the primary tumor, and will assess the extent to which TTF/gene expression molecular profile at diagnosis may help guide choice of therapies at relapse.

Summary of Research Findings

As presented in further detail in Project 3 and the Pathology Core, we have identified approximately 736 archival tumor samples from our Tissue Bank that match eligibility criteria for inclusion in this trial. We are now in the process of assessing in detail the quality of RNA, DNA, and protein that is available from these specimens prior to making a final selection of the subset of 150 that will be used for full analysis under PROSPECT. In addition, tissue microarrays have already been constructed on 327 of these 736 samples and we have completed staining each of these for the immunohistochemical (IHC) assessment of more than 100 relevant biomarkers. Initial biostatistical assessments on a subset of markers (cytoplasmic, membrane and/or nuclear staining for CA IX, COX2, CTR1, DcR2, DNMT1, ERCC1, HIF-1 α , Ki67, p14ARF, p16 INK4a, p21 WAF1/CIP1, p53, RB, pRB, SHARP2, SURVIVIN, TGF β , VEGF, GLUT4, RhoA, Folate Receptor alpha, and RFC1) revealed in univariate analysis that cytoplasmic staining for HIF-1 α and nuclear staining for pRB correlated significantly with overall survival. Factors correlating with time to relapse include membrane expression of CA IX and p16. Factors correlating with relapse with borderline significance ($p < 0.10$) included ERCC1, RB, and TGF β .

Several of the markers correlated significantly with the stage and with the lung cancer type. Higher N stage was associated with significantly decreased expression of cytoplasmic and nuclear CTR1, cytoplasmic DNMT1, and cytoplasmic RB. Compared to squamous cell carcinomas, adenocarcinomas had significantly higher expression of TGF β , CTR1, cytoplasmic DNMT1, cytoplasmic ERCC1, VEGF, p16, p14AR, FOLR1, and RhoA and significantly lower expression of SHARP, CA IX, nuclear DNMT1, nuclear ERCC1, nuclear RB, SURVIVIN, p21WAF and p53. High expression of FOLR1 in adenocarcinomas is of interest since it might explain the greater efficacy of the multitargeted, antifolate agent pemetrexed in adenocarcinomas than in squamous cell carcinomas.

Collection of prospective tumor samples is also going well. Of the 300 blood and tissue samples proposed over the course of the project, we have collected 291 tissue samples between August 2007 and May 2009. Blood samples have been collected from 283 patients; both blood and tissue samples have been collected in 231 patients. We had proposed to collect tissue samples from 100 patients who received neoadjuvant chemotherapy, and to date we have collected 74. Tissues from an additional 100 neoadjuvant patients have been accessed from our preexisting tissue bank specimens. Hence, we are ahead of schedule on specimen procurement for the project.

In Project 3, expression profiles in tumors from patients in Project 2 who received neoadjuvant chemotherapy will be compared to those in patients who did not. Tumors surviving neoadjuvant chemotherapy will be regarded as a model of acquired resistance. In related work, we found that tumors exposed to chemotherapy or targeted therapies within the previous 3 months had decreased expression of the copper/platinum transporter CTR1¹, suggesting a mechanism by which exposure to a broad range of agents could secondarily lead to resistance to cisplatin and carboplatin.

In last year's report, we also outlined preliminary work that had been performed using exponential decay nonlinear regression analysis of patient survival plots, and conclusions that had been drawn. This previous work defined the process to be used for future correlations of the biomarker data with patient outcomes.

Key Research Accomplishments

- Collected tumor specimens on 291 lung cancer patients (including 74 who had received neoadjuvant chemotherapy).
- Collected blood samples on 283 lung cancer patients (including 64 who received neoadjuvant chemotherapy).
- Performed preliminary assessment of impact of 18 biomarkers on survival, and their correlation with stage and tumor type.

Conclusions

During this project period, we identified and are currently assessing the quality of RNA, DNA, and protein that is available from these tumor specimens prior to the full analysis under PROSPECT. Specimen collection continues at a brisk pace and will further our goal of predicting future sites of relapse by examining the molecular profiles associated with the patient tissues. Further analysis is needed to assess the extent to which TTF/gene expression molecular profile at diagnosis may help guide choice of therapies at relapse.

Project 3: Molecular Profiling of Non-Small Cell Lung Cancer Tissue Specimens and Serum and Plasma Samples: Correlation with Patient Response and Tumor Resistance to Chemotherapy.

(Leader: Dr. Ignacio Wistuba; Co-Leaders: Lin Ji and John Minna)

Hypothesis:

In Project 3, we hypothesize that systematic molecular profiling of surgically resected non-small cell lung cancer (NSCLC) tissue specimens using therapeutic target-focused (TTF) and mRNA approaches, along with serum phosphopeptide screening and plasma DNA analysis, will lead to the following results:

1. Validation in patients' tissue specimens of molecular signatures obtained from NSCLC cell lines that are associated with *in vitro* and *in vivo* (xenograft) resistance of NSCLC cell lines to chemotherapeutic and targeted agents.
2. Identification of molecular profiling signatures associated with NSCLC sensitivity or resistance to chemotherapeutic agents that can identify NSCLC patients most likely to respond to a given targeted therapeutic agent.
3. Development and validation of serum phosphopeptide profiles and plasma DNA markers associated with NSCLC patient response and tumor resistance to chemotherapeutic agents.

Objectives:

The greatest obstacle to creating effective treatments for lung cancer is the development of resistance to both chemotherapeutic and targeted agents. In this highly integrated and translational program project, we tackle one of the most clinically significant problems in lung cancer: the prediction of patient response to therapy, especially in the context of tumor resistance to current standard chemotherapies. The main objectives of this project are as follows:

- a) To profile surgically resected tumor tissue specimens obtained from NSCLC patients to validate molecular signatures found in the TTF and mRNA profiles developed in Project 1. These profiles will be compared with molecular signatures obtained from NSCLC cell lines

that are associated with *in vitro* and *in vivo* (xenograft) resistance to chemotherapeutic and targeted agents.

- b) By comparing NSCLC tumor specimens (collected in Project 2) from patients who have received preoperative chemotherapy and from those who have not, to validate TTF and mRNA signatures that are found in Project 1 to be associated with resistance to therapy and with the activation of resistance-associated molecular pathways or that are found in Project 1 to be potentially exploitable as new therapeutic targets.
- c) To identify serum and plasma biomarkers as surrogate markers to predict the response of NSCLC patients to neoadjuvant chemotherapy and to predict patient outcome.
- d) To provide tissue- and serum-based molecular profile signatures or markers to Project 2 that can predict the clinical outcome of NSCLC patients who had undergone surgical resection with curative intent, with or without neoadjuvant therapy.

This interdisciplinary research proposal for profiling cell lines, tumor tissue, and serum samples from NSCLC patients requires extensive histopathological, molecular, and immunohistochemical studies, which will be coordinated and/or performed by the Pathology Core (see Pathology Core's report).

Specific Aims:

Aim 1: To validate, in retrospectively collected NSCLC tumor tissue specimens, the TTF and mRNA profiles predictive of the *in vitro* and *in vivo* (xenograft) resistance of NSCLC cell lines to chemotherapeutic and targeted agents.

Summary of proposal: We will select 150 surgically-resected NSCLC tumor specimens from The University of Texas Lung SPORE (UT-SPORE) Tissue Bank for TTF and mRNA profiling. Using those 150 frozen archival NSCLC tumor tissues, we will perform reverse-phase protein array (RPPA), multiplex bead-based protein analysis (MBA) and Affymetrix U133 Plus 2.0 array to validate the molecular signatures developed in Project 1. Then, we will compare the profile signatures obtained from the NSCLC tumor specimens with the signatures obtained from NSCLC cell lines in Project 1 that predict the *in vitro* and *in vivo* resistance to chemotherapeutic and targeted agents. Finally, using formalin-fixed and paraffin-embedded tissue specimens, we will validate the expression of proteins abnormally represented in the molecular profiling analyses of NSCLC tumor specimens by using tissue microarrays (TMAs) and semiquantitative immunohistochemical (IHC) methods.

Summary of Research Findings

In March 2009, Dr. Li Mao (former Co-Leader) left the institution to accept a position at the University of Maryland at Baltimore. Dr. Wistuba has accepted the task of taking over Dr. Mao's responsibilities on this project and will continue to provide leadership in this capacity.

During the second year of this grant, we have achieved the following: 1) We finalized the selection and processing of all surgically resected NSCLC tissue specimens needed for molecular profiling as proposed in Aim 1; 2) We refined the profiling plan of NSCLC tissue specimens, and we expanded our profiling plans to include miRNA and DNA; 3) We explored alternative approaches for the molecular profiling of tissue specimens, such as formalin-fixed and paraffin-embedded (FFPE) samples; 4) In collaboration with Project 4 (Dr. A. Tsao), we performed a comprehensive molecular profiling of malignant pleural mesothelioma (MPM) tissue specimens and cell lines. The detailed progress update is as follows:

1. Selection and processing of all surgically resected NSCLC tissue specimens needed for molecular profiling as proposed in Aim 1. To develop molecular signatures (from mRNA and miRNA profiles, and reverse phase protein array, RPPA) in NSCLC specimens, we extracted RNA and DNA from frozen tumor and normal tissue from over 600 NSCLCs with annotated clinicopathologic information, including outcomes (recurrence-free and overall survival). We are currently in the process of selecting 250 stages I to IIIA surgically resected NSCLCs for the profiling experiments. Of these, 125 cases will have received adjuvant chemotherapy and 125 cases will not.

a) Detailed histopathological analysis of NSCLC frozen tissue specimens. In collaboration with the Pathology Core, detailed histopathological analysis was performed using a technique developed in-house called the “shaving method” (please see Pathology Core report for additional detail). This technique uses 5- μ m-thick haematoxylin-eosin (H&E)-stained histology sections obtained at 4 levels of the tissue specimen that are alternated by two sets of thirty 20- μ m thick sections obtained for DNA, RNA, and protein extractions. For detailed histopathological analysis, each tumor and normal H&E-stained section was examined by an experienced lung cancer pathologist to assess the percentage of tumor vs. adjacent normal tissues and, most importantly, the percentage of malignant cells vs. tumor non-malignant stromal (inflammatory, vascular and fibroblasts) cells and normal cells present in the adjacent normal tissue. In addition, tumor cell viability has been addressed by examining the presence of necrosis and hemorrhage. Detailed histopathological analysis was performed on 661 NSCLC tumors. These 661 cases represent 90% of 736 NSCLC cases we selected from the UT-Lung SPORE Tissue Bank. Paired normal and tumor samples were found in 634 (96%) of cases. Among these 661 tumor cases, 353 contain >70% tumor content and >50% tumor cell content. In addition, we are in the process of digitalization of all slides for future comparisons of these detailed histopathological analyses.

b) DNA and RNA extraction from NSCLC frozen tissue specimens. DNA was extracted from 1,294 samples, including 773 tumor and 613 normal samples; paired normal and tumor samples were found in 541 cases (88%). The average DNA concentration among these samples was 267 ng/ μ l (0.9 -5.631 ng/ μ l) and total micrograms obtain from extraction was 102.8 μ g (0.1-3549 μ g). RNA was extracted from 1,302 samples, which include 550 tumors with 76 duplicate samples. These represent 75% of 736 NSCLCs selected from our UT-Lung SPORE Tissue Bank. Paired normal and tumor samples were found in 537 cases (98%). In these samples, the average RNA concentration was 776 ng/ μ l (3.4-4758 ng/ μ l) and total micrograms obtained from extraction was 158 (0.3 – 3214 μ g). An overview of the characteristics of the DNA and RNA extracted is shown in Table 1. The extraction of proteins for RPPA is pending, and will be completed during the third year of this grant; however, the appropriate laboratory protocols for this work have been developed.

As we mentioned in our previous report, a large variability in DNA and RNA quantities as expressed in micrograms is observed in the NSCLC tissue specimens. The quality of RNA obtained for our mRNA (Affymetrix) profiling analysis seems reasonable and meets our expectations. The average RNA Integrity Number (RIN; Agilent Bioanalyzer) for our samples is 5.8 (Affymetrix 340 NSCLC samples have recommended RIN>5.0), and thus, these samples are eligible for mRNA Affymetrix profiling studies.

Table 1. Summary of the characteristics of the DNA and RNA extracted from 387 NSCLC cases.

	DNA				RNA			
	Tumor		Normal		Tumor		Normal	
	Average	SD	Average	SD	Average	SD	Average	SD
Quantity (μg)	102.8	408.23	38.5	113.7	57.8	104.2	80.3	151.9
Concentration ($\text{ng}/\mu\text{l}$)	267.29	879.68	227.5	638.4	688.9	1182.4	539.6	616.8
RNA Integrity	--	--	--	--	5.8	3.2	5.5	2.6

c) Selection of cases for RNA and DNA profiling. More than 300 cases have been selected for profiling with the following criteria: a) frozen tumor tissue with $\geq 70\%$ tumor content per histology quality control; b) frozen tumor tissue with $\geq 30\%$ of malignant cell content; c) mRNA RIN ≥ 4 ; and, d) available clinical data (adjuvant therapy status).

2. Profiling plan of NSCLC tissue specimens. We have defined the molecular profiling analysis to be performed on the 250 NSCLCs selected as follows: a) miRNA profiling using the Agilent human miRNA microarray Rel12.0 (Agilent Technologies, Inc., Santa Clara, California, USA); b) mRNA Affymetrix profiling using the U133 Plus 2.0 chips array; c) DNA array comparative genomic hybridization (aCGH) using the 244K Agilent array. We are currently in the process of aliquotting the RNA and DNA samples for the various profiling platforms. We plan to complete all these molecular profiling during the third year of the grant.

3. Alternative approaches for the molecular profiling of tissue specimens. Formalin-fixed paraffin-embedded (FFPE) samples are widely available, and provide valuable sources for study molecular basis of diseases files of tumors and the association between molecular changes and clinical outcomes. Due to the degradation and chemical alteration that occurs when RNAs are extracted from FFPE samples, the use of microarrays for gene expression analysis in FFPE samples has been largely hampered. New technology and methodologies have been developed to extract RNA, and new array platforms have been designed to measure gene expression in FFPE samples. In this study, we have shown that microarray analysis of FFPE samples, after strict quality control and careful data processing, can be used to build a robust prognosis signature for NSCLC. We analyzed 75 FFPE tumor samples from NSCLCs. RNA was isolated from each sample using Response Genetics kit (Response Genetics). The Affymetrix 133 2+ microarray platform was used to obtain gene expression profiles.

Major findings. A set of 1,400 genes passed the FFPE sample microarray data quality control criteria, and we refer to this gene set as the “robust genes set” (RGS). On the basis of the expression of these robust genes, patients could be divided into two groups; notably, the patient samples in Group 1 were primarily squamous lung cancer (82%), whereas the patient samples in Group 2 were primarily adenocarcinoma lung cancer (93%; $P < 0.0001$).

To investigate whether the two groups defined by RGS expression profiles have different clinical prognoses, we drew Kaplan-Meier curves for both overall survival (OS) time and recurrence-free survival (RFS) time for two groups (Figure 1). Of interest, Group 1 showed significantly shorter OS time (median survival time = 3 years) compared to Group 2 (median survival time was not reached; $P = 0.017$ from log-rank test). Group 1 also had shorter RFS time (median PFS = 2.4 year) compared to Group 2 (median RFS = 4.2 year; $P = 0.09$ from log-rank test). The association between RGS groups and death or disease progression was independent of stage

(HR=4.38, $P=0.012$ for OS; HR=2.15, $P=0.059$ for RFS). After showing the strong associations between the groups defined by RGS expression profiles and the clinical outcomes, we explored whether the RGS expression profile can be used to predict the lung cancer patients' survival.

First, we randomly divided 55 patients into training (25 samples) and testing (30 samples) sets. We built a prediction model using 1,400 RGS values through a supervised principle component analysis approach

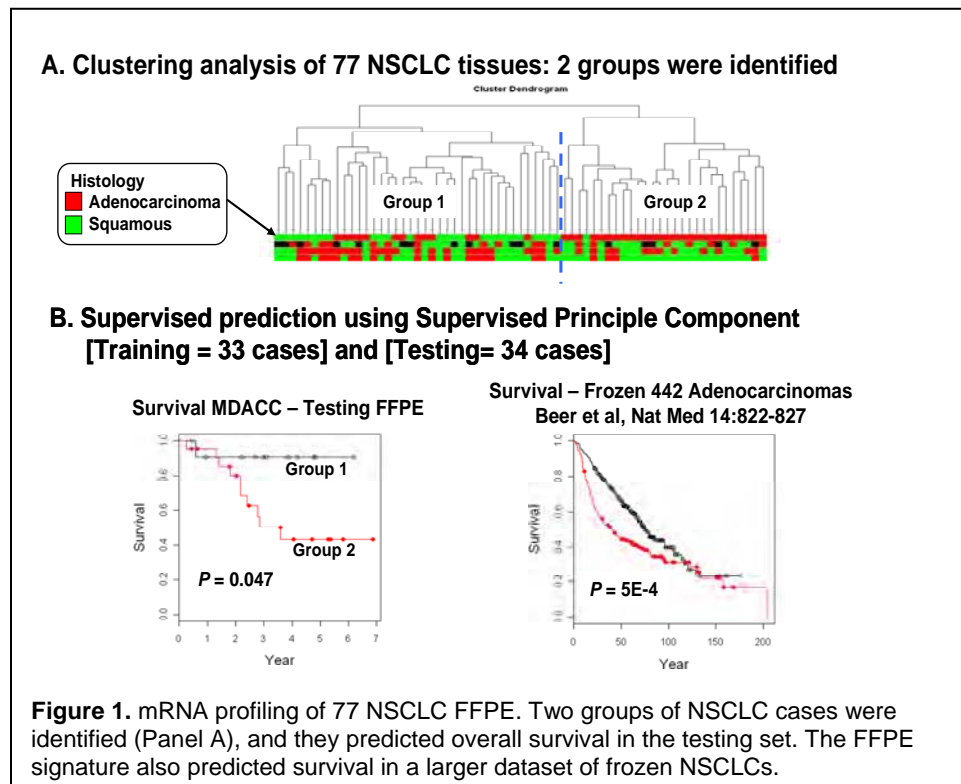


Figure 1. mRNA profiling of 77 NSCLC FFPE. Two groups of NSCLC cases were identified (Panel A), and they predicted overall survival in the testing set. The FFPE signature also predicted survival in a larger dataset of frozen NSCLCs.

using the training data, and then validated this prediction model using the testing data. We found that the predicted low-risk group has significant longer survival time than the predicted high-risk group (median OS=2.78 years for high-risk group, and median OS for low-risk group was not reached, $P=0.013$). We then demonstrated that our RGS can be used to train and test the prediction models in frozen

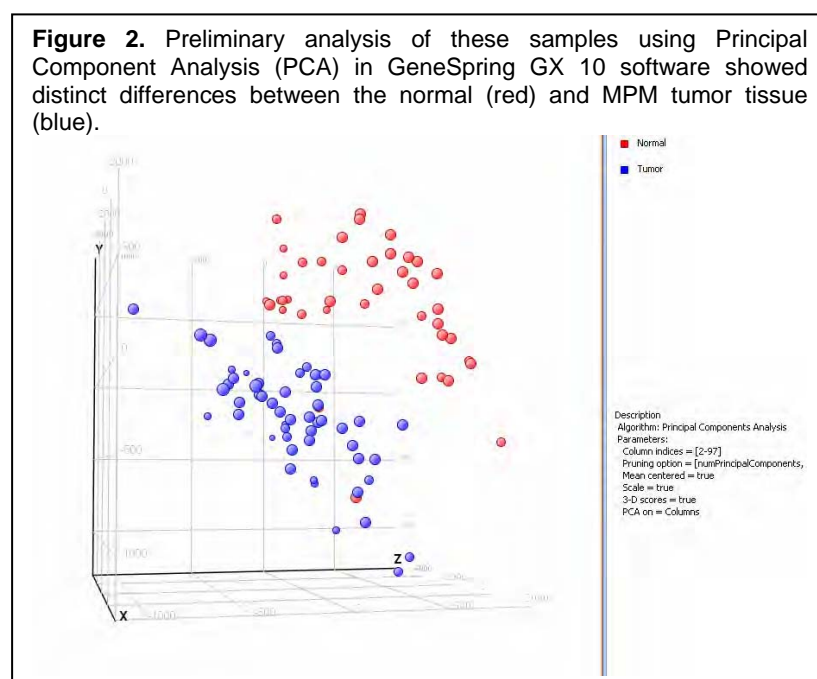
samples using one of the largest independent lung cancer microarray data sets, the recently published NCI Director's Consortium for the study of lung cancer that included 442 resected NSCLCs. Thus, using the FFPE signature, we predicted that the low-risk group had a significantly longer survival time than the predicted high-risk group (median OS=2 years for high-risk group, and median OS for low-risk group = 4.5 years, $P=0.00013$) (Figure 1). A manuscript is currently in preparation with these data.

4. Comprehensive molecular profiling of malignant pleural mesothelioma (MPM) tissue and cell lines specimens. In collaboration with Project 4 (Dr. A. Tsao), we performed a comprehensive profiling analysis of 53 MPM tissue specimens and 5 MPM cell lines.

a) MPM RNA and DNA Extraction. We extracted total RNA from 89 MPM tissue samples, representing 53 cases, using the TRI Reagent (Applied Biosystems, Ambion, USA) according to the manufacturer's instructions. These 53 cases include 36 cases with paired-normal controls (adjacent and non-tumor tissue) and comprise epitheloid (n=38), biphasic (n=8), and sarcomatoid (n=7) histotypic distribution of cases. The tumor tissue was "shaved" (see previous description of method) prior to extraction, which, based on our preliminary studies, allows higher yield and quality of RNA to be obtained as well as facilitates subsequent analysis of the tissue. The histological analysis was carried out by a pathologist and showed that about 68% of the samples had greater than 70% tumor content. The RNA was quantified using the Nanodrop-1000 spectrophotometer (Nanodrop Technologies, Wilmington, Delaware, USA) and the quality was determined on the RNA Nano-chip using the Agilent 2100 Bioanalyzer. The

spectrophotometric analysis showed that more than 35% of the samples had a 260/280 nm absorbance ratio of equal to or greater than 2.0 with an average yield of 435 ng/ μ l. The Nano-chip determined that 67% of the samples had RIN values \geq 5.

b) MPM Messenger RNA profiling. 250 nanograms of total RNA from each of the 89 samples were sent to the M. D. Anderson Cancer Center MicroArray Core Facility for analysis where they were labeled via the double *in-vitro* transcription (IVT) protocol and hybridized onto Affymetrix U133 Plus 2.0 chips. These chips determine the relative expression level of more than 47,000 transcripts representing most of the human genes. The Core facility scanned the chips and has delivered the data to Dr. Kevin Coombes (Bioinformatics Core) for subsequent analysis. Preliminary analysis of these samples using Principal Component Analysis (PCA) in GeneSpring GX 10 software (Agilent Technologies, Inc., Santa Clara, California, USA) showed distinct differences between the normal (red) and tumor tissue (blue) (Figure 2).



c) MPM MicroRNA profiling.

The same set of 89 samples that were profiled for mRNA was also profiled in Dr. Wistuba's lab for microRNA content using the Agilent human miRNA microarray. Human miRNA Microarray Rel12.0 arrays contain approximately 866 human and 89 human viral miRNAs, which represent the complete content sourced from the Sanger miRBase v 12.0. Slides were scanned on an Agilent microarray scanner (model G2565A) at 100% sensitivity and 5 micron settings at the U.T.M.D.A.C.C Genomics Core facility. Feature Extraction software version

10.5.1 was used for image analysis and quality assessment to obtain primary data, which was further analyzed for data reduction and cluster analysis using the GeneSpring GX version 10.

d) DNA profiling. DNA was isolated from tissue shavings using the DNazol Reagent (Molecular Research Center, Inc, Cincinnati, OH, USA). As with the RNA, spectrophotometric analysis was used to determine the quantity and purity of the samples, while quality was assessed on the DNA chip using the Agilent 2100 Bioanalyzer. The spectrophotometric analysis showed that more than 37% of the samples had a 260/280 nm absorbance ratio of equal to or greater than 1.8 with an average yield of 150 ng/ μ l. The DNA chip determined that 99% of the samples had molecular weight greater than 10 kilobases. Of the 53 cases, about 47 tumor cases will be analyzed for SNP and copy number variations using the Human IM-duo platform (Illumina, Inc., San Diego, CA, USA), which contains more than 1 million SNP's along with copy number variation content.

e) Protein Profiling. We are in the process of extracting proteins from these 89 samples for Reverse Phase Protein Array (RPPA) analysis using the protocol obtained from Dr. John

Heymach's lab (Project 1). The protein lysates will be printed with the help of Dr. Heymach's lab for the RPPA analysis.

f) MPM Cell line Profiling Update. We have acquired from various sources about 17 mesothelial and mesothelioma cell lines with a good distribution of different histotypes, including at least 4 epithelioid, 2 biphasic, and 2 sarcomatoid morphological types. Of these, six cell lines have already been profiled for messenger RNA and miRNA content. Other cell lines are awaiting their characterization as genuine mesothelioma cell lines. DNA from these cell lines has been sent to the MDACC Microarray Core facility for SNP and copy number analysis on the Affymetrix SNP 6.0 platform. Additionally, we have obtained protein lysates from these cell lines to print RPPAs in Dr. Heymach's laboratory (Project 1).

To explore the role of epigenetically mediated up-regulation of miRNAs in MPM, we performed pharmacological unmasking of miRNA expression in cell lines. miRNAs have emerged as key players in human carcinogenesis. Recently, studies have shown that some miRNAs can be epigenetically up-regulated by aberrant hypermethylation in human cancer. Five cell lines, including one normal mesothelial (Met5A) and five MPMs (epithelioid H2452, biphasic H211 and unclassified H28 and H2052) were treated *in vitro* with the demethylating agent 5-aza-cytidine (5-Aza; 1 μ M) and SAHA (2.5 μ M) for 96 hrs. After RNA extraction (Trizol), miRNA profiling was performed by Agilent human microRNA kit v2. A total of 299 (51%) miRNA were up-regulated (two-fold) after the treatment in a normal mesothelial Met5A cell line, but fewer miRNAs were upregulated in the malignant cell lines: 171 (29%) in H2452, 79 (13.5%) in H211, 55 (9.4%) in H28, and 56 (9.6%) in H2052. We detected 167 (55.9%) miRNAs that were exclusively up-regulated in Met5A, 56 (32.7%) in H2452, 21 (26.6%) in H 211, 16 (29.1%), in H28, and 18 (32.1%) in H2052. Among all unique miRNA, only 17 (let-7b, let-7c, let-7f-2, miR-302c, miR-328, miR-510, miR-125b-1, miR-16-1, miR-223, miR-302b, miR-383, miR-551b, miR-922, miR-148a, miR-18b, miR-302d, miR-326) have been previously associated with human carcinogenesis. Interestingly, one miRNA (miR-148a) has been associated with a microRNA tumor metastasis signature. The number of total and unique miRNA upregulated after 5-Aza and SAHA was lower in MPM cell lines compared with normal Met5A cell line. Up-regulation of unique miRNAs was found to be associated with cell lines obtained from some specific subtypes of MPM. The identification of metastasis-associated miR-148a suggests a potential biomarker for metastasis in this highly malignant neoplasm.

Aim 2: To develop TTF and mRNA signatures of NSCLC resistance to chemotherapy, and identify chemoresistance-associated targets/pathways as new therapeutic targets.

Summary of proposal: Whereas Aim 1 focuses on the identification in archived tumor specimens of TTF and mRNA molecular profiles detected in NSCLC cell lines, the main focus of Aim 2 is to determine whether the molecular signatures in the tumor specimens correlate with patient response to neoadjuvant chemotherapy. From the clinical trial in Project 2, we will use specimens from 100 NSCLC patients who received neoadjuvant therapy and had surgical resection with curative intent (cases) and from 200 NSCLC patients who had surgical resection but did not receive neoadjuvant therapy (controls) to perform RPPA, MBA, and Affymetrix U133 Plus 2.0 array analyses. Then, we will compare the TTF and mRNA profile signatures obtained from these NSCLC tumor specimens with signatures obtained in Project 1 to predict the *in vitro* and *in vivo* resistance of NSCLC cell lines to therapy. Those data will be provided to Project 2 for correlation with clinical characteristics, including prognosis and metastasis. Finally, using formalin-fixed and paraffin-embedded tissue specimens, we will validate the expression of proteins abnormally represented in the molecular profiling analyses in NSCLC tumor specimens from all patients enrolled in Project 2 by using TMAs and semiquantitative IHC methods.

Summary of Research Findings

During the second year of this program, in collaboration with the Pathology Core, we have mainly focused on the identification, characterization, and processing of tissue specimens from surgically resected NSCLC obtained from patients who have received neoadjuvant chemotherapy. From the 736 NSCLC cases selected in the first year, we have identified 147 (20%) patients who have received neoadjuvant chemotherapy. Our goal to obtain 100 NSCLC cases with neoadjuvant therapy has, therefore, been reached.

Selection of prospectively collected cases: Since the activation of the PROSPECT laboratory protocol on August 2007, the Pathology Core has collected fresh and FFPE tissue specimens from 79 cases that have received neoadjuvant chemotherapy. Our goal to obtain 100 prospectively collected NSCLC cases with neoadjuvant treated group was also reached this year.

Processing of the tissues and molecular profiling (mRNA and protein): These experiments will begin after specimen profiling in Aim 1 is completed. We expect to initiate these experiments by the end of the third year of the grant.

Additional tissue sets for profiling studies: As reported last year, Dr. Li Mao signed a collaborative agreement with the Intergroupe Francophone de Cancérologie Thoracique (IFCT) to obtain up to 250 frozen lung tumor tissues from patients enrolled in IFCT-0002 clinical trial (a open-labelled, multicentric, randomized phase III study), which was designed to define the best timing of neoadjuvant chemotherapies. These samples will be used to identify a gene expression signature of resistance to platinum-based chemotherapies. Samples of 170 of these cases were received in Dr. Mao's laboratory, and are now going through histology quality control process. As Dr. Mao has recently relocated to another institution, Dr. Wistuba has assumed responsibility for these analyses.

Pathological analysis of NSCLC response to neoadjuvant therapy. In collaboration with Dr. Wistuba, Drs. Abujiang Pataer and Stephen G. Swisher from the Departments of Thoracic and Cardiovascular Surgery at M.D. Anderson Cancer Center have initiated a study on the assessment of the pathological response to chemotherapy in NSCLC. Our main goal is to determine whether pathologic and radiological features can predict response after chemotherapy of lung cancer and identify the potential biomarkers that possible to assist in the selection of patients for specific therapies in the future. The identification of genes involved in chemo-resistance may also allow development of novel therapies to enhance the clinical efficacy of chemotherapy. We plan to accomplish the following three specific goals: (1) Evaluate surgically resected patients treated with neoadjuvant chemotherapy. (2) Determine whether pathologic or radiologic criteria of chemotherapy response are associated with long-term survival. (3) Determine the role of biomarkers with chemotherapy response.

Histological recognition of cases in which neoadjuvant therapy has been given and the description of the extent of the residual tumor will become increasingly important in prognostication and in evaluating postoperative therapeutic options. We identified 147 patients from 2001-2005 in which neoadjuvant therapy was received before surgical resection. The clinical and pathological information have been obtained in all cases. To refine histological parameters for tumor regression and describe patterns of tumor reaction to therapy, we collected 133 formalin-fixed and paraffin-embedded tissues specimens from the Thoracic Malignancy Tissue Bank and PROSPECT Pathology Core. In those specimens, 129 cases have frozen tissue. Histological patterns of treatment-induced tumor regression were analyzed

included viable tumor, necrosis, fibrosis, mixed inflammatory infiltrate, foamy macrophages, and giant cells. Figures 3A, B, C, and D show typical examples of the histopathology of tumors associated with no or extensive response to treatment. In most tumors, fibrosis was present; in some cases fibrosis was the predominant manifestation of treatment response (Figure 3C). In some response cases, the foamy macrophages were associated with multinucleated giant cells with cholesterol clefts (Figures 3C and D). We then determined the size reduction by radiological assessment in 100 cases. Figures 3E, F, G, and H show typical examples of the radiology of tumors associated with no or extensive response to treatment. In some tumors, the induction of radiological size was observed (Figures 3E and F). The 56% radiological size reduction was recorded in different cases (Figures 3G and H). We next will analyze the correlation of pathological or radiological features with patient outcomes. We will construct Kaplan-Meier estimated survival curves for disease-free survival, progression-free survival, and overall survival, and we will use Cox proportional hazards models in our study. We will determine the correlation between extent of visible cancer cells or fibrosis and radiological estimate of size reduction. We will identify chemo-resistant and chemo-sensitive groups based on radiological or pathological features for biomarker discovery.

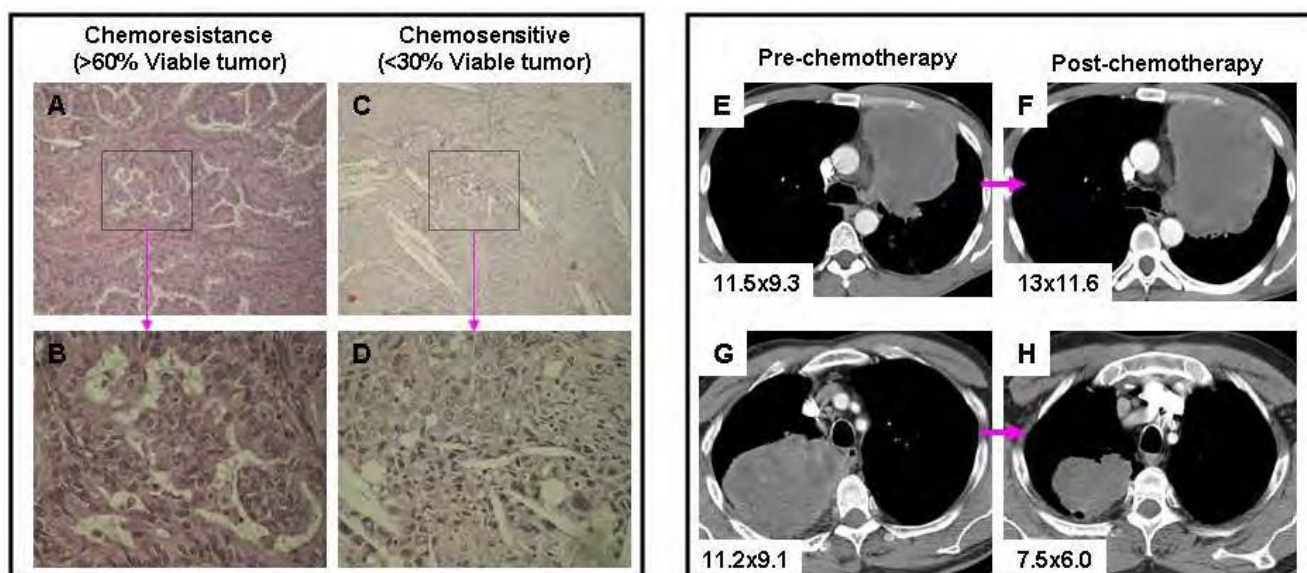
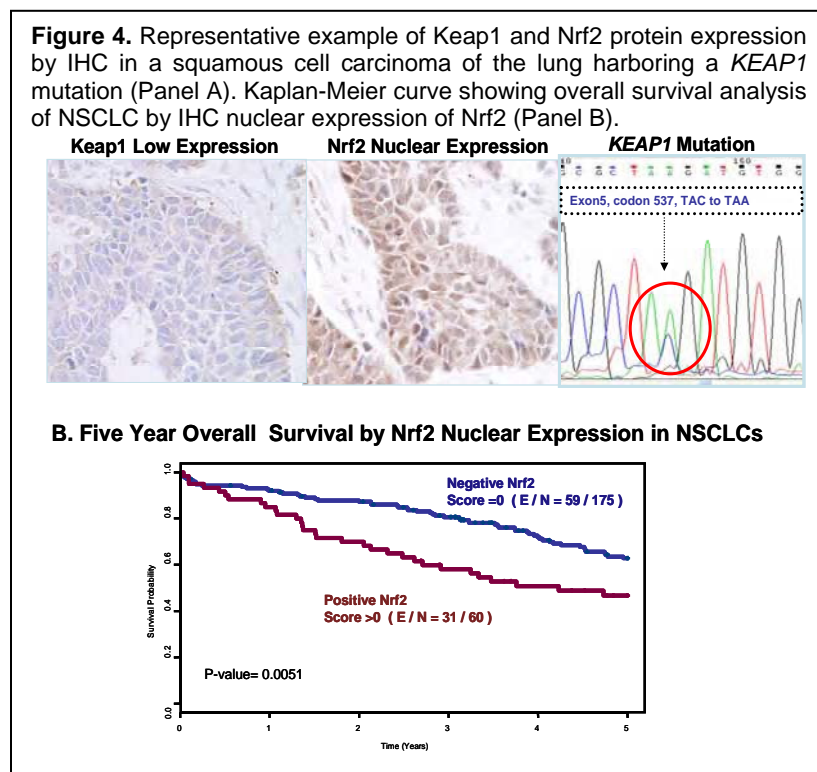


Figure 3. Typical examples of the histopathology and radiology of tumors associated with no response (A, B, E and F) or extensive response to treatment (C, D, G and H).

In addition, during the second year of the grant, we have developed 3 additional projects to investigate in NSCLC novel biomarkers related or potentially related to resistance to chemotherapy. These studies are the following: a) Expression of Keap1 and Nrf2 in NSCLC; b) Expression of cell membrane receptors in NSCLC; and c) Expression of cancer stem cell markers in NSCLC. The ultimate goal is to test if the expression of these markers associates with resistance to chemotherapy in this disease. A brief description of these projects and the major findings includes the following:

a) Keap1 and Nrf2 expression in NSCLC correlates with clinicopathological features. Nuclear factor erythroid-2 related factor 2 (Nrf2) is a transcription factor associated with *in vitro* resistance to chemotherapy. Kelch-like ECH-associated protein 1 (Keap1) is a cytoplasmic repressor of Nrf2. KEAP1 inactivation is a relatively frequent genetic alteration in NSCLC, and leads to Nrf2 activation. We investigated the IHC expression of nuclear Nrf2 and cytoplasmic Keap1 proteins in 304 surgically resected NSCLC tissues in tissue microarrays

(adenocarcinomas, n=190; squamous cell carcinomas, n=114) (Figure 4). We correlated those findings with patients' clinicopathological features and, in adenocarcinomas, with *EGFR* and *KRAS* mutations. We also examined the expression of Nrf2 and Keap1 using whole tissue sections in 79 NSCLC tumors (36 chemo-naïve and 43 treated with neoadjuvant chemotherapy). We detected Nrf2 expression in 26% (77/299) of NSCLCs, and expression was significantly higher in squamous cell carcinoma (43/112, 38%) compared with adenocarcinoma (34/188, 18%; $P=0.0001$). In adenocarcinomas, Nrf2 was not expressed in *EGFR* mutant (0/23) compared with wild-type tumors (31/145, 21%; $P=0.009$). Keap1 expression score was significantly higher in squamous cell carcinoma compared with adenocarcinoma ($P<0.0001$). In patients with NSCLC stage I/II, who did not receive adjuvant or neoadjuvant treatment, Nrf2 overexpression significantly correlated with poor overall survival in multivariate analysis (HR=2.468; 95% CI 1.468, 4.151; $P=0.0007$).



In patients with squamous cell carcinoma histology, low Keap1 expression correlated with poor overall survival (HR=0.479; 95% CI 0.260, 0.882; $P=0.018$). *KEAP1* mutation (exons 2-5) was detected in 1/20 tumors examined. Normal bronchial epithelia adjacent to NSCLC tumors did not show Nrf2 expression, suggesting that a field-effect phenomenon related to Nrf2 expression was not present. We conclude that: 1) increased expression of Nrf2 and decreased expression of Keap1 are relatively frequent abnormalities in NSCLC, especially in squamous cell carcinoma histology; and 2)

altered IHC expression of these markers correlates with NSCLC patients' outcome. The identification of the subset of patients with abnormal expression of Nrf2 may be important for better selection of treatment in NSCLC.

b) IHC expression of membrane transporters correlates with histology of NSCLC. Folate receptor alpha (FOLR1), reduced folate carrier 1 (RFC1), copper transporter receptor 1 (CTR1), glucose 4 (GLUT4) and RHOA regulate uptake of molecules and drugs inside the cell. FOLR1 and RFC1 are overexpressed in epithelial tumors and are potential therapeutic targets and tumor biomarkers. IHC protein expression of FOLR1, RFC1, CTR1, GLUT4 and RHOA was examined in 320 surgically resected NSCLCs placed in tissue microarrays, including 202 adenocarcinomas and 110 squamous carcinomas, and correlated with patients' clinicopathological characteristics. A semi-quantitative IHC score was obtained assessing the intensity of immunostaining and percentage of positive tumor cells. The pattern of IHC expression varied in malignant cells, with FOLR1, RFC1 and GLUT4 expressed in the membrane and cytoplasm, CTR1 expressed in the cytoplasm and nucleus, and RHOA expressed only in the cytoplasm. In all cases, expression in tumor cells was higher than in non-malignant lung epithelial cells.

Tumor stromal IHC expression was frequently detected, especially in endothelial cells, lymphocytes, macrophages, and fibroblasts. Adenocarcinomas showed significantly higher expression compared with squamous cell carcinoma for most markers, including membrane ($P<0.001$) and cytoplasmic ($P<0.001$) FOLR1, cytoplasmic ($P<0.001$) and nuclear ($P<0.004$) CTR1, and cytoplasmic RHOA ($P<0.001$). Female NSCLC patients had significantly higher expression of membrane and cytoplasmic FOLR1 ($P=0.01$) compared with male patients. Smoking patients demonstrated significantly lower expression of membrane ($P<0.001$) and cytoplasmic FOLR1 ($P<0.002$), and higher expression of membrane ($P=0.04$) and cytoplasmic ($P=0.03$) GLUT4, and membrane RFC1 ($P=0.01$) when compared with never-smokers. In adenocarcinomas, the presence of *EGFR* mutations correlated with higher expression of membrane FOLR1 ($P<0.002$), and *KRAS* mutation with higher expression of membrane GLUT4 ($P<0.004$) and lower expression of nuclear CTR1 ($P=0.02$). We conclude: 1) membrane transporters proteins are overexpressed in NSCLC compared to normal lung epithelium; 2) significant differences were found between adenocarcinomas and squamous lung cancer in both tumor cells and the tumor microenvironment; and 3) differences were found in tumors of males and females, between tumors from never- and ever-smokers, and between tumors with *EGFR* or *KRAS* mutations. The different patterns of transporter expression may explain the superior response of NSCLC patients with adenocarcinoma histology to pemetrexed.

c) Expression of stem cell markers in NSCLC and correlation with clinicopathologic features.

Cancer stem cells (CSCs) represent a minority population of self-renewing tumor cells that are believed to play an important role in tumor development and metastasis, and in resistance to therapy. Although some CSC markers have been described in NSCLC, no comprehensive characterization of multiple CSC markers has been undertaken in this disease. It has been hypothesized that the CSCs may be responsible for tumor resistance to therapy. Our aim was to investigate the pattern of protein expression of a panel of CSC-related markers in a large series of NSCLCs, and to correlate those findings with patients' clinicopathologic characteristics. We examined protein expression by IHC of 287 NSCLCs (178 adenocarcinomas, and 109 squamous cell carcinomas, SCC) with a panel of seven CSC markers: EZH2, SOX2, CD24, CD44, C-kit, BMI-1 and Oct3/4. The pattern of expression of these markers was correlated with patients' and tumors' clinicopathologic characteristics, including outcome of the disease. In adenocarcinomas, CSC markers expression was correlated with the *EGFR* and *KRAS* mutation status of the tumors. Expression of EZH2, SOX2, CD44, CD24 and C-kit was detected in a subset of NSCLC tumors, and no expression of BMI-1 and Oct3/4 was detected in any tumor specimen. The pattern of expression for these markers varied according to NSCLC clinicopathologic characteristics, including tumor histology and pathological stage, and patients' smoking history. Both EZH2 and SOX2 nuclear protein expression were significantly higher in SCC than adenocarcinoma ($P<0.001$). Conversely, CD44 membrane ($P<0.001$) and CD24 cytoplasmic ($P<0.05$) expression were significantly higher in adenocarcinoma than in SCC. We identified a subset of NSCLCs having membrane CD44 high/CD24 low or negative expression. In adenocarcinomas, EZH2, CD44, and CD24 expression levels were significantly ($P <0.001$) higher in current smokers than never or former smokers. The presence of *EGFR* mutation in lung adenocarcinomas correlated significantly with low EZH2 ($P=0.03$) and high CD44 ($P=0.032$) membrane expression. Interestingly, in multivariate analysis and examining the expression scores as continuous variables, high nuclear expression of EZH2 correlated significantly with worse recurrence-free survival (HR=1.006; $P=0.0035$) and overall survival (HR=1.005; $P=0.0202$) in stages I/II lung adenocarcinoma. We thus have provided a characterization of multiple CSC markers in a large series of NSCLCs. Our findings indicate that a different pattern of CSC markers expression is detected in adenocarcinomas and squamous cell carcinomas of the lung, and their expression correlates with patients' clinicopathologic features, including survival. The understanding of the role of CSC in NSCLC tumor development

and progression may provide opportunities to design novel strategies to prevent and treat this disease.

Aim 3: To identify surrogate serum phosphopeptide profiles and plasma DNA markers associated with NSCLC tumor resistance and patient response to neoadjuvant chemotherapy.

We will identify serum samples from the UT-SPORE Tissue Bank that match the NSCLC tumor resection specimens examined in Aim 1. We will use these serum samples for phosphopeptide profiling and peptide mapping by ProteinChip array-based surface-enhanced laser-desorption-ionization (SELDI) mass spectrometry (MS) and laser desorption/ionization (LDI) mass spectrometry (MS)/MS to compare serum phosphopeptides with TTF and mRNA profiles. The phosphopeptide MS profiles from retrospective specimens will later be used as references and controls for the prospective serum proteomic analysis. As in Aim 2, we will use serum samples collected prospectively in Project 2 from 100 NSCLC cases undergoing neoadjuvant chemotherapy and 200 NSCLC controls undergoing surgery without neoadjuvant chemotherapy, and, when relevant, at the time of relapse. Using these serum specimens, we will perform phosphopeptide profiling on ProteinChip arrays by SELDI-MS to measure the temporal changes in serum phosphopeptides before and after the therapeutic intervention. We will use LDI-QSTAR-MS/MS and liquid chromatography (LC)-MS/MS to identify specific serum phosphopeptides that are determined by SELDI-MS to be relevant to targeted therapeutic response and acquired resistance in lung cancer patients. In addition, we will compare serum phosphopeptide profiles with TTF (RPPA and MBA) profiles, mRNA profiles, and TMAs and IHC analysis developed in Project 1 and in Aims 1 and 2 of this project. This comparison will identify TTF serologic molecular signatures and elucidate the biologic pathways potentially associated with patient response and tumor resistance to targeted therapeutic agents. Finally, in collaboration with Project 2 we will perform correlation analysis of these NSCLC serum phosphopeptide profile signatures with patients' clinical characteristics to predict lung cancer, cancer progression, cancer stages, and overall survival rate; to characterize serum phosphopeptide proteomic patterns and signatures in correlation to tumor recurrence, clinical response to adjuvant chemotherapeutic and targeted agents, and development of resistance; and to identify serum phosphopeptide markers as surrogate predictors of patient outcome.

Moreover, in Aim 3 we will quantify total circulating plasma DNA and methylation-specific DNA in all 300 patients with NSCLC enrolled in the Project 2 clinical trial. The circulating DNA levels will be correlated with patients' clinicopathologic characteristics. Any changes in these levels during chemotherapy and after surgery will be correlated with patient response to neoadjuvant therapy and patient outcome after surgery. The correlation between circulating methylated DNA levels and tumor DNA methylation will also be examined in a selected panel of patients.

Summary of Research Findings

Protein phosphorylation is a dynamic, post-translational modification that plays a critical role in the regulation of a wide spectrum of biological events and cellular functions including signal transduction, gene expression, cell proliferation, and apoptosis. We have developed a functional proteomics technique using the ProteinChip array-based SELDI-TOF-MS analysis for high throughput profiling of phosphoproteins/phosphopeptides in human serum for the early detection and diagnosis as well as for the molecular staging of human cancer. We have been able to use this proteomics platform to selectively isolate, profile, and identify phosphopeptides present in a highly complex mixture prepared from human lung cancer patient serum samples. We have identified a phosphopeptide with a 1752.3 Da mass as Alpha-1-acid glycoprotein 1

precursor (A1AG1), a potential target of multiple protein tyrosine kinases including EGFR, and a novel ligand of nicotinic acetylcholine receptor (nAChR) protein subunits. We found that the AIAG1 phosphopeptide is significantly upregulated in cancer serum samples (more than 10-fold increase in mass peak intensity, $P = 0.0024$) by SELDI-TOF-Spectrometry analysis. The upregulated phosphorylated AIAG1 has also been detected by phospho-AIAG1-specific ELISA analysis in the serum samples of the early stage (Stage I) lung cancer patients and ever smokers and in human lung cancer cell lines. We also detected the interaction of AIAG1 protein with nAChR- $\alpha 4$, $\beta 2$, and $\alpha 7$ subunits by immuno-precipitation and immuno-blotting analysis, suggesting a role of AIAG1 as a potential ligand of nAChR proteins in regulation of nAChR-mediated signaling pathway in lung cancer carcinogenesis. Further characterization of AIAG1 expression and biological activity in larger population of lung cancer patient serum samples and in lung cancer cell lines *in vitro* and *in vivo* will provide validation of using the phospho- A1AG1 peptide as a novel serum biomarker for early lung cancer detection and intervention.

We plan to further validate phosphopeptide profiling in large group of lung cancer patient serum samples, and to analyze AIAG1 and Phospho-AIAG1 in lung cancer cell lines, serum, and tissue samples. During the next project period, we will functionally characterize AIAG1/aChR subunits interaction and signaling in lung cancer cell lines. Investigations into the modulation of serum and cellular phospho-AIAG1 in response to tyrosine kinase inhibitors (TKIs) or tobacco carcinogens will begin, and we will elucidate the role of AIAG1 in the EGFR/AKT signaling pathway in lung cancer carcinogenesis, diagnosis, and prognosis.

Key Research Accomplishments

- Performed extraction of DNA and RNA of over 600 NSCLC and 53 MPM with annotated clinicopathologic information for profiling analysis.
- Developed an mRNA prognostic signature for NSCLC using FFPE tissue specimens.
- Performed mRNA and miRNA molecular profiling in 53 MPM tumor and cell line specimens.
- Collected >200 frozen NSCLC tissue specimens from patients who received neoadjuvant therapy, and evaluated the pathological response to chemotherapy in 133 cases.
- Characterized NSCLC tissue specimens for novel biomarkers associated to resistance to chemotherapy in lung cancer, including Nrf2/Keap1, membrane transporters and cancer stem cell markers.

Conclusions

During the second project period, we reached our collection goal of NSCLC tissues from patients who received neoadjuvant chemotherapy, and finalized the extraction of DNA and RNA for molecular profiling of chemo-naïve surgically resected NSCLCs. We have initiated the molecular profiling of lung cancer, and developed an NSCLC prognostic mRNA signature using FFPE tissues. We are in the process of completing comprehensive (mRNA, miRNA, DNA and protein) profiling analyses of MPM tissue and cell line specimens.

Project 4: Target Modulation Following Induction Treatment With Dasatinib in Patients With Malignant Pleural Mesothelioma (MPM) and Identification of New Therapeutic Targets/Strategies for MPM

(Leaders: Drs. Anne Tsao, Reza Mehran)

Hypothesis:

We hypothesize that dasatinib, a broad spectrum ATP-competitive inhibitor for oncogenic tyrosine kinases (BCR-ABL, SRC, c-Kit, PDGFR, and ephrin receptor kinases), may be a new therapeutic agent in malignant pleural mesothelioma (MPM). We also believe that conducting therapeutic target-focused (TTF) molecular and gene profiling (Affymetrix arrays) will lead to development of other novel therapies for MPM.

Specific aims:

Aim 1: Conduct a phase I clinical trial with the primary endpoint of biomarker modulation using dasatinib as induction therapy in patients with resectable MPM.

- 1a. Determine the effects of dasatinib induction therapy on selected tumor biomarkers (activated Src, PDGFR, VEGFR) pre- and post-induction therapy.
- 1b. Determine the modulatory effects of dasatinib on selected biomarkers of survival and apoptosis (PI3K/AKT, bcl-xL, caspases), proliferation (IGFR, Ki-67), angiogenesis (IL-8, bFGF, TNF- α), epithelial-mesenchymal transition (TNF- β , E-cadherin, c-Kit/Slug) and invasion/migration (Ephrin, MMP) in tumor specimens pre- and post- induction therapy.
- 1c. Determine the effects of induction dasatinib therapy on tumor mean vessel density, cell apoptosis, and the proliferation index.
- 1d. Determine the modulatory effects of dasatinib on serum, platelet, and pleural effusion markers of survival (PI3K/AKT, bcl-xL, caspases), proliferation (IGFR, Src), angiogenesis (soluble VEGFR, VEGF, PDGF, IL-8, bFGF, TNF- α), and invasion/migration (Ephrin, MMP).
- 1e. Determine the drug concentration of dasatinib in tumor and serum.
- 1f. Assess the effects of dasatinib and cytoreductive surgery on the serum mesothelin-related peptide (SMRP) level.
- 1g. Assess the safety and toxicity profile of induction dasatinib in patients with resectable MPM.

Aim 2: Conduct radiographic correlates of tumor response and clinical outcome with positron-emission technology-computer tomography (PET-CT).

Aim 3: Explore and develop new therapeutic targets and treatment strategies for MPM in tumor specimens collected from Specific Aim1 and in MPM cell lines.

- 3a. Determine key signaling pathways involved in tumor resistance or sensitivity to dasatinib using therapeutic target-focused (TTF) molecular and global gene expression profiling on MPM tumor specimens pre- and post- induction dasatinib therapy.
- 3b. Determine the sensitivity of a panel of MPM cell lines to targeted agents tested in Project 1 via TTF profiling and DATs (drug and therapeutic target siRNA).

Summary of Research Findings

It should be noted that Dr. Reza Mehran has replaced Dr. David Rice as Co-Leader of this project, due to Dr. Rice's increased responsibilities with other programmatic activities. As shown

in his appended biosketch, Dr. Mehran brings long-standing expertise in the management of thoracic malignancies, and leadership of large, complex clinical studies.

We designed a biomarker-based neoadjuvant trial from our preclinical studies during the previous project period. The trial is intended to show that dasatinib, a multi-targeted Src kinase inhibitor, has activity against MPM and target-specificity to Src Tyr419. Untreated MPM patients underwent extended surgical staging (ESS) with multiple biopsies along the future surgical incision line to account for tumor heterogeneity and evaluate for sarcomatoid features. If deemed a surgical candidate for either pleurectomy/decortication (P/D) or extrapleural pneumonectomy (EPP), patients received 4 weeks of oral dasatinib (70 mg BID) followed by P/D or EPP. If either a radiographic or molecular response (de-phosphorylation of Src Tyr419 in tumor) was observed, an additional 2 years of dasatinib maintenance after adjuvant radiotherapy and systemic chemotherapy was scheduled for the affected patients. Serum/blood/platelets and pleural effusion were collected for exploratory analysis of peripheral surrogate biomarkers. The primary endpoint of this trial is biomarker modulation of Src Tyr419; secondary endpoints include response, survival, safety/toxicity, and biomarker modulation in tumor/serum/platelets/pleural effusion.

Fourteen patients have been accrued to this trial from April 2008 to April 2009; ten have successfully completed the ESS, neoadjuvant dasatinib, and P/D (n=6) or EPP (n=4). Two patients are currently receiving neoadjuvant dasatinib, 2 patients were deemed to not be surgical candidates due to a rapid decline in PS, and one patient was found to have bilateral mesothelioma. The main side effects recorded for dasatinib were grade 1-2 anemia, nausea, vomiting, anorexia, electrolyte abnormalities, fatigue, and anxiety. Grade 3 toxicities included hyperkalemia (1), infection - pneumonia (1), and hypoxia (1). There were no grade 4-5 toxicities recorded for these patients. Post-surgical grade 3 toxicity included anemia, electrolyte abnormalities, arrhythmia, HTN, and pleural effusion; one grade 4 episode of hyperglycemia was seen. After 4 weeks of neoadjuvant dasatinib therapy, there was one non-evaluable patient, one recorded PD, eight SD, and two minor responses. In the two patients with a radiographic response by PET-CT, their anatomic response correlated with a molecular response, with dephosphorylation of SrcTyr419 observed in their tumor tissue. Based on these clinical results, we found that conducting biomarker-based clinical trials with novel agents in MPM is feasible and necessary to further our understanding of this deadly disease. There is preliminary evidence that a subgroup of MPM patients may gain clinical benefit from dasatinib therapy, and that modulation of p-Src Tyr419 in MPM tumor tissue is a reasonable pharmacodynamic marker for dasatinib treatment. Future translational studies will correlate the outcome and tumor p-Src Tyr419 with peripheral surrogate markers for response and evaluate potential pathways of resistance to dasatinib therapy in tumor tissue. The optimal multi-modality treatment for resectable malignant pleural mesothelioma (MPM) still remains unknown. No prior neoadjuvant trials with targeted agents have been published due to limited funding and eligible patients.

In other related efforts, in collaboration with this project and Project 3, the Pathology Core has constructed a MPM tissue microarray containing 76 surgically resected tumor cases, including epitheloid, sarcomatoid, and biphasic histology types, with well-annotated clinicopathologic information. This TMA has been used to characterize the expression of several IHC markers (please see Pathology Core report for further detail). The Pathology Core has also collected, banked, and characterized MPM tumor tissue from 10 patients enrolled in the MPM dasatinib clinical trial who underwent video-assisted thoracoscopy (VAT) and extrapleural pneumonectomy (EPP). A total of 172 (91 baseline [VAT] and 81 at surgery [EPP]) fresh frozen

and formalin-fixed tumor tissue specimens have been obtained, processed, and characterized by the Pathology Core.

Key Research Accomplishments

- Demonstrated that the Src Tyr419 biomarker is accurately predicting for radiographic response in patients receiving dasatinib therapy.
- Enrolled 14 patients on the clinical trial.
- Contributed specimens used in construction of an MPM tissue microarray and 172 MPM tumor tissue specimens from the clinical trial to the MPM tissue bank.

Conclusions

We have demonstrated that this novel trial design is feasible and preliminary evidence suggests that our Src Tyr419 biomarker is accurately predicting for radiographic response in patients receiving dasatinib therapy. There is a subpopulation of MPM patients that may derive clinical benefit from oral dasatinib therapy. MPM is a very heterogeneous tumor, and molecular profiling will be necessary in future studies to ultimately optimize targeted therapy in this disease.

Preliminary evidence suggests that modulation of p=Src Ty⁴¹⁹ is a feasible, reasonable pharmacodynamic biomarker for dasatinib. Future plans include correlating outcome and tumor p-Src tyr⁴¹⁹ to peripheral surrogate markers in blood/serum/platelets and pleural effusion, and to analyze pathways of resistance in MPM tumors.

Project 5: Development of a Novel Multi-Biomarker System Using Quantum Dot Technology for Assessments of Prognosis of NSCLC and Prediction of Outcome of EGFR-Targeted Therapy

(Leader: Dr. Zhuo (Georgia) Chen; Co-Leaders: Drs. Fadlo Khuri, Dong Shin, Ruth O'Regan, Shi-Yong Sun)

Quantum dots (QDs) provide sharper fluorescent signals than organic dyes and can detect multi-biomarkers simultaneously in the same material, allowing quantification and correlation of molecular signature with cellular response to targeted therapies.

Hypothesis:

A multi-biomarker system using quantum dot (QD) technology will enhance accuracy in assessment of prognosis of non-small cell lung cancer (NSCLC) and prediction of outcome of epidermal growth factor receptor (EGFR)-targeted therapy.

Specific Aims:

Specific Aim 1: Development of QD-Abs and imaging systems for detection and quantification of multi-biomarkers (MBM) using lung cancer cell lines.

Summary of Research Findings

Specific Aim 1 was completed in 2008. Major findings were reported last year and were published in *Nanotechnology*. Our results illustrated that QD-immunocytochemistry (ICC)-based technology can not only quantify basal level of multiplex biomarkers but can also track

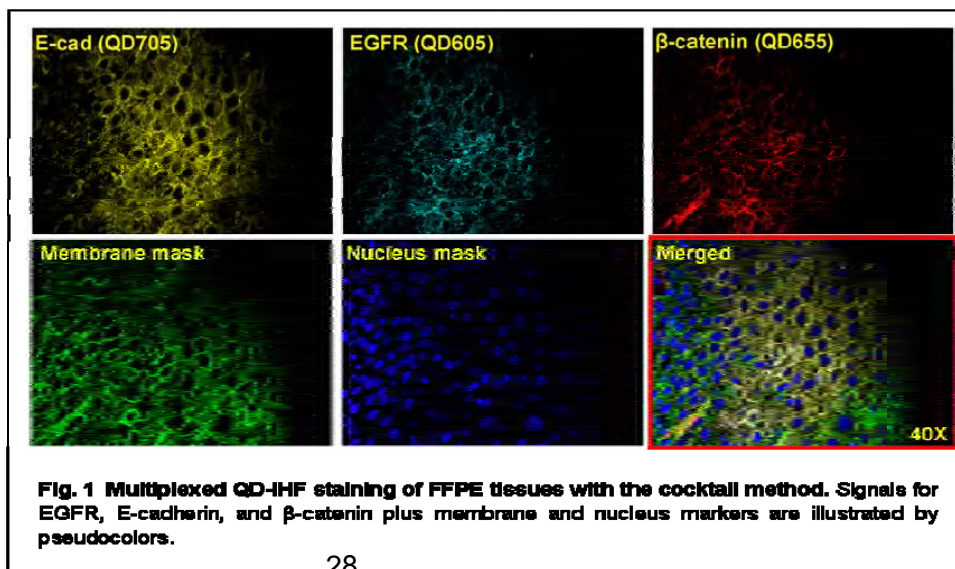
the localization of biomarkers upon biostimulus. With this new technology, we found that EGFR and E-cad were located mainly in the cytoplasm in EGFR-TKI-insensitive cells; however, in EGFR-TKI-sensitive cells, they were found mainly on the cell membrane. After induction with EGF, both EGFR and E-cad internalized to the cytoplasm, but the internalization capability in EGFR-TKI-sensitive cells was greater than that in EGFR-TKI-insensitive cells. The quantification also showed that the inhibition of EGF-induced EGFR and E-cad internalization by erlotinib in the sensitive cells was stronger than that measured in the insensitive cells. These studies demonstrate that there are substantial differences between EGFR-TKI-insensitive and EGFR-TKI-sensitive cancer cells in EGFR and E-cad expression and localization, both at the basal level and in response to EGF and erlotinib. QD-based analysis facilitates the understanding of the features of EGFR-TKI-insensitive vs. EGFR-TKI-sensitive cancer cells and may ultimately be useful for the prediction of patients' response to EGFR-targeted therapy.

Specific Aim 2: Verification of QD-Abs for detection and quantification of MBM by comparison with conventional IHC using paraffin-embedded tissues and evaluation of their prognostic value in NSCLC.

Summary of Research Findings

Nanoparticle QDs are ideal materials for multiplexed biomarker detection, localization, and quantification; however, working conditions for the application of QD in staining of formalin-fixed and paraffin-embedded (FFPE) specimens need to be optimized. Both direct and indirect methods are available for QD-based immunohistofluorescence (QD-IHF) staining, but the direct method has been considered laborious and costly. In this study, we optimized and compared the indirect QD-IHF single-staining procedure using QD-secondary antibody conjugates and QD-streptavidin conjugates. Problems associated with sequential multiplex staining were identified quantitatively. A method using a QD cocktail solution was developed allowing simultaneous staining with three antibodies against E-cadherin, EGFR, and β -catenin in FFPE tissues. The expression of each biomarker was quantified and compared using the cocktail and the sequential method. Our results demonstrated that the QD signal for each multiplexed biomarker was more consistent and stable using the cocktail method than the sequential method, providing a unique tool for potential research and clinical applications (Figure 1). A quantification method for multiplexing three biomarkers (EGFR, E-cadherin, and β -catenin plus DAPI in FFPE tissues) was developed using the CRi Nuance spectral system (Figure 2).

We also validated the QD-IHF procedures. The validation included: 1) the comparison of single biomarker detection using conventional immunohistochemistry (IHC) with QD-based immunohistofluorescence (IHF); and 2) the comparison of biomarker signals from samples stained with single QD IHF in serial sections to biomarker signals from the same



proteins but from samples stained simultaneously with multiple QD IHF. FFPE tissue sections from 30 FFPE tissue samples were used for the validation. Both Pearson's and Spearman's tests show significant correlation between IHC and QD-IHF for the single-marker staining tests (EGFR: correlation coefficient $R = 0.8-0.9$, $p < 0.00001$; E-cadherin: $R = 0.9$, $p < 0.00001$; β -catenin: $R = 0.7-0.8$, $p < 0.00001$) and for the singleplex versus multiplex tests (EGFR: $R = 0.8-0.9$, $p < 0.00001$; E-cadherin: $R = 0.8$, $p < 0.00001$; β -catenin: $R = 0.7-0.8$, $p < 0.00001$) (Figure 3).

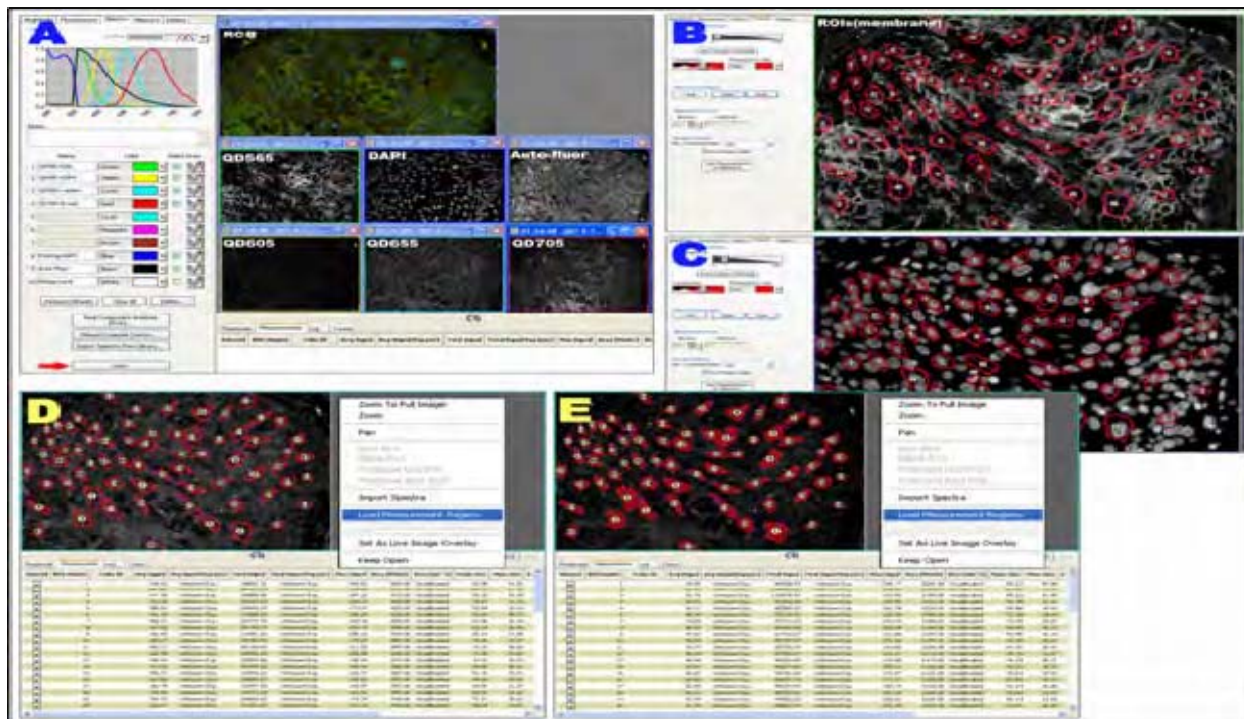
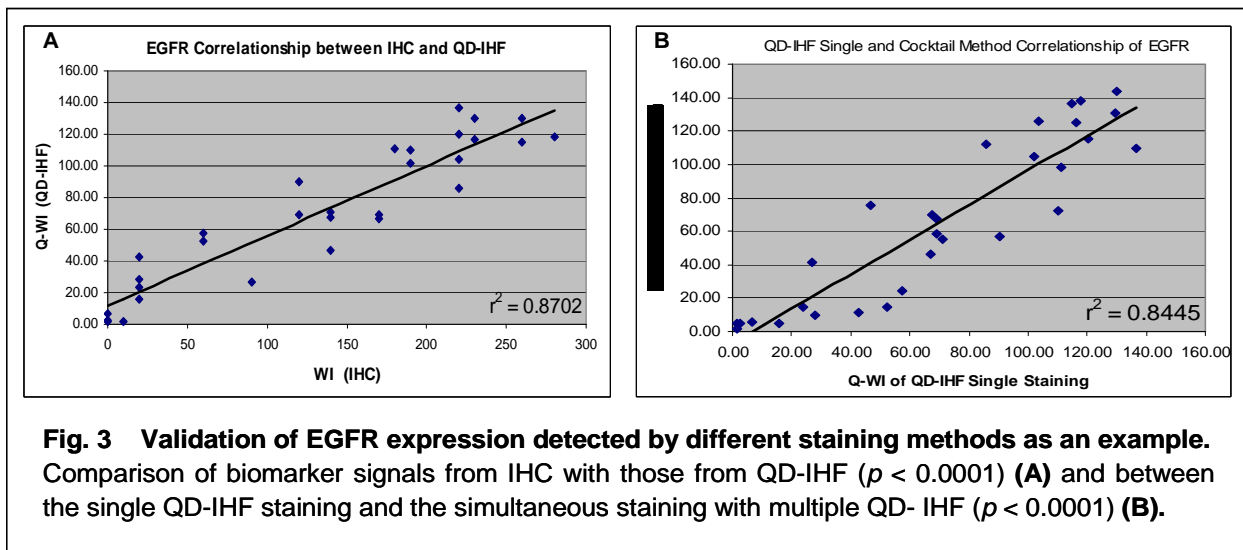


Fig. 2 Identification of region of interest for single-cell quantification. A. Obtaining RGB Image and unmixing each QD signal; B. Manually identifying the region of interests (ROIs) (membrane) in the unboxed "membrane mask" signal window; C. Confirming the ROIs in the "nucleus mask" window; D and E. Obtaining membrane or total quantification results after defining the different ROIs. Ten images were randomly acquired from each sample and at least 60 cells were randomly analyzed in each image.



To complete this specific aim, tissue samples (including tumor specimens and adjacent normal tissues) from 94 cases of NSCLC with relevant clinical information were collected for IHC and QD-IHF staining (Figure 4). Quantification of QD-IHF is still ongoing. For quantification of IHC results, Weighted Index {WI = [percentage of positive stain x intensity score (0, 1+, 2+, and 3+)] x100} and ratio of membrane to total staining (RMT = signal of membrane stain/signal of total stain) were recorded. Preliminary statistical analysis of IHC showed that both expression and membrane localization of all three biomarkers in tumor tissue are significantly different from those in the adjacent normal tissue (Table 1). Development and validation of QD-IHF for the second set of biomarkers relevant to mTor pathway is ongoing.

Table 1: Summary of the Semi-quantification of IHC

	EGFR (WI)	% Membrane	E-cadherin (WI)	% Membrane	β -catenin (WI)	% Membrane
Normal	36.0	40.7	179.2	89.7	158.4	82.7
Tumor	97.4	31.1	136	50	130.2	50.4
p-Value*	1.34E-16	2.12E-04	2.44E-11	1.28E-28	7.47E-09	1.49E-29

* Paired t-test

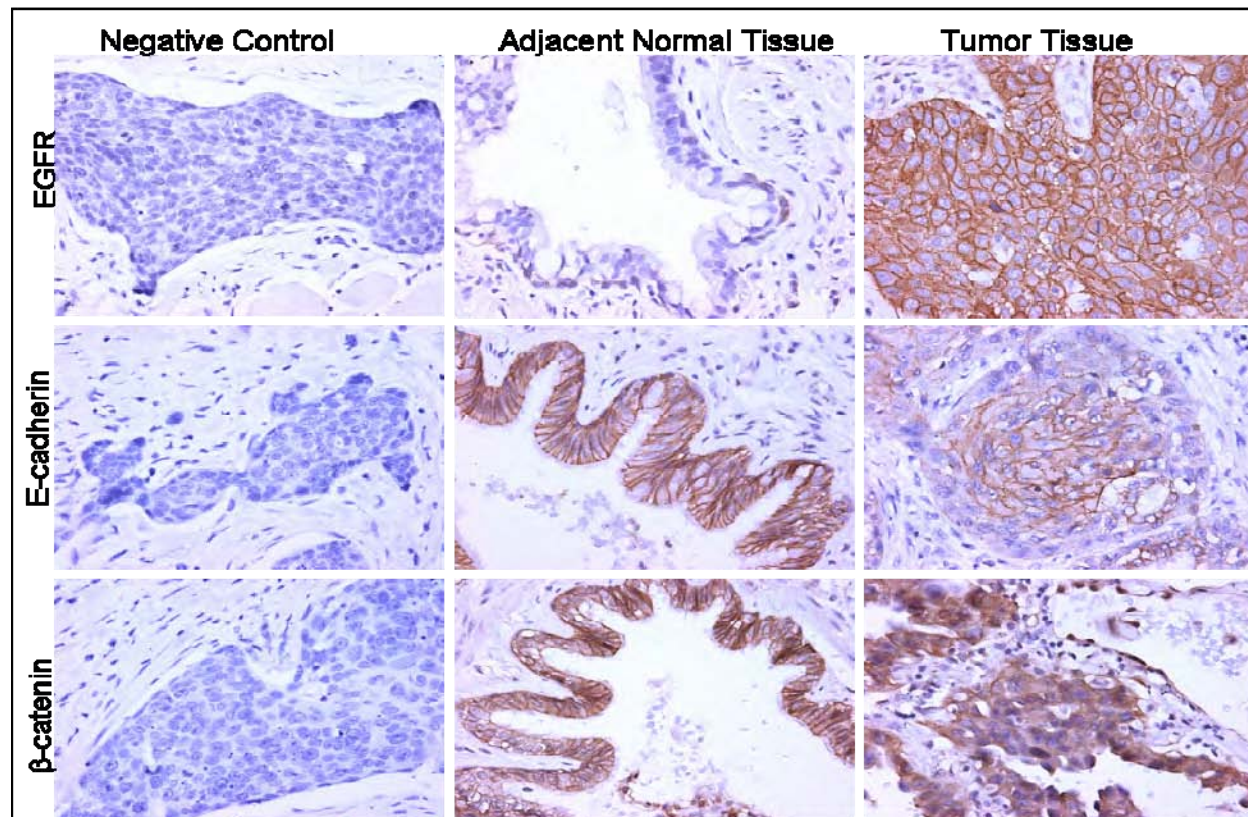


Fig 4. Representative IHC staining of EGFR, E-cadherin, and β -catenin in both adjacent normal and tumor tissues. Expression of EGFR is significantly higher in tumor tissues than that in the adjacent normal tissue, while expressions of E-cadherin and β -catenin are less and more internalized in the tumor tissues than those in the adjacent normal epithelia. We expect that simultaneously characterizing these features in the same tissue using QD-IHF will correlate more precisely the biology with progression of these tumor cells. (Magnification 400X)

Specific Aim 3: Correlation of the MBM detected by QD-Abs with outcomes of chemotherapies and EGFR- targeted therapy using resectable NSCLC tissues.

Summary of Research Findings

This study was proposed for years 3 and 4 of this grant; thus, are no updates for this Specific Aim.

Key Research Accomplishments

- Optimized and validated QD-staining conditions for multiplexing three biomarkers (EGFR, E-cadherin, and β -catenin) in both cell lines and FFPE tissues.
- Developed a quantification method for QD signals using the CRi Nuance spectral system.
- Collected training set materials including 94 cases of NSCLC and their adjacent normal tissues, and entered clinical information into a database for further analysis.
- Completed staining of the three biomarkers in the 94 pairs of the NSCLC tissues by both IHC and QD-IHF methods. The imaging and statistical analyses are ongoing.

Conclusions

In the past year, we completed the proposed cell line studies in Specific Aim 1 and published the results in *Nanotechnology*. Our findings provide new biomarkers and QD methodology in predicting sensitivity to EGFR-targeting therapy which can be applied to tumor tissue specimens for clinical application. Furthermore, clarifying substantial differences between EGFR-TKI sensitive and insensitive cancer cells will help to understand the mechanism of EGFR-targeted resistance and facilitate the development of new targeted therapies. During the project period, we focused on optimization and validation of a quantification strategy for using QD-based IHF. These studies provided a solid foundation for analyzing biomarker expressions in NSCLC tissues. Using this strategy, we have completed the immunostaining of three biomarkers - EGFR, E-cadherin, and β -catenin - in 94 pairs of the patients' tissue samples. Further imaging and statistical analyses of these stains will answer an important question of whether quantification of multiplex biomarkers by QD-IHF can provide more accurate correlation to patient's prognosis and the other relevant clinical information than a single biomarker analysis.

Pathology Core

(Director: Dr. Ignacio Wistuba)

The Pathology Core is an essential component of the PROSPECT program. The Pathology Core plays an important role by collecting, processing and distributing tissue and serum specimens obtained from Clinical Trials on NSCLC (Project 2) and malignant pleural mesothelioma (MPM; Project 4) for molecular profiles and biomarker analysis. **Our objectives (functions) are as follows:**

1. Develop and maintain a repository of tissue and serum specimens from patients with non-small cell lung carcinoma (NSCLC) and malignant pleural mesothelioma (MPM).
2. Process NSCLC cell lines and tissue specimens for histopathologic and molecular analyses.
3. Perform and evaluate immunohistochemical (IHC) analysis in human tumor tissue specimens and mouse xenograft tissues.

Objective 1. Develop and maintain repository of tissue and serum specimens from patients with lung cancer and malignant pleural mesothelioma (MPM).

Summary of Research Findings

Selection of lung cancer and mesothelioma specimens available in Thoracic Malignancy Tissue Bank. As reported last year, we identified 1,385 non-small cell lung cancer (NSCLC) tumor specimens as potential cases for PROSPECT Projects 2 and 3, including the major histology types adenocarcinoma (n=729) and squamous cell carcinoma (n=414). Of those specimens, we stored frozen tumor tissue available from patients who have consented to their tissue to be banked and used for research purposes. We selected 736 NSCLC cases for Project 3 and 4; 147 of the 736 (20%) NSCLC cases have received neoadjuvant chemotherapy. In addition, more than 4,011 NSCLC cases with formalin-fixed and paraffin-embedded (FFPE) tissues available have been identified and specimens banked. All the cases retrieved are under histopathological review and classified according to the 2004 WHO Pathology Classification for lung cancer. Peripheral mononuclear blood cells (PMBC) and serum samples collected during the surgical resection from 464 NSCLC and 36 MPM patients are also available. As reported last year, we have identified 108 MPMs with frozen tumor tissue available for PROSPECT

Project 4. FFPE tissues from 91 MPMs have been collected, and clinical and pathological information have been obtained in all cases.

Prospective collection and banking of lung cancer and mesothelioma specimens for PROSPECT projects. Since the activation of the PROSPECT laboratory project on August 2007, the Pathology Core has collected fresh and formalin-fixed tissue specimens from 272 NSCLC and 19 MPM surgically resected cases (Table 1). During this period of time, 347 surgeries for lung cancer and mesothelioma have been performed, and we have collected tissue specimens in 84% of them. From those, snap-frozen normal and tumor tissue have been collected in all cases. In addition, we have obtained and banked tumor specimens in RNAlater® (Ambion, Austin, TX) (n=115 samples), 12% dimethyl sulfoxide (DMSO)-preserved samples (n=122 samples), and OCT-embedded for frozen sectioning (n=96 samples). From the 272 NSCLC cases, 79 patients have received neoadjuvant chemotherapy. Blood specimens (serum and PMBC) have collected, processed, and banked in 283 out of 347 surgeries (69%). Of interest, tissue and blood specimens have been obtained in 231 cases (67%).

Table 1. Summary of prospectively collected tumor tissue specimens from NSCLC and MPM cases.

Histology	Number of Cases
Adenocarcinoma	160
Squamous cell carcinoma	63
Large cell carcinoma	4
Other NSCLC	41
No tumor present	4
Total Lung Tumors	272
Malignant Mesothelioma	19

Thoracic Malignancy Tissue Bank Database. To improve the handling of tissue and blood specimens, our institution developed a Web-based tissue banking system, named TissueStation. We also have a Microstrategy Report Services system (Oracle-based), which allows us to run reports and retrieve data from the TissueStation database. Both applications (TissueStation and Microstrategy) have been instrumental to the success of the Pathology Core in obtaining and banking tissue and blood specimens from NSCLC and MPM patients.

Objective 2. Process NSCLC cell lines and tissue specimens for histopathological and molecular analyses.

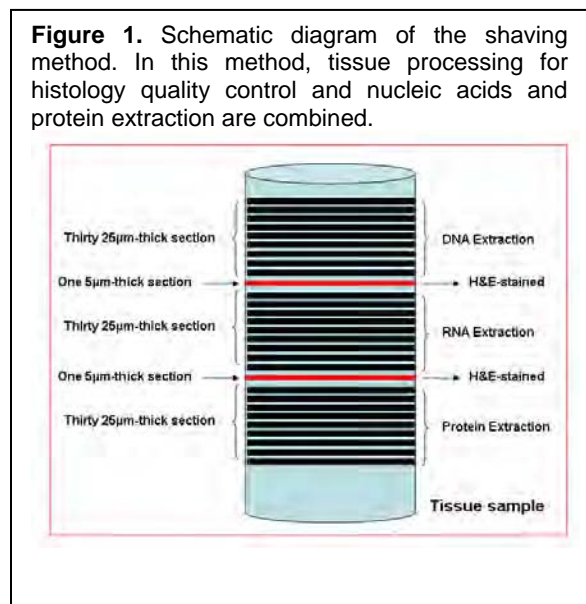
Summary of Research Findings

Cell Lines. a) **Lung Cancer.** In collaboration with Project 1 (Drs. J. Heymach and J. Minna), we have developed a repository of 48 NSCLC cell lines and 2 normal bronchial epithelial cells; b) **Mesothelioma.** In collaboration with Projects 3 and 4 (Drs. I. Wistuba and A. Tsao, respectively), we have acquired 17 mesothelial and mesothelioma cell lines (Table 2) with a good distribution of different histotypes including 4 epitheloid, 2 biphasic and 2 sarcomatoid MPMs. Some of these are currently being characterized by immunohistochemistry (IHC) using 7 different markers to distinguish them as authentic mesothelioma cell lines. Three of these IHC markers, Cytokeratin 5/6, calretinin and mesothelin, are seen frequently in MPM tumors, whereas CEA (carcinoembryonic antigen), B72.3, CD15 (LeuM1) and TTF-1 (thyroid

transcription factor-1) are rarely seen in these tumor cells and, therefore, represent negative controls. For all these cell lines, several frozen vials have been obtained and stored for future work. In addition, RNA, DNA, and protein have been extracted and stored. Importantly, FFPE pellets have been prepared in all cell lines to be used as control for IHC and fluorescent in situ hybridization (FISH) experiments. Both NSCLC and MPM cell lines are being STR DNA fingerprinted in the DNA core for their authentication in the M. D. Anderson Molecular Cytogenetics Core facility.

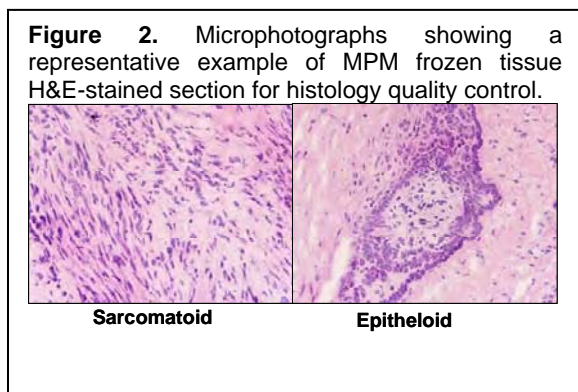
Table 2. List of MPM and normal mesothelial cells stored in the Pathology Core

Cell line	Type	Source
HMeso	MPM	Dr. Harvey Pass
HP-3	MPM	Dr. Harvey Pass
HP-4	MPM	Dr. Harvey Pass
HP-5	MPM	Dr. Harvey Pass
HP-6	MPM	Dr. Harvey Pass
HP-7	MPM	Dr. Harvey Pass
HP-9	MPM	Dr. Harvey Pass
HP-10	MPM	Dr. Harvey Pass
HCT-4012	Pleural Mesothelial (Telomerase- transformed)	Dr. Adi Gazdar
Met-5A	Pleural Mesothelial (SV40- transformed)	ATCC
MSTO-211H	MPM, Biphasic	ATCC
H28	MPM, Epitheloid	ATCC
H2052	MPM, Epitheloid	ATCC
H2452	MPM, Epitheloid	ATCC
JL-1	MPM, Epitheloid	DSMZ
DM-3	MPM, Sarcomatoid	DSMZ
RS-5	MPM, Sarcomatoid	DSMZ



Tissue Processing for RNA, DNA and Protein Extractions. In collaboration with Project 3 (Drs. I. Wistuba, A. Corvalan and S. Suraokar), frozen tumor and normal tissue from 613 NSCLCs and 53 MPMs obtained from the Thoracic Tissue Bank (see Objective 1) have been processed for the extraction of nucleic acids and proteins. For extractions, a detailed histopathological analysis was performed using a technique developed in-house called the “shaving method” (Figure 1). This technique uses 5-µm-thick haematoxylin-eosin (H&E)-stained histology sections obtained at four levels of the tissue specimen that are alternated by two sets of thirty 20-µm thick sections obtained for DNA, RNA, and protein extractions. All the shaving processing has been performed using RNase-free conditions. The

microtome and blades were routinely cleaned with ethanol (70%) to avoid any risk of degradation of RNA by RNase. After cutting, all samples have been stored in an -30°C freezer until the extractions are ready to be performed.



Histology Quality Control of Tissue Specimens.

For detailed histopathological analysis, each tumor H&E-stained section was examined by an experienced lung cancer pathologist to assess the percentage of tumor versus adjacent normal tissues, the percentage of malignant cells versus tumor non-malignant stromal (inflammatory, vascular and fibroblasts) cells, and normal cells present in the adjacent normal tissue. In addition, tumor cell viability has been addressed by examining the presence of necrosis and hemorrhage in the tissues. For NSCLC, a detailed

histopathological analysis was performed on 1,543 slides, 797 of which were tumor slides, and 661 corresponded to unique tumors. These 661 cases represent 90% of the 736 NSCLC available in UT-Lung SPORE Tissue Bank. Paired normal and tumor samples were found in 634 (96%) of cases. Among these 661 tumor cases, 353 contain >70% tumor content and >50% tumor cell content. In addition, we are in the process of digitalization of all slides for future comparisons of detailed histopathological analyses. For MPM, the histology quality control was performed in 159 slides of tumor tissue and 108 of corresponding normal tissue (Figure 2). All these H&E-stained sections are being scanned and digital images stored in an Aperio slide scanner (Aperio Technology) for future analysis.

MPM Tissue Microarray. In collaboration with Projects 3 and 4, we have constructed a MPM tissue microarray containing 76 surgically resected tumor cases, including epithelioid, sarcomatoid, and biphasic histology types, with well-annotated clinicopathologic information. This TMA has been used to characterize the expression of several IHC markers (see Objective 3).

MPM Clinical Trial Tissue Collection and Processing. In collaboration with Project 4, the Pathology Core has collected, banked, and characterized MPM tumor tissue from 10 patients enrolled in the MPM dasatinib clinical trial who underwent video-assisted thoracoscopy (VAT) and extrapleural pneumonectomy (EPP). A total of 172 (91 baseline [VAT] and 81 at surgery [EPP]) fresh frozen and formalin-fixed tumor tissue specimens have been obtained, processed, and characterized by the Pathology Core.

Objective 3. Perform and evaluate immunohistochemical (IHC) analysis in human tumor tissue specimens and mouse xenograft tumor specimens.

Summary of Research Findings

The Pathology Core has assisted and performed IHC analysis for a number of markers using TMAs and whole sections in tumor tissue specimens of NSCLC and MPM in collaboration with Projects 2 (Dr. D. Stewart), 3 (Dr. I. Wistuba), and 4 (Dr. A. Tsao).

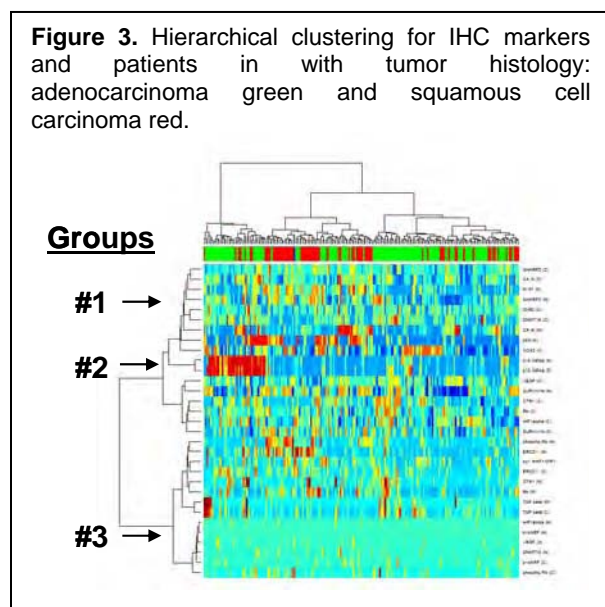
Project 2. Using IHC, 18 proteins associated with senescence, proliferation, apoptosis and other tumor-related phenomena (Table 3) have been examined in a set of NSCLC TMAs containing

330 tumors, including 220 adenocarcinomas and 110 squamous cell carcinomas. Annotated clinicopathologic information, including overall and recurrence-free survival with a median follow-up of 7.2 years, is available in all these cases. The IHC data obtained are being analyzed by the Biostatistics and Bioinformatics Core (Dr. K. Coombes) (Figure 3). From the preliminary analysis, at least 3 groups of patients have been identified by the expression of the IHC markers examined. The clinicopathologic characteristics of these cases, including their outcome is currently under evaluation.

Table 3. List of IHC markers examined in NSCLC TMAs in collaboration with Project 2.

p53	CTR1	ERCC1	SHARP2
p21	RB	SURVIVIN	DcR2
Ki67	p16 INK4a	HIF1 α	TUNEL
COX2	p14 ARF	CA IX	
DNMT1	TGF β	VEGF	

In addition, in collaboration with Project 2, we have examined IHC expression of cell membrane



transporters, including copper transporter receptor 1(CTR1), glucose 4 (GLUT4) and RHOA, and folate receptor alpha (FOLR1) and reduced folate carrier 1 (RFC1) in TMAs from NSCLC and MPM. The data on NSCLC have been presented in the 2009 AACR Meeting (Poster, April 2009, Denver, CO) and will be presented in the IASLC World Lung Cancer meeting (oral presentation, July 2009, San Francisco, CA). A manuscript is in preparation.

Project 3. In collaboration with this Project, a series of cancer stem cell (CSC) markers have been examined by IHC using NSCLC TMAs (n=330 cases), including EZH2, SOX2, CD24, CD44, C-kit, BMI-1, HEY1, HEY2, and Oct3/4. These data will be presented as an oral presentation in the IASLC World Lung Cancer meeting (oral presentation, July 2009, San

Francisco, CA), and a manuscript is in preparation. In addition, the Pathology Core has contributed to the analysis of Keap1/Nrf2 proteins and genes expression in NSCLC TMAs and frozen tissue specimens.

Project 4. The MPM TMAs have been utilized to characterize the expression of several markers, including markers related to epithelial-to-mesenchymal transition (EMT; 5 IHC markers), angiogenesis (PFGFR β ; 2 IHC markers and FISH for the gene), and cell membrane transporters (5 IHC markers). In addition, the recently acquired MPM cell lines from Dr. Harvey Pass are currently being characterized by IHC using 7 different markers to distinguish them as authentic mesothelioma cell lines, including cytokeratin 5/6, calretinin, mesothelin, CEA, B72.3, CD15, and TTF-1. Finally, the Pathology Core has optimized and examined by IHC the expression of total Src and p-Src (Tyr 416), as well as Ki67 in nearly 100 MPM tissue samples obtained from patients enrolled in the dasatinib clinical trial.

Key Research Accomplishments

- Collected prospective frozen tissue specimens from 272 NSCLC and 19 MPM cases, including 79 NSCLC cases treated with neo-adjuvant chemotherapy.
- Established a NSCLC and MPM cell line repository at the M. D. Anderson Cancer Center in collaboration with Projects 1 and 4.
- Performed extraction with detailed histology quality control of 613 NSCLCs and 53 MPMs tumor and corresponding normal tissues, which will be used for profiling analysis (Project 3).
- Collected, processed, and analyzed 172 MPM tumor tissue specimens from patients enrolled in the dasatinib clinical trial (Project 4).

Conclusions

During the second year, the PROSPECT Pathology Core has achieved and exceeded its goals for the second year by prospectively collecting frozen tissue specimens from 272 NSCLC and 19 MPM cases, including 79 NSCLC cases treated with neo-adjuvant chemotherapy. We have expanded the MPM cell line repository to 17 cell lines. The Pathology Core has played an important role in the processing of NSCLC and MPM tissue specimens for profiling, and in the characterization of tissue specimens on the expression of protein expression by immunohistochemistry.

Biostatistics/Bioinformatics Core

(Director: Dr. J. Jack Lee; Co-Director: Kevin Coombes)

In close collaboration with the Pathology Core and each of the five main projects, the Biostatistics and Data Management Core (BDMC) for the Department of Defense (DoD) PROSPECT lung cancer research program is a comprehensive, multi-lateral resource for designing clinical and basic science experiments; developing and applying innovative statistical methodology, data acquisition and management, and statistical analysis; and publishing translational research generated by this research proposal. We deliver planned and tailored statistical analyses for rapid communication of project results among project investigators, and by collaborating with all project investigators to facilitate the timely publication of scientific results.

The main objectives of the Biostatistics and Data Management Core are to:

1. Provide the statistical design, sample size, and power calculations for each project.
2. Develop a secure, internet-driven, Web-based database application to integrate data generated by the five proposed projects and the Pathology Core of the PROSPECT research project.
3. Develop a comprehensive, Web-based database management system for tissue specimen tracking and distribution and for a central repository of all biomarker data.
4. Provide all statistical data analyses, including descriptive analysis, hypothesis testing, estimation, and modeling of prospectively generated data.
5. Provide prospective collection, entry, quality control, and integration of data for the basic science, pre-clinical, and clinical studies in the PROSPECT grant.
6. Provide study monitoring and conduct of the neoadjuvant clinical trial that ensures patient safety by timely reporting of toxicity and interim analysis results to various institutional review boards (IRBs), the UTMDACC data monitoring committee, the DoD, and other regulatory agencies.

7. Generate statistical reports for all projects.
8. Collaborate with all project investigators and assist them in publishing scientific results.
9. Develop and adapt innovative statistical and genomic methods pertinent to biomarker-integrated translational lung cancer studies.

Summary of Research Findings

In the second funding year, the BDMC continued to work with all project investigators in providing biostatistics and data management support. The accomplishments are summarized below.

Biostatistics. We worked with clinical investigators to provide the biostatistical support in the development and revision of PROSPECT protocols. We provided statistical reports on a monthly basis to update the accrual, randomization, and demographic data for all projects involved.

We have developed and evaluated the statistical methodology used for comparing various test statistics for response adaptive randomization (*BMC Medical Research Methodology*). We have also placed emphasis on applying the Emax model, the interaction index, and the bivariate thin plate splines for drug interaction assessment in combination studies (*Frontiers of Biosciences*).

In collaboration with the University of Texas Lung SPORE, we continued to work on developing semantic database models for the assay data being generated by both the PROSPECT projects and the Lung SPORE projects (*PLoS ONE, AMIA Annu Symp Proc*).

We continue to work on developing statistical methods for processing and analyzing the reverse-phase protein array (RPPA) data that continue to be generated as part of the PROSPECT study of lung cancer (*BMC Bioinformatics, Bioinformatics*).

We have performed (and continue to perform) analyses of PROSPECT data. Although these analyses have not yet resulted in publications, they are expected to do so in future project periods. These analyses include:

1. Analysis of an initial set of immunohistochemically stained tissue microarray data looking at markers of prognosis in lung cancer samples. Univariate analysis identified a number of markers that appear to be related either to important clinical covariates or to clinically relevant outcomes (overall survival, disease-free survival, or recurrence-free survival). We are in the process of performing multivariate analyses to identify robust signatures of these outcomes using the same kinds of methods have been developed in the field of gene expression microarrays.
2. We have developed a novel method to find comparative signatures of drug response by simultaneously modeling the differential response of cell lines to two different drugs. This method was developed using RPPA data and dose response data from both lung cancer and head and neck cancer cell lines; the lung cancer data was collected as part of the PROSPECT grant.
3. We are preparing a statistical methods manuscript that uses models to evaluate methods that simultaneously discover markers and identify subsets of patients who receive greater benefit from certain drugs in a multi-arm clinical trial.
4. We have recently received a full set of combined Affymetrix gene expression data and Agilent microarray measurements of miRNA expression. Analysis is underway, with the first step being to analyze each technology separately to discover new prognostic markers. At a

later stage, we will integrate the data by accounting for known or predicted interactions between miRNA and mRNA molecules.

Data Management. The PROSPECT database development takes advantage of the ReVITALization effort from the DoD-sponsored VITAL program due to the similarity between the two databases developed for these projects. To tailor the database for the PROSPECT-specific needs, database extensions were made to allow the collection and management of data from multiple studies including the neoadjuvant studies, adjuvant studies, and regular chemotherapy studies. In addition, the PROSPECT database was developed to extend the ReVITALization database in VITAL to provide additional clinical, pathological, and biomarker data repositories and tissue tracking. In this funding period, we continue our database development effort and make updates to improve the function and usability of the database.

The SQL Server 2005 database and ASP.NET web application is implemented with VB.net language. Queries and SQL 2005 reports are provided. Secure Socket Layer (SSL) and secured database passwords are used to keep data transaction protected and confidential. The tissue data include clinical and pathological data.

1) The database's clinical module contains the following Web forms:

- Patient Information
- Social History (Alcohol and Smoking history)
- Medical History
- Other Malignancy
- Treatments (Surgery, Chemotherapy, Radiotherapy and Other Treatments)
- Clinical Staging
- Follow up

2) The pathological module contains the following Web forms:

- Primary and Metastasis data (Diagnosis and Surgery Specimens)
- Histology
- Staging and Tumor Information: Cancer staging (TNM classification) is automatically determined by the system based on the tumor information provided.
- Tissue Bank (Frozen Tissue and Paraffin)

3) Reports: Several Excel reports are provided for clinical and pathological modules.

- Clinical Report
- Pathological Report
- Patient Report
- Accession Report
- General Information Report
- Other Malignancy Report
- Surgery Report
- Chemotherapy Report
- Radiotherapy Report
- Other Treatment Report
- Staging Report
- Follow up Report
- Histology Diagnosis Report

4) Dictionaries: The database gives control for the users to update dictionaries; however, dictionary deletion is prohibited.

Key Research Accomplishments

- Developed a secured, Web-based database application to assist the study conduct.
- Performed database maintenance, training, and support.
- Provided data integrity and data correction.
- Updated dictionaries and added data fields.
- Updated project reports.
- Provided more links to make data navigation easier.

Reportable Outcomes

A web-based database application is developed and deployed at:

https://insidebiostat/DMI_PROSPECT/Common/Login.aspx

Conclusions

In collaboration with clinical investigators, research nurses, the Biomarker Core, and basic scientists, the Biostatistics and Data Management Core has continued to deliver biostatistics and data management support as proposed. Further support and analysis will be provided in the future project period.

KEY RESEARCH ACCOMPLISHMENTS

PROJECT 1

- Completed protein profiling and gene expression profiling for 50 NSCLC cell lines.
- Derived baseline gene expression signatures predictive of response by correlating mRNA expression with drug response.
- Derived proteomic drug response signatures by correlating proteomic profiles with drug response data for a variety of drugs.
- Using baseline proteomic profiles, markers of radiation sensitivity and resistance were identified in lung cancer cell lines (Yordy et al., ASTRO 2008; Yordy et al., ASCO 2008).
- Identified factors associated with age and sex differences in NSCLC (Herynk et al., Proceeding of the Flight Attendants Medical Research Institute, 2009) (Herynk et al., Proceedings of the International Association for the Study of Lung Cancer, 2009).
- Identified SRC as a potential biomarker of response to the EGFR inhibitor.

PROJECT 2

- Collected tumor specimens on 291 lung cancer patients (including 74 who had received neoadjuvant chemotherapy).
- Collected blood samples on 283 lung cancer patients (including 64 who received neoadjuvant chemotherapy).
- Performed preliminary assessment of impact of 18 biomarkers on survival, and their correlation with stage and tumor type.

PROJECT 3

- Performed extraction of DNA and RNA of over 600 NSCLC and 53 MPM with annotated clinicopathologic information for profiling analysis.
- Developed an mRNA prognostic signature for NSCLC using FFPE tissue specimens.
- Performed mRNA and miRNA molecular profiling in 53 MPM tumor and cell line specimens.
- Collected >200 frozen NSCLC tissue specimens from patients who received neoadjuvant therapy, and evaluated the pathological response to chemotherapy in 133 cases.
- Characterized NSCLC tissue specimens for novel biomarkers associated to resistance to chemotherapy in lung cancer, including Nrf2/Keap1, membrane transporters and cancer stem cell markers.

PROJECT 4

- Demonstrated that the Src Tyr419 biomarker is accurately predicting for radiographic response in patients receiving dasatinib therapy.
- Enrolled 14 patients on the clinical trial.
- Contributed specimens used in construction of an MPM tissue microarray and 172 MPM tumor tissue specimens from the clinical trial to the MPM tissue bank.

PROJECT 5

- Optimized and validated QD-staining conditions for multiplexing three biomarkers (EGFR, E-cadherin, and β -catenin) in both cell lines and FFPE tissues.
- Developed a quantification method for QD signals using the CRi Nuance spectral system.
- Collected training set materials including 94 cases of NSCLC and their adjacent normal tissues, and entered clinical information into a database for further analysis.
- Completed staining of the three biomarkers in the 94 pairs of the NSCLC tissues by both IHC and QD-IHF methods. The imaging and statistical analyses are ongoing.

PATHOLOGY CORE

- Collected prospective frozen tissue specimens from 272 NSCLC and 19 MPM cases, including 79 NSCLC cases treated with neo-adjuvant chemotherapy.
- Established a NSCLC and MPM cell line repository at the M. D. Anderson Cancer Center in collaboration with Projects 1 and 4.
- Performed extraction with detailed histology quality control of 613 NSCLCs and 53 MPMs tumor and corresponding normal tissues, which will be used for profiling analysis (Project 3).
- Collected, processed, and analyzed 172 MPM tumor tissue specimens from patients enrolled in the dasatinib clinical trial (Project 4).

BIostatistics AND DATA MANAGEMENT CORE

- Developed a secured, Web-based database application to assist the study conduct.
- Performed database maintenance, training, and support.
- Provided data integrity and data correction.
- Updated dictionaries and added data fields.
- Updated project reports.
- Provided more links to make data navigation easier.

REPORTABLE OUTCOMES

Publications (Attached in Appendix A)

Blanco R, Iwakawa R, Tang M, Kohno T, Angulo B, Pio R, Montuenga LM, Minna JD, Yokota J, Sanchez-Cespedes M. A gene-alteration profile of human lung cancer cell lines. *Human Mutation*. 2009 May 20. PMID: 19472407.

Deus HF, Stanislaus R, Behrens C, Wistuba I, Minna JD, Garner HR, Swisher SG, Roth J, Correa A, Broom B, Coombes K, Almeida JS. Data driven semantic integration of translational lung cancer research at M.D. Anderson Cancer Center. *American Medical Informatics Association Annual Symposium Proceedings*. 2008 Nov 6:927. PMID: 18999102.

Deus HF, Stanislaus R, Viegas DF, Behrens C, Wistuba II, Minna JD, Garner HR, Swisher SG, Roth JA, Correa AM, Broom B, Coombes K, Chang A, Vogel LH, Almeida JS. A semantic web management model for integrative biomedical informatics. *PLoS ONE*. 2008 Aug 13;3(8):e2946. PMCID: PMC2491554.

Gazdar AF, Minna JD. Deregulated EGFR signaling during lung cancer progression: mutations, amplicons, and autocrine loops. *Cancer Prevention Research*. 2008 Aug;1(3):156-60. PMID: 19138950.

Ji L, Roth JA. Tumor suppressor FUS1 signaling pathway. *Journal of Thoracic Oncology*. 2008 Apr;3(4):327-30. PMID: 18379348.

Huang DH, Su L, Peng XH, Zhang H, Khuri FR, Shin DM, Chen ZG. Quantum dot-based quantification revealed differences in subcellular localization of EGFR and E-cadherin between EGFR-TKI sensitive and insensitive cancer cells. *Nanotechnology*. 2009 Jun 3;20(22):225102. PMID: 19433879.

Larsen JE, Spinola M, Gazdar AF, Minna JD. An overview of the molecular biology of lung cancer. Lung Cancer: Principles and Practice, 4th edition. Philadelphia: Lippincott Williams & Wilkins, 2009.

Neeley ES, Kornblau SM, Coombes KR, Baggerly KA. Variable slope normalization of reverse phase protein arrays. *Bioinformatics*. 2009 Jun 1;25(11):1384-9. PMID: 19336447.

Shames DS, Minna JD. IP6K2 is a client for HSP90 and a target for cancer therapeutics development. *Proceedings of the National Academy of Science U S A*. 2008 Feb 5;105(5):1389-90. PMCID: PMC2234151.

Sos ML, Koker M, Weir BA, Heynck S, Rabinovsky R, Zander T, Seeger JM, Weiss J, Fischer F, Frommolt P, Michel K, Peifer M, Mermel C, Girard L, Peyton M, Gazdar AF, Minna JD, Garraway LA, Kashkar H, Pao W, Meyerson M, Thomas RK. PTEN loss contributes to erlotinib resistance in EGFR-mutant lung cancer by activation of Akt and EGFR. *Cancer Research*. 2009 Apr 15;69(8):3256-61. PMID: 19351834.

Sos ML, Michel K, Zander T, Weiss J, Frommolt P, Peifer M, Li D, Ullrich R, Koker M, Fischer F, Shimamura T, Rauh D, Mermel C, Fischer S, Stückrath I, Heynck S, Beroukhi R, Lin W,

Winckler W, Shah K, LaFramboise T, Moriarty WF, Hanna M, Tolosi L, Rahnenführer J, Verhaak R, Chiang D, Getz G, Hellmich M, Wolf J, Girard L, Peyton M, Weir BA, Chen TH, Greulich H, Barretina J, Shapiro GI, Garraway LA, Gazdar AF, Minna JD, Meyerson M, Wong KK, Thomas RK. Predicting drug susceptibility of non-small cell lung cancers based on genetic lesions. *Journal of Clinical Investigation*. 2009 Jun;119(6):1727-40. doi: 10.1172/JCI37127. PMID: PMC2689116.

Stanislaus R, Carey M, Deus HF, Coombes KR, Hennessy BT, Mills GB, Almeida JS. RPPAML/RIMS: A meta data format and an information management system for reverse phase protein arrays. *BMC Bioinformatics*. 2008 Dec 22;9:555. PMID: PMC2639439.

Stewart D, Issa JP, Kurzrock R, Nunez M, Jelinek J, Hong D, Yasuhiro O, Guo Z, Gupta S, Wistuba I. Decitabine effect on tumor global DNA methylation and other parameters in a phase I trial in refractory solid tumors and lymphomas. *Clinical Cancer Research*. 2009 Jun 1;15(11):3881-8. PMID: 19470736.

Zhang L, Wei Q, Mao L, Liu W, Mills GB, Coombes KR. Serial dilution curve: a new method for analysis of reverse phase protein array data. *Bioinformatics*. 2009 Mar 1;25(5):650-4. PMID: PMC2647837.

Manuscripts submitted, in revision, or in review (Attached in Appendix A)

Huang, D.H., Peng, H.X., Su, L., Wang, D.S., Khuri, F.R., Shin, D.M., Chen, Z.G., Optimization and Comparison of Multiplexed Quantum Dot Immunohistofluorescence. *Biomaterials*. Submitted, 2009.

Imai H, Sunaga N, Shimizu Y, Yanagitani N, Kaira K, Tomizawa Y, Ishizuka T, Minna JD, Mori M. Overexpression of CXCL12 and its receptors CXCR4 and CXCR7 in lung cancer: CXCL12 as a potential molecular target for lung cancer. *Genes Chromosomes Cancer*. Submitted, 2009.

Jayachandran G, Roth, Ji L. Analysis of Protein-protein Interaction using ProteinChip Array-based SELDI-TOF Mass Spectrometry. Methods in Molecular Biology. The Humana Press, 2009. (in press).

Jeong Y, Xie Y, Xiao G, Xie XJ, Behrens C, Girard L, Patz Jr EF, Wistuba II, Minna JD, Mangelsdorf DJ. Nuclear Receptor Expression Defines a Set of Prognostic Biomarkers for Lung Cancer. *Cancer Cell*. (Submitted CANCER-CELL-S-09-00260), 2009.

Ji L, Jayachandran G, Roth J. High Throughput Profiling of Serum Phosphoproteins/peptides Using the SELDI-TOF-MS Platform. Methods in Molecular Biology. The Humana Press, 2009. (in press).

Kong M, Lee JJ. Applying Emax Model and Bivariate Thin Plate Splines to Assess Drug Interactions. *Frontiers of Biosciences*. In press, 2009.

Lee JJ, Gu X A simulation study for comparing testing statistics in response-adaptive randomization. *BMC Medical Research Methodology*. (in revision).

Lee JJ, Lin HY, Liu DD, Kong M. Applying Emax model and interaction index for assessing drug interaction in combination studies. *Frontiers of Biosciences*. In press, 2009.

Ramos AH, Dutt A, Mermel C, Perner S, Cho J, Lafargue CJ, Johnson LA, Tanaka K, Bass AJ, Barretina J, Weir BA, Beroukhir R, Thomas RK, Minna J, Chirieac LR, Lindeman NI, Beer DG, Wagner P, Wistuba II, Rubin MA, Meyerson M. Amplification of PDGRA and KIT in Non-small Cell Lung Cancer. *Cancer Research*. (CAN-08-4331 submitted), 2009.

Stewart, DJ. Non-small cell lung cancer patient survival when assessed as a first order nonlinear process: effect of therapy and stage. Submitted for publication.

Abstracts (Attached in Appendix A)

Byers LA, Tran HT, Tumula PK, Du Z, Herynk M, Minna JD, Heymach JV. Cytokine and angiogenic factor (CAF) profiling of non-small cell lung cancer cell lines identifies secreted proteins associated with response to chemotherapy and targeted agents. ASCO-NCI-EORTC Annual Meeting on Molecular Markers in Cancer. Hollywood ,FL. October 2008.

Gold K, Lee JJ, Rice D, Tse W, Stewart DJ, Wistuba R, Herbst R, Lippman SL, Hong WK, Kim ES. Phase II pilot study of neoadjuvant docetaxel and cisplatin followed by adjuvant erlotinib in patients with I-III non-small cell lung cancer (NSCLC). ASCO Annual Meeting, Orlando, FL, June 2009.

Herynk MH, Hanrahan E, Lin HY, Cascone T, Yan S, Byers L, Yordy J, Lee JJ, Heymach JV (2009) Secreted Cytokine and Angiogenic Factor (CAF) profiles associated with age and sex in NSCLC. Proceedings of the Flight Attendants Medical Research Institute.

Huang, D., Hoyt, C. C., Peng, H., Wang, D., Zhang, H., Khuri, K. R., Shin, D. M., Chen, Z(G). Development of a quantum dots (QDs)-based quantification method for multiplexed biomarkers in prediction of metastasis. AACR Annual Meeting, Denver, CO, April 2009.

Mehran R, Gil J, Rice D, Swisher S, Lee JJ, Lippman S, Pisters, Blumenschein G, Hong WK, Tsao AS. Phase I trial of neoadjuvant dasatinib in patients with respectable malignant pleural mesothelioma. ASCO Annual Meeting, Orlando, FL, June 2009.

Nunez MI, Behrens C, Woods DM, Lin H, Prudkin L, Suraokar M, Girard L, Minna J, Lee JJ, Hofstetter W, Franklin W, Moran CA, Stewart DJ, Wistuba II. Immunohistochemical expression of membrane transporters correlates with histology type of non-small cell lung carcinoma. AACR Annual Meeting, Denver, CO. April, 2009.

Solis L, Behrens C, Bekele BN, Ozburn N, Moran CA, Minna JD, Suroakar M, Stewart DJ, Swisher SG, Corvalan AH, Wistuba II. Keap1 and Nrf2 expression in non-small cell lung carcinoma correlates with clinico-pathological features. AACR Annual Meeting, Denver, CO. April 2009.

Sunaga N, Imai H, Shimizu K, Kakegawa S, Shames D, Girard L, Minna J, Mori M. Overexpression of epiregulin is associated with KRAS mutations, aggressive phenotypes and regulates the growth of non-small cell lung cancer. IASLC World Lung Cancer meeting, July 2009. San Francisco, CA.

Suraokar M, Corvalan A, Chow CW, Gazdar A, Moran C, Raso G, Mehran R, Tsao A, Wistuba I. Integrating microRNA and mRNA expression profiles identified a small set of unique genes up regulated in malignant pleural mesothelioma (MPM). 2009 AACR Meeting, April 2009, Denver, CO.

Yordy JS, Byers LA, Davies M, Mills G, Ju Z, Ang KK, Heymach JV. Protein Expression Profiling Identifies Markers of Radiation Sensitivity and Resistance in the NCI 60 Cell Lines. ASCO-NCI-EORTC Annual Meeting on Molecular Markers in Cancer. Hollywood, FL. October, 2008.

Yordy JS, Byers LA, Davies M, Molkenkine D, Nanjundan M, Raju U, Mills G, Minna J, Coombes K, Ang KK, Heymach JV. Reverse Phase Protein Arrays Reveal Biomarkers of Radiation Sensitivity and Resistance in Head and Neck and Lung Cancer Cell Lines. ASTRO Translational Advances in Radiation Oncology and Cancer Imaging Symposium. Arlington, VA. October, 2008.

Presentations

Corvalan A, Suraokar M, Zou X, Chow CW, Gazdar A, Moran C, Raso G, Mehran R, Tsao A, Wistuba I. Profiling in pharmacologically re-expressed microRNAs by 5-azacytidine and SAHA identified a metastasis associated miR-148b in malignant pleural mesothelioma cell lines. Accepted for oral presentation in the IASLC World Lung Cancer meeting, July 2009, San Francisco, CA.

Herynk MH, Hanrahan E, Lin HY, Cascone T, Yan S, Byers L, Yordy J, Lee JJ, Heymach JV. Secreted Cytokine and Angiogenic Factor (CAF) profiles associated with age and sex in NSCLC. Accepted for poster presentation in the IASLC World Lung Cancer meeting, July 2009. San Francisco, CA.

Nunez M, Behrens C, Lin H, Prudkin K, Suraokar M, Woods DM, Girard L, Minna J, Lee JJ, Hofstetter W, Franklin W, Moran CA, Franklin W, Hong WK, Stewart D, Wistuba I. Immunohistochemical Expression of Membrane Transporters Correlates with Histology of Non-Small Cell Lung Carcinoma. Poster presentation, 2009 AACR Meeting, April 2009, Denver, CO.

Nunez MI, Behrens C, Woods DM, Lin H, Suraokar M, Girard L, Minna J, Lee JJ, Hofstetter W, Franklin W, Moran CA, Hong WK, Stewart DJ, Wistuba II. Enriched Tumor Expression of Folate Transporters Correlates With Adenocarcinoma Histology Type, Female Gender and Presence of EGFR Mutation in Non-Small Cell Lung Carcinoma. Accepted for oral presentation in the IASLC World Lung Cancer meeting, July 2009, San Francisco, CA.

Raso G, Corvalan A, Behrens C, Basey A, Mendoza G, Roth J, Moran C, Wistuba I. Importance of Histopathology Quality Control of Non-Small Cell Lung Cancer Tissue Specimens for DNA/RNA Extraction and Profiling Analysis. Poster presentation, International Society for Biological and Environmental Repositories (ISBER) 2009 Annual Meeting, May 2009 in Portland, OR.

Solis L, Behrens C, Bekele BN, Ozburn N, Moran CA, Minna JD, Suroakar M, Stewart DJ, Swisher SG, Corvalan AH, Wistuba II. Keap1 and Nrf2 expression in non-small cell lung carcinoma correlates with clinico-pathological features. AACR Annual Meeting, Denver, CO. April 2009. Poster presentation, 2009 AACR Meeting, April 2009, Denver, CO.

Suraokar M, Corvalan A, Chow CW, Gazdar A, Moran C, Raso G, Mehran R, Tsao A, Wistuba I. Integrating microRNA and mRNA expression profiling using a novel algorithm identified a small set of unique genes upregulated in malignant pleural mesothelioma (MPM). Poster presentation, 2009 AACR Meeting, April 2009, Denver, CO.

Tsao, A. Phase I trial of cisplatin, pemetrexed, and imatinib mesylate in chemo-naive patients with unresectable malignant pleural mesothelioma. Accepted for poster discussion in the IASLC World Lung Cancer meeting, July 2009, San Francisco, CA.

Yuan P, Behrens C, Huang J, Spinola M, Prudkin L, Dong W, Yin GG, Moran C, Kim E, Zhou BB, Minna J, Wistuba I. Expression of Stem Cell Markers in Non-Small Cell Lung Carcinoma (NSCLC) and Correlation with Clinico-pathologic Features. Accepted for oral presentation in the IASLC World Lung Cancer meeting, July 2009, San Francisco, CA.

CONCLUSIONS

PROJECT 1: RPPA proteomic profiling and gene expression profiling for a large number of cell lines was performed and has provided the bases for identifying intracellular signaling pathways and proteins associated with sensitivity and resistance to chemotherapies and targeted agents in NSCLC cell lines and tumor samples. These profiles will allow for multiple biomarker analyses. One of the identified markers, SRC-3, was found to be correlated with resistance to EGFR inhibitors. Inhibition of SRC-3 in a gefitinib-resistant cell line was able to reverse resistance to the inhibitor. These results show that the model is successful at identifying relevant biological targets that, when inhibited, are able to reverse resistance to a targeted agent. Our findings will be further investigated by correlating RPPA of tumor samples with clinical outcomes in samples from the BATTLE-1 trial and other clinical samples with the goal of developing predictive markers that can guide treatment selection and identify new targets in NSCLC.

PROJECT 2: During this project period, we identified and are currently assessing the quality of RNA, DNA, and protein that is available from these tumor specimens prior to the full analysis under PROSPECT. Specimen collection continues at a brisk pace and will further our goal of predicting future sites of relapse by examining the molecular profiles associated with the patient tissues. Further analysis is needed to assess the extent to which TTF/gene expression molecular profile at diagnosis may help guide choice of therapies at relapse.

PROJECT 3: During the second project period, we reached our collection goal of NSCLC tissues from patients who received neoadjuvant chemotherapy, and finalized the extraction of DNA and RNA for molecular profiling of chemo-naïve surgically resected NSCLCs. We have initiated the molecular profiling of lung cancer, and developed an NSCLC prognostic mRNA signature using FFPE tissues. We are in the process of completing comprehensive (mRNA, miRNA, DNA and protein) profiling analyses of MPM tissue and cell line specimens.

PROJECT 4: We have demonstrated that this novel trial design is feasible and preliminary evidence suggests that our Src Tyr419 biomarker is accurately predicting for radiographic response in patients receiving dasatinib therapy. There is a subpopulation of MPM patients that may derive clinical benefit from oral dasatinib therapy. MPM is a very heterogeneous tumor, and molecular profiling will be necessary in future studies to ultimately optimize targeted therapy in this disease.

Preliminary evidence suggests that modulation of p=Src Ty⁴¹⁹ is a feasible, reasonable pharmacodynamic biomarker for dasatinib. Future plans include correlating outcome and tumor p-Src tyr⁴¹⁹ to peripheral surrogate markers in blood/serum/platelets and pleural effusion, and to analyze pathways of resistance in MPM tumors.

PROJECT 5: In the past year, we completed the proposed cell line studies in Specific Aim 1 and published the results in *Nanotechnology*. Our findings provide new biomarkers and QD methodology in predicting sensitivity to EGFR-targeting therapy which can be applied to tumor tissue specimens for clinical application. Furthermore, clarifying substantial differences between EGFR-TKI sensitive and insensitive cancer cells will help to understand the mechanism of EGFR-targeted resistance and facilitate the development of new targeted therapies. During the project period, we focused on optimization and validation of a quantification strategy for using QD-based IHF. These studies provided a solid foundation for analyzing biomarker expressions in NSCLC tissues. Using this strategy, we have completed the immunostaining of three biomarkers - EGFR, E-cadherin, and β -catenin - in 94 pairs of the

patients' tissue samples. Further imaging and statistical analyses of these stains will answer an important question of whether quantification of multiplex biomarkers by QD-IHF can provide more accurate correlation to patient's prognosis and the other relevant clinical information than a signal biomarker analysis.

PATHOLOGY CORE: During the second year, the PROSPECT Pathology Core has achieved and exceeded its goals for the second year by prospectively collecting frozen tissue specimens from 272 NSCLC and 19 MPM cases, including 79 NSCLC cases treated with neo-adjuvant chemotherapy. We have expanded the MPM cell line repository to 17 cell lines. The Pathology Core has played an important role in the processing of NSCLC and MPM tissue specimens for profiling, and in the characterization of tissue specimens on the expression of protein expression by immunohistochemistry.

BIOSTATISTICS AND DATA MANAGEMENT CORE: In collaboration with clinical investigators, research nurses, the Biomarker Core, and basic scientists, the Biostatistics and Data Management Core has continued to deliver biostatistics and data management support as proposed. Further support and analysis will be provided in the future project period.

APPENDIX A

Abstracts and Publications

APPENDIX B

Biostatistics Workflow and Database Overview

APPENDIX C

New Investigator Biosketches

A Gene-Alteration Profile of Human Lung Cancer Cell Lines

Raquel Blanco,¹ Reika Iwakawa,² Moying Tang,¹ Takashi Kohno,² Barbara Angulo,¹ Ruben Pio,³ Luis M. Montuenga,³ John D. Minna,⁴ Jun Yokota,² and Montse Sanchez-Cespedes^{1*}

¹Lung Cancer Group, Molecular Pathology Programme, Centro Nacional de Investigaciones Oncológicas (CNIO), Madrid, Spain; ²Biology Division, National Cancer Center Research Institute, Tokyo, Japan; ³Division of Oncology, Centro para la Investigación Médica Aplicada (CIMA), University of Navarra, Pamplona, Spain; ⁴Hamon Center for Therapeutic Oncology Research, University of Texas Southwestern Medical Center, Dallas, Texas

Communicated by Arupa Ganguly

Received 17 December 2008; accepted revised manuscript 12 March 2009.

Published online in Wiley InterScience (www.interscience.wiley.com). DOI 10.1002/humu.21028

ABSTRACT: Aberrant proteins encoded from genes altered in tumors drive cancer development and may also be therapeutic targets. Here we derived a comprehensive gene-alteration profile of lung cancer cell lines. We tested 17 genes in a panel of 88 lung cancer cell lines and found the rates of alteration to be higher than previously thought. Nearly all cells feature inactivation at *TP53* and *CDKN2A* or *RB1*, whereas *BRAF*, *MET*, *ERBB2*, and *NRAS* alterations were infrequent. A preferential accumulation of alterations among histopathological types and a mutually exclusive occurrence of alterations of *CDKN2A* and *RB1* as well as of *KRAS*, epidermal growth factor receptor (*EGFR*), *NRAS*, and *ERBB2* were seen. Moreover, in non-small-cell lung cancer (NSCLC), concomitant activation of signal transduction pathways known to converge in mammalian target of rapamycin (mTOR) was common. Cells with single activation of *ERBB2*, *PTEN*, or *MET* signaling showed greater sensitivity to cell-growth inhibition induced by erlotinib, LY294002, and PHA665752, respectively, than did cells featuring simultaneous activation of these pathways, underlining the need for combined therapeutic strategies in targeted cancer treatments. In conclusion, our gene-alteration landscape of lung cancer cell lines provides insights into how gene alterations accumulate and biological pathways interact in cancer.

Hum Mutat 30,1–8, 2009. © 2009 Wiley-Liss, Inc.

KEY WORDS: lung cancer; oncogenes; tumor suppressors; tyrosine kinase inhibitors

Introduction

Characterization of accumulated genetic alterations in cancer cells is important not only to understand tumor biology, but also to guide drug design and select patients who might benefit from a given targeted cancer therapy. The promise of using proteins

encoded by mutated cancer genes, mainly kinases encoded by oncogenes, as molecular targets for the development of novel therapies, drives endeavors to identify novel mutated cancer genes and to create catalogues of somatic mutations in cancer [Wang et al., 2004; Sjoblom et al., 2006; Greenman et al., 2007; Thomas et al., 2007]. The paradigm of the latter is the Catalogue of Somatic Mutations in Cancer (COSMIC) database of the Wellcome Trust Sanger Institute (www.sanger.ac.uk/cosmic) [Forbes et al., 2006], which brings together data on the mutation status of hundreds of cancer-related genes in primary tumors and cancer cell lines from a wide variety of tumor types.

In the particular case of lung cancer, several gene alterations are known to contribute to its development, including activating mutations and gene amplification at the oncogenes *BRAF* (MIM# 164757), epidermal growth factor receptor (*EGFR*) (MIM# 131550), *ERBB2* (MIM# 164870), *KRAS* (MIM# 190070), *NRAS* (MIM# 164790), *PIK3CA* (MIM# 1171834), *MYC* (MIM# 190080), *MYCL1* (MIM# 164850), and *MYCN* (MIM# 164840), as well as inactivating intragenic mutations, homozygous deletions, and promoter hypermethylation at the tumor suppressor genes *BRG1/SMARCA4* (MIM# 603254), *LKB1/STK11* (MIM# 602216), *PTEN* (MIM# 601728), *CDKN2A* (MIM# 600160), *RB1* (MIM# 180200), and *TP53* (MIM# 191170) [Sanchez-Cespedes 2007; Medina et al., 2008]. Some of these gene alterations are known to be specific to lung tumor histologies [Westra et al., 1993; Otterson et al., 1994; Kelley et al., 1995; Sanchez-Cespedes, 2007; Medina et al., 2008]. In addition, it is also well established that some gene alterations are mutually exclusive, as is the case for pairs of genes, such as *KRAS* and *EGFR*, or *CDKN2A* and *RB1* [Otterson et al., 1994; Lynch et al., 2004; Paez et al., 2004], that encode proteins acting in the same signaling pathway. However, a profile of alterations at multiple well-known cancer genes in a large panel of lung cancers has never been reported. This limits our understanding of how gene alterations are distributed among lung tumors and how they interact with one another.

Here, we attempt to delineate the gene-alteration profile of lung cancer cell lines by screening for alterations of seventeen well-known cancer genes, including point mutations at *AKT1* (MIM# 164730) and *EML4-ALK* (MIM# 607442 for *EML4* and MIM# 105590 for *ALK*) fusions, a small inversion within chromosome 2p recently reported in a small subset of non-small-cell lung cancers (NSCLCs) [Carpten et al., 2007; Soda et al., 2007]. We examined the association between the genetic alteration profile and the response to specific small molecule inhibitors.

Additional Supporting Information may be found in the online version of this article. Raquel Blanco and Reika Iwakawa contributed equally to the present work.

*Correspondence to: Montse Sanchez-Cespedes, Cancer Epigenetics and Biology Program-PEBC, Catalan Institute of Oncology (ICO), Bellvitge Biomedical Research Institute (IDIBELL), Hospital Duran i Reynals, Av. Gran Via s/n km 2.7, 08907 - L'Hospitalet de Llobregat-Barcelona, Spain. E-mail: mscscespedes@iconcologia.net

Material and Methods

Cell Lines

Cells were maintained in culture flasks in either DMEM (A549, NCI-H1299, NCI-H23, Calu-3, NCI-H522, and EBC1) or RPMI 1640 (NCI-H446, NCI-H1650, NCI-H460, and NCI-N417) (Invitrogen, Carlsbad, CA) supplemented with 10% (v/v) fetal bovine serum, 2 mM L-glutamine, 50 mg/ml penicillin/streptomycin, and 2.5 µg/ml fungizone. Cultures were kept at 37°C in a humidified atmosphere of 5% CO₂/95% air. DNA, RNA, and protein were extracted using standard protocols.

Screening for Gene Mutations and Deletions

Screening for mutations in *AKT1* (exon 3), *BRAF* (exons 11 and 15), *MET* (MIM# 164860) (exons 16–20), *ERBB2* (exon 20), *EGFR* (exons 18–21), *NRAS* (codons 12, 13, and 61), *PIK3CA* (exons 1, 9, and 20), *PTEN* (exons 2–9), and *CDKN2A* (exons 1–3) was performed by directly sequencing PCR products using primers and conditions that have been previously described [Matsumoto et al., 2007; Angulo et al., 2008; Medina et al., 2008], or that are available upon request. Nucleotide numbering reflects cDNA numbering with +1 corresponding to the A of the ATG transition initiation codon in the reference sequence. We considered the presence of homozygous deletions when there was a reproducible absence of PCR product of one or more consecutive exons. The mutational status of *STK11*, *SMARCA4*, *KRAS*, and *TP53* was either determined for those cases with incomplete/conflicting information or gathered from previous publications [Harbors et al., 1988; Yokota et al., 1988; Otterson et al., 1994; Shimizu et al., 1994; Matsumoto et al., 2007; Angulo et al., 2008] (Supp. Table S1) or from the Wellcome Trust Sanger Institute's Cancer Cell Line Project website (www.sanger.ac.uk/cosmic). In those cases where mutation/deletion data were not available, cells with a reported absence of RB protein expression were classified as *RBI*-mutant. The presence of the *EML4-ALK* fusion gene was tested according to previously published conditions [Soda et al., 2007].

Promoter Hypermethylation

The determination of promoter hypermethylation at *CDKN2A* was evaluated by bisulfite treatment of the genomic DNA and subsequent methylation-specific PCR, using previously published protocols [Esteller et al., 2001].

Real-Time Quantitative Genomic PCR for Determining Gene Amplification

To determine *MET*, *ERBB2*, *MYC*, *MYCL*, and *MYCN* amplification we used quantitative real-time genomic PCR. The conditions and primers used for *MYC*, *MYCN* and *MYCL* have been previously described [Medina et al., 2008]. *ERBB2* and *MET* primers and PCR conditions are available upon request. The copy number of genomic DNA was measured by SYBR green using an ABI Prism 7900 Sequence Detector (Applied Biosystems, Foster City, CA).

Inhibitors and Viability Assay

Rapamycin (mammalian target of rapamycin [mTOR] inhibitor) and LY-294002 (PI3K inhibitor) were obtained from Calbiochem (La Jolla, CA) and PHA665752 (MET inhibitor) from Tocris Bioscience (Ellisville, MI). Erlotinib (N-(3-ethynyl-

phenyl)-6,7-bis(2-methoxyethoxy)-4-quinazolinamine) (EGFR inhibitor) was a gift from Roche Pharmaceuticals (Mannheim, Germany). Erlotinib tablets were ground to powder and dissolved in pure dimethyl sulfoxide (DMSO) to the desired concentration. For the cell-survival assays, cells were seeded at a density of 5,000 cells/well (15,000 cells/well for N417) on 96-well plates. They were allowed to recover for 12 hr before adding the drugs. Cells were exposed to various concentrations of each drug for 48 or 72 hr, and then the viable cell number was measured by the 3-(4,5-dimethylthiazol-2)-2,5-diphenyltetrazolium bromide (MTT) assay. Briefly, 10 µl of a solution of 5 mg/ml MTT (Sigma Chemical, Zwijndrecht, The Netherlands) was added to each well. After incubation for 3 hr at 37°C, the medium was discarded, the formed formazan crystals were dissolved in 100 µl DMSO and absorbance was determined at 596 nm by means of a microplate reader (Bio-Rad, Hercules, CA). Viabilities were expressed as a percentage of the untreated controls. The 50% growth inhibition (IC₅₀) was determined from the dose-response curve. Results are presented as the median of at least two independent experiments performed in triplicate for each cell line and each compound.

Antibodies and Western Blot Analysis

Anti-phospho-AKT (S473), anti-AKT, anti-S6, anti-phospho-S6 (S235/236), anti-phospho-MET (Y1234/Y1235), and anti-MET were obtained from Cell Signaling Technology (Beverly, MA). For western blotting, cells were seeded in 12-well culture plates and, after incubating for 24 hr with the designated drug, were scraped from the dishes into lysis buffer. Forty micrograms (µg) of total protein were separated by SDS-PAGE, transferred to a PVDF membrane, and blotted with the appropriate antibody according to the manufacturer's instructions.

Results

Gene Alteration Profiles of a Lung Cancer Cell Line Panel

To accurately determine the frequency of point mutations and homozygous/intragenic deletions of known cancer genes in lung cancer, avoiding the masking effect of the admixture with nonmalignant cells, we chose to screen cancer cell lines, including small-cell lung cancer (SCLC), squamous cell carcinomas (SCC), adenocarcinomas (AC), large-cell carcinomas (LCC), and carcinoids. Eighty-eight lung cancer cell lines were tested for alterations at 17 genes: *AKT1*, *BRAF*, *MET*, *EGFR*, *ERBB2*, *KRAS*, *STK11*, *MYC*, *MYCL*, *MYCN*, *NRAS*, *PIK3CA*, *PTEN*, *CDKN2A*, *RBI*, and *TP53*, as well as the *EML4-ALK* fusion. Alterations were present in all genes except *AKT1*. The *EML4-ALK* fusion was never detected. A total of 98% (86/88) of the cell lines had alterations of at least at one of the genes tested (Supp. Table S1 and Supp. Fig. S1). As expected, alterations in tumor-suppressor genes were homozygous whereas they were often heterozygous in oncogenes. Although two different heterozygous *TP53* mutations were detected in three cell lines, these mutations are likely to have occurred in each of both alleles resulting in the complete and biallelic inactivation of the *TP53* gene. The frequency of alterations when considering all histological types, from the highest to the lowest, were ranked as follows: *TP53* (79%), *CDKN2A* (59%), *RBI* (35%), *STK11* (27%), *MYC*-family (20%), *KRAS* (17%), *PTEN* (11%), *PIK3CA* (8%), *EGFR* (7%), *NRAS* (6%), *MET* (5%), *BRAF* (2%), and *ERBB2* (2%). The present study does not extend to mutation analysis at another key tumor-suppressor gene, *SMARCA4*, which has recently been found to be frequently altered in NSCLC [Medina

et al., 2008]. Data on the mutation status of *SMARCA4* for some cell lines is also provided in Supp. Table S1.

To determine possible cell culture artifacts we compared the mutational profile of lung cancer cell lines and lung primary tumors. The mutational status of the *TP53*, *STK11*, *KRAS*, *PIK3CA*, *EGFR*, and *BRAF* genes was available for non-small-cell lung primary tumors [Angulo et al., 2008]. The ranking of the most commonly mutated genes in lung primary tumors (*TP53*>*KRAS*>*STK11*>*EGFR*>*PIK3CA*>*BRAF*) was very similar to that in cell lines. However, the frequency of mutations at any gene in primary tumors was about half that in lung cancer cell lines (Supp. Fig. S2), suggesting a reduced effectiveness in the detection of gene alterations in primary tumors, probably due to contamination by normal cells. Alternatively, it is also possible that primary tumors are more heterogeneous than cell lines with respect to the accumulated genetic alterations. Since there are models for stepwise accumulation of genetic alterations both for lung AC and SCC, we can not completely discard that these differences arise as a consequence of different progression stages between the tumors and cell lines analyzed.

Gene Alterations and Histopathological Correlations

The distribution of gene alterations among patient characteristics and tumor histopathologies are summarized in Table 1. As previously described, alterations in *CDKN2A* and *STK11* were preferentially found in NSCLC, whereas alterations in *PTEN*, *RBI*, and in the *MYC* family of genes, especially *MYCL* and *MYCN*, were more common in SCLC. It is also interesting to note that mutations at other components of the *EGFR/KRAS* signal transduction pathway, i.e., *EGFR*, *ERBB2*, *BRAF*, and *NRAS*, predominate in lung AC. The differences did not reach statistical significance probably due to the few number of cell lines with mutations at those genes. However, when combined together, mutations at any of the different components of the *KRAS* pathway (*EGFR*, *ERBB2*, *KRAS*, *NRAS*, and *BRAF*) were significantly more frequent in lung AC as compared to SCCs ($P < 0.05$; Fisher's exact test) and in NSCLC as compared to SCLC ($P < 0.00005$; Fisher's exact test). Alterations at *TP53* were present in a similar frequency in both SCLC and NSCLC, indicating that its inactivation is required for the development of all histopathological types of lung cancer. Although very low frequency, mutations at *PIK3CA* were also found in NSCLC and SCLC. The mutations found in the later correspond to novel variants that need verification.

As previously reported, mutations at *KRAS* and *EGFR* predominate in tumors from Caucasian and Asian patients, respectively. However, a new observation that arises from our study is the accumulation of alterations at the *MYC*-family of gene in tumors from patients of Caucasian origin ($P < 0.05$; Fisher's exact test). No associations were detected between alterations at any gene and gender, or age, nor were gene alterations seen to have accumulated in tumors of older patients. Rather than a definitive observation, the lack of association between the presence of mutations at *EGFR* and *KRAS* with tumors from nonsmokers and smokers, respectively, is likely due to the lack of information on the smoking habit of many the individuals.

Identification of Novel Variants

In addition to well-known somatic mutations with an oncogenic effect within the helical and kinase domains of *PIK3CA* [Samuels et al., 2004; Gymnopoulos et al., 2007; Angulo et al., 2008], we identified two novel variants, both located near well-

characterized mutation hotspots. One of these is an insertion of 387 nt after the termination codon TGA that results in the duplication of amino acids 1,051 to 1,068 (Fig. 1B) and the other is a p.D1029Y substitution. Since no matched normal DNA was available for these cell lines, we could not test whether these mutations are germline polymorphisms or tumor-specific mutations. Four cell lines carried *MET* alterations, including gene amplification and two novel variants, p.L1158F (in the HCC15 cells) and p.T1259K (in the H1963 cells) (Fig. 1B and C). Again, due to the lack of normal matched DNA for these cell lines we could not verify the somatic nature of the amino acid substitutions. However, the absence of constitutive *MET* activation indicated by the lack of pMET^{Y1234/Y1235} in these cell lines strongly argues against an oncogenic role for the variants (Fig. 1D). The H441, Calu3, HCC366, and HCC78 cells that were reported to have high levels of pMET^{Y1234/Y1235} [Rikova et al., 2007] did not feature gene amplification or point mutations within the hotspots tested here.

Cooperation of Several Biological Pathways in Lung Carcinogenesis

It is widely accepted that alterations of genes in the same biological pathways are not redundant in cancer cells. Accordingly, genes that are altered in a mutually exclusive manner are likely to encode proteins that act in the same biological pathway. This hypothesis has been extensively borne out in lung cancer cells by the lack of concomitant alterations at *RBI* and *CDKN2A*, and at *EGFR* and *KRAS*. Our data also confirm the mutually exclusive nature of these pairs of alterations (Fig. 1A). Likewise, alterations at *ERBB2* and *NRAS* did not occur in the same cell lines or in cells carrying *EGFR* and *KRAS* mutations, consistent with their participation in the same signal transduction pathway. *PTEN* and *PIK3CA*, which are both encoding proteins that modulate the intracellular levels of the phosphoinositide-3,4,5-trisphosphate (PIP3), were also found to be mutated in a mutually exclusive manner. Only one cell line, Lu134, with a homozygous deletion at *PTEN*, had a concomitant change at *PIK3CA*. The *PIK3CA* variant is a p.D1029Y substitution, which has not been described before and for which there is no evidence of its somatic nature. On the other hand, there were concomitant *BRAF*- and *NRAS*-activating mutations in the H2087 lung adenocarcinoma cells. The somatic nature of the p.L597V mutation in *BRAF* was confirmed after sequencing the DNA of the corresponding lymphoblastoid line (BL-H2087). On the other hand, simultaneous mutations in signal transduction pathways that are known to converge in the modulation of mTOR activity, such as *MET*, *PIK3CA/PTEN*, *STK11*, and *KRAS/EGFR/NRAS/ERBB2*, were present in some cell lines, implying cooperation in cancer development. Namely, 17 (28%) of the 61 NSCLC cell lines carried single mutations, whereas 16 (26%) and two (3%) of them carried double and triple mutations, respectively, in any of this group of genes.

Correlation of Acquired Genetic Alterations With Sensitivity to Small Molecule Inhibitors

To understand a possible effect of these genetic alterations on the primary resistance to tyrosine kinase inhibitors (TKIs) and other small molecule inhibitors, we selected a panel of 10 lung cancer cell lines with a known genetic background for *KRAS*, *STK11*, *EGFR*, *PTEN*, *PIK3CA*, and *MET*, and tested the sensitivity to treatment with inhibitors of PI3K (LY294002), mTOR (rapamycin), *MET* (PHA665752), and *EGFR* (erlotinib). As

Table 1. Distribution of the Indicated Mutations Among the Different Characteristics of the Lung Cancer Cell Lines

	TP53		CDKN2A		RBI		STK11		ANY (MYC, MYCL, MYCN)		KRAS ^a		PTEN		PIK3CA		EGFR ^b		NRAS ^b		MET		BRAF ^b		ERBB2 ^b		ANY (KRAS, EGFR, NRAS, BRAF, ERBB2)		
	WT	MUT	WT	MUT	WT	MUT	WT	MUT	WT	MUT	WT	MUT	WT	MUT	WT	MUT	WT	MUT	WT	MUT	WT	MUT	WT	MUT	WT	MUT	WT	MUT	
Total	17	70	36	52	47	26	63	24	70	18	72	15	78	10	81	7	82	6	83	5	81	4	86	2	86	2	57	29	
	80%		59%		36%		31%		20%		17%		11%		8%		7%		6%		5%		2%		2%		33%		
Age (years)																													
≤40	10	9	3	7	5	1	7	3	10	0	6	3	8	2	10	0	5	2	7	0	9	1	7	0	6	1	4	6	
40–60	38	10	17	21	24	12	27	11	27	11	14	5	35	3	37	1	15	2	16	1	36	2	15	1	16	1	24	13	
≥60	30	3	15	15	12	10	23	6	25	5	10	3	25	5	27	3	9	0	8	2	29	1	10	1	10	0	24	6	
Gender																													
Female	17	5	7	10	8	4	11	6	13	4	5	4	15	2	16	1	9	1	9	1	16	0	9	1	9	1	9	7	
Male	66	7	28	38	38	19	49	16	52	14	27	9	58	8	60	6	23	4	25	2	61	3	26	1	26	1	48	18	
Origin																													
Asian	32	5	12	20	19	6	24	8	30	2	17	2	29	3	29	3	10	5	14	2	31	1	15	0	15	0	23	8	
Black	5	0	3	2	2	3	4	1	4	1	1	1	5	0	5	0	2	0	2	0	3	1	2	0	2	0	4	1	
Caucasian	38	9	19	19	22	14	28	9	27	11	12	7	31	7	36	2	15	1	14	2	36	0	14	2	14	2	24	14	
									$P < 0.05^*$								$P < 0.07^*$												
Smoker																													
Yes	34	7	21	13	16	16	26	7	25	9	10	4	27	7	33	1	11	1	11	1	30	2	10	2	11	1	23	11	
No	9	1	8	2	7	7	8	1	8	1	4	2	8	1	8	1	4	0	3	1	8	0	4	0	4	0	6	3	
HIST																													
AC	39	6	33	8	31	1	24	15	34	5	30	9	38	1	37	2	33	6	36	3	38	1	37	2	37	2	18	21	
SCC	13	2	11	3	10	6	9	4	12	1	12	1	11	2	12	1	13	0	12	1	11	0	13	0	13	0	11	2	
									$P = 0.15$																		$P < 0.05$		
LCC	9	2	7	2	7	1	5	4	7	2	5	4	8	1	7	2	9	0	8	1	9	0	9	0	9	0	4	5	
SCLC	24	6	17	22	2	19	23	0	15	9	24	0	19	5	22	2	24	0	24	0	23	1	24	0	24	0	23	0	
Others ^c	3	1	2	1	2	1	2	1	2	1	2	1	2	1	3	0	3	0	3	0	1	0	3	0	3	0	2	1	
HIST																													
NSCLC	61	9	52	13	48	44	3	38	23	53	8	47	13	57	4	56	5	55	6	56	5	58	3	59	2	59	2	35	29
SCLC	24	6	17	22	2	19	23	0	15	9	23	0	19	5	22	2	24	0	24	0	23	1	24	0	24	0	23	0	
									$P < 0.05$																		$P < 0.00005$		

^aAnalysis performed only for the adenocarcinoma and large-cell carcinoma cell lines.

^bAnalysis performed only for the adenocarcinoma cell lines.

^cIncludes the following categories: one mesothelioma, one carcinoma, and one neuroendocrine.

*Asian vs. Caucasian comparison.

HIST, histopathological type.

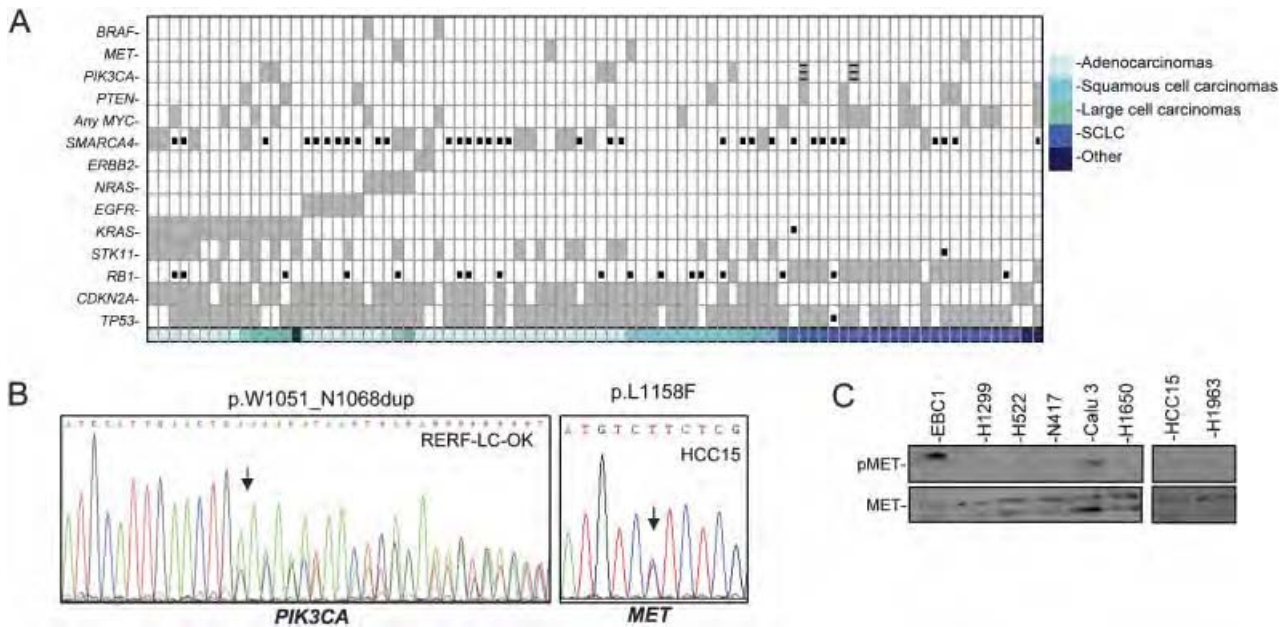


Figure 1. Gene alterations in lung cancer cell lines. **A:** Profile of genes altered in human lung cancer cell lines. The presence of alterations is indicated by gray bars. Black squares indicate no data. The black lines in the *PIK3CA* oncogene refer to the two variants of unknown oncogenic potential. The histopathology is also shown. **B:** *PIK3CA* and *MET* variants in the RERF-LC-OK and HCC15 cell lines. Nucleotide numbering reflects cDNA numbering with +1 corresponding to the A of the ATG transition initiation codon in the reference sequence. **C:** *MET* gene amplification in lung cancer cell lines revealed by quantitative PCR. The relative *MET* copy number was determined by comparison with an unrelated control locus, *MDH2*, on chromosome 7q11. Cells with *MET* amplification are indicated with an arrow. **D:** Western blot anti-phospho-MET (pMET^{Y1234/Y1235}) and anti-MET (MET) in the indicated cell lines. Constitutive MET activation is present in the EBC-1 and Calu-3 cells, but not in the HCC15 and H1963 cells, which carry gene variants of unknown biological significance.

subrogate markers to test the ability of the drug to inhibit its target molecule we measured the levels of pAKT^{Ser473} (for PI3K and EGFR inhibitors), pS6^{Ser235/236} (for mTOR inhibitor), and pMET^{Y1234/Y1235} (for MET inhibitor). The calculated IC₅₀ for the different compounds is summarized in Figure 2A. A marked genotype–drug sensitivity association was observed for the Calu-3 and EBC-1 cells, which were highly responsive to growth inhibition triggered by erlotinib and PHA665752 compounds, respectively. The effectiveness of these treatments was also measured by their ability to decrease phosphorylation at their target molecules or at downstream effectors (Fig. 2B). We did not observe a low IC₅₀ in response to treatment with PHA665752, in the H1963 or HCC15 cell lines (data not shown). These carry amino acid substitutions at the tyrosine kinase domain of *MET*, which is further indication that these variants are not functionally significant. Similarly, the Calu-3 cells that carry high levels of MET phosphorylation (Fig. 1D) but do not exhibit gene amplification or mutations were insensitive to PHA665752. Interestingly, the H522 cells evidenced a strong sensitivity to PHA665752. These cells neither carry amplification/point mutations at *MET* nor MET phosphorylation. Thus, the characterization of the gene alterations underlying the sensitivity of these cells to MET inhibitors will be of interest. Although the differences were not as marked, we also noted that sensitivity to LY294002, as indicated by the lower IC₅₀, was increased in the H446 and N417 cell lines, both of which are *PTEN*-deficient. Similarly, the lowest IC₅₀ to rapamycin was observed for the N417, H446, EBC-1, and Calu-3 cells (Fig. 2A and B). Some of these cells carry constitutive activation of AKT due to the presence of *PTEN* inactivation (the N417 and H446), or to *ERBB2* gene amplification (Calu-3). Intriguingly, the triple mutant *KRAS-STK11-PIK3CA* (H460) and *EGFR-PTEN* (H1650) cells were extremely resistant to rapamycin, LY294002, and erlotinib. Thus, we investigated the effect of the

combined treatment with erlotinib and LY294002 on cell growth, and found that the addition of erlotinib significantly increased the efficiency of cell-growth inhibition of the LY294002 compound in H1650 cells, but not in H460 cells (Fig. 3A and B).

Discussion

We provide a detailed gene-alteration profile of lung cancer cells of distinct histologies. In full compliance with Knudson's two-hit hypothesis [Knudson, 1971], mutations in tumor suppressors, but not in oncogenes, were always homozygous. We also confirmed the disproportionately high frequency of occurrence of some gene alterations in specific histological types, which probably reflects differences in the cell type of origin. The overall profile of genes mutated in lung cancer was comparable between lung primary tumors and lung cancer cell lines. However, the frequency of mutations at any gene was higher in cell lines, which strongly implies a masking effect due to the admixture of nonmalignant cells that hinders the detection of point mutations and insertions/deletions in the primary tumors. This obstacle has been noted before [Sanchez-Cespedes, 2007; Thomas et al., 2006] and is a significant problem that may be solved by the use of a novel generation of sequencers [Thomas et al., 2006], or by other technical approaches like careful microdissection of tumor cells.

TP53 was the most frequently altered gene in the lung cancer cell lines. Nearly 80% of the cell lines carry alterations of this tumor suppressor. Similarly, alterations at the cell cycle components, either *RB* or *CDKN2A*, were also extremely common. The high frequency of *TP53* and *CDKN2A/RB1* alterations in all histopathologies is a demonstration of their important role in lung cancer development. It is tempting to speculate that *TP53* and *CDKN2A/RB1* inactivation in lung cancer may be universal and are thus a requisite for the evolution of lung tumors.

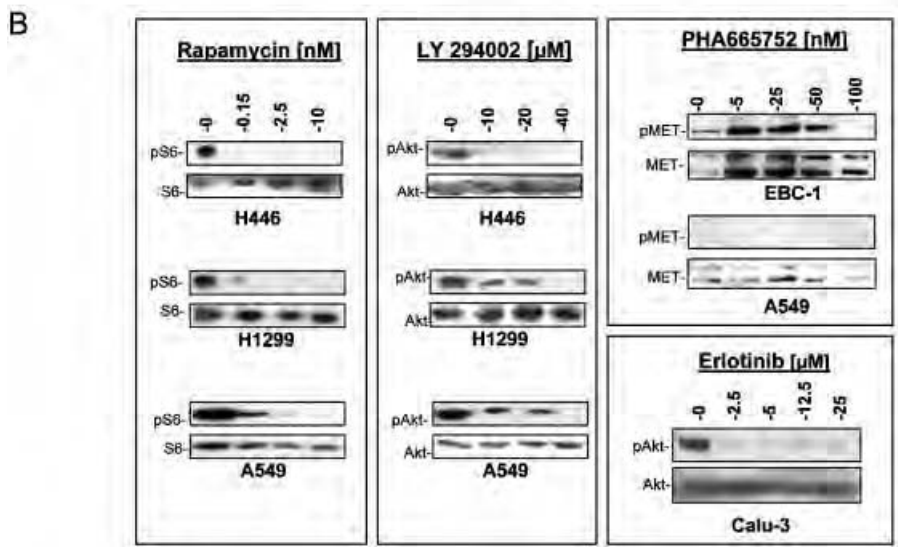
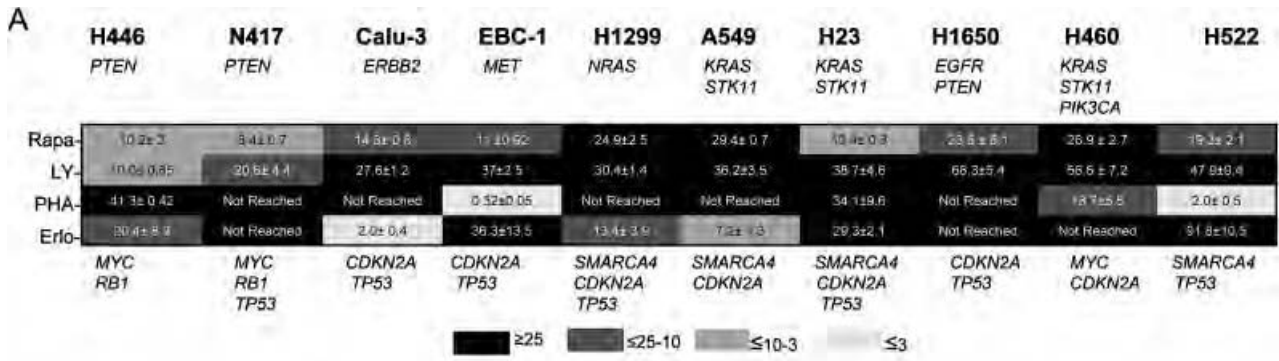


Figure 2. Genotype of the cell lines and sensitivity to specific inhibitors. **A:** The IC₅₀ (μM) for each compound (RAPA, rapamycin; LY, LY294002, PHA, PHA665752; and Erlotinib) is indicated within the boxes. Treatments were applied for 72 hr. **B:** Immunoblotting analysis depicting the decreased phosphorylation of the indicated protein upon administering increasing concentrations of the compound. Treatments were applied for 24 hr.

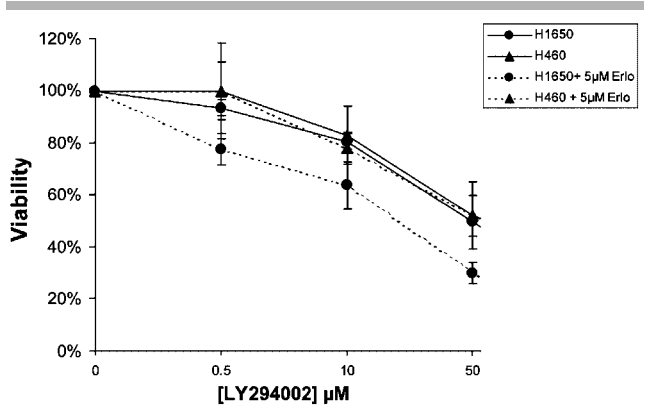


Figure 3. Cell-growth inhibition upon administering combined LY294002 and erlotinib treatment. Lines represent the cell survival relative to untreated controls of the MTT assays in the H1650 and H460 cells treated with increasing concentrations of LY294002, alone or with 5 μM erlotinib for 72 hr. Error bars indicate the standard deviation of three replicates.

Conversely, alterations at some oncogenes, such as *BRAF*, *ERBB2*, and *MET*, were infrequent.

It was remarkable the differences in the activation of components of the *KRAS* pathway among the lung cancer

histopathologies. While alterations at any of the *BRAF*, *EGFR*, *ERBB2*, *KRAS*, or *NRAS* was significantly more common in AC as compared to SCC, virtually none of the SCLC carry alterations at any of those genes. This strongly points out towards completely different mechanisms of carcinogenesis for NSCLC and SCLC and likely accounts for the distinct clinical behavior of both types of lung cancer.

Although mutations outside the hotspots may increase the frequency of alterations at these genes to some extent, it seems certain that their contribution will be confined to a small subset of lung tumors. However, given that the encoded proteins are targets for small molecule inhibitors, the context in which these mutations arise (e.g., histological type, concomitant mutations at other genes) needs to be better understood. We confirmed the lack of concomitant mutations in those genes encoding proteins acting in the same biological pathway, such as *CDKN2A/RB1*, *KRAS/EGFR/ERBB2*, and *PIK3CA/PTEN*. Apart from these, simultaneous alterations were found in most of the other genes. Intriguingly, we also found that *BRAF-NRAS*, were genetically altered in the same cells, suggesting that the collaboration of the encoded proteins affects the development of the cancer. Similarly, it was previously reported that *BRAF* mutations involving codons other than 600 or 601 were highly likely to co-occur with a RAS family mutation [Thomas et al., 2007]. It is interesting to note the frequent concomitant activation of signal transduction pathways

that converge in the modulation of mTOR activity upon different stimuli, such as *KRAS/EGFR/ERBB2*, *PIK3CA/PTEN*, and *STK11* [Corradetti and Guan, 2006].

Selective small inhibitors against molecules that participate in different signaling pathways have been approved or are at various stages of development for clinical use in cancer patients. In this new scenario of targeted therapies, the response to a given therapeutic drug is likely to depend on the genetic background of the tumor. Similarly to previous observations [McDermott et al., 2007], our present results show how lung cancer cells with single alterations at *MET*, *PTEN*, or *ERBB2/EGFR* are sensitive to *MET* (PHA665752), *PI3K* (LY294002), and *EGFR* (erlotinib) inhibitors, respectively. However, this does not hold true in cells with activation of multiple signaling pathways, suggesting that there are interconnections among pathways that enable cells to bypass the negative effects on cell growth triggered by the small inhibitor. We found that in the originally resistant *EGFR/PTEN* double-mutant cells, erlotinib sensitized the cells to the effect of the LY294002 compound, which suggests that the use of drug combination strategies could improve sensitivity to specific therapies. Current efforts to understand the mechanisms of tumor resistance, especially to TKIs in lung cancer, further support this hypothesis [Rikova et al., 2007; Engelman et al., 2007]. Guo et al. [2008] reported that in *EGFR*-mutant cells which are sensitive to *EGFR* inhibitors, *EGFR* drives other receptors tyrosine kinases (RTKs) and a network of downstream signaling that collapse with drug treatment. In these cells, secondary drug resistance appears through the generation of novel gene alterations at another RTK, *MET*, preventing such collapse and thus bypassing the inhibitory effect of the drug. Taken together these observations are strong evidence that different signal transduction pathways assemble in networks, through the use of some common components. Beyond the contribution to the understanding of cell biology, our observations draw attention to the need to stratify tumors according to their genotype and histology and suggest that the combination of pathway-selective therapies will eventually be required for the treatment of many solid tumors.

Acknowledgments

We would like to acknowledge the support of Spanish Ministerio de Educación (SAF2005-00626) and Instituto de Salud Carlos III (RTICC), Grants-in-Aid from the Ministry of Health, Labor and Welfare for the 3rd-term Comprehensive 10-years Strategy for Cancer Control and for Cancer Research (16-1), a Grant-in-Aid for the Program for Promotion of Fundamental studies in Health Sciences of the National Institute of Biomedical Innovation (NiBio), NCI Lung Cancer SPORE (P50CA70907), and DOD PROSPECT (W81XWH-07-1-0306). R.B. is supported by a postdoctoral contract from the Fondo de Investigaciones Sanitarias (FIS). We also acknowledge the technical assistance of the Genomics Unit at the CNIO.

References

Angulo B, Suarez-Gauthier A, Lopez-Rios F, Medina PP, Conde E, Tang M, Soler G, Lopez-Encuentra A, Cigudosa JC, Sanchez-Cespedes M. 2008. Expression signatures in lung cancer show a profile for *EGFR*-mutant tumors and identifies selective *PIK3CA* overexpression by gene amplification. *J Pathol* 214:347–356.

Carpten JD, Faber AL, Horn C, Donoho GP, Briggs SL, Robbins CM, Hostetter G, Boguslawski S, Moses TY, Savage S, Uhlik M, Lin A, Du J, Qian YW, Zeckner DJ, Tucker-Kellogg G, Touchman J, Patel K, Mousset S, Bittner M, Schevitz R, Lai MH, Blanchard KL, Thomas JE. 2007. A transforming mutation in the pleckstrin homology domain of *AKT1* in cancer. *Nature* 448:439–444.

Carrtero J, Medina PP, Pio R, Montuenga LM, Sanchez-Cespedes M. 2004. Novel and natural knockout lung cancer cell lines for the *LKB1/STK11* tumor suppressor gene. *Oncogene* 23:4037–4040.

Corradetti MN, Guan KL. 2006. Upstream of the mammalian target of rapamycin: do all roads pass through mTOR? *Oncogene* 25:6347–6360.

Engelman JA, Zejnullahu K, Mitsudomi T, Song Y, Hyland C, Park JO, Lindeman N, Gale CM, Zhao X, Christensen J, Kosaka T, Holmes AJ, Rogers AM, Cappuzzo F, Mok T, Lee C, Johnson BE, Cantley LC, Janne PA. 2007. *MET* amplification leads to gefitinib resistance in lung cancer by activating *ERBB3* signaling. *Science* 316:1039–1043.

Esteller M, Corn PG, Baylin SB, Herman JG. 2001. A gene hypermethylation profile of human cancer. *Cancer Res* 61:3225–3229.

Forbes S, Clements J, Dawson E, Bamford S, Webb T, Dogan A, Flanagan A, Teague J, Wooster R, Futreal PA, Stratton MR. 2006. COSMIC 2005. *Br J Cancer* 94:318–322.

Fujita T, Kiyama M, Tomizawa Y, Kohno T, Yokota J. 1999. Comprehensive analysis of *p53* gene mutation characteristics in lung carcinoma with special reference to histological subtypes. *Int J Oncol* 15:927–934.

Greenman C, Stephens P, Smith R, Dalgleish GL, Hunter C, Bignell G, Davies H, Teague J, Butler A, Stevens C, Edkins S, O'Meara S, Vastrik I, Schmidt EE, Avis T, Barthorpe S, Bhamra G, Buck G, Choudhury B, Clements J, Cole J, Dicks E, Forbes S, Gray K, Halliday K, Harrison R, Hills K, Hinton J, Jenkinson A, Jones D, Menzies A, Mironenko T, Perry J, Raine K, Richardson D, Shepherd R, Small A, Tofts C, Varian J, Webb T, West S, Widawa S, Yates A, Cahill DP, Louis DN, Goldstraw P, Nicholson AG, Brasseur F, Looijenga L, Weber BL, Chiew YE, DeFazio A, Greaves MF, Green AR, Campbell P, Birney E, Easton DF, Chenevix-Trench G, Tan MH, Khoo SK, Teh BT, Yuen ST, Leung SY, Wooster R, Futreal PA, Stratton MR. 2007. Patterns of somatic mutation in human cancer genomes. *Nature* 446:153–158.

Guo A, Villén J, Kornhauser J, Lee KA, Stokes MP, Rikova K, Possemato A, Nardone J, Innocenti G, Wetzel R, Wang Y, MacNeill J, Mitchell J, Gygi SP, Rush J, Polakiewicz RD, Comb MJ. 2008. Signaling networks assembled by oncogenic *EGFR* and *c-Met*. *Proc Natl Acad Sci USA* 105:692–697.

Gymnopoulos M, Elsliger MA, Vogt PK. 2007. Rare cancer-specific mutations in *PIK3CA* show gain of function. *Proc Natl Acad Sci USA* 104:5569–5574.

Harbors JW, Lai SL, Whang-Peng J, Gazdar AF, Minna JD, Kaye FJ. 1988. Abnormalities in structure and expression of the human retinoblastoma gene in SCLC. *Science* 241:353–357.

Horowitz JM, Park SH, Bogenmann E, Cheng JC, Yandell DW, Kaye FJ, Minna JD, Dryja TP, Weinberg RA. 1990. Frequent inactivation of the retinoblastoma anti-oncogene is restricted to a subset of human tumor cells. *Proc Natl Acad Sci USA* 87:2775–2779.

Kashii T, Mizushima Y, Monno S, Nakagawa K, Kobayashi M. 1994. Gene analysis of *K-*, *H-ras*, *p53*, and retinoblastoma susceptibility genes in human lung cancer cell lines by the polymerase chain reaction/single-strand conformation polymorphism method. *J Cancer Res Clin Oncol* 120:143–148.

Kaye FJ, Kratzke RA, Gerster JL, Horowitz JM. 1990. A single amino acid substitution results in a retinoblastoma protein defective in phosphorylation and oncoprotein binding. *Proc Natl Acad Sci USA* 87:6922–6926.

Kelley MJ, Nakagawa K, Steinberg SM, Mulshine JL, Kamb A, Johnson BE. 1995. Differential inactivation of *CDKN2* and *Rb* protein in non-small-cell and small-cell lung cancer cell lines. *J Natl Cancer Inst* 87:756–761.

Knudson AG. 1971. Mutations and cancer: statistical study of a retinoblastoma. *Proc Natl Acad Sci USA* 68:820–823.

Lynch TJ, Bell DW, Sordella R, Gurubhagavata S, Okimoto RA, Brannigan BW, Harris PL, Haslerat SM, Supko JG, Haluska FG, Louis DN, Christiani DC, Settleman J, Haber DA. 2004. Activating mutations in the epidermal growth factor receptor underlying responsiveness of non-small-cell lung cancer to gefitinib. *N Engl J Med* 350:2129–2139.

Matsumoto S, Iwakawa R, Takahashi K, Kohno T, Nakanishi Y, Matsuno Y, Suzuki K, Nakamoto M, Shimizu E, Minna JD, Yokota J. 2007. Prevalence and specificity of *STK11* genetic alterations in lung cancers. *Oncogene* 26:5911–5918.

McDermott U, Sharma SV, Dowell L, Greninger P, Montagut C, Lamb J, Archibald H, Raudales R, Tam A, Lee D, Rothenberg SM, Supko JG, Sordella R, Ulkus LE, Iafraite AJ, Maheswaran S, Njauw CN, Tsao H, Drew L, Hanke JH, Ma XJ, Erlander MG, Gray NS, Haber DA, Settleman J. 2007. Identification of genotype-correlated sensitivity to selective kinase inhibitors by using high-throughput tumor cell line profiling. *Proc Natl Acad Sci USA* 104:19936–19941.

Medina PP, Romero OA, Kohno T, Montuenga LM, Pio R, Yokota J, Sanchez-Cespedes M. 2008. Frequent *BRG1/SMARCA4*-inactivating mutations in human lung cancer cell lines. *Human Mut* 29:617–622.

Mitsudomi T, Viallet J, Mulshine JL, Linnola RI, Minna JD, Gazdar AF. 1991. Mutations of *ras* genes distinguish a subset of non-small-cell lung cancer cell lines from small-cell lung cancer cell lines. *Oncogene* 6:1353–1362.

Mitsudomi T, Steinberg SM, Nau MM, Carbone D, D'Amico D, Bodner S, Oie HK, Linnola RI, Mulshine JL, Minna JD, Gazdar AF. 1992. *p53* gene mutations in non-small-cell lung cancer cell lines and their correlation with the presence of *ras* mutations and clinical features. *Oncogene* 7:171–180.

- Mori N, Yokota J, Akiyama T, Sameshima Y, Okamoto A, Mizoguchi H, Toyoshima K, Sugimura T, Terada M. 1990. Variable mutations of the RB gene in small-cell lung carcinoma. *Oncogene* 5:1713–1717.
- Murakami Y, Katahira M, Makino R, Hayashi K, Hirohashi S, Sekiya T. 1991. Inactivation of the retinoblastoma gene in a human lung carcinoma cell line detected by single-strand conformation polymorphism analysis of the polymerase chain reaction product of cDNA. *Oncogene* 6:37–42.
- Otterson GA, Kratzke RA, Coxon A, Kim YW, Kaye FJ. 1994. Absence of p16INK4 protein is restricted to the subset of lung cancer lines that retains wildtype RB. *Oncogene* 9:3375–3378.
- Paez JG, Janne PA, Lee JC, Tracy S, Greulich H, Gabriel S, Herman P, Kaye FJ, Lindeman N, Boggon TJ, Naoki K, Sasaki H, Fujii Y, Eck MJ, Sellers WR, Johnson BE, Meyerson M. 2004. EGFR mutations in lung cancer: correlation with clinical response to gefitinib therapy. *Science* 304:1497–1500.
- Phelps RM, Johnson BE, Ihde DC, Gazdar AF, Carbone DP, McClintock PR, Linnoila RI, Matthews MJ, Bunn Jr PA, Carney D, Minna JD, Mulshine JL. 1996. NCI-Navy Medical Oncology Branch cell line data base. *J Cell Biochem Suppl* 24:32–91.
- Rikova K, Guo A, Zeng Q, Possemato A, Yu J, Haack H, Nardone J, Lee K, Reeves C, Li Y, Hu Y, Tan Z, Stokes M, Sullivan L, Mitchell J, Wetzell R, Macneill J, Ren JM, Yuan J, Bakalarski CE, Villen J, Kornhauser JM, Smith B, Li D, Zhou X, Gygi SP, Gu TL, Polakiewicz RD, Rush J, Comb MJ. 2007. Global survey of phosphotyrosine signaling identifies oncogenic kinases in lung cancer. *Cell* 131:1190–1203.
- Sameshima Y, Matsuno Y, Hirohashi S, Shimosato Y, Mizoguchi H, Sugimura T, Terada M, Yokota J. 1992. Alterations of the p53 gene are common and critical events for the maintenance of malignant phenotypes in small-cell lung carcinoma. *Oncogene* 7:451–457.
- Samuels Y, Wang Z, Bardelli A, Silliman N, Ptak J, Szabo S, Yan H, Gazdar A, Powell SM, Riggins GJ, Willson JK, Markowitz S, Kinzler KW, Vogelstein B, Velculescu VE. 2004. High frequency of mutations of the PIK3CA gene in human cancers. *Science* 304:554.
- Sanchez-Cespedes M. 2003. Dissecting the genetic alterations involved in lung carcinogenesis. *Lung Cancer* 40:111–121.
- Sanchez-Cespedes M. 2007. A role for LKB1 gene in human cancer beyond the Peutz-Jeghers syndrome. *Oncogene* 26:7825–7832.
- Schauer IE, Siriwardana S, Langan TA, Sclafani RA. 1994. Cyclin D1 overexpression vs. retinoblastoma inactivation: implications for growth control evasion in non-small cell and small cell lung cancer. *Proc Natl Acad Sci USA* 91:7827–7831.
- Shapiro GI, Edwards CD, Kobzik L, Godleski J, Richards W, Sugarbaker DJ, Rollins BJ. 1995. Reciprocal Rb inactivation and p16INK4 expression in primary lung cancers and cell lines. *Cancer Res* 55:505–509.
- Shimizu E, Coxon A, Otterson GA, Steinberg SM, Kratzke RA, Kim YW, Fedorko J, Oie H, Johnson BE, Mulshine JL, et al. 1994. RB protein status and clinical correlation from 171 cell lines representing lung cancer, extrapulmonary small cell carcinoma, and mesothelioma. *Oncogene* 9:2441–2448.
- Sjoblom T, Jones S, Wood LD, Parsons DW, Lin J, Barber TD, Mandelker D, Leary RJ, Ptak J, Silliman N, Szabo S, Buckhaults P, Farrell C, Meeh P, Markowitz SD, Willis J, Dawson D, Willson JK, Gazdar AF, Hartigan J, Wu L, Liu C, Parmigiani G, Park BH, Bachman KE, Papadopoulos N, Vogelstein B, Kinzler KW, Velculescu VE. 2006. The consensus coding sequences of human breast and colorectal cancers. *Science* 314:268–274.
- Soda M, Choi YL, Enomoto M, Takada S, Yamashita Y, Ishikawa S, Fujiwara S, Watanabe H, Kurashina K, Hatanaka H, Bando M, Ohno S, Ishikawa Y, Aburatani H, Niki T, Sohara Y, Sugiyama Y, Mano H. 2007. Identification of the transforming EML4-ALK fusion gene in non-small-cell lung cancer. *Nature* 448:561–566.
- Sumitomo K, Shimizu E, Shinohara A, Yokota J, Sone S. 1999. Activation of RB tumor suppressor protein and growth suppression of small cell lung carcinoma cells by reintroduction of p16INK4 gene. *Int J Oncol* 14:1075–1080.
- Thomas RK, Nickerson E, Simons JF, Janne PA, Tengs T, Yuza Y, Garraway LA, LaFramboise T, Lee JC, Shah K, O'Neill K, Sasaki H, Lindeman N, Wong KK, Borras AM, Gutmann EJ, Dragnev KH, DeBiasi R, Chen TH, Glatt KA, Greulich H, Desany B, Lubeski CK, Brockman W, Alvarez P, Hutchison SK, Leamon JH, Ronan MT, Turenchalk GS, Egholm M, Sellers WR, Rothberg JM, Meyerson M. 2006. Sensitive mutation detection in heterogeneous cancer specimens by massively parallel picoliter reactor sequencing. *Nat Med* 12:852–855.
- Thomas RK, Baker AC, DeBiasi RM, Winckler W, Laframboise T, Lin WM, Wang M, Feng W, Zander T, MacConaill L, Lee JC, Nicoletti R, Hatton C, Goyette M, Girard L, Majumdar K, Ziaugra L, Wong KK, Gabriel S, Beroukhi R, Peyton M, Barretina J, Dutt A, Emery C, Greulich H, Shah K, Sasaki H, Gazdar A, Minna J, Armstrong SA, Mellinghoff IK, Hodi FS, Dranoff G, Mischel PS, Cloughesy TF, Nelson SF, Liau LM, Mertz K, Rubin MA, Moch H, Loda M, Catalona W, Fletcher J, Signoretti S, Kaye F, Anderson KC, Demetri GD, Dummer R, Wagner S, Herlyn M, Sellers WR, Meyerson M, Garraway LA. 2007. High-throughput oncogene mutation profiling in human cancer. *Nat Genet* 39:347–351.
- Wang Z, Shen D, Parsons DW, Bardelli A, Sager J, Szabo S, Ptak J, Silliman N, Peters BA, van der Heijden MS, Parmigiani G, Yan H, Wang TL, Riggins G, Powell SM, Willson JK, Markowitz S, Kinzler KW, Vogelstein B, Velculescu VE. 2004. Mutational analysis of the tyrosine phosphatome in colorectal cancers. *Science* 304:1164–1166.
- Westra WH, Slebos RJ, Offerhaus GJ, Goodman SN, Evers SG, Kensler TW, Askin FB, Rodenhuis S, Hruban RH. 1993. K-ras oncogene activation in lung adenocarcinomas from former smokers. Evidence that K-ras mutations are an early and irreversible event in the development of adenocarcinoma of the lung. *Cancer* 72:432–438.
- Yandell DW, Campbell TA, Dayton SH, Petersen R, Walton D, Little JB, McConkie-Rosell A, Buckley EG, Dryja TP. 1989. Oncogenic point mutations in the human retinoblastoma gene: their application to genetic counseling. *N Engl J Med* 321:1689–1695.
- Yokota J, Akiyama T, Fung YK, Benedict WF, Namba Y, Hanaoka M, Wada M, Terasaki T, Shimosato Y, Sugimura T, Terada M. 1988. Altered expression of the retinoblastoma (RB) gene in small-cell carcinoma of the lung. *Oncogene* 3:471–475.

Background

The Challenge

The Lung Cancer SPORE at The University Texas MD Anderson Cancer Center and Southwestern Medical School requires the integration of heterogeneous multi-institutional sources comprising both molecular and clinical data.

The Technology

We describe a novel method for converging domain specific experimental ontologies that relies on propagating permissions in Resource Description Framework (RDF) triplets rather than the single access point of conventional relational databases.

The challenge is addressed by combining Semantic Web data reposition with code distribution. The S3DB Core Model [1,2] was used to represent each data element on the Lung Cancer Dataset as RDF triples.

Conclusions

The use of the traditional web 1.0 tools to manage translational datasets is not appropriate as they typically include not only clinical but molecular data as well.

Using a Semantic Web management model for integration such as S3DB, experimental data may be queried using Semantic Web Technologies such as, for example, SPARQL, the query language for RDF.

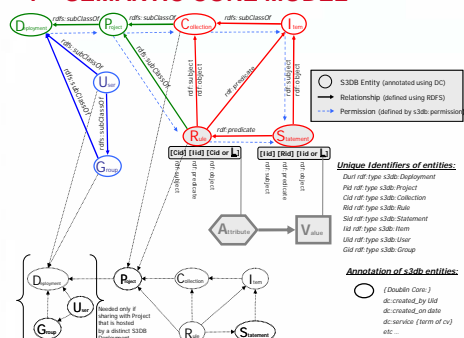
Publications

[1] Almeida JS, C Chen, R Gorlitsky, R Stanislaus, M Aires-de-Sousa, P Eleuterio, JA Carrico, A Maretzek, A Bohn, A Chang, F Zhang, R Mitra, GB Mills, X Wang, HF Deus (2006) Data integration gets 'Sloppy'. Nature Biotechnology 24(9): 1070-1071. [PMID: 16964209].

[2] Deus FH, R Stanislaus1, DF Veiga, C Behrens, II Wistuba, JD Minna, HR Garner, SG Swisher, JA Roth, AM Correa, B Broom, K Coombes, A Chang, LH Vogel, JS Almeida (2008) A Semantic Web management model for integrative biomedical informatics. PLoS ONE. Aug 13; 3(8):e2946 [PMID: 18698353].

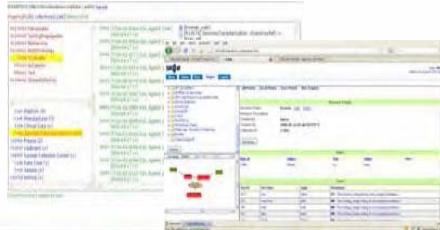
Software Design Patterns

1 – SEMANTIC CORE MODEL



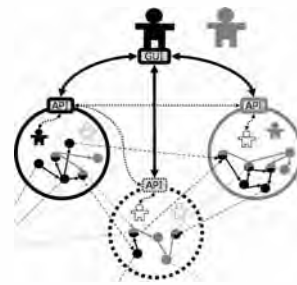
Core data model developed for S3DB (supported by version 3.0 onwards). This diagram can be read starting from the most fundamental data unit, the Attribute-Value pair (filled hexagonal and square symbols). Each element of the pair is object of two distinct triples, one describing the domain of discourse, the **Rules**, and the other made of **Statements** where that domain is populated to instantiate relationships between entities. The latter includes the actual **Values**. Surrounding these two nuclear collection of triples, is the resolution of **Collection** and its instantiation as Item that define the relationship between the individual elements of **Rules** and **Statements**. The resulting structure is then organized in **Projects** in such a way that the domain of discourse can nevertheless be shared with other **Projects**, in the same or in a distinct deployment of S3DB. Finally, a propagation of **User** permissions (dashed line) is defined such that the distribution of the data structures can be traced.

Generic interfaces



2 – PERMISSION MIGRATION AND DATA ACCESS

Distinct users, with identities (solid icon) managed in distinct S3DB deployments (circular compartments), which they control separately, share a distributed and overlapping data structure (arrows between symbols) that they also manage independently: some data elements are shared (mixed color symbols) others are not. This will require the identity verification to propagate between deployments peer-to-peer (P2P, dotted lines), including to deployments where neither user maintains an identity (dotted circular compartment). This is in contrast with the conventional approach of having distinct users manage insular deployments with permissions managed at the access point level.

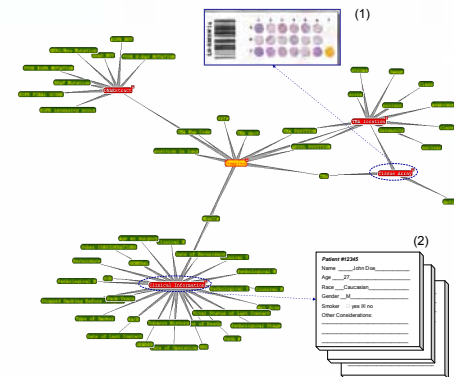


What S3DB provides is a web service for data discovery that can be accessed through a RESTfull API. Generic interfaces and stand alone analytic applications query the data elements using a SPARQL endpoint, available with each deployment of S3DB, to perform queries that are distributed by the deployments where the data is kept.

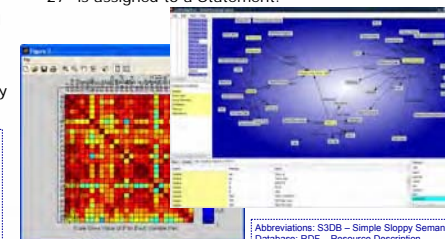
S3DB Fact Sheet:

Availability: <http://s3db.org>.
Source code: PHP (5+); License: GNU GPL.
Downloads: ~2/day since Jan 2008; Registered deployments: 248.
API: REST (Representation State Transfer).
I/O: RDF, XML, tab-delimited.
Client applications: <http://bioinformaticstation.org>.

3 – DOMAIN REPRESENTATION



Relevant data elements of the domain, such as individual images of the Tissue Microarrays (1) and Personal Health Record (2) data are assigned to each element of the S3DB Core Model by the domain expert. The concepts of Sample and Tissue Microarray, for example, are assigned to Collections (red and yellow nodes) and the relationships between two Collections or between a Collection and an attribute such as "Age" (green nodes) are assigned to the Rules (grey lines). Elements that represent instances of Collections are assigned to Items, for for example, "Patient #12345" is assigned to an Item of the Collection "Clinical Data". Finally, the value for a given attribute, such as "Age 27" is assigned to a Statement.



Abbreviations: S3DB – Simple Sloppy Semantic Database; RDF – Resource Description Framework; TCGA – The Cancer Genome Atlas; SPARQL – Sparsed RDF Query Language

A Semantic Web Management Model for Integrative Biomedical Informatics

Helena F. Deus^{1,2}, Romesh Stanislaus¹, Diogo F. Veiga¹, Carmen Behrens³, Ignacio I. Wistuba^{3,4}, John D. Minna⁵, Harold R. Garner^{5,6,7,8,9}, Stephen G. Swisher¹⁰, Jack A. Roth¹⁰, Arlene M. Correa¹⁰, Bradley Broom¹, Kevin Coombes¹, Allen Chang¹, Lynn H. Vogel^{1,11}, Jonas S. Almeida^{1*}

1 Department of Bioinformatics and Computational Biology, The University of Texas M.D. Anderson Cancer Center, Houston, Texas, United States of America, **2** Instituto de Tecnologia Química e Biológica, Universidade Nova de Lisboa, Lisboa, Portugal, **3** Department of Thoracic/Head and Neck Medical Oncology, The University of Texas M.D. Anderson Cancer Center, Houston, Texas, United States of America, **4** Department of Pathology, The University of Texas M.D. Anderson Cancer Center, Houston, Texas, United States of America, **5** Hamon Center for Therapeutic Oncology Research, Simmons Cancer Center, University of Texas Southwestern Medical Center, Dallas, Texas, United States of America, **6** Department of Internal Medicine, University of Texas Southwestern Medical Center, Dallas, Texas, United States of America, **7** Eugene McDermott Center for Human Growth and Development, University of Texas Southwestern Medical Center, Dallas, Texas, United States of America, **8** Center for Biomedical Inventions, University of Texas Southwestern Medical Center, Dallas, Texas, United States of America, **9** Department of Biochemistry, University of Texas Southwestern Medical Center, Dallas, Texas, United States of America, **10** Department of Thoracic and Cardiovascular Surgery, The University of Texas M.D. Anderson Cancer Center, Houston, Texas, United States of America, **11** Department of Biomedical Informatics, Columbia University, New York, New York, United States of America

Abstract

Background: Data, data everywhere. The diversity and magnitude of the data generated in the Life Sciences defies automated articulation among complementary efforts. The additional need in this field for managing property and access permissions compounds the difficulty very significantly. This is particularly the case when the integration involves multiple domains and disciplines, even more so when it includes clinical and high throughput molecular data.

Methodology/Principal Findings: The emergence of Semantic Web technologies brings the promise of meaningful interoperation between data and analysis resources. In this report we identify a core model for biomedical Knowledge Engineering applications and demonstrate how this new technology can be used to weave a management model where multiple intertwined data structures can be hosted and managed by multiple authorities in a distributed management infrastructure. Specifically, the demonstration is performed by linking data sources associated with the Lung Cancer SPORC awarded to The University of Texas MD Anderson Cancer Center at Houston and the Southwestern Medical Center at Dallas. A software prototype, available with open source at www.s3db.org, was developed and its proposed design has been made publicly available as an open source instrument for shared, distributed data management.

Conclusions/Significance: The Semantic Web technologies have the potential to address the need for distributed and evolvable representations that are critical for systems Biology and translational biomedical research. As this technology is incorporated into application development we can expect that both general purpose productivity software and domain specific software installed on our personal computers will become increasingly integrated with the relevant remote resources. In this scenario, the acquisition of a new dataset should automatically trigger the delegation of its analysis.

Citation: Deus HF, Stanislaus R, Veiga DF, Behrens C, Wistuba II, et al. (2008) A Semantic Web Management Model for Integrative Biomedical Informatics. PLoS ONE 3(8): e2946. doi:10.1371/journal.pone.0002946

Editor: Eshel Ben-Jacob, Tel Aviv University, Israel

Received: March 25, 2008; **Accepted:** July 12, 2008; **Published:** August 13, 2008

Copyright: © 2008 Deus et al. This is an open-access article distributed under the terms of the Creative Commons Attribution License, which permits unrestricted use, distribution, and reproduction in any medium, provided the original author and source are credited.

Funding: This work was supported in part by the National Heart, Lung and Blood Institute (NHLBI), by the National Cancer Institute (NCI) of the US National Institutes of Health (NIH), and by the Center for Clinical and Translational Sciences under contracts no. N01-HV-28181, P50 CA70907, and 1UL1RR024148, respectively. The authors also acknowledge support by the PREVIS project, contract number LSHM-CT-2003-503413 from the European Union Commission.

Competing Interests: The authors have declared that no competing interests exist.

* E-mail: jalmeida@mdanderson.org

Introduction

Data management and analysis for the life sciences

“The laws of Nature are written in the language of mathematics” famously said Galileo. However, in recent years efforts to analyze the increasing amount and diversity of data in the Life Sciences has been correspondingly constrained not so much by our ability to read it as by the challenge of organizing it. The urgency of this task and the reward of even partial success in its accomplishment have caused the interoperability between diverse digital representations to take center stage [1–5]. Presently,

for those in the Life Sciences enticed by Galileo’s pronouncement, the effort of collecting data is no longer focused solely on field/bench work. Instead, it often consists of painfully squeezing the pieces of the systemic puzzle from the digital media where the raw data is held hostage [6]. It is only then that a comprehensive representation amenable to mathematical modeling really becomes available [7]. This is not a preoccupation exclusive to the Life Sciences. Integration of software applications is also the driving force behind new information management systems architectures that seek to eliminate the boundaries to interoperability between data and services. This preoccupation indeed

underlies the emergence of service oriented architectures [8–11], even more so in its event driven dynamic generalization [12]. It also underlies the development of novel approaches to software deployment (Figure 1) that juggle data structures between server and client applications. Presently, a particularly popular design pattern is the usage-centric Web 2.0 [13,14] which seeks a delicate balance in the distribution of tasks between client and server in order to diminish the perception of a distinction between local and remote computation.

Semantic web technologies [3,15–21] represent the latest installment of web technology development. In what is being unimaginatively designated as Web 3.0[22,23], a software development design pattern is proposed where the interoperability boundaries between data structures, not just between the systems that produce them, is set to disappear. The defining characteristic of this environment is that one can retrieve data and information by specifying their desired properties instead of explicitly (syntactically) specifying their physical location. The desirability of this design can clearly be seen in systems in which clinical records are matched with high throughput molecular profiles, each of which stem from very distinct environments and are often the object of very different access management regulations.

Inadequacy of conventional systems for Translational Research

On the one hand, high throughput molecular Biology core facilities and improved medical record systems are able to

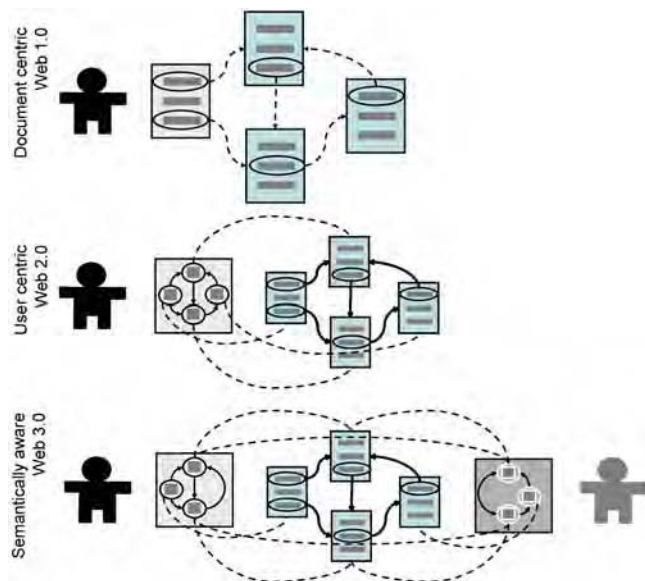


Figure 1. Three generations of design patterns for web-based applications. The original design (“1.0”) consists of collections of hypertext documents that are syntactically (dashed lines) interoperable (traversing between them by clicking on the links), regardless of the domain content. The user centric web 2.0 applications use internal representations of the external data structures. This representation is asynchronously updated from the reference resources which are now free to have a specialized interoperation between domain contents. An example of this approach is that followed by AJAX-based interfaces. Finally, the ongoing emergence of the semantic web promises to produce service oriented systems that are semantically interoperable such that the interface application reacts to domains of knowledge specifically. At this level all applications tend to be web-interoperable with peer-to-peer architectures complementing the client-server design of w1.0 and w2.0.

doi:10.1371/journal.pone.0002946.g001

document individual data elements with increasing detail. On the other hand, researchers producing the data and models that critically advance the understanding of biological phenomena are increasingly separated from their use by the specialization inherent in each of these activities. Consequently, bridging between the information systems of basic research and their clinical application becomes a necessary foundation for any translational exploits of new biomedical knowledge[3,24]. The alternative, using conventional data representations where the data models cannot evolve, typically requires the biomedical community to complement the data representation with a clandestine and inefficient flurry of datasets exchanged as spreadsheets through email.

Foundations for a novel solution

As others before us[5], we have argued previously for the use of semantic web formats as the foundation for developing more flexible and articulated data management and analytical bioinformatics infrastructures[20]. A software prototype was then produced following those technical specifications to provide a flexible web-based data sharing environment within which a management model can be identified[24]. In this third report we describe the resulting core model supporting distributed and portable data representation and management. In practice this translates into a small application deployed in multiple locations rather than a large infrastructure at a single central location. The open source prototype application described here has been made public[25]. All deployments support a common data management and analysis infrastructure with no constraints on the actual data structures described.

A very brief history of data

The formatting of data sets as portable text mirrors the same three stages described for web-based applications in Figure 1. As described in Figure 2, data representation has been evolving from tabular text formats (“flat files”), to self described hierarchical trees of tags (extended markup languages, XML), and finally to the subject-predicate-object triples of Resource Description Framework (RDF)[26]. We have been active participants in these transformations [24,27,28], and like many others concluded that in order to bridge the fragmentation between distinct data structures, we needed to break down the data structures themselves[20], that is, to reduce the interoperable elements to RDF triples[29]. In addition to its directed labeled graph nature, RDF formats[29] have a second defining characteristic: each of the three elements has a Uniform Resource Identifier (URI), which, for the purposes of this very brief introduction, can be thought as a unique locator capable of directing an application to the desired content or service. It is also interesting to note that at each level of this three-stage progression (Figure 2) we find data elements that have “matured”, that is, that present a stable representation which remains useful to specialized tools. When this happens we find that those elements remain convenient representations preserved whole within more fragmented formats. For example, we find no advantages in breaking down mzXML[30] representations of mass spectrometry based proteomics data. Instead, these data structures are used as objects of regular RDF triples. The mzXML proteomics data structure offers an paradigmatic illustration of the evolution of ontologies as efforts to standardize data formats[31]. It would be interesting to understand if the lengthy effort headed by the Human Proteomics Organization, HUPO, to integrate it reflects the difficulty to justify reforming[32] a representation that remains useful[33].

The advancement towards a more abstract, more global and more flexible representation of data is by no means unique to the Life Sciences. However, because of the exceptional diversity of

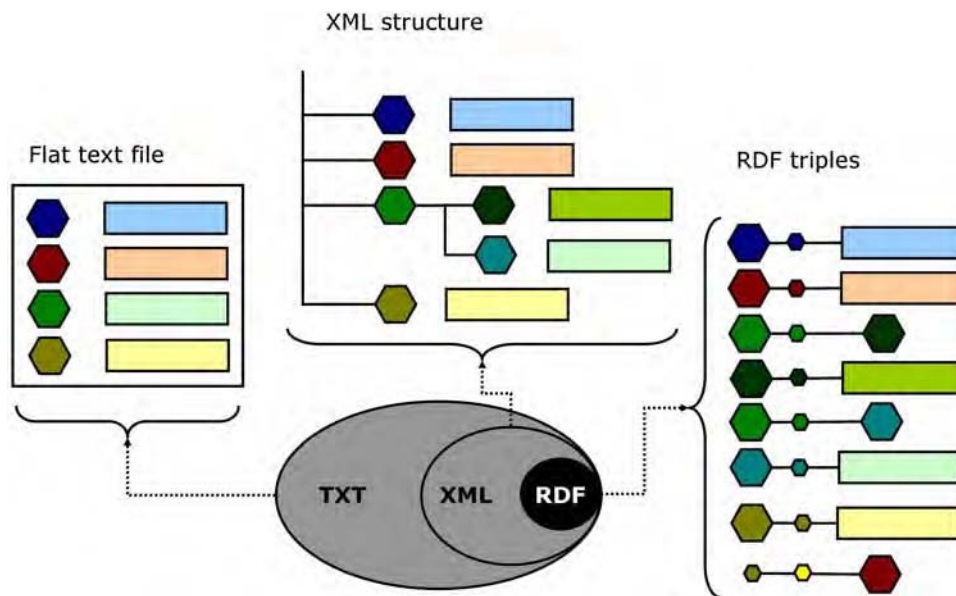


Figure 2. Evolution of formats for individual datasets. Hexagons, rectangles and small circles indicate data elements, respectively, attributes, their values, and relations. First, flat file formats such as fasta or the GeneBank data model were proposed to collect attribute-value pairs about an individual data entry. The use of tagging by extended markup languages (XML) allowed for the embedding of additional detail and further definition of the nature of the hierarchical structure between data elements. More recently, the resource description framework (RDF) further generalized the XML tree structure into that of a network where the relationship between resources (nodes) is a resource itself. Furthermore, the referencing of each resource by a unique identifier (URI) implies that the data elements can be distributed between distinct documents or even locations.
doi:10.1371/journal.pone.0002946.g002

that domain's fluidity, the Life Sciences are where the Semantic Web may find its most interesting challenge and as well, hopefully, where it will find its most compelling validation[15].

Mathematics for data models

It has not been lost to the swelling ranks of Systems Biologists that the reduction of data interoperability to the ternary representation of *relations* [34] brings the topic solidly back to the Galilean fold of Mathematics as a language. The reduction of data structures to globally referenced dyadic relations (functions of two variables), such as those of the Entity-Relationship (ER) model, brings in rich feeds from the vein of Logic. In the process, and beyond Galileo's horizon, assigning a description logic value[35–37] to some RDF predicates (for example, specifying that something is part of or, on the contrary, is distinct from something else) allows the definition of procedures. This further elaboration of RDF has the potential to transform data management into an application of knowledge engineering, and more specifically of artificial intelligence (AI). This reclassification reflects the dilution of the distinction between data management and data analysis that is apparent even in an introduction as brief as this one. Another clear indication of this transformation is that it re-ignites the opposition between data-driven and rule-driven designs for semantic web representation[38–42], a recurring topic in AI. It is important to note that the management model proposed here is orthogonal to that discussion. Its purpose is solely to enable the distribution[43] of a semantic data management system that can withstand changes in the domain of discourse, independently of the rationale for the changes themselves.

Software engineering for Bioinformatics

This overview of modern trends in integrative data management is as significant for what is covered as for what is missed – what management models should be used to control the generation and

transformation of the data model? It is interesting to note that the management models that associate access permissions with the population of a data model have traditionally been the province of software engineering. This may at first appear to be a reasonable solution. Since instances of a data structure in conventional databases are contained in a defined digital media, permission management is an issue of access to the system itself. However, this ceases to be the case with the semantic web RDF triples because they weave data structures that can expand indefinitely between multiple machines. Presently, the formalisms to manage data in the semantic web realm are still in the early stages of development, notably by the World Wide Web consortium (W3C) SKOS initiative (Simple Knowledge Organization Systems). This initiative recently issued a call[44] for user cases where good design criteria can be abstracted and recommendations be issued on standard formats. As expected[15], the Life Sciences present some of the most convoluted user cases in which a multitude of naive domain experts effectively need to maintain data structures that are as diverse and fluid as the experimental evidence they describe[24].

Materials and Methods

The most extreme combination of heterogeneous data structures and the need for very tight control of access is arguably found in applications to Personalized Medicine, such as those emerging for cancer treatment and prevention. At the Univ. Texas MDAnderson Cancer Center at Houston and the Southwestern Medical Center at Dallas we have deployed the S3DB semantic web prototype to engage the community of translational researchers of the University of Texas Lung Cancer SPOR [45] in identifying a suitable management model. This exercise involved over one hundred researchers and close to half a million data entries, of clinical and molecular nature. Right at its onset integrating access permissions in the definition of the data models was identified as an absolute necessity by the participants, as

anticipated by the SKOS group. As a consequence, a data driven “core model”, S3DBcore, that accommodates management specifications as part of data representation, was developed and is described here. The software used is provided with open source at www.s3db.org. Only open source tools were used in development of this web-based web-service: PHP 5 was used for server side programming and both MySQL and PostgreSQL were tested as the relational backbone for PHP’s database abstraction class. At the same location detailed documentation about S3DB’s Application Programming Interface (API) is also provided.

Results

Units of representation

The most fundamental representation of data is that of attribute-value (AV) pairs, for example, <color, “blue”>. The generic data management infrastructure proposed here can be described as that of encapsulating AV pairs through the use of another fundamental unit of representation, the Entity-Relation-Entity model (ER), such as <sky, has, color>. Each entity can then be associated with one or more AV pairs using the entity-attribute-value EAV model, for example, <sky, color, “blue”>. Fast forwarding three decades of computer science and knowledge engineering and we reach the present day development of a representation framework where each element of the triple is a resource with a unique identifier, with the third element of the triple having the option of being a literal, that is, of having an

actual value rather than a placeholder. This single sentence very broadly describes the Resource Description Framework (RDF) which is at the foundation of the ongoing development of the Semantic Web[29], just like hypertext (HTML) was the enabling format for the original Web. It is important to note that the evolution of representation formats typically takes place through generalization of the existing ones. For example, extended markup language-based files (XML) are still text files, and RDF documents are still XML structures (Figure 2). As noted earlier, this succession is closely paralleled by refinements of software design patterns (Figure 1). This reification process is often driven by the necessity to maintain increasingly complex data at a simpler level of representation where they remain intelligible for those who generate and use the data. Accordingly, in the next section triple relations will be weaved around the AV pair with that exact purpose: to produce a core model that is simple enough to be usable by naïve users that need to interact with heterogeneous data hosted in a variety of machines (Figure 3), yet sophisticated enough to support automated implementation.

Weaving a distributed information management system

The objective of this exercise is to produce a data management model that can be distributed through multiple deployments of the Database Management Systems (DBMS) which implies a mechanism for migration access permissions. Simultaneously, this model should allow different domain experts to evolve their own data models without compromising pre-existing data. Achieving these

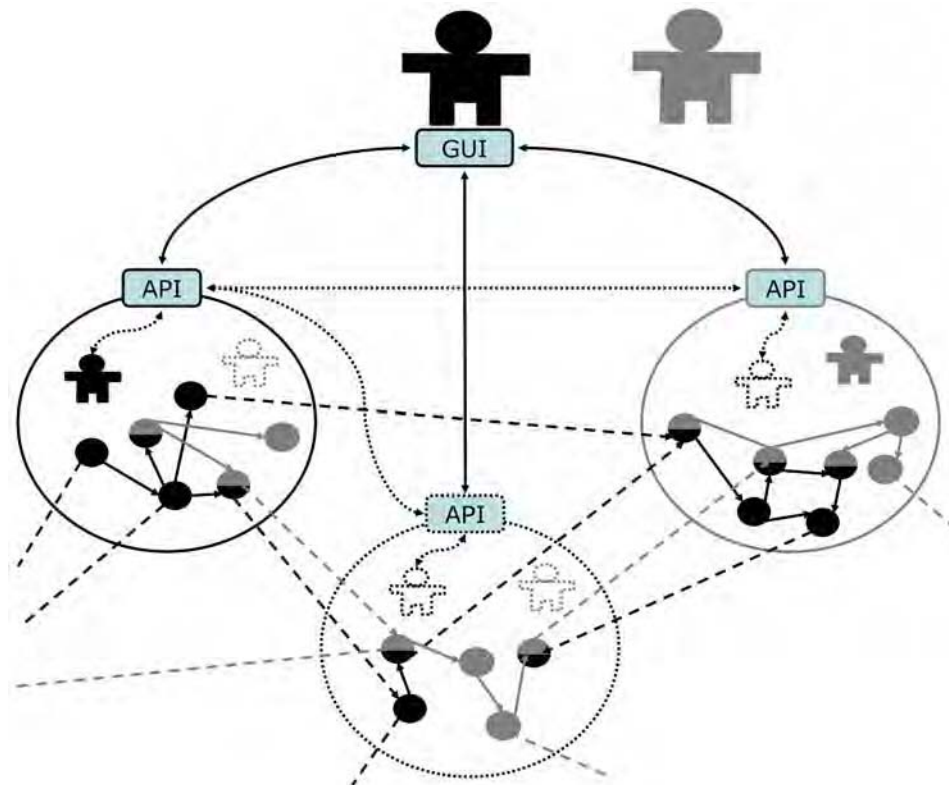


Figure 3. Illustration of the desirable functionality: distinct users, with identities (solid icon) managed in distinct S3DB deployments (circular compartments), which they control separately, share a distributed and overlapping data structure (arrows between symbols) that they also manage independently: some data elements are shared (mixed color symbols) others are not. This will require the identity verification to propagate between deployments peer-to-peer (P2P, dotted lines), including to deployments where neither user maintains an identity (dotted circular compartment). This is in contrast with the conventional approach of having distinct users manage insular deployments with permissions managed at the access point level.
doi:10.1371/journal.pone.0002946.g003

two goals simultaneously can only be realized if the proposed distributed system is composed of node applications that are not only syntactically interoperable, but also semantically transparent. For a discussion of the absolute need for evolvable data models in the Life Sciences see [24]. That report is also where the DBMS prototype, S3DB, was first introduced (version 1.0). Finally, the Application Programming Interface (API) needs to support the semantic interoperability in a way that spans multiple deployments (Figure 3). The data model developed to achieve these goals is described in Figure 4.

A Core data management model that is universal and distributed

The directed labeled graph nature of RDF triples, coupled with their reliance on unique identifiers (as URIs), enables data structures to be scattered between multiple machines while permitting different domains of discourse to use the same data elements differently. However, those two characteristics alone do not address the

management issue: how to decide when, where and what can be viewed, inserted, deleted and by whom. It is clear that the conventional approach of dealing with permissions at the level of access to the data store is not appropriate to the Life Sciences[5] where multiple disciplines and facilities are contributing to a partially overlapping representation of the system. It cannot be overstated that this is particularly the case when the system is designed to host clinical data. To solve this problem we have developed a core data model where membership and permission can migrate with the data. We have also developed a prototype application to support such a distributed data management system (Figure 3), which we make freely available with open source[25].

Discussion

The proposed core model is detailed in Figure 4 and will be now discussed in more detail. This diagram is best understood chronologically, starting with the very basic and nuclear collection

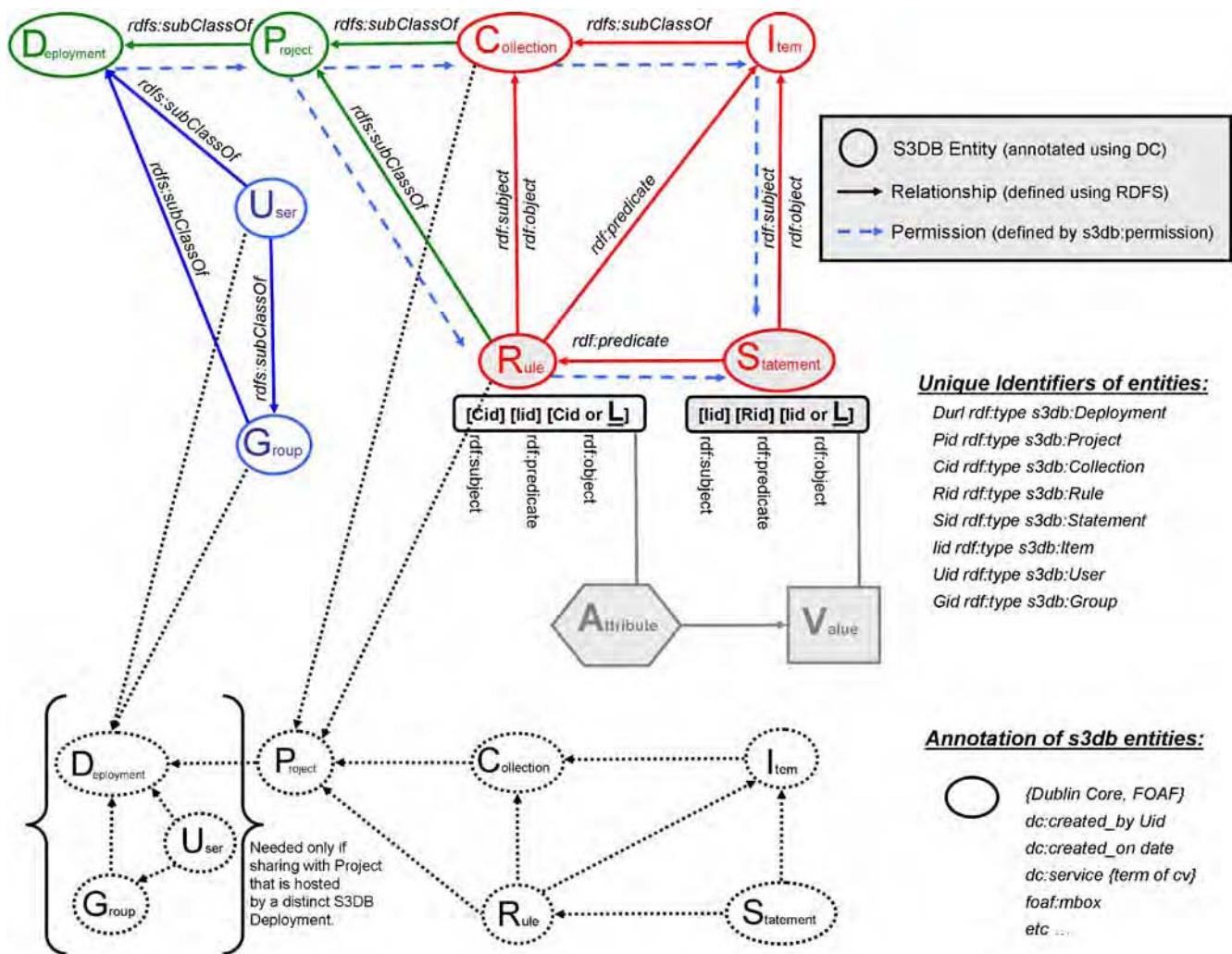


Figure 4. Core model developed for S3DB (supported by version 3.0 onwards). This diagram can be read starting from the most fundamental data unit, the Attribute-Value pair (filled hexagonal and square symbols). Each element of the pair is object of two distinct triples, one describing the domain of discourse, the Rules, and the other made of Statements where that domain is populated to instantiate relationships between entities. The latter includes the actual Values. Surrounding these two nuclear collection of triples, is the resolution of Collection and its instantiation as Item that define the relationship between the individual elements of Rules and Statements. The resulting structure is then organized in Projects in such a way that the domain of discourse can nevertheless be shared with other Projects, in the same or in a distinct deployment of S3DB. Finally, a propagation of user permissions (dashed line) is defined such that the distribution of the data structures can be traced. See text for a more detailed description. doi:10.1371/journal.pone.0002946.g004

of attribute-value pairs and then proceeding to their encapsulation by three consecutive layers – the semantic schema, assignment of membership and, finally the permission propagation.

Schema

The first layer of encapsulation is the definition and use of a domain of discourse (elements in red in Figure 4). This was achieved in typical RDF fashion by defining two sets of triples, one defining a set of rules and the second, the statements, using them. As discussed elsewhere [24], there are good reasons to equip those who generate the data with the tools to define and manage their own domains of knowledge. The ensuing incubation of experimental ontologies was facilitated by an indexing scheme that mimics the use of subject, verb, object in natural languages. This indexing is achieved by recognizing *Collections* and the *Items* they contain as elements of the two sets of nuclear triples (*Rules* and *Statements*).

Organization

The second layer of formal encapsulation corresponds to the assignment of membership. This process extends the designation of *Items* in the previous level, by assigning the *Collections* that contain them and *Rules* that relate them to *Projects* that are hosted by individual *Deployments* of the prototype S3DB application. In the diagram, the membership dependencies are accordingly labeled as *rdfs:subClassOf* [29]. Note that memberships can also be established with remote resources (dotted lines in Figure 4), that is, between resources of distinct deployments. Defining remote memberships presents little difficulty in the RDF format because each element of the triple is referred to by a universal identifier (a URI), unique across deployments. On the other hand, managing permission to access the remote content is a much harder problem, which we will address by supporting migration of identity. The alternative solution to migration of identities is migrating the contents along membership lines. However, that was, unsurprisingly, found to be objectionable by users with a special attention to privacy and confidentiality issues. It would also present some logistic challenges for larger datasets. In contrast, the definition of a temporary, portable, identity key or token needed for migration of identity is typically incommensurably smaller than the content it permits access.

Permissions

The final layer of encapsulation defines *Users* and *Groups* within *Deployments* and controls their permissions to the data (blue in Figure 4). As with rest of the core model, the identification of proposed management of permissions was directed by user cases. That exercise determined that user identities should be maintained by specific *Deployments* of S3DB but also that they may be temporarily propagated to other deployments. That solution, illustrated in Figure 3, allows one application to request the verification of an identity in a remote deployment, which then verifies it in the identity's source deployment and assigns it a temporary key or token, say, for one hour. All that is propagated is a unique alphanumeric string, the temporary token, paired with the user's URI. No other user information is exchanged. As a consequence, for the remainder of the hour, the identification will be asynchronously available in both deployments, which enables the solution described in Figure 3, where a single interface can manipulate multiple components of a large, distributed systems level representation of the target data. Interestingly, because the multiple deployments of S3DB are accessed independently by multiple deployments of various applications, the mode of syntactic interoperation is *de facto* peer-to-peer. The propagation of permissions flows in the sequence indicated by the dashed blue

lines in Figure 4. When a permission level is not defined for a resource, say for a *Item*, then it is borrowed from the parent entity, in this example, from the corresponding *Collection*. When there is a conflict then the most restrictive option is selected. For example a conflict can arise for a *Statement* which inherits permissions from both *Rules* and *Collections*. Another frequent example happens when a user belongs to multiple groups with distinct permissions to a common target resource.

Permission management is a particularly thorny issue in life sciences applications because of the management of multiple data provenances. Relying on distributed hosting of the complementary data sources compounds the management of multiple permissions even further because it also involves multiple permission management systems. Finally, permission management is often treated *ad hoc* by the management systems themselves where it is resolved as access permission to the system as a whole rather than being specified in the data representation. Because each source often describes a specialized domain, it is guarded with understandable zeal. We argue here that propagation of permissions is the only practical solution to determine how much information is to be revealed in different contexts. Consequently, whereas the relationships between the 8 S3DB entities (oval symbols in Figure 4) are defined using RDF schema[26] (RDFS), and their tagging uses the well established Dublin Core[46], the permission propagation layer is a novel component of the proposed management model. In order to respond to widest range of the user cases driving model identification, the propagation was defined by three parameters, view, edit, and use. Each of these parameters can have three values, 0, 1 or 2, corresponding to, respectively, no permission, permission only on entries submitted by the user, and permission on all entries of that resource. *Users* and *Groups* (blue entities in Figure 4) can have these three types of permissions on *Projects*, *Collections*, *Rules*, *Items* and *Statements*. Among those five entities, additional permissions can be issued, for example, a *Project* may have specific permissions on *Collections* and *Rules*. *Collections* may have further permissions on their *Items*. The same reasoning, in reverse, establishes what should happen when permission is not specifically defined for a given entity. For example, for a *Statement* the permission would be inherited from the parent entities, *Item* and *Rule*. If those two entities did not specify specific permissions for the target statement, then those are searched upstream (Figure 4) until reaching the *Project* or even *Deployment* level. According to this mechanism, the conventional role of a system administrator corresponds to a user with permissions 222 at Deployment level. It is worth recalling that propagation of permissions between data elements in distinct S3DB deployments happens through the sharing the membership in external *Collections* and *Rules* (dotted lines), not through extending the permission inheritance beyond the local deployment. This is not a behavior explicitly imposed on the distributed deployment; it emerges naturally from the fact that *Rule* sharing specifies a permission which, remote or local, interrupts the permission inheritance. In practice both the user of the interface and the programmer using the API can ignore the intricacies of this process, which was identified to be the intuitive, sensible, propagation of permissions that we found naive users to expect in user-case exercises.

Portability

This discussion would not be complete without unveiling some defining technical details about how portability is addressed by this design. So far we have been loosely equating “unique identifiers” with the use of Uniform Resource Identifiers (URI). More specifically, the right hand side of Figure 4 includes a list of eight

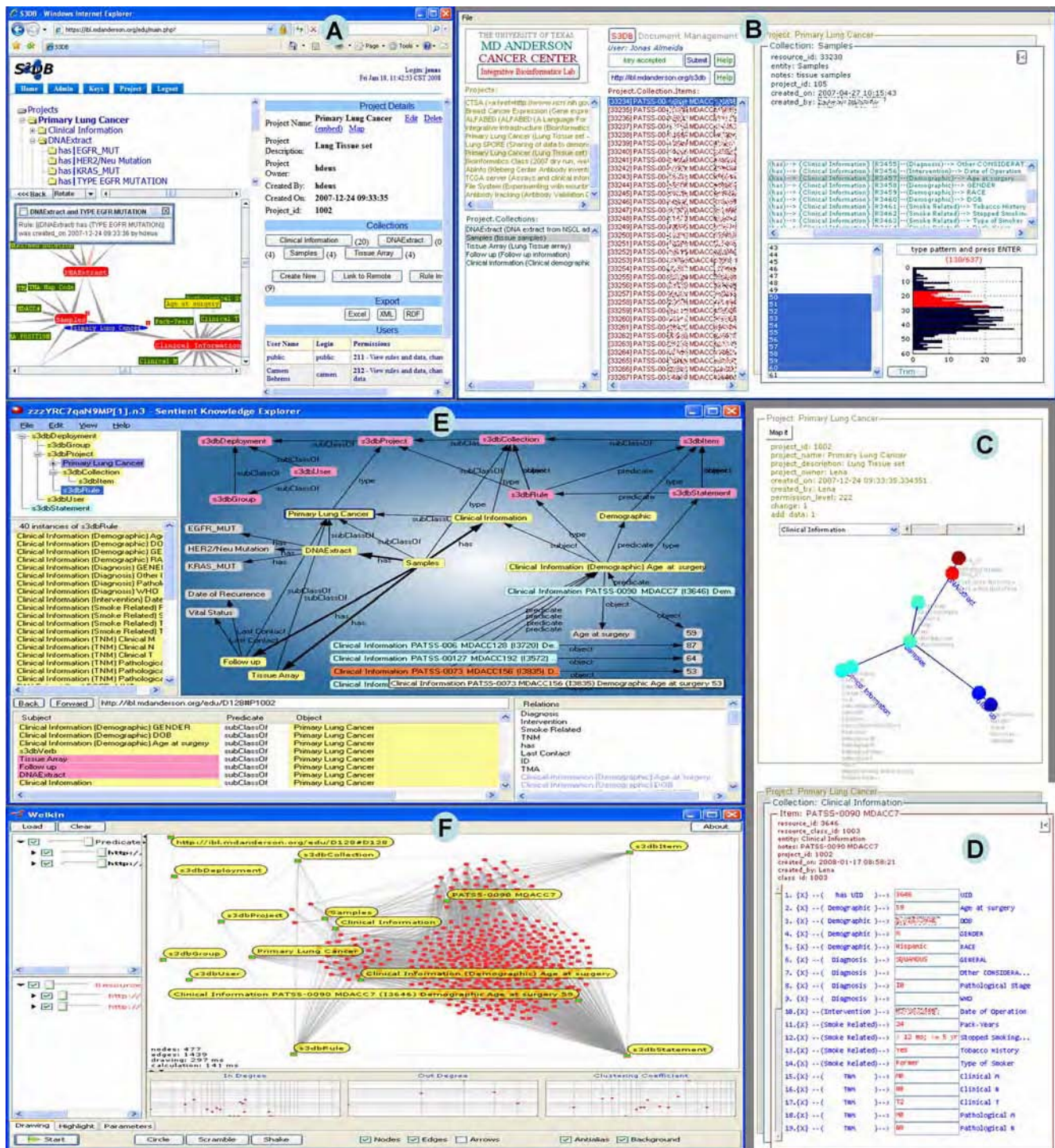


Figure 5. Snapshots of interfaces using S3DB's API (Application Programming Interface). These applications exemplify why the semantic web designs can be particularly effective at enabling generic tools to assist users in exploring data documenting very specific and very complex relationships. Snapshot A was taken from S3DB's web interface, which is included in the downloadable package[25]. This interface was developed to assist in managing the database model and, therefore, is centered on the visualization and manipulation of the domain of discourse, its *Collections of Items* and *Rules* defining the documentation of their relations. The application depicted on snapshots B–D describe a document management tool S3DBdoc, freely available as a Bioinformatics Station module (see Figure 6). The navigation is performed starting from the Project (C), then to the *Collection* (B) and finally to the editing of the *Statements* about an *Item* (D). The snapshot B illustrates an intermediate step in the navigation where the list of *Items* (in this case samples assayed by tissue arrays, for which there is clinical information about the donor) is being trimmed according to the properties of a distant entity, Age at Diagnosis, which is a property of the Clinical Information *Collection* associated with the sample that originated the array results. This interaction would have been difficult and computationally intensive to manage using a relational architecture. The RDF formatted query result produced by the API was also visualized using a commercial tool, Sentient Knowledge Explorer (IO-Informatics Inc), shown in snapshot E, and by Welkin, developed by the digital inter-operability SIMILE project at the Massachusetts Institute of Technology. See text for discussion of graphic representations by these tools. To protect patient confidentiality some values in snapshots B and D are scrambled and numeric sample and patient identifiers elsewhere are altered.
doi:10.1371/journal.pone.0002946.g005

types of locally unique identifiers that can be assigned to the same number of entities that define the core model. It is easy to see how this indexing can be made globally unique by concatenating them with the *Deployment's* ID, itself unique, for example using its URL. Indeed this is what is supported by the accompanying prototype software, with a generalizing twist with very significant consequences: *Did* can either be the deployment address or anything that indicates what that address is. For example, it can indicate an HTML document or even an entry in a database where this address is specified. More interestingly, it can also be a simple alphanumeric code that is maintained at www.s3db.org in association with the actual URL of the target deployment. The flexible global indexing achieved by either scenario allows the manipulation of entire databases management systems as portable data structures. It also allows for novel management solutions through manipulation of the DBMS logical structure. For example, defining a *Did* as 'localhost' would have the effect of severing all logical connections to any usage outside that of the server machine. None of these more fanciful configurations were validated with the Lung Cancer SPORE user community even if they are fully supported by the accompanying prototype. Nevertheless, its possibility enables some interesting scenarios for data management and indeed for Knowledge Engineering.

User Interfaces

The ultimate test for a data management model is the intuitiveness of what it communicates through the user interface[47,48]. The structure of S3DBcore offers some useful guidelines in this regard. The experimental values are represented in a combination of *Items* and *Statements* (Figure 4). There are two routes to that endpoint. One possibility is to take the document management approach of navigating from *Projects* to *Collections*, then to their *Items* and finally to the *Statements*. This is the scenario that will suit data centric activities such as querying and updating existing data or inserting new data. A real, working example of how that interface may look is depicted in Figure 5-B, which details an intermediate step between selecting a *Project* (Figure 5-B), and identifying and manipulating an individual entry made of multiple statements about an *Item* (Fig. 5-D). The mechanism used to distribute rich graphics applications and their interoperation with S3DB is detailed in Figure 6. Another possibility is to navigate from the *Project* to the collection of *Rules*, most likely represented as a directed labeled graph network, and then browse the *Statements* as an instantiation of the *Rules*, exemplified by another snapshot of a working application, Figure 5-A. This application is the standard web-based user interface distributed with S3DB package[25]. Unlike the bookkeeping approach of the document centric model (Figure 5-B), the rule centric view (Figure 5-A) is most suitable to investigate the relationship between different parts of the domain of knowledge and to incubate[24] a more comprehensive and exact version of the ontology. However, and this may be the most relevant point, since S3DB's API returns query results as RDF, any RDF browser can be used to explore it. This point is illustrated in figures 5E and F where, respectively, a commercial semantic web knowledge explorer (Sentient, IO-Informatics Inc) and Welkin, a popular RDF browser developed at the Massachusetts Institute of Technology, are used to visualize the same S3DB Lung Cancer project depicted in Figs. 5A and B. Whereas the former is designed as a tool for knowledge discovery, the latter offers a global view of distributed data structures. The value of the core model described in Figure 4 as a management template for individual data elements will be apparent upon close inspection of Fig. 5E. The different colors, automatically set by Sentient KE, distinguish the core model (pink), where permission management takes place, from the instantiation of

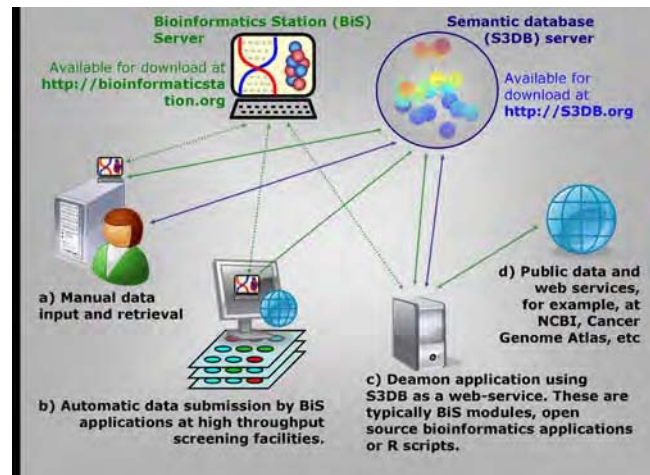


Figure 6. Prototype infrastructure for integrated data management and analysis being tested by the Univ. Texas Lung cancer SPORE. The system is based on two components, a network of universal semantic database servers and a code distribution server that delivers applications in response to the use of ontology. Four distinct user cases are represented, a–d, which rely on a combination of download of interpreted code (green arrows) or direct access to web-based graphic user interfaces or web-based API (blue arrows, in the latter case using Representational State Transfer, REST). The dotted lines represent regular updating of the application, propagating improvements in the application code.

doi:10.1371/journal.pone.0002946.g006

their entities, in yellow. These two layers describe the context for individual entries specifying the age at surgery of 5 patients. The same display includes access to molecular work on tumor samples, in this case using tissue arrays and DNA extracts. The distinct domains are therefore integrated in an interoperable framework in spite of the fact that they are maintained, and regularly edited, by different communities of researchers. As a consequence, the database can evolve with the diversification of data gathering methodologies and with the advancement in understanding the underlying processes. In figure 5F it can be seen that MIT's Welkin RDF visualizer easily distinguished the query results as the interplay of 4 collections of 380 *Statements* about 41 *Items* from 5 *Collections* related by 40 *Rules*. For comparison, see Figure 5E where one of its *Statements* is labeled (describing that Age of patient providing pathology sample #90 with Clinical Information #I3646 is 90 years old), along with the parent entities. For examples of other *Statements* about the same *Item* see Fig. 5D. For examples of other statements of the same nature (about the same domain), see 4 statements listed at the bottom-right of Figure 5E.

Conclusion

The Semantic Web[15] technologies have the potential to address the need for distributed and evolvable representations that are critical for systems Biology and translational biomedical research. As this technology is incorporated into application development we can expect that both general purpose productivity software and domain specific software installed on our personal computers will become increasingly integrated with the relevant remote resources. In this scenario, the acquisition of a new dataset should automatically trigger the delegation of its analysis. The relevance of this achievement becomes very clear when we note that what prevents a new microarray result from being of immediate use to the experimental Biologist acquiring it is not the computational capability of the experimentalist's machine. Biostatisticians do not

necessarily have more powerful machines than molecular Biologists. Moreover, in neither case is high end computation expected to be performed in the client machine[8]. Rather, once data gathering and data analysis applications become semantically interoperable, at the very least, those who acquire the illustrative microarray data should expect their own machines to automatically trigger its sensible analysis by background subtraction, normalization and basic multivariate exploratory analysis such as dimensionality reduction and clustering. As a consequence, the quantitative scientist's role can be focused on defining the sensibility of alternative contexts of data generation.

The consequences of semantic integration are just as advantageous for those dedicated to data analysis. Statistical analysts typically spend the majority of their time parsing raw datasets rather than assessing the reasonableness of alternative analytical routes. This contrasts with the critical need to validate any given analysis by comparing results produced by alternative configurations applied to independent experimental evidence. It is this final step that ultimately determines the sensibility of the data analysis procedures triggered by the acquisition of data. In summary, any data management and analysis system that will scale for systems level analysis in the Life Sciences has to be semantically interoperable if automated validation is to be attainable.

In this report, we have demonstrated the design of a semantic web data model, S3DBcore, capable of delivering the desired

features of distribution and evolvability. This solution relies on RDF triples, the language developed to enable the semantic web in the same fashion that HTML was developed to enable the original web. However, collections of *subject-predicate-object* triples do not establish a management model by themselves. That exercise requires the encapsulation of the data within two additional layers, one confining membership and another permitting access. The effort of identifying management models for information systems has conventionally been the property of technology deployment. This is not feasible when the challenge is scaled to the level of complexity and distribution of Systems Biology. This report describes such a working management model and the authors also make its prototype deployment freely available with open source. In conclusion, a distributed integrated data management and analysis system might look like the prototype infrastructure described in Figure 6 which is based on a semantic database backbone coupled to a code distribution server reacting to the domain of discourse being used.

Author Contributions

Conceived and designed the experiments: HFD CB IW JSA. Performed the experiments: HFD JSA. Analyzed the data: HFD JSA. Contributed reagents/materials/analysis tools: HFD RS DVF CB JDM HRG SGS JAR AMC BB KC AC LHV JSA. Wrote the paper: JSA.

References

- Blake JA, Bult CJ (2006) Beyond the data deluge: data integration and bio-ontologies. *J Biomed Inform* 39: 314–320.
- Komatsoulis GA, Warzel DB, Hartel FW, Shanbhag K, Chilukuri R, et al. (2007) caCORE version 3: Implementation of a model driven, service-oriented architecture for semantic interoperability. *J Biomed Inform*.
- Ruttenberg A, Clark T, Bug W, Samwald M, Bodenreider O, et al. (2007) Advancing translational research with the Semantic Web. *BMC Bioinformatics* 8 Suppl 3: S2.
- Brazhnik O, Jones JF (2007) Anatomy of data integration. *J Biomed Inform* 40: 252–269.
- Hendler J (2003) Communication. *Science and the semantic web. Science* 299: 520–521.
- Wiley HS, Michaels GS (2004) Should software hold data hostage? *Nat Biotechnol* 22: 1037–1038.
- Wass J (2006) Integrating Knowledge. *Bio-IT World* 5: 22.
- Foster I (2005) Service-oriented science. *Science* 308: 814–817.
- Hey T, Trefethen AE (2005) Cyberinfrastructure for e-Science. *Science* 308: 817–821.
- Nadkarni PM, Miller RA (2007) Service-oriented architecture in medical software: promises and perils. *J Am Med Inform Assoc* 14: 244–246.
- Bridges MW (2007) SOA in healthcare, Sharing system resources while enhancing interoperability within and between healthcare organizations with service-oriented architecture. *Health Manag Technol* 28: 6, 8, 10.
- Gomadani R, Ramaswamy, Sheth, Verma (2007) A Semantic Framework for Identifying Events in a Service Oriented Architecture. *IEEE International Conference on Web Services ICWS 2007*: 545–552.
- Musser J (2006) *Web 2.0 Principles and Best Practices*; O'Reilly T, ed. O'Reilly Media, Inc.
- Kamel Boulos MN, Wheeler S (2007) The emerging Web 2.0 social software: an enabling suite of sociable technologies in health and health care education. *Health Info Libr J* 24: 2–23.
- Berners-Lee T, Hall W, Hendler J, Shadbolt N, Weitzner DJ (2006) Computer science. *Creating a science of the Web. Science* 313: 769–771.
- Berners-Lee T, Hendler J (2001) Publishing on the semantic web. *Nature* 410: 1023–1024.
- Gordon PM, Trinh Q, Sensen CW (2007) Semantic Web Service provision: a realistic framework for Bioinformatics programmers. *Bioinformatics* 23: 1178–1180.
- Neumann E, Prusak L (2007) Knowledge networks in the age of the Semantic Web. *Brief Bioinform* 8: 141–149.
- Post IJ, Roos M, Marshall MS, Driel RV, Breit TM (2007) A semantic web approach applied to integrative bioinformatics experimentation: a biological use case with genomics data. *Bioinformatics*.
- Wang X, Gorlitsky R, Almeida JS (2005) From XML to RDF: how semantic web technologies will change the design of 'omic' standards. *Nat Biotechnol* 23: 1099–1103.
- Feigenbaum L, Martin S, Roy MN, Szekely B, Yung WC (2007) Boca: an open-source RDF store for building Semantic Web applications. *Brief Bioinform* 8: 195–200.
- Borland J (2007) A Smarter Web. *Technology Review* March/April.
- Green H (2007) A Web That Thinks Like You. *Businessweek* 28.
- Almeida JS, Chen C, Gorlitsky R, Stanislaus R, Aires-de-Sousa M, et al. (2006) Data integration gets 'Sloppy'. *Nat Biotechnol* 24: 1070–1071.
- s3db 2.0.
- Robu I, Robu V, Thirion B (2006) An introduction to the Semantic Web for health sciences librarians. *J Med Libr Assoc* 94: 198–205.
- Silva S, Gouveia-Oliveira R, Marezek A, Carrico J, Gudnason T, et al. (2003) EURISWEB—Web-based epidemiological surveillance of antibiotic-resistant pneumococci in day care centers. *BMC Med Inform Decis Mak* 3: 9.
- Stanislaus R, Chen C, Franklin J, Arthur J, Almeida JS (2005) AGML Central: web based gel proteomic infrastructure. *Bioinformatics* 21: 1754–1757.
- Ivan Herman RS, DanBrickley (2007) Resource Description Framework (RDF). *The World Wide Web Consortium*.
- Pedrioli PG, Eng JK, Hubley R, Vogelzang M, Deutsch EW, et al. (2004) A common open representation of mass spectrometry data and its application to proteomics research. *Nat Biotechnol* 22: 1459–1466.
- Orchard S, Jones AR, Stephan C, Binz PA (2007) The HUPO pre-congress Proteomics Standards Initiative workshop. *HUPO 5th annual World Congress. Long Beach, CA, USA 28 October-1 November 2006. Proteomics* 7: 1006–1008.
- Orchard S, Montechi-Palazzi L, Deutsch EW, Binz PA, Jones AR, et al. (2007) Five years of progress in the Standardization of Proteomics Data 4(th) Annual Spring Workshop of the HUPO-Proteomics Standards Initiative April 23–25, 2007 Ecole Nationale Supérieure (ENS), Lyon, France. *Proteomics* 7: 3436–3440.
- Klimek J, Eddes JS, Hohmann L, Jackson J, Peterson A, et al. (2007) The Standard Protein Mix Database: A Diverse Data Set To Assist in the Production of Improved Peptide and Protein Identification Software Tools. *J Proteome Res*.
- Aho JDU AV (1979) Universality of data retrieval languages. *Proceedings of the 6th ACM SIGACT-SIGPLAN symposium on Principles of programming languages*. pp 110–119.
- Aranguren ME, Bechhofer S, Lord P, Sattler U, Stevens R (2007) Understanding and using the meaning of statements in a bio-ontology: recasting the Gene Ontology in OWL. *BMC Bioinformatics* 8: 57.
- Lam HY, Marengo L, Shepherd GM, Miller PL, Cheung KH (2006) Using web ontology language to integrate heterogeneous databases in the neurosciences. *AMIA Annu Symp Proc*. pp 464–468.
- Zhang S, Bodenreider O, Golbreich C (2006) Experience in reasoning with the foundational model of anatomy in OWL DL. *Pac Symp Biocomput*. pp 200–211.
- Miller M, Rifaich R (2006) Wrestling with SUMO and bio-ontologies. *Nat Biotechnol* 24: 22–23; author reply 23.
- Musen MA, Lewis S, Smith B (2006) Wrestling with SUMO and bio-ontologies. *Nat Biotechnol* 24: 21; author reply 23.
- Stoeckert C, Ball C, Brazma A, Brinkman R, Causton H, et al. (2006) Wrestling with SUMO and bio-ontologies. *Nat Biotechnol* 24: 21–22; author reply 23.
- Blake J (2004) Bio-ontologies-fast and furious. *Nat Biotechnol* 22: 773–774.
- Soldatova LN, King RD (2005) Are the current ontologies in biology good ontologies? *Nat Biotechnol* 23: 1095–1098.

43. Merelli E, Armano G, Cannata N, Corradini F, d'Inverno M, et al. (2007) Agents in bioinformatics, computational and systems biology. *Brief Bioinform* 8: 45–59.
44. Antoine Isaac JP, Daniel Rubin (2007) SKOS Use Cases and Requirements.
45. The University of Texas Lung Cancer SPORE. P50 CA70907.
46. Baker T (2005) A Common Grammar for Diverse Vocabularies: The Abstract Model for Dublin Core. *Lecture Notes in Computer Science* 3815: 495.
47. Good BM, Wilkinson MD (2006) The Life Sciences Semantic Web is full of creeps! *Brief Bioinform* 7: 275–286.
48. Neumann E (2005) A life science Semantic Web: are we there yet? *Sci STKE* 2005: pe22.

Deregulated *EGFR* Signaling during Lung Cancer Progression: Mutations, Amplicons, and Autocrine Loops

Adi F. Gazdar and John D. Minna

One or more members of the family of epidermal growth factor receptor (*EGFR*) genes are overexpressed or otherwise deregulated in virtually all epithelial tumors, including non-small cell lung cancers (NSCLC). This and related observations on the importance of protein phosphorylation and the discovery that the first identified oncogene, *v-Src*, is a protein kinase led John Mendelsohn and Gordon Sato to select *EGFR* as the first target of molecular targeted therapy more than 20 years ago (1, 2). *EGFR* family members are deregulated in cancers by the following three fundamental mechanisms: activating gene mutations, increased gene copy number (via amplification or polysomy), and altered ligand expression (with possible formation of autocrine loops; ref. 3). Two reports in this issue of the journal advance our understanding of the role of all three mechanisms in the pathogenesis and progression of NSCLC (4, 5). Before discussing these reports, however, we will present background information on *EGFR* signaling and its deregulation in cancers.

Reversible protein phosphorylation as a crucial regulator of many essential cell functions has been elucidated over the past 50 years. A superfamily of more than 500 highly conserved protein kinase genes contains about 2% of the genome (6). Specific kinases phosphorylate serine/threonine or tyrosine residues or have dual specificity. The tyrosine kinases, which catalyze the transfer of γ phosphate of ATP to tyrosine residues on protein substrates, fall into two classes: transmembrane receptors (receptor tyrosine kinase) and nonreceptors. Subclass I of the receptor tyrosine kinases is the *EGFR* family, which consists of four members: *EGFR* (or *EGFR1*, *ERBB2*, *HER1*), *EGFR2* (or *ERBB2*, *HER2*), *EGFR3* (or *ERBB3*, *HER3*), and *EGFR4* (or *ERBB4*, *HER4*; ref. 3). Receptor-ligand interaction results in formation of homodimers or heterodimers (between family members), activation of the intrinsic kinase domain, and phosphorylation of specific tyrosine residues in the cytoplasmic tail of the receptor. The phosphorylated residues become docking sites for multiple proteins, which in turn activate downstream signaling pathways including the *PI3K/AKT* pro-survival, *STAT* transcription, and *RAS/RAF/MEK* proliferation pathways.

Eleven members of the EGF family have been identified as ligands for the *EGFR* family. *HER2* is not ligand activated be-

cause of its unique extracellular spatial structure but is the preferred dimerization partner for other family members; its heterodimers preferentially enhance ligand binding (7). *EGFR3* is "kinase dead" (i.e., it lacks intrinsic kinase activity) and, as with *HER2*, functions via heterodimerization. The EGF ligands show specificity for multiple homodimers or heterodimers (7). Epregrulin is a pan-*EGFR* family ligand that preferentially activates heterodimeric receptor complexes (8). The EGF ligands are produced as transmembrane precursors that are cleaved into their soluble forms by proteases ("shed-dases") of the ADAM family (especially ADAM10 and ADAM17) or by matrix metalloproteinases, a process known as ectodomain shedding (9). Other receptor pathways also may activate *EGFR* signaling by activating the *EGFR* pathway via "cross talk" and/or "transactivation." An important new example of this with relevance to *EGFR* is the inflammatory cytokine interleukin-6, which activates the Janus-activated kinase/signal transducer and activator of transcription system, which in turn activates *EGFR* pathway signaling. High levels of interleukin-6 have been described in many cancers, including *EGFR*-mutant lung cancers, providing an additional method for *EGFR* activation and a new therapeutic target.

NSCLC cells can produce and release several of the EGF ligands (10–12). Under certain circumstances, the membrane-anchored isoforms and soluble growth factors also may act as biologically active ligands. Therefore, depending on the circumstances, these ligands may induce juxtacrine, autocrine, paracrine, and/or endocrine signaling (13). Establishing *EGFR* autocrine loops renders the cells sensitive to inhibition by tyrosine kinase inhibitors (10, 12). Zhou et al. (14) described the presence of an autocrine heregulin-*EGFR3* loop associated with up-regulation of the sheddase ADAM10. Inhibiting ADAM10 with a specific inhibitor prevented the processing and activation of multiple EGF ligands. Recent reports indicate that breast and NSCLC cells (especially those with *EGFR* mutations) may produce large amounts of interleukin-6, activating another autocrine loop that drives tumorigenesis (15, 16).

Mutations of *EGFR* may target many regions of the gene, especially the extracellular domain in glioblastomas (17) and the kinase domain in lung cancers (18, 19). *EGFR* mutations may play a major role in lung tumorigenesis but also leave lung tumor cells dependent on *EGFR* signaling pathway activation for growth and survival ("oncogene addiction"; refs. 19, 20). Therefore, inhibition of *EGFR* signaling by tyrosine kinase inhibitors rapidly leads to apoptosis and growth cessation. In the 4 years since the discovery of the mutations, however, it was realized that primary tumor response and resistance to tyrosine kinase inhibitors are influenced by many factors, including mutations, mutation type, and copy numbers of *EGFR*; *EGFR3* activation; *KRAS* mutations; *MET* amplification, and others (21–23). Therefore, although some studies

Authors' Affiliations: Hamon Center for Therapeutic Oncology Research and the Simmons Cancer Center, UT Southwestern Medical Center, Dallas, Texas Received 04/15/2008; accepted 04/22/2008.

Grant support: NCI Lung Cancer Specialized Program of Research Excellence grant P50CA70907, Early Detection Research Network, National Cancer Institute, and Department of Defense VITAL and PROSPECT grants.

Requests for reprints: Adi F. Gazdar, UT Southwestern Medical Center, Building NB8.206, 6000 Harry Hines Boulevard, Dallas, TX 75390-8593. Phone: 214-648-4921; Fax: 214-648-4940; E-mail: adi.gazdar@utsouthwestern.edu.

©2008 American Association for Cancer Research.

doi:10.1158/1940-6207.CAPR-08-0080

(usually from single institutions analyzing highly selected patient populations) have shown very high response rates of EGFR-mutant tumors to tyrosine kinase inhibitors, large multi-institutional clinical trials have often failed to show a survival benefit of this approach, although increased copy number of *EGFR* (and *HER2* in some series) was associated with a good treatment outcome (24, 25). Although *EGFR* mutations and copy number gains may occur independently, they occur together more frequently than alone (26, 27). In addition, as with glioblastomas (17), the mutant allele is preferentially amplified in such cases (26). Therefore, “triple whammy” tumors (i.e., those with mutations, copy number gains, and mutant allele-specific amplifications) are in all probability highly oncogene addicted and likely to show dramatic and sustained responses to appropriate targeted therapies. Autocrine loops and other derangements of EGFR signaling are frequent in all forms of NSCLC, which therefore may involve tumors with more than three EGFR aberrations, or “multiple whammy” tumors.

The finding that all of these different mechanisms activate EGFR signaling in lung cancers signifies the presence and great importance of strong selective pressures on the EGFR signaling pathway in these cancers. This selectivity was dramatically highlighted by the finding of *EGFR* tyrosine kinase domain mutations, but lung cancer use of all these alternative mechanisms is equally important in underscoring the key role of the EGFR pathway in driving lung cancer pathogenesis. Of course, these findings also highlight how versatile tumor cells are in finding ways to activate the pathway. On a related note, the relapse and subsequent drug resistance of lung cancers that had responded to EGFR-targeting drugs (such as EGFR tyrosine kinase inhibitors) show the resourcefulness of these cancers in finding other ways to use the EGFR or other pathways (e.g., *KRAS*, *c-MET*) to ward off extinction. Relapse and resistance also highlight the need for tools that can determine whether the pathway is active in and identify “sensitive” therapeutic target(s) for individual lung cancers. It is also important to realize that the target is constantly changing, and thus different therapeutic options are needed at different disease stages.

We now evaluate the contributions of the articles by Zhang et al. (4) and Tang et al. (5) in the context of the EGFR signaling background detailed above. Lung cancer has a high mortality that usually is due to the development of metastatic lesions. Although relatively few studies have directly compared the molecular changes in primary tumors with those in corresponding metastatic tumors, the metastatic phenotype is characterized by changes in multiple cellular pathways (28). The study by Zhang et al. (4) was stimulated by previous work from their laboratory showing that epiregulin is one of the several highly expressed EGF ligands in EGFR-mutant NSCLC cells (10). This group tested the hypothesis that epiregulin is involved in the development of the metastatic phenotype. Immunostaining studies confirmed their previous observation that primary NSCLC tumors with localized disease stages frequently (in 65% of cases) expressed the ligand. They reported a significant correlation between ligand expression and advanced nodal stage (stage II) and a trend toward shorter survival. *In vitro* studies confirmed the role of epiregulin in promoting tumor growth and invasion. These analyses show a clear role for epiregulin in tumor cell survival, inva-

sion, and metastasis. Because epiregulin can stimulate multiple members of the *EGFR* receptor family, activation of both *EGFR* and *EGFR3* signaling may contribute to carcinogenesis. Because ligand expression is much more frequent than are *EGFR* mutations or copy number gains, these findings provide further evidence that autocrine loops may be the major mechanism by which *EGFR* signaling is deregulated in all histologic forms of NSCLC. Future studies should comprehensively analyze all 11 EGF ligands found in lung cancers because other members of this ligand group may have similar tumor-promoting actions.

As mentioned earlier, *EGFR* mutations and copy gains occur frequently in the same tumors. Previous studies have shown widespread field effects throughout the respiratory epithelium of smokers (29, 30), suggesting that tobacco exposure damages the entire respiratory epithelium. Most *EGFR* mutations occur in lung cancers of lifetime never smokers, which have a largely unknown etiology (31). In their earlier work, the authors carefully microdissected histologically normal respiratory epithelium from small airways surrounding mutation-containing tumors (32); often present in airways within or near the tumor but seldom in distant sites, the mutations reflected a limited field effect. Therefore, exposure and damage seem to be much more limited in never smokers than in current or former smokers. In their present study, Tang et al. conducted a more extensive field study, assessing the presence of mutations and copy number gains (by fluorescence *in situ* hybridization technique) in primary NSCLC, corresponding metastases, and histologically normal respiratory epithelium. As in their previous study, mutations and EGFR protein overexpression were a localized field effect. The key present findings are that copy number gains were absent in normal epithelium and were distributed heterogeneously in primary tumors and more evenly in metastases. Tang et al. (5) have answered the question, “Which came first, the chicken (copy number gains) or the egg (mutations)?” The finding of mutant allele-specific gains gives the nod to the egg.

The prototype *EGFR* gene is not the only EGFR pathway gene amplified in NSCLC. A recent report describes amplification of other pathway members including *HER2*, *SHC1*, and *AKT* (33). Our unpublished work indicates that other pathway genes including *KRAS* and *BRAF* may also be amplified in NSCLC. Although mutations of pathway genes are usually mutually exclusive, single tumors may contain copy number gains for multiple genes or a single pathway mutation and one or more pathway gene copy number gains.¹

Two other recently published studies (34, 35) are consistent with the findings of Tang et al. (5). Cancers arise as a result of multistage processes, and a lesion known as atypical adenomatous hyperplasia is recognized as a precursor or premalignant lesion for peripheral lung adenocarcinomas. Atypical adenomatous hyperplasia lesions progress to noninvasive cancers known as bronchioloalveolar carcinomas as defined by the strict criteria of WHO classification (36). Bronchioloalveolar carcinoma tumors may become invasive and eventually metastatic. Early invasive cancers may contain invasive and noninvasive components that can be microdissected and examined separately. By examining the various stages of lung

¹ Unpublished data.

pathogenesis for *EGFR* mutations and copy gains, both reports (34, 35) conclude that mutations are early, preinvasive changes, whereas copy number gains are later events associated with the invasive phenotype (Fig. 1).

All of these findings are consistent with the hypothesis that mutations precede copy number gains, which may be associated with the metastatic phenotype. Therefore, mutations are likely to show little or no heterogeneity in primary or metastatic tumors, and copy number gains may be absent or

heterogeneously distributed in primary tumors and relatively evenly distributed within metastatic sites. Further work will be needed to confirm that copy number gains are part of the metastatic phenotype.

What are the clinical implications of these findings? The data of Zhang et al. (4) suggest that about two thirds of all NSCLCs express at least one of the EGF ligands. Testing the expression of the other 10 known ligands in this cohort presumably would have shown an even higher percentage. The

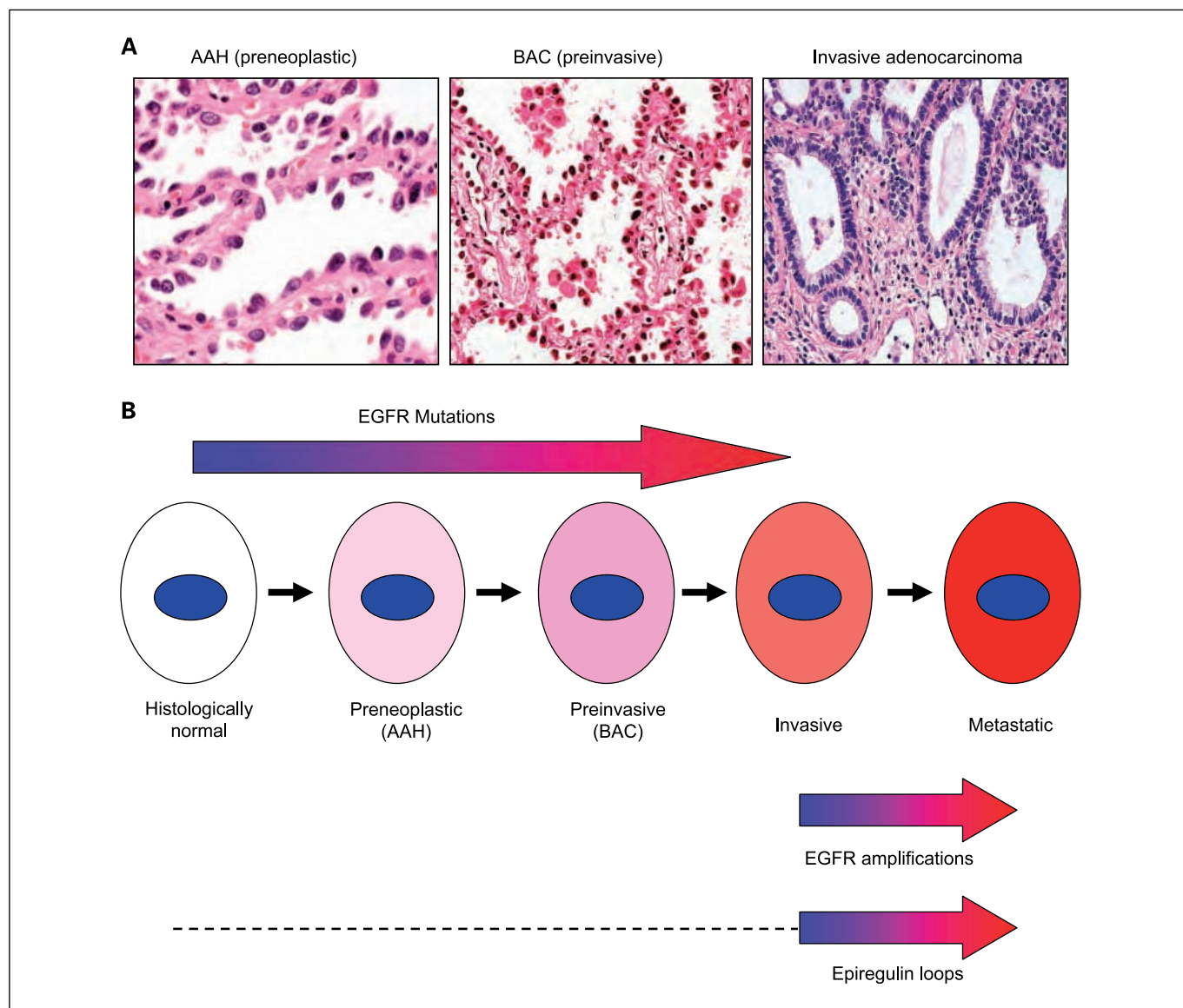


Fig. 1. Deregulation of the *EGFR* gene during the multistage pathogenesis of peripheral lung adenocarcinomas. **A**, peripheral adenocarcinomas are believed to arise from preneoplastic lesions known as atypical adenomatous hyperplasias (AAH), which first progress to a preinvasive neoplastic stage called bronchioloalveolar carcinoma (BAC). Foci of invasion may develop in the fibrotic centers of bronchioloalveolar carcinomas, which then are called invasive adenocarcinomas, although noninvasive elements may persist at the edges of the tumors. Metastases ultimately develop (not shown). **B**, from the article by Tang et al. (5) and from the literature cited in the text, *EGFR* mutations commence early during pathogenesis and can be detected in histologically normal respiratory epithelium near tumors (localized field effect). Mutations are more frequent in preneoplastic (atypical adenomatous hyperplasia) and preinvasive (bronchioloalveolar carcinoma) stages than in normal epithelium. Therefore, there is relatively little heterogeneity of mutations in invasive carcinomas, and the mutations contribute to tumor pathogenesis. In contrast, gene copy number gains, often in the form of amplifications, commence relatively late in pathogenesis, usually at the tumor stage. They are more frequent in metastatic lesions, suggesting that they may be progression events involved in the metastatic phenotype. Much less is known about the timing of epiregulin loops (either autocrine, paracrine, or juxtacrine). From the data of Zhang et al. (4), however, it would seem that epiregulin loops can be detected in primary invasive tumors but are more frequent or active during the metastatic stage. The dashed line indicates that the timing of the appearance of these loops during earlier preinvasive stages is unknown.

expression of EGFR protein in most NSCLCs, including squamous cell carcinomas, raises the question of what mechanism causes deregulation. Mutations and copy number gains explain only a minority of these cases and probably are not important mechanisms in squamous cell carcinomas. As suggested by the data of Zhang et al. (4), activation of autocrine (or paracrine or juxtacrine) loops is an attractive alternative mechanism. If this loop is dependent on continued EGFR signaling and is inhibited by tyrosine kinase inhibitor therapy, as suggested by the data, this would be a plausible explanation for why some nonmutant tumors of all histologic types with nearly diploid copy number respond to tyrosine kinase inhibitor therapy (24, 37). Future retrospective and prospective studies are needed to determine whether EGF ligand expression is an additional predictive factor for tyrosine kinase inhibitor response. The concept that the driving force behind many or most NSCLC tumors is EGF ligand receptor loops offers the clinician the following additional avenues for potential targeted therapies: preventing sheddase up-regulation or activity, preventing ligand production directly or by inhibition of the loop at a more upstream stage, targeting the soluble form of the ligand, and preventing ligand-receptor interaction.

With the identification of deregulated expression of EGF family ligands in lung cancer pathogenesis, we can now consider using the relevant ligands for early cancer diagnosis, identifying key therapeutic targets, and as biomarkers to monitor response to chemoprevention or very early treatment. Because the ligands are soluble, they potentially could be detected in blood or bronchial lavage specimens in addition to biopsy and brushing specimens. Furthermore, while exploring their diagnostic and therapeutic targeting roles, we need to understand the molecular mechanisms leading to the deregulated expression of these ligands. Copy number changes, mutations, promoter alterations (including epigenetic changes), the role of specific transcription factors

(such as the lineage-specific oncogene *TITF1*), and altered miRNA expression are all potential mechanisms that need to be explored, as does ligand expression in cancer stem cells.

Another major clinical interest is to understand the sequential appearance of molecular changes during multistage pathogenesis. The appearance of *EGFR* mutations at a preinvasive and even at a premalignant phase creates opportunities to use *EGFR* mutation markers for risk identification, early detection, and prevention, particularly for never smokers, who are at most risk for *EGFR*-mutant tumors and for whom no such markers currently exist (31). Early *EGFR* mutations also have important implications for the study of *EGFR* tyrosine kinase inhibitors in the adjuvant/second primary tumor prevention setting. Whereas mutations seem to be initiating events, copy number gains are related to progression and metastatic events. Therefore, heterogeneity may occur both within the primary tumor and between the primary tumor and metastatic sites. These considerations are important if copy number gains are used as a marker for selecting targeted therapies, and they indicate the importance of testing for this marker in tumor samples obtained immediately before therapy versus relying on marker data from earlier samples.

The reports of Zhang et al. and Tang et al. in this issue of the journal shed new light on the highly complex, multifaceted, and as yet incompletely understood nature of the *EGFR* signaling pathway. This pathway in NSCLCs and in the bronchial epithelium of patients at a high lung-cancer risk will be a critical focus of diagnostic, preventive, and therapeutic efforts for the foreseeable future.

Disclosure of Potential Conflicts of Interest

No potential conflicts of interest were disclosed.

References

- Cohen P. Protein kinases—the major drug targets of the twenty-first century? *Nat Rev Drug Discov* 2002;1:309–15.
- Mendelsohn J. Antibody-mediated EGF receptor blockade as an anticancer therapy: from the laboratory to the clinic. *Cancer Immunol Immunother* 2003;52:342–6.
- Hynes NE, Lane HA. ERBB receptors and cancer: the complexity of targeted inhibitors. *Nature reviews* 2005;5:341–54.
- Zhang J, Iwanaga K, Choi CC, et al. Intratumoral epigulgin is a marker of advanced disease in non-small cell lung cancer patients and confers invasive properties on *EGFR*-mutant cells. *Cancer Prev Res*. In press 2008.
- Tang X, Varella-Garcia M, Xavier AC, et al. *EGFR* abnormalities in the pathogenesis and progression of lung adenocarcinoma. *Cancer Prev Res*. In press 2008.
- Manning G, Plowman GD, Hunter T, Sudarsanam S. Evolution of protein kinase signaling from yeast to man. *Trends Biochem Sci* 2002;27:514–20.
- Citri A, Yarden Y. EGF-ERBB signalling: towards the systems level. *Nat Rev Mol Cell Biol* 2006;7:505–16.
- Shelly M, Pinkas-Kramarski R, Guarino BC, et al. Epigulgin is a potent pan-ErbB ligand that preferentially activates heterodimeric receptor complexes. *J Biol Chem* 1998;273:10496–505.
- Hynes NE, Schlange T. Targeting ADAMs and ERBBs in lung cancer. *Cancer cell* 2006;10:7–11.
- Fujimoto N, Wislez M, Zhang J, et al. High expression of ErbB family members and their ligands in lung adenocarcinomas that are sensitive to inhibition of epidermal growth factor receptor. *Cancer Res* 2005;65:11478–85.
- Volante M, Saviozzi S, Rapa I, et al. Epidermal growth factor ligand/receptor loop and downstream signaling activation pattern in completely resected nonsmall cell lung cancer. *Cancer* 2007;110:1321–8.
- Wu W, O'Reilly MS, Langley RR, et al. Expression of epidermal growth factor (EGF)/transforming growth factor- α by human lung cancer cells determines their response to EGF receptor tyrosine kinase inhibition in the lungs of mice. *Mol Cancer Ther* 2007;6:2652–63.
- Singh AB, Harris RC. Autocrine, paracrine and juxtacrine signaling by *EGFR* ligands. *Cell Signal* 2005;17:1183–93.
- Zhou BB, Peyton M, He B, et al. Targeting ADAM-mediated ligand cleavage to inhibit HER3 and *EGFR* pathways in non-small cell lung cancer. *Cancer Cell* 2006;10:39–50.
- Schafer ZT, Brugge JS. IL-6 involvement in epithelial cancers. *J Clin Invest* 2007;117:3660–3.
- Gao SP, Mark KG, Leslie K, et al. Mutations in the *EGFR* kinase domain mediate STAT3 activation via IL-6 production in human lung adenocarcinomas. *J Clin Invest* 2007;117:3846–56.
- Frederick L, Eley G, Wang XY, James CD. Analysis of genomic rearrangements associated with *EGFRvIII* expression suggests involvement of Alu repeat elements. *Neuro-oncol* 2000;2:159–63.
- Shigematsu H, Gazdar AF. Somatic mutations of epidermal growth factor receptor signaling pathway in lung cancers. *Int J Cancer* 2006;118:257–62.
- Sharma SV, Bell DW, Settleman J, Haber DA. Epidermal growth factor receptor mutations in lung cancer. *Nature reviews* 2007;7:169–81.
- Gazdar AF, Shigematsu H, Herz J, Minna JD. Mutations and addition to *EGFR*: the Achilles 'heel' of lung cancers? *Trends Mol Med* 2004;10:481–6.
- Engelman JA, Cantley LC. The role of the ErbB family members in non-small cell lung cancers sensitive to epidermal growth factor receptor kinase inhibitors. *Clin Cancer Res* 2006;12:4372–6s.
- Pao W, Wang TY, Riely GJ, et al. *KRAS* mutations and primary resistance of lung adenocarcinomas to gefitinib or erlotinib. *PLoS Med* 2005;2:e17.
- Riely GJ, Politi KA, Miller VA, Pao W. Update on epidermal growth factor receptor mutations in non-small cell lung cancer. *Clin Cancer Res* 2006;12:7232–41.
- Shepherd FA, Rosell R. Weighing tumor biology in treatment decisions for patients with non-small

- cell lung cancer. *J Thorac Oncol* 2007;2 Suppl 2: S68–76.
25. Cappuzzo F, Varella-Garcia M, Shigematsu H, et al. Increased HER2 gene copy number is associated with response to gefitinib therapy in epidermal growth factor receptor-positive non-small-cell lung cancer patients. *J Clin Oncol* 2005; 23:5007–18.
 26. Nomura M, Shigematsu H, Li L, et al. Polymorphisms, mutations, and amplification of the EGFR gene in non-small cell lung cancers. *PLoS Med* 2007;4:e125.
 27. Okabe T, Okamoto I, Tamura K, et al. Differential constitutive activation of the epidermal growth factor receptor in non-small cell lung cancer cells bearing EGFR gene mutation and amplification. *Cancer Res* 2007;67:2046–53.
 28. Minn AJ, Gupta GP, Siegel PM, et al. Genes that mediate breast cancer metastasis to lung. *Nature* 2005;436:518–24.
 29. Mao L, Lee JS, Kurie JM, et al. Clonal genetic alterations in the lungs of current and former smokers [see comments]. *J Natl Cancer Inst* 1997;89: 857–62.
 30. Wistuba II, Lam S, Behrens C, et al. Molecular damage in the bronchial epithelium of current and former smokers. *J Natl Cancer Inst* 1997;89:1366–73.
 31. Sun S, Schiller JH, Gazdar AF. Lung cancer in never smokers—a different disease. *Nat. Rev* 2007;7:778–90.
 32. Tang X, Shigematsu H, Bekele BN, et al. EGFR tyrosine kinase domain mutations are detected in histologically normal respiratory epithelium in lung cancer patients. *Cancer Res* 2005;65:7568–72.
 33. Lockwood WW, Chari R, Coe BP, et al. DNA amplification is a ubiquitous mechanism of oncogene activation in lung and other cancers. *Oncogene*. In press 2008.
 34. Soh J, Toyooka S, Ichihara S, et al. Sequential molecular changes during multistage pathogenesis of small peripheral adenocarcinomas of the lung. *J Thorac Oncol* 2008;3:340–7.
 35. Yatabe Y, Takahashi T, Mitsudomi T. Epidermal growth factor receptor gene amplification is acquired in association with tumor progression of EGFR-mutated lung cancer. *Cancer Res* 2008;68: 2106–11.
 36. Brambilla E, Travis WD, Colby TV, Corrin B, Shimosato Y. The new World Health Organization classification of lung tumours. *Eur Respir J* 2001; 18:1059–68.
 37. Tsao MS, Sakurada A, Cutz JC, et al. Erlotinib in lung cancer—molecular and clinical predictors of outcome. *N Engl J Med* 2005;353:133–44.

Tumor Suppressor FUS1 Signaling Pathway

Lin Ji, PhD, and Jack A. Roth, MD

Abstract: FUS1 is a novel tumor suppressor gene identified in the human chromosome 3p21.3 region where allele losses and genetic alterations occur early and frequently for many human cancers. Expression of FUS1 protein is absent or reduced in the majority of lung cancers and premalignant lung lesions. Restoration of wt-FUS1 function in 3p21.3-deficient non-small cell lung carcinoma cells significantly inhibits tumor cell growth by induction of apoptosis and alteration of cell cycle kinetics. Here we present recent findings indicating that FUS1 induces apoptosis through the activation of the intrinsic mitochondrial-dependent and Apaf-1-associated pathways and inhibits the function of protein tyrosine kinases including EGFR, PDGFR, AKT, c-Abl, and c-Kit. Intravenous administration of a nanoparticle encapsulated FUS1 expression plasmid effectively delivers FUS1 to distant tumor sites and mediates an antitumor effect in orthotopic human lung cancer xenograft models. This approach is the rationale for an ongoing FUS1-nanoparticle-mediated gene delivery clinical trial for the treatment of lung cancer.

Key Words: Tumor suppressor gene, FUS1, Signaling pathway, Lung cancer.

(*J Thorac Oncol.* 2008;3: 327–330)

Cytogenetic and allelotyping studies of fresh tumors and tumor cell lines have shown that allele losses and genetic alterations on the short arm of chromosome 3p (3p25, 3p21–22, 3p14, and 3p12–13) are among the most frequent and earliest genomic abnormalities involved in a wide spectrum of human cancers, including lung^{1–6} and breast.^{7–9} Multiple overlapping homozygous deletions have also been found in the 3p21.3 region, spanning a 120 kb genomic locus in human lung and breast cancer cell lines.^{10,11} Chromosomal abnormalities in the 3p21.3 region have been frequently detected in smoke-damaged respiratory epithelium and preneoplastic lesions.^{10,12–13} These findings suggest that one or more putative

3p21.3 tumor suppressor genes function as “gatekeepers” in the molecular pathogenesis of lung and other human cancers.^{10,12,14} The novel FUS1 gene is one of the nine candidate TSGs (*CACNA2D2*, *PL6*, *101F6*, *FUS1*, *BLU*, *RASSF1*, *NPRL2*, *HYAL2*, and *HYAL1*) that were identified in this region.^{1,14–17} In this review, we will describe a pathway involved in FUS1-mediated tumor suppression and discuss potential translational applications of the FUS1 TSG for human lung cancer therapy.

Inactivation of FUS1 In Lung Cancer Pathogenesis

The FUS1 gene may be inactivated in human cancer cell lines and primary tumors by haploinsufficiency.^{16,17} Although single allele loss is common, only a few missense mutations and C-terminal deletion mutations have been identified in primary lung cancer samples, and there is no evidence for promoter hypermethylation.^{6,16,17} FUS1 mRNA transcripts could be detected on Northern blots of RNAs prepared from some lung cancer cell lines, but no endogenous FUS1 protein could be detected in a majority of non-small cell lung carcinoma (NSCLC) cells and almost all of the small-cell lung cancer (SCLC) cell lines tested.^{6,16,17} Myristoylation of the FUS1 N-terminus is required for tumor suppressor activity.¹⁷ A loss of expression coupled with a myristoylation defect of the FUS1 protein was detected in primary lung cancers. The myristoylation defective FUS1 protein has a greatly reduced half-life and is subject to rapid proteosomal degradation.¹⁷ Using a tissue microarray of 303 lung cancers, loss or reduction of FUS1 expression was detected in 100% of SCLCs and 82% of NSCLCs.¹⁸ In NSCLCs, loss or reduction of FUS1 expression was associated with significantly worse overall patient survival. Squamous metaplasia and dysplasia expressed significantly lower levels of FUS1 than did normal and hyperplastic bronchial epithelia. Lee et al.¹⁹ showed the translation of FUS1 was significantly down-regulated by microRNA-378 targeting the 3'UTR of FUS1 mRNA and the ectopic expression of miR-378 enhanced cell survival, tumor growth, and angiogenesis. A genetically engineered mouse with a targeted disruption of the FUS1 gene developed signs of autoimmune disease, showed an increased frequency of spontaneous vascular tumor formation, and had defects in natural killer cell maturation coupled with IL-15 insufficiency.²⁰ These findings suggest that loss of FUS1 expression may play an important role in the early pathogenesis of lung cancer.

Section of Thoracic Molecular Oncology, Department of Thoracic and Cardiovascular Surgery, The University of Texas M. D. Anderson Cancer Center, Houston, Texas.

Disclosure: Drs. Roth and Ji have filed patents on the FUS1 gene which has been licensed by Introgen Therapeutics, Inc. Dr. Roth is a paid consultant and owns stock in Introgen Therapeutics, Inc.

Address for correspondence: Lin Ji, PhD, Department of Thoracic and Cardiovascular Surgery, Unit 445, The University of Texas. M. D. Anderson Cancer Center, P.O. Box, 301402, Houston, Texas 77230-1402. E-mail: lji@mdanderson.org

Copyright © 2008 by the International Association for the Study of Lung Cancer

ISSN: 1556-0864/08/0304-0327

The Role of FUS1 in the Intrinsic Apoptotic Signaling Pathway

We previously used recombinant adenoviruses or *N*-[1-(2,3-dioleoyloxy)propyl]-*N,N,N*-trimethylammonium chloride/cholesterol nanoparticle-complexed plasmid vectors to introduce FUS1 and other genes into lung cancer cells.^{14,15,17,21,22} FUS1 showed the most potent proapoptotic activity in human lung cancer cells among these candidate 3p21.3 TSGs.^{15–17,23} To identify the pathway involved in FUS1-mediated apoptosis, we used a ProteinChip array-based SELDI-MS spectrometry to analyze all of the protein species in complexes immunoprecipitated by anti-FUS1-antibodies. The apoptotic protease-activating factor 1 (Apaf-1) was identified as a potential cellular target of FUS1 protein by its direct protein–protein interaction (Figure 1). A computer-based analysis of the functional domains and signaling motifs within the amino acid sequence of FUS1 and Apaf-1 proteins reveals Class II and Class I PDZ^{24,25} protein–protein interaction motifs at the C-termini of FUS1 and Apaf-1 proteins, respectively, providing a structural bases for FUS1-Apaf-1 protein–protein interaction. Apaf-1 plays an important role in the mitochondria-dependent apoptotic pathway.^{26–28} A relatively high level of endogenous Apaf-1 protein was universally detected in lung cancer cells. These Apaf-1 proteins

appeared to be functionally inactive, as indicated by their lack of intrinsic ATPase activity, which is essential for Apaf-1-mediated caspase activation and apoptosis induction in both cancer cells deficient in FUS1 expression and in normal cells with low level of endogenous FUS1 expression.^{28,29} We showed that activation of endogenous FUS1 in normal cells in response to stress, such as UV irradiation, and the forced expression of FUS1 in FUS1-deficient tumor cells can trigger cytochrome C release from mitochondria into the cytosol and cause FUS1 binding to Apaf-1 and recruit it to critical cellular locations, thus, activating Apaf-1 in situ, initiating Apaf-1-mediated caspase activation, and inducing apoptosis.^{17,30,31} Although our proposed mechanism remains to be validated by identifying all of the components in this complicated apoptotic apparatus and their dynamic interactions, our findings support a role for loss of FUS1 expression as a critical event in lung cancer pathogenesis.

Inhibition of Tyrosine Kinase Signaling by FUS1

We found that reactivating FUS1 in 3p21.3-deficient lung cancer cells inhibited their growth and induced apoptosis, in part, by inhibiting protein tyrosine kinases (PTKs) such as EGFR, PDGFR, c-Abl, c-Kit, and AKT (Figure 1). A

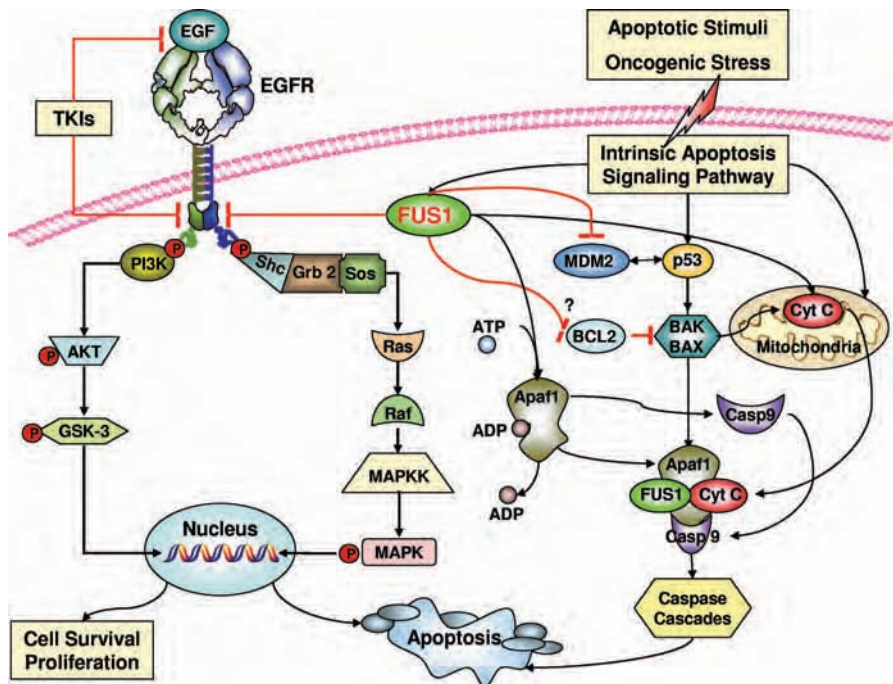


FIGURE 1. Schema of the FUS1 pathway. Activation of FUS1 in normal cells in response to apoptotic stimuli, stress, or restoration of wt-FUS1 function by ectopic gene transfer in FUS1-deficient tumor cells activates the intrinsic mitochondrial apoptosis pathway. Activation of FUS1 triggers cytochrome c (Cyt C) release from the inner membrane of mitochondria to the cytosol, selectively and directly interacts with Apaf-1 and recruits it to a critical subcellular location, and activates Apaf-1 by induction of its ATPase activity in situ thus facilitating downstream Apaf-1-mediated apoptosome assembly, caspase activation, and apoptosis induction. Activation of FUS1 may also block MDM2-associated proteolytic degradation of p53 and enhance the p53-dependent apoptotic pathway. The potent tumor suppressor activity of FUS1 is also in part mediated by its inhibition of multiple oncogenic protein tyrosine kinases (PTKs) including EGFR, PDGFR, c-Abl, c-Kit, and AKT that are up-regulated in cancer cells. FUS1-mediated inactivation of these oncogenic PTKs leads to induction of apoptosis and inhibition of tumor cell proliferation and survival.

computer-based homology modeling of the FUS1 protein sequence and structure³² predicts a potential protein kinase A activation site, and an A kinase anchoring protein homology motif.¹⁷ It has been shown that a FUS1 peptide derived from FUS1 protein sequence in a region that was deleted in a mutant *FUS1* gene detected in some lung cancer cell lines inhibits a constitutively active recombinant c-Abl tyrosine kinase and the full length c-Abl kinase *in vitro*.³³ Platelet-derived growth factors (PDGFs) play a crucial role in cell migration, proliferation, apoptosis, and cell survival. Forced expression of wt-FUS1 by nanoparticle-mediated gene transfer in the PDGFR β -expressing SCLC H69 and H417 cell lines inactivated PDGFR β and its downstream targets, PI3K and AKT kinases, as shown by marked reduction in PTK phosphorylation.

We explored the ability of FUS1 expression to overcome gefitinib resistance in NSCLC cells. We found that reexpression of wt-FUS1 by *FUS1*-nanoparticle-mediated gene transfer into FUS1-deficient and gefitinib-resistant NSCLC cell lines that have wt-EGFR sensitized them to gefitinib treatment and synergistically induced apoptosis. FUS1 nanoparticle treatment alone or with gefitinib in gefitinib-resistant NSCLC cells markedly inactivated EGFR and AKT, as shown by decreased phosphorylation levels of these proteins, and activated caspase-3, caspase-9, and PARP, as shown by the increased cleavage of their precursor proteins on Western blots. Together, these results suggest that combination treatment with FUS1 and PTK inhibitors may be a useful therapeutic strategy for human lung cancer.

Translational Applications of FUS1 for Lung Cancer Therapy

We initiated a dose escalation Phase I clinical trial of FUS1-nanoparticles in patients with chemotherapy refractory stage IV lung cancer. In this clinical trial, a FUS1 expression plasmid in a nanoparticle is injected intravenously in stage IV lung cancer patients who had progressed after cisplatin combination chemotherapy. The trial continues to accrue patients.

We have also explored the combined effects of the FUS1-nanoparticles with conventional chemotherapy and external beam radiotherapy.³¹ Forced expression by *FUS1*-nanoparticle-mediated gene transfer sensitized NSCLC cells to cisplatin or γ -radiation, resulting in a 3- to 8-fold increase in inhibition of tumor cell viability and induction of apoptosis in *FUS1*-transfected cells. Systemic treatment with a combination of *FUS1* nanoparticles and cisplatin in a human lung cancer orthotopic mouse model synergistically enhanced the therapeutic efficacy of cisplatin.

We evaluated the combined effects of FUS1 and the TSG p53 on tumor cell growth and apoptosis induction in NSCLC cells cotransfected with *FUS1*- and *p53*.³⁰ We found that coexpression of wt-p53 with wt-FUS1, but not the myristoylation mutant (mt-FUS1), synergistically inhibited cell proliferation and induced apoptosis in human NSCLC cells. We also found that coexpression of FUS1 and p53 enhanced the sensitivity of NSCLC cells to treatments with the DNA-damaging agents γ -radiation and cisplatin. We found that the observed synergistic tumor suppression by FUS1 and p53 correlated with FUS1-mediated down-regula-

tion of MDM2 expression resulting in the accumulation and stabilization of p53 protein and the up-regulation of Apaf-1 expression with activation of the caspase cascade (Figure 1). Our results demonstrate an important role for FUS1 in modulating chemo- and radiosensitivities of lung cancer cells and suggest that an optimal combination of molecular therapeutics, such as the proapoptotic tumor suppressor *FUS1*-nanoparticle and conventional anticancer agents, such as cisplatin, may be an effective treatment strategy for human lung cancer.

ACKNOWLEDGMENTS

Our research is supported by the National Cancer Institute, the National Institutes of Health (SPORE P50CA070907; UO1CA105352; RO1CA116322); Department of Defense Lung Cancer Programs (DAMD17-02-1-0706 and W81XWH-07-1-0306).

REFERENCES

- Lerman MI, Minna JD. The 630-kb lung cancer homozygous deletion region on human chromosome 3p21. 3: identification and evaluation of the resident candidate tumor suppressor genes. The International Lung Cancer Chromosome 3p21. 3 Tumor Suppressor Gene Consortium. *Cancer Res* 2000;60:6116–6133.
- Minna JD, Fong K, Zochbauer-Muller S, et al. Molecular pathogenesis of lung cancer and potential translational applications. *Cancer J* 2002; 8(Suppl 1):S41–S46.
- Sekido Y, Fong KM, Minna JD. Molecular genetics of lung cancer. *Ann Rev Med* 2003;54:73–87.
- Wistuba II, Gazdar AF, Minna JD. Molecular genetics of small cell lung carcinoma. *Semin Oncol* 2001;28:3–13.
- Yan PS, Shi H, Rahmatpanah F, et al. Differential distribution of DNA methylation within the RASSF1A CpG island in breast cancer. *Cancer Res* 2003;63:6178–6186.
- Zabarovsky ER, Lerman MI, Minna JD. Tumor suppressor genes on chromosome 3p involved in the pathogenesis of lung and other cancers. *Oncogene* 2002;21:6915–6935.
- Maitra A, Wistuba II, Washington C, et al. High-resolution chromosome 3p allelotyping of breast carcinomas and precursor lesions demonstrates frequent loss of heterozygosity and a discontinuous pattern of allele loss. *Am J Pathol* 2001;159:119–130.
- Miller BJ, Wang D, Krahe R, et al. Pooled analysis of loss of heterozygosity in breast cancer: a genome scan provides comparative evidence for multiple tumor suppressors and identifies novel candidate regions. *Am J Hum Genetics* 2003;73:748–767.
- Yang Q, Yoshimura G, Mori I, et al. Chromosome 3p and breast cancer. *J Hum Genetics* 2002;47:453–459.
- Wistuba II, Behrens C, Virmani AK, et al. High resolution chromosome 3p allelotyping of human lung cancer and preneoplastic/preinvasive bronchial epithelium reveals multiple, discontinuous sites of 3p allele loss and three regions of frequent breakpoints. *Cancer Res* 2000;60: 1949–1960.
- Daly MC, Xiang RH, Buchhagen D, et al. A homozygous deletion on chromosome 3 in a small cell lung cancer cell line correlates with a region of tumor suppressor activity. *Oncogene* 1993;8:1721–1729.
- Zochbauer-Muller S, Gazdar AF, Minna JD. Molecular pathogenesis of lung cancer. *Annu Rev Physiol* 2002;64:681–708.
- Wistuba II, Lam S, Behrens C, et al. Molecular damage in the bronchial epithelium of current and former smokers. *J Natl Cancer Inst* 1997;89: 1366–1373.
- Ji L, Minna JD, Roth JA. 3p21. 3 tumor suppressor cluster: prospects for translational applications. *Future Oncol* 2005;1:79–92.
- Ji L, Nishizaki M, Gao B, et al. Expression of several genes in the human chromosome 3p21. 3 homozygous deletion region by an adenovirus vector results in tumor suppressor activities *in vitro* and *in vivo*. *Cancer Res* 2002;62:2715–2720.
- Kondo M, Ji L, Kamibayashi C, et al. Overexpression of candidate tumor suppressor gene FUS1 isolated from the 3p21. 3 homozygous

- deletion region leads to G1 arrest and growth inhibition of lung cancer cells. *Oncogene* 2001;20:6258–6262.
17. Uno F, Sasaki J, Nishizaki M, et al. Myristoylation of the FUS1 protein is required for tumor suppression in human lung cancer cells. *Cancer Res* 2004;64:2969–2976.
 18. Prudkin L, Behrens C, Liu DD, et al. Loss and reduction of FUS1 protein expression is a frequent phenomenon in the pathogenesis of lung cancer. *Clin Cancer Res* 2008;14:41–47.
 19. Lee DY, Deng Z, Wang CH, et al. MicroRNA-378 promotes cell survival, tumor growth, and angiogenesis by targeting SuFu and Fus-1 expression. *Proc Natl Acad Sci USA* 2007;104:20350–20355.
 20. Jakubowska A, Gronwald J, Menkiszak J, et al. Autoimmunity, spontaneous tumorigenesis, and IL-15 insufficiency in mice with a targeted disruption of the tumour suppressor gene *Fus1*. *J Pathol* 2007;211:591–601.
 21. Ohtani S, Iwamaru A, Deng W, et al. Tumor suppressor 101F6 and ascorbate synergistically and selectively inhibit non-small cell lung cancer growth by caspase-independent apoptosis and autophagy. *Cancer Res* 2007;67:6293–6303.
 22. Ueda K, Kawashima H, Ohtani S, et al. The 3p21. 3 tumor suppressor NPRL2 plays an important role in cisplatin-induced resistance in human NSCLC cells. *Cancer Res* 2006;66:9682–9690.
 23. Ito I, Ji L, Tanaka F, et al. Liposomal vector mediated delivery of the 3p *FUS1* gene demonstrates potent antitumor activity against human lung cancer *in vivo*. *Cancer Gene Ther* 2004;11:733–739.
 24. Fanning AS and Anderson JM. Protein modules as organizers of membrane structure. *Cur Opin Cell Biol* 1999;11:432–439.
 25. Nourry C, Grant SG, Borg JP. PDZ domain proteins: plug and play! *Sci STKE* 2003;2003:RE7.
 26. Acehan D, Jiang X, Morgan DG, et al. Three-dimensional structure of the apoptosome: implications for assembly, procaspase-9 binding, and activation. *Mol Cell* 2002;9:423–432.
 27. Riedl SJ, Salvesen GS, Riedl SJ, et al. The apoptosome: signalling platform of cell death. *Nat Rev Mol Cell Biol* 2007;8:405–413.
 28. Riedl SJ, Li W, Chao Y, et al. Structure of the apoptotic protease-activating factor 1 bound to ADP. *Nature* 2005;434:926–933.
 29. Bao Q, Riedl SJ, Shi Y, et al. Structure of Apaf-1 in the auto-inhibited form: a critical role for ADP. *Cell Cycle* 2005;4:1001–1003.
 30. Deng W, Kawashima H, Wu G, et al. Synergistic tumor suppression by coexpression of FUS1 and p53 is associated with down-regulation of murine double minute-2 and activation of the apoptotic protease-activating factor 1-dependent apoptotic pathway in human non-small cell lung cancer cells. *Cancer Res* 2007;67:709–717.
 31. Deng WG, Wu G, Ueda K, et al. Enhancement of antitumor activity of cisplatin in human lung cancer cells by tumor suppressor FUS1. *Cancer Gene Ther* 2007;15:29–39.
 32. Lee D, Redfern O, Orengo C. Predicting protein function from sequence and structure. *Nat Rev Mol Cell Biol* 2007;8:995–1005.
 33. Lin J, Sun T, Ji L, et al. Oncogenic activation of c-Abl in non-small cell lung cancer cells lacking FUS1 expression: Inhibition of c-Abl by the tumor suppressor gene product *Fus1*. *Oncogene* 2007;26:6989–6996.

Quantum dot-based quantification revealed differences in subcellular localization of EGFR and E-cadherin between EGFR-TKI sensitive and insensitive cancer cells

Dong-hai Huang^{1,2}, Ling Su¹, Xiang-hong Peng¹,
Hongzheng Zhang¹, Fadlo R Khuri¹, Dong M Shin¹ and
Zhuo (Georgia) Chen^{1,3}

¹ Department of Hematology and Medical Oncology, Winship Cancer Institute, Emory University School of Medicine, Atlanta, GA, USA

² Department of Otolaryngology—Head and Neck Surgery, Xiang-Ya Hospital, Central South University, Changsha, Hunan, People's Republic of China

E-mail: gzchen@emory.edu

Received 5 February 2009, in final form 24 March 2009

Published 12 May 2009

Online at stacks.iop.org/Nano/20/225102

Abstract

Nanoparticle quantum dots (QDs) provide sharper and more photostable fluorescent signals than organic dyes, allowing quantification of multiple biomarkers simultaneously. In this study, we quantified the expression of epidermal growth factor receptor (EGFR) and E-cadherin (E-cad) in the same cells simultaneously by using secondary antibody-conjugated QDs with two different emission wavelengths (QD605 and QD565) and compared the cellular distribution of EGFR and E-cad between EGFR-tyrosine kinase inhibitor (TKI)-insensitive and -sensitive lung and head and neck cancer cell lines. Relocalization of EGFR and E-cad upon treatment with the EGFR-TKI erlotinib in the presence of EGF was visualized and analyzed quantitatively. Our results showed that QD-immunocytochemistry (ICC)-based technology can not only quantify basal levels of multiple biomarkers but also track the localization of the biomarkers upon biostimulation. With this new technology we found that in EGFR-TKI-insensitive cells, EGFR and E-cad were located mainly in the cytoplasm; while in sensitive cells, they were found mainly on the cell membrane. After induction with EGF, both EGFR and E-cad internalized to the cytoplasm, but the internalization capability in sensitive cells was greater than that in insensitive cells. Quantification also showed that inhibition of EGF-induced EGFR and E-cad internalization by erlotinib in the sensitive cells was stronger than that in the insensitive cells. These studies demonstrate substantial differences between EGFR-TKI-insensitive and -sensitive cancer cells in EGFR and E-cad expression and localization both at the basal level and in response to EGF and erlotinib. QD-based analysis facilitates the understanding of the features of EGFR-TKI-insensitive versus -sensitive cancer cells and may be used in the prediction of patient response to EGFR-targeted therapy.

1. Introduction

In recent years, the science of nanotechnology has been combined with the disciplines of biology and medicine

³ Address for correspondence: Department of Hematology and Medical Oncology, Winship Cancer Institute, Emory University School of Medicine, 1365-C Clifton Road, Suite C3086, Atlanta, GA 30322, USA.

to provide advantages in molecular detection, imaging, diagnostics, and therapeutics in the cancer field [1, 2]. Quantum dots (QDs) are nanoscale particles made from inorganic semiconductors and have large molar extinction coefficients which are 10–50 times larger than those of organic dyes. QDs have superior signal brightness, photostability, longer excited-state lifetimes, and optimized signal-to-background ratios compared with organic dyes [3]. QDs can be covalently linked to biological molecules such as peptides, proteins, and nucleic acids [4, 5]. Thus, they are ideal imaging materials for molecular profiling [3–6]. A significant advantage of QDs over immunofluorescence using organic dyes and fluorescence-activated cell sorting (FACS) is that QDs can both visualize and quantify multiple biomarkers simultaneously in the same material because they have a long excitation and narrow emission spectra and can be excited simultaneously through one appropriate excitation source. This allows the quantification and correlation of molecular signatures with cellular response to targeted therapies [6, 7].

Epidermal growth factor receptor (EGFR) is a 170 kDa transmembrane protein with intrinsic tyrosine kinase activity that regulates cell growth in response to binding of its ligands, including epidermal growth factor (EGF) and transforming growth factor- α (TGF- α). Overexpression of EGFR and its ligand TGF- α is reportedly observed in 50–90% of non-small cell lung carcinoma (NSCLC) [8, 9] and 80–90% of squamous cell carcinoma of the head and neck (SCCHN) specimens [10–13]. Several studies have demonstrated that EGFR overexpression correlates with reduced disease-free and overall survival [13–18]. Therefore, many strategies including using specific tyrosine kinase inhibitors (TKI) and monoclonal antibodies to target EGFR have been developed for the treatment of NSCLC and SCCHN. However, resistance to EGFR-TKI treatment has been observed in lung, SCCHN, and other types of cancer [19]. The relationship between EGFR expression and a patient's response to EGFR-targeted therapy is currently not clear [20–23].

Recent publications suggest that an epithelial-to-mesenchymal transition (EMT) is a determinant of the sensitivity of cancer cells to EGFR inhibition [24–26]. E-cadherin (E-cad) expression in NSCLC and SCCHN tissue specimens has been reported in several studies and is correlated with tumor progression and metastasis [27–33]. Restoring E-cad expression enhanced sensitivity to EGFR-targeted therapy [34], suggesting that E-cad expression may be required for successful targeting of EGFR. Although the hypothesis that E-cad and EGFR may interact was proposed more than ten years ago [35], the effect of the molecular relationship between EGFR and E-cad on EGFR-targeted therapy is currently unclear. Recently, we examined the expression and localization of E-cad and EGFR in both SCCHN tissue specimens and cell line models and found that not only expression but also localization of EGFR and E-cad had clinical relevance in predicting lymph node metastasis and patient survival [36]. Therefore, quantification of EGFR and E-cad localization at a basal level and in response to EGFR ligands and EGFR-TKIs should facilitate our understanding of the mechanism of resistance to EGFR-targeted therapy.

This current study reports the use of QD-based immunocytochemistry (QD-ICC) per-cell quantification analyses to study the expression and subcellular localization of EGFR and E-cad. QD-based quantification allows comparison of the expression of these two proteins between EGF-TKI-sensitive and -insensitive NSCLC and SCCHN cancer cell lines, thereby elucidating one mechanism for cellular resistance to EGFR-targeted therapy and providing a basis for the prediction of response to EGFR-targeted therapy.

2. Materials and methods

2.1. Cell lines

NSCLC cell lines H1703, H460, H292 and H322 were kindly provided by Dr Shi-Yong Sun (Emory University Winship Cancer Institute, Atlanta GA); H460 and H1703 are EGFR-TKI-insensitive and H292 and H322 are -sensitive cell lines [25]. The SCCHN cell line 686LN was established from a lymph node metastasis of a primary base of tongue SCC. 686LN-M4e is a highly metastatic cell line generated by *in vivo* selection from 686LN that has low metastatic potential in the lymph node of the nude mouse as described previously [37]. The SCCHN cell line 686LN-R30 is an EGFR-TKI-insensitive cell line established from 686LN by single cell cloning after challenging with gradually increased concentrations of gefitinib. Additional SCCHN cell lines UPCI-37A and -37B were established from larynx (epiglottis) at the University of Pittsburgh Cancer Institute (Pittsburgh, PA); UPCI-37A was from a primary tumor, while UPCI-37B was from lymph node metastases. These cell lines were maintained as monolayer cultures in RPMI 1640 medium (NSCLC cells) or DMEM/F12 50/50 medium (SCCHN cells) supplemented with 10% heat-inactivated fetal bovine serum (FBS). All cells were maintained in a humidified incubator at 37°, 5% CO₂.

2.2. QD-based immunocytochemistry (QD-ICC)

The cells were seeded onto an 8-well chamber slide (Lab-Tek Permanox™ slide, Rochester, NY) and starved for 24 h (in FBS-free medium). The cells were then incubated with or without erlotinib (0–2.5 μ M) for 2 h and stimulated with 100 ng ml⁻¹ EGF (Invitrogen, Carlsbad, CA) for 30 min at 37°C. The cells were fixed with 4% paraformaldehyde, permeabilized with 0.25% Triton-X-100/PBS for 10 min, blocked with 10% goat serum, and incubated with primary antibodies, rabbit anti-EGFR (clone 1005, 1:200 dilution, Santa Cruz Biotechnology, Santa Cruz, CA) and mouse anti-E-cad (clone 36, 1:400 dilution, BD Biosciences, Franklin Lakes, NJ) simultaneously. After washing with phosphate-buffered saline (PBS), the cells were incubated with QD-secondary antibody conjugates (QD 605 goat F(ab')₂ anti-rabbit IgG; QD 565 goat F(ab')₂ anti-mouse IgG, 1:100 dilution, Invitrogen, Carlsbad, CA) in a cocktail solution at 37°C (figure 1). These QDs are made of semiconductor materials, including cadmium mixed with selenium or tellurium which has been coated with an additional semiconductor shell (zinc sulfide) to improve the optical properties of the material. Cell nuclei were

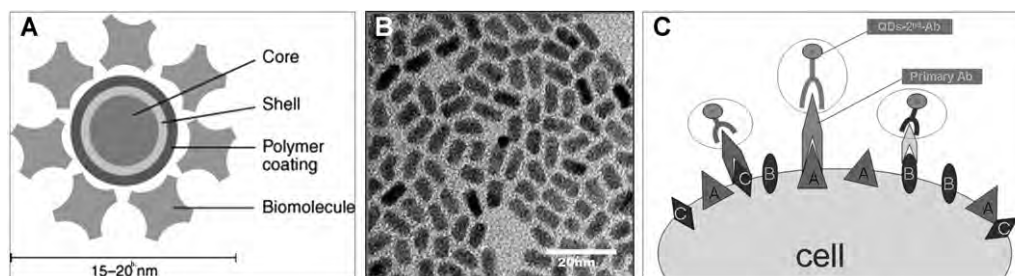


Figure 1. (A) Schematic diagram of the overall structure of a QD-secondary antibody conjugate. The layers represent the distinct structural elements of the QD nanocrystal conjugates, and are roughly to scale (adapted from Invitrogen). (B) TEM image of core-shell QD nanoparticles at 200 000 \times magnification (adapted from Invitrogen). (C) Cartoon showing cocktail QD-based immunocytochemistry (QD-ICC) with QD-secondary antibody conjugates. Several proteins presented as A, B and C can be detected simultaneously by specific primary antibodies plus appropriate secondary antibodies conjugated with QDs.

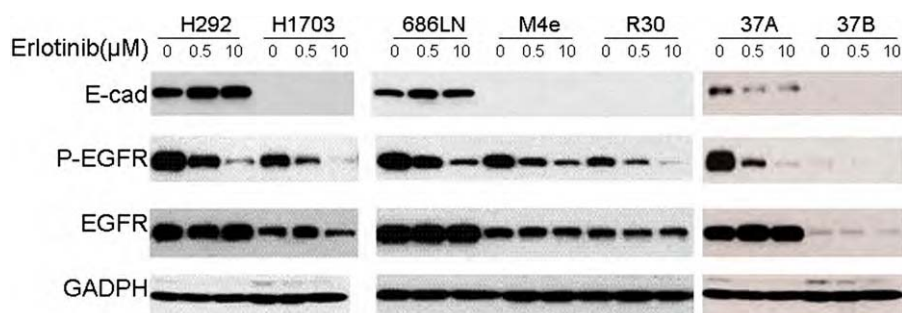


Figure 2. Immunoblotting of cancer cells treated with erlotinib. Lung cancer cell lines H292 and H1703, head and neck cancer cell lines 686LN, 686LN-M4e, 686LN-R30, UPCI-37A and -37B were treated with erlotinib at concentrations of 0.5 and 10 μ M for 72 h. G3PDH served as a loading control.

counterstained using 4',6-diamidino-2-phenylindole (DAPI, Invitrogen, Carlsbad, CA). Mouse and rabbit IgG were used as negative controls.

For tracking the endosome and lysosome distribution of EGFR in both EGF-TKI-sensitive and -insensitive cell lines, the cells were stimulated with 100 ng ml⁻¹ EGF for 30, 60 or 120 min at 37 °C. The mixed primary antibodies were rabbit anti-EGFR (clone 1005, 1:200 dilution, Santa Cruz Biotechnology, Santa Cruz, CA) plus mouse anti-EEA1, an early endosome marker (clone 10, 1:800 dilution, BD Biosciences, Franklin Lakes, NJ), or mouse anti-CD63, a late endosome/lysosome marker (clone H5C6, 1:800 dilution, BD Biosciences, Franklin Lakes, NJ). The staining procedures were the same as the above.

2.3. QD spectral imaging and signal quantification

An Olympus microscope IX71 with a CRi Nuance spectral imaging and quantifying system (CRi Inc., Woburn, MA), was used to observe and quantify the QD signal. All cubed image files were collected from the cell slides at 10 nm wavelength intervals from 500 to 800 nm, with an auto exposure time per wavelength interval at 400 \times magnification. Taking the cube with a long wavelength bandpass filter allowed transmission of all emission wavelengths above 450 nm. Both separated and combined QD images were established after determining the QD spectral library and unmixing the cube. We removed background for accurate quantification of the QD signals. For

quantification of the QD signal on cellular membranes and in the cytoplasm with Nuance software, we obtained both total and manually marked membrane QD signals which showed the correct QD wavelength in 50 cells from 10 randomly selected fields on the cell slides. The signal unit (au) was defined as the average fluorescence signal intensity per exposure time (ms) which was obtained from the Nuance software. The relative internalization of EGF-induced EGFR or E-cad was defined as [1-(membrane signal with EGF/membrane signal without EGF)] \times 100%.

2.4. Immunoblotting analysis

Immunoblotting was performed as described in our previous studies [37, 38]. Primary antibodies for immunoblotting were monoclonal antibodies against E-cad (clone G-10, 1:1000 dilution), polyclonal antibodies against phospho-EGFR (Tyr 1045, 1:500 dilution), and EGFR (clone 1005, 1:500 dilution) (Santa Cruz Biotechnology, Santa Cruz, CA). An antibody against G3PDH (1:3000 dilution, Trevigen, Inc., Gaithersburg, MD) was used as an internal control.

2.5. Fluorescence-activated cell sorting (FACS)

After starving the cells for 24 h, erlotinib (0.1–2.5 μ M) was added to the cells 2 h before stimulation with EGF-Alexa Fluor-488 (100 ng ml⁻¹, Invitrogen, Carlsbad, CA) for 30 min. Then the cells were washed with acetic acid (0.2 M, plus

0.5 M NaCl, pH 2.8) to remove the uninternalized membrane receptor, and suspended in 2% bovine serum albumin (BSA) with 0.05% Na₃N in PBS. FACS was used to examine EGFR internalization. Cells incubated with EGF-488 at 4 °C were used as the negative control. Relative internalization was defined as (FITC + cells/total cells) × 100%.

2.6. Statistical analysis

All results represent the average of at least three separate experiments and are expressed as mean ± SD unless otherwise indicated. Statistical analysis was performed using a *t*-test. $P < 0.05$ was considered as statistically significant.

3. Results and discussion

3.1. Basal level and localization of EGFR and E-cad

To understand EGFR-TKI resistance, we tested 9 lung and head and neck cancer cell lines: H1703, H460, H292, H322; 686LN, 686LN-R30, 686LN-M4e; UPCI-37A and -37B. Among them H292, H322, 686LN, UPCI-37A are sensitive to EGFR-TKI and H1703, H460, 686LN-R30, 686LN-M4e, and UPCI-37B are insensitive cell lines. Alterations in the levels of E-cad, p-EGFR, and total EGFR in the presence or absence of erlotinib were studied by immunoblotting (figure 2). The data showed that although p-EGFR levels were reduced by 0.5 μM erlotinib in the EGFR-TKI-insensitive cell lines H1703, 686LN-M4e, 686LN-R30 and 37B cells, almost no growth inhibition was observed in these cells, by treatment with erlotinib at this concentration (data not shown). Thus, reduction of activated EGFR did not correlate with growth inhibition by erlotinib in the EGFR-TKI-insensitive cell lines. Furthermore, the insensitive cell lines had lower total levels of EGFR and E-cad than the sensitive cell lines.

Since immunoblotting can only show the total level of each protein, QD-ICC combined with its interrelated imaging and quantification system was used to obtain the quantified colocalization of the related proteins in the same sample. Figure 3 shows membrane and cytoplasmic distribution of E-cad and EGFR in EGFR-TKI-sensitive and -insensitive cells. Results of the quantification show that the mean of the average E-cad membrane signal in four sensitive cell lines was 0.512 ± 0.110 au, while that in five insensitive cells was only 0.307 ± 0.055 au ($P < 0.008$; table 1). The mean of the average EGFR membrane signal in the sensitive cell lines was 1.413 ± 0.448 au compared with 0.443 ± 0.076 au in insensitive cells ($P < 0.002$; table 1). QD-based quantification also confirmed that not only membrane but also total protein levels of both EGFR and E-cad were lower in the insensitive cell lines than in the sensitive cell lines (data not shown).

These observations are consistent with our recent studies on human tissues and animal and cell line models of head and neck cancer, which identified three populations of tumor cells, including those with high membrane expression of EGFR and E-cad and those with low and mostly cytoplasmic expression of EGFR and E-cad [36]. To further understand these cells, we asked two fundamental questions, (i) how these cells respond

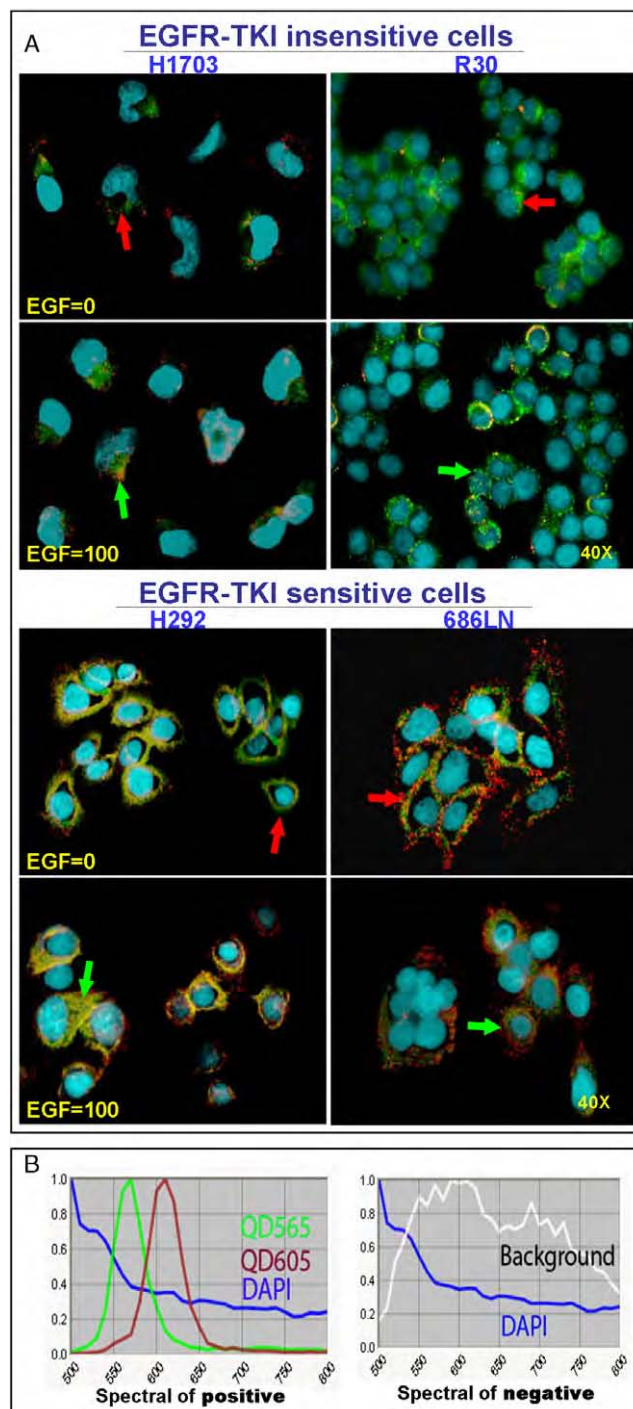


Figure 3. (A) Colocalization of EGFR (QD605, red) and E-cad (QD565, green) in the absence or presence of EGF. EGFR and E-cad expression levels were imaged by an Olympus microscope IX71 with a CRi spectral imaging and quantifying system. Yellow indicates colocalization of EGFR (red) and E-cad (green). (B) Spectral image of positive staining (including QDs 565, QDs 605, and DAPI signals) and negative staining (only background and DAPI signals).

to EGFR ligands such as EGF, and (ii) what happens when EGFR-TKI is applied to the EGFR-activated cells?

The cocktail solution for QD-secondary antibody conjugates was prepared in PBS, as recommended by the QD

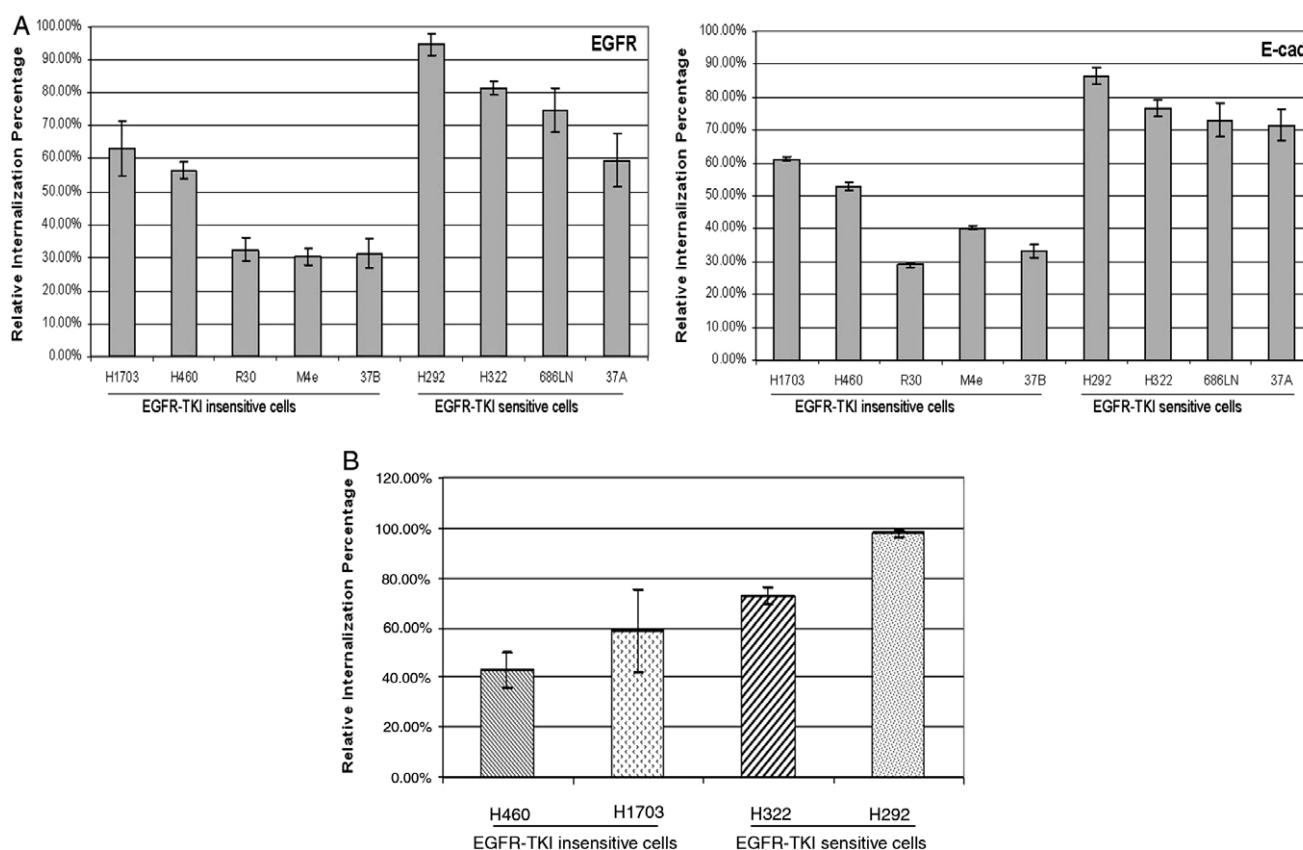


Figure 4. (A) Comparison of internalization of E-cad and EGFR induced by EGF in EGFR-TKI-insensitive and -sensitive cell lines measured by a CRi Nuance system. Relative internalization was defined as $[1 - (\text{membrane EGFR with EGF} / \text{membrane EGFR without EGF})] \times 100\%$. (B) Comparison of EGF-induced EGFR internalization measured by FACS. Relative internalization was defined as $(\text{FITC} + \text{cells} / \text{total cells}) \times 100\%$.

manufacturer, Invitrogen Cooperation, and is suggested not to affect the stability of their QDs. Our study confirmed that the QD signals in PBS appeared in the correct wavelength with reasonable sensitivity (see figure 3). Although there may be some signal interference between the two QDs, our objective is to compare the signals of QD565 (EGFR) and QD605 (E-cad) between different cell lines or between different treatments, not between QD565 and QD605; thus, any alteration in signal level due to the cocktail solution is unlikely to affect our experimental results.

3.2. Response to EGF-induced EGFR internalization

In order to characterize the differences between these two types of cell lines, relocalization of EGFR and E-cad was quantified by different QD signals simultaneously after induction with EGF. We found that both EGFR and E-cad internalized to the cytoplasm in EGFR-TKI-sensitive cell lines upon addition of EGF. In contrast, in -insensitive cells, these dynamic changes were not clearly observed (figure 3). Quantification showed that the capability of EGF to induce EGFR and E-cad internalization was much greater in sensitive cells than in insensitive cells. In detail, the percentage of relative EGFR internalization in the sensitive cells was 1.39–2.21-fold greater and the E-cad internalization was 1.65–2.00-fold greater than that in the insensitive cells (figure 4(A)). EGFR internalization

induced by EGF was confirmed with conventional FACS (figure 4(B)), which showed that in sensitive cells, the percentage of relative internalization of EGFR was 72.97–97.99%, compared with only 42.82–58.59% in insensitive cells. These results are similar to those from the QD-ICC analysis.

3.3. Erlotinib inhibition of EGF-induced EGFR internalization

QD quantification showed that erlotinib at $0.5 \mu\text{M}$ inhibited EGF-induced EGFR internalization by 30.90–63.59% in the sensitive cells as compared with the untreated control, whereas in the insensitive cells the inhibitory effect was only 5.28–11.47% (figures 5 and 6(A)). Erlotinib at $0.5 \mu\text{M}$ also had a significant inhibitory effect on E-cad internalization in sensitive cells. Quantified QD-ICC showed that in the sensitive cells, the inhibition of EGF-induced E-cad internalization was 30.03–46.62%, compared with 3.52–9.60% in the insensitive cells (figure 6(A)). FACS analysis also confirmed that inhibition of EGFR internalization by erlotinib was dose-dependent in both EGFR-TKI-insensitive and -sensitive cell lines (figures 5 and 6(B)), but the inhibition was much stronger in sensitive than insensitive cells.

EGFR-targeted therapies have been both tested in clinical trials and used in clinical practice. Among them, erlotinib

Table 1. Quantified results of E-cad and EGFR membrane signals. (Note: Average membrane signals of E-cad (QD565) and EGFR (QD605) between EGFR-TKI-insensitive (H1703, H460, R30, M4e, and 37B) and -sensitive (H292, H322, 686LN, and 37A) cell lines were determined manually with CRi Nuance software as described in the Materials and methods section. au = fluorescence average signal intensity per exposure time (ms) (Avg. signal/exp.)

1st Ab/cell lines	EGF = 0		EGF = 100	
	Avg. signal/exp. (au)	STD. (au)	Avg. signal/exp. (au)	STD. (au)
EGFR				
H1703	0.312	0.018	0.121	0.007
H460	0.222	0.009	0.105	0.013
R30	0.377	0.012	0.268	0.047
M4e	0.320	0.011	0.191	0.030
37B	0.305	0.015	0.204	0.021
H292	0.574	0.050	0.077	0.024
H322	0.440	0.019	0.103	0.026
686LN	0.634	0.080	0.170	0.052
37A	0.401	0.050	0.115	0.047
E-cad				
H1703	0.565	0.111	0.208	0.083
H460	0.465	0.032	0.202	0.024
R30	0.385	0.074	0.260	0.058
M4e	0.412	0.145	0.287	0.050
37B	0.387	0.012	0.266	0.004
H292	1.867	0.116	0.102	0.032
H322	1.463	0.070	0.273	0.022
686LN	1.526	0.152	0.385	0.066
37A	0.796	0.094	0.323	0.079

is orally bioavailable and has various effects on tumor cells expressing EGFR. It can inhibit phosphorylation of EGFR, ERK and AKT and induce G1 arrest and apoptosis. Phase III clinical trials have demonstrated its efficacy in inhibiting tumor progression [39]. However, the response rate to erlotinib or other EGFR-targeted therapies is limited [19, 40], around 10–20% [41]. Therefore, pre-selection of those patients who may benefit most from EGFR-targeted therapies is necessary. The current challenge is to define sensitive biomarkers and develop reliable methods to predict EGFR-targeting sensitivity.

Expression of the EMT biomarker E-cad correlates with tumor progression and metastasis [27–33] and has been reported to be related to a reduced sensitivity to EGFR-TKI [25]. Currently the effect of the molecular relationship between EGFR and E-cad on EGFR-targeting therapy is unclear. Our recent findings showed that not only expression but also localization of EGFR and E-cad had clinical relevance in predicting lymph node metastasis and patient survival [36]. Lee *et al* found that EGF treatment downregulates E-cad and upregulates vimentin in cervical cancer cells [42]. Lo *et al* also reported that EGF reduced E-cad expression and increased that of mesenchymal proteins [43]. Rho *et al* indicated that induction of EMT may contribute to the decreased efficacy of therapy in primary and acquired resistance to gefitinib [44]. In this study, we demonstrated quantitatively that EGFR and E-cad internalization mediated by EGF and inhibition of this internalization by erlotinib were greater in the sensitive cells than in the insensitive cells. These quantifications of EGFR and

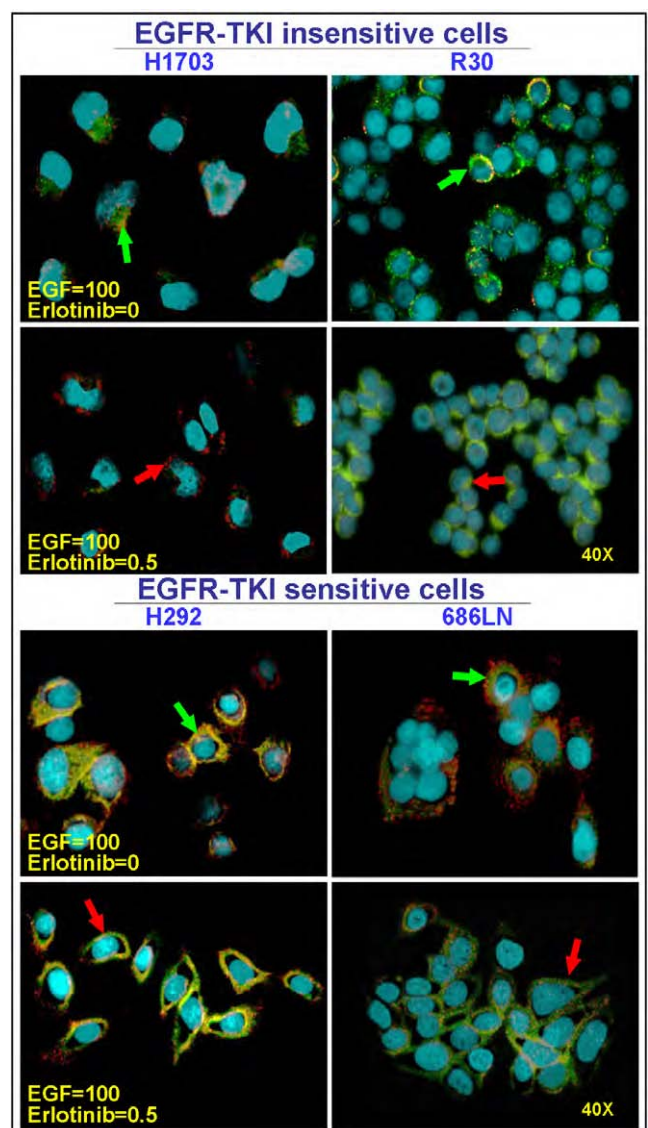


Figure 5. Localization of EGFR (QD605, red) and E-cad (QD565, green) induced by EGF with or without erlotinib. Images were taken by an Olympus microscope IX71 with a CRi spectral imaging and quantifying system. Yellow indicates colocalization of EGFR (red) and E-cad (green).

E-cad localization in response to EGFR ligands and EGFR-TKI will facilitate our understanding of the mechanism of resistance to EGFR-targeted therapy.

Several mechanisms have been considered to contribute to cancer cell resistance to EGFR-targeted therapy in lung and head and neck cancer, including overexpression of EGFR ligand [11], increased EGFR gene copy numbers [45, 46] overexpression of other members of the EGFR family [47], and the existence of the EGFRvIII mutation [48]. In addition, in lung cancer, a secondary mutation in the EGFR gene, T790M, and amplification of the MET proto-oncogene were also suggested to contribute to EGFR-targeting resistance [49, 50]. Our recent study of human head and neck cancer tissues has identified an additional possibility: that the cytoplasmic localization of EGFR, rather than EGFR expression, along

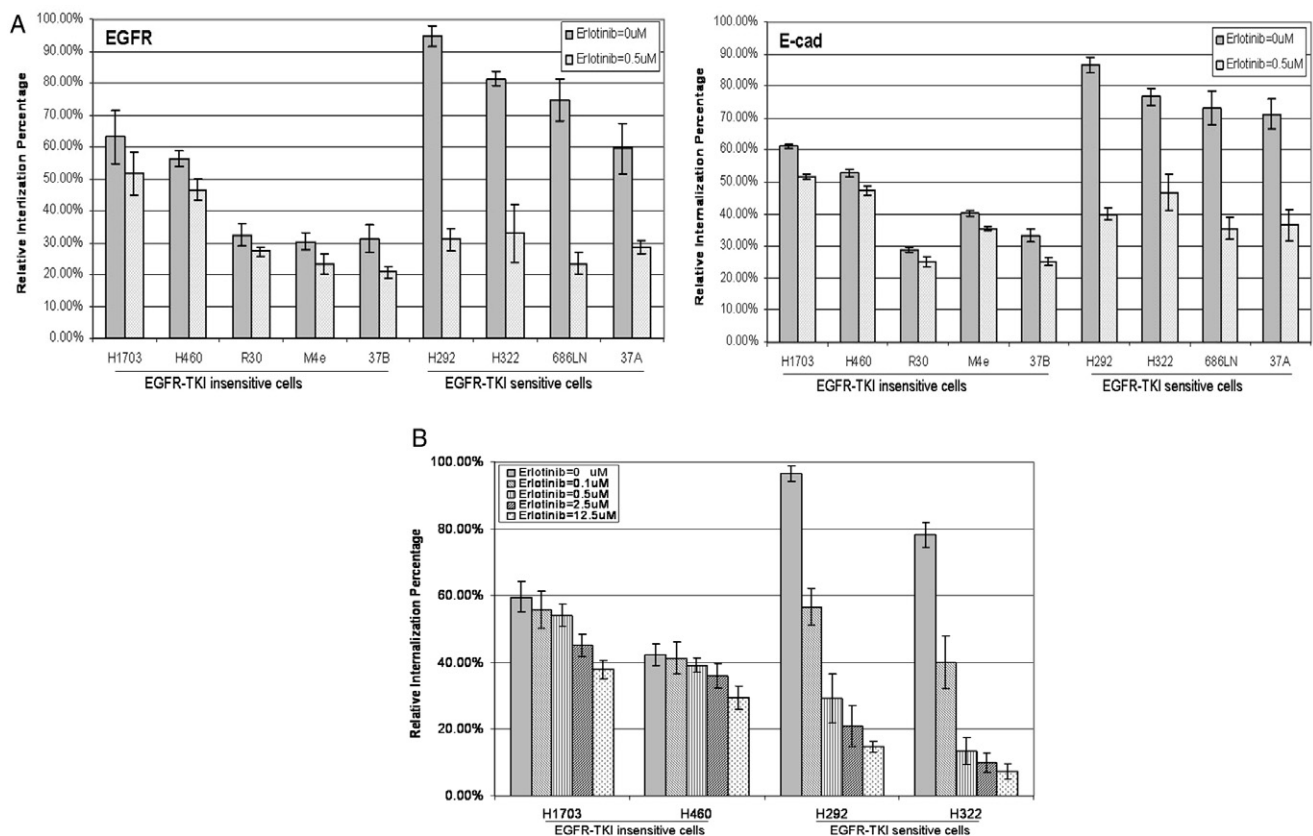


Figure 6. (A) Comparison of erlotinib-mediated inhibition of EGF-induced internalization of EGFR and E-cad quantified by a CRi Nuance system. Relative internalization was defined as $[1 - (\text{membrane EGFR induced with EGF} / \text{membrane EGFR without EGF and erlotinib})] \times 100\%$. (B) Comparison of erlotinib-mediated inhibition of EGF-induced EGFR internalization measured by FACS. Erlotinib was used at a range of concentrations as indicated in the figure. Relative internalization was defined as $(\text{FITC}^+ \text{ cells} / \text{total cells}) \times 100\%$.

with reduction of E-cad may explain the clinical findings of poor response to EGFR-TKI and particularly, therapeutic antibody against the extracellular portion of EGFR [36]. In the current study, all of the lung cancer cell lines contain wild type EGFR [25]. We also sequenced the head and neck cancer cell lines 686LN, 686LN-M4e, and 686LN-R30 and found neither gain of function nor loss of function mutations in these cell lines (data not shown). Therefore, the resistance phenotype of these cell lines is not derived from EGFR gene mutations. Rather, this study supports our new explanation for EGFR-targeting resistance.

Using QD-based ICC and CRi spectral imaging software, we have developed a quantification method to record dynamic processes in cancer cells in response to the EGFR ligand EGF and erlotinib. The quantification results are consistent with those obtained by FACS, but QD imaging has the advantage over FACS of providing visualization of the cellular localization of the proteins studied. In this study, we have clarified three important features of lung and head and neck cancer cells that are insensitive to EGFR-TKI, at least in this population. First, these cells have lower levels of membrane and total EGFR than sensitive cells. Second, the insensitive cells showed lower levels of EGFR internalization induced by EGF than the sensitive cells, suggesting the biological activity of these cells may not rely mainly on EGFR ligand-mediated signal transduction. Third, our previous

publication and others have shown that EGFR-TKI inhibits EGFR internalization induced by EGF [41, 51]. These results suggest that quantification of membrane expression of EGFR and E-cad may serve as biomarkers in predicting the efficacy of EGFR-targeted therapy, at least for one population of lung and head and neck cancer patients. Further clarification of the substantial differences between EGFR-TKI-insensitive and -sensitive cancer cells will help to define the mechanism of resistance to EGFR-targeted agents and facilitate the development of new targeted therapies.

3.4. Subcellular localization of EGFR in the endosome and lysosome

After the binding of EGF, EGFR dimerizes, autophosphorylates and then internalizes. Concomitantly, these ligand-receptor complexes cluster into clathrin-coated pits, internalize into early endosomes, and then either recycle back to the cell surface or eventually traffic to lysosomes for degradation [52]. Nishimura *et al* demonstrated efficient endocytosis of the EGF-EGFR complex and rapid endocytosis of phosphorylated EGFR via the early/late endocytic pathway in the PC9 NSCLC cell line [51, 53]. Strong evidence indicates that endosome-localized EGFR plays an important role in cell signaling [51, 52, 54].

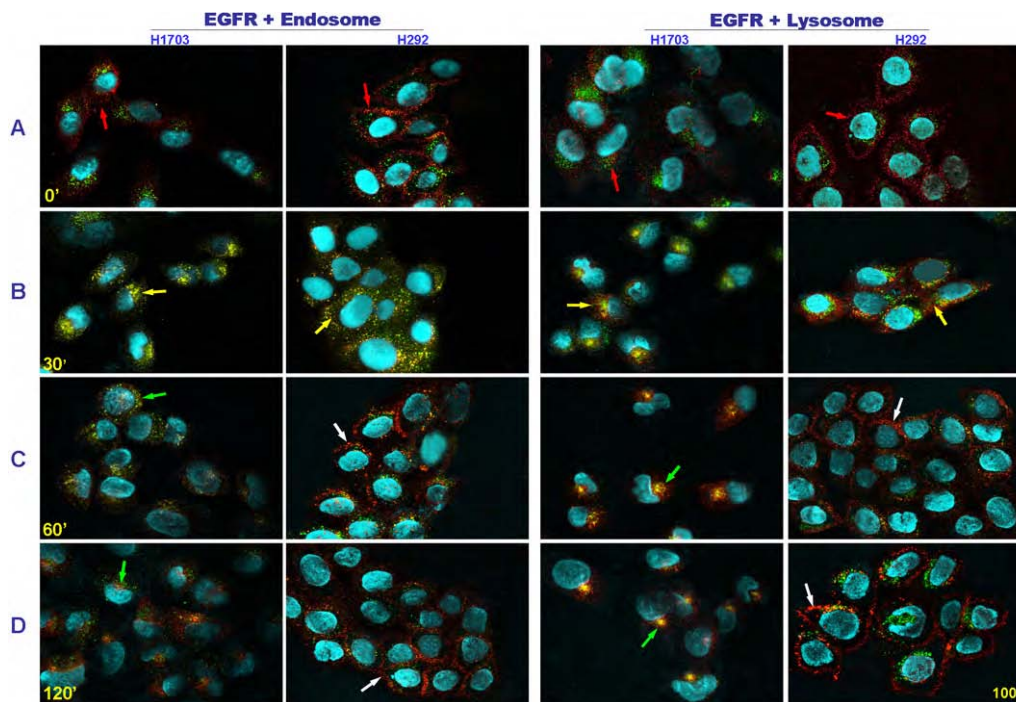


Figure 7. Colocalization of EGFR with the early endosome and lysosome. EGFR was tracked with QDs605 (red), and the early endosome and late endosome/lysosome were tracked with QDs565 (green). Yellow color indicates the colocalization of EGFR and early endosome or late endosomes/lysosomes.

To further understand the differences in intracellular distribution of EGFR between EGFR-TKI-sensitive and -insensitive cell lines, NSCLC cell lines H292, H322, H1703, and H460 were double-stained with antibodies specific to EGFR and either the early endosome marker EEA1 or the late endosome/lysosome marker CD63. EEA1 and CD63 are distributed within the endocytic organelles at a high concentration in early endosomes and late endosomes/lysosomes, respectively. Using the QD-ICC method, we compared EGFR subcellular localization in endosomes and lysosomes between the sensitive and insensitive cancer cells after stimulating with EGF at different time points. In the absence of EGF, the majority of EGFR was colocalized within large swollen vacuoles in the perinuclear region in insensitive cells, while in the sensitive cells, EGFR staining was found mainly on the cell membrane. In the absence of EGF, EGFR did not colocalize with either the early endosomes or the late endosomes/lysosomes in either the sensitive or insensitive cancer cell lines. After 30 min stimulation by EGF, EGFR was mainly colocalized with the early endosomes in both cell types. In most sensitive cells, EGFR colocalized mainly with early endosomes 60 min after EGF stimulation, and was recycled back to the cell membrane after 60–120 min, with only a little EGFR colocalized with late endosomes/lysosomes. In contrast, in most of the insensitive cells, EGFR was colocalized with late endosomes/lysosomes as early as 30 min after EGF stimulation, and colocalization was retained up to 120 min (figure 7).

Our results demonstrate that in the insensitive cells, EGFR was distributed mainly in late endosomes/lysosomes, where completed maturation of lysosomes by fusing with

the late endosomes occurred. In contrast, in the sensitive cells, after stimulation with EGF, EGFR internalized through intracellular endocytic trafficking from the membrane via the early endosomes toward both the membrane (major) and the late endosomes/lysosomes (minor). These results show that endocytosis of the EGF-EGFR complex occurs via different endocytic pathways in EGFR-TKI-sensitive versus -insensitive cancer cells.

4. Conclusions

In summary, our study provides a potential new strategy for using a QD methodology in the prediction of sensitivity to EGFR-targeted therapy. There are many advantages in using QD-based image analysis instead of conventional fluorescent dyes: (i) the fluorescent signal generated by QDs is more stable than that of organic dyes, and QDs are more resistant to photobleaching; (ii) QDs have broad excitation spectra and narrow emission spectra as compared with organic dyes, facilitating quantification of the image; (iii) through the judicious choice of an appropriate excitation source, multiple color QDs may be excited simultaneously, allowing quantification of multiple biomarkers on the same sample.

In this study, QD-based quantification methodologies facilitated the analysis of subcellular distributions of multiple biomarkers, EGFR and E-cad, providing new biomarkers for the prediction of sensitivity to EGFR-targeted therapy, which can be further developed for clinical application to tumor tissue specimens. Our findings highlight substantial differences between EGFR-TKI-sensitive and -insensitive cancer cells in the cellular localizations of EGFR and E-cad, which will

help to define the mechanisms of resistance to EGFR-targeted agents. Quantification of multiple proteins by QDs may help to monitor the effect of EGFR-targeted therapy on EGFR downstream signaling molecules as well as EGFR parallel pathways which may serve as new therapeutic targets for treatment of cancer.

Acknowledgments

Grant support: DOD Grant W81XWH-07-1-0306 Project 5 to ZC and GCC Distinguished Scholar Award to FRK, DMS, and ZC. We thank Dr Anthea Hammond for her critical reading of the manuscript.

References

- [1] Ferrari M 2005 *Nat. Rev.* **5** 161–71
- [2] Nie S, Xing Y, Kim G J and Simons J W 2007 *Annu. Rev. Biomed. Eng.* **9** 257–88
- [3] Smith A M, Gao X and Nie S 2004 *Photochem. Photobiol.* **80** 377–85
- [4] Whaley S R, English D S, Hu E L, Barbara P F and Belcher A M 2000 *Nature* **405** 665–8
- [5] Chan W C and Nie S 1998 *Science* **281** 2016–8
- [6] Wu X, Liu H, Liu J, Haley K N, Treadway J A, Larson J P, Ge N, Peale F and Bruchez M P 2003 *Nat. Biotechnol.* **21** 41–6
- [7] Xing Y *et al* 2007 *Nat. Protoc.* **2** 1152–65
- [8] Giaccone G 2005 *Ann. Oncol.* **16** 538–48
- [9] Hirsch F R, Scagliotti G V, Langer C J, Varella-Garcia M and Franklin W A 2003 *Lung Cancer* **41** S29–42
- [10] Ang K K, Berkey B A, Tu X, Zhang H Z, Katz R, Hammond E H, Fu K K and Milas L 2002 *Cancer Res.* **62** 7350–6
- [11] Grandis J R and Twardy D J 1993 *Cancer Res.* **53** 3579–84
- [12] Astsaturov I, Cohen R B and Harari P 2006 *Expert Rev. Anticancer Ther.* **6** 1179–93
- [13] Kalyankrishna S and Grandis J R 2006 *J. Clin. Oncol.* **24** 2666–72
- [14] Rubin Grandis J, Melhem M F, Gooding W E, Day R, Holst V A, Wagener M M, Drenning S D and Twardy D J 1998 *J. Natl. Cancer Inst.* **90** 824–32
- [15] Maurizi M, Almadori G, Ferrandina G, Distefano M, Romanini M E, Cadoni G, Benedetti-Panici P, Paludetti G, Scambia G and Mancuso S 1996 *Br. J. Cancer* **74** 1253–7
- [16] Yamanaka Y, Friess H, Kobrin M S, Buchler M, Beger H G and Korc M 1993 *Anticancer Res.* **13** 565–9
- [17] Neal D E, Sharples L, Smith K, Fennelly J, Hall R R and Harris A L 1990 *Cancer* **65** 1619–25
- [18] Franklin W A, Veve R, Hirsch F R, Helfrich B A and Bunn P A Jr 2002 *Sem. Oncol.* **29** 3–14
- [19] Bates S E and Fojo T 2005 *Clin. Cancer Res.* **11** 7203–5
- [20] Cappuzzo F *et al* 2005 *J. Natl. Cancer Inst.* **97** 643–55
- [21] Tsao M S *et al* 2005 *New Engl. J. Med.* **353** 133–44
- [22] Perez-Soler R, Chachoua A, Hammond L A, Rowinsky E K, Huberman M, Karp D, Rigas J, Clark G M, Santabarbara P and Bonomi P 2004 *J. Clin. Oncol.* **22** 3238–47
- [23] Parra H S, Cavina R, Latteri F, Zucali P A, Campagnoli E, Morengi E, Grimaldi G C, Roncalli M and Santoro A 2004 *Br. J. Cancer* **91** 208–12
- [24] Shrader M, Pino M S, Brown G, Black P, Adam L, Bar-Elil M, Dinney C P and McConkey D J 2007 *Mol. Cancer Therapeut.* **6** 277–85
- [25] Thomson S, Buck E, Petti F, Griffin G, Brown E, Ramnarine N, Iwata K K, Gibson N and Haley J D 2005 *Cancer Res.* **65** 9455–62
- [26] Yauch R L *et al* 2005 *Clin. Cancer Res.* **11** 8686–98
- [27] Bremnes R M, Veve R, Gabrielson E, Hirsch F R, Baron A, Bemis L, Gemmill R M, Drabkin H A and Franklin W A 2002 *J. Clin. Oncol.* **20** 2417–28
- [28] Bowie G L, Caslin A W, Roland N J, Field J K, Jones A S and Kinsella A R 1993 *Clin. Otolaryngol. Allied Sci.* **18** 196–201
- [29] Bosch F X, Andl C, Abel U and Kartenbeck J 2005 *Int. J. Cancer* **114** 779–90
- [30] Kurtz K A, Hoffman H T, Zimmerman M B and Robinson R A 2006 *Otolaryngol. Head Neck Surg.* **134** 142–6
- [31] Kyzas P A, Stefanou D, Batistatou A, Agnantis N J, Nakanishi Y, Hirohashi S and Charalabopoulos K 2006 *Am. J. Surg. Pathol.* **30** 185–93
- [32] Retera J M, Leers M P, Sulzer M A and Theunissen P H 1998 *J. Clin. Pathol.* **51** 891–4
- [33] Choi Y S, Shim Y M, Kim S H, Son D S, Lee H S, Kim G Y, Han J and Kim J 2003 *Eur. J. Cardiothorac. Surg.* **24** 441–9
- [34] Witta S E *et al* 2006 *Cancer Res.* **66** 944–50
- [35] Jawhari A U, Farthing M J and Pignatelli M 1999 *J. Pathol.* **187** 155–7
- [36] Muller S, Su L, Tighiouart M, Saba N, Zhang H, Shin D M and Chen Z G 2008 *Cancer* **113** 97–107
- [37] Zhang X, Su L, Pirani A A, Wu H, Zhang H, Shin D M, Gernert K M and Chen Z G 2006 *Clin. Exp. Metastasis* **23** 209–22
- [38] Chen Z, Zhang X, Li M, Wang Z, Wieand H S, Grandis J R and Shin D M 2004 *Clin. Cancer Res.* **10** 5930–9
- [39] Wacker B, Nagrani T, Weinberg J, Witt K, Clark G and Cagnoni P J 2007 *Clin. Cancer Res.* **13** 3913–21
- [40] Dassonville O, Bozec A, Fischel J L and Milano G 2007 *Crit. Rev. Oncol. Hematol.* **62** 53–61
- [41] Wheeler D L, Huang S, Kruser T J, Nechrebecki M M, Armstrong E A, Benavente S, Gondi V, Hsu K T and Harari P M 2008 *Oncogene* **27** 3944–56
- [42] Lee M Y, Chou C Y, Tang M J and Shen M R 2008 *Clin. Cancer Res.* **14** 4743–50
- [43] Lo H W, Hsu S C, Xia W, Cao X, Shih J Y, Wei Y, Abbruzzese J L, Hortobagyi G N and Hung M C 2007 *Cancer Res.* **67** 9066–76
- [44] Rho J K, Choi Y J, Lee J K, Ryoo B Y, Na I I, Yang S H, Kim C H and Lee J C 2008 *Lung Cancer* **63** 219–26
- [45] Chung C H *et al* 2006 *J. Clin. Oncol.* **24** 4170–6
- [46] Temam S, Kawaguchi H, El-Naggar A K, Jelinek J, Tang H, Liu D D, Lang W, Issa J P, Lee J J and Mao L 2007 *J. Clin. Oncol.* **25** 2164–70
- [47] Erjala K, Sundvall M, Junttila T T, Zhang N, Savisalo M, Mali P, Kulmala J, Pulkkinen J, Grenman R and Elenius K 2006 *Clin. Cancer Res.* **12** 4103–11
- [48] Sok J C *et al* 2006 *Clin. Cancer Res.* **12** 5064–73
- [49] Engelman J A *et al* 2007 *Science* **316** 1039–43
- [50] Kobayashi S B T, Dayaram T, Jänne P A, Kocher O, Meyerson M, Johnson B E, Eck M J, Tenen D G and Halmos B 2005 *New Engl. J. Med.* **352** 786–92
- [51] Nishimura Y, Berezcky B and Ono M 2007 *Histochem. Cell Biol.* **127** 541–53
- [52] Sorkin A and Von Zastrow M 2002 *Nat. Rev. Mol. Cell Biol.* **3** 600–14
- [53] Nishimura Y, Yoshioka K, Berezcky B and Itoh K 2008 *Mol. Cancer* **7** 42
- [54] Wang Y, Pennock S, Chen X and Wang Z 2002 *Sci. STKE* **2002** PL17

Variable slope normalization of reverse phase protein arrays

E. Shannon Neeley^{1,2,*}, Steven M. Kornblau³, Kevin R. Coombes²
and Keith A. Baggerly²

¹Department of Statistics, Rice University, ²Department of Bioinformatics and Computational Biology and

³Department of Stem Cell Transplantation and Cellular Therapy, University of Texas M.D. Anderson Cancer Center, Houston, TX, USA

Received on June 12, 2008; revised on February 27, 2009; accepted on March 24, 2009

Advance Access publication March 31, 2009

Associate Editor: Thomas Lengauer

ABSTRACT

Motivation: Reverse phase protein arrays (RPPA) measure the relative expression levels of a protein in many samples simultaneously. A set of identically spotted arrays can be used to measure the levels of more than one protein. Protein expression within each sample on an array is estimated by borrowing strength across all the samples, but using only within array information. When comparing across slides, it is essential to account for sample loading, the total amount of protein printed per sample. Currently, total protein is estimated using either a housekeeping protein or the sample median across all slides. When the variability in sample loading is large, these methods are suboptimal because they do not account for the fact that the protein expression for each slide is estimated separately.

Results: We propose a new normalization method for RPPA data, called variable slope (VS) normalization, that takes into account that quantification of RPPA slides is performed separately. This method is better able to remove loading bias and recover true correlation structures between proteins.

Availability: Code to implement the method in the statistical package R and anonymized data are available at <http://bioinformatics.mdanderson.org/supplements.html>.

Contact: sneeley@stats.byu.edu

Supplementary information: Supplementary data are available at *Bioinformatics* online.

1 INTRODUCTION

Protein arrays have been used in many contexts to measure protein expression in a high-throughput format (Becker *et al.* 2006; Grote *et al.* 2008; Hennessy *et al.* 2007; Herrmann *et al.* 2003; Kornblau *et al.* 2009; Kreutzberger 2006; Park *et al.* 2008). Assays that measure protein are able to address questions about post-translational modifications and protein pathway relationships that genomic studies alone cannot answer (Nishizuka *et al.* 2003b). Several different protein array formats have been developed, but they can be dichotomized into forward and reverse phase assays (Liotta *et al.* 2006). In forward phase arrays, numerous capture antibodies are printed on the array, which is then exposed to a single protein sample, allowing the simultaneous measurement of

the level of multiple targets in a single sample. In reverse phase arrays, numerous protein samples are printed in discrete spots on the array, which is then probed with a single validated antibody, simultaneously measuring the level of a single protein in multiple samples. One reverse phase approach that uses lysed homogenized samples is the protein lysate or reverse phase protein array (RPPA) first described by Paweletz *et al.* (2001). Since then, RPPAs have been used by several groups worldwide to study the protein behavior in diseases (Chan *et al.* 2004; Herrmann *et al.* 2003; Jiang *et al.* 2006; Korf *et al.* 2008; Kornblau *et al.* 2009; Mendes *et al.* 2007; Park *et al.* 2008; Stevens *et al.* 2008; Zhang *et al.* 2009).

RPPAs have been used to address a number of biological questions. For example, RPPAs were used to study proteomic signatures of signaling pathways in various types of cancer including prostate (Grubb *et al.*, 2003; Paweletz *et al.*, 2001), breast (Akkiprik *et al.*, 2006), glioma (Jiang *et al.*, 2006), follicular lymphoma (Gulmann *et al.*, 2005) and leukemia (Kornblau *et al.*, 2009). Calvert *et al.* (2007), Nishizuka *et al.* (2003a) and Mendes *et al.* (2007) all found protein signatures that were able to distinguish between diseases or subtypes of disease. Other studies that use RPPAs to study proteins relating to pathway dysregulation or drug response in cancer or other diseases include Ma *et al.* (2006); Wulfkühle *et al.* (2003), Nishizuka *et al.* (2003b), Chan *et al.* (2004), Zha *et al.* (2004), Shankavaram *et al.* (2007) and Kim *et al.* (2008).

The RPPA assay is described in detail in Paweletz *et al.* (2001) (see also Charboneau *et al.*, 2002; Espina *et al.*, 2004; Liotta *et al.*, 2006; Tibes *et al.*, 2006). Briefly, biological samples are lysed, resulting in solutions that contain the protein of interest in unknown amounts. These sample lysates are spotted onto a nitrocellulose backed array in a dilution series. The array is then hybridized with a specific antibody validated to recognize only the protein of interest. Next, the array is incubated with a biotinylated secondary antibody that recognizes and binds to the primary antibody. Finally, streptavidin-linked labels (such as dyes) are introduced and bound to the biotin. When the array is processed, the labels can be observed and measured. It is assumed that the amount of label corresponds to the amount of protein at the spot. The processed arrays are scanned and the resulting images are analyzed with array software (we use MicroVigene®, VigeneTech, Carlisle, MA) that measures the foreground and background intensities of the label at each spot. RPPA ‘raw data’ consists of these measurements of foreground and background intensity at each spot on the array. Figure 1 shows an

*To whom correspondence should be addressed.

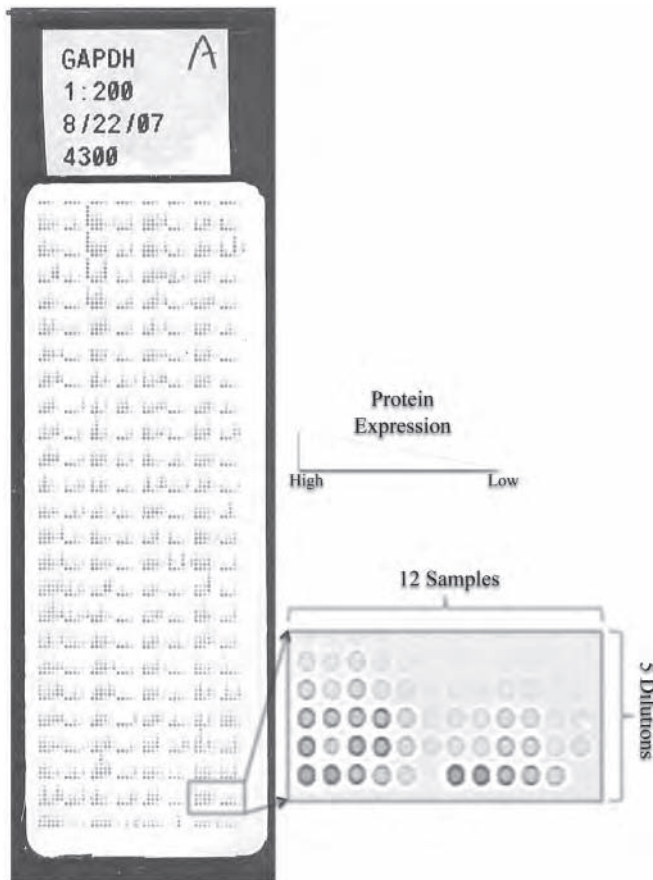


Fig. 1. Image of an example RPPA with 1152 separate dilution series. Each dilution series is printed in 5-spot 1/2 dilutions. The zoom-in box shows 12 dilution series on the array. The darker the spot, the higher the amount of protein. Some of the spots do not appear on the array or in the zoom-in box because there was no label (i.e. protein) at the spot.

example of an RPPA slide with details of a few samples in their dilution series. The darker spots contain more protein than the lighter spots.

The reverse phase nature of RPPAs allows the levels of only one protein to be measured per array. Thus, RPPA experiments involve multiple arrays each printed identically with the same samples but probed with different antibodies. Such a set of arrays allows for estimation of sample effects that can go undetected with one array.

Similar to other array formats, this data undergoes a series of preprocessing steps before a formal analysis. The three main preprocessing steps are background subtraction, quantification and normalization. RPPA processing steps are performed sequentially:

- (1) *Background correction*: the background spot intensities are used to subtract baseline or non-specific signal from the foreground spot intensities.
- (2) *Quantification*: the background adjusted spot intensities from each dilution series are mapped into one number, the protein expression, that represents the amount of protein in the sample relative to the other samples on the array.
- (3) *Normalization*: the estimated relative sample expressions are adjusted to account for known sources of variation.

In this article, we focus on the normalization step. Specifically, we discuss current practices for estimating and correcting array and sample effects, with more focus on sample effects. We also propose a new normalization model that corrects array and sample effects based on the assumption that the protein expression estimates from each array are potentially on slightly different scales due to random variability in the quantification step.

Row and sample effects are assumed to be additive on the log scale:

$$x_{jp} = \lambda_j + \delta_p + c_{jp} \quad (1)$$

where x_{jp} is the estimated relative log expression in sample j on array p , λ_j is the effect due to sample j , δ_p is the effect due array p and c_{jp} is the relative protein log expression with sample and array effects removed. Array effects are due to the fact that each array is quantified separately and protein expression is relative within slides. Sample effects occur when different amounts of total protein are unintentionally spotted on the array for different samples. Array and sample effects are further discussed in the next section.

The model we propose is a slight variation. The following simple modification to Equation (1) can improve normalized results when there is large variation in the sample effects:

$$x_{jp} = (\lambda_j + \delta_p + c_{jp})\gamma_p. \quad (2)$$

Here, the γ_p term refers to a protein specific quantity that helps to account for error in estimating the sample protein expressions.

In order to motivate this model, we briefly discuss the quantification step. This is the only step that has been explicitly addressed in RPPA data (see Hu *et al.*, 2007; Mircean *et al.*, 2005; Nishizuka *et al.*, 2003b; Tabus *et al.*, 2006; and Supplementary Material).

The purpose of the quantification is to estimate the relative amount of protein in a sample as compared with the other samples on the same array using information from the dilution series and the observed intensities. This is accomplished by establishing a model relationship between the observed spot intensities and unknown relative expressions. Various groups have developed methods for RPPA quantification including models that use only sample information (Mircean *et al.*, 2005; Nishizuka *et al.*, 2003b) and 'joint sample' models that borrow strength from all samples on the array (Hu *et al.*, 2007; Tabus *et al.*, 2006). We use a joint sample model developed by our group at MD Anderson, called 'SuperCurve'. This model is explained in detail in the Supplementary Material. Briefly, a three parameter logistic equation is used to model the dependency of the observed intensity on the unknown protein expression. There is one overall logistic curve estimated for the whole array and individual protein expressions are estimated as offsets from the overall curve. The logistic equation parameters and sample protein expressions are estimated iteratively (see Supplementary Material).

Sample protein expressions are estimated relative to the other samples on the array, and are reported without units. Since most estimation models, including SuperCurve, compute log expression values, in this article, we treat all expressions as on the log scale.

Array quantification is performed individually for each array. We have observed that this separate estimation of protein expression can result in unexpected multiplicative effects. For example, one experiment that we ran involved more samples than could be printed on a single array. We randomly allocated each sample to one of two groups, balancing for all potentially explanatory covariates that

we could identify in advance. These two groups of samples were then printed on two parallel sets of arrays, which were interrogated with the same sets of antibodies. Due to the randomization, we knew that the distributions of protein expression for a given antibody should be the same for Groups 1 and 2. However, comparison of the expression distributions showed an unexpected shift in scale due to slightly different estimates of the slopes in the logistic curves used in the quantification of these arrays. These small differences are a result of error in the estimates of the logistic parameters. However, while the differences in slope estimates were slight, the range of sample loadings was broad, so the final expression estimates (and the protein clusters) were quite different. It is important to note that while this experiment (with samples split across arrays) first led us to identify the problem, these shifts in logistic slope are also present [and can be fixed with variable slope (VS) normalization] in the more common design context where all samples are printed on one array.

The usual normalization model in Equation (1) fails to capture the fact that protein expression is estimated separately for each slide and each array can have slightly different slopes in the overall logistic curve. Small errors in the slope parameter of the logistic curve can result in large variation if not properly accounted for.

The proposed model, Equation (2), adjusts for variability in slide-to-slide expression estimates when adjusting for sample loading. The γ_p term refers to a protein-specific quantity that accounts for potentially differing slopes in the sigmoidal slope from the curve estimated with quantification methods described in Tabus *et al.* (2006), Hu *et al.* (2007) and the Supplementary Material. We call the new approach VS normalization because it accounts for variation in the estimated slope parameters from the calibration curve estimated in the quantification step.

2 METHODS

Normalization, using either Equations (1) or (2), requires estimation of both array and sample effects. Equation (2) additionally requires estimating multiplicative array effects. We first address additive array and sample effects and then the multiplicative array effects.

2.1 Array and sample effects

Array effects, δ_p in Equations (1) and (2), are actually common and even expected since each slide is quantified separately and expression estimates are relative within slides. These effects are corrected by normalizing expression to the median slide expression estimate so that each array has the same median expression.

Sample effects, λ_j , occur when the amount of total protein that is spotted on the array, the sample loading, varies from sample to sample. Unintentionally printing differing amounts of total protein for each sample can result in false conclusions of differential expression. Although efforts are made when the array is being printed to equalize total protein, this is often an unavoidable problem. For example, the same number of cells can be used in each biological sample, but if the size of the cells differs, then samples with larger cells will have more protein.

Sample loading has been estimated with a ‘housekeeping’ (HK) protein, such as β -Actin, as in Jiang *et al.* (2006) and Mendes *et al.* (2007). A HK protein is a protein that should be present in the same amount for all samples so differences in expression reflect differences in sample loading. However, in reality there is no protein that meets this expectation, and the expression levels of HK proteins can be quite variable. We refer to normalization with Equation (1), estimating λ_j with a HK protein, as HK normalization.

Another method that is used to estimate sample loading for the j -th sample is to use the median protein expression estimate for sample j across all the arrays, $\lambda_j = \text{median}_j(x_{jp})$. This method assumes, first, that all the arrays were printed in a similar manner and, second, that most proteins will not be abnormally expressed but the few that are will still be noticed after normalization to the median. It is important to note that this method requires a set of arrays with the same samples. Normalization with Equation (1) but estimating λ_j with the median is called median loading (ML) normalization.

2.2 Multiplicative protein effects

The array-specific multiplicative effects, γ_p , in model 2 are partially confounded with the additive protein effects, δ_p . We outline a method that we have found to be effective in estimating parameters and performing sample loading normalization according to the VS normalization model.

First, write (2) as

$$x_{jp} = (\lambda_j + c_{jp})\gamma_p + \delta_p\gamma_p. \quad (3)$$

The confounded term, $\delta_p\gamma_p$, is lumped together as the overall protein effect and estimated with the median of protein p across all samples [$\widehat{\gamma_p\delta_p} = \text{median}_p(x_{jp})$]. Moving this term to the left-hand side, (3) can be written as

$$x_{jp} - \widehat{\gamma_p\delta_p} = \gamma_p(\lambda_j + c_{jp}). \quad (4)$$

We will not be able to estimate the exact γ_p 's, but taking the ratio of (4) for two values of p will allow estimation of the relative γ_p 's. This ratio will be

$$\frac{x_{jp_1} - \widehat{\gamma_{p_1}\delta_{p_1}}}{x_{jp_2} - \widehat{\gamma_{p_2}\delta_{p_2}}} = \frac{\gamma_{p_1}(\lambda_j + c_{jp_1})}{\gamma_{p_2}(\lambda_j + c_{jp_2})} \approx \frac{\gamma_{p_1}}{\gamma_{p_2}} \quad (5)$$

where

$$\frac{(\lambda_j + c_{jp_1})}{(\lambda_j + c_{jp_2})} \approx 1$$

since we assume that most c_{jp} 's will be small relative to λ_j . We also assume that the γ_p 's have an expected value of 1 and a small variance. They should realistically have a range of around 0.5–1.5 so that there should not be a danger of ratios behaving badly as the denominator gets close to 0. We define $\hat{x}_{jp} \equiv x_{jp} - \widehat{\gamma_p\delta_p}$, hence Equation (5) implies that $\hat{x}_{jp_1}/\hat{x}_{jp_2}$ estimates the ratio $\gamma_{p_1}/\gamma_{p_2}$. This ratio can be estimated by regressing \hat{x}_{jp_1} on \hat{x}_{jp_2} . Since there is no preferred direction (we could just as easily regress \hat{x}_{jp_2} on \hat{x}_{jp_1}) we use perpendicular least squares (de Groen, 1996; Rencher, 1995). The logs of these ratios are used to set up a system of equations whose solution yields estimates of the $\log \hat{\gamma}_p$'s: the system is made non-singular by setting

$$\frac{1}{K} \sum_p^K \log \gamma_p = 0.$$

VS normalization is the process of adjusting the matrix \hat{x}_{jp} by dividing each column by the appropriate $\hat{\gamma}_p$, and subtracting from each row the appropriate $\hat{\lambda}_j = \text{median}_j(x_{jp})$ to obtain the estimate of c_{jp} .

3 SIMULATIONS

We ran simulations to compare VS, ML and HK normalization. We randomly generated 30 proteins, each with 200 samples, from independent standard normal distributions. Array and samples effects were generated according to the following distributions, based on empirical data:

$$\lambda_j \sim N(-2, 16) \quad (6)$$

$$\delta_p \sim N(-1, 4) \quad (7)$$

$$\log \gamma_p \sim N(0, 0.01) \quad (8)$$

The ‘HK protein’ was modeled as:

$$x_{j\text{phouse}} = \lambda_j + \epsilon_j \sim N(0, 0.5). \quad (9)$$

Table 1. Results of the simulation comparing the \widehat{MSE} s of HK, ML and VS normalization

Contrast	HK MSE	ML MSE	VS MSE	Low MSE
1 Correlated columns	0.023	0.029	0.005	0.002
2 Differential expression	3.429	3.506	2.431	2.000

The theoretical minimum (Low) is also shown. We looked at two contrasts: (i) the correlation between two columns that should have a correlation of 0.6 and (ii) the difference between an unexpressed sample and a sample with spiked in expression (with a value of 5) within the same protein.

In comparing the three methods, we wanted to assess the ability of each (i) to recover true protein correlation and (ii) to detect differential expression. To this end, two protein expression vectors were generated to have a correlation of 0.6, and another was ‘spiked’ with expression by adding a constant to one of the samples.

After each simulation, we performed normalization with the three methods and computed (i) correlation between correlated proteins and (ii) differential expression. Each target was compared with the truth using an estimated mean squared error (\widehat{MSE}) defined as

$$\widehat{MSE} = \text{var}(\hat{\theta}_i) + \left(\theta - \frac{1}{n} \sum \hat{\theta}_i\right)^2 \quad (10)$$

where θ is the true value of the contrast (i.e. true correlation or true differential expression), and $\hat{\theta}_i$ is the value of the contrast for the i -th simulation.

Table 1 shows the \widehat{MSE} of the contrasts after 1000 simulations. The \widehat{MSE} for VS normalization is better than both the other methods in every case and is good at maintaining correlation between proteins with known correlation.

The last column of the table shows the ‘Lowest’ \widehat{MSE} or what the \widehat{MSE} would be if the parameters were known. This number is not 0 because of randomness in the data.

We performed a second set of simulations in which we varied the simulation parameters, including the number of proteins, the number of samples and the SDs of λ_j , δ_p and γ_p in Equations (6–8). The results of this simulations (shown in the Supplementary Material) similarly show that VS normalization performs as well or better than the other methods in all situations. The differences are most dramatic, however, when the variability in the sample loadings is large.

We ran a third simulation to compare only VS normalization with ML normalization when clustering proteins. We generated 30 proteins with 200 samples from a multivariate normal distribution with a covariance structure that allowed for five correlated groups as follows: Group 1, $N=3$, $r=0.4$; Group 2, $N=10$, $r=0.2$; Group 3, $N=5$, $r=0.2$; Group 4, $N=5$, $r=0.5$; and Group 5, $N=7$, $r=0.3$. The column, row and slope effects were generated according to Equations (6–8). Figure 2 shows a plot of the ‘true’, observed and normalized data matrices from a typical simulation.

It is easy to distinguish between groups for the true data, but grouping becomes scrambled after the row and column effects are introduced. ML normalization is able to separate some of the groups but still leaves many proteins scrambled. VS normalization is able to recover and separate all the groups present in the ‘true’ matrix. This example illustrates the strength of VS normalization to recover true correlation structure between proteins in the presence of high sample loading variability.

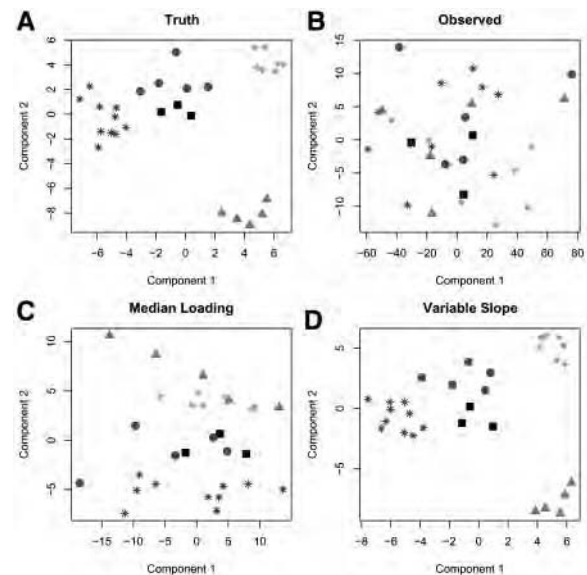


Fig. 2. The first two principal components plotted against each other for the true data matrix (A), the observed data matrix (B), the data matrix after ML normalization (C) and the data matrix after VS normalization (D). There are five groups each plotted in a different shade and symbol (every point represents a different protein/array). Each panel is shown in principal component space so rotation of axes is arbitrary; it is only important how the points group together. VS normalization is able to recover the group structure observed in the ‘true’ matrix, while ML normalization only recovers one of the groups.

4 EXAMPLE WITH LEUKEMIA DATA

We applied the normalization methods to an RPPA experiment studying protein signatures in leukemia. A series of 138 lysate arrays were printed with either blood or marrow samples from 360 patients with acute lymphoblastic leukemia (ALL). Each sample was printed in duplicate on the array; each replicate was printed in a five spot, 2-fold dilution series. We used *SuperCurve* (see supplementary Material) to estimate protein expression for each dilution series.

The sample loadings for this data are quite variable. Figure 3 shows the protein expression for two extreme samples across all of the arrays. Figure 3A plots the expression before any loading normalization, showing that two samples can differ by nearly 8 U on a log₂ scale (a 256-fold difference) just due to sample loading. Figure 3(B–D) plots protein expression for the same two samples after HK, ML and VS normalizations. There is still a slight loading bias after HK normalization, but the other two methods are able to correct this.

We performed hierarchical clustering of the 138 proteins, using average linkage for the linkage method and Pearson’s correlation coefficient for the distance metric. For both VS and ML normalization methods, we checked the robustness of the protein clusters using bootstrap clustering (Kerr and Churchill, 2001; Pollard and van der Laan, 2005). HK normalization is excluded here because it did not remove all sample loading bias (Fig. 3). The idea behind bootstrap clustering is to see how often each pair of proteins clusters together in a set of bootstrapped samples. Based on the median split silhouette statistic (see Pollard and van der Laan 2005), we assumed nine clusters. Figure 4 shows the

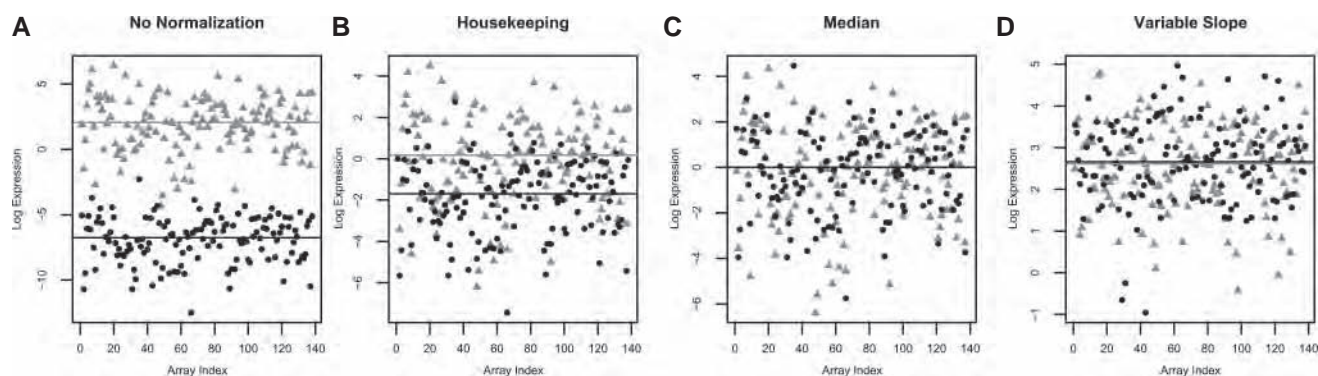


Fig. 3. Protein expression for two extreme samples (a low expressed sample in black and a high expressed sample in gray) from an RPPA experiment with 138 slides. (A–D) The expression for the two samples across all arrays in the set. The array index is plotted on the x -axis and the estimated log expression is plotted on the y -axis. When there is no normalization, there is nearly an $8 \log_2$ unit difference in expression (256-fold) between these samples primarily due to sample loading effects. HK normalization mostly corrects for sample loading, but there is still a 4-fold sample loading bias that the HK protein does not fix. Both median and VS normalization completely correct this level of observed sample loading bias. Note that there are differences in scale in each of the plots.

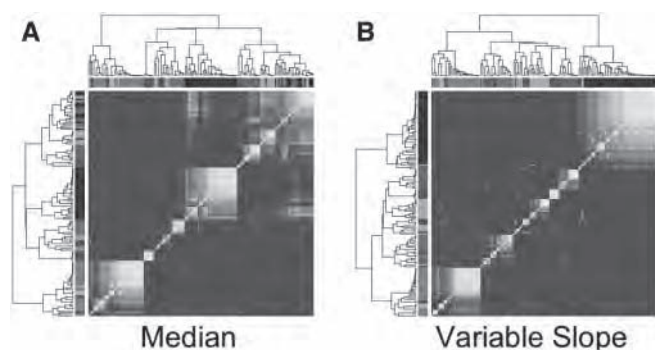


Fig. 4. Bootstrap Cluster results after ML (A) and VS normalization (B). The colors on the margin were assigned based on group membership after clustering the VS normalized data matrix. The marginal colors are present only to show that there is some shift in group membership depending on the normalization method. The clusters found after VS normalization seem to be more robust.

results of a bootstrap cluster test with 500 bootstrapped samples after ML and VS normalizations. The figure ranges from perfectly yellow, meaning the proteins always cluster in the same group, to perfectly blue meaning the proteins never cluster in the same group (color version online). There are nine marginal colors that were assigned based on group membership of the proteins after the hierarchical cluster of the VS normalized data matrix. The colors in the margins of the plot are arbitrary, only used to illustrate change in group membership. The figure demonstrates that there is change in protein group membership depending on the normalization method used, confirming that the normalization approach is an important consideration. Although it is not possible to say which grouping is correct, the clusters found after VS normalization appear more robust, as seen by the tighter yellow squares along the diagonal.

We attempted to determine which normalization method is most consistently correct. The ALL samples were each printed in duplicate on the array, so we performed hierarchical clustering with each set of replicates separately after both VS and ML normalization methods. Clustering with each replicate set should produce the same clusters,

since the same set of samples is used. We counted the number of protein pairs that clustered together using the samples from one replicate but did not cluster together using the samples from the other replicate and divided this count by the total number of protein pairs. The count is interpreted as the percentage of protein pairs that did not cluster consistently. For the ALL samples from the set of 138 arrays, ML normalization inconsistently clustered 24% of the protein pairs while VS normalization inconsistently clustered 17% of the protein pairs. After filtering out non-informative samples, ML normalization inconsistency dropped to 18% and VS normalization inconsistency dropped to 12%. Both results are consistent with VS normalization as the preferred method.

5 DISCUSSION

Protein arrays are not currently in as widespread use as genomic arrays or other proteomic techniques; however, they are becoming more common. Several different groups have published analyses using RPPA technology (Gulmann *et al.* 2005; Hennessy *et al.* 2007; Jiang *et al.* 2006; Korf *et al.* 2008; Kornblau *et al.* 2009; Park *et al.* 2008; Tibes *et al.* 2006). Furthermore, RPPAs can be produced with common laboratory materials and techniques, making them more accessible than genomic arrays or mass spectrometry. As this technology becomes more common, appropriate preprocessing of the data will be even more important.

It is not a trivial problem to determine the best way or ways to normalize RPPA data. We have presented a traditional framework for correcting sample and array effects. We further introduced a slight modification to the standard procedure, the VS normalization method, which normalizes for total protein while taking into account error that can be introduced during the quantification step. Namely, since each array is quantified separately, slight variations in the estimated logistic slope of the dose response curve can create problems if ignored. The VS model better explains observed behavior and matches our knowledge of protein expression estimation. We have shown through simulation and an example with real data that how the VS method can recover true group correlations better than simply normalizing to the median of the samples or to a HK protein. We have also pointed out that the usual practice of

normalization to a HK protein can be problematic both because of difficulties in finding a true HK protein and failures to remove all sample loading bias.

The impact of the multiplicative protein effect, γ_p in Equation (2), depends on variability in the sample loadings. Since the γ_p 's are centered close to one, when the sample loadings have small variability, the impact of γ_p will also be small. However, the relatively small values of γ_p can have a large impact when variability in the sample loadings is large, as for example in the ALL data cited here. In these cases, it is especially important to correct for both additive and multiplicative protein effects. The type of sample contributes to how big the sample loading problem can be. Cell lines, for example, are not nearly as variable as tissue samples and usually do not have such large variations in sample loading across the samples.

The problem of sample loading is not something that can be resolved or even seen with just one array. Simulations not shown here suggest that at least 20 arrays (proteins) are adequate to provide good estimates of total protein, though fewer arrays can indicate a sample loading problem.

This is the first attempt that we know of to combine information across arrays in an RPPA study instead of focusing on each arrays individually.

Better estimation of the VS model parameters might be achieved with other estimation methods, such as with an iterative approach. In the future, we will investigate this possibility and how better estimates can improve results more. Although this procedure was developed for RPPAs, it can have application to any array assay in which different samples are printed together on the same array.

Conflict of Interest: none declared.

REFERENCES

- Akkiprik, M. *et al.* (2006) Dissection of signaling pathways in fourteen breast cancer cell lines using reverse-phase protein lysate microarray. *Technol. Cancer Res. Treat.*, **5**, 543–551.
- Becker, K.-F. *et al.* (2006) Clinical proteomics: new trends for protein microarrays. *Curr. Med. Chem.*, **13**, 1831–1837.
- Calvert, V.S. *et al.* (2007) A systems biology approach to the pathogenesis of obesity-related nonalcoholic fatty liver disease using reverse phase protein microarrays for multiplexed cell signaling analysis. *Hepatology*, **46**, 166–172.
- Chan, S.M. *et al.* (2004) Protein microarrays for multiplex analysis of signal transduction pathways. *Nat. Med.*, **10**, 1390–1396.
- Charboneau, L. *et al.* (2002) Utility of reverse phase protein arrays: applications to signalling pathways and human body arrays. *Brief. Funct. Genomic Proteomic*, **1**, 305–315.
- de Groen, P.P.N. (1996) An introduction to total least squares. *Nieuw Arch. Wiskd.*, **14**, 237.
- Espina, V. *et al.* (2004) Protein microarray detection strategies: focus on direct detection technologies. *J. Immunol. Methods*, **290**, 121–133.
- Grote, T. *et al.* (2008) Validation of reverse phase protein array for practical screening of potential biomarkers in serum and plasma: accurate detection of CA19-9 levels in pancreatic cancer. *Proteomics*, **8**, 3051–3060.
- Grubb, R.L. *et al.* (2003) Signal pathway profiling of prostate cancer using reverse phase protein arrays. *Proteomics*, **3**, 2142–2146.
- Gulmann, C. *et al.* (2005) Proteomic analysis of apoptotic pathways reveals prognostic factor in follicular lymphoma. *Clin. Cancer Res.*, **11**, 5847–5855.
- Hennessy, B. *et al.* (2007) Pharmacodynamic markers of perifosine efficacy. *Clin. Cancer Res.*, **13**, 7421–7431.
- Herrmann, P.C. *et al.* (2003) Mitochondrial proteome: altered cytochrome c oxidase subunit levels in prostate cancer. *Proteomics*, **3**, 1801–1810.
- Hu, J. *et al.* (2007) Nonparametric quantification of protein lysate arrays. *Bioinformatics*, **23**, 1986–1994.
- Jiang, R. *et al.* (2006) Pathway alterations during glioma progression revealed by reverse phase protein lysate arrays. *Proteomics*, **6**, 2964–2971.
- Kerr, M.K. and Churchill, G.A. (2001) Bootstrapping cluster analysis: assessing the reliability of conclusions from microarray experiments. *Proc. Natl Acad. Sci. USA*, **98**, 8961–8965.
- Kim, W. *et al.* (2008) A novel derivative of the natural agent deguelin for cancer chemoprevention and therapy. *Cancer Prev. Res.*, **1**, 577–587.
- Korf, U. *et al.* (2008) Quantitative protein microarrays for time-resolved measurements of protein phosphorylation. *Proteomics*, **8**, 4603–4612.
- Kornblau, S. *et al.* (2009) Functional proteomic profiling of AML predicts response and survival. *Blood*, **113**, 154–164.
- Kreutzberger, J. (2006) Protein microarrays: a chance to study microorganisms. *Appl. Microbiol. Biotechnol.*, **70**, 383–390.
- Liotta, L.A. *et al.* (2006) Protein microarrays: meeting analytical challenges for clinical applications. *Clin. Cancer Res.*, **12**, 4583–4589.
- Ma, Y. *et al.* (2006) Predicting cancer drug response by proteomic profiling. *Drug Discov. Today*, **11**, 1007–1011.
- Mendes, K.N. *et al.* (2007). Analysis of signaling pathways in 90 cancer cell lines by protein lysate array. *J. Proteome Res.*, **6**, 2753–2767.
- Mircean, C. *et al.* (2005) Robust estimation of protein expression ratios with lysate microarray technology. *Bioinformatics*, **21**, 1935–1942.
- Nishizuka, S. *et al.* (2003a) Diagnostic markers that distinguish colon and ovarian adenocarcinomas: identification by genomic, proteomic, and tissue array profiling. *Cancer Res.*, **63**, 5243–5250.
- Nishizuka, S. *et al.* (2003b) Proteomic profiling of the NCI-60 cancer cell lines using new high-density reverse-phase lysate microarrays. *Proc. Natl Acad. Sci. USA*, **100**, 14229–14234.
- Park, M. *et al.* (2008) A quantitative analysis of N-myc downstream regulated gene 2 (NDRG 2) in human tissues and cell lysates by reverse-phase protein microarray. *Clin. Chim. Acta*, **387**, 84–89.
- Paweletz, C.P. *et al.* (2001) Reverse phase protein microarrays which capture disease progression show activation of pro-survival pathways at the cancer invasion front. *Oncogene*, **20**, 1981–1989.
- Pollard, K. and van der Laan, M.J. (2005) *Bioinformatics and Computational Biology Solutions Using R and Bioconductor*, ch. 13. Springer, New York, pp. 209–228.
- Rencher, A.C. (1995) *Methods of Multivariate Analysis*. John Wiley & Sons, Inc., New York.
- Shankavaram, U.T. *et al.* (2007) Transcript and protein expression profiles of the NCI-60 cancer cell panel: an integrative microarray study. *Mol. Cancer Ther.*, **6**, 820–832.
- Stevens, E. *et al.* (2008) Predicting cisplatin and trabectedin drug sensitivity in ovarian and colon cancers. *Mol. Cancer Ther.*, **7**, 10–18.
- Tabus, I. *et al.* (2006) Nonlinear modeling of protein expressions in protein arrays. *IEEE Trans. Signal Processing*, **54**, 2394–2407.
- Tibes, R. *et al.* (2006) Reverse phase protein array: validation of a novel proteomic technology and utility for analysis of primary leukemia specimens and hematopoietic stem cells. *Mol. Cancer Ther.*, **5**, 2512–2521.
- Wulfkuhle, J.D. *et al.* (2003) Signal pathway profiling of ovarian cancer from human tissue specimens using reverse-phase protein microarrays. *Proteomics*, **3**, 2085–2090.
- Zhang, L. *et al.* (2009) Serial dilution curve: a new method for analysis of reverse phase protein array data. *Bioinformatics*, **25**, 650–654.
- Zha, H. *et al.* (2004) Similarities of prosurvival signals in Bcl-2-positive and Bcl-2-negative follicular lymphomas identified by reverse phase protein microarray. *Lab. Invest.*, **84**, 235–44.

PTEN Loss Contributes to Erlotinib Resistance in EGFR-Mutant Lung Cancer by Activation of Akt and EGFR

Martin L. Sos,¹ Mirjam Koker,¹ Barbara A. Weir,⁵ Stefanie Heynck,¹ Rosalia Rabinovsky,⁶ Thomas Zander,² Jens M. Seeger,³ Jonathan Weiss,¹ Florian Fischer,¹ Peter Frommolt,⁴ Kathrin Michel,¹ Martin Peifer,¹ Craig Mermel,^{5,6} Luc Girard,⁹ Michael Peyton,⁹ Adi F. Gazdar,^{9,10} John D. Minna,^{9,11} Levi A. Garraway,^{5,6,7} Hamid Kashkar,³ William Pao,¹² Matthew Meyerson,^{5,6,7,8} and Roman K. Thomas^{1,2,13}

¹Max-Planck-Institute for Neurological Research with Klaus-Joachim Zülch Laboratories of the Max-Planck-Society and the Medical Faculty of the University of Köln, ²Department I of Internal Medicine and Center of Integrated Oncology, University of Köln, ³Institute for Medical Microbiology, Immunology and Hygiene, and ⁴Institute for Medical Statistics, Informatics and Epidemiology, Köln, Germany; ⁵The Broad Institute of Harvard and MIT, Cambridge, Massachusetts; ⁶Department of Medical Oncology and ⁷Center for Cancer Genome Discovery, Dana-Farber Cancer-Institute, and ⁸Department of Pathology, Harvard Medical School, Boston, Massachusetts; ⁹Hamon Center for Therapeutic Oncology Research, and Departments of ¹⁰Pathology and ¹¹Internal Medicine and Pharmacology, University of Texas Southwestern Medical Center, Dallas, Texas; ¹²Human Oncology and Pathogenesis Program, Memorial Sloan-Kettering Cancer Center, New York, New York; and ¹³Chemical Genomics Center of the Max-Planck-Society, Dortmund, Germany

Abstract

Clinical resistance to epidermal growth factor receptor (EGFR) inhibition in lung cancer has been linked to the emergence of the EGFR T790M resistance mutation or amplification of *MET*. Additional mechanisms contributing to EGFR inhibitor resistance remain elusive. By applying combined analyses of gene expression, copy number, and biochemical analyses of EGFR inhibitor responsiveness, we identified homozygous loss of *PTEN* to segregate EGFR-dependent and EGFR-independent cells. We show that in EGFR-dependent cells, *PTEN* loss partially uncouples mutant EGFR from downstream signaling and activates EGFR, thereby contributing to erlotinib resistance. The clinical relevance of our findings is supported by the observation of *PTEN* loss in 1 out of 24 primary EGFR-mutant non-small cell lung cancer (NSCLC) tumors. These results suggest a novel resistance mechanism in *EGFR*-mutant NSCLC involving *PTEN* loss. [Cancer Res 2009;69(8):3256–61]

Introduction

Activating mutations in the epidermal growth factor receptor (EGFR) are present in ~10% of non-small cell lung cancers (NSCLC) in Caucasian patients and in up to 40% of East-Asian patients. By contrast, EGFR mutations are much more rare in African Americans. These mutations lead to the “addiction” of mutant cells to the oncogenic signals driven by mutant EGFR. This dependency is thought to be the cause of the clinical observations that *EGFR*-mutant tumors shrink when treated with EGFR inhibitors (1, 2). Eventually, these tumors recur; in ~60% to 70% (3) of cases, this has been linked to the emergence of either the T790M resistance mutation of EGFR or amplification of *MET* (2–4). However, a mechanistic explanation for acquired resistance in the remaining cases is lacking.

Note: Supplementary data for this article are available at Cancer Research Online (<http://cancerres.aacrjournals.org/>).

Requests for reprints: Roman K. Thomas, Max-Planck-Institute for Neurological Research, Gleueler Street 50, Cologne 50931, Germany. Phone: 49-221-472-6259; Fax: 49-221-472-6298; E-mail: nini@nf.mpg.de.

©2009 American Association for Cancer Research.
doi:10.1158/0008-5472.CAN-08-4055

Here, we used a large collection of genomically characterized NSCLC cell lines in order to derive genomic features that segregate EGFR-dependent from EGFR-independent EGFR-mutant lung tumor cells. We combined computational, biochemical, and cellular approaches to identify novel, clinically relevant mechanisms uncoupling EGFR-dependent tumors from downstream signaling.

Materials and Methods

A detailed description of all methods is given in the Supplementary Methods. As part of a larger effort to characterize the genomes of NSCLC, we have collected 84 NSCLC cell lines, which we analyzed for chromosomal gene copy number alterations, mutations, as well as transcriptional changes. The detailed description of this collection will be published elsewhere. Here, a subset of 53 of these cell lines was studied (Supplementary Table S1). Hierarchical clustering was performed using dCHIP. Genomic lesions differentiating between erlotinib-sensitive and erlotinib-insensitive cells were analyzed by inferring the mean copy number of chromosomal windows from five contiguous loci. Statistical analyses were performed using R.

Results and Discussion

In order to analyze oncogene dependencies in lung cancer, we used a collection of 84 NSCLC cell lines that we have recently characterized in-depth genomically and phenotypically (Supplementary Table S1).¹⁴

We performed hierarchical clustering of gene expression data of 53 of these lines. In this analysis, the *EGFR*-mutant cell line, H1650, did not share a cluster with all other *EGFR*-mutant cell lines (Fig. 1A). This cell line has previously been reported to be erlotinib-resistant, despite lacking known resistance mechanisms (Fig. 1A; ref. 5).

Confirming these observations, H1650 cells were erlotinib-resistant with a half-maximal inhibitory concentration (IC₅₀) of 2.13 μmol/L (Fig. 1B). As previously reported, *EGFR*-mutant HCC827 cells were erlotinib-sensitive (IC₅₀, 0.02 μmol/L), whereas H1975 cells expressing both the erlotinib-sensitizing L858R mutation and the T790M resistance mutation were resistant (IC₅₀ > 10 μmol/L; Fig. 1B; refs. 5, 6). Treatment with 100 nmol/L of

¹⁴M.L. Sos et al., under revision.

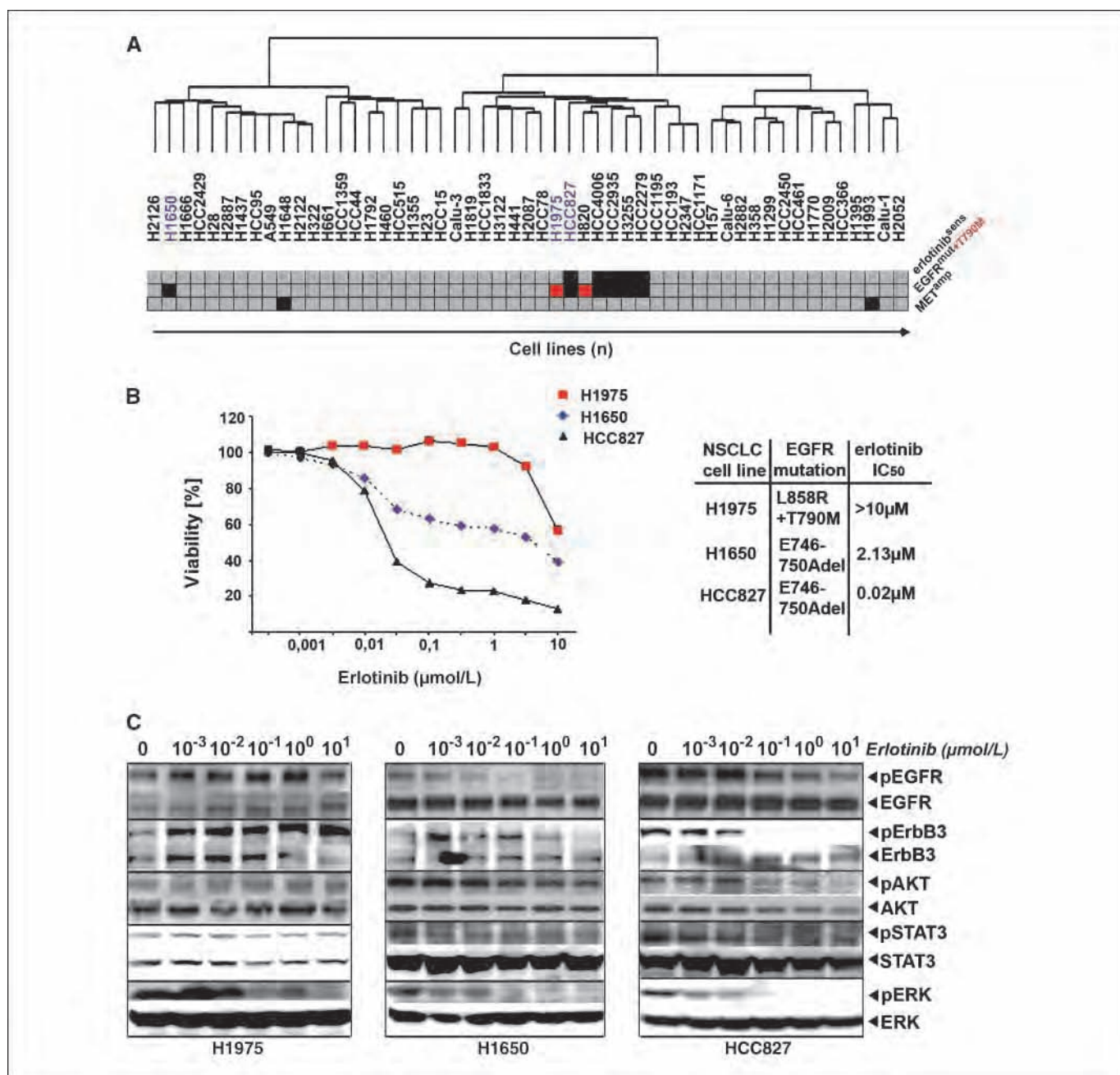


Figure 1. An EGFR independence signature in H1650 cells. *A*, hierarchical clustering of 53 NSCLC cells according to gene expression. Erlotinib sensitivity ($IC_{50} < 1 \mu\text{mol/L}$, red; $IC_{50} > 1 \mu\text{mol/L}$, gray) and *EGFR* mutations (*EGFR*-mutant, black; T790M, red; *EGFR* wild-type, gray) as well as *MET* amplification (black). *B*, left, cellular viability as a function of erlotinib dose for all three cell lines studied. Right, mutation status and IC_{50} values. *C*, cells were treated with different doses of erlotinib. Activation of *EGFR* and downstream signaling pathways was determined by analyzing the amount of phosphorylated versions of the respective proteins in comparison with their total levels using phosphorylation-specific antibodies.

erlotinib led to the dephosphorylation of *EGFR* in H1650 and HCC827 but not in H1975 cells (Fig. 1C). However, although the dephosphorylation of *EGFR* was accompanied by a reduction in p-Akt levels in erlotinib-sensitive HCC827 cells, H1650 cells retained high levels of p-Akt despite inhibition of *EGFR* (Fig. 1C). By contrast, erlotinib-mediated inhibition of known signal transducers of the *EGFR* such as ErbB3, STAT3, and ERK was similar to the levels observed in HCC827, consistent with the uncoupling of mutant *EGFR* from downstream survival signaling at the level of Akt (Fig. 1C).

We speculated that chromosomal aberrations might be causatively involved in this phenotype and sought for chromosomal regions displaying differential copy numbers between H1650 cells and the *EGFR*-mutant and erlotinib-sensitive cell lines. We identified 13 H1650-specific chromosomal loci harboring nine known genes, including a chromosomal region affected by homozygous deletion 3' to the locus containing the tumor suppressor gene *PTEN* (Fig. 2A; ref. 7). Furthermore, when analyzing the transcription of *IGFBP2*, a marker predictive of *PTEN* loss in glioblastoma (8), H1650 was the highest scoring line

in our panel (data not shown). PTEN counteracts Akt activation by dephosphorylating phosphatidylinositol-3,4,5-triphosphate (PIP3), the product of class I phosphoinositide-3-kinases (7, 9). Because *PTEN* loss has been shown to be involved in EGFR inhibitor resistance in some tumor cell lines (10, 11) and in glioblastoma patients (12), we reasoned that *PTEN* loss might also be involved in the EGFR-independent phenotype of H1650. Furthermore, lack of PTEN protein expression has previously been speculated to be involved in erlotinib resistance in H1650 cells (13, 14).

To determine whether loss of PTEN protein in H1650 cells (13, 14) might be caused by genomic loss, we mapped the *PTEN* locus by quantitative PCR. Fine-mapping followed by long-distance PCR revealed that the homozygous deletion (spanning 16.8 kb) leads to the deletion of the 3' part of exon 8 and the entire exon 9 (Fig. 2B). The deletion results in a COOH-terminally truncated protein that could only be detected using antibodies against NH₂-terminal

epitopes (Fig. 2C). Previous functional genetics experiments have shown a critical role of the COOH-terminal part of PTEN (15). Thus, the COOH-terminal deletion in H1650 cells might be causally involved in uncoupling mutant EGFR from downstream Akt survival signaling.

We next analyzed a panel of 140 primary lung adenocarcinomas (predominantly Caucasian patients), annotated for copy number alterations and mutations in 623 genes, for the presence of co-occurring lesions in *PTEN* and *EGFR* (16, 17). We found co-occurrence of homozygous deletion of *PTEN* and *EGFR* mutation in 1 out of 24 samples with *EGFR* mutations (Fig. 2D). Thus, primary resistance of EGFR-mutant NSCLC might, in rare cases, be due to homozygous loss of *PTEN*. Furthermore, we found hemizygous loss of chromosome 10 to be significantly enriched in *EGFR*-mutant patients in the cohort of 140 primary samples ($P = 0.012$; data not shown). Loss of the other allele by mutation

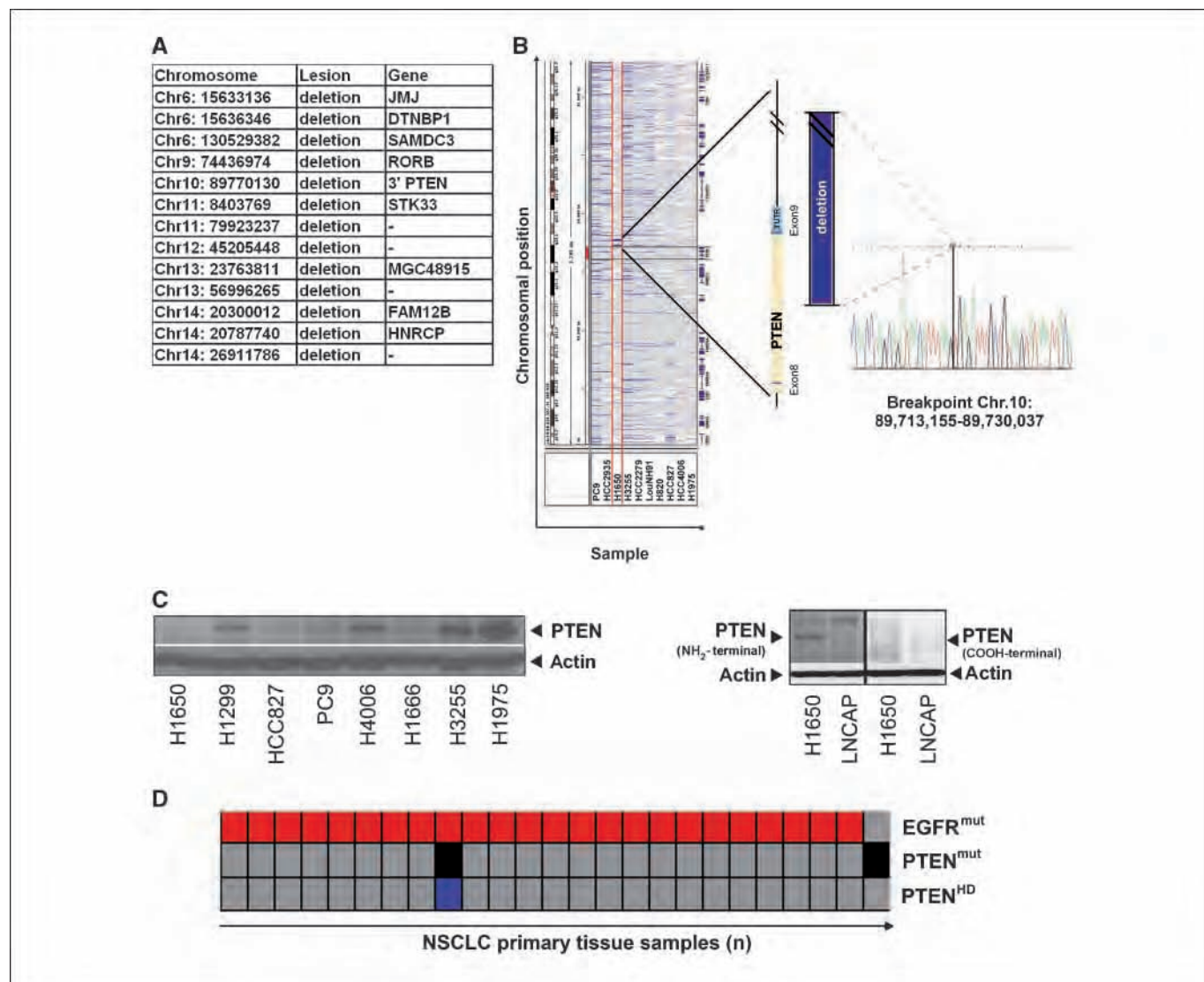


Figure 2. Genomic characterization of *PTEN* loss in H1650 cells. **A**, list of genes affected by differential lesions between H1650 cells and EGFR-mutant and erlotinib-sensitive cell lines. **B**, left, screenshot showing chromosomal aberrations at chromosome 10 (Integrative Genomics Viewer; <http://www.broad.mit.edu/igv/>) of all *EGFR*-mutant cells. Middle, 3'-region mapping of *PTEN* using quantitative PCR reveals a homozygous deletion deleting parts of exon 8 and the entire exon 9. Right, the sequence bridging the breakpoint. **C**, left, PTEN protein status determined using immunoblotting in different NSCLC cell lines. Right, NH₂-terminal and COOH-terminal PTEN detection by immunoblotting. LNCAP cells, known to express a truncated version of *PTEN*, served as controls. **D**, analysis of *EGFR* mutations (red) and homozygous deletions of *PTEN* (black) and *PTEN* mutations (blue) in 140 lung cancer biopsy specimens.

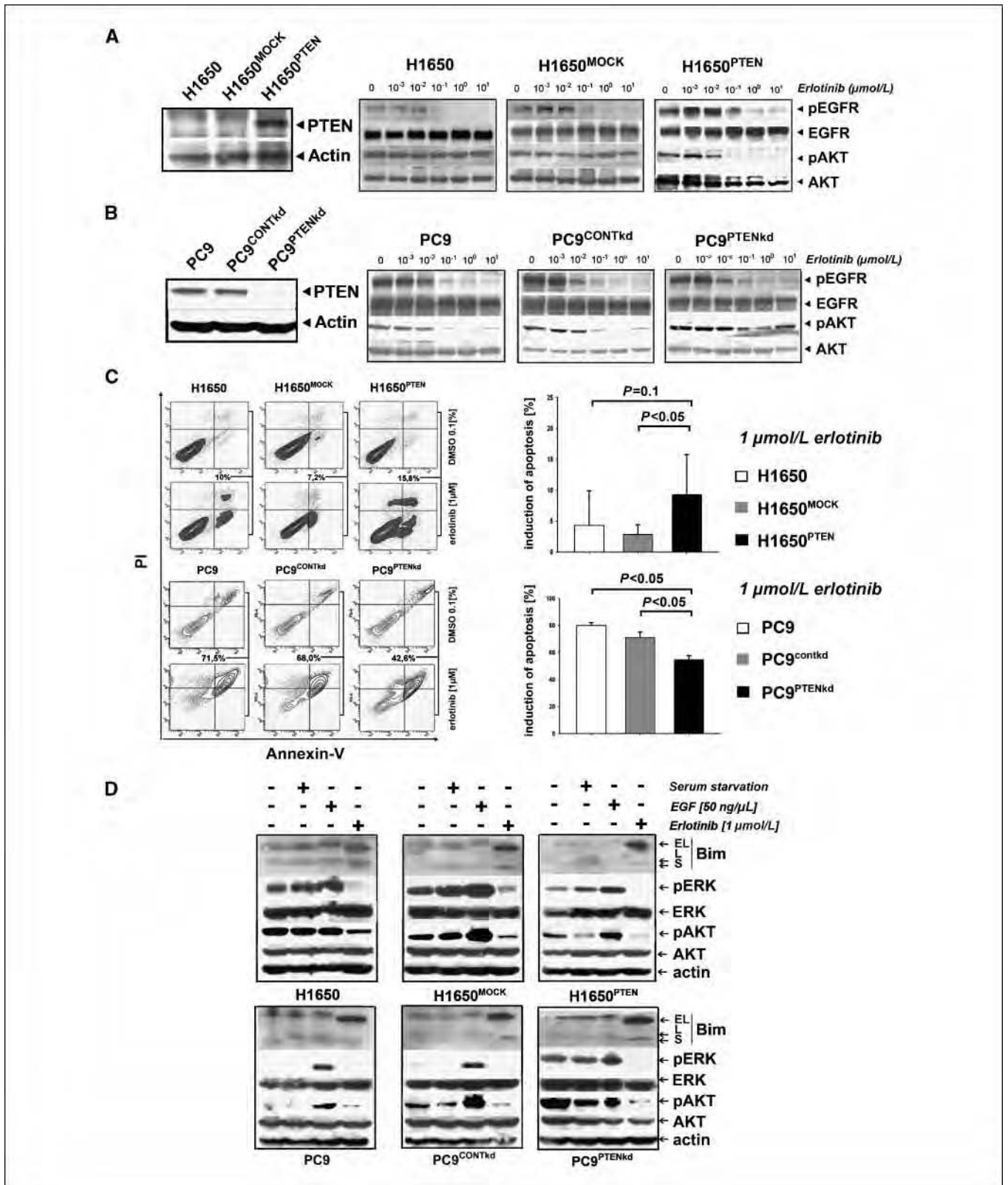


Figure 3. Erlotinib resistance in EGFR-mutated NSCLC with PTEN loss. *A, left*, in H1650^{PTEN} cells, PTEN levels were determined by immunoblotting. *Right*, levels of phospho-EGFR and phospho-AKT were assessed by immunoblotting in H1650, H1650^{MOCK}, and H1650^{PTEN} cells treated with erlotinib. *B, left*, in PC9^{PTENkd} cells, PTEN levels were determined by immunoblotting. *Right*, levels of phospho-EGFR and phospho-AKT were assessed in PC9, PC9^{CONTkd}, and PC9^{PTENkd} cells treated with erlotinib. *C, left*, percentage of apoptotic cells (in %, analyzed by measuring the fraction of cells positive for Annexin V and/or propidium iodide by flow cytometry) after treatment with either erlotinib (1 μmol/L) or control. *Right*, cumulative histograms of apoptosis induction. *D*, levels of Bim (EL, extra long; L, long; S, short), phospho-ERK, phospho-pAKT, and actin were measured after serum starvation (serum starvation "+"), EGF stimulation (EGF "+"), or treatment with erlotinib (1 μmol/L erlotinib "+") for 24 h.

might thus confer acquired resistance in patients initially responding to EGFR inhibition. This notion is also supported by a previous study reporting favorable survival of *EGFR*-mutant patients with high expression of PTEN (18).

We reconstituted wild-type *PTEN* in H1650 cells by stable retroviral expression (Fig. 3A). Reconstitution of *PTEN* restored coupling of the EGFR signal to downstream Akt signaling as evidenced by dephosphorylation of both EGFR and Akt upon erlotinib treatment (Fig. 3A). Cellular proliferation of H1650^{PTEN} cells treated with erlotinib was virtually identical to that seen in the parental cells (data not shown) but combinatorial treatment of H1650 cells with erlotinib and an AKT inhibitor led to a reduction of viability when compared with cells treated with erlotinib alone (Supplementary Fig. S1). However, when analyzing the fraction of cells undergoing apoptosis upon treatment with erlotinib, we observed an increase of apoptotic H1650^{PTEN} cells when compared with the parental and the mock-transduced cells (Fig. 3C). Thus, *PTEN* reconstitution increases the susceptibility to erlotinib-induced apoptosis in H1650 cells.

We next silenced *PTEN* in *EGFR*-mutant and erlotinib-sensitive PC9 cells by lentiviral short hairpin RNAs (Fig. 3B). Similar to our observation in the parental H1650 cells, *PTEN* loss in PC9 cells (PC9^{PTENkd}) induced the uncoupling of EGFR and downstream Akt signaling as shown by continuous Akt phosphorylation under

erlotinib treatment (Fig. 3B). Again, recapitulating our observations in H1650 cells, silencing of *PTEN* expression in PC9 cells led to a significant decrease in the fraction of apoptotic cells when treated with erlotinib (Fig. 3C). Induction of apoptosis in both *PTEN*-proficient and *PTEN*-deficient cells was paralleled by activation of the proapoptotic protein Bim, recently shown to play a key role in erlotinib-induced apoptosis in *EGFR*-mutant NSCLC (refs. 19, 20; Fig. 3D). Thus, the differential induction of apoptosis is not mediated through modulation of Bim levels. Interestingly, in PC9^{PTENkd} cell lines, we observed the activation of Erk under steady-state and serum-starved conditions, whereas *PTEN*-proficient cells hardly showed Erk activity (Fig. 3D). Thus, *PTEN* loss partially uncouples EGFR signaling from downstream Akt survival signaling, activates ERK, and contributes to EGFR inhibitor resistance.

While analyzing the activity of Akt in *PTEN*-deficient H1650 and PC9^{PTENkd} *EGFR*-mutant cells, we observed an increase in phospho-EGFR when compared with *PTEN*-proficient cells. In PC9^{PTENkd} cells, complete deactivation of EGFR was achieved at 750 nmol/L of erlotinib, whereas in parental and control PC9 cells, 250 nmol/L of erlotinib was sufficient to fully dephosphorylate the receptor (Fig. 4A). Thus, the resistance phenotype observed in *PTEN*-deficient H1650 cells may be partially explained by the prolonged activation of EGFR under treatment with EGFR tyrosine

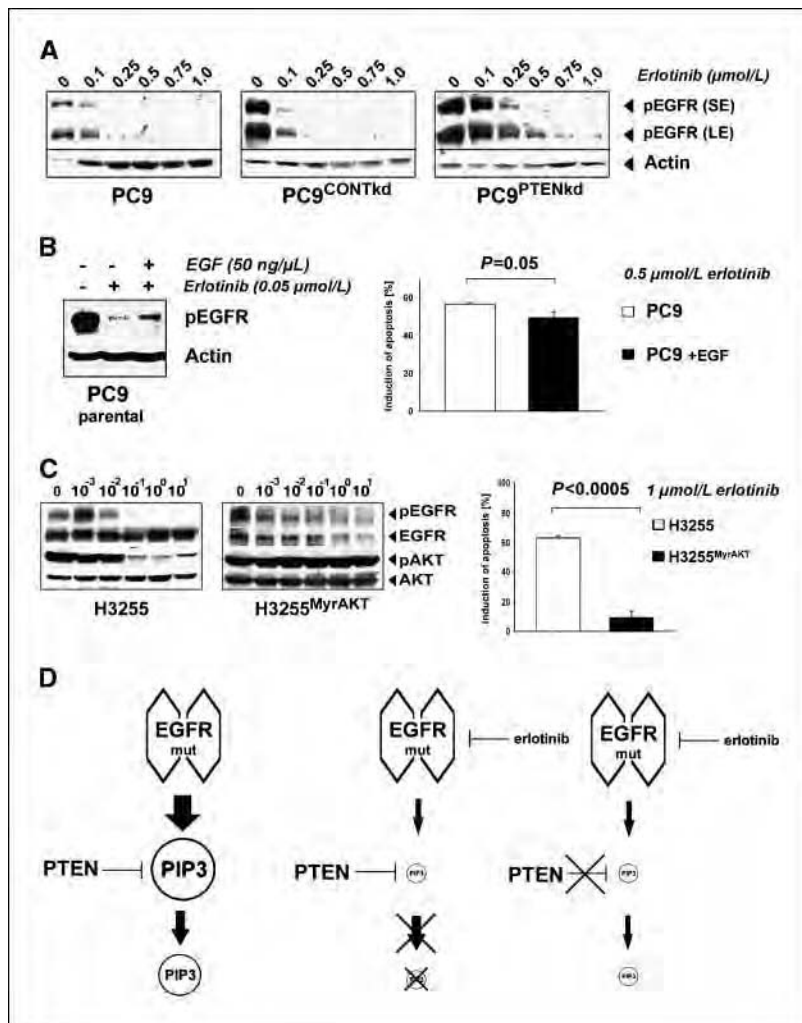


Figure 4. *PTEN* loss activates EGFR. *A*, phospho-EGFR was detected by immunoblotting after short exposure (*SE*) and long exposure (*LE*) in PC9, PC9^{CONTkd}, and PC9^{PTENkd} cells. Actin levels served as a loading control. *B*, *left*, levels of phospho-EGFR of PC9^{PTENkd} and PC9 cells treated with erlotinib were determined (+/- EGF) under serum starvation. *Right*, apoptosis (%) after erlotinib treatment (0.5 μmol/L) in the given cells. *C*, *left*, phospho-EGFR and phospho-AKT in H3255 and H3255^{MyrAKT} cells were assessed by immunoblotting. *Right*, the fraction of apoptotic cells (in %) in the given cells. *D*, a simplified model explaining our observations: in *EGFR*-mutant cells, EGFR is the sole input for production of PIP3. Inhibiting EGFR dramatically reduces the input into PIP3 production. Therefore, the lack of negative regulation of PIP3 production by loss of *PTEN* is limited.

kinase inhibitors. To test whether *PTEN* loss-induced EGFR activation may be mimicked by stimulation of EGFR in *PTEN*-proficient PC9 cells, we treated parental PC9 cells with a combination of erlotinib and EGF (Fig. 4B). We observed an induction of phospho-EGFR by dual EGF stimulation and EGFR inhibition resembling the situation in *PTEN*-deficient cells (Fig. 4B). Confirming the functional relevance of *PTEN* loss-induced EGFR activation, this treatment also led to a reduction of the fraction of apoptotic cells (Fig. 4B).

Finally, we asked whether survival signaling activated by loss of *PTEN* is equivalent to immediate activation of Akt. We introduced a constitutively active allele of Akt (MyrAkt) into *EGFR*-mutant and erlotinib-sensitive H3255 cells. As expected, levels of phospho-Akt but not of phospho-EGFR levels remained elevated in H3255^{MyrAkt} cells under erlotinib treatment (Fig. 4C). Furthermore, this pronounced Akt activity was associated with erlotinib resistance ($P < 0.0005$) of H3255^{MyrAkt} cells when measuring apoptosis (Fig. 4C). Thus, immediate and constitutive activation of Akt is more effective than *PTEN* loss to induce erlotinib resistance in *EGFR*-mutant NSCLC cells.

Others have recently shown that *PTEN* loss leads to robust EGFR inhibitor resistance in cells lacking *EGFR* mutations (10, 11). Our findings in *EGFR*-mutant NSCLC cells differ from these observations, as the phenotype elicited by *PTEN* loss was less dominant. This discrepancy may be explained by the fact that *EGFR*-mutant NSCLC cells are exclusively dependent on EGFR signaling for their survival. Thus, erlotinib-mediated inhibition of EGFR as the sole input of PIP3 production may only partially be rescued by *PTEN* loss (Fig. 4D).

In summary, we have shown that in-depth genomic and phenotypic analyses of large cell line collections can be applied to identify a novel cell biology phenotype. Here, computational genomic analyses implied homozygous deletion of *PTEN* as a candidate for EGFR inhibitor resistance. Functional studies revealed that *PTEN* loss induces a significant reduction in apoptosis sensitivity in *EGFR*-mutant cells by activation of Akt and EGFR. We speculate that activation of Erk in *PTEN*-deficient cells (Fig. 3D) may lead to transcriptional up-regulation of EGFR ligands, such as amphiregulin (21). Moreover, *PTEN* loss and *EGFR* mutation co-occurred in 1 out of 24 *EGFR*-mutant patients in a genomic analysis of 140 lung adenocarcinomas, thus confirming the clinical relevance of our findings. Thus, *PTEN* loss may represent an additional mechanism of initial or acquired resistance to erlotinib-induced apoptosis in *EGFR*-mutant NSCLC.

Disclosure of Potential Conflicts of Interest

No potential conflicts of interest were disclosed.

Acknowledgments

Received 10/21/08; revised 2/20/09; accepted 2/24/09; published OnlineFirst 4/7/09.

Grant support: R.K. Thomas is a fellow of the International Association for the Study of Lung Cancer; and is supported by the Deutsche Krebshilfe (107954), the Fritz-Thyssen-Stiftung (10.08.2.175), and the NGFN-Plus Program of the German Ministry of Science and Education (BMBF, 01GS08100). J.D. Minna is supported by grants from the Specialized Programs of Research Excellence P50CA70907, DOD PROSPECT, and the Longenbaugh Foundation.

The costs of publication of this article were defrayed in part by the payment of page charges. This article must therefore be hereby marked *advertisement* in accordance with 18 U.S.C. Section 1734 solely to indicate this fact.

We thank Dr. Ingo Mellinghoff for sharing unpublished results.

References

- Sharma SV, Fischbach MA, Haber DA, Settleman J. "Oncogenic shock": explaining oncogene addiction through differential signal attenuation. *Clin Cancer Res* 2006;12:4392-5.
- Thomas RK, Greulich H, Yuza Y, et al. Detection of oncogenic mutations in the EGFR gene in lung adenocarcinoma with differential sensitivity to EGFR tyrosine kinase inhibitors. *Cold Spring Harb Symp Quant Biol* 2005;70:73-81.
- Engelman JA, Janne PA. Mechanisms of acquired resistance to epidermal growth factor receptor tyrosine kinase inhibitors in non-small cell lung cancer. *Clin Cancer Res* 2008;14:2895-9.
- Bean J, Brennan C, Shih JY, et al. MET amplification occurs with or without T790M mutations in EGFR mutant lung tumors with acquired resistance to gefitinib or erlotinib. *Proc Natl Acad Sci U S A* 2007;104:20932-7.
- Guo A, Villen J, Kornhauser J, et al. Signaling networks assembled by oncogenic EGFR and c-Met. *Proc Natl Acad Sci U S A* 2008;105:692-7.
- Sos ML, Zander T, Thomas RK, Staratschek-Jox A, Claassen J, Wolf J. Expression of signaling mediators downstream of EGF-receptor predict sensitivity to small molecule inhibitors directed against the EGF-receptor pathway. *J Thorac Oncol* 2008;3:170-3.
- Stambolic V, Suzuki A, de la Pompa JL, et al. Negative regulation of PKB/Akt-dependent cell survival by the tumor suppressor PTEN. *Cell* 1998;95:29-39.
- Mehrian-Shai R, Chen CD, Shi T, et al. Insulin growth factor-binding protein 2 is a candidate biomarker for PTEN status and PI3K/Akt pathway activation in glioblastoma and prostate cancer. *Proc Natl Acad Sci U S A* 2007;104:5563-8.
- Sansal I, Sellers WR. The biology and clinical relevance of the PTEN tumor suppressor pathway. *J Clin Oncol* 2004;22:2954-63.
- Yamasaki F, Johansen MJ, Zhang D, et al. Acquired resistance to erlotinib in A-431 epidermoid cancer cells requires down-regulation of MMAC1/PTEN and up-regulation of phosphorylated Akt. *Cancer Res* 2007;67:5779-88.
- She QB, Solit DB, Ye Q, O'Reilly KE, Lobo J, Rosen N. The BAD protein integrates survival signaling by EGFR/MAPK and PI3K/Akt kinase pathways in PTEN-deficient tumor cells. *Cancer Cell* 2005;8:287-97.
- Mellinghoff IK, Wang MY, Vivanco I, et al. Molecular determinants of the response of glioblastomas to EGFR kinase inhibitors. *N Engl J Med* 2005;353:2012-24.
- McDermott U, Sharma SV, Dowell L, et al. Identification of genotype-correlated sensitivity to selective kinase inhibitors by using high-throughput tumor cell line profiling. *Proc Natl Acad Sci U S A* 2007;104:19936-41.
- Rikova K, Guo A, Zeng Q, et al. Global survey of phosphotyrosine signaling identifies oncogenic kinases in lung cancer. *Cell* 2007;131:1190-203.
- Georgescu MM, Kirsch KH, Akagi T, Shishido T, Hanafusa H. The tumor-suppressor activity of PTEN is regulated by its carboxyl-terminal region. *Proc Natl Acad Sci U S A* 1999;96:10182-7.
- Weir BA, Woo MS, Getz G, et al. Characterizing the cancer genome in lung adenocarcinoma. *Nature* 2007;450:893-8.
- Ding L, Getz G, Wheeler DA, et al. Somatic mutations affect key pathways in lung adenocarcinoma. *Nature* 2008;455:1069-75.
- Endoh H, Yatabe Y, Kosaka T, Kuwano H, Mitsudomi T. PTEN and PIK3CA expression is associated with prolonged survival after gefitinib treatment in EGFR-mutated lung cancer patients. *J Thorac Oncol* 2006;1:629-34.
- Gong Y, Somwar R, Politi K, et al. Induction of BIM is essential for apoptosis triggered by EGFR kinase inhibitors in mutant EGFR-dependent lung adenocarcinomas. *PLoS Med* 2007;4:e294.
- Deng J, Shimamura T, Perera S, et al. Proapoptotic BH3-only BCL-2 family protein BIM connects death signaling from epidermal growth factor receptor inhibition to the mitochondrion. *Cancer Res* 2007;67:11867-75.
- Toulany M, Baumann M, Rodemann HP. Stimulated PI3K-AKT signaling mediated through ligand or radiation-induced EGFR depends indirectly, but not directly, on constitutive K-Ras activity. *Mol Cancer Res* 2007;5:863-72.



Predicting drug susceptibility of non–small cell lung cancers based on genetic lesions

Martin L. Sos,¹ Kathrin Michel,¹ Thomas Zander,² Jonathan Weiss,¹ Peter Frommolt,³ Martin Peifer,¹ Danan Li,⁴ Roland Ullrich,¹ Mirjam Koker,¹ Florian Fischer,¹ Takeshi Shimamura,⁴ Daniel Rauh,⁵ Craig Mermel,^{4,6} Stefanie Fischer,¹ Isabel Stückerath,¹ Stefanie Heynck,¹ Rameen Beroukhi,^{4,6} William Lin,^{4,6} Wendy Winckler,^{4,6} Kinjal Shah,^{4,6} Thomas LaFramboise,⁷ Whei F. Moriarty,^{4,6} Megan Hanna,^{4,6} Laura Tolosi,⁸ Jörg Rahnenführer,⁹ Roel Verhaak,^{4,6} Derek Chiang,^{4,6} Gad Getz,⁶ Martin Hellmich,³ Jürgen Wolf,² Luc Girard,¹⁰ Michael Peyton,¹⁰ Barbara A. Weir,^{4,6} Tzu-Hsiu Chen,^{4,6} Heidi Greulich,^{4,6} Jordi Barretina,^{4,6,11} Geoffrey I. Shapiro,⁴ Levi A. Garraway,^{4,6,11,12} Adi F. Gazdar,^{10,13} John D. Minna,^{10,14} Matthew Meyerson,^{4,6,11,12} Kwok-Kin Wong,^{4,15} and Roman K. Thomas^{1,2,5}

¹Max Planck Institute for Neurological Research, Klaus-Joachim-Zülch Laboratories of the Max Planck Society, and University of Köln Medical Faculty, ²Department I of Internal Medicine and Center of Integrated Oncology Köln-Bonn, and ³Institute of Medical Statistics, Informatics and Epidemiology, University of Köln, Cologne, Germany. ⁴Department of Medical Oncology, Dana-Farber Cancer Institute, Harvard Medical School, Boston, Massachusetts, USA. ⁵Chemical Genomics Center of the Max Planck Society, Dortmund, Germany. ⁶Broad Institute of MIT and Harvard, Cambridge, Massachusetts, USA. ⁷Department of Genetics, Case Western Reserve University School of Medicine, Cleveland, Ohio, USA. ⁸Max Planck Institute for Informatics, Saarbrücken, Germany. ⁹Department of Statistics, Technical University of Dortmund, Dortmund, Germany. ¹⁰Hamon Center for Therapeutic Oncology Research, University of Texas Southwestern Medical Center, Dallas, Texas, USA. ¹¹Center for Cancer Genome Discovery, Dana-Farber Cancer Institute, Harvard Medical School, Boston, Massachusetts, USA. ¹²Department of Medicine, Brigham and Women's Hospital and Harvard Medical School, Boston, Massachusetts, USA. ¹³Department of Pathology and ¹⁴Departments of Internal Medicine and Pharmacology, University of Texas Southwestern Medical Center, Dallas, Texas, USA. ¹⁵Ludwig Center, Dana-Farber Cancer Institute, Harvard Medical School, Boston, Massachusetts, USA.

Somatic genetic alterations in cancers have been linked with response to targeted therapeutics by creation of specific dependency on activated oncogenic signaling pathways. However, no tools currently exist to systematically connect such genetic lesions to therapeutic vulnerability. We have therefore developed a genomics approach to identify lesions associated with therapeutically relevant oncogene dependency. Using integrated genomic profiling, we have demonstrated that the genomes of a large panel of human non–small cell lung cancer (NSCLC) cell lines are highly representative of those of primary NSCLC tumors. Using cell-based compound screening coupled with diverse computational approaches to integrate orthogonal genomic and biochemical data sets, we identified molecular and genomic predictors of therapeutic response to clinically relevant compounds. Using this approach, we showed that *v-Ki-ras2* Kirsten rat sarcoma viral oncogene homolog (KRAS) mutations confer enhanced Hsp90 dependency and validated this finding in mice with KRAS-driven lung adenocarcinoma, as these mice exhibited dramatic tumor regression when treated with an Hsp90 inhibitor. In addition, we found that cells with copy number enhancement of *v-abl* Abelson murine leukemia viral oncogene homolog 2 (ABL2) and ephrin receptor kinase and *v-src* sarcoma (Schmidt-Ruppin A-2) viral oncogene homolog (avian) (SRC) kinase family genes were exquisitely sensitive to treatment with the SRC/ABL inhibitor dasatinib, both in vitro and when it xenografted into mice. Thus, genomically annotated cell-line collections may help translate cancer genomics information into clinical practice by defining critical pathway dependencies amenable to therapeutic inhibition.

Introduction

The dynamics of ongoing efforts to fully annotate the genomes of all major cancer types are reminiscent of those of the Human Genome Project. The analysis of somatic gene copy number alterations and gene mutations associated with cancer (both

here referred to as *lesions*) will thus provide the genetic landscape of human cancer in the near future. The medical implications of these endeavors are exemplified by the success of molecularly targeted cancer therapeutics in genetically defined tumors: the ERBB2/Her2-targeted (where ERBB2 is defined as *v-erb b2 eryth-*

Authorship note: Martin L. Sos, Kathrin Michel, Thomas Zander, Peter Frommolt, and Jonathan Weiss contributed equally to this work.

Conflict of interest: R.K. Thomas has received research support from AstraZeneca. J. Wolf has received research support from Novartis and Roche. A.F. Gazdar has served as a consultant/lecturer for AstraZeneca, Genentech, and Boehringer Mannheim. L.A. Garraway has received research support from and served as a consultant for Novartis. M. Meyerson is a consultant for and received research funding from Novartis. M. Meyerson is an inventor on a patent describing EGFR mutation testing as a diagnostic test.

Nonstandard abbreviations used: 17-AAG, 17-(allylamino)-17-demethoxygeldanamycin; ABL2, *v-abl* Abelson murine leukemia viral oncogene homolog 2; BCR, breakpoint cluster region; BRAF, *v-raf* murine sarcoma viral oncogene homolog B1; 17-DMAG, 17-(dimethylaminoethylamino)-17-demethoxygeldanamycin; ERBB2, *v-erb b2* erythroblastic leukemia viral oncogene homolog 2, neuro/glioblastoma-derived oncogene homolog (avian); GI₅₀, half-maximal growth inhibitory concentrations; GISTIC, Genomic Identification of Significant Targets in Cancer; KIT, *v-kit* Hardy-Zuckerman 4 feline sarcoma viral oncogene homolog; KNN, K-nearest-neighbor; KRAS, *v-Ki-ras2* Kirsten rat sarcoma viral oncogene homolog; LOH, loss of heterozygosity; NSCLC, non–small cell lung cancer; PIK3CA, phosphoinositide-3-kinase, catalytic, α polypeptide; SRC, *v-src* sarcoma (Schmidt-Ruppin A-2) viral oncogene homolog (avian); TESP, Target-Enriched Sensitivity Prediction.

Citation for this article: *J. Clin. Invest.* 119:1727–1740 (2009). doi:10.1172/JCI37127.



roblastic leukemia viral oncogene homolog 2, neuro/glioblastoma-derived oncogene homolog [avian]) antibody trastuzumab shrinks tumors in women with *ERBB2*-amplified breast cancer (1); the *ABL/KIT/PDGFR* (where *ABL* is defined as *v-abl Abelson murine leukemia viral oncogene homolog* and *KIT* is defined as *v-kit Hardy-Zuckerman 4 feline sarcoma viral oncogene homolog*) inhibitor imatinib induces responses in patients with chronic myeloid leukemia carrying the *BCR/ABL* (where *BCR* is defined as *breakpoint cluster region*) translocation (2, 3) as well as in patients with gastrointestinal stromal tumors and melanomas bearing mutations in *KIT* (4) or *PDGFRA* (5); and finally, *EGFR*-mutant lung tumors are highly sensitive to the *EGFR* inhibitors gefitinib and erlotinib (6–8). In most cases, such discoveries were made after the completion of clinical trials; as yet no robust mechanism currently exists that permits systematic identification of lesions causing therapeutically relevant oncogene dependency prior to initiation of such clinical trials.

The use of cancer cell lines allows systematic perturbation experiments *in vitro*, yet the validity and clinical interpretability of these widely used models have been questioned. In some notable instances, pathways may lose function when grown in culture (9). In addition, cell lines are frequently thought to be genomically disarrayed and unstable and therefore likely poorly representative of primary tumors. Furthermore, the genetic diversity of histopathologically defined classes of tumors is often substantial, e.g., the clinical tumor entity non-small cell lung cancer (NSCLC) comprises *EGFR*- and *KRAS*-mutant (where *KRAS* is defined as *v-Ki-ras2 Kirsten rat sarcoma viral oncogene homolog*) lung adenocarcinomas as well as *KRAS*-mutant squamous-cell lung cancers. Thus, any representative preclinical model would need to capture the nature of lesions of primary tumors as well as their distribution in the histopathologically defined cohort.

Recent reports have credentialed the use of cancer cell lines in preclinical drug target validation experiments (10–13). Building on the foundation of these studies, we have now established a cell-line collection that enables systematic prediction of drug activity using global profiles of genetic lesions in NSCLC. Given the genomic diversity of a particular cancer type, we reasoned that in-depth preclinical analyses of activity of cancer therapeutics in tumor cells would require *both* thorough genomic analysis of a large cell-line collection of a single tumor entity *and* high-throughput cell-line profiling, followed by genomic prediction of compound activity.

We set out to systematically annotate the genomes of a large panel of NSCLC cell lines in order to determine whether such a collection reflects the genetic diversity of primary NSCLC tumors. We further determined the phenotypic validity of this collection and analyzed drug activity as a function of genomic lesions in a systematic fashion. Finally, we confirmed the validity of our predictors *in vitro* and in lung cancer mouse models. Such complementary efforts may provide a framework for future preclinical analyses of compound activity, taking into account the multitude of genetic lesions in histopathologically defined cancer types.

Results

A genomically validated collection of NSCLC cell lines. Eighty-four NSCLC cell lines were collected from various sources (Supplemental Table 1; supplemental material available online with this article; doi:10.1172/JCI37127DS1) and formed the basis for all subsequent experiments. Cell lines were derived from tumors representing all major subtypes of NSCLC tumors, including adenocarcinoma, squamous-cell carcinoma, and large-cell carcinoma.

The genomic landscape of these cell lines was characterized by analyzing gene copy number alterations using high-resolution SNP arrays (250K Sty1). We used the statistical algorithm Genomic Identification of Significant Targets in Cancer (GISTIC) to distinguish biologically relevant lesions from background noise (14). The application of GISTIC revealed 16 regions of recurrent, high-level copy number gain (inferred copy number > 2.14) and 20 regions of recurrent copy number loss (inferred copy number < 1.86) (Supplemental Tables 2 and 3). Overall, we identified focal peaks with a median width of 1.45 Mb (median 13.5 genes/region) for amplifications and 0.45 Mb for deletions (median 1 gene/region). These regions contained lesions known to occur in NSCLC (e.g., deletion of *LRP1B* [2q], *FHIT* [3p], *CDKN2A* [9p]; amplification of *MYC* [8q], *EGFR* [7p] and *ERBB2* [17q]; Figure 1A and Supplemental Table 2). Furthermore, within broad regions of copy number gain, we also identified amplification of *TTF1* (14q) and *TERT* (5p) (Figure 1A and Supplemental Table 2), recently identified by large-scale genomic profiling of primary lung adenocarcinomas (15–17).

Analysis of homozygous deletions as well as loss of heterozygosity (LOH) is typically hampered by admixture of nontumoral cells in primary tumors. The purity of cell-line DNA permitted identification of previously unknown homozygous deletions and regions of LOH, including LOH events resulting from uniparental disomy (e.g., copy-neutral events) (Supplemental Table 4). In this analysis, known genes such as *MTAP* (9p) and *LATS2* (13q) were altered by homozygous deletions (18, 19) and we found what we believe are novel homozygous deletion of genes such as *TUBA2* (Supplemental Table 4). Of note, most of these regions could also be identified in primary NSCLC tumors as deleted (15); however, inferred copy numbers only inconsistently showed LOH or homozygous deletions, indicating admixture of normal diploid DNA (Supplemental Table 4). Thus, while a recent large-scale cancer profiling study (15) enabled insight into the genomic landscape of lung adenocarcinoma, the use of pure populations of tumor cells further afforded discovery of previously unrecognized regions of homozygous deletions and LOH.

We next compared the profile of significant amplifications and deletions in this cell-line collection with that of a set of 371 primary lung adenocarcinomas (15). This comparison revealed a striking similarity between the 2 data sets (Figure 1A) but not between NSCLC cell lines and gliomas or melanomas (Supplemental Figure 1, A and B). A quantitative analysis of similarity by computing correlations of the false discovery rate (*q* value) confirmed the similarity of primary lung cancer and lung cancer cell lines ($r = 0.77$) and the lack of similarity of lung cancer cell lines and primary gliomas (14) ($r = 0.44$), melanoma cell lines (11) ($r = 0.44$), or ovarian tumors ($r = 0.38$; Supplemental Figure 1C). As a control, repeated random splitting of the lung cancer cell-line data and computation of internal similarity resulted in correlation coefficients between 0.82 and 0.86, whereas we found no correlation with normal tissue ($r = 0.0195$; Supplemental Figure 1C). These results demonstrate that the genomic copy number landscape of NSCLC cell lines reflects that of primary NSCLC tumors, while tumors or cell lines of other lineages show a much lower degree of similarity (20, 21). Furthermore, the distribution of oncogene mutations in the cell lines (Supplemental Table 5) was similar to that in primary NSCLC tumors, with a high prevalence of mutations in the *KRAS* and *EGFR* genes (22–25) and rare occurrence of phosphoinositide-3-kinase, catalytic, α polypeptide (*PIK3CA*) and v-raf murine sarcoma viral oncogene homolog B1 (*BRAF*) mutations (Figure 1B). These results further validate our cell-line collection on a genetic level.

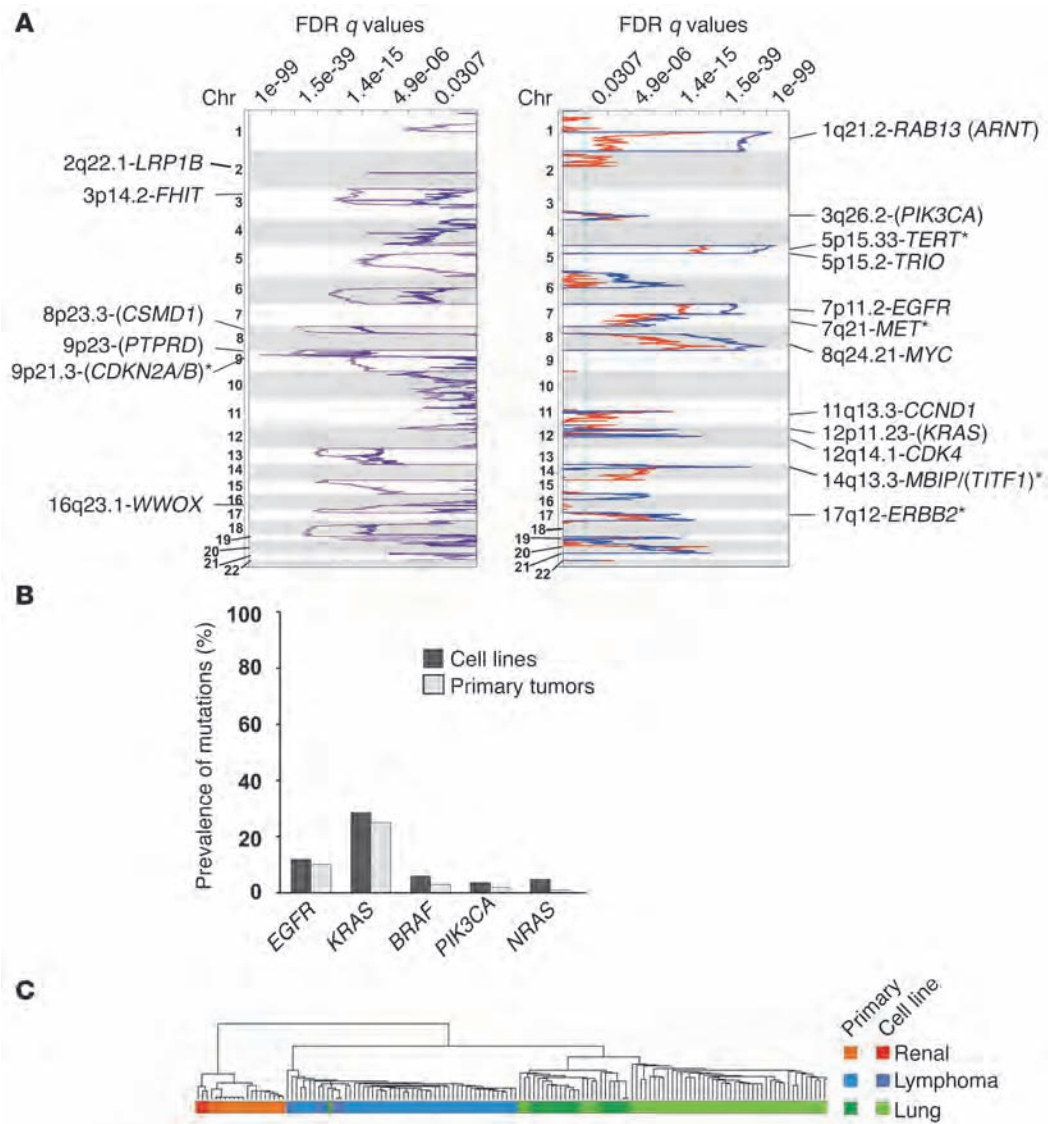


Figure 1

Genomic validation of 84 NSCLC cell lines. **(A)** Chromosomal copy number changes of NSCLC cell lines are plotted against those of 371 primary NSCLC tumors. The q values (false discovery rates) for each alteration (x axis) are plotted at each genome position (y axis). Left panel shows chromosomal losses (cell lines, purple; primary tumors, dark blue); right panel shows chromosomal gains (cell lines, red; primary tumors, blue). Genomic positions corresponding to even-numbered chromosomes are shaded; dotted lines indicate centromeres; green lines, q value cutoff (0.25) for significance. Genes represent known targets of mutation in lung adenocarcinomas. Putative targets near peaks are given in parentheses. Genes identified by GISTIC using stringent filtering criteria for peak border detection are marked by asterisks. **(B)** Oncogene mutations present in NSCLC cell lines (black bars) are plotted according to their relative frequencies in comparison with primary lung tumors (gray bars) (22–25). **(C)** Transcriptional profiles of primary renal cell carcinomas (orange) and corresponding cell lines (red); primary lung tumors (dark green) and lung cancer cell lines (light green); primary lymphomas (blue) and lymphoma cell lines (purple) were analyzed by hierarchical clustering. To reduce noise, probe sets were filtered prior to clustering (coefficient of variation from 1.0 through -10.0 , present call rate, 20%; absolute expression greater than 100 in more than 20% of samples).

The availability of both copy number alteration and oncogene mutation data of the NSCLC cell lines enabled us to analyze the interactions of both types of lesions (Supplemental Figure 2). Hierarchical clustering of lesions robustly grouped both mutations and amplification of *EGFR* in 1 subcluster (ratio Q of observed vs. expected cooccurrence: $Q = 4.38$, $P = 0.001$), while *KRAS* mutations consistently grouped in a distinct cluster. These findings corroborate prior observations in vivo in which mutations in *KRAS* and *EGFR* were mutually exclusive while *EGFR* mutation and *EGFR* amplification

frequently cooccurred (23, 26, 27). Moreover, these results suggest that these mutations influence the particular signature of genomic alterations in the affected tumors. Finally, in unsupervised hierarchical cluster analyses of gene expression data, primary lung cancer specimens (28) and lung cancer cell lines shared 1 cluster (Figure 1C), while renal cell carcinomas (29) and lymphomas (30) as well as the corresponding cell lines clustered in a separate group.

In summary, in-depth comparative analysis of orthogonal genomic data sets of a large panel of NSCLC cell lines and primary

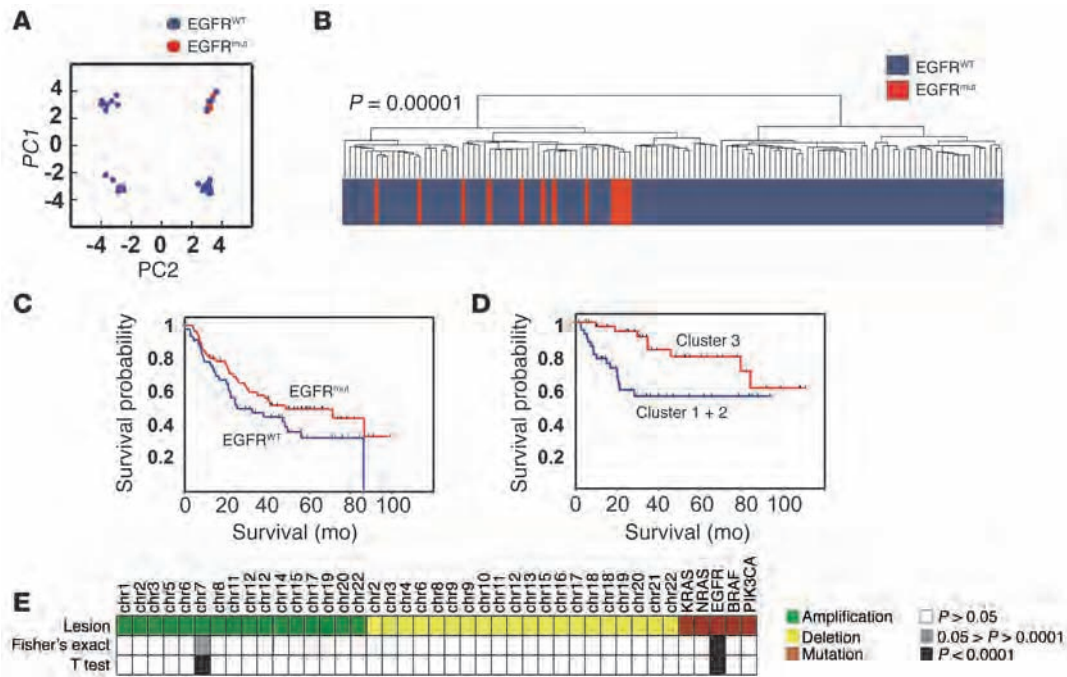


Figure 2

Robustness of phenotypic properties of EGFR-mutant lung cancer cells in vivo. (A) The first 2 principal components (PC1 and PC2) distinguish cell lines with mutated (mut) *EGFR* (red dots) and WT *EGFR* (blue dots) ($n = 54$). (B) The signature (fold change greater than 2; absolute difference, 100; $P < 0.01$) of *EGFR*-mutant cell lines ($n = 8/54$) was used for hierarchical clustering of 123 primary adenocarcinomas (35) annotated for the presence (*EGFR*^{mut}, red bars) or absence (*EGFR*^{WT}, dark blue bars) of *EGFR* mutations. (C) Probability of survival was estimated for all 123 primary adenocarcinomas with known *EGFR* mutation status following grouping according to relative abundance of 337 RNA transcripts identified as differentially expressed between *EGFR*-mutant and *EGFR* WT cell lines. *EGFR*-mutant tumors ($n = 13$) were excluded from survival analyses. Survival probabilities are depicted as Kaplan-Meier survival estimate curves. (D) The same analysis was performed using 86 lung tumors from Beer et al. (37) with available survival data. Two groups were formed according to relative abundance of the *EGFR* mutation-specific genes, and survival analysis was performed as in D. (E) The association between presence (amplification, green; mutation, red; deletion, yellow) of genetic lesions identified in the cell lines and sensitivity of the respective cell lines to treatment with the *EGFR* inhibitor erlotinib was analyzed by Welch's *t* test and Fisher's exact test. Significant lesions are marked by gray ($P < 0.05$) or black ($P < 0.0001$) boxes.

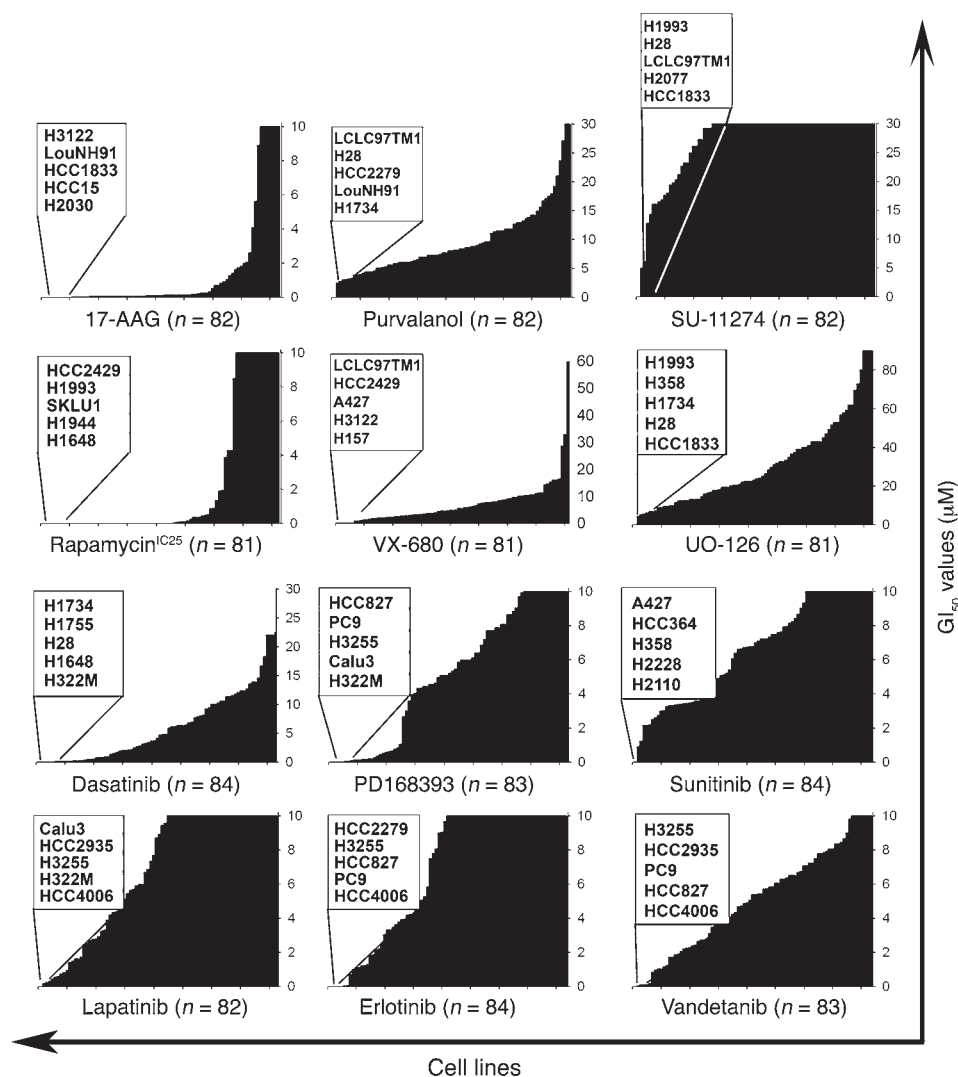
tumors demonstrates that these cell lines reflect the genetic and transcriptional landscape of primary NSCLC tumors.

EGFR mutations define phenotypic properties of lung tumors in vitro and in vivo. Activated oncogenes typically cause a transcriptional signature that can be used to identify tumors carrying such oncogenes (31, 32). However, we consistently failed to identify a gene expression signature characteristic of *EGFR*-mutant tumors (33, 34) using a gene expression data set of 123 primary lung adenocarcinomas (35) annotated for mutations in *EGFR* (data not shown). We therefore reasoned that the cellular purity of our cell lines ($n = 54$ analyzed on U133A) might enable the determination of such a signature and the application of this signature in primary tumors. We applied principal component analyses on the variable genes and found a remarkable grouping of all *EGFR* mutated cell lines ($n = 8/54$), with a significant dissociation already in the first principal component (Welch's *t* test on the distribution of eigenvalues: $P = 0.0005$) contributing 14.5% to the overall variance (Figure 2A). Similar results were obtained by hierarchical clustering (data not shown). Using genes differentially expressed in *EGFR*-mutant cell lines (including T790M) as a surrogate feature (Supplemental Table 6), all of the *EGFR*-mutant primary tumors (35) were grouped in a distinct cluster ($P = 0.00001$) when performing hierarchical clustering (Figure 2B). This result was also recapitulated when selecting genes differentially expressed in erlotinib-sensitive

($GI_{50} < 0.1 \mu M$, $n = 5/54$ vs. $GI_{50} > 2 \mu M$, $n = 45$, where GI_{50} indicates half-maximal growth inhibitory concentration) cell lines (Supplemental Figure 3A). Furthermore, patients with tumors expressing the signature of *EGFR* mutated cell lines had better overall survival than those whose tumors did not (Figure 2C) (36). The power of our *EGFR*^{mut} signature to predict survival was confirmed, employing the data published by Beer and colleagues (Figure 2D) (37). This effect was even observed when excluding *EGFR*-mutant tumors ($n = 13$) from the analysis (Figure 2C). Thus, expression signatures extracted in vitro can be used to identify biologically diverse tumors in vivo (38).

Others have recently characterized a transcriptional signature of *EGFR*-mutant NSCLC using a small set of cell lines (39). However when analyzing primary lung adenocarcinomas with the signature described by Choi et al., *EGFR*-mutant samples were randomly distributed across the data set (Supplemental Figure 3B). This finding further highlights the importance of using large cell-line collections in order to represent the overall genomic diversity of primary tumors.

Recent studies have linked the presence of *EGFR* mutations in lung adenocarcinomas to clinical response to the *EGFR* inhibitors erlotinib and gefitinib (6–8). However, retrospective studies aimed at determining predictive markers for *EGFR* inhibition yielded heterogeneous results, implicating *EGFR* mutations and/or

**Figure 3**

Sensitivity profiles of compounds determined by high-throughput cell-line screening. GI_{50} values (y axes) for 12 compounds are shown for the successfully screened (Supplemental Table 5) cell lines (x axes show individual cell lines). Due to the fact that rapamycin typically fails to completely abrogate cellular proliferation (79), the 25% inhibitory concentration is shown for these compounds. Bars represent GI_{50} (GI_{25} values in the case of rapamycin, y axis) throughout the cell-line collection (x axis) ranked according to sensitivity. The maximum concentration is adapted to the GI_{50} value (GI_{25} values in the case of rapamycin; 10 μ M for 17-AAG, erlotinib, vandetanib, lapatinib, sunitinib, rapamycin, and PD168393; 30 μ M for SU-11274, dasatinib, and purvalanol; 60 μ M for VX-680; 90 μ M for UO126) of resistant cell lines. The 5 most sensitive cell lines for each compound are highlighted in table form.

EGFR amplifications among others as predictive of response or patient outcome (40–42). We set out to systematically identify genetic lesions associated with sensitivity to erlotinib by including all global lesion data from our genomics analyses rather than focusing on *EGFR*-associated lesions. We established a high-throughput cell-line screening pipeline that enables systematic chemical perturbations across the entire cell-line panel followed by automated determination of GI_{50} values (43) to determine erlotinib sensitivity for all cell lines. We next analyzed the distribution of genetic lesions in erlotinib-sensitive compared with insensitive cell lines (Supplemental Tables 5 and 7) and further compared the mean sensitivity of cell lines with and without the respective genetic lesions. In both analyses, *EGFR* mutations were the best single-lesion predictor of erlotinib sensitivity (Figure 2E and Supplemental Table 7; Fisher's exact test; $P = 6.9 \times 10^{-8}$). Furthermore, we found a less stringent association with amplification of *EGFR* (Fisher's exact test; $P = 1.4 \times 10^{-4}$); however, only *EGFR* mutations were significant predictors of erlotinib sensitivity when we adjusted for multiple hypothesis testing using Bonferroni's correction (data not shown). We next used signal-to-noise-based feature selection combined with the

K-nearest-neighbor (KNN) algorithm (44, 45) to build a multilesson predictor of erlotinib sensitivity. The best performing multilesson predictor comprised *EGFR* mutations, amplification of *EGFR*, and lack of *KRAS* mutations (Figure 2E and Supplemental Table 7), which have all been implicated in determining responsiveness of NSCLC patients to *EGFR* inhibitors (6–8, 27, 40, 41, 46). We note that in our data set, as in previously published reports (6–8, 27, 40, 41, 46), *EGFR* amplification and mutation were correlated, whereas *KRAS* mutations were mutually exclusive with either lesion (Supplemental Figure 2). Thus, our observation confirms the overall predominant role of *EGFR* mutations in predicting responsiveness to *EGFR* inhibition, and it provides an explanation for the finding of *EGFR* amplification as being predictive of response as well. Our findings also corroborate prior clinical reports establishing *KRAS* mutations as a resistance marker for *EGFR* inhibition therapy. Together, these results imply that essential transcriptional and biological phenotypes of the original tumors are preserved in the cell lines, a necessary requirement for application of such collections as proxies in preclinical drug target validation efforts.

Differential activity of compounds in clinical development in NSCLC cell lines. Having validated the cell-line collection by demonstrating its

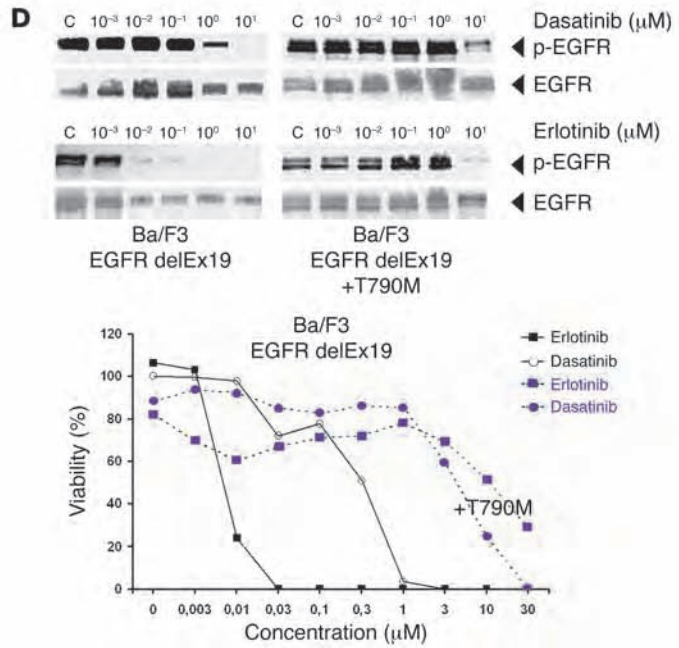
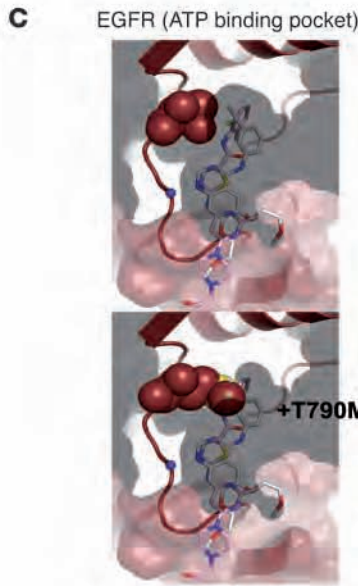
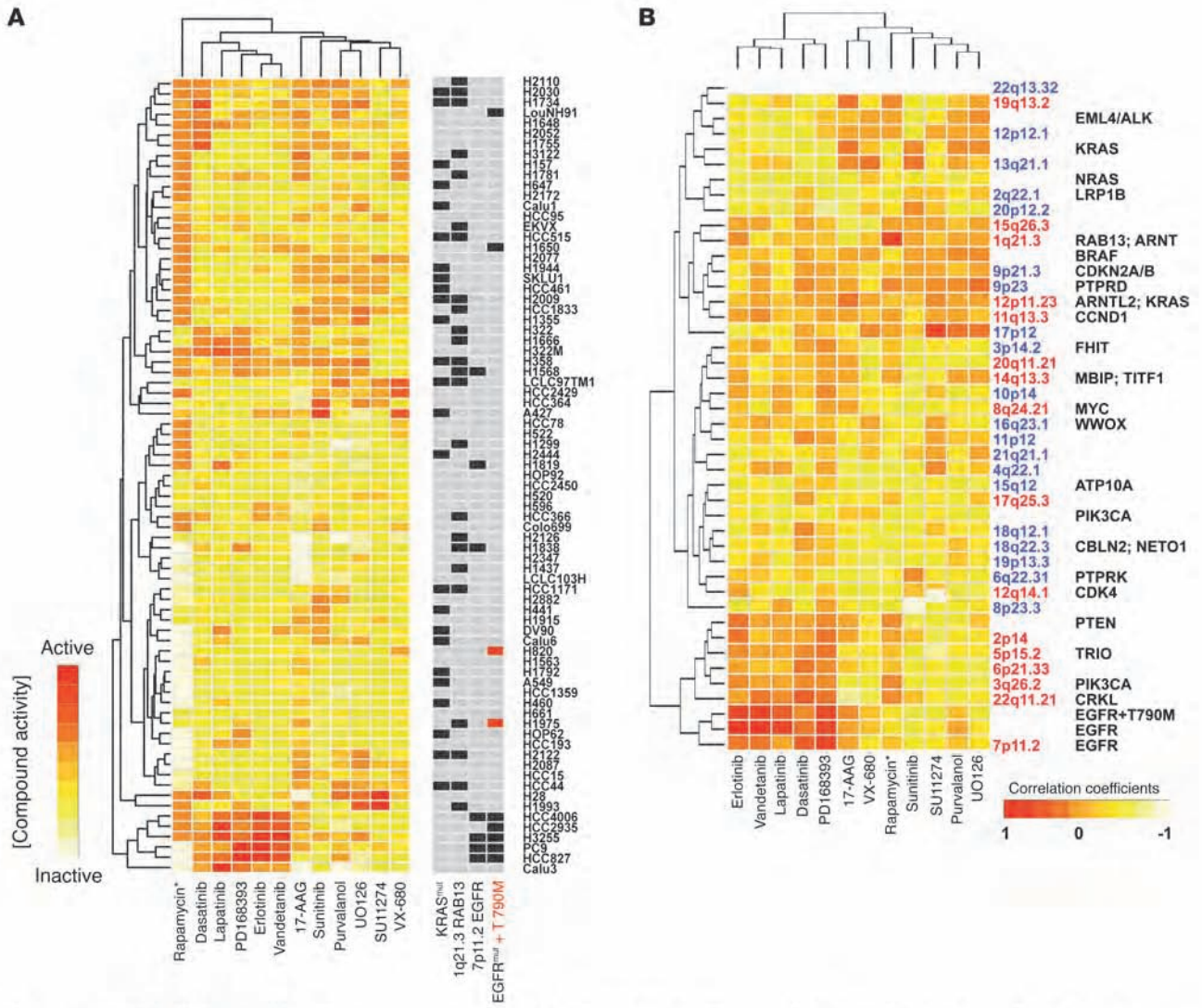




Figure 4

Hierarchical clustering of compound activity uncovers mutated *EGFR* as a target for dasatinib activity. (A) Displayed is a hierarchical cluster of cell lines and compounds, clustered according to GI_{50} values (red, high compound activity; white, low compound activity) after logarithmic transformation and normalization. 77 cells reached full compound coverage. The presence (black) or absence (gray) of selected lesions is annotated in the right panel. (B) Correlation of activity of compounds to presence of amplifications (red) and deletions (blue) as well as oncogene mutations (mut) was used for hierarchical clustering. Putative target genes inside and bordering (*) the region defined by GISTIC are annotated. (C) Upper panel shows that binding mode of erlotinib (white) to WT *EGFR*. Dasatinib (pink) is modeled into the ATP-binding site of *EGFR*. The 2-amino-thiazole forms 2 hydrogen bonds with the hinge region of the kinase. Lower panel shows that the chloro-methyl-phenyl ring of dasatinib binds to a hydrophobic pocket near the gatekeeper Thr790 and helix C and will clash with the Met side chain of the *EGFR* drug-resistance mutation T790M. (D) Upper panel shows that Ba/F3 cells ectopically expressing mutant *EGFR* with (delEx19 + T790M) or without (delEx19) the T790M mutation were treated for 12 hours with the either dasatinib or erlotinib, and phospho-*EGFR* and *EGFR* levels were detected by immunoblotting. Lower panel shows that the same cells were treated for 96 hours with either dasatinib or erlotinib and viability was assessed. Growth inhibition relative to untreated cells (y axis) is shown as a function of compound concentrations.

genomic and phenotypic similarity to primary NSCLC tumors, we reasoned that adding complex phenotypic data might elicit additional insights into the impact cancer genotypes have on cell biology phenotypes. In our initial pilot screening experiment, we profiled all cell lines against erlotinib and subsequently extended our assay to 11 additional inhibitors that were either under clinical evaluation or showed high activity in preclinical models; these compounds target a wide spectrum of relevant proteins in cancer (Supplemental Figure 4). We treated all cell lines with these compounds and determined GI_{50} values (GI_{25} respectively; Supplemental Table 5). The resulting sensitivity patterns (Figure 3) revealed that while some of the compounds exhibited a pronounced cytotoxic activity in a small subset of cell lines (e.g., erlotinib, vandetanib, VX-680), others were active in most of the cell lines, with only a minority being resistant [e.g., 17-(allylamino)-17-demethoxygeldanamycin (17-AAG)]. Only 2 cell lines (<2%) were resistant to all of the compounds (Supplemental Table 5), suggesting that most NSCLC tumors might be amenable to targeted treatment. Overall, these observations are highly reminiscent of patient responses in clinical trials in which limited subsets of patients experience partial and, rarely, complete response while the majority of patients exhibit stable disease, no change, or progression.

Identification of relevant compound targets by similarity profiling. As an initial approach to identification of shared targets of inhibitors, we performed hierarchical clustering based on the similarity of sensitivity profiles (Figure 4A) and based on the correlation between sensitivity and genomic lesion profiles (Figure 4B). Erlotinib and vandetanib exhibited the highest degree of similarity, pointing to mutant *EGFR* as the critical target of vandetanib in NSCLC tumor cells (Figure 4, A and B) (47, 48). The high degree of correlation ($r = 0.91$; $P < 0.001$) of cell-line GI_{50} values for both compounds as well as structural modeling of vandetanib binding in the *EGFR* kinase domain, which revealed a binding mode identical to that of erlotinib, further corroborate this notion (Supplemental Figure 5A). This model predicted that binding of both compounds would be prevented by the T790M resistance muta-

tions of *EGFR* (48–50); accordingly, murine Ba/F3 cells ectopically expressing erlotinib-sensitizing mutations of *EGFR* together with T790M (51) were completely resistant to erlotinib and vandetanib (Supplemental Figure 5, B and C).

In addition to the ERBB2/*EGFR* inhibitor lapatinib, vandetanib, and the irreversible *EGFR* inhibitor PD168393 (52), the SRC/*ABL* (where SRC is defined as *v-src sarcoma [Schmidt-Ruppin A-2] viral oncogene homolog [avian]*) inhibitor dasatinib (53) shared a cluster with the *EGFR* inhibitor erlotinib, although at a much lower potency than erlotinib (Figure 4, A and B). Molecular modeling of dasatinib binding to *EGFR* predicted a binding mode similar to that of erlotinib (Figure 4C), with a steric clash of erlotinib and dasatinib with the erlotinib resistance mutation T790M (49, 50, 54, 55) (Figure 4C). We therefore formally validated *EGFR* as a relevant dasatinib target in tumor cells by showing cytotoxicity as well as *EGFR* dephosphorylation (56) elicited by this compound in Ba/F3 cells ectopically expressing mutant *EGFR* but not in those coexpressing the T790M resistance allele (Figure 4D). Thus, large-scale phenotypic profiling coupled to computational prediction formally validated a relevant tumor-cell target of an FDA-approved drug using a systematic unbiased approach. It is noteworthy that a trial of dasatinib in patients with acquired erlotinib resistance is currently ongoing (trial ID: NCT00570401; <http://clinicaltrials.gov/ct2/show/NCT00570401?term=NCT00570401&rank=1>; based on previously reported biochemical findings (54) and our results, we predict limited clinical activity in those patients in whom erlotinib resistance is due to the *EGFR* resistance mutation T790M.

Supervised learning identifies predictors for inhibitor responsiveness. We have shown that hierarchical clustering can identify compounds with overlapping target specificities within a screening experiment. We now set out to extend our analyses to additional computational approaches to predict inhibitor responsiveness from global lesion data in a systematic fashion. To this end, we applied supervised learning methods as we did for erlotinib (see above). Applying this method, we identified robust, genetic lesion-based predictors for the majority of the tested compounds (Supplemental Table 7).

UO126 is a MEK inhibitor that also showed enhanced activity in a subset of the lung cancer cell-line collection. Here, the supervised approach identified chromosomal gains of 1q21.3 affecting the genes *ARNT* and *RAB13* as being robustly associated with UO126 sensitivity (Fisher's exact test, copy number threshold 2.14, $P = 0.02$; Supplemental Figure 6 and Supplemental Table 7). In order to validate this finding in an independent data set, we made use of the NCI-60 cancer cell-line panel (57) in which hypothemycin was used as a MEK inhibitor (12). This cross-platform validation revealed that 1q21.3 gain predicted sensitivity to MEK inhibition in both data sets (Fisher's exact test, $P = 0.03$, NCI-60 collection; Supplemental Figure 6).

In our initial cluster analysis, we found that *KRAS* mutations correlated with sensitivity to the Hsp90 inhibitor 17-AAG, a geldanamycin derivative (Figure 4B). Recapitulating this observation, we found *KRAS* mutations to be predictive of 17-AAG sensitivity, even when applying our KNN-based prediction approach (Fisher's exact test, $P = 0.029$; Figure 5A and Supplemental Table 7). Confirming this observation in an independent cell-line model, we found the distribution of geldanamycin sensitivity and *KRAS* mutation in the NCI-60 cell-line collection to be strikingly similar to that observed in our panel ($P = 0.049$; Figure 5A).

In 17-AAG-sensitive cells, Hsp90 inhibition led to robust induction of apoptosis (Supplemental Figure 7A). In order to gain mech-

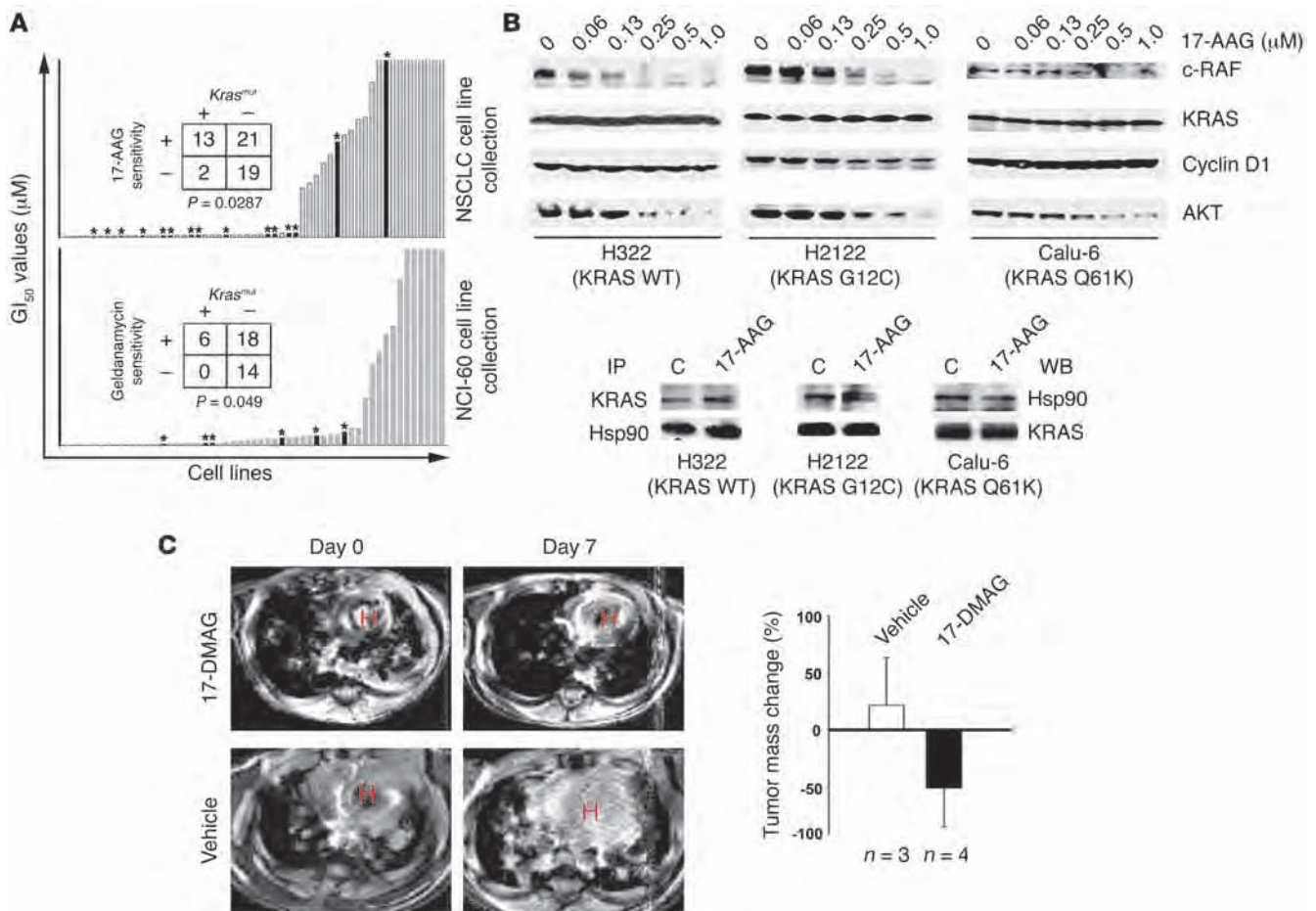


Figure 5 *KRAS* mutations predict response to inhibition of Hsp90 in vitro and in vivo. **(A)** The sensitive and resistant cell lines were sorted according to their GI_{50} values and annotated for the presence of *KRAS* mutations (asterisks and black columns). Bar height represents the respective GI_{50} values. The association of *KRAS* mutations and 17-AAG sensitivity ($GI_{50} < 0.07 \mu M =$ sensitive; $GI_{50} > 0.83 \mu M =$ resistant; according to the lower and upper 25th percentiles) was calculated by Fisher’s exact test for the lung cancer data set (upper panel) and for the NCI60 data set (lower panel). **(B)** Upper panel shows that whole-cell lysates of the indicated *KRAS* WT and *KRAS* mutated cell lines treated with different concentrations of 17-AAG were analyzed for levels of c-RAF, KRAS, cyclin D1, and AKT by immunoblotting. Lower panel shows that extracts of the indicated cells treated with either control (C) or 0.5 μM (H322 and Calu-6) or 1 μM (H2122) of 17-AAG were subjected to coimmunoprecipitation with antibodies to either KRAS (top) or Hsp90 (bottom); immunoprecipitates were analyzed for levels of Hsp90 (top) or KRAS (bottom) by immunoblotting. Noncontiguous bands run on the same gel are separated by a black line (H2122). WB, Western blot. **(C)** Displayed are coronal MRI scans of *lox-stop-lox*^{KRAS^{G12D}} mice before and after 7 days of treatment with either 17-DMAG or vehicle. The areas of lung tumors were manually segmented and measured on each magnetic resonance slice, and total tumor volume reduction was calculated for all mice treated with 17-DMAG ($n = 4$) and placebo ($n = 3$). SD of tumor volume in the cohort of treated and untreated mice was calculated and is depicted as error bars.

anistic insight into *KRAS* dependency on Hsp90 chaperonage, we first confirmed the specificity of our *KRAS* antibody (Supplemental Figure 7C). Using conditions under which EGFR coprecipitated with Hsp90 in *EGFR*-mutant cells (Supplemental Figure 7B) (58), we found *KRAS* to be bound to Hsp90 as well (Figure 5B). However, while 17-AAG treatment depleted mutant EGFR from Hsp90 (Supplemental Figure 7B), *KRAS* binding to Hsp90 was not affected by this treatment (Figure 5B). Furthermore, cellular *KRAS* protein levels were also not reduced by 17-AAG (Figure 5B). These findings are surprising, as other oncogenes, such as EGFR or BRAF, known to be dependent on Hsp90 chaperonage are depleted from the complex after treatment with 17-AAG (58, 59). However, reduction of viability of *KRAS*-mutant cells treated with 17-AAG is accompanied by depletion of c-RAF and AKT (60) (Figure 5B). Since both c-RAF

and AKT are known Hsp90 clients (59, 61), we hypothesize that this observation might rely on the activation of the AKT and RAF/MEK/ERK signaling pathways by mutant *KRAS* (62, 63).

To further validate the power of *KRAS* mutations to predict response to Hsp90 inhibition, we employed a *lox-stop-lox*^{KRAS^{G12D}} mouse model that enables the study of *KRAS*-driven lung adenocarcinomas in vivo (64). Mice with established lung tumors induced by nasal inhalation of adenoviral *Cre* (64) were either treated with the water-soluble geldanamycin Hsp90 inhibitor 17-(dimethylaminoethylamino)-17-demethoxygeldanamycin (17-DMAG) or placebo. Whereas no tumor shrinkage was observed in the placebo-treated mice after 1-week treatment (Figure 5C and Supplemental Figure 8), substantial regression of established tumors was observed in 3 out of 4 mice receiving 17-DMAG, with a tumor volume reduction

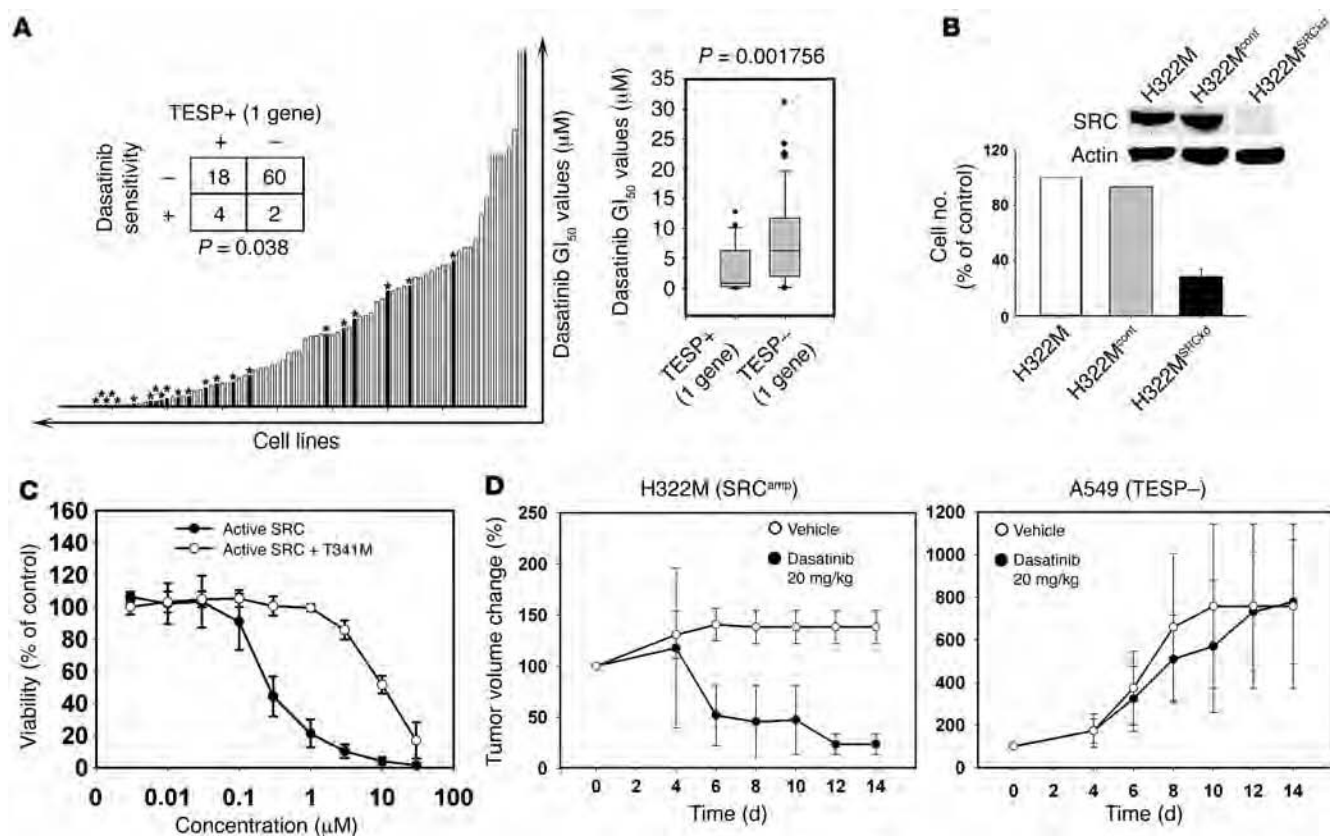


Figure 6

Identification of functionally relevant targets for dasatinib activity. **(A)** Left panel shows that cell lines with copy number gain involving at least 1 gene encoding dasatinib target are labeled with asterisks and black columns. The probability of these cells being dasatinib sensitive was calculated by Fisher's exact test. In right panel, dasatinib GI₅₀ values are shown as box plots (representing the 25th to 75th percentile; whisker representing the 95th percentile; dots representing outliers) for cell lines with (TESP+ 1 gene) and without (TESP- 1 gene) copy number gain of dasatinib target genes (Wilcoxon test). **(B)** H322M cells harboring amplified SRC were either left untreated or transduced with an empty vector control (H322M^{cont}) or with shRNA targeting SRC (H322M^{SRCKd}). After puromycin selection, levels of SRC in H322M cells transduced with the indicated vectors were analyzed by immunoblotting (top). The H322M^{SRCKd} lanes were run on the same gel but were noncontiguous, as indicated by the white line. Viability was quantified by cell counting. Error bars represent SD between different experiments. **(C)** H322M cells were transduced with vectors encoding either active SRC or active SRC with a gatekeeper mutation SRC (T341M). Stable cells were treated with dasatinib for 96 hours. Viability is shown as percentage of untreated controls. Error bars indicate SD of 3 independent experiments. **(D)** Dasatinib-sensitive (TESP+; H322M) or -resistant cells (TESP-; A549) were grown s.c. in nude mice. After 14 days of treatment (vehicle, dasatinib), tumor volumes were measured as diameters. SD of tumor volume in the cohort of treated and untreated mice was calculated and is depicted as error bars.

of up to 80% (Figure 5C and Supplemental Figure 8). Although responses were transient as those seen in 17-DMAG-treated transgenic mice with EGFR-driven lung carcinomas (data not shown), these findings validate our observation that KRAS mutation predicts response to Hsp90 inhibition in vivo.

Compound target gene enrichment predicts sensitivity. We have used similarity profiling and supervised learning approaches that led to the identification of predictive markers based on significant lesions found in our data set as defined by GISTIC. However, the advantage of statistically defining relevant lesions in a given data set limits the utility of lesions occurring at low frequency and/or amplitude to be used as predictors for compound sensitivity. We therefore developed an additional approach, denoted *Target-Enriched Sensitivity Prediction (TESP)*, which enables inclusion of statistically underrepresented yet biologically relevant lesions.

Amplification of drug-target genes has been demonstrated to predict vulnerability to target-specific compounds in ERBB2-

amplified breast cancer and EGFR-amplified lung cancer (1, 46). We therefore speculated that chromosomal copy number alterations of biochemically defined drug targets could be used for prediction of sensitivity to other tyrosine kinase inhibitors as well. To this end, we used tyrosine kinase inhibitor targets defined by the quantitative dissociation constant as determined in quantitative kinase assays (65). As a proof of principle, we determined whether copy number gain in EGFR is associated with sensitivity to erlotinib (40). In our systematic approach, cell lines inhibited by erlotinib at clinically achievable dosages (up to 1 μM) were highly enriched for amplification of EGFR (P = 0.00023; Supplemental Figure 9A). We next tested our prediction model for lapatinib, a specific inhibitor of ERBB2 and EGFR, clinically approved for ERBB2-positive breast cancer (66). Again, we observed cell lines inhibited by lapatinib (n = 82) below clinically achievable dosage of 1 μM to be significantly enriched in the subgroup of cell lines with amplification of



ERBB2 or *EGFR* (Fisher's exact test, $P = 0.009$; data not shown). Thus, TESP enables discovery of clinically relevant genotype-phenotype relationships.

Encouraged by these findings, we set out to test our approach for compounds inhibiting a wide range of kinases, such as dasatinib (65). We determined the distribution of GI_{50} values of cell lines with chromosomal copy number gain (copy number > 3) affecting at least 1 or 2 of either one of the genes encoding the most biochemically sensitive dasatinib targets and compared these to the distribution of GI_{50} values of cells without copy number gain at these genomic positions (Figure 6A, Supplemental Table 8, and Supplemental Figure 9B). As hypothesized, these groups were significantly distinct in the distribution of GI_{50} values ($P = 1.8 \times 10^{-3}$ when 1 gene was affected and $P = 4.6 \times 10^{-3}$ when 2 of the target genes were affected by copy number gain; Figure 6A and Supplemental Figure 9B). In particular, this predictor comprised copy number gain at the loci of gene family members of ephrin receptor kinases (*EPHA3*, *EPHA5*, and *EPHA8*), SRC kinases (*SRC*, *FRK*, *YES1*, *LCK*, and *BLK*), and *ABL2*, suggesting that NSCLC cells harboring such lesions might be exquisitely sensitive to therapeutic inhibition of the encoded proteins. The probability that cell lines with copy number gain at either 1 or 2 of these genes will be sensitive to dasatinib treatment ($GI_{50} < 100$ nM) increases up to 5.6-fold (gain of 1 gene) and 15.8-fold (gain of 2 genes), respectively, when compared with cells without copy number gain at these loci (Figure 6A and Supplemental Figure 9B). In contrast, copy number gain involving loci encoding biochemically less sensitive dasatinib targets failed to show enrichment of sensitive cell lines (data not shown).

In cells with copy number gain of biochemically defined dasatinib target genes, dasatinib treatment led to robust induction of apoptosis (data not shown). Importantly, copy number gain of at least one of either of these genes is present in 12.9% (copy number > 3) of several hundred primary lung adenocarcinomas (15) (data not shown), thus emphasizing the potential clinical relevance of our predictor.

In the dasatinib-sensitive cell-line H322M harboring amplified *SRC*, dasatinib treatment led to dephosphorylation of *SRC* at low nanomolar doses, paralleling growth inhibition at similar concentrations (Supplemental Figure 9C). In order to determine whether the genes in our dasatinib predictor are causatively linked with the activity of dasatinib, we silenced *SRC* by lentiviral shRNA in H322M cells (Figure 6B). When compared with parental cells or cells expressing the control vector, H322M-*SRC*-knockdown (*H322M^{SRCKD}*) cells showed a massive reduction in cellular proliferation (Figure 6B) and increase in cell death (data not shown). In order to further validate activated *SRC* as the relevant dasatinib target in H322M cells, we expressed an activated allele of *SRC* together with a sterically demanding mutation at the gatekeeper position of the ATP-binding pocket (T341M) (67); this mutation and the analogous mutations in Bcr-Abl and *EGFR* (see above) induce on-target drug resistance (67) by displacing the compound from the ATP-binding pocket. As hypothesized, expression of the T341M gatekeeper mutation but not of *SRC* alone rescued dasatinib-induced cell death in H322M cells (Figure 6C). These results formally validate *SRC* as the relevant dasatinib target in *SRC*-amplified NSCLC cells.

We also validated *EPHA3* as a relevant target in H28 cells with gain of *EPHA3* by showing decreased viability of these cells upon stable knockdown of *EPHA3* (Supplemental Figure 10).

We next transplanted cells with or without copy number gain of *SRC* into nude mice. Mice were treated with either dasatinib or placebo on a daily application schedule. Again confirming our

in-vitro observations, robust tumor shrinkage was observed in mice transplanted with cells harboring copy number gain of *SRC* (H322M) (Figure 6D) receiving dasatinib. In contrast, no tumor shrinkage was observed in mice transplanted with cells predicted to be resistant against dasatinib (A549) and in all mice treated with placebo (Figure 6D). We consistently failed to grow *EPHA3*-amplified H28 cells in nude mice; HCC515 cells were therefore chosen as another model of NSCLC with gain of *EPHA3*. Dasatinib treatment of established HCC515 tumors also induced significant tumor shrinkage (data not shown).

Together, these results show that in NSCLC, copy number gain of ephrin receptor or *SRC* family member genes and *ABL2* may render tumor cells dependent on these kinases, thus exposing a vulnerability to therapeutic inhibition with dasatinib.

Discussion

Here, we show that diverse analytical approaches of multiple orthogonal genomic and chemical perturbation data sets pertinent to a large collection of cancer cell lines afford insights into how somatic genetic lesions impact cell biology and therapeutic response in cancer. Such data sets provide a rich source for different computational approaches that each yield complementary, accurate, and valid predictors of inhibitor sensitivity. The basis for such predictions is a panel of genomically annotated NSCLC cell lines that is representative of the genetic diversity, the transcriptional profile, and the phenotypic properties of primary NSCLC tumors. The overall functional biological validity of our approach is supported by the observation that *EGFR* mutations are the strongest predictor of sensitivity to the *EGFR* inhibitor erlotinib. Others have similarly observed high activity of *EGFR* inhibitors in *EGFR*-mutant NSCLC cell lines (6, 13, 68), supporting the validity of our unbiased computational approach employing systematic global measurements of genetic lesions.

Applying systematic similarity profiling using computationally defined significant genetic lesions, we also identified predictors for compounds currently in clinical use or trials. Specifically, in an unbiased manner, we confirmed *EGFR* mutations not only to predict sensitivity to *EGFR* inhibitors (erlotinib, PD168393, vandetanib) (6–8, 47, 52) but also to the *SRC*/*ABL* inhibitor dasatinib (54, 56). We formally demonstrated that *EGFR* is the *relevant* target of dasatinib in *EGFR*-mutant cells by showing the lack of activity of this compound in Ba/F3 cells expressing the T790M resistance allele of *EGFR*. Thus, exploring multiple orthogonal genomic and chemical data sets enabled the formal definition of a *relevant* tumor-cell target of an FDA-approved drug.

In addition, we performed supervised identification of predictors for drug sensitivity. A noteworthy finding is the role of *KRAS* mutation as a predictor of sensitivity to 17-AAG. Independent validation of the predictor for an Hsp90 inhibitor in a transgenic murine lung cancer model strengthens the robustness of our approach. Given the high prevalence of cancer patients with mutated *KRAS* and their unfavorable prognosis, this finding might be of clinical importance, as Hsp90 inhibitors (e.g., 17-AAG, IPI-504, NVP-AUY922) are currently under clinical evaluation.

Finally, our compound target-enrichment approach for prediction of sensitivity led to the observation of exquisite vulnerability of cells with copy number gain of ephrin receptor and *SRC* family genes as well as *ABL2* to dasatinib treatment. As a proof of principle we validated our prediction model in great depth for the relevance of *SRC* amplification for dasatinib activity in vitro



and *in vivo*. Thus, copy number gain affecting one of these genes may render tumor cells dependent on the encoded kinases, thereby defining potential biomarkers for successful treatment of NSCLC patients with dasatinib, an FDA-approved drug.

In summary, we have established a genomically, phenotypically, and functionally validated tool for studying drug activity mechanisms in the laboratory. Our results strengthen the notion that multiple orthogonal data sets pertinent to large cancer cell-line collections may offer an as-yet-unmatched potential for exploring the cell-biological impact of novel compounds in genomically defined cancer types. Such cell-line collections may advance molecularly targeted treatment of cancer by providing a tool for preclinical molecular drug target validation on the basis of the genetic lesion signature characteristic of individual tumors.

Methods

Cells. The cell-line collection generated by A.F. Gazdar, J. Minna, and colleagues (69, 70) formed the basis of this collection. Further cell lines were obtained from ATCC, DSMZ (German Collection of Microorganisms and Cell Cultures, Germany), and our own or other cell culture collections. Details on all cell lines are listed in Supplemental Table 1, including providers and culture conditions. Cells were routinely controlled for infection with mycoplasma by MycoAlert (Cambrex) and were treated with antibiotics according to a previously published protocol (71) in case of infection.

SNP arrays. Genomic DNA was extracted from cell lines using the Puregene kit (QIAGEN) and hybridized to high-density oligonucleotide arrays (Affymetrix) interrogating 238,000 SNP loci on all chromosomes except Y, with a median intermarker distance of 5.2 kb (mean 12.2 kb). Array experiments were performed according to the manufacturer's instructions. SNPs were genotyped by the Affymetrix Genotyping Tools software, version 2.0. SNP array data of 371 primary samples were obtained from the Tumor Sequencing Project (processed data file viewable in GenePattern's SNP viewer: dataset.snp; <http://www.broad.mit.edu/cancer/pub/tsp/>) (15). We applied what we believe is a novel and general method for GISTIC (14) to analyze the data sets. In brief, each genomic marker was scored according to an integrated measure of the prevalence and amplitude of copy number changes (and only prevalence in the case of LOH), and the statistical significance of each score was assessed by comparison with the results expected from the background aberration rate alone. The GISTIC algorithm was run using 2 different pairs of copy number thresholds: copy number 4 (amplifications); 1 (deletions); and copy number 2.14 (amplifications); 1.87 (deletions) to reflect focal and broad events, respectively. For the sake of simplicity, we refer to these settings using only the amplification threshold.

Detection of homozygous deletions. For identification of homozygous deletions, SNP data were filtered for 5 coherent SNPs exhibiting copy numbers of less than 0.5. The analysis was focused on focal losses, excluding entire chromosomal arms. Information about genes located in a region of homozygous deletion was based on hg17 build of the human genome sequence from the University of California Santa Cruz (<http://genome.ucsc.edu>).

Analysis of cooccurring lesions. The analysis was performed computing ratios of observed versus expected cooccurrence frequency of individual lesions. Hierarchical clustering of mutation data combined to quantitative copy number changes that were dichotomized was performed using the reciprocal cooccurrence ratio as distance measure with average linkage method. As the adequate threshold for occurrence of copy number lesions depends on the overall level of copy number alteration for that specific lesion, the sum of these ratios for 3 distinct thresholds was used.

Mutation detection. Mutation status of known oncogene mutations in the genes *EGFR*, *BRAF*, *ERBB2*, *PIK3CA*, *NRAS*, *KRAS*, *ABLI*, *AKT2*, *CDK4*, *FGFR1*, *FGFR3*, *FLT3*, *HRAS*, *JAK2*, *KIT*, *PDGFR α* , and *RET* was determined

by mass-spectrometric genotyping. Mutation status of these genes for all cell lines was published previously (22). In addition, the genes *EGFR*, *BRAF*, *ERBB2*, *PIK3CA*, *KRAS*, *TP53*, *STK11*, *PTEN*, and *CDKN2A* were bi-directionally sequenced following PCR amplification of all coding exons.

Expression arrays. Expression data for 54 of the cell lines were obtained using Affymetrix U133A arrays. RNA extraction, hybridization, and scanning of arrays were performed using standard procedures (35). CEL files from U133A arrays were preprocessed using the dChip software (<http://biosun1.harvard.edu/complab/dchip/>; built date May 5, 2008). We compared the cell lines with cell lines and primary tumors from lung cancer (28), renal cell carcinomas (29, 72), and lymphoma (30, 73) data sets obtained from GEO (<http://www.ncbi.nlm.nih.gov/geo/>) by hierarchical clustering. Data were processed by standard procedures; normalization was performed in dChip. For comparison of NSCLC cell lines (U133A) and primary tumors, we used data on adenocarcinomas from Bhattacharjee and colleagues generated on U95Av2 arrays (35). We selected genes that we found differentially expressed between cell lines with mutant *EGFR* and WT *EGFR* (fold change between groups >2, 90% CI; absolute difference >100, $P < 0.01$) and between erlotinib-sensitive and erlotinib-resistant cell lines (erlotinib-sensitive [$GI_{50} < 0.1 \mu M$] vs. erlotinib-resistant [$GI_{50} > 2 \mu M$], fold change >2, 90% CI; absolute difference >100, $P < 0.005$). For principal component analysis, the R language for statistical computing was used. Variable transcripts were identified using the following filtering criteria: coefficient of variation 1.9 through 10, 40% present call rate. The first principal component described 14.5% of the overall variance, the second 9.6%, and the third 8.2%. Using a cutoff of 1400 in the eigenvalue, samples were grouped according to the first principal component.

Cell-based screening. All compounds were purchased from commercial suppliers or synthesized in house, dissolved in DMSO, and stored at $-80^{\circ}C$. Cells were plated into sterile microtiter plates using a Multidrop instrument (Thermo Scientific) and cultured overnight. Compounds were then added in serial dilutions. Cellular viability was determined after 96 hours by measuring cellular ATP content using the CellTiter-Glo Assay (Promega). Plates were measured on a Mithras LB 940 Plate Reader (Berthold Technologies). GI_{50} values were determined from the preimage under the growth inhibition curve, where the latter was smoothed according to the logistic function with the parameters appropriately chosen. For these analyses, we have established a semiautomated pipeline as what we believe to be a novel R package (43).

Lesion-based prediction of compound sensitivity. For lesion-based prediction of sensitivity, 3 different approaches were applied. First, the most sensitive and most resistant samples were chosen according to their sensitivity profile. Where the sensitivity profile of the corresponding compound did not allow a clear distinction between resistant and sensitive cell lines, groups were defined by the 25th and 75th percentiles. We used Fisher's exact test to evaluate the association between the activity of the compound and the presence of significant lesions as defined by GISTIC. For this purpose, the cell-line panel was divided according to the presence of each lesion. The logarithmically transformed GI_{50} values pertinent to each group were now compared by a 2-sample Welch's *t* test. In order to avoid an artificially low variance, the Welch's *t* tests were based on a fixed variance determined as the mean of the variances that were clearly distinct from zero (>0.1). Details of this procedure are presented in the publication by Solit and colleagues (12).

In a next step, multilesion predictors of sensitivity were calculated using feature selection, with subsequent validation by a KNN algorithm with a leave-one-out strategy (45), in which the same choice of samples was used as above for Fisher's exact test: For all but 1 sample, genetic lesions strongly discriminating between sensitive and resistant cell lines were selected and the prediction was validated by the remaining left-out sample. Copy number data were dichotomized to ensure a better comparability with the mutation data. Five different thresholds were used to



dichotomize the copy numbers: 2.14, 2.46, 2.83, 3.25, and 4 for amplified loci; and 1.87, 1.62, 1.41, 1.23, and 1 for deletions. The collection of features and the threshold for the dichotomization were selected for which the leave-one-out validation showed best performance and was taken as the best combined predictor to the respective compound. As a measure to select the setting with the largest predictive strength, the Youden index (sensitivity + specificity - 1) was used.

For example, the best erlotinib single gene predictor was obtained when the lesion data were dichotomized using the thresholds 3.25 and 1.23, respectively. Cell lines with a GI_{50} of less than 0.07 μ M were considered sensitive. For the predictor, the same cutoff values were used. Best performance in the leave-one-out cross validation was obtained using 15 features, $k = 3$ neighbors, and the cosine-based metric. Due to the problem of multiple hypothesis testing, the significance of the above Welch's t tests as well as Fisher's exact tests should be understood in an explorative rather than confirmative sense.

The NCI-60 cancer cell-line panel was used for validation of our findings (http://dtp.nci.nih.gov/mtargets/mt_index.html). Since the MEK inhibitor UO126 and the Hsp90 inhibitor 17-AAG were not covered by the collection of pharmacological data, we analyzed the association of the respective lesions to hypothemycin (MEK inhibitor) and to geldanamycin (17-AAG is a geldanamycin derivative) instead. Significance of association was analyzed by Fisher's exact test. Due to strongly discordant GI_{50} values, the cell lines HOP62 and A549 were excluded from the analysis with respect to the Hsp90 inhibitors. The thresholds for 1q21.3 amplification were set according to the overall distribution of copy number changes in the respective data sets (2.7 corresponding to 33% of the NSCLC cell lines; 2.4 corresponding to 33% of the NCI-60 collection).

All Fisher's exact tests, Welch's t tests (all 2-tailed), and Wilcoxon tests were performed using R version 2.7.1 (<http://www.wpic.pitt.edu/WPIC-CompGen/hclust/hclust.htm>). A level of significance of 5% was chosen. For cluster analysis, the R routine "hclust" was used.

Structural modeling of compound binding. The crystal structures of dasatinib bound to ABL kinase (pdb code 2IVU; ref. 74) and vandetanib bound to the RET kinase (pdb code 2IVU; ref. 75) were aligned to the kinase domain of EGFR bound to erlotinib (pdb code 1M17; ref. 76) using PyMOL software, 1.1beta (DeLano Scientific LLC). Based on the structural alignment of ABL with EGFR, the binding mode for dasatinib in EGFR is identical to that of the dasatinib-Abl complex. Figures of the structures were prepared using PyMOL.

Western blot analyses. Whole-cell lysates were prepared in NP40 lysis buffer (50 mmol/l Tris-HCl, pH 7.4, 150 mmol/l NaCl, 1% NP40) supplemented with protease and phosphatase inhibitor I and II cocktails (Merck) and clarified by centrifugation. Proteins were subjected to SDS-PAGE on 12% gels, except where indicated. Western blotting was done as described previously (77). The EGFR (no. 2232), the AKT (no. 9272), and the phospho-SRC (Tyr⁴¹⁶) (no. 2101) antibodies were both purchased from Cell Signaling Technology. The SRC (GD11) antibody was purchased from Millipore. The Hsp90 antibody (16F1) was purchased from Stressgen (Assay Designs). The phospho-EGFR (Tyr¹⁰⁶⁸) antibody was purchased from BioSource (Invitrogen). The cyclin D1 (DCS-6), the c-RAF (C-20), and the actin (C-11) antibody were purchased from Santa Cruz Biotechnology Inc. The KRAS (234-4.2) antibody was purchased from Calbiochem.

Immunoprecipitation. For the detection of complexes of Hsp90 with KRAS or EGFR and vice versa, whole-cell lysate (0.5–1 mg) in NP40 lysis buffer was incubated with Agarose A/G Plus pre-conjugated with the Hsp90 or KRAS antibody (see Western blot analyses). Immunoprecipitates were washed in NP40 lysis buffer, boiled in sample buffer, and subjected to SDS-PAGE followed by Western blotting using an anti KRAS, Hsp90, or EGFR antibody to detect complex formation.

Apoptosis assays. Cells were plated in 6-well plates after 24 hours of incubation, treated with 17-AAG for 72 hours, and finally harvested after trypsinization. Then cells were washed with PBS, resuspended in annexin V binding buffer, and finally stained with annexin V-FITC and propidium iodide. FACS analysis was performed on a FACSCanto flow cytometer (BD Biosciences), and results were calculated using FACSDiva Software, version 5.0.

Transfection and infection. Replication-incompetent retroviruses were produced from pBabe-based vectors by transfection into the Phoenix 293-TL packaging cell line (Orbigen) using the calcium precipitation method. Replication-incompetent lentiviruses were produced from pLKO.1-puro based vectors containing the shRNA insert (<http://www.broad.mit.edu/node/563>) by cotransfection of 293-TL cells with pMD.2 and pCMVd.8.9 helper plasmids using reagent Trans-LT (Mirus). Cells were infected with viral supernatants in the presence of polybrene. After 24 hours, medium was changed and cell lines were selected with 1–2 μ g/ml puromycin, from which stable transduced clonal cell lines were derived.

Site-directed mutagenesis. All mutations (Y530F; T341M) were introduced into the c-SRC ORF with the QuikChange XL II Mutagenesis Kit (Stratagene) following the instructions of the manufacturer. Oligonucleotides covering the mutations were designed with the software provided by Stratagene, and each mutant was confirmed by sequencing.

17-DMAG treatment in LSL-KRAS mice. The lox-stop-lox-KRAS (LSL-KRAS) mouse lung cancer model has been described elsewhere (64). Seven mice were imaged by MRI at 12 to 20 weeks after adeno-CRE treatments to document initial tumor volume. The mice were then divided into 17-DMAG (LC Laboratories) and placebo treatment groups, with 4 and 3 mice in each group, respectively. 17-DMAG was formulated in saline and given through tail-vein injection at 20 mg/kg/d dosing schedule. Mice were imaged by MRI after 1 week of drug treatment and sacrificed for further histological analysis thereafter. The protocol for animal work was approved by the Dana-Farber Cancer Institute Institutional Animal Care and Use Committee, and the mice were housed in a pathogen-free environment at the Harvard School of Public Health.

MRI scanning and tumor volume measurement. Mice were anesthetized with 1% isoflurane; respiratory and cardiac rates were monitored with BioTrig Software, version BT1 (Bruker BioSpin). Animals were imaged in the coronal planes with a rapid acquisition with relaxation enhancement (RARE) sequence ($Tr = 2000$ ms; TE effect = 25 ms, where Tr = pulse repetition time and TE = minimum echo time), using 17×1 mm slices to cover the entire lung. Matrix size of 128×128 and field of view (FOV) of 2.5×2.5 cm² were used for all imaging. The areas of lung tumors were manually segmented and measured using ImageJ software (version 1.33; <http://rsbweb.nih.gov/ij/>) on each magnetic resonance slice. Total tumor volume was calculated by adding tumor areas from all 17 slices (78). Note that MRI cannot clearly distinguish tumor lesions and postobstruction pneumonia that is induced by bronchial tumors of this particular tumor model.

Xenograft models. All animal procedures were in accordance with the German Laws for Animal Protection and were approved by the local animal protection committee and the local authorities (Bezirksregierung Köln). Tumors were generated by s.c. injections of 5×10^6 tumor cells into *nu/nu* athymic male mice. When tumors had reached a size of about 50 mm³, animals were randomized into 2 groups, control (vehicle) and dasatinib-treated mice. All controls were dosed with the same volume of vehicle. Mice were treated daily by oral gavage of 20 mg/kg dasatinib. The vehicle used was propylene glycol/water (1:1). Tumor size was monitored every 2 days by measuring perpendicular diameters. Tumor volumes were calculated from the determination of the largest diameter and its perpendicular diameter according to the equation [tumor volume = $a \times (b^2/2)$], where a = tumor width and b = tumor length].



Acknowledgments

We thank William Pao and William Sellers for helpful discussions and comments on the manuscript. We thank Andreas Janzer for help with immunoblotting experiments and Diana Wagner-Stippich for excellent technical assistance. Roman Thomas is a fellow of the International Association for the Study of Lung Cancer (IASLC). Stefanie Fisher holds a Köln Fortune fellowship. This work was supported by grants from the Deutsche Krebshilfe (107954 to Roman Thomas) and the German Ministry of Science and Education (BMBF) as part of the German National Genome Research Network (NGFNplus) program (01GS08100 to Roman Thomas). John Minna is supported by grants from SPOR (P50CA70907), DOD PROSPECT, and the Longenbaugh Foundation. Jordi Barretina holds a Beatriu de Pinós fellowship from the Departament d'Educació i Universitats de la Generalitat de Catalunya. K.-K. Wong was supported by NIH grants R01 CA122794 and R01 AG2400401; Dana-Farber/Harvard Cancer Center Lung

Cancer Specialized Program of Research Excellence (SPOR) grant P50 CA090578; and the Cecily and Robert Harris Foundation.

Received for publication August 12, 2008, and accepted in revised form March 25, 2009.

Address correspondence to: Roman Thomas, Max Planck Institute for Neurological Research, Gleueler Str. 50, 50931 Köln, Germany. Phone: 49-221-4726-259; Fax: 49-221-4726-298; E-mail: nini@nf.mpg.de. Or to: Kwok-Kin Wong, Department of Medical Oncology, Dana-Farber Cancer Institute, Harvard Medical School, 44 Binney St., Boston, Massachusetts 02115, USA. Phone: (617) 632-6084; Fax: (617) 582-7839; E-mail: kwong1@partners.org. Or to: Matthew Meyerson, Department of Medical Oncology, Dana-Farber Cancer Institute, Harvard Medical School, 44 Binney St., Boston, Massachusetts 02115, USA. Phone: (617) 632-4768; Fax: (617) 582-7880; E-mail: matthew_meyerson@dfci.harvard.edu.

- Slamon, D.J., et al. 2001. Use of chemotherapy plus a monoclonal antibody against HER2 for metastatic breast cancer that overexpresses HER2. *N. Engl. J. Med.* **344**:783–792.
- Druker, B.J., et al. 2001. Activity of a specific inhibitor of the BCR-ABL tyrosine kinase in the blast crisis of chronic myeloid leukemia and acute lymphoblastic leukemia with the Philadelphia chromosome. *N. Engl. J. Med.* **344**:1038–1042.
- Druker, B.J., et al. 2001. Efficacy and safety of a specific inhibitor of the BCR-ABL tyrosine kinase in chronic myeloid leukemia. *N. Engl. J. Med.* **344**:1031–1037.
- Hodi, F.S., et al. 2008. Major response to imatinib mesylate in KIT-mutated melanoma. *J. Clin. Oncol.* **26**:2046–2051.
- Heinrich, M.C., et al. 2003. Kinase mutations and imatinib response in patients with metastatic gastrointestinal stromal tumor. *J. Clin. Oncol.* **21**:4342–4349.
- Paez, J.G., et al. 2004. EGFR mutations in lung cancer: correlation with clinical response to gefitinib therapy. *Science*. **304**:1497–1500.
- Lynch, T.J., et al. 2004. Activating mutations in the epidermal growth factor receptor underlying responsiveness of non-small-cell lung cancer to gefitinib. *N. Engl. J. Med.* **350**:2129–2139.
- Pao, W., et al. 2004. EGF receptor gene mutations are common in lung cancers from “never smokers” and are associated with sensitivity of tumors to gefitinib and erlotinib. *Proc. Natl. Acad. Sci. U. S. A.* **101**:13306–13311.
- Sasai, K., et al. 2006. Shh pathway activity is down-regulated in cultured medulloblastoma cells: implications for preclinical studies. *Cancer Res.* **66**:4215–4222.
- Neve, R.M., et al. 2006. A collection of breast cancer cell lines for the study of functionally distinct cancer subtypes. *Cancer Cell.* **10**:515–527.
- Lin, W.M., et al. 2008. Modeling genomic diversity and tumor dependency in malignant melanoma. *Cancer Res.* **68**:664–673.
- Solit, D.B., et al. 2006. BRAF mutation predicts sensitivity to MEK inhibition. *Nature*. **439**:358–362.
- McDermott, U., et al. 2007. Identification of genotype-correlated sensitivity to selective kinase inhibitors by using high-throughput tumor cell line profiling. *Proc. Natl. Acad. Sci. U. S. A.* **104**:19936–19941.
- Beroukhi, R., et al. 2007. Assessing the significance of chromosomal aberrations in cancer: Methodology and application to glioma. *Proc. Natl. Acad. Sci. U. S. A.* **104**:20007–20012.
- Weir, B.A., et al. 2007. Characterizing the cancer genome in lung adenocarcinoma. *Nature*. **450**:893–898.
- Kendall, J., et al. 2007. Oncogenic cooperation and coamplification of developmental transcription factor genes in lung cancer. *Proc. Natl. Acad. Sci. U. S. A.* **104**:16663–16668.
- Kwei, K.A., et al. 2008. Genomic profiling identifies TITF1 as a lineage-specific oncogene amplified in lung cancer. *Oncogene*. **27**:3635–3640.
- Schmid, M., et al. 1998. Homozygous deletions of methylthioadenosine phosphorylase (MTAP) are more frequent than p16INK4A (CDKN2) homozygous deletions in primary non-small cell lung cancers (NSCLC). *Oncogene*. **17**:2669–2675.
- Chen, C.F., Yeh, S.H., Chen, D.S., Chen, P.J., and Jou, Y.S. 2005. Molecular genetic evidence supporting a novel human hepatocellular carcinoma tumor suppressor locus at 13q12.11. *Genes Chromosomes Cancer*. **44**:320–328.
- Jong, K., et al. 2007. Cross-platform array comparative genomic hybridization meta-analysis separates hematopoietic and mesenchymal from epithelial tumors. *Oncogene*. **26**:1499–1506.
- Greshock, J., et al. 2007. Cancer cell lines as genetic models of their parent histology: analyses based on array comparative genomic hybridization. *Cancer Res.* **67**:3594–3600.
- Thomas, R.K., et al. 2007. High-throughput oncogene mutation profiling in human cancer. *Nat. Genet.* **39**:347–351.
- Sharma, S.V., Bell, D.W., Settleman, J., and Haber, D.A. 2007. Epidermal growth factor receptor mutations in lung cancer. *Nat. Rev. Cancer*. **7**:169–181.
- Bamford, S., et al. 2004. The COSMIC (Catalogue of Somatic Mutations in Cancer) database and website. *Br. J. Cancer*. **91**:355–358.
- Aviel-Ronen, S., Blackhall, F.H., Shepherd, F.A., and Tsao, M.S. 2006. K-ras mutations in non-small-cell lung carcinoma: a review. *Clin. Lung Cancer*. **8**:30–38.
- Kaye, F.J. 2005. A curious link between epidermal growth factor receptor amplification and survival: effect of “allele dilution” on gefitinib sensitivity? *J. Natl. Cancer Inst.* **97**:621–623.
- Pao, W., et al. 2005. KRAS mutations and primary resistance of lung adenocarcinomas to gefitinib or erlotinib. *PLoS Med.* **2**:e17.
- Lu, Y., et al. 2006. A gene expression signature predicts survival of patients with stage I non-small cell lung cancer. *PLoS Med.* **3**:e467.
- Lenburg, M.E., et al. 2003. Previously unidentified changes in renal cell carcinoma gene expression identified by parametric analysis of microarray data. *BMC Cancer*. **3**:31.
- Hummel, M., et al. 2006. A biologic definition of Burkitt’s lymphoma from transcriptional and genomic profiling. *N. Engl. J. Med.* **354**:2419–2430.
- Lamb, J., et al. 2003. A mechanism of cyclin D1 action encoded in the patterns of gene expression in human cancer. *Cell*. **114**:323–334.
- Bild, A.H., et al. 2006. Oncogenic pathway signatures in human cancers as a guide to targeted therapies. *Nature*. **439**:353–357.
- Balko, J.M., et al. 2006. Gene expression patterns that predict sensitivity to epidermal growth factor receptor tyrosine kinase inhibitors in lung cancer cell lines and human lung tumors. *BMC Genomics*. **7**:289.
- Dzadzadziszko, R., et al. 2006. Epidermal growth factor receptor messenger RNA expression, gene dosage, and gefitinib sensitivity in non-small cell lung cancer. *Clin. Cancer Res.* **12**:3078–3084.
- Bhattacharjee, A., et al. 2001. Classification of human lung carcinomas by mRNA expression profiling reveals distinct adenocarcinoma subclasses. *Proc. Natl. Acad. Sci. U. S. A.* **98**:13790–13795.
- Eberhard, D.A., et al. 2005. Mutations in the epidermal growth factor receptor and in KRAS are predictive and prognostic indicators in patients with non-small-cell lung cancer treated with chemotherapy alone and in combination with erlotinib. *J. Clin. Oncol.* **23**:5900–5909.
- Beer, D.G., et al. 2002. Gene-expression profiles predict survival of patients with lung adenocarcinoma. *Nat. Med.* **8**:816–824.
- Nevins, J.R., and Porti, A. 2007. Mining gene expression profiles: expression signatures as cancer phenotypes. *Nat. Rev. Genet.* **8**:601–609.
- Choi, K., Creighton, C.J., Stivers, D., Fujimoto, N., and Kurie, J.M. 2007. Transcriptional profiling of non-small cell lung cancer cells with activating EGFR somatic mutations. *PLoS ONE*. **2**:e1226.
- Cappuzzo, F., et al. 2005. Epidermal growth factor receptor gene and protein and gefitinib sensitivity in non-small-cell lung cancer. *J. Natl. Cancer Inst.* **97**:643–655.
- Hirsch, F.R., et al. 2005. Increased epidermal growth factor receptor gene copy number detected by fluorescence in situ hybridization associates with increased sensitivity to gefitinib in patients with bronchioloalveolar carcinoma subtypes: a Southwest Oncology Group Study. *J. Clin. Oncol.* **23**:6838–6845.
- Sequist, L.V., Bell, D.W., Lynch, T.J., and Haber, D.A. 2007. Molecular predictors of response to epidermal growth factor receptor antagonists in non-small-cell lung cancer. *J. Clin. Oncol.* **25**:587–595.
- Frommolt, P., and Thomas, R.K. 2008. Standardized high-throughput evaluation of cell-based compound screens. *BMC Bioinformatics*. **9**:475.
- Reich, M., et al. 2006. GenePattern 2.0. *Nat. Genet.* **38**:500–501.



45. Golub, T.R., et al. 1999. Molecular classification of cancer: class discovery and class prediction by gene expression monitoring. *Science*. **286**:531-537.
46. Tsao, M.S., et al. 2005. Erlotinib in lung cancer - molecular and clinical predictors of outcome. *N. Engl. J. Med.* **353**:133-144.
47. Arao, T., et al. 2004. Small in-frame deletion in the epidermal growth factor receptor as a target for ZD6474. *Cancer Res.* **64**:9101-9104.
48. Ichihara, E., et al. 2008. Emergence of the EGFR T790M mutation in a lung adenocarcinoma cell line after vandetanib treatment. In *Proceedings of the 99th Annual Meeting of the American Association for Cancer Research*. April 12-16. San Diego, California, USA. AACR. Philadelphia, Pennsylvania, USA. 678.
49. Kobayashi, S., et al. 2005. EGFR mutation and resistance of non-small-cell lung cancer to gefitinib. *N. Engl. J. Med.* **352**:786-792.
50. Pao, W., et al. 2005. Acquired resistance of lung adenocarcinomas to gefitinib or erlotinib is associated with a second mutation in the EGFR kinase domain. *PLoS Med.* **2**:e73.
51. Yuza, Y., et al. 2007. Allele-dependent variation in the relative cellular potency of distinct EGFR inhibitors. *Cancer Biol. Ther.* **6**:661-667.
52. Sos, M.L., et al. 2008. Expression of signaling mediators downstream of EGF-receptor predict sensitivity to small molecule inhibitors directed against the EGF-receptor pathway. *J. Thorac. Oncol.* **3**:170-173.
53. Shah, N.P., et al. 2004. Overriding imatinib resistance with a novel ABL kinase inhibitor. *Science*. **305**:399-401.
54. Carter, T.A., et al. 2005. Inhibition of drug-resistant mutants of ABL, KIT, and EGF receptor kinases. *Proc. Natl. Acad. Sci. U. S. A.* **102**:11011-11016.
55. Yun, C.H., et al. 2007. Structures of lung cancer-derived EGFR mutants and inhibitor complexes: mechanism of activation and insights into differential inhibitor sensitivity. *Cancer Cell.* **11**:217-227.
56. Song, L., Morris, M., Bagui, T., Lee, F.Y., Jove, R., and Haura, E.B. 2006. Dasatinib (BMS-354825) selectively induces apoptosis in lung cancer cells dependent on epidermal growth factor receptor signaling for survival. *Cancer Res.* **66**:5542-5548.
57. Shoemaker, R.H. 2006. The NCI60 human tumour cell line anticancer drug screen. *Nat. Rev. Cancer.* **6**:813-823.
58. Shimamura, T., Lowell, A.M., Engelman, J.A., and Shapiro, G.I. 2005. Epidermal growth factor receptors harboring kinase domain mutations associate with the heat shock protein 90 chaperone and are destabilized following exposure to geldanamycins. *Cancer Res.* **65**:6401-6408.
59. Grbovic, O.M., et al. 2006. V600E B-Raf requires the Hsp90 chaperone for stability and is degraded in response to Hsp90 inhibitors. *Proc. Natl. Acad. Sci. U. S. A.* **103**:57-62.
60. Shields, J.M., Pruitt, K., McFall, A., Shaub, A., and Der, C.J. 2000. Understanding Ras: 'it ain't over 'til it's over'. *Trends Cell Biol.* **10**:147-154.
61. Basso, A.D., et al. 2002. Akt forms an intracellular complex with heat shock protein 90 (Hsp90) and Cdc37 and is destabilized by inhibitors of Hsp90 function. *J. Biol. Chem.* **277**:39858-39866.
62. Lim, K.H., and Counter, C.M. 2005. Reduction in the requirement of oncogenic Ras signaling to activation of PI3K/AKT pathway during tumor maintenance. *Cancer Cell.* **8**:381-392.
63. Ji, H., et al. 2007. Mutations in BRAF and KRAS converge on activation of the mitogen-activated protein kinase pathway in lung cancer mouse models. *Cancer Res.* **67**:4933-4939.
64. Jackson, E.L., et al. 2001. Analysis of lung tumor initiation and progression using conditional expression of oncogenic K-ras. *Genes Dev.* **15**:3243-3248.
65. Karaman, M.W., et al. 2008. A quantitative analysis of kinase inhibitor selectivity. *Nat. Biotechnol.* **26**:127-132.
66. Geyer, C.E., et al. 2006. Lapatinib plus capecitabine for HER2-positive advanced breast cancer. *N. Engl. J. Med.* **355**:2733-2743.
67. Du, J., et al. 2009. Bead-based profiling of tyrosine kinase phosphorylation identifies SRC as a potential target for glioblastoma therapy. *Nat. Biotechnol.* **27**:77-83.
68. Tracy, S., et al. 2004. Gefitinib induces apoptosis in the EGFR L858R non-small-cell lung cancer cell line H3255. *Cancer Res.* **64**:7241-7244.
69. Gazdar, A.F., and Minna, J.D. 1996. NCI series of cell lines: an historical perspective. *J. Cell Biochem. Suppl.* **24**:1-11.
70. Phelps, R.M., et al. 1996. NCI-Navy Medical Oncology Branch cell line data base. *J. Cell Biochem. Suppl.* **24**:32-91.
71. Uphoff, C.C., and Drexler, H.G. 2005. Eradication of mycoplasma contaminations. *Methods Mol. Biol.* **290**:25-34.
72. Shankavaram, U.T., et al. 2007. Transcript and protein expression profiles of the NCI-60 cancer cell panel: an integrative microarray study. *Mol. Cancer Ther.* **6**:820-832.
73. Rinaldi, A., et al. 2006. Genomic and expression profiling identifies the B-cell associated tyrosine kinase Syk as a possible therapeutic target in mantle cell lymphoma. *Br. J. Haematol.* **132**:303-316.
74. Tokarski, J.S., et al. 2006. The structure of Dasatinib (BMS-354825) bound to activated ABL kinase domain elucidates its inhibitory activity against imatinib-resistant ABL mutants. *Cancer Res.* **66**:5790-5797.
75. Knowles, P.P., et al. 2006. Structure and chemical inhibition of the RET tyrosine kinase domain. *J. Biol. Chem.* **281**:33577-33587.
76. Stamos, J., Sliwkowski, M.X., and Eigenbrot, C. 2002. Structure of the epidermal growth factor receptor kinase domain alone and in complex with a 4-anilinoquinazoline inhibitor. *J. Biol. Chem.* **277**:46265-46272.
77. Shimamura, T., et al. 2006. Non-small-cell lung cancer and Ba/F3 transformed cells harboring the ERBB2 G776insV_G/C mutation are sensitive to the dual-specific epidermal growth factor receptor and ERBB2 inhibitor HKI-272. *Cancer Res.* **66**:6487-6491.
78. Li, D., et al. 2007. Therapeutic anti-EGFR antibody 806 generates responses in murine de novo EGFR mutant-dependent lung carcinomas. *J. Clin. Invest.* **117**:346-352.
79. O'Reilly, K.E., et al. 2006. mTOR inhibition induces upstream receptor tyrosine kinase signaling and activates Akt. *Cancer Res.* **66**:1500-1508.

Decitabine Effect on Tumor Global DNA Methylation and Other Parameters in a Phase I Trial in Refractory Solid Tumors and Lymphomas

David J. Stewart, Jean-Pierre Issa, Razelle Kurzrock, Maria I. Nunez, Jaroslav Jelinek, David Hong, Yasuhiro Oki, Zhong Guo, Sanjay Gupta, and Ignacio I. Wistuba

Abstract **Purpose:** By hypomethylating genes, decitabine may up-regulate factors required for chemotherapeutic cytotoxicity. Platinum-resistant cells may have reduced expression of the copper/platinum transporter CTR1. **Experimental Design:** Thirty-one patients with refractory malignancies received decitabine 2.5 to 10 mg/m² on days 1 to 5, and 8 to 12 or 15 to 20 mg/m² on days 1 to 5. Tumor was assessed for DNA methylation (by LINE assays), apoptosis, necrosis, mitoses, Ki67, DNA methyltransferase (DNMT1), CTR1, and p16. **Results:** Febrile neutropenia was dose limiting. One thymoma patient responded. Decitabine decreased tumor DNA methylation (from median 51.2% predecitabine to 43.7% postdecitabine; $P = 0.01$, with effects at all doses) and in peripheral blood mononuclear cells (from 65.3-56.0%). There was no correlation between tumor and peripheral blood mononuclear cells. Patients starting decitabine ≤ 3 versus > 3 months after last prior cytotoxic or targeted therapy had lower predecitabine tumor CTR1 scores ($P = 0.02$), higher p16 ($P = 0.04$), and trends ($P = 0.07$) toward higher tumor methylation and apoptosis. Decitabine decreased tumor DNMT1 for scores initially > 0 ($P = 0.04$). Decitabine increased tumor apoptosis ($P < 0.05$), mitoses (if initially low, $P = 0.02$), and CTR1 (if initially low, $P = 0.025$, or if ≤ 3 months from last prior therapy, $P = 0.04$). Tumor CTR1 scores correlated inversely with methylation ($r = -0.41$, $P = 0.005$), but CTR1 promoter was not hypermethylated. Only three patients had tumor p16 promoter hypermethylation. P16 scores did not increase. Higher blood pressure correlated with lower tumor necrosis ($P = 0.03$) and a trend toward greater DNA demethylation ($P = 0.10$). **Conclusions:** Exposure to various cytotoxic and targeted agents might generate broad pleiotropic resistance by reducing CTR1 and other transporters. Decitabine decreases DNA methylation and augments CTR1 expression through methylation-independent mechanisms.

Hypermethylation by DNA methyltransferase (DNMT) helps regulate gene expression, and tumor suppressor gene hypermethylation promotes tumorigenesis (1-4). Altered gene methylation may also cause chemotherapy resistance (5). Many factors underlie chemotherapy resistance (6), but dose-response curve flattening at higher doses (7) suggests that deficiency of

factors required for cytotoxicity may be particularly important. For example, platinum-resistant cells may have hypermethylation of the MLH1 mismatch repair gene that is important in triggering platinum cytotoxicity (8) or may have a pleiotropic reduction in transporters (9, 10) that is potentially reversible by the DNMT inhibitor decitabine (9). The copper transporter CTR1 contributes to cellular platinum uptake (11). Platinum exposure rapidly decreases CTR1 expression, thereby reducing further platinum influx (12).

DNMT inhibitors tested clinically include decitabine (5-aza-2'-deoxycytidine; refs. 2, 4, 13-16), 5-azacytidine (4), and MG-98 (17). Decitabine inhibits DNMT, depletes DNMT1 through proteosomal degradation (18), induces global DNA hypomethylation, and increases expression of specific genes through mechanisms both dependent on (2, 16) as well as independent of (2, 4) promoter hypomethylation.

Of administration schedules tested in leukemias, 1-hour low-dose decitabine infusions days 1 to 5 \pm days 8 to 12 every 4 weeks may be particularly effective therapeutically (13-15, 19) and in demethylating DNA (14, 19). Low decitabine doses

Authors' Affiliation: M. D. Anderson Cancer Center, Houston, Texas
Received 9/5/08; revised 2/13/09; accepted 3/2/09; published OnlineFirst 5/26/09.
Grant support: NIH grants UO1 CA062461-10, R21 CA112895-01A1, Cancer Center Support Grant number 5-P30 CA16672-32, and by Department of Defense grant number W81XWH-07-1-0306.

The costs of publication of this article were defrayed in part by the payment of page charges. This article must therefore be hereby marked *advertisement* in accordance with 18 U.S.C. Section 1734 solely to indicate this fact.

Note: J-P. Issa, R. Kurzrock, and I.I. Wistuba contributed equally.

Requests for reprints: David J. Stewart, Department of Thoracic/Head and Neck Medical Oncology, University of Texas M. D. Anderson Cancer Center, Houston, TX 77030. Phone: 713-792-6363; Fax: 713-792-1220; E-mail: dstewart@mdanderson.org.

© 2009 American Association for Cancer Research.
doi:10.1158/1078-0432.CCR-08-2196

Translational Relevance

(a) Decitabine reduces DNA methylation in solid tumors, and should be assessed for its ability to increase expression of factors required for efficacy of other agents. (b) Peripheral blood mononuclear cells should not be used as surrogates for decitabine effect in tumor. (c) Exposure within the previous 3 months to a wide range of chemotherapy and targeted agents is associated with decreased copper/platinum uptake transporter CTR1 and with a trend to increased DNA methylation. Hence, many agents might reduce subsequent platinum uptake. We will explore the possibility that other transporters are also down-regulated, that this is a mechanism underlying epigenetic broad cross-resistance, and that agents that do not require uptake into cells (e.g., antibodies) could combine more effectively with chemotherapy agents than do small molecules (which require uptake into cells). (d) Decitabine increases CTR1 expression, suggesting that it should be further evaluated for its ability to reduce platinum resistance.

(sufficient to cause DNA hypomethylation) seemed to be more effective than higher cytotoxic doses in leukemia and myelodysplasia (13–15). Low-dose decitabine can also restore hemoglobin F production in sickle cell anemia (4, 20).

Because low-dose daily decitabine is effective in leukemias, we defined the maximum tolerated dose of this schedule in patients with refractory solid tumors and lymphomas and assessed decitabine effect on tumor and peripheral blood mononuclear cell (PBMC) DNA methylation and on tumor necrosis, apoptosis, mitoses, Ki67, CTR1, DNMT1, and the tumor suppressor gene p16 (which may be inactivated by hypermethylation; ref. 21). Because drug delivery may vary with tissue blood flow (22) and because tumor blood flow is more sensitive to blood pressure than is normal tissue blood flow (23, 24), we also assessed effect on decitabine effect of day 1 systolic blood pressure (SBP). Drug uptake into tumors may also vary with tumor pH (25). Hence, we also assessed effect of factors that might be related to tumor pH, including serum lactate dehydrogenase (LDH; because LDH5 converts pyruvate to lactate in tumors; ref. 26), glucose (because administration of a glucose load may reduce tumor extracellular pH; ref. 27), CO₂ (because administration of a bicarbonate load may raise tumor pH; ref. 28), and chloride.

Materials and Methods

Eligibility criteria for this Institutional Review Board–approved protocol included written informed consent, solid tumor or lymphoma refractory to standard therapy, biopsiable tumor, and adequate organ function. Dose-limiting toxicity was defined as febrile neutropenia, grade 4 thrombocytopenia lasting >2 wk, treatment-related bleeding, or clinically significant ≥grade 3 nonhematologic toxicity occurring with the first therapy cycle. Decitabine was supplied by the National Cancer Institute Division of Cancer Treatment and Diagnosis under a Collaborative and Research Development Agreement.

Patients received decitabine i.v. over 1 h daily, with ≥6 patients per cohort. Cohorts 1, 2, and 3 received decitabine 2.5, 5, and 10 mg/m²/d days 1 to 5 and 8 to 12 of each 4-wk cycle. Because substantial myelosuppression (but less than maximum tolerated dose) was seen in cohort 3, and because updated data from leukemia studies (19) suggested that administration of low-dose decitabine days 1 to 5 was as effective as days 1 to 5 and 8 to 12, cohorts 4 and 5, respectively, received 15 and 20 mg/m²/d on days 1 to 5 only. Granulocyte colony-stimulating factor was added for cohort 5. Tumor biopsies were done on all patients prior to decitabine and again on cycle 1 day 12 (within a few hours of the final cycle 1 dose for cohorts 1 to 3 and 7 d after last decitabine for cohorts 4 and 5). PBMCs were collected on the days of tumor biopsies. Computed tomography scans to evaluate tumor size were first repeated after cycle 1.

Tumors were characterized histopathologically with respect to tumor type, % necrosis, number of mitoses, % of cells with nuclear staining for Ki67 (29), and apoptosis by terminal deoxynucleotidyl transferase–mediated dUTP nick end labeling (TUNEL) assay (30). Global tumor and PBMC DNA methylation (% of CpG islands methylated) was assessed by LINE assays (31). Change in DNA methylation was calculated by dividing absolute change (day 12 minus day 1) by the day 1 value and multiplying by 100. Promoter methylation for *p16* and *CTR1* genes was assessed by pyrosequencing, as previously described (32).

Table 1. Patient characteristics

Patient characteristic	No. of patients
Total	31
Gender: male	17
Female	14
Median age (range)	53 (20-75)
Tumor type: malignant melanoma	6
Renal cell carcinoma	3
Breast carcinoma	4
Cutaneous T-cell lymphoma/ mycosis fungoides	3
Thymoma/thymic carcinoma	4
Adenocystic carcinoma	2
Head & neck squamous carcinoma	2
Neuroendocrine carcinomas	2
Desmoplastic tumor	1
Other carcinomas	4
Dose Level (mg/m ² /d): 2.5 × 10 d	6
5 × 10 d	6
10 × 10 d	7
15 × 5 d	6
20 × 5 days	6
Months from last therapy: median (range)	
Last cytotoxic therapy	3 (1-31)
Last platinum (n = 22)	9.5 (1.5-50)
Last cytotoxic or targeted therapy	2 (1-18)
No. of prior systemic regimens: median (range)	5 (1-14)
No. of prior targeted agents: median (range)	2 (0-6)
No. of patients previously treated with targeted agents:	
Thalidomide	5
Bevacizumab	7
Interferon α	9
EGFR inhibitor (gefitinib, erlotinib, cetuximab, PKI-166)	8
Histone deacetylase inhibitors	3
No. of other prior targeted agents	21

Table 2. Grade ≥ 3 toxicity with first cycle decitabine

Decitabine mg/m ² /d × no. days	2.5 × 10	5 × 10	10 × 10	15 × 5	20 × 5
No. of cycles	6	6	7	6	6
Toxicity:	No. of cycles with toxicity				
Neutropenia: grade 3		2	1	2	1
Grade 4			5	3	5
Febrile neutropenia grade 3					2
Nonneutropenic infection grade 3		1	1		
Platelets: grade 3			1		
Grade 4			1	1	
Anemia grade 3			1		1
Fatigue/↓Phosphate	1				
Fatigue grade 3					1
Hyperglycemia*			2		
Renal vein thrombus*			1		

*Probably unrelated.

For immunohistochemistry, 5- μ m-thick formalin-fixed and paraffin-embedded tumor tissue sections were deparaffinized and hydrated. Sections were stained using mouse antibodies for Ki67 (monoclonal, clone MIB1; dilution, 1:200; 90-min incubation at room temperature; Dako, Inc.), CTR1 (polyclonal; dilution, 1:400; 90-min incubation at room temperature; Gene Tex, Inc.), DNMT1 (polyclonal; dilution, 1:100; 90-min incubation at room temperature; Santa Cruz Biotechnology), and p16 (monoclonal, clone JC8; dilution, 1:50; 60-min incubation at 37°C; Lab Vision Co.). As secondary antibody, Envision Plus Dual Link-labeled polymer (Dako, Inc.) was used. Apoptosis was studied using TUNEL assay (Promega Co.) according to manufacturer recommendations, but the diaminobenzidine reaction was stopped at 3 min.

Cytoplasmic CTR1, DNMT1, and p16 expression was quantified using a 4-value intensity score (0-3+). The cytoplasmic expression score (range, 0-300) was then obtained by multiplying the intensity score by the percent tumor cells staining. Nuclear CTR1, DNMT1, and Ki67 expression was reported as the percentage of positive nuclei among tumor cells assessed. For TUNEL assessment, we counted the number of positive apoptotic cells plus apoptotic bodies in 10 high power fields ($\times 40$; ref. 30). Changes in these scores and in number of mitoses per high power field, % necrosis, and apoptosis were calculated by subtracting day 1 values from day 12 values (baseline 0 values precluded calculation as % changes). Assessments were blinded with respect to drug dose, cohort, and % DNA methylation.

GraphPad Prism 5.0 was used for statistical calculations using two-tailed nonparametric tests (Spearman tests for correlations, Wilcoxon signed-rank tests for paired comparisons, and Mann-Whitney and Kruskal-Wallis tests for comparison of two groups or more than two groups, respectively). Small sample size precluded multivariate analyses. For dichotomization of continuous variables, cut-points were chosen arbitrarily by inspection of the data to try to maximize differences between higher and lower value groups.

Results

The trial accrued 31 patients from September, 2004 to March, 2007. Patient demographics are outlined in Table 1 and first-cycle toxicity in Table 2. First-cycle dose-limiting febrile neutropenia developed in two of six cohort five patients. Febrile neutropenia also developed during a later cycle of therapy in one patient in cohort 2. The dose recommended for phase II trials is 10 mg/m²/d days 1 to 5, and 8 to 12 or 15 mg/m²/d days 1 to 5 (with granulocyte colony-stimulating factor).

Time to progression and response. Median time to progression (TTP) was 7.1 (range, 4 to 29) weeks. There was one partial remission (thymoma). At first planned re-evaluation at 4 weeks, 17 of 28 evaluable patients had disease stability (including 3 minor responses in cutaneous T-cell lymphoma, malignant melanoma, and appendiceal adenocarcinoma, respectively). Tumor characteristics were similar in patients with partial or minor responses versus stability or progression. Fifteen patients received 1 decitabine cycle, 10 received 2, and 6 received 3 to 7 cycles. Tumor growth was the most frequent reason for therapy discontinuation.

Cohorts 4 to 5 had a shorter median TTP (4.5 versus 10 weeks; $P = 0.02$) and a trend toward greater increase in tumor size with first cycle (12.6% versus 7.0%; $P = 0.17$) than cohorts 1 to 3. Neither outcome correlated significantly with decitabine dose ($r = -0.24$ and $r = 0.22$, respectively) or with tumor characteristics, although there were slight trends toward TTP correlations with tumor type (median of 6.0 weeks for epithelial tumors versus 8.4 weeks for others; $P = 0.10$), number of mitoses ($r = -0.34$; $P = 0.09$), apoptosis score ($r = 0.34$; $P = 0.17$), and DNMT1 score ($r = -0.32$; $P = 0.12$) and toward tumor size change correlations with mitoses ($r = 0.32$; $P = 0.13$) and CTR1 score ($r = 0.40$; $P = 0.07$).

Time from last prior therapy and predecitabine tumor characteristics. Patients with shorter times from last prior cytotoxic or targeted therapies had a trend toward higher predecitabine tumor DNA methylation (55.2% for ≤ 3 months from last therapy versus 39.6% for > 3 months, $P = 0.07$; Fig. 1A). They also tended to have higher apoptosis scores ($r = -0.44$; $P = 0.07$) and had significantly higher p16 scores (Fig. 1B). Patients with last therapy ≤ 3 months before decitabine had lower predecitabine CTR1 scores than did those > 3 months from last therapy (median score 90 versus 285; $P = 0.02$). CTR1 scores correlated more closely with time from last targeted or cytotoxic therapy (Fig. 1C) than with time only from last cytotoxic therapy (Fig. 1D), or time from last platinum ($r = -0.13$; $P = 0.63$). CTR1 score was not significantly different for patients who had versus had not received a platinum agent previously (median scores 100 versus 110; $P = 0.69$). Time from last therapy did not correlate with number of mitoses ($r = 0.04$), Ki67 positivity ($r = -0.01$), % necrosis ($r = -0.09$), or DNMT1 score ($r = -0.009$).

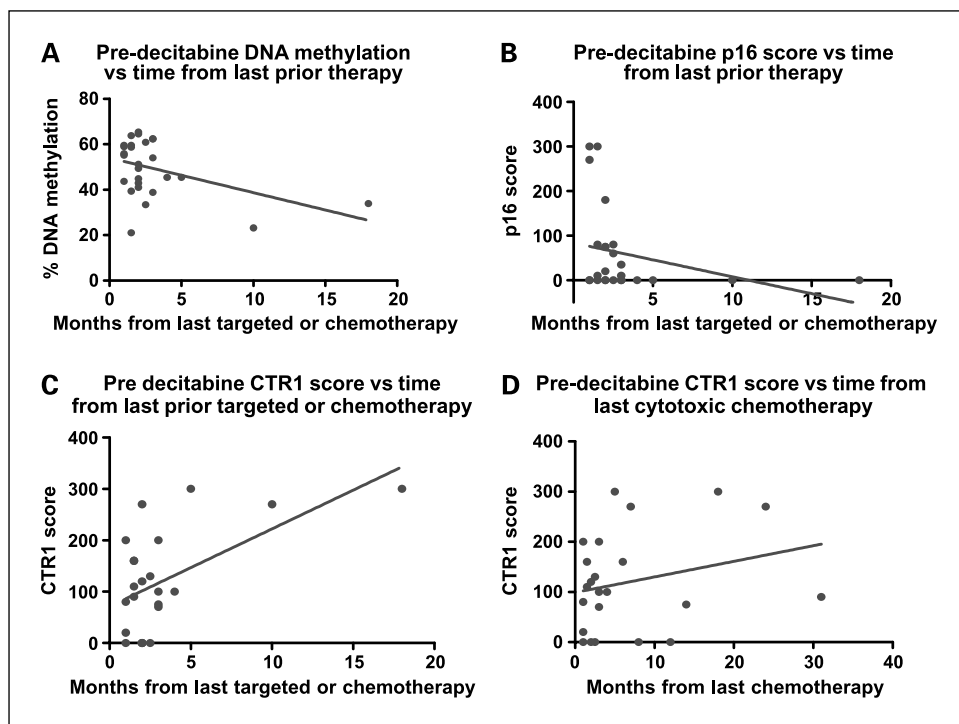


Fig. 1. Tumor characteristics and time from last prior therapy. *A*, predecitabine tumor DNA methylation versus time from last prior cytotoxic or targeted therapy ($P = 0.07$ for <3 versus >3 mo). *B*, predecitabine p16 score versus time from last prior cytotoxic or targeted therapy ($r = -0.42$; $P = 0.04$). *C*, predecitabine CTR1 score versus time from last prior cytotoxic or targeted therapy ($r = 0.34$; $P = 0.11$; $P = 0.02$ for >3 versus ≤ 3 mo). *D*, predecitabine CTR1 versus time from last prior cytotoxic chemotherapy ($r = 0.22$; $P = 0.32$).

Effect of decitabine on tumor global DNA methylation. In paired comparisons, there was a significant reduction in global tumor DNA methylation with decitabine, with a median relative reduction in tumor DNA methylation of 6% (mean, 8%; range, 52% decrease to 24% increase). Reduction in tumor DNA methylation was seen at all decitabine dose levels (median relative decreases 6%, 3%, 2.5%, and 12% with 25, 50, 75, and 100 mg/m²/cycle, respectively; $P = 0.16$ for 100 mg/m²/cycle versus others combined) and in all cohorts (median relative decreases 6%, 3%, 15%, 2.5%, and 4% in cohorts 1 to 5, respectively; $P = 0.052$ for cohort 3 versus others combined; Fig. 2A). Change in methylation did not correlate significantly with predecitabine tumor characteristics, although there tended to be greater reduction in methylation in tumors with more baseline mitoses ($r = -0.40$; $P = 0.07$).

Change in PBMC DNA methylation. PBMCs did not correlate significantly with tumors with respect to either DNA methylation (predecitabine and postdecitabine; $r = 0.22$; $P = 0.09$) or change in DNA methylation ($r = 0.02$; $P = 0.91$). Change in tumor DNA methylation was less than change in PBMC DNA methylation (PBMC median change, -14%; range, 47% reduction to 23% increase; $P = 0.04$ for tumor versus PBMC).

Gender and tumor type. Tumor DNA methylation was 52.5% in females versus 47.4% in males ($P = 0.73$), and methylation change was -8.4% versus -3.3% in females versus males ($P = 0.39$). "Standard" epithelial tumors tended to have slightly higher predecitabine methylation than did other tumor types (melanomas, lymphomas, thymomas, neuroendocrine carcinomas, desmoplastic tumors; 55.5% versus 45.4%; $P = 0.13$), and epithelial tumors had less DNA methylation change with decitabine (median reduction, 2.6% versus 11.2%; $P = 0.026$).

DNMT1 scores. Although cytoplasmic staining for DNMT1 was noted in 16 of 25 evaluable samples, nuclear staining

was only evident in 8. Predecitabine, cytoplasmic DNMT1 scores did not correlate with DNA methylation (Table 3), and changes in these parameters with decitabine also did not correlate ($r = -0.29$). For tumors with predecitabine scores of >0 , there was a reduction in cytoplasmic DNMT1 scores with decitabine (Table 4).

p16 scores. Predecitabine p16 score did not correlate with DNA methylation, but did correlate with apoptosis (Table 3), and was higher in epithelial tumors than in other types (median score, 75 versus 0; $P = 0.01$). Change in p16 score did not correlate with change in DNA methylation ($r = 0.04$), and decitabine had little effect on p16 scores (Table 4). Only 1 of 12 tumors initially negative for p16 converted to positive. Predecitabine p16 promoter methylation was less than or equal to the background noise level (10%) in 25 of 28 evaluable tumors. The 3 with higher baseline levels went from 46% to 37%, 27% to 23%, and 16% to 47%, respectively, with p16 remaining undetectable in the first 2, and going from 10/300 to undetectable in the third.

CTR1 score. CTR1 staining was predominantly cytoplasmic, with nuclear staining identified in only six predecitabine and five postdecitabine samples. CTR1 scores were slightly lower in epithelial tumors than in other tumor types (median score, 80 versus 125; $P = 0.15$). Predecitabine CTR1 score was significantly higher in tumors with >7 versus ≤ 7 mitoses (Table 3). In paired comparisons, CTR1 scores increased significantly with decitabine when initial scores were <200 and in patients starting decitabine ≤ 3 months after last prior therapy (Table 4; Fig. 2B and C). CTR1 change did not vary significantly with dose or cohort. Although there was a strong inverse correlation between CTR1 score and methylation (Table 3; Fig. 2D), change in CTR1 score did not correlate significantly with change in methylation ($r = 0.23$), and CTR1 promoter methylation was $<10\%$ (background noise level) in

all evaluable tumor samples (24 predecitabine, 26 postdecitabine) and in all 36 cell lines tested.

DNA methylation and markers of proliferation and cell death, tumor size change, and TTP. Mitoses and Ki67 tended to increase with decitabine in tumors in which they were initially low and apoptosis increased significantly, but necrosis did not change (Table 4). Predecitabine DNA methylation did not correlate with mitoses, Ki67, % necrosis, or apoptosis (Table 3), and also did not correlate with tumor size change over first therapy cycle ($r = -0.20$) or with TTP ($r = 0.20$). Similarly, change in DNA methylation did not correlate significantly with change in any of mitoses ($r = 0.07$), Ki67 ($r = 0.16$), apoptosis ($r = 0.002$), necrosis ($r = -0.38$; $P = 0.08$), or tumor size ($r = -0.26$) or with TTP ($r = 0.29$; $P = 0.20$). Despite the lack of correlation of predecitabine methylation and methylation change with these factors, postdecitabine methylation did correlate with postdecitabine mitoses ($r = -0.56$; $P = 0.002$) and Ki67 ($r = -0.43$; $P = 0.04$), with a trend to an association with TTP ($r = 0.29$; $P = 0.15$).

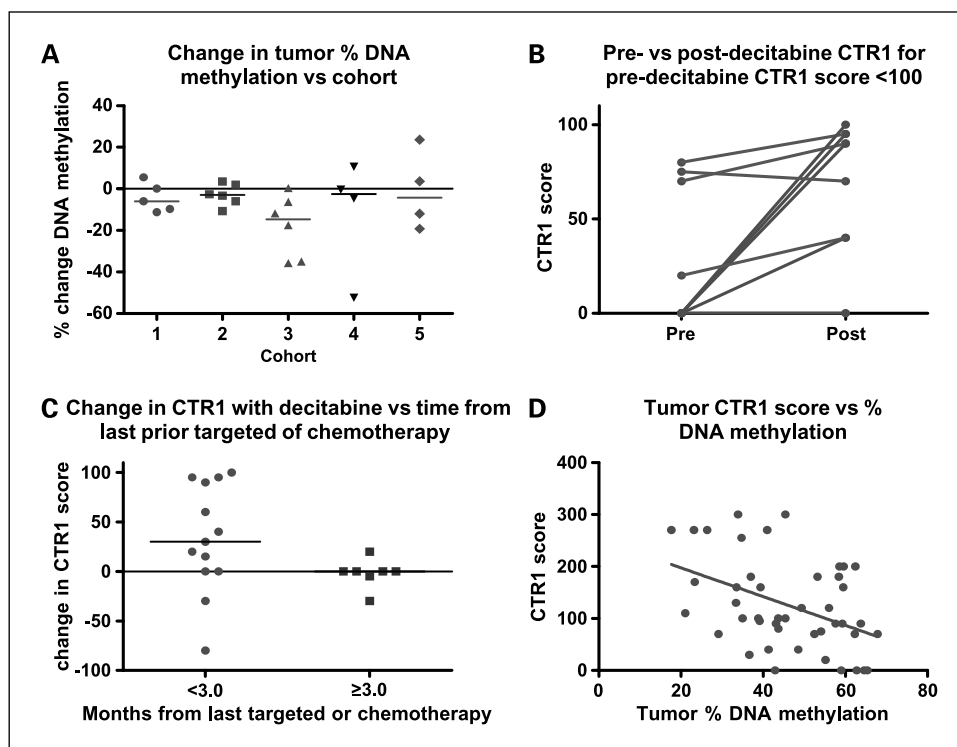
Blood pressure and pH factors. Patients with SBP <120 versus ≥ 120 mm Hg had significantly higher predecitabine tumor necrosis (median, 40% versus 15%; $P = 0.03$). For SBP <140 versus ≥ 140 mm Hg, first cycle tumor size change was 7.5% versus 15.6% ($P = 0.03$), whereas DNA methylation change was -3.3% versus -11.6% ($P = 0.10$). If SBP is multiplied by dose/cycle (because both higher SBP and higher dose might increase tumor exposure to drug), DNA methylation change was -12% versus -3% for patients with values $\geq 9,000$ versus $<9,000$ ($P = 0.04$). There was a trend toward a greater reduction in DNA methylation with higher predecitabine serum LDH ($r = -0.38$; $P = 0.058$), possibly because LDH also correlated with predecitabine mitoses ($r = 0.40$; $P = 0.04$). There were no correlations of interest between serum glucose, chloride or CO_2 , and changes in DNA methylation.

Discussion

This daily $\times 5$ to 10 decitabine regimen was well tolerated in very heavily pretreated solid tumor and lymphoma patients. Neutropenia was dose limiting. Decitabine reduced global DNA methylation, particularly in nonepithelial tumors in this study. In leukemias, dose-response curves for decitabine-induced demethylation flatten at higher doses (33). Although the relationship between dose and effect was not statistically significant in our study, trends to increased demethylation with both higher decitabine doses and with higher SBP [which might augment tumor blood flow (23, 24), thereby enhancing drug delivery; ref. 22] suggest a dose-response effect, as previously suggested for 6-hour decitabine infusions in solid tumors (16). However, methylation decreased even with lowest doses tested, and the changes we noted at lower doses were comparable with those previously reported at higher doses using 6-hour decitabine infusions (16).

In our study, we saw a median relative reduction in tumor DNA methylation of 6% (mean, 8%; range, 52% decrease to 24% increase), with a median 12% decrease in methylation at the highest dose tested (100 $\text{mg}/\text{m}^2/\text{cycle}$). In comparison, using a single 6-hour i.v. infusion of decitabine in combination with carboplatin, Appleton et al. (16) noted a mean demethylation of the *MAGE1A* promoter of 3.5% in tumor at their decitabine maximum tolerated dose of 90 $\text{mg}/\text{m}^2/\text{cycle}$, with a maximal demethylation of 6.8%. Although we reported a relative change in % DNA methylation, it was not clear whether Appleton et al. (16) were reporting a relative or an absolute change in methylation. Aparicio et al. (34) administered decitabine 20 to 40 mg/m^2 to solid tumor patients as a 72-h continuous i.v. infusion, and detected decreased promoter methylation for some genes in some patients, but they did not report the degree of demethylation. Furthermore, in their

Fig. 2. Change in tumor characteristics with decitabine. **A**, change in tumor % DNA methylation versus cohort (across all cohorts, $P = 0.40$; cohort 3 versus combined others: median, -15% versus -3%; $P = 0.052$). **B**, predecitabine versus postdecitabine CTR1 score for predecitabine CTR1 of <100 (median, 0 versus 90; paired $P = 0.02$, increase in 8 of 10). **C**, change in CTR1 score with decitabine for patients with last prior therapy <3 versus ≥ 3 mo before decitabine (median, 30 versus 0; $P = 0.03$). **D**, tumor CTR1 score versus % DNA methylation predecitabine and postdecitabine ($r = -0.41$; $P = 0.005$).



study, methylation was instead increased in some patients, and change in methylation did not correlate with decitabine dose (34). Schrupp et al. (35) also gave decitabine 60 to 90 mg/m² as a continuous i.v. infusion to solid tumor patients, and postdecitabine, they noted increased expression of 75 genes but decreased expression of 324 genes, and they did not report % change in DNA methylation. Overall, the available data from our study and others suggests that decitabine is able to reduce DNA methylation in solid tumors. The effect of dose is unclear, but our data and Appleton's data suggest that higher doses within the range tolerated may have a greater effect. The effect of schedule of drug administration is also unclear. There is no indication that our daily 1-h infusion schedule was any less effective than more prolonged administration schedules.

PBMC DNA methylation was not a reliable surrogate for tumor methylation. We and others (16) found a greater decitabine effect on methylation in PBMCs than in tumors, possibly due to differences in kinetics or drug accessibility. DNA synthesis is required for decitabine incorporation into DNA, for DNMT entrapment and for DNA demethylation (36), in keeping with the trend noted toward greater demethylation in tumors with more predecitabine mitoses.

Decitabine promotes proteosomal degradation of DNMT (18), and DNMT1 was decreased in tumors in which it was detectable predecitabine by our immunohistochemistry methods, although changes in DNMT1 and methylation did not correlate. The previously reported proteosomal degradation of DNMT1 in cell lines was seen predominantly in the cell nucleus (18), although we found mainly cytoplasmic changes in DNMT1 in our study. We are unaware of any other clinical assessments of effect of decitabine on DNMT1 expression, by immunohistochemistry. Because the functional role of DNMT1 is within the cell nucleus, it is unclear whether the changes in cytoplasmic expression of DNMT1 we detected are of any biological significance.

In secondary exploratory analyses (which should be interpreted cautiously in light of small patient numbers, population heterogeneity, multiplicity of analyses, and use of semiquantitative immunohistochemistry), mitoses and Ki67 tended to increase with decitabine when initially low, postdecitabine mitoses, and Ki67 correlated inversely with postdecitabine methylation, and TTP tended to be shorter with low postdecitabine methylation, suggesting that, although decitabine increases apoptosis, it may also enhance proliferation by up-regulating pro-

growth signaling pathways. The association of shorter TTP with schedule could possibly indicate that effect on proliferation varies with decitabine schedule, although patient selection might also account for this. Hence, decitabine might be better used in combination with other agents as a potential resistance modulator rather than being used alone in solid tumors.

Platinum-resistant cell lines may have reduced CTR1 (a copper transporter that plays a role in cellular platinum uptake; ref. 37) and multiple other membrane transporters (9, 10), and decitabine may up-regulate some transporters in platinum-resistant cells (9). We hypothesized that the dose-response curve flattening seen at higher chemotherapy doses in non-small cell lung cancer and other malignancies could be explained in part by down-regulation and saturation of factors required for drug efficacy, including various transporters (7). Here, we found that, compared with tumors not recently treated, tumors treated recently with any cytotoxic or targeted therapy had significantly less CTR1 but increased p16 and trends to increased methylation and apoptosis. Although *CTR1* promoter was not hypermethylated, there was a strong negative correlation between global DNA methylation and CTR1 score, and administration of decitabine (which activates gene expression through mechanisms both dependent on and independent of promoter hypomethylation; refs. 2, 4) significantly increased CTR1 score for those with initial scores of <200 and for patients who had received their last prior therapy <3 months earlier. Hence, DNA hypermethylation may play an indirect role in decreasing CTR1 expression (for example, by decreasing cell proliferation), and decitabine may be effective at increasing its expression by up-regulating expression of factors that in turn promote CTR1 expression. We are currently also assessing expression of other transporters in these tumors. Alternatively, it remains possible that the increase in CTR1 is a more nonspecific effect of chemotherapy administration and that agents with other mechanisms of action would also increase CTR1 expression. Against this possibility is the observation that CTR1 expression increased with increasing time from last therapy with other agents.

In keeping with published cell line (9) and xenograft (8) data, our observations suggest a potential role for decitabine as a resistance modulator in tumors with reduced transporters. Although other dose-schedules have been ineffective (38, 39), combining multiple day decitabine administration with platinum in chemo-naïve patients could be of interest. DNA synthesis (during either cell division or DNA repair) is

Table 3. Spearman coefficients for correlations between predecitabine tumor characteristics

	<i>n</i>	P16 score	CTR1 score	DNMT1 score	Tumor % DNA methylation	Apoptosis score	% necrosis	% Ki67 positive
No. of Mitoses	26	-0.14	0.39* (<i>P</i> = 0.06)	0.17	0.004	-0.13	0.17	0.14
Ki67% positive	23	0.26	0.19	0.04	0.07	-0.04	-0.36 (<i>P</i> = 0.09)	
% necrosis	27	-0.22	-0.08	-0.25	-0.20	-0.18		
Apoptosis score	18	0.53 (<i>P</i> = 0.03)	0.03	-0.21	0.12			
Tumor % DNA methylation	27	0.21	-0.45 (<i>P</i> = 0.04)	-0.15				
DNMT1 score	25	0.02	0.34 (<i>P</i> = 0.11)					
CTR1 score	23	0.05						
P16 score	25							

NOTE: Only *P* values <0.20 are shown.

*Predecitabine CTR1 score was significantly higher in tumors with >7 mitoses than in those with ≤7 (200 vs 85, *P* = 0.02).

Table 4. Postdecitabine vs predecitabine tumor characteristics

Factor	n*	Predecitabine		Postdecitabine		Wilcoxon signed rank (paired) P
		Median	Range	Median	Range	
No. of mitoses:						
All	24	2.0	0-15	3.5	0-28	0.12
If predecitabine mitoses \leq 7	18	1.5	0-7	3.0	0-28	0.02
% tumor cells expressing Ki67:						
All	20	20	0-70	22.5	0-85	0.53
If predecitabine Ki67 \leq 25	14	7.5	5-25	12.5	5-75	0.15
% of tumor that is necrotic:						
All	25	20	0-90	20	0-70	0.32
If predecitabine necrosis $>$ 30%	8	65	40-90	35	0-70	0.02
If predecitabine necrosis \leq 30%	17	5	0-30	5	0-50	0.30
Apoptosis score	17	22	2-230	49	0-269	0.049
% DNA methylated:						
Tumor	25	51.2	21.1-65.4	43.7	17.7-67.9	0.01
Blood	30	65.3	39.5-74.1	56.0	33.8-64.5	$<$ 0.001
DNMT1 cytoplasmic score:						
All	23	30	0-280	50	0-180	0.56
If predecitabine DNMT1 $>$ 0	16	120	20-280	95	0-180	0.04
DNMT1 nuclear score						
All	23	0	0-110	0	0-40	0.50
If predecitabine DNMT1 $>$ 0	7	10	5-110	5	0-40	0.50
CTR1 score:						
All	21	100	0-300	95	0-300	0.22
If predecitabine CTR1 $<$ 200	15	75	0-160	90	0-255	0.025
If predecitabine CTR1 $<$ 100	9	0	0-80	90	0-100	0.02
If \leq 3 months from last therapy	17	80	0-270	95	0-270	0.04
P16 score	24	5	0-300	0	0-300	0.96
% of tumor that is stroma	26	40	0-90	50	1-90	0.97
% of tumor that is fibrosis	26	30	0-60	35	0-80	0.49

*Number for which both the predecitabine and postdecitabine value is known and the predecitabine value satisfies any criteria specified in left column.

required for decitabine-induced hypomethylation (36). Platinum binding to DNA generates DNA repair (6). Hence, platinum could potentiate DNA demethylation by augmenting decitabine incorporation into DNA, whereas DNA demethylation could potentially inhibit emergence of resistance to the platinum.

Decitabine may also augment epidermal growth factor receptor (EGFR) expression and restore sensitivity to EGFR inhibitors (40), suggesting a role for decitabine in reversing some types of acquired resistance to EGFR inhibitors. Furthermore, our observation here that CTR1 expression may be reduced by recent exposure to targeted therapies may help explain why addition of small molecule EGFR inhibitors to chemotherapy in non-small cell lung cancer adds little (41, 42), whereas addition of anti-EGFR antibodies to chemotherapy may improve outcome (43). Cellular uptake of small molecules could hypothetically be reduced by down-regulation of membrane transporters, whereas antibodies would not require cellular uptake.

Correlation of low SBP with increased tumor necrosis is in keeping with tumor blood flow being particularly sensitive to SBP (23, 24). The additional observations that high SBP corre-

lated with greater tumor growth with first decitabine cycle, but decitabine-induced demethylation was greater with increased SBP (possibly through improved drug delivery) suggest testing of a strategy to maintain SBP at low levels between chemotherapy cycles but to adjust medications to promote high SBP during chemotherapy administration and distribution.

Although the effect of decitabine on DNA methylation and other parameters was modest, our data support further exploration of decitabine as a resistance-modulating agent. Patients most likely to benefit may be those most recently treated with other agents and those with lowest expression of drug transporters.

Disclosure of Potential Conflicts of Interest

No potential conflicts of interest were disclosed.

Acknowledgments

We thank M.D. Anderson Cancer Center for making funding available for required tumor biopsies and Dr. Anthony Murgu from CTEP, National Cancer Institute, for his help and support in this project.

References

- Kim JS, Kim H, Shim YM, Han J, Park J, Kim DH. Aberrant methylation of the FHIT gene in chronic smokers with early stage squamous cell carcinoma of the lung. *Carcinogenesis* 2004;25:2165-71.
- Oki Y, Aoki E, Issa JP. Decitabine-bedside to bench. *Crit Rev Oncol Hematol* 2007;61:140-52.
- Baylin SB, Herman JG, Graff JR, Vertino PM, Issa JP. Alterations in DNA methylation: a fundamental aspect of neoplasia. *Adv Cancer Res* 1998;72:141-96.
- Ghoshal K, Bai S. DNA methyltransferases as targets for cancer therapy. *Drugs Today (Barc)* 2007;43:395-422.

5. Chekhun VF, Lukyanova NY, Kovalchuk O, Tryndyak VP, Pogribny IP. Epigenetic profiling of multidrug-resistant human MCF-7 breast adenocarcinoma cells reveals novel hyper- and hypomethylated targets. *Mol Cancer Ther* 2007;6:1089-98.
6. Stewart DJ. Mechanisms of resistance to cisplatin and carboplatin. *Crit Rev Oncol Hematol* 2007;63:12-31.
7. Stewart DJ, Chiritescu G, Dahrouge S, Banerjee S, Tomiak EM. Chemotherapy dose-response relationships in non-small cell lung cancer and implied resistance mechanisms. *Cancer Treat Rev* 2007;33:101-37.
8. Plumb JA, Strathdee G, Sludden J, Kaye SB, Brown R. Reversal of drug resistance in human tumor xenografts by 2'-deoxy-5-azacytidine-induced demethylation of the hMLH1 gene promoter. *Cancer Res* 2000;60:6039-44.
9. Shen DW, Su A, Liang XJ, Pai-Panandiker A, Gottesman MM. Reduced expression of small GTPases and hypermethylation of the folate binding protein gene in cisplatin-resistant cells. *Br J Cancer* 2004;91:270-6.
10. Liang XJ, Shen DW, Gottesman MM. A pleiotropic defect reducing drug accumulation in cisplatin-resistant cells. *J Inorg Biochem* 2004;98:1599-606.
11. Safaei R, Howell SB. Copper transporters regulate the cellular pharmacology and sensitivity to Pt drugs. *Crit Rev Oncol Hematol* 2005;53:13-23.
12. Holzer AK, Katano K, Klomp LW, Howell SB. Cisplatin rapidly down-regulates its own influx transporter hCTR1 in cultured human ovarian carcinoma cells. *Clin Cancer Res* 2004;10:6744-9.
13. Kantarjian HM, O'Brien S, Huang X, et al. Survival advantage with decitabine versus intensive chemotherapy in patients with higher risk myelodysplastic syndrome: comparison with historical experience. *Cancer* 2007;109:1133-7.
14. Issa JP, Gharibyan V, Cortes J, et al. Phase II study of low-dose decitabine in patients with chronic myelogenous leukemia resistant to imatinib mesylate. *J Clin Oncol* 2005;23:3948-56.
15. Issa JP, Garcia-Manero G, Giles FJ, et al. Phase I study of low-dose prolonged exposure schedules of the hypomethylating agent 5-aza-2'-deoxycytidine (decitabine) in hematopoietic malignancies. *Blood* 2004;103:1635-40.
16. Appleton K, Mackay HJ, Judson I, et al. Phase I and pharmacodynamic trial of the DNA methyltransferase inhibitor decitabine and carboplatin in solid tumors. *J Clin Oncol* 2007;25:4603-9.
17. Stewart DJ, Donehower RC, Eisenhauer EA, et al. A phase I pharmacokinetic and pharmacodynamic study of the DNA methyltransferase 1 inhibitor MG98 administered twice weekly. *Ann Oncol* 2003;14:766-74.
18. Ghoshal K, Datta J, Majumder S, et al. 5-Aza-deoxycytidine induces selective degradation of DNA methyltransferase 1 by a proteasomal pathway that requires the KEN box, bromo-adjacent homology domain, and nuclear localization signal. *Mol Cell Biol* 2005;25:4727-41.
19. Kantarjian H, Oki Y, Garcia-Manero G, et al. Results of a randomized study of 3 schedules of low-dose decitabine in higher-risk myelodysplastic syndrome and chronic myelomonocytic leukemia. *Blood* 2007;109:52-7.
20. Koshy M, Dorn L, Bressler L, et al. 2-deoxy 5-azacytidine and fetal hemoglobin induction in sickle cell anemia. *Blood* 2000;96:2379-84.
21. Digel W, Lubbert M. DNA methylation disturbances as novel therapeutic target in lung cancer: preclinical and clinical results. *Crit Rev Oncol Hematol* 2005;55:1-11.
22. Lutz RJ, Galbraith WM, Dedrick RL, Shrager R, Mellett LB. A model for the kinetics of distribution of actinomycin-D in the beagle dog. *J Pharmacol Exp Ther* 1977;200:469-78.
23. Suzuki M, Hori K, Abe I, Saito S, Sato H. A new approach to cancer chemotherapy: selective enhancement of tumor blood flow with angiotensin II. *J Natl Cancer Inst* 1981;67:663-9.
24. Guichard M, Lespinasse F, Trotter M, Durand R, Chaplin D. The effect of hydralazine on blood flow and misonidazole toxicity in human tumour xenografts. *Radiother Oncol* 1991;20:117-23.
25. Raghunand N, Gillies RJ. pH and drug resistance in tumors. *Drug Resist Updat* 2000;3:39-47.
26. Koukourakis MI, Giatromanolaki A, Sivridis E. Lactate dehydrogenase isoenzymes 1 and 5: differential expression by neoplastic and stromal cells in non-small cell lung cancer and other epithelial malignant tumors. *Tumour Biol* 2003;24:199-202.
27. Kozin SV, Shkarin P, Gerweck LE. The cell transmembrane pH gradient in tumors enhances cytotoxicity of specific weak acid chemotherapeutics. *Cancer Res* 2001;61:4740-3.
28. Raghunand N, He X, van Sluis R, et al. Enhancement of chemotherapy by manipulation of tumour pH. *Br J Cancer* 1999;80:1005-11.
29. Barbareschi M, Girlando S, Mauri FM, et al. Quantitative growth fraction evaluation with MIB1 and Ki67 antibodies in breast carcinomas. *Am J Clin Pathol* 1994;102:171-5.
30. Labat-Moleur F, Guillermet C, Lorimier P, et al. TUNEL apoptotic cell detection in tissue sections: critical evaluation and improvement. *J Histochem Cytochem* 1998;46:327-34.
31. Yang AS, Estecio MR, Doshi K, Kondo Y, Tajara EH, Issa JP. A simple method for estimating global DNA methylation using bisulfite PCR of repetitive DNA elements. *Nucleic Acids Res* 2004;32:e38.
32. Colella S, Shen L, Baggerly KA, Issa JP, Krahe R. Sensitive and quantitative universal Pyrosequencing methylation analysis of CpG sites. *Bio-techniques* 2003;35:146-50.
33. Yang AS, Doshi KD, Choi SW, et al. DNA methylation changes after 5-aza-2'-deoxycytidine therapy in patients with leukemia. *Cancer Res* 2006;66:5495-503.
34. Aparicio A, Eads CA, Leong LA, et al. Phase I trial of continuous infusion 5-aza-2'-deoxycytidine. *Cancer Chemother Pharmacol* 2003;51:231-9.
35. Schrupp DS, Fischette MR, Nguyen DM, et al. Phase I study of decitabine-mediated gene expression in patients with cancers involving the lungs, esophagus, or pleura. *Clin Cancer Res* 2006;12:5777-85.
36. Issa JP. DNA methylation as a therapeutic target in cancer. *Clin Cancer Res* 2007;13:1634-7.
37. Ishida S, Lee J, Thiele DJ, Herskowitz I. Uptake of the anticancer drug cisplatin mediated by the copper transporter Ctr1 in yeast and mammals. *Proc Natl Acad Sci U S A* 2002;99:14298-302.
38. Pohlmann P, DiLeone LP, Cancellala AI, et al. Phase II trial of cisplatin plus decitabine, a new DNA hypomethylating agent, in patients with advanced squamous cell carcinoma of the cervix. *Am J Clin Oncol* 2002;25:496-501.
39. Schwartzmann G, Schunemann H, Gorini CN, et al. A phase I trial of cisplatin plus decitabine, a new DNA-hypomethylating agent, in patients with advanced solid tumors and a follow-up early phase II evaluation in patients with inoperable non-small cell lung cancer. *Invest New Drugs* 2000;18:83-91.
40. Montero AJ, Diaz-Montero CM, Mao L, et al. Epigenetic inactivation of EGFR by CpG island hypermethylation in cancer. *Cancer Biol Ther* 2006;5:1494-501.
41. Herbst RS, Prager D, Hermann R, et al. TRIBUTE: a phase III trial of erlotinib hydrochloride (OSI-774) combined with carboplatin and paclitaxel chemotherapy in advanced non-small-cell lung cancer. *J Clin Oncol* 2005;23:5892-9.
42. Herbst RS, Giaccone G, Schiller JH, et al. Gefitinib in combination with paclitaxel and carboplatin in advanced non-small-cell lung cancer: a phase III trial-INTACT 2. *J Clin Oncol* 2004;22:785-94.
43. Butts CA, Bodkin D, Middleman EL, et al. A. Randomized phase II study of gemcitabine plus cisplatin, with or without cetuximab, as first-line therapy for patients with advanced or metastatic non small-cell lung cancer. *J Clin Oncol* 2007;25:5777-84.

Editorial Manager(tm) for Biomaterials
Manuscript Draft

Manuscript Number:

Title: Optimization and Comparison of Multiplexed Quantum Dot Based Immunohistofluorescence

Article Type: FLA Original Research

Section/Category: Biomaterials & Nanotechnology

Keywords: Quantum dots
Immunohistofluorescence
Nanocrystals
Spectral imaging

Corresponding Author: Dr. Zhuo (Georgia) Chen,

Corresponding Author's Institution: Emory University Winship Cancer Institute

First Author: Dong-hai Huang

Order of Authors: Dong-hai Huang; Xiang-hong Peng; Ling Su; Dongsheng Wang; Fadlo R Khuri; Dong M Shin; Zhuo (Georgia) Chen

Abstract: Nanoparticle quantum dots (QDs) are ideal materials for multiplexed biomarker detection, localization, and quantification. Both direct and indirect methods are available for QD-based immunohistofluorescence (QD-IHF) staining; however, the direct method has been considered laborious and costly. In this study, we optimized and compared the indirect QD-IHF single staining procedure using QD-secondary antibody conjugates and QD-streptavidin conjugates. Problems associated with sequential multiplex staining were identified quantitatively. A method using a QD cocktail solution was developed allowing simultaneous staining with three antibodies against E-cadherin, EGFR, and β -catenin in formalin-fixed and paraffin-embedded (FFPE) tissues. The expression of each biomarker was quantified and compared using the cocktail and the sequential method. Our results demonstrated that the QD signal for each multiplexed biomarker was more consistent and stable using the cocktail method than the sequential method, providing a unique tool for potential research and clinical applications.

***Mandatory Author Declaration** **Author Declaration**

Dear Editor:

We the undersigned declare that this manuscript is original, has not been published before and is not currently being considered for publication elsewhere.

We wish to confirm that there are no known conflicts of interest associated with this publication and there has been no significant financial support for this work that could have influenced its outcome.

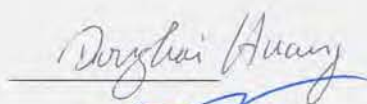
We confirm that the manuscript has been read and approved by all named authors and that there are no other persons who satisfied the criteria for authorship but are not listed. We further confirm that the order of authors listed in the manuscript has been approved by all of us.

We confirm that we have given due consideration to the protection of intellectual property associated with this work and that there are no impediments to publication, including the timing of publication, with respect to intellectual property. In so doing we confirm that we have followed the regulations of our institutions concerning intellectual property.

We understand that the Corresponding Author is the sole contact for the Editorial process (including Editorial Manager and direct communications with the office). He/she is responsible for communicating with the other authors about progress, submissions of revisions and final approval of proofs. We confirm that we have provided a current, correct email address which is accessible by the Corresponding Author and which has been configured to accept email from biomaterials@online.be.

Signed by all authors as follows:

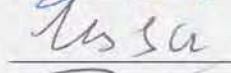
Dong-hai Huang



Xiang-hong Peng



Ling Su



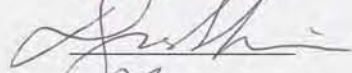
Dongsheng Wang



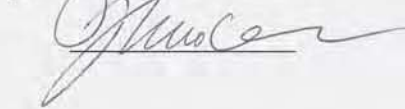
Fadlo R. Khuri



Dong M. Shin



Zhuo (Georgia) Chen



Title of the manuscript "Optimization and Comparison of Multiplexed Quantum Dot Based Immunohistofluorescence"



EMORY

WINSHIP
CANCER
INSTITUTE

June 6th, 2008

Professor D.F. Williams
Editor-in-Chief
Biomaterials Editorial Office
Department of Clinical Engineering, University of Liverpool
P.O. Box 147, Liverpool L69 3BX, UK

Dear Professor Williams:

Enclosed is a copy of our manuscript entitled “Optimization and Comparison of Multiplexed Quantum Dot Immunohistofluorescence” for publication in *Biochemical and Biophysical Research Communications* as a Research Article.

To the best of our knowledge, this manuscript is the first report using quantified data to guide the optimization of conditions for quantum dot (QD) immunohistofluorescence staining and to develop a cocktail QD procedure, allowing simultaneous staining of three antibodies. Our results demonstrate that the QD signal for each multiplexed biomarker was more consistent and stable using the cocktail method than a sequential method, providing a unique tool for multiplexing biomarkers in research and clinical applications.

All authors of this research paper have directly participated in the planning, execution, and/or analysis of the study and have read and agreed to the contents of the final version submitted. The data presented in the manuscript have not been published or copyrighted in any other scientific journal, nor are under consideration for publication. The contents of this manuscript will not be copyrighted, submitted, or published elsewhere while acceptance by this Journal is under consideration.

Your favorable consideration of this manuscript is appreciated.

Sincerely,

A handwritten signature in cursive script, appearing to read 'Zhuo Chen'.

Zhuo (Georgia) Chen, Ph.D.
Associate Professor of Hematology and Medical Oncology
Emory Winship Cancer Institute

1
2
3
4
5
6
7
8
9
10
11
12
13
14
15
16
17
18
19
20
21
22
23
24
25
26
27
28
29
30
31
32
33
34
35
36
37
38
39
40
41
42
43
44
45
46
47
48
49
50
51
52
53
54
55
56
57
58
59
60
61
62
63
64
65

Optimization and Comparison of Multiplexed Quantum Dot Based Immunohistofluorescence

Dong-hai Huang^{a, b}, Xiang-hong Peng^a, Ling Su^a, Dongsheng Wang^a, Fadlo R. Khuri^a, Dong M. Shin^a, Zhuo (Georgia) Chen^{a,*}

^a Department of Hematology and Medical Oncology, Winship Cancer Institute, Emory University School of Medicine, Atlanta, Georgia, 30322, USA

^b Department of Otolaryngology-Head and Neck Surgery, Xiang-Ya Hospital, Central South University, Changsha, Hunan, 410008, P.R. China

***Corresponding author:** Zhou (Georgia) Chen, Department of Hematology and Medical Oncology, Winship Cancer Institute, Emory University School of Medicine, 1365-C Clifton Road, Suite C3086, Atlanta, GA 30322. Phone: 404-778-3977; Fax: 404-778-5520; Email: gzchen@emory.edu.

1
2
3
4
5
6
7
8
9
10
11
12
13
14
15
16
17
18
19
20
21
22
23
24
25
26
27
28
29
30
31
32
33
34
35
36
37
38
39
40
41
42
43
44
45
46
47
48
49
50
51
52
53
54
55
56
57
58
59
60
61
62
63
64
65

Abstract

Nanoparticle quantum dots (QDs) are ideal materials for multiplexed biomarker detection, localization, and quantification. Both direct and indirect methods are available for QD-based immunohistofluorescence (QD-IHF) staining; however, the direct method has been considered laborious and costly. In this study, we optimized and compared the indirect QD-IHF single staining procedure using QD-secondary antibody conjugates and QD-streptavidin conjugates. Problems associated with sequential multiplex staining were identified quantitatively. A method using a QD cocktail solution was developed allowing simultaneous staining with three antibodies against E-cadherin, EGFR, and β -catenin in formalin-fixed and paraffin-embedded (FFPE) tissues. The expression of each biomarker was quantified and compared using the cocktail and the sequential method. Our results demonstrated that the QD signal for each multiplexed biomarker was more consistent and stable using the cocktail method than the sequential method, providing a unique tool for potential research and clinical applications.

1
2
3
4
5
6
7
8
9
10
11
12
13
14
15
16
17
18
19
20
21
22
23
24
25
26
27
28
29
30
31
32
33
34
35
36
37
38
39
40
41
42
43
44
45
46
47
48
49
50
51
52
53
54
55
56
57
58
59
60
61
62
63
64
65

1. Introduction

In recent years, nanotechnology has rapidly developed and is used in molecular detection, imaging, diagnostics, and therapeutics in the cancer field [1, 2]. Quantum dots (QDs) are nanoscale particles made from inorganic semiconductors that can produce different fluorescence signals depending on their size and components. QDs have superior signal brightness, photostability, relatively long excited-state lifetimes, and optimized signal-to-background ratios compared with organic dyes [3]. QDs can be covalently linked to biological molecules such as peptides, proteins, and nucleic acids, as well as streptavidin [4, 5]. Due to their long excitation and narrow emission spectra, QDs can be excited simultaneously through one appropriate excitation source. Together these properties render QDs ideal for multiplexed biological imaging. They have been used for both molecular and cellular labeling [3-7].

Many researchers reported that QDs can immunostain more than three biomarkers in formalin-fixed paraffin-embedded (FFPE) tissues using QD-based immunohisto-fluorescence (QD-IHF) [8-11]. To date, several different staining procedures have been utilized, including direct and indirect staining, such as QDs linked to primary antibody and QDs linked to secondary antibody or streptavidin, respectively [9, 10, 12, 13]. Although the direct staining method (QDs linked directly to a primary antibody) is straightforward, some primary antibodies may not survive the QD conjugation process. The conformation and function of the primary antibody may be changed and its binding properties are likely altered by covalent modifications at either $-NH_2$ or $-COOH$ sites [9, 14]. Furthermore, the reagent costs are considerable because each conjugation reaction requires up to 300 μ g antibody (Invitrogen protocol) and the yield of QD-antibody-conjugates is usually low. Since each primary antibody is covalently conjugated to just one type of QD, changing antibody for a certain QD probe is not possible once the conjugation is completed. Many researchers have abandoned the direct staining method since these problems can be avoided by indirect QD staining methods.

The main advantages of indirect QD staining are its flexibility, lower costs, and the reduced constraints on primary antibodies. Although many studies have described detailed protocols for tissue specimen preparation, multicolor QD staining, and image

1
2
3
4 processing [8, 9, 15], they did not provide detailed discussion and quantitative analysis in
5 optimizing their multiplexed biomarker staining procedures. In this study, we compared
6 multiple QD staining in a sequential order with that in a simultaneous combination while
7 using different methods, QD-secondary antibody conjugates and QD-streptavidin
8 conjugates, and quantitatively evaluated these staining methods for each of the tested
9 biomarkers.

16 2. Materials and methods

19 2.1. Materials.

22 Mouse anti-human E-cadherin (E-cad) was purchased from BD Biosciences
23 (Franklin Lakes, NJ, USA), rabbit anti-human epidermal growth factor receptor (EGFR)
24 was from BioGenex (San Ramon, CA, USA), and goat anti-human β -catenin was from
25 R&D Systems (Minneapolis, MN, USA). All of the primary antibodies were diluted with
26 antibody diluents (Dako, Carpinteria, CA, USA). QD-secondary antibody conjugates
27 (*QD-2nd Ab*) and QD-streptavidin conjugates (*QD-streptavidin*): Qdots[®] 565 goat F(ab')₂
28 anti-mouse IgG conjugates, Qdots[®] 605 goat F(ab')₂ anti-rabbit IgG conjugates, Qdots[®]
29 655 rabbit F(ab')₂ anti-goat IgG conjugates, and Qdots[®] streptavidin conjugates (565,605,
30 655nm) were bought from Invitrogen (Carlsbad, CA, USA) and diluted with 6% bovine
31 serum albumin (BSA) (Sigma, St. Louis, MO) in phosphate buffered saline (PBS).
32 Ready-to-use biotinylated goat anti-mouse/rabbit/goat IgG (biotinylated 2nd Ab) was
33 obtained from Vector Laboratories (Burlingame, CA, USA). Spectrofluoremeter was
34 from QuantaMaster™ UV VIS, Photon Technology International (PTI).

47 2.2. Human tissue samples.

50 Using an Institutional Review Board-approved consent for tissue acquisition,
51 specimens for this study were obtained from surgical specimens from patients who were
52 diagnosed at Emory University Hospital with squamous cell carcinoma of the head and
53 neck (SCCHN), whose initial treatment was surgery, and who had not received prior
54 treatment with radiation and/or chemotherapy. The clinical information on the samples
55 was obtained from the surgical pathology files in the Department of Pathology at Emory
56
57
58
59
60
61
62
63
64
65

1
2
3
4 University according to the regulations of the Health Insurance Portability and
5 Accountability Act. After a routine process to generate formalin-fixed, paraffin-
6 embedded (FFPE) samples, the blocks were sectioned to 4 μm each and mounted on
7 coated slides. Each sample was analyzed by a pathologist after hematoxylin and eosin
8 (H&E) staining.
9

14 2.3. *Single QD-IHF staining with QD-2nd Ab or QD-streptavidin.*

17 Before QD-IHF staining, we confirmed the primary antibodies were suitable for IHC
18 and selected FFPE samples which were strongly positive for staining of the primary
19 antibodies as positive control slides. Then, dilution and incubation conditions for the
20 primary antibody and QD-conjugates were optimized by quantification for QD-IHF
21 staining. (1) The QD-IHF procedure with QD-2nd Ab was briefly as follows (shown in
22 cartoon in Fig. 1A). After deparaffinization and rehydration, antigen retrieval was
23 performed using citric acid (10 mM, pH6.0) in microwave at 95 °C for 10 min. The tissue
24 slides were blocked with 5% normal goat serum (Dako) for 10 min before the primary
25 antibody incubation (E-cad 1: 2,000 dilution, EGFR 1:150 dilution, or β -catenin 1:2,000
26 dilution) for 1 hour at 37°C. Followed by three washes with PBS (5 min each), the slides
27 were incubated with QD [QD 565 goat F(ab')₂ anti-mouse IgG conjugates, QD 605 goat
28 F(ab')₂ anti-rabbit IgG conjugates, or QD 655 rabbit F(ab')₂ anti-goat IgG conjugates
29 accordingly] in 6% BSA for 1 hour at 37°C. After washing with PBS 3 times, the nuclei
30 were counterstained with 4',6-diamidino-2-phenylindole (DAPI) (Invitrogen, Carlsbad,
31 CA, USA). The slides were mounted with CytosealTM 60 mounting medium (Richard-
32 Allan Scientific, MI). (2) For QD-IHF staining with QD-streptavidin (shown in cartoon in
33 Fig. 1B), slides were prepared as above. After the primary antibody incubation, slides
34 were incubated with biotinylated 2nd Ab for 20 min at room temperature (RT), and
35 washed 3 times with PBS (5 min). Slides were incubated with QD 565, QD 605, or QD
36 655-streptavidin (1:100) in 6% BSA for 1 hour at 37°C and washed with PBS (5 min) for
37 3 times. After nuclei counterstaining and mounting, the slides were kept in the dark at
38
39
40
41
42
43
44
45
46
47
48
49
50
51
52
53
54
55
56
57
58
59
60
61
62
63
64
65

1
2
3
4
5 4°C for visualizing and quantifying. Mouse, rabbit or goat IgG was used as a negative
6
7 control.

8
9
10 2.4. *Sequential QD-IHF staining with QD-streptavidin.*

11
12
13 Slide selection and preparation were the same as for single QD-IHF staining.
14 Primary antibodies used for sequential staining were as described above. After the
15 primary antibody E-cad incubation (1:2,000 dilution), the slides were incubated with the
16 biotinylated 2nd Ab for 20 min at RT and washed 3 times with PBS (5 min each). Slides
17 were then incubated with QD 565-streptavidin (1:100) in 6% BSA for 1 hour at 37°C and
18 washed with PBS (5 min each) 3 times. After staining the first biomarker with QDs, the
19 staining procedure was repeated from the blocking step, except the primary antibody and
20 QD conjugates were replaced with EGFR (1:150) and QD 605-streptavidin (1:100),
21 respectively. Then the slides were mounted after nuclear counterstaining. For QD signal
22 comparison, we also switched the staining sequence from EGFR with QD 565-
23 streptavidin staining as the first step to E-cad with QD 605-streptavidin staining as the
24 second. Mouse and rabbit IgG was used as a negative control.
25
26
27
28
29
30
31
32
33
34
35
36

37 2.5. *Multiple QD-IHF staining with cocktail or sequential method.*

38
39
40 Before QD-IHF staining, slide selection was confirmed as strongly positive for E-
41 cad, EGFR, and β -catenin expression. (1) For the cocktail staining method (shown in
42 cartoon in Fig. 4A(i)), we chose primary antibodies of distinct species origins, including
43 mouse anti-human E-cad, rabbit anti-human EGFR, and goat anti-human β -catenin.
44 Therefore, for QD-2nd Abs, we selected QD 565 goat F(ab')₂ anti-mouse IgG, QD 605
45 goat F(ab')₂ anti-rabbit IgG, and QD 655 rabbit F(ab')₂ anti-goat IgG, respectively. After
46 preparation steps, the slides were incubated with the three primary antibodies against E-
47 cad (1:2,000), EGFR (1:150), and β -catenin (1:2,000) simultaneously for 1 hour at 37°C.
48 After washing with PBS 3 times, the three QD-2nd Abs in a cocktail solution at 1:100
49 dilution were added to the slides with further incubation for 1 hour at 37°C. Slides were
50
51
52
53
54
55
56
57
58
59
60
61
62
63
64
65

1
2
3
4 washed 3 times in PBS, counterstained, mounted, and stored as described above. (2) For
5
6 the sequential method (shown in cartoon in Fig. 4A(ii)), the additional biomarker β -
7
8 catenin was stained by incubation with QD 655-streptavidin following staining for E-cad
9
10 with QD 565-streptavidin and EGFR with QD 605-streptavidin as above. The IgG with
11
12 the same host species as the 2nd Ab was used as a negative control.
13

14 2.6. *QD spectral imaging and signal quantification.*

15
16
17 An Olympus Microscope IX71 with CRi Nuance spectral imaging and quantifying
18
19 system (CRi Inc., Woburn, MA) was used to observe and quantify the QD signals. All
20
21 cubed image files were collected from the FFPE tissue slides at 10-nm wavelength
22
23 intervals from 500 to 800 nm with an auto exposure time at 200 \times magnification. Taking
24
25 the cube with a long wavelength bandpass filter allowed transmission of all emission
26
27 wavelengths above 450 nm. Both mixed and separated QD images were established after
28
29 determining the QD spectral library and unmixing the cube. Background and auto-
30
31 fluorescence were removed for accurate quantification of each QD signal. For
32
33 comparison of the QD signals, we defined the measurement threshold as the same. An
34
35 arbitrary unit (a.u.) was defined as the average fluorescence signal intensity per exposure
36
37 time (ms), which was obtained directly from the Nuance software. Ten randomly selected
38
39 fields in each sample slide were used for quantification. Data are presented as a mean of
40
41 ten readings with standard deviation (SD).

42 3. Results

43 3.1. *Optimization of QD-IHF single staining conditions*

44
45
46 The quantification results were used to evaluate the optimized working conditions. It
47
48 was found that (1) the same antigen retrieval method as used in IHC also performed well
49
50 in QD-IHF staining of FFPE samples; (2) the optimized working conditions for primary
51
52 antibodies in IHC also worked well for QD-IHF; (3) incubation of the QD-conjugates
53
54 from Invitrogen at 10-20nM, 37 $^{\circ}$ C for 1 hour was sufficient to reach a balance of the
55
56 maximum staining effect with minimized non-specific binding. Non-specific binding
57
58
59
60
61
62
63
64
65

1
2
3
4 increased when enhancing the concentration and the incubation time of QD-conjugates.
5
6 There was almost no significant difference in the intensity of QD signal when the
7
8 concentration of QD-conjugates reached 20nM, but the non-specific binding increased
9
10 directly (data not shown), suggesting that the QD binding was saturated at 20nM; (4)
11
12 multiple PBS washing up to three times did not reduce the QD signal intensity. The
13
14 effects of other washing buffers, such as PBS with Tween-20 (PBS-T) or Tris-buffered
15
16 saline with Tween-20 (TBS-T), were similar to that of PBS.
17

18 3.2. *Comparison of QD-IHF single staining with QD-2nd Ab or QD-streptavidin*

19
20
21 For indirect QD-IHF staining of FFPE tissues, either QD-2nd Ab or QD-streptavidin
22
23 (Fig. 1A, B) can be selected. To evaluate these two methods, we compared the signals
24
25 when using the same concentration and incubation time for both QD conjugates. It was
26
27 found that the signal when staining with QD-2nd Ab was lower than that with QD-
28
29 streptavidin (Fig. 1C, D). The quantification results also showed that the average
30
31 intensity from QD-streptavidin staining was 1.36-1.73-fold greater than that from QD-2nd
32
33 Ab staining (Fig. 1E).
34

35 3.3. *Comparison of QD signals at different steps in QD-IHF sequential staining*

36
37
38 To investigate whether the intensity of the QD signal at the first step changes or not
39
40 after the following biomarker staining and many washing steps, we initially tested
41
42 sequential QD-IHF staining of E-cad with QD565-streptavidin followed by EGFR with
43
44 QD605-streptavidin, and then altered this sequence. The staining signals from the two
45
46 experiments were quantified and compared. It was found that the QD intensity of E-cad
47
48 staining when stained first was 0.104 ± 0.050 compared with 0.534 ± 0.132 when stained
49
50 second (Fig. 2). Similarly, the intensity of EGFR staining when stained first was
51
52 0.189 ± 0.104 compared with 0.565 ± 0.098 when stained second (Fig. 2).
53

54 3.4. *Comparison of QD-IHF cocktail method with the sequential method*

55
56
57 In order to avoid the decrease in signal observed with sequential staining, we applied
58
59 three mixed primary antibodies with distinct species origins to the tissue slides and then
60
61
62
63
64
65

1
2
3
4 incubated the relevant QD 2nd-Abs in a cocktail solution in order to make the IHF
5 staining efficient and simple [Fig. 3A(i)]. The level of each QD signal obtained from the
6 cocktail method was quantified and compared to that from the sequential method. It was
7 found that each of the QD signals obtained by the QD-IHF cocktail method was
8 consistent (Fig. 3B). The intensities of E-cad, EGFR and β -catenin were 0.318 ± 0.015 ,
9 0.309 ± 0.034 , and 0.362 ± 0.036 , respectively (Fig. 3D). In contrast, the signals from the
10 sequential staining method were not consistent (Fig. 3C). Intensities of the second and the
11 third signals were 1.57-2.20– and 5.80-8.24–fold higher than the first signal, respectively
12 (Fig. 3D).
13
14
15
16
17
18
19
20
21

22 3.5. *Stability of each QD in the cocktail solution*

23
24
25 As recommended by the QD manufacturer, Invitrogen Cooperation, we diluted the
26 three QDs with 6% BSA in PBS solution, and tested the signal intensity of the QDs either
27 singly or in a cocktail solution using a spectrofluorometer. Our study confirmed that the
28 QD signals in PBS appeared in the expected wavelength with reasonable sensitivity (Fig.
29 4). The fluorescence intensity of each QD was not altered in the cocktail solution
30 compared to the single QD solution (Fig. 4). Furthermore, our study has demonstrated
31 that the intensity of each single QDs at the same concentration was different – in the
32 order of QD 655 > QD 605 > QD 565 (Fig. 4).
33
34
35
36
37
38
39
40

41 4. Discussion

42
43
44 The antigen retrieval method, dilution, and incubation condition of the antibody are
45 the main factors that affect the results of immunostaining FFPE tissues. There are several
46 issues that should be addressed before immunostaining with QD-bioconjugates: (1) Do
47 the optimized working conditions for IHC work well for QD-IHF? (2) How to control the
48 dilution ratio for QD-conjugates and the incubation conditions to obtain a balance
49 between an optimal signal and minimized non-specific binding? (3) How to optimize the
50 QD-IHF staining procedure, especially in multiple staining? Most researchers use the
51 same retrieval method and incubation conditions for primary antibodies when conducting
52 IHC and IHF stained with QDs as their experience. In this study, after evaluated
53
54
55
56
57
58
59
60
61
62
63
64
65

1
2
3
4 systematically with quantification data, it was confirmed that the same antigen retrieval
5 method, the optimized working conditions for primary antibodies in IHC also worked
6 well for QD-IHF. For QD-conjugates from Invitrogen, the best concentration is at 10-
7 20nM. And for washing buffers, there is no difference between PBS, PBS-T, and TBS-T.
8
9

10
11 Either QD-2nd Ab conjugates or QD-streptavidin conjugates can be selected for
12 indirect QD-IHF staining. Although many studies have described detailed protocols [8, 9,
13 15], they did not provide detailed quantitative analysis to compare these two methods. It
14 was found that the signal when staining with QD-2nd Ab was lower than that with QD-
15 streptavidin at the same concentration and incubation time for both QD conjugates. The
16 staining with QD-streptavidin had some amplification effect. These finding is similar
17 with others reports.
18
19

20
21 For multiplex QD staining, the sequential staining method is used by most
22 researchers [8, 12]. Many researchers had this question -- how about the staining effect of
23 each QD? It was found that the QD intensity when stained first was lower than the signal
24 when stained second. This result indicated that after the initial biomarker staining,
25 following the second blocking and washing steps, the intensity of the first QD signal was
26 reduced. These problems should be considered for multiplex QD staining with sequential
27 method. In order to achieve the best staining of each biomarker using the QD-IHF
28 sequential method, theoretically, the QD with higher intensity is recommended to be used
29 at the first step to balance the decreasing signal when staining with QD-IHF in a
30 sequential manner.
31
32

33
34 In order to avoid this problem in sequential staining, we investigated a new method -
35 - selected three primary antibodies with distinct species origins and incubated
36 simultaneously to the tissue slides, and then incubated the relevant QD 2nd-Abs
37 conjugates in a cocktail solution. It was named QD-IHF cocktail method. After quantified
38 and compared with the sequential method, it was found that each of the QD signals
39 obtained by the QD-IHF cocktail method was consistent, not like sequential method.
40
41

42
43 Because the properties of nanocrystals are highly dependent on the surface
44 environment, it is always a consideration whether the stability with respect to the optical
45 emission peak maximum and color purity of the QDs in such a cocktail solution may be
46 changed. After testing with a spectrofluorometer, it was confirmed that the fluorescence
47
48
49
50
51
52
53
54
55
56
57
58
59
60
61
62
63
64
65

1
2
3
4 intensity of each QD was not altered in the cocktail solution compared to the single QD
5
6 solution.

7
8 But one of the drawbacks of the cocktail method is that it can be challenging to find
9
10 more than 4 primary antibodies with distinct species origins for simultaneous IHF
11
12 staining, which limits the use of this method to for more than 4 biomarkers. In the case of
13
14 multiplexing more than 4 biomarkers, the cocktail plus the sequential method may be
15
16 applied.

17 18 **5. Conclusion**

19
20
21 In summary, we demonstrated that the signal intensities using the QD-streptavidin-
22
23 based staining method were higher than those with QD-2nd Ab. QD staining signals using
24
25 the cocktail method were more consistent and stable than those obtained using the
26
27 sequential method. In order to achieve the optimal signal for each biomarker in a QD-IHF
28
29 multiplexed staining procedure, the staining method selection and QD intensity should be
30
31 considered.

32 33 **Acknowledgements**

34
35
36 This study was supported by DOD Grant W81XWH-07-1-0306 Project 5 and GCC
37
38 Distinguished Scholar Award. We thank Dr. Ximei Qian for testing QD fluorescence
39
40 intensity and Dr. Anthea Hammond for her critical reading of the manuscript.
41
42
43
44
45
46
47
48
49
50
51
52
53
54
55
56
57
58
59
60
61
62
63
64
65

1
2
3
4 **References**
5

- 6 1. Ferrari M. Cancer nanotechnology: opportunities and challenges. *Nature reviews*
7 2005;5(3):161-171.
- 8 2. Nie S, Xing Y, Kim GJ, Simons JW. Nanotechnology applications in cancer.
9 *Annual review of biomedical engineering* 2007;9:257-288.
- 10 3. Smith AM, Gao X, Nie S. Quantum dot nanocrystals for in vivo molecular and
11 cellular imaging. *Photochemistry and photobiology* 2004;80(3):377-385.
- 12 4. Whaley SR, English DS, Hu EL, Barbara PF, Belcher AM. Selection of peptides
13 with semiconductor binding specificity for directed nanocrystal assembly. *Nature*
14 2000;405(6787):665-668.
- 15 5. Chan WC, Nie S. Quantum dot bioconjugates for ultrasensitive nonisotopic
16 detection. *Science (New York, NY)* 1998;281(5385):2016-2018.
- 17 6. Wu X, Liu H, Liu J, Haley KN, Treadway JA, Larson JP, et al.
18 Immunofluorescent labeling of cancer marker Her2 and other cellular targets with
19 semiconductor quantum dots. *Nature biotechnology* 2003;21(1):41-46.
- 20 7. Gao X. Multifunctional quantum dots for cellular and molecular imaging. *Conf*
21 *Proc IEEE Eng Med Biol Soc* 2007;2007:524-525.
- 22 8. Sweeney E, Ward TH, Gray N, Womack C, Jayson G, Hughes A, et al.
23 Quantitative multiplexed quantum dot immunohistochemistry. *Biochemical and*
24 *biophysical research communications* 2008;374(2):181-186.
- 25 9. Xing Y, Chaudry Q, Shen C, Kong KY, Zhau HE, Chung LW, et al.
26 Bioconjugated quantum dots for multiplexed and quantitative immunohistochemistry.
27 *Nature protocols* 2007;2(5):1152-1165.
- 28 10. Fountaine TJ, Wincovitch SM, Geho DH, Garfield SH, Pittaluga S. Multispectral
29 imaging of clinically relevant cellular targets in tonsil and lymphoid tissue using
30 semiconductor quantum dots. *Mod Pathol* 2006;19(9):1181-1191.
- 31 11. True LD, Gao X. Quantum dots for molecular pathology: their time has arrived. *J*
32 *Mol Diagn* 2007;9(1):7-11.
- 33 12. Shi C, Zhou G, Zhu Y, Su Y, Cheng T, Zhau HE, et al. Quantum dots-based
34 multiplexed immunohistochemistry of protein expression in human prostate cancer cells.
35 *Eur J Histochem* 2008;52(2):127-134.
- 36 13. Yang D, Chen Q, Wang W, Xu S. Direct and indirect immunolabelling of HeLa
37 cells with quantum dots. *Luminescence* 2008;23(3):169-174.
- 38 14. Resch-Genger U, Grabolle M, Cavaliere-Jaricot S, Nitschke R, Nann T. Quantum
39 dots versus organic dyes as fluorescent labels. *Nature methods* 2008;5(9):763-775.
- 40 15. Tholouli E, Sweeney E, Barrow E, Clay V, Hoyland JA, Byers RJ. Quantum dots
41 light up pathology. *The Journal of pathology* 2008;216(3):275-285.
- 42
- 43
- 44
- 45
- 46
- 47
- 48
- 49
- 50
- 51
- 52
- 53
- 54
- 55
- 56
- 57
- 58
- 59
- 60
- 61
- 62
- 63
- 64
- 65

Figure Legends

Fig. 1 Comparison of single QD-IHF staining using QD-2nd Ab with QD-streptavidin. *A.* Cartoon showing single QD-IHF staining with QD-2nd Ab conjugates; *B.* Cartoon showing single QD-IHF staining with QD-streptavidin conjugates; *C.* RGB image of E-cad QD-IHF staining with QD 565-2nd Ab; *D.* RGB image of E-cad QD-IHF staining with QD 565-streptavidin; *E.* Signal intensity comparison between QD-2nd Ab and QD-streptavidin.

Fig. 2 Comparison of the first signal with the second signal in a sequential QD-IHF staining. *A.* E-cad with QD 565-streptavidin as the first biomarker and EGFR with QD 605-streptavidin as the second; *B.* EGFR with QD 605-streptavidin as the first biomarker and E-cad with QD 565-streptavidin as the second; *(i)* unmixed first signal; *(ii)* unmixed second signal; *(iii)* quantification comparison between these two biomarkers.

Fig. 3 Comparison of the QD-IHF cocktail method with the sequential method. *A(i).* Cartoon showing cocktail QD-IHF staining with QD-2nd Ab conjugates, “1” illustrates the addition of different QDs simultaneously; *A(ii).* Cartoon showing sequential QD-IHF staining with QD-streptavidin conjugates, “1, 2, 3” represent the addition of QDs at different steps; *B.* Cocktail QD-IHF staining of E-cad+EGFR+ β -catenin with QD 565+605+655 2nd Ab-conjugates; *C.* Sequential QD-IHF staining of E-cad, EGFR, and β -catenin with QD 565-, 605- and 655-streptavidin conjugates respectively; *(i)* unmixed E-cad (QD 565) signal; *(ii)* unmixed EGFR (QD 605) signal; *(iii)* unmixed β -catenin (QD 655) signal; *D.* Quantified signal comparison between these two methods.

Fig. 4 Comparison of QD fluorescence intensity in single QD or cocktail PBS solutions. Fluorescence intensity of each of the three QDs was detected by QuantaMaster™ UV VIS, (Photon Technology International, Birmingham, NJ).

Fig. 1

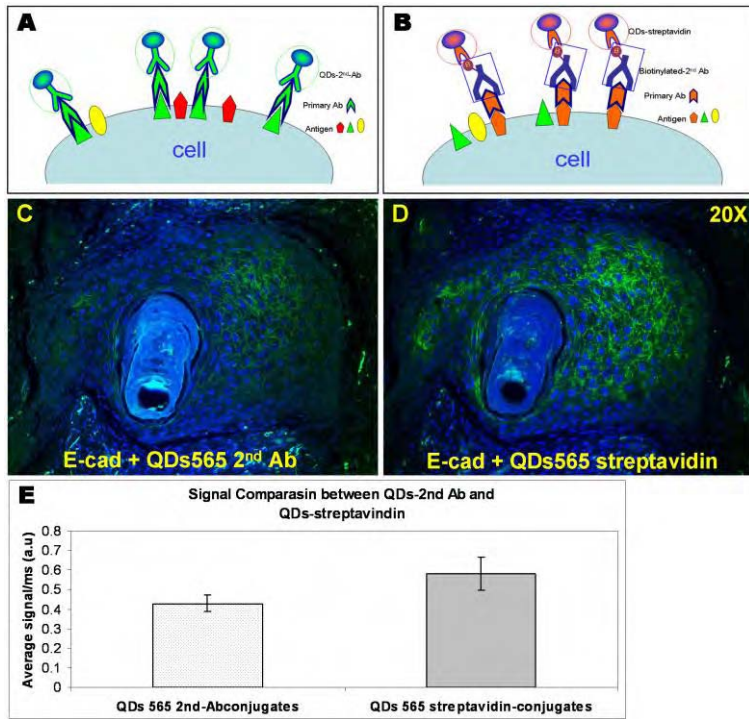


Fig. 2

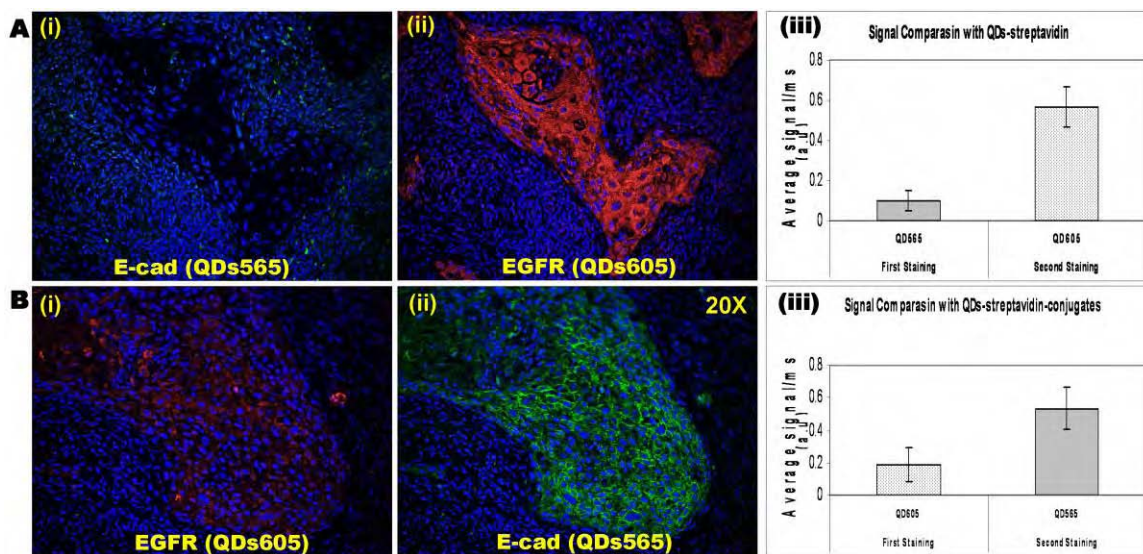


Fig. 3

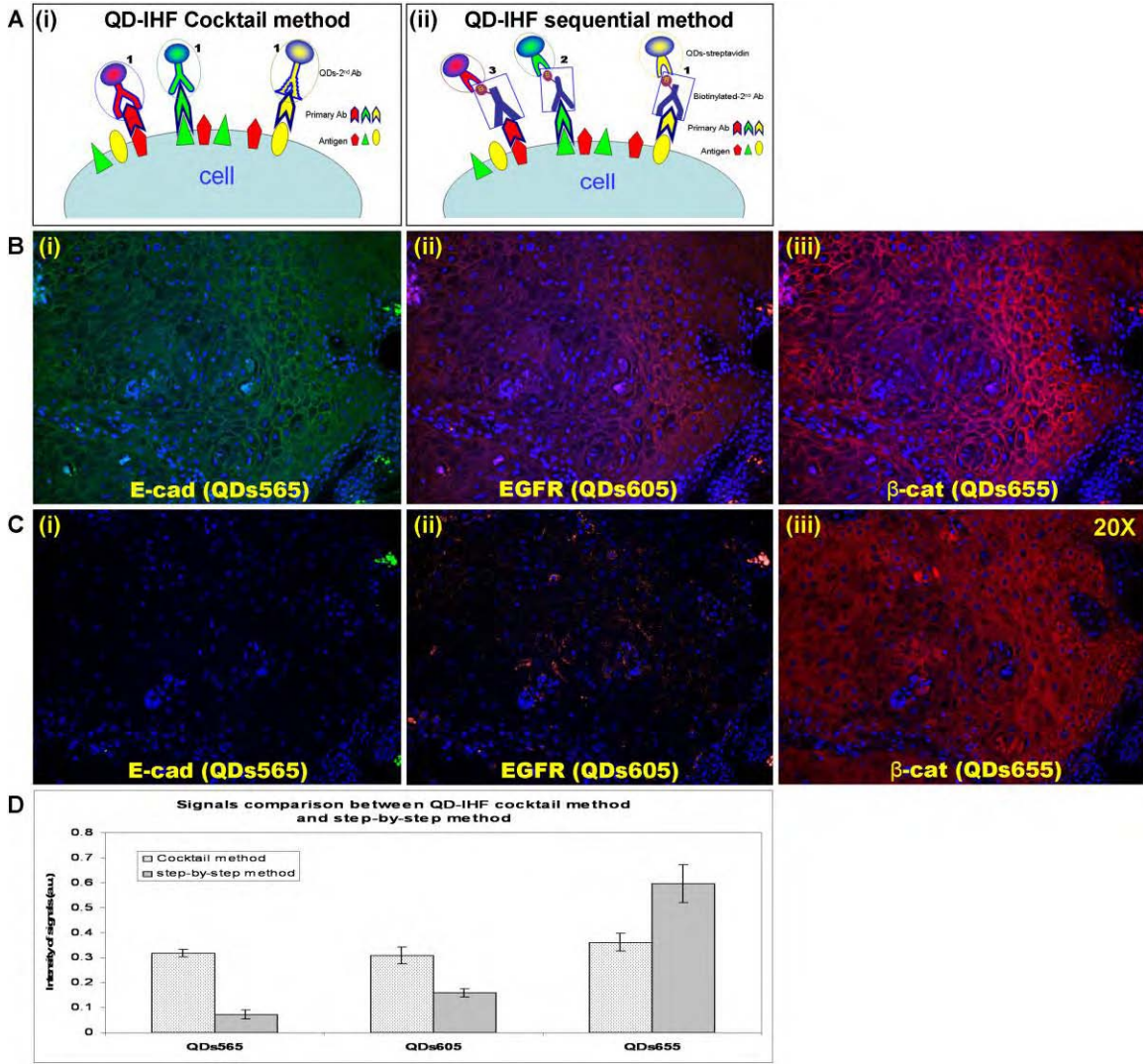
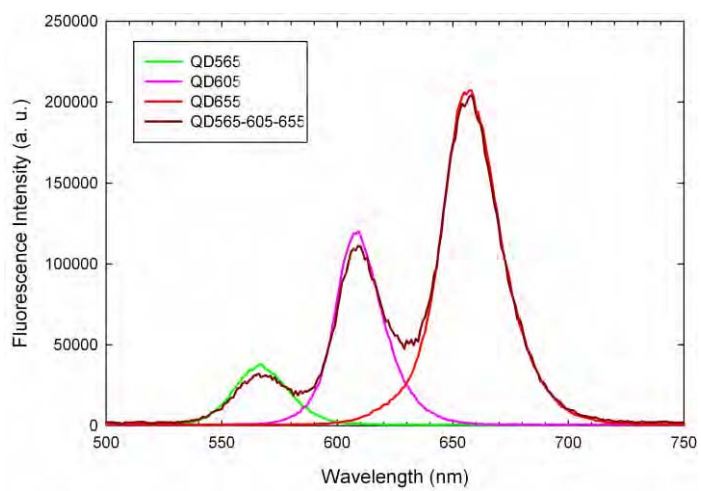


Fig. 4



CXCL12 and its receptors CXCR4 and CXCR7 as potential molecular targets for lung cancer

Journal:	<i>Genes, Chromosomes and Cancer</i>
Manuscript ID:	draft
Wiley - Manuscript type:	Research Article
Keywords:	lung cancer, therapeutic molecular target, CXCL12, CXCR4, CXCR7



P
er Review

1
2
3
4
5
6 **CXCL12 and its receptors CXCR4 and CXCR7 as potential molecular targets for**
7 **lung cancer**
8
9

10
11
12
13 **Hisao Imai¹, Noriaki Sunaga^{*1}, Yasuo Shimizu¹, Noriko Yanagitani¹, Kyoichi**
14 **Kaira¹, Yoshio Tomizawa², Tamotsu Ishizuka¹, Ryusei Saito², John D Minna³ and**
15 **Masatomo Mori¹**
16
17

18
19
20 ¹Department of Medicine and Molecular Science, Gunma University Graduate School
21 of Medicine, 3-39-15 Showa-machi, Maebashi, Gunma 371-8511, Japan
22
23

24
25 ²Department of Respiratory Medicine, National Nishigunma Hospital, 2854 Kanai,
26 Shibukawa, Gunma 377-8511, Japan
27
28

29
30 ³Hamon Center for Therapeutic Oncology Research, University of Texas Southwestern
31 Medical Center at Dallas, 6000 Harry Hines Blvd., Dallas, Texas 75390-8593, USA
32
33

34
35
36 *Correspondence to: Noriaki Sunaga, M.D., Department of Medicine and Molecular
37 Science, Gunma University Graduate School of Medicine, 3-39-15 Showa-machi,
38 Maebashi, Gunma 371-8511, Japan
39
40

41
42
43 Tel: 81-27-220-8136, Fax: 81-27-220-8136
44

45
46 E-mail address: nsunaga@showa.gunma-u.ac.jp
47
48
49

50 **Running title:** Role of CXCL12 in lung cancer.
51

52 **Key words:** CXCL12, CXCR4, CXCR7, lung cancer, therapeutic molecular target.
53

54 **Abbreviations used are:** SCLC, small cell lung cancer; NSCLC, non-small cell lung
55 cancer; RNA interference, RNAi; siRNA, small interfering RNA.
56
57
58
59
60

ABSTRACT

The interaction between the chemokine CXCL12 and the two receptors, CXCR4 and CXCR7, is thought to play a role in tumor growth and metastasis in human cancers. However, the expression of CXCL12, CXCR4 and CXCR7 and their role in lung cancer is not fully elucidated. Here we examined the expression of CXCL12, CXCR4 and CXCR7 in 23 small cell lung cancer (SCLC) cell lines and 32 non-small cell lung cancer (NSCLC) cell lines. CXCL12, CXCR4 and CXCR7 were overexpressed in lung cancer cell lines compared with human non-malignant lung epithelial cells (N=6). CXCR4 levels were significantly higher in SCLCs than those in NSCLCs, while there were no differences in the levels of both CXCL12 and CXCR7 between SCLCs and NSCLCs. Frequencies of CXCL12, CXCR4 and CXCR7 overexpression were 45%, 80% and 16%, respectively, and CXCL12 expression was positively associated with expression of CXCR4 and CXCR7. RNA interference-mediated CXCL12 knockdown inhibited cell growth and migration in a CXCL12-overexpressing lung cancer cells, and the effect involved inactivation of the MEK-ERK pathway. Furthermore, treatment with an anti-CXCL12 neutralizing antibody inhibited cell growth in four of CXCL12-overexpressing lung cancer cell lines but not in CXCL12 non-expressing lines. The results demonstrate that: CXCL12, CXCR4 and CXCR7 are concomitantly overexpressed in lung cancers; CXCR4 is abundantly expressed in SCLCs compared with NSCLCs; and that CXCL12 is required for lung cancer cell growth and migration via the MEK-ERK signaling pathway. Thus, inhibition of CXCL12 activity could be a novel therapeutic approach in lung cancer.

INTRODUCTION

Lung cancer is the leading cause of cancer-related death in U.S (Jemal, et al. 2007) and worldwide. Lung cancer is divided into two major histological types: small cell lung cancer (SCLC) and non-small cell lung cancer (NSCLC). Despite improvements in therapy, most patients with lung cancer will die, in most cases from metastatic disease (Minna, et al. 2002). Accordingly, there is a major need for identification of novel therapeutic targets and elucidating mechanisms of growth and metastasis in lung cancer.

Chemokines, structurally related, small (8-14kDa) polypeptide signaling molecules, bind to and activate seven-transmembrane G-protein-coupled chemokine receptors (Murphy 1996). Chemokines are expressed by many tumor types and are implicated in tumor cell growth, invasion, and metastasis (Balkwill 2004). Chemokine (C-X-C motif) ligand 12 (CXCL12)/stromal cell-derived factor 1 (SDF-1), a 10kDa secreted protein, is a homeostatic chemokine that signals through chemokine (C-X-C motif) receptor 4 (CXCR4), a G protein-coupled receptor, which in turn plays a role in hematopoiesis, development, and organization of the immune system (Kryczek, et al. 2007). The interaction between CXCL12 and CXCR4 is implicated in cell proliferation, migration, adhesion, angiogenesis, and metastasis in many cancers including breast, lung, ovary, pancreas, prostate, neuroblastoma, hepatic cell carcinomas (Geminder, et al. 2001; Kryczek, et al. 2005; Mochizuki, et al. 2004; Mori, et al. 2004; Muller, et al. 2001; Phillips, et al. 2003; Sutton, et al. 2007; Tang, et al. 2007). Recently, CXCR7/RDC1 was identified as a second receptor for CXCL12 (Balabanian, et al. 2005) and may function in regulating growth of breast, lung and prostate cancers (Miao, et al. 2007; Wang, et al. 2008). However, of how CXCL12 with its receptors, CXCR4 and CXCR7, play a role in the development of lung cancer is unknown.

1
2
3
4
5
6
7
8
9
10
11
12
13
14
15
16
17
18
19
20
21
22
23
24
25
26
27
28
29
30
31
32
33
34
35
36
37
38
39
40
41
42
43
44
45
46
47
48
49
50
51
52
53
54
55
56
57
58
59
60

In the present study, we found that CXCL12, CXCR4 and CXCR7 were overexpressed in lung cancer cell lines compared to non-malignant lung epithelial cells. CXCL12 overexpression was positively associated with the overexpression of its receptors CXCR4 and CXCR7, suggesting the concomitant expression of CXCL12 and the receptors in an autocrine manner. And RNA interference (RNAi)-mediated knockdown of CXCL12 expression in over-expressing lung cancer cells led to the inhibition of cell proliferation, colony formation and migration as well as the dephosphorylation of MEK and ERK. Furthermore, blocking CXCL12 activity with the CXCL12 neutralizing antibody could inhibit cell growth in four CXCL12-overexpressing lung cancers. These results suggest that CXCL12 could play a major role in the biologic behavior and be a new therapeutic target for lung cancer.

MATERIALS AND METHODS

Cell lines. We used 23 SCLC cell lines and 32 NSCLC cell lines, all of which were obtained from the Hamon Center collection (University of Texas Southwestern Medical Center)(Phelps, et al. 1996). Normal human bronchial epithelial cells (NHBE), small-airway epithelial (SAEC) cells and immortalized human bronchial epithelial cells (BEAS-2B, HBEC1, HBEC3 and HBEC4) were used as non-tumor lung controls. NHBE and SAEC were obtained from Clonetics (San Diego, CA), and BEAS-2B was obtained from ATCC. HBEC1, HBEC3, and HBEC4 cells were recently generated by the authors (Ramirez, et al. 2004). Cancer cells were cultured with RPMI 1640 with 5% fetal bovine serum, and human bronchial epithelial cells were cultured with Keratinocyte-SFM (Invitrogen, Carlsbad, CA) medium containing 25 µg/mL bovine pituitary extract (Invitrogen) and 5 ng/mL epidermal growth factor (Invitrogen).

Quantitative real-time RT-PCR. The expression of the *CXCL12*, *CXCR4* and *CXCR7* genes was examined by quantitative real-time RT-PCR as previously described (Suzuki, et al. 2004). Briefly, total RNA was extracted using the RNeasy mini kit (Qiagen, Valencia, CA), and cDNA was synthesized using 2 µg of total RNA with the SuperScript II First-Strand Synthesis using oligo (dT) primer system (Invitrogen) according to the manufacturer's instructions. Primers and probes for *CXCL12*, *CXCR4* and *CXCR7* were purchased from Applied Biosystems (Tokyo, Japan). For the quantitative analysis, the *TBP* gene was used as an internal reference gene to normalize input cDNA. PCR was performed in a reaction volume of 20 µl, including 2 µl cDNA using the Gene Amp 7700 Sequence Detection System and software (Applied Biosystems). The comparative Ct method was used to compute relative expression

1
2
3
4
5
6 values. The cutoff value of mean plus 3 SD of non-tumor lung cell lines (N=6) was
7
8 used to define overexpression.
9

10
11 **Preparation and transfection of synthetic small interfering RNA (siRNA).** Two
12
13 siRNAs were used that target different sites of *CXCL12* mRNA, which were purchased
14
15 from Dharmacon Inc (Lafayette, CO). A siRNA against Tax (the human leukemia
16
17 virus gene) was used as a negative control (Sunaga, et al. 2004). siRNAs were
18
19 transfected into cells by using Oligofectamine transfection reagent (Invitrogen) as a
20
21 previously described method (Sunaga, et al. 2004) and after 72 h, cells were harvested
22
23 for further analysis.
24
25
26
27

28
29 **MTT assay.** Cell viability was measured using the 3-(4,5
30
31 dimethylthiazol-2yl)-2,5-diphenyl-tetrazolium bromide (MTT) Cell Growth Assay Kit
32
33 (Chemicon International, Temecula, CA) according to the manufacturer's protocol.
34
35 Twenty-four hr after transfection with siRNAs, trypan blue-negative viable cells were
36
37 re-plated and cultured in 96-well plates in replicates of 8. After 72 h, cells were then
38
39 incubated with 0.5 mg/ml MTT for 4 hr at 37°C. After MTT withdrawal, the resulting
40
41 blue formazan cristae were solubilized, and absorbance was read at 570/630nm using a
42
43 microtiter plate reader. As for the CXCL12 neutralizing assay, cells were treated with
44
45 3 µg/ml of the anti-human CXCL12/SDF-1 antibody (R&D Systems, Minneapolis, MN)
46
47 or 3 µg/ml of the IgG1 isotype control antibody (R&D Systems) and MTT assay was
48
49 performed after 72 h.
50
51
52
53
54

55
56 **Colony formation assay.** The *in vitro* growth characteristics were tested by a colony
57
58 formation assay (Sunaga, et al. 2004). Briefly, after 48 h of siRNA transfection, cells
59
60 were harvested, and 500 of trypan blue-negative viable cells were re-plated in each well

1
2
3
4
5
6 of 6-well plates. The cells were cultured in RPMI1640 supplemented with 5% serum,
7
8 and surviving colonies were counted 14 days later after staining with methylene blue.
9

10
11 **Migration assay.** Cell migration was measured in a modified Boyden chamber as
12 previously described (Yokomizo, et al. 1997). Briefly, polycarbonate filters with 8 μm
13 pores (Neuroprobe, Gaithersburg, MD) were coated with 100 $\mu\text{g}/\text{ml}$ of collagen (Elastin
14 Products Company, Owensville, MO) in 0.5 M acetic acid for 16 h. The coated filter
15 was then placed on a 12-blind-well chemotaxis chamber (Neuroprobe) containing cells
16 (10^5 cells in 100 μl per well) were loaded into the upper wells. The cells were
17 incubated for 15 min before being loaded. After incubation at 37°C in 5% CO_2 for 4 h,
18 the filter was disassembled. The upper side of the filter was then scraped free of cells.
19 The cells on the lower side of the filter were fixed with methanol and stained with a
20 Diff-Quick staining kit (International Reagent, Kobe, Japan). The number of cells that
21 migrated to the lower side of the filter was counted.
22
23
24
25
26
27
28
29
30
31
32
33
34
35
36
37
38

39 **Western Blot Analysis.** The cells were grown to 80 to 90% confluency and harvested,
40 and cellular proteins were extracted with lysis buffer (40 mM HEPES-NaOH [pH 7.4],
41 1% NP40, 0.5% sodium deoxycholate, 0.1% SDS, 150 mM NaCl) containing Complete
42 Mini, a cocktail of protease inhibitors (Roche, Indianapolis, IN). Total protein was
43 separated on a SDS-polyacrylamide gel and electroblotted to nitrocellulose membranes
44 (BIORAD, Hercules, CA). After blocking with 5% bovine serum albumin and 0.1%
45 Tween 20 in Tris-buffered saline, membranes were incubated at room temperature for 3
46 h with rabbit polyclonal anti-phospho-MEK (mitogen-activated protein
47 kinase/extracellular signal-related kinase) 1/2 (Ser217/221) (Cell Signaling, Beverly,
48 MA), rabbit polyclonal anti-phospho-p44/42 MAP Kinase (ERK; Thr202/Tyr204; Cell
49
50
51
52
53
54
55
56
57
58
59
60

1
2
3
4
5
6 Signaling), rabbit polyclonal anti- MEK1/2(Ser217/221) (Cell Signaling), rabbit
7 polyclonal anti- p44/42 MAP Kinase (p-ERK; Thr202/Tyr204) (Cell Signaling), rabbit
8 polyclonal anti-Akt (Cell Signaling) and rabbit polyclonal anti-phospho-Akt (Ser473;
9 Cell Signaling), antibodies. The membranes then were developed with horseradish
10 peroxidase linked whole antibody (GE healthcare, UK) by Super Signal
11 chemiluminescence substrate (Pierce, Rockford, IL).
12
13
14
15
16
17
18
19
20

21 **Statistical Analysis.** For comparison of gene expression levels, unpaired t test with
22 Welch's correction was used between two groups, and Kruskal-Wallis test with
23 Dunn's Multiple Comparison test was used between three groups. Fisher's exact test
24 was used to compare frequencies. One-way ANOVA with Bonferroni's posthoc test
25 was used for comparison between groups in MTT assay, colony formation assay, and
26 migration assay. All statistical analyses were performed using the GraphPad Prism
27 version 5.0 software program for Windows (GraphPad Software, San Diego, CA). *P*
28 values<0.05 were considered to be statistically significant.
29
30
31
32
33
34
35
36
37
38
39
40
41
42
43
44
45
46
47
48
49
50
51
52
53
54
55
56
57
58
59
60

RESULTS

Overexpression of CXCL12, CXCR4 and CXCR7 in lung cancer cell lines.

We first examined the expression of *CXCL12*, *CXCR4* and *CXCR7* mRNA in 55 lung cancer cell lines (32 NSCLCs and 23 SCLCs) by the quantitative real-time RT-PCR analysis. When the expression levels in lung cancers were normalized to the mean value obtained from six different non-tumor lung cell lines, the mean levels of *CXCL12*, *CXCR4* and *CXCR7* in lung cancers were 41, 1277 and 2.7, respectively. The expression levels of *CXCL12* (Fig. 1A) and *CXCR4* (Fig. 1B) were significantly higher in lung cancer cells than the non-tumor cells ($P < 0.01$ for *CXCL12*, and $P < 0.0001$ for *CXCR4*). *CXCR7* levels were also high in lung cancer cells but the difference was of borderline significance compared with the levels of the non-tumor cells ($P = 0.058$; Fig. 1C). *CXCR4* expression levels were significantly higher in SCLCs than in NSCLCs (Fig. 1E; $P < 0.001$), while there was no significant difference in the levels of *CXCL12* (Fig. 1D) or *CXCR7* (Fig. 1F) between SCLCs and NSCLCs. The results demonstrate that *CXCL12*, *CXCR4* and *CXCR7* are overexpressed in lung cancers and *CXCR4* expression is relatively abundant, especially in SCLC.

Positive association of the expression status between CXCL12 and its receptors CXCR4 and CXCR7

If overexpression was defined as more than the mean level plus 3 SD in the non-tumor lung cells, frequencies of *CXCL12*, *CXCR4* and *CXCR7* overexpression in lung cancer cell lines were 45%, 80% and 16%, respectively (Table 1). SCLCs overexpressed all of these genes with higher frequencies compared with NSCLCs, although no significant difference was observed. *CXCL12* overexpression was positively associated with the

1
2
3
4
5
6 overexpression of CXCR4 ($P=0.008$) and CXCR7 ($P=0.008$), and the presence of
7
8 overexpression of either CXCR4 or CXCR7 ($P=0.015$; Table 2), indicating the
9
10 concomitant expression of CXCL12 and its receptors, CXCR4 and CXCR7.
11
12

13 14 15 **Effect of RNAi-mediated CXCL12 knockdown on cell growth and migration in** 16 17 **lung cancer cells.** 18

19
20 Since the biological significance of CXCL12 overexpression in lung cancer is obscure,
21
22 we assessed the effect of CXCL12 gene silencing on the cell growth in
23
24 CXCL12-overexpressing lung cancer cell lines by using RNA interference (RNAi)
25
26 technology. Two siRNAs against different sites of *CXCL12* mRNA were used to
27
28 verify that the effect of CXCL12 siRNA is specific. A siRNA against the *Tax* gene was
29
30 used as a negative control (Sunaga, et al. 2004). siRNAs against CXCL12 and *Tax*
31
32 were transfected into A549 cells that overexpress CXCL12, and the effect on gene
33
34 silencing was monitored by real-time RT-PCR. Two siRNAs against CXCL12 led to a
35
36 marked reduction of *CXCL12* mRNA expression at 72 h post-transfection in comparison
37
38 to the levels in untreated cells and they both gave similar results ($P<0.01$; Fig. 2), while
39
40 the treatment with Oligofectamine or *Tax* siRNA did not significantly affect the
41
42 expression levels. Thus, RNAi-mediated knockdown of CXCL12 expression
43
44 successfully reduced the *CXCL12* mRNA level in A549 cells.
45
46
47
48
49

50
51 The effect of CXCL12 knockdown on cell proliferation of A549 cells was
52
53 examined by an MTT assay. Knockdown of CXCL12 expression led to significant
54
55 inhibition of cell proliferation in A549 cells ($P<0.0001$; Fig. 3) while the treatment with
56
57 Oligofectamine or *Tax* siRNA did not affect the cell proliferation. In H1299 NSCLC
58
59 cells that lack CXCL12 expression, the treatment with CXCL12 siRNAs as well as the
60

1
2
3
4
5
6
7 treatment with Oligofectamine or Tax siRNA did not affect cell proliferation (Fig. 3).
8
9 We further employed the colony formation assay to assess the effect of CXCL12
10 siRNAs on cell growth in A549 cells. RNAi-mediated CXCL12 knockdown
11 significantly inhibited colony formation in A549 cells ($P<0.01$; Fig. 4A, B) but not in
12 H1299 cells (Fig. 4B). These results indicate that CXCL12 is required for *in vitro* cell
13 growth in lung cancer cells that overexpress CXCL12.
14
15
16
17
18
19

20 We next examined the effect of RNAi-mediated CXCL12 knockdown on cell
21 migration in A549 cells. CXCL12 knockdown mediated resulted in a significant
22 attenuation in cell migration ($P<0.0001$; Fig. 5) while the treatment with
23 Oligofectamine or *Tax* siRNA did not inhibit the migration. The results indicate that
24 CXCL12 plays a role in migration of *CXCL12*-overexpressing lung cancer cells.
25
26
27
28
29
30
31
32
33

34 **Growth inhibition of CXCL12-overexpressing lung cancer cells by the** 35 **anti-CXCL12 neutralizing antibody.** 36 37

38 We further examined the effect of an anti-CXCL12 neutralizing antibody on cell
39 proliferation in four of CXCL12-overexpressing lung cancer cell lines A549, HCC95,
40 H1264 and H661. The CXCL12 levels of A549, HCC95, H1264 and H661 were 317,
41 557, 210 and 157, respectively, when the expression levels were normalized by the
42 mean level of the six non-tumor lung cell lines. Viable cells were significantly
43 reduced to 32% in A549, 47% in HCC95, 49% in H1264 and 32% in H661 by the
44 treatment with the CXCL12 neutralizing antibody at a concentration of 3 $\mu\text{g}/\text{ml}$ (Fig. 6;
45 $P<0.001$ in all lines) but not by the treatment with the control antibody. On the other
46 hand, the neutralization of CXCL12 did not affect cell proliferation in lung cancer cell
47 lines H1299 and H2009, in which CXCL12 expression levels were undetectable (Fig. 6).
48
49
50
51
52
53
54
55
56
57
58
59
60

1
2
3
4
5
6 These results demonstrate that blocking CXCL12 activity led to inhibition of cell
7 proliferation in CXCL12-overexpressing lung cancer cells but not in lung cancer cells
8 lacking CXCL12 expression.
9
10
11
12

13
14
15 **RNAi-mediated Knockdown of CXCL12 expression led to the inactivation of**
16 **MEK-ERK pathways.**
17

18
19 In order to elucidate mechanisms as to how CXCL12 overexpression regulated signal
20 transduction in lung cancer cells, the effect of RNAi-mediated knockdown of CXCL12
21 on phosphorylation of MEK, ERK and Akt was examined. In A549 cells,
22 RNAi-mediated CXCL12 knockdown reduced the levels of phosphorylated MEK and
23 phosphorylated ERK (Fig. 7), while CXCL12 knockdown did not affect the levels of
24 phosphorylated Akt (Fig. 7). The results suggest that cell growth in
25 CXCL12-overexpressing lung cancer cells involved in activation of the MEK-ERK
26 pathways.
27
28
29
30
31
32
33
34
35
36
37
38
39
40
41
42
43
44
45
46
47
48
49
50
51
52
53
54
55
56
57
58
59
60

DISCUSSION

Several lines of evidence have indicated that CXCL12-CXCR4 interactions plays a role in tumor growth and metastasis in lung cancer. In previous studies, CXCR4 was shown to be abundantly expressed in SCLC and CXCL12-induced activation of CXCR4 enhanced cell invasion and adhesion through integrin activation (Burger, et al. 2003; Hartmann, et al. 2005; Kijima, et al. 2002). Recently, elevated CXCR4 expression was observed in NSCLC cell lines and NSCLC tumors, and CXCR4 expression was implicated in the metastatic potential of NSCLC (Oonakahara, et al. 2004; Phillips, et al. 2003; Su, et al. 2005). Consistent with these findings, we observed CXCR4 overexpression in lung cancer cell lines. Considering that most of lung cancer cell lines we used here were established from advanced tumors with metastasis and came from the metastatic lesions (Phelps, et al. 1996), it is likely that CXCR4 overexpression is associated with high metastatic potential in lung cancer. In addition, we found that CXCR4 expression was relatively more abundant in SCLC cells versus NSCLC cells.

In contrast to the evidence available for CXCR4, there are few studies assessing the expression of CXCL12 and the recently identified receptor CXCR7 (Balabanian, et al. 2005) in lung cancers. In agreement with a previous study showing that CXCL12 was expressed in the majority of NSCLC tumors (Wald, et al. 2006), we confirmed the CXCL12 overexpression in lung cancer cell lines. On the other hand, we also found that 15 (47%) of NSCLC lines and 8 (35%) of SCLC lines exhibited lower or undetectable CXCL12 expression compared with non-tumor lung cells. A recent study by Suzuki et al. reported that CXCL12 was silenced by aberrant methylation correlated with poor prognosis in NSCLCs (Suzuki, et al. 2008). Of note, they also demonstrated that positive expression of CXCL12 was correlated with lymph

1
2
3
4
5
6 node involvement, advanced stage, and poor prognosis in NSCLC tumors. Therefore,
7
8 it is likely that CXCL12 may have opposite functions depending on the cellular context
9
10 as are other proteins (e.g. RAS (Crespo and Leon 2000) and CAV1 (Sunaga, et al.
11
12 2004)) shown to have such opposite functions. This may explain why RNAi-mediated
13
14 CXCL12 knockdown or the treatment with a CXCL12 neutralizing antibody did not
15
16 affect cell growth in CXCL12-nonexpressing NSCLC lines in the current study.
17
18 Further studies with some functional assays should be needed to elucidate whether
19
20 CXCL12 can act as a tumor suppressor in lung cancers, in which CXCL12 is silenced
21
22 by the promoter hypermethylation.
23
24
25

26
27 As for CXCR7, recent studies have reported that CXCR7 is abundantly
28
29 expressed in various types of human cancer cell lines including one NSCLC cell line
30
31 A549 (Burns, et al. 2006) and contributes to tumor development and progression in lung
32
33 and breast cancers (Miao, et al. 2007). The current results of CXCR7 overexpression
34
35 in lung cancer cells support their findings and suggest that CXCR7 as well as CXCR4
36
37 implicates in lung cancer development by interacting with CXCL12.
38
39
40

41 Chemokines display autocrine and paracrine roles related to growth and
42
43 metastasis of human cancers including lung cancer (Strieter, et al. 2004). The
44
45 autocrine CXCL12-CXCR4 system has been shown to be involved in tumor
46
47 development (Kryczek, et al. 2007; Raman, et al. 2007; Uchida, et al. 2007). In this
48
49 study, we found the concomitant expression of CXCL12 and its receptors CXCR4 and
50
51 CXCR7 in lung cancer cells, suggesting the existence of autocrine
52
53 CXCL12-CXCR4/CXCR7 system in lung cancer cells and that CXCL12 could be an
54
55 autocrine growth factor.
56
57
58

59 Reserchers have demonstrated the interaction with CXCL12 to the receptors
60

1
2
3
4
5
6 has a proliferative effect on various types of cancer cells (Darash-Yahana, et al. 2004;
7
8 Katayama, et al. 2005; Marchesi, et al. 2004; Scotton, et al. 2002; Sutton, et al. 2007)
9
10 including SCLC cells (Kijima, et al. 2002) and plays an essential role in tumor invasion
11
12 and metastasis (Balkwill 2004) as previously described that migration of lung cancer
13
14 cells was enhanced in response to CXCL12 (Phillips, et al. 2005) or by forced
15
16 expression of CXCR4 (Su, et al. 2005). Here we used RNAi methodology, a different
17
18 approach from these previous studies, in order to elucidate the function of endogenous
19
20 CXCL12 in lung cancer cells. Our findings that RNAi-mediated CXCL12 knockdown
21
22 inhibited cell proliferation, colony formation and migration in CXCL12-overexpressing
23
24 lung cancer cells suggest that CXCL12, which is expressed and secreted from cancer
25
26 cells, can act as an activator of cell proliferation and migration in lung cancer. The
27
28 results of growth inhibitory effect by CXCL12 knockdown prompted us to examine
29
30 whether a CXCL12 neutralizing antibody could inhibit cell growth in
31
32 CXCL12-overexpressing lung cancer cells. Our observation of a marked decrease in
33
34 cell viability by the anti-CXCL12 antibody indicates that the interaction of
35
36 CXCL12-CXCR4/CXCR7 might be critical for cell growth and inhibition of CXCL12
37
38 has therapeutic potential for lung cancers, in which the interaction is active. Further
39
40 studies *in vivo* will be needed to elucidate the therapeutic effectiveness of anti-CXCL12
41
42 antibody for lung cancer.
43
44
45
46
47
48
49

50 It has been reported that CXCL12 has multiple functions via regulation of
51
52 MAPK and PI3K-Akt signaling pathways (Kryczek, et al. 2007; Liang, et al. 2007;
53
54 Wang, et al. 2000). In the present study, RNAi-mediated CXCL12 knockdown
55
56 decreased phosphorylation of MEK and ERK in lung cancer cells. In agreement with
57
58 the previous studies (Arai, et al. 2006; Huang, et al. 2007; Mori, et al. 2004; Tang, et al.
59
60

1
2
3
4
5
6 2007), the current results suggest that CXCL12-CXCR4 interaction can activate
7
8 MEK-ERK signaling pathway, which in turn promotes cell proliferation and migration
9
10 (Huang, et al. 2004; Shaul and Seger 2007). The effect of CXCL12 knockdown on
11
12 Akt phosphorylation was also examined since previous studies indicated the ability of
13
14 CXCL12 to induce activation of Akt (Wang, et al. 2000). However, Akt
15
16 phosphorylation was not affected by knockdown of CXCL12 expression; therefore the
17
18 PI3K-Akt pathway seems to be irrelevant to the CXCL12-CXCR4/CXCR7 interaction
19
20 at least in lung cancer cells.
21
22
23
24

25 In conclusion, our expression analysis for CXCL12, CXCR4 and CXCR7 with
26
27 a large number of lung cancer cell lines demonstrates that these genes are concomitantly
28
29 overexpressed in lung cancer cells. RNAi-mediated CXCL12 knockdown led to
30
31 inhibition of cell growth and migration as well as dephosphorylation of MEK and ERK
32
33 in CXCL12-overexpressing lung cancer cells, suggesting that
34
35 CXCL12-CXCR4/CXCR7 interactions play a role in the development of lung cancer
36
37 through the activation of MEK and ERK pathway. The growth-inhibitory effect of the
38
39 CXCL12 neutralizing antibody in CXCL12-overexpressing lung cancer cells provides
40
41 the possibility that inhibition of CXCL12 activity could be a novel therapeutic approach
42
43 in lung cancer. Further studies will be needed to elucidate whether CXCL12
44
45 expression could be a biomarker and therapeutic target for lung cancer.
46
47
48
49
50
51
52
53
54
55
56
57
58
59
60

CONFLICT OF INTEREST STATEMENT

All authors have no financial or personal relationships with other people or organizations that could inappropriately influence our work.

ACKNOWLEDGMENTS

We thank Dr. Adi F. Gazdar of the University of Texas Southwestern Medical Center for providing all lung cancer cell lines and immortalized human bronchial epithelial cells. We also thank Dr Michael Peyton the University of Texas Southwestern Medical Center and Drs. Shuichi Okada, Mitsuyoshi Utsugi, Tadayoshi Kawata and Hironobu Iijima of the Gunma University Graduate School of Medicine for technical support and critical comments for this study. This work was supported in part by Grant 18790532 (to N.S.) from the Ministry of Education, Culture, Sports, Science and Technology, Japan, and Lung Cancer SPORE (P50CA70907), DOD PROSPECT, and Longenbaugh Foundation Grants (JDM).

FIGURE LEGENDS

Figure 1. Comparison of mRNA levels of the (A) *CXCL12*, (B) *CXCR4* and (C) *CXCR7* genes relative to those of the *TBP* gene between lung cancer cell lines (N=55) and nontumor lung cell lines (N=6) as measured by quantitative real-time RT-PCR analysis. The expressions of (D) *CXCL12*, (E) *CXCR4* and (F) *CXCR7* were also compared between SCLC and NSCLC cell lines. The expression levels were normalized by mean level of the non-tumor cells. Bars indicate the means of the relative *CXCL12*, *CXCR4* and *CXCR7* expression.

Figure 2. RNAi-mediated knockdown of *CXCL12* mRNA expression. NT: treatment with medium alone; Oligo: treatment with Oligofectamine reagent alone. A549 cells were transfected with 100 nM siRNAs against either *CXCL12* (SDF1-1 and SDF1-2) or Tax. After 72 h, cells were harvested and quantitative real-time RT-PCR was performed. Columns represent the mean *CXCL12* mRNA levels \pm SD (bars) obtained from three independent experiments. Treatment with medium alone was set at 100%. *, $P < 0.01$.

Figure 3. RNAi-mediated knockdown of *CXCL12* expression inhibited cell proliferation in *CXCL12*-overexpressing A549 cells but not in *CXCL12*-nonexpressing H1299 cells as measured by an MTT assay. siRNAs were transfected into the cells, and MTT assay was performed in replicates of 8 at 4 days after transfection. Columns represent the mean \pm SD (bars). Treatment with medium alone was set at 100%. *, $P < 0.0001$.

1
2
3
4
5
6
7
8
9 **Figure 4.** CXCL12 siRNAs inhibited colony formation in CXCL12-overexpressing
10 A549 cells but not in CXCL12-nonexpressing H1299 cells. After 48 h of siRNA
11 transfection, cells were replated for colony formation assay in liquid culture, and after
12 14 days, surviving colonies were stained with methylene blue. (A) Stained colonies of
13 A549 cells are shown. (B) *Columns* represent the mean \pm SD (*bars*) obtained from
14 three independent experiments. Treatment with medium alone was set at 100%. *,
15 $P < 0.01$.
16
17
18
19
20
21
22
23
24
25
26

27 **Figure 5.** CXCL12 siRNA inhibited migration of CXCL12-overexpressing A549 cells
28 as measured by migration assay. After 48 h of siRNA transfection, 10^5 cells/well of
29 12-blind-well chemotaxis chamber were loaded. *Columns* represent the mean \pm SD
30 (*bars*) obtained from three independent experiments. Treatment with medium alone
31 was set at 100%. *, $P < 0.0001$.
32
33
34
35
36
37
38
39
40
41

42 **Figure 6.** The CXCL12 neutralizing antibody inhibited cell proliferation in
43 CXCL12-overexpressing lung cancer cell lines (A549, HCC95, H1264 and H661) but
44 not in CXCL12-nonexpressing lung cancer cell lines (H1299 and H2009). Cells were
45 treated with the anti-CXCL12 neutralizing antibody (3 $\mu\text{g/ml}$) or the IgG1 control
46 antibody (3 $\mu\text{g/ml}$) for 72 h and cell proliferation was measured by MTT assay.
47
48
49
50
51
52
53
54
55
56
57
58
59
60
Columns represent the mean \pm SD (*bars*) obtained from four independent experiments.
Nontreatment was set at 100%. *, $P < 0.0001$.

1
2
3
4
5
6
7
8
9
10
11
12
13
14
15
16
17
18
19
20
21
22
23
24
25
26
27
28
29
30
31
32
33
34
35
36
37
38
39
40
41
42
43
44
45
46
47
48
49
50
51
52
53
54
55
56
57
58
59
60

Figure 7. RNAi-mediated knockdown of CXCL12 reduced on the levels of phosphorylated MEK (p-MEK) and phosphorylated ERK (p-ERK) but not phosphorylated Akt (p-Akt). Cells were harvested at 72 h post-transfection of siRNAs and Western blotting was performed. Fifteen μ g of total protein were loaded in each lane.

For Peer Review

REFERENCES

- 1
2
3
4
5
6
7
8
9
10
11 Arai A, Aoki M, Weihua Y, Jin A, Miura O. 2006. CrkL plays a role in SDF-1-induced
12 activation of the Raf-1/MEK/Erk pathway through Ras and Rac to mediate
13 chemotactic signaling in hematopoietic cells. *Cell Signal* 18(12):2162-71.
14
15
16
17
18 Balabanian K, Lagane B, Infantino S, Chow KY, Harriague J, Moepps B,
19 Arenzana-Seisdedos F, Thelen M, Bachelier F. 2005. The chemokine
20 SDF-1/CXCL12 binds to and signals through the orphan receptor RDC1 in T
21 lymphocytes. *J Biol Chem* 280(42):35760-6.
22
23
24
25
26
27 Balkwill F. 2004. Cancer and the chemokine network. *Nat Rev Cancer* 4(7):540-50.
28
29
30
31 Burger M, Glodek A, Hartmann T, Schmitt-Graff A, Silberstein LE, Fujii N, Kipps TJ,
32 Burger JA. 2003. Functional expression of CXCR4 (CD184) on small-cell lung
33 cancer cells mediates migration, integrin activation, and adhesion to stromal
34 cells. *Oncogene* 22(50):8093-101.
35
36
37
38
39 Burns JM, Summers BC, Wang Y, Melikian A, Berahovich R, Miao Z, Penfold ME,
40 Sunshine MJ, Littman DR, Kuo CJ and others. 2006. A novel chemokine
41 receptor for SDF-1 and I-TAC involved in cell survival, cell adhesion, and tumor
42 development. *J Exp Med* 203(9):2201-13.
43
44
45
46
47
48 Crespo P, Leon J. 2000. Ras proteins in the control of the cell cycle and cell
49 differentiation. *Cell Mol Life Sci* 57(11):1613-36.
50
51
52
53 Darash-Yahana M, Pikarsky E, Abramovitch R, Zeira E, Pal B, Karplus R, Beider K,
54 Avniel S, Kasem S, Galun E and others. 2004. Role of high expression levels of
55 CXCR4 in tumor growth, vascularization, and metastasis. *Faseb J*
56
57
58
59
60 18(11):1240-2.

- 1
2
3
4
5
6 Geminder H, Sagi-Assif O, Goldberg L, Meshel T, Rechavi G, Witz IP, Ben-Baruch A.
7
8 2001. A possible role for CXCR4 and its ligand, the CXC chemokine stromal
9 cell-derived factor-1, in the development of bone marrow metastases in
10 neuroblastoma. *J Immunol* 167(8):4747-57.
11
12
13
14
15
16 Hartmann TN, Burger JA, Glodek A, Fujii N, Burger M. 2005. CXCR4 chemokine
17 receptor and integrin signaling co-operate in mediating adhesion and
18 chemoresistance in small cell lung cancer (SCLC) cells. *Oncogene*
19 24(27):4462-71.
20
21
22
23
24
25 Huang C, Jacobson K, Schaller MD. 2004. MAP kinases and cell migration. *J Cell Sci*
26 117(Pt 20):4619-28.
27
28
29
30 Huang YC, Hsiao YC, Chen YJ, Wei YY, Lai TH, Tang CH. 2007. Stromal cell-derived
31 factor-1 enhances motility and integrin up-regulation through CXCR4, ERK and
32 NF-kappaB-dependent pathway in human lung cancer cells. *Biochem Pharmacol*
33 74(12):1702-12.
34
35
36
37
38
39 Jemal A, Siegel R, Ward E, Murray T, Xu J, Thun MJ. 2007. Cancer statistics, 2007. *CA*
40 *Cancer J Clin* 57(1):43-66.
41
42
43
44 Katayama A, Ogino T, Bandoh N, Nonaka S, Harabuchi Y. 2005. Expression of CXCR4
45 and its down-regulation by IFN-gamma in head and neck squamous cell
46 carcinoma. *Clin Cancer Res* 11(8):2937-46.
47
48
49
50
51 Kijima T, Maulik G, Ma PC, Tibaldi EV, Turner RE, Rollins B, Sattler M, Johnson BE,
52 Salgia R. 2002. Regulation of cellular proliferation, cytoskeletal function, and
53 signal transduction through CXCR4 and c-Kit in small cell lung cancer cells.
54 *Cancer Res* 62(21):6304-11.
55
56
57
58
59
60 Kryczek I, Lange A, Mottram P, Alvarez X, Cheng P, Hogan M, Moons L, Wei S, Zou L,

- 1
2
3
4
5
6 Machelon V and others. 2005. CXCL12 and vascular endothelial growth factor
7 synergistically induce neoangiogenesis in human ovarian cancers. *Cancer Res*
8
9 65(2):465-72.
10
11
12
13 Kryczek I, Wei S, Keller E, Liu R, Zou W. 2007. Stroma-derived factor
14 (SDF-1/CXCL12) and human tumor pathogenesis. *Am J Physiol Cell Physiol*
15
16 292(3):C987-95.
17
18
19
20 Liang Z, Brooks J, Willard M, Liang K, Yoon Y, Kang S, Shim H. 2007.
21 CXCR4/CXCL12 axis promotes VEGF-mediated tumor angiogenesis through
22 Akt signaling pathway. *Biochem Biophys Res Commun* 359(3):716-22.
23
24
25
26
27 Marchesi F, Monti P, Leone BE, Zerbi A, Vecchi A, Piemonti L, Mantovani A, Allavena
28 P. 2004. Increased survival, proliferation, and migration in metastatic human
29 pancreatic tumor cells expressing functional CXCR4. *Cancer Res*
30
31 64(22):8420-7.
32
33
34
35
36 Miao Z, Luker KE, Summers BC, Berahovich R, Bhojani MS, Rehemtulla A, Kleer CG,
37 Essner JJ, Nasevicius A, Luker GD and others. 2007. CXCR7 (RDC1) promotes
38 breast and lung tumor growth in vivo and is expressed on tumor-associated
39 vasculature. *Proc Natl Acad Sci U S A* 104(40):15735-40.
40
41
42
43
44
45
46 Minna JD, Roth JA, Gazdar AF. 2002. Focus on lung cancer. *Cancer Cell* 1(1):49-52.
47
48
49
50 Mochizuki H, Matsubara A, Teishima J, Mutaguchi K, Yasumoto H, Dahiya R, Usui T,
51 Kamiya K. 2004. Interaction of ligand-receptor system between
52 stromal-cell-derived factor-1 and CXC chemokine receptor 4 in human prostate
53 cancer: a possible predictor of metastasis. *Biochem Biophys Res Commun*
54
55 320(3):656-63.
56
57
58
59
60 Mori T, Doi R, Koizumi M, Toyoda E, Ito D, Kami K, Masui T, Fujimoto K, Tamamura

- 1
2
3
4
5
6 H, Hiramatsu K and others. 2004. CXCR4 antagonist inhibits stromal
7 cell-derived factor 1-induced migration and invasion of human pancreatic cancer.
8
9 Mol Cancer Ther 3(1):29-37.
10
11
12
13 Muller A, Homey B, Soto H, Ge N, Catron D, Buchanan ME, McClanahan T, Murphy E,
14 Yuan W, Wagner SN and others. 2001. Involvement of chemokine receptors in
15 breast cancer metastasis. Nature 410(6824):50-6.
16
17
18
19
20 Murphy PM. 1996. Chemokine receptors: structure, function and role in microbial
21 pathogenesis. Cytokine Growth Factor Rev 7(1):47-64.
22
23
24
25 Oonakahara K, Matsuyama W, Higashimoto I, Kawabata M, Arimura K, Osame M.
26
27 2004. Stromal-derived factor-1alpha/CXCL12-CXCR 4 axis is involved in the
28 dissemination of NSCLC cells into pleural space. Am J Respir Cell Mol Biol
29 30(5):671-7.
30
31
32
33
34 Phelps RM, Johnson BE, Ihde DC, Gazdar AF, Carbone DP, McClintock PR, Linnoila
35 RI, Matthews MJ, Bunn PA, Jr., Carney D and others. 1996. NCI-Navy Medical
36 Oncology Branch cell line data base. J Cell Biochem Suppl 24:32-91.
37
38
39
40
41 Phillips RJ, Burdick MD, Lutz M, Belperio JA, Keane MP, Strieter RM. 2003. The
42 stromal derived factor-1/CXCL12-CXC chemokine receptor 4 biological axis in
43 non-small cell lung cancer metastases. Am J Respir Crit Care Med
44 167(12):1676-86.
45
46
47
48
49
50 Phillips RJ, Mestas J, Gharaee-Kermani M, Burdick MD, Sica A, Belperio JA, Keane
51 MP, Strieter RM. 2005. Epidermal growth factor and hypoxia-induced
52 expression of CXC chemokine receptor 4 on non-small cell lung cancer cells is
53 regulated by the phosphatidylinositol 3-kinase/PTEN/AKT/mammalian target of
54 rapamycin signaling pathway and activation of hypoxia inducible factor-1alpha.
55
56
57
58
59
60

- 1
2
3
4
5
6 J Biol Chem 280(23):22473-81.
7
8
9 Raman D, Baugher PJ, Thu YM, Richmond A. 2007. Role of chemokines in tumor
10 growth. *Cancer Lett* 256(2):137-65.
11
12
13 Ramirez RD, Sheridan S, Girard L, Sato M, Kim Y, Pollack J, Peyton M, Zou Y, Kurie
14 JM, Dimaio JM and others. 2004. Immortalization of human bronchial epithelial
15 cells in the absence of viral oncoproteins. *Cancer Res* 64(24):9027-34.
16
17
18
19
20 Scotton CJ, Wilson JL, Scott K, Stamp G, Wilbanks GD, Fricker S, Bridger G, Balkwill
21 FR. 2002. Multiple actions of the chemokine CXCL12 on epithelial tumor cells
22 in human ovarian cancer. *Cancer Res* 62(20):5930-8.
23
24
25
26
27 Shaul YD, Seger R. 2007. The MEK/ERK cascade: from signaling specificity to diverse
28 functions. *Biochim Biophys Acta* 1773(8):1213-26.
29
30
31
32 Strieter RM, Belperio JA, Burdick MD, Sharma S, Dubinett SM, Keane MP. 2004. CXC
33 chemokines: angiogenesis, immunoangiostasis, and metastases in lung cancer.
34 *Ann N Y Acad Sci* 1028:351-60.
35
36
37
38
39 Su L, Zhang J, Xu H, Wang Y, Chu Y, Liu R, Xiong S. 2005. Differential expression of
40 CXCR4 is associated with the metastatic potential of human non-small cell lung
41 cancer cells. *Clin Cancer Res* 11(23):8273-80.
42
43
44
45
46 Sunaga N, Miyajima K, Suzuki M, Sato M, White MA, Ramirez RD, Shay JW, Gazdar
47 AF, Minna JD. 2004. Different roles for caveolin-1 in the development of
48 non-small cell lung cancer versus small cell lung cancer. *Cancer Res*
49 64(12):4277-85.
50
51
52
53
54
55 Sutton A, Friand V, Brule-Donneger S, Chaigneau T, Ziol M, Sainte-Catherine O, Poire
56 A, Saffar L, Kraemer M, Vassy J and others. 2007. Stromal cell-derived
57 factor-1/chemokine (C-X-C motif) ligand 12 stimulates human hepatoma cell
58
59
60

- 1
2
3
4
5
6 growth, migration, and invasion. *Mol Cancer Res* 5(1):21-33.
7
8
9 Suzuki M, Mohamed S, Nakajima T, Kubo R, Tian L, Fujiwara T, Suzuki H, Nagato K,
10 Chiyo M, Motohashi S and others. 2008. Aberrant methylation of CXCL12 in
11 non-small cell lung cancer is associated with an unfavorable prognosis. *Int J*
12 *Oncol* 33(1):113-9.
13
14
15 Suzuki M, Sunaga N, Shames DS, Toyooka S, Gazdar AF, Minna JD. 2004. RNA
16 interference-mediated knockdown of DNA methyltransferase 1 leads to
17 promoter demethylation and gene re-expression in human lung and breast cancer
18 cells. *Cancer Res* 64(9):3137-43.
19
20
21
22
23
24
25
26
27 Tang CH, Tan TW, Fu WM, Yang RS. 2007. Involvement of matrix metalloproteinase-9
28 in stromal cell-derived factor-1/CXCR4 pathway of lung cancer metastasis.
29 *Carcinogenesis*.
30
31
32
33
34 Uchida D, Onoue T, Tomizuka Y, Begum NM, Miwa Y, Yoshida H, Sato M. 2007.
35 Involvement of an autocrine stromal cell derived factor-1/CXCR4 system on the
36 distant metastasis of human oral squamous cell carcinoma. *Mol Cancer Res*
37 5(7):685-94.
38
39
40
41
42
43
44 Wald O, Izhar U, Amir G, Avniel S, Bar-Shavit Y, Wald H, Weiss ID, Galun E, Peled A.
45 2006. CD4⁺CXCR4^{high}CD69⁺ T cells accumulate in lung adenocarcinoma. *J*
46 *Immunol* 177(10):6983-90.
47
48
49
50
51 Wang J, Shiozawa Y, Wang J, Wang Y, Jung Y, Pienta KJ, Mehra R, Loberg R,
52 Taichman RS. 2008. The role of CXCR7/RDC1 as a chemokine receptor for
53 CXCL12/SDF-1 in prostate cancer. *J Biol Chem* 283(7):4283-94.
54
55
56
57 Wang JF, Park IW, Groopman JE. 2000. Stromal cell-derived factor-1alpha stimulates
58 tyrosine phosphorylation of multiple focal adhesion proteins and induces
59
60

1
2
3
4
5
6 migration of hematopoietic progenitor cells: roles of phosphoinositide-3 kinase
7
8 and protein kinase C. *Blood* 95(8):2505-13.
9

10
11 Yokomizo T, Izumi T, Chang K, Takawa Y, Shimizu T. 1997. A G-protein-coupled
12
13 receptor for leukotriene B4 that mediates chemotaxis. *Nature* 387(6633):620-4.
14
15
16
17
18
19
20
21
22
23
24
25
26
27
28
29
30
31
32
33
34
35
36
37
38
39
40
41
42
43
44
45
46
47
48
49
50
51
52
53
54
55
56
57
58
59
60

For Peer Review

Table 1. Frequencies of overexpression of CXCL12 and its receptors CXCR4 and CXCR7 in lung cancer cell lines.

	Number of the overexpressed cell lines (%)		
	Total	SCLC	NSCLC
CXCL12	25 (45)	14 (61)	11 (34)
CXCR4	44 (80)	21 (91)	23 (72)
CXCR7	9 (16)	5 (22)	4 (13)

For Peer Review

Table 2. Correlation between the expression of CXCL12 and its receptors CXCR4 and CXCR7 in lung cancer cell lines.

	CXCR4(+)	CXCR4(-)	CXCR7(+)	CXCR7(-)	CXCR4(+) or CXCR7(+)	CXCR4(-) and CXCR7(-)
CXCL12 (+)	24	1	8	17	24	1
CXCL12 (-)	20	10	1	29	21	9

For Peer Review

Fig. 1

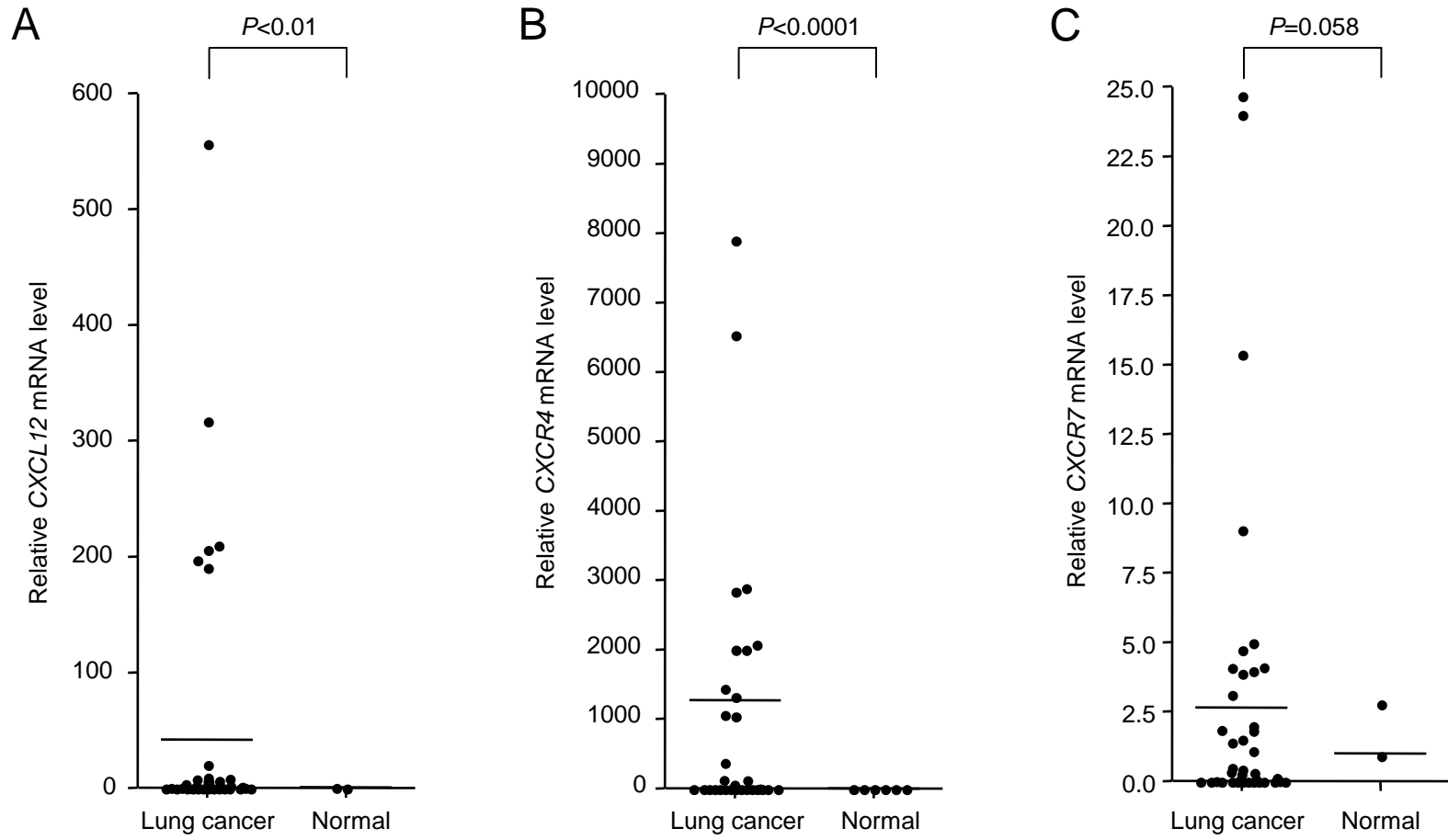


Fig. 1

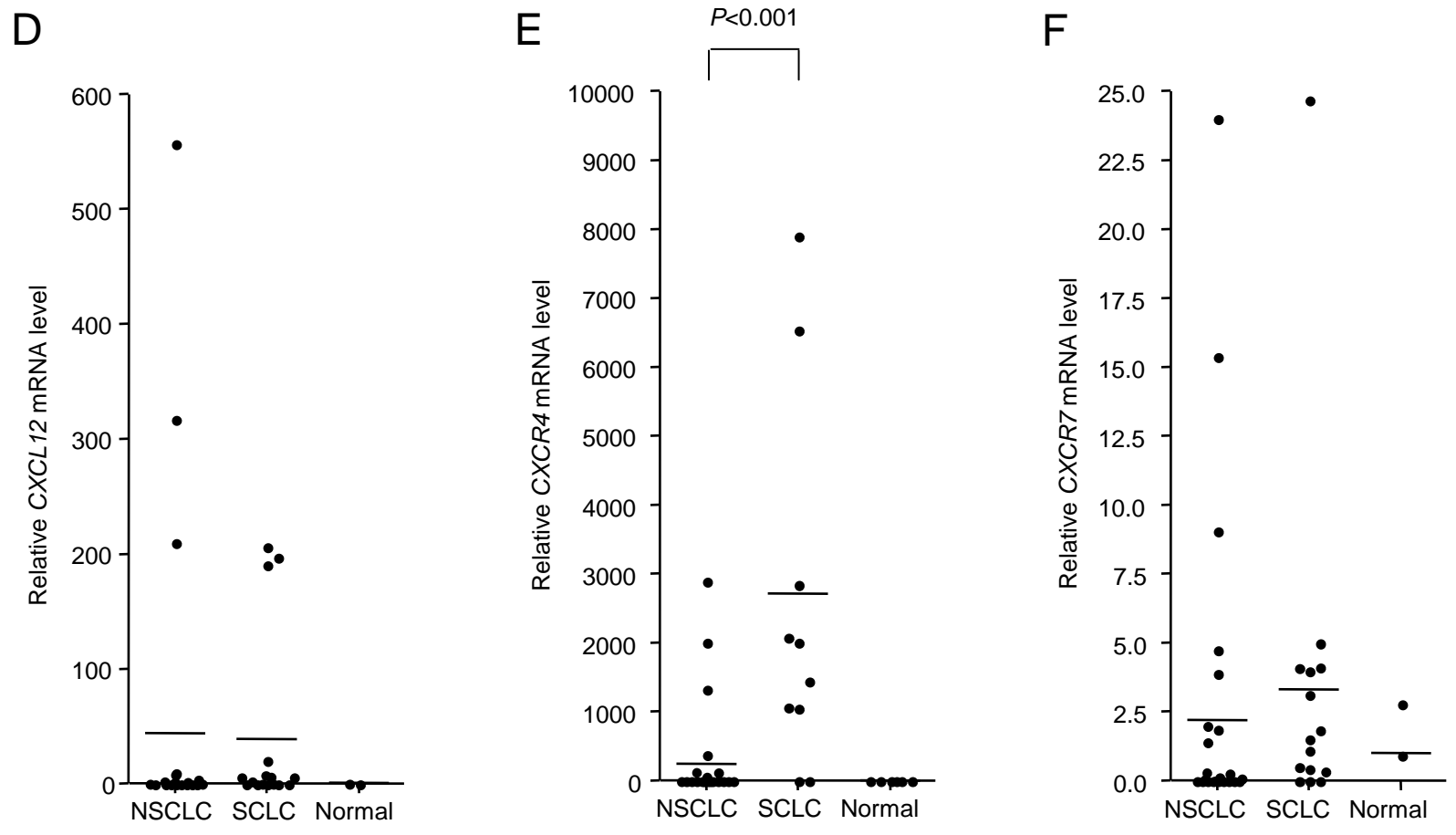


Fig. 2

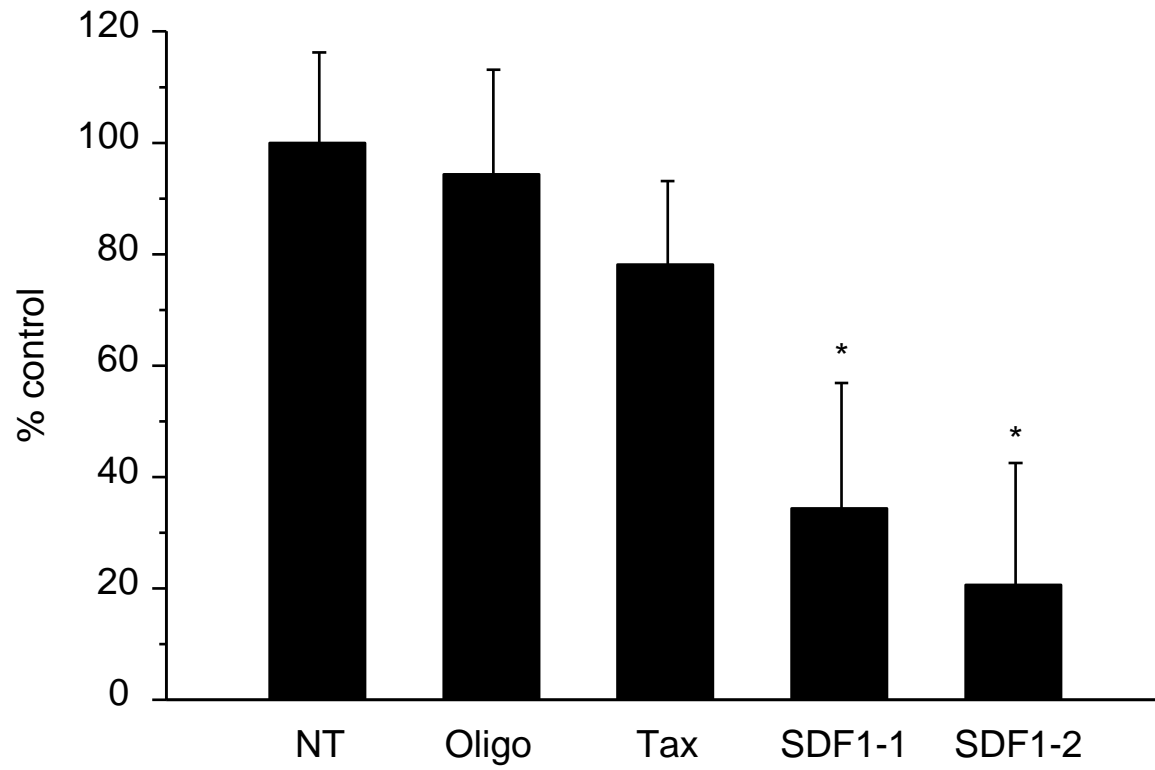


Fig. 3

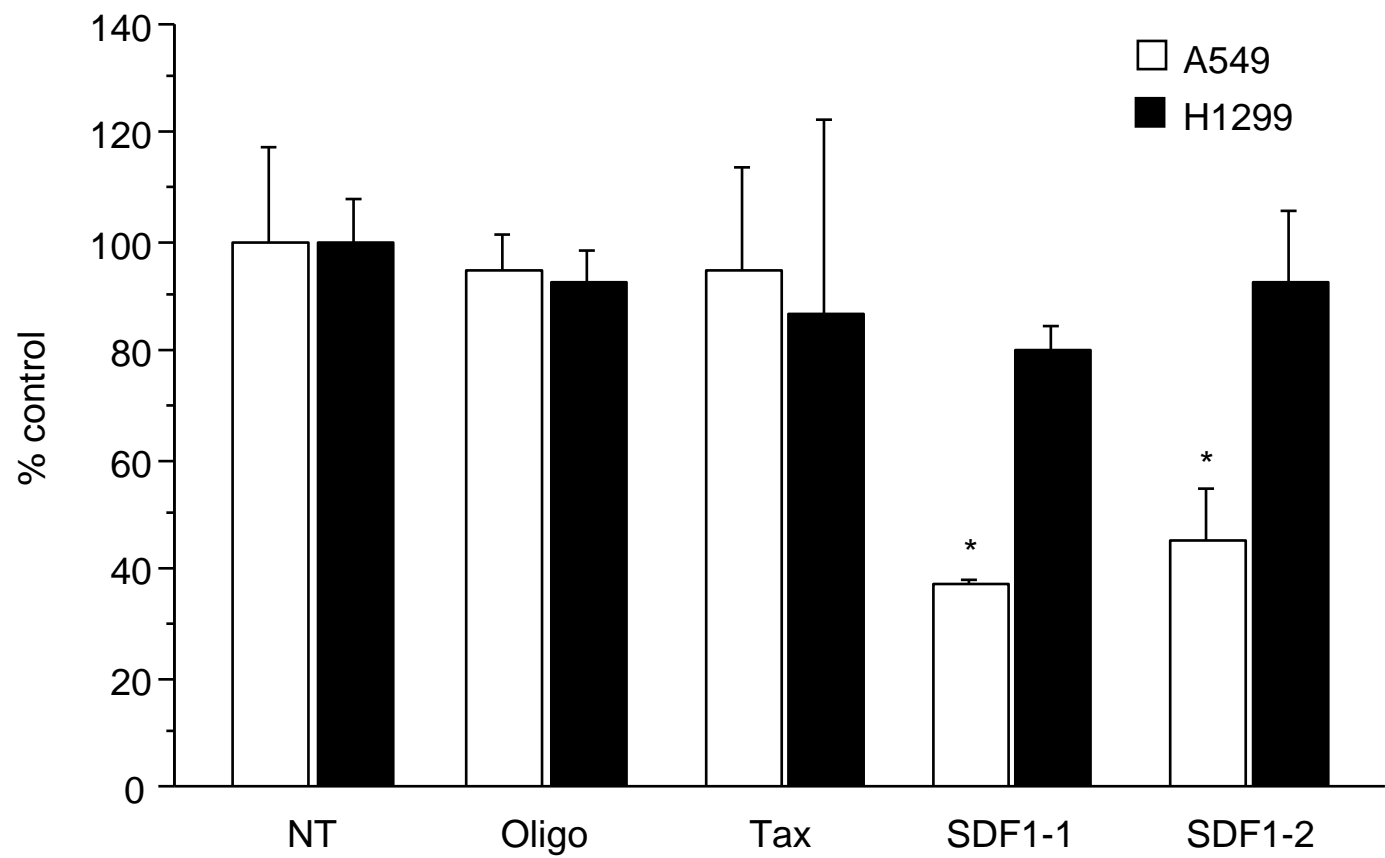
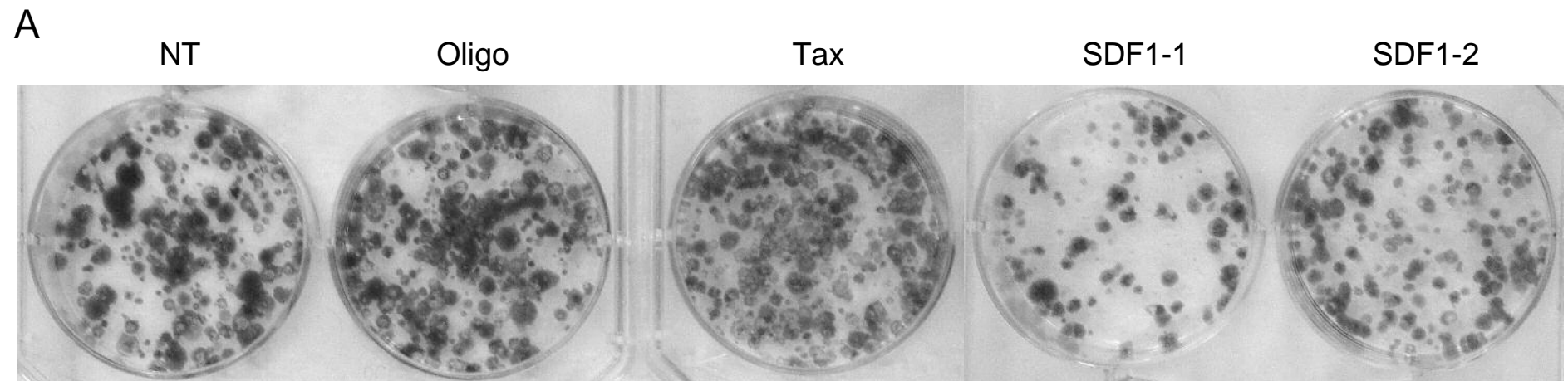


Fig. 4



B

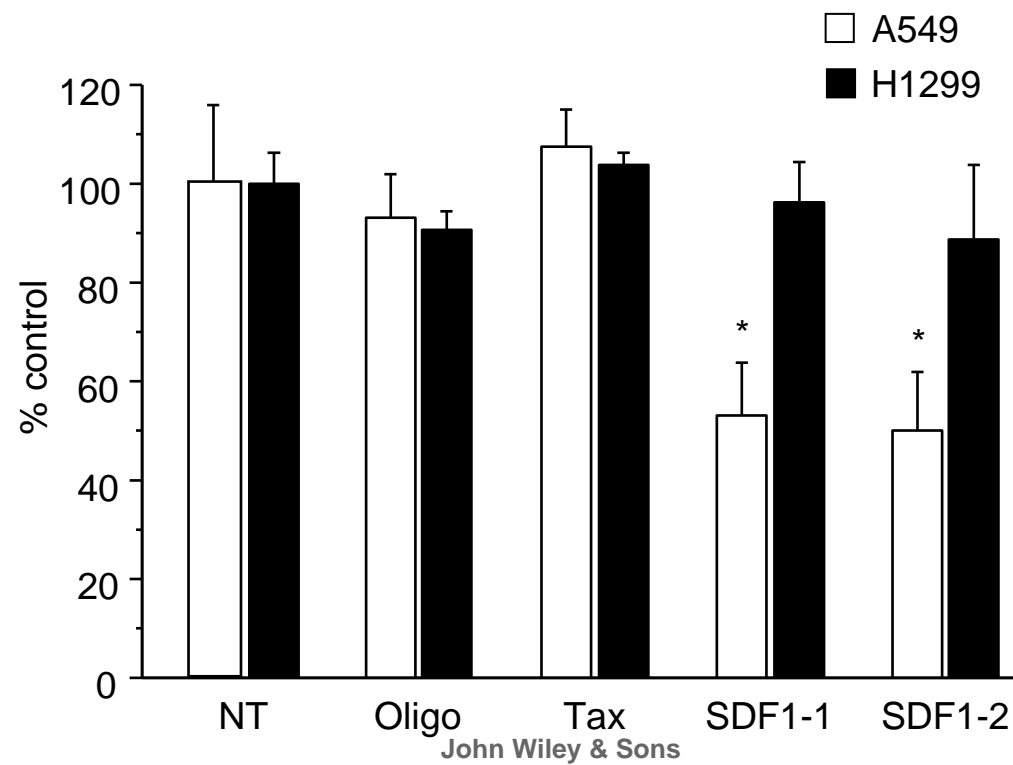


Fig. 5

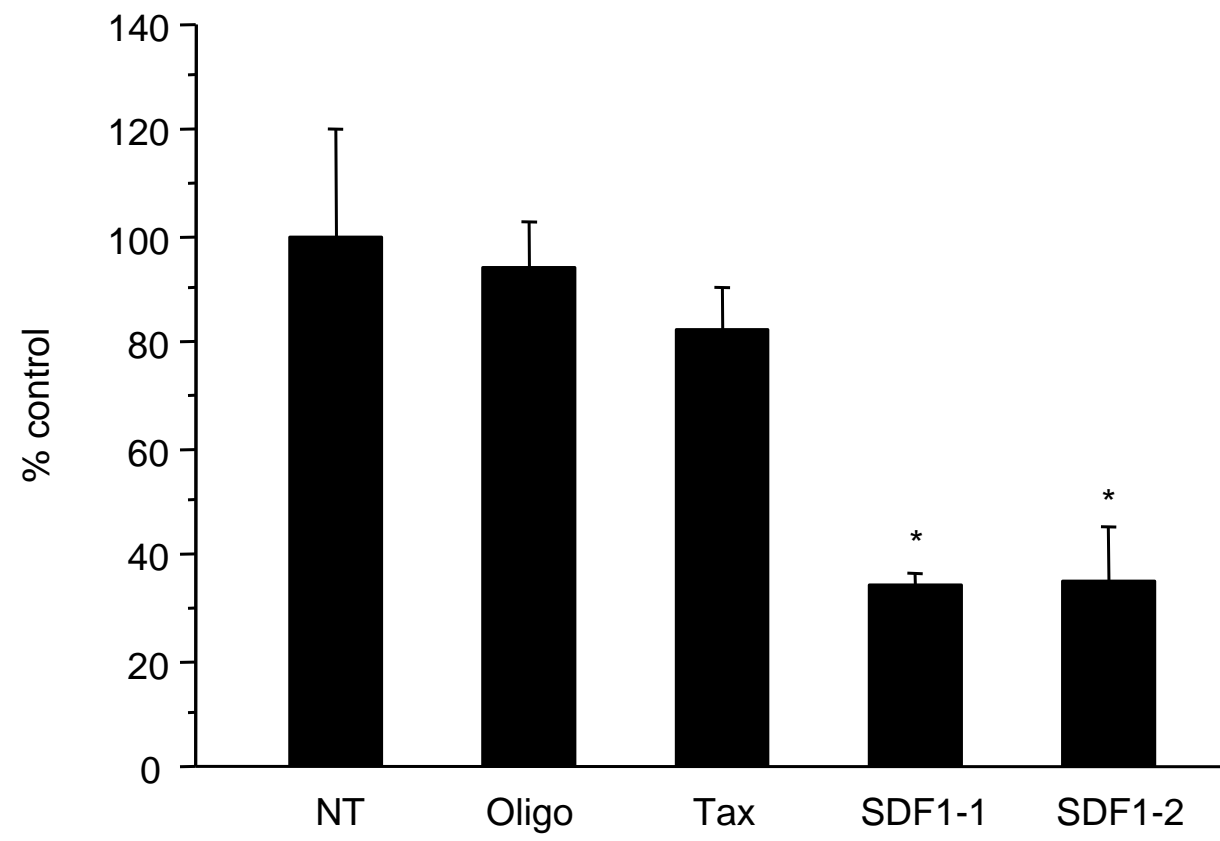


Fig. 6

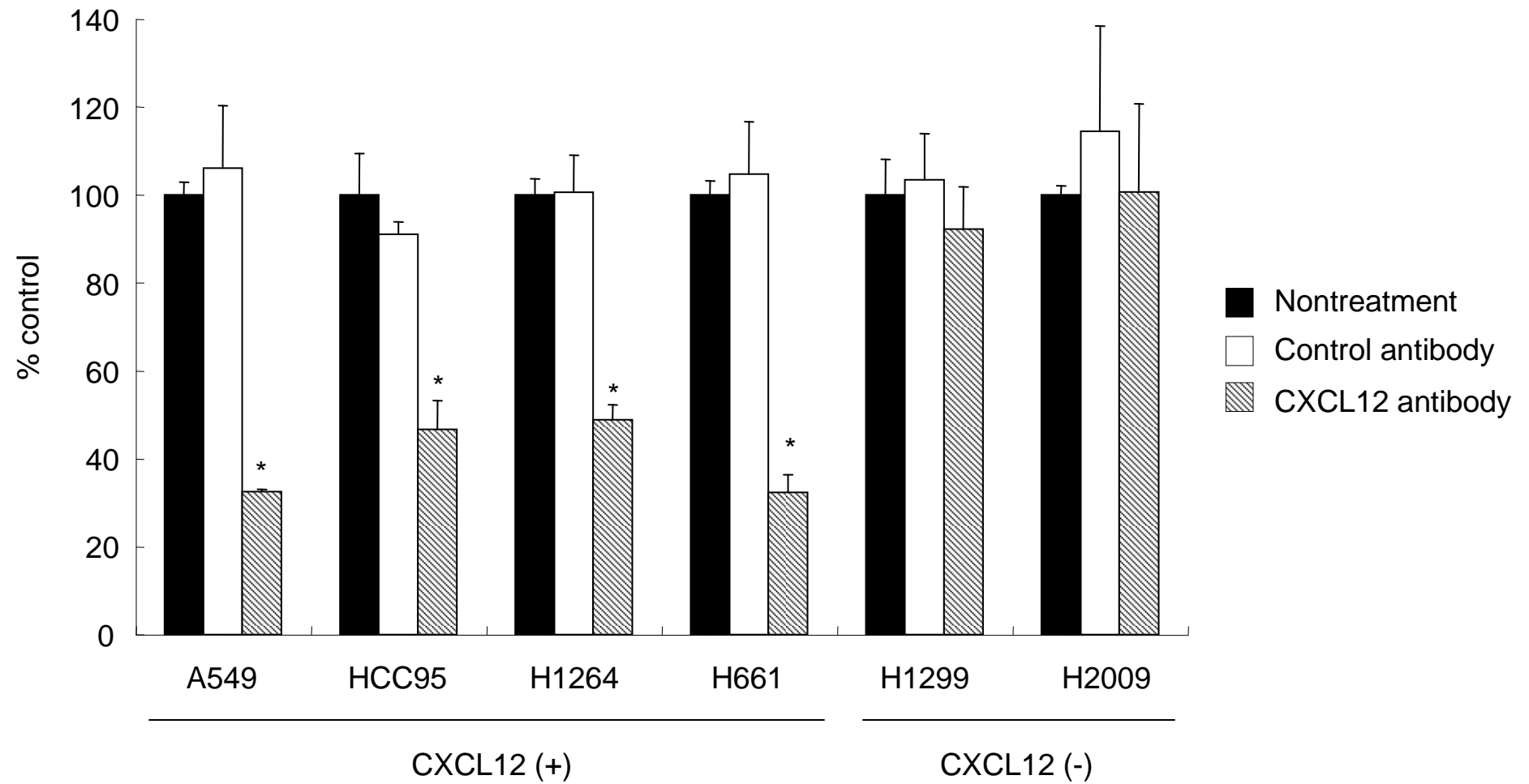
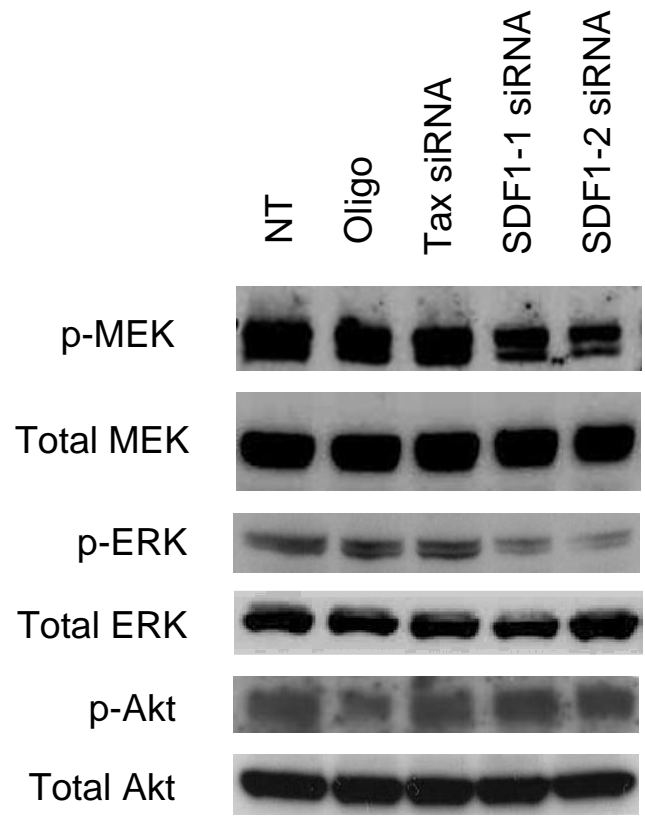


Fig. 7



Elsevier Editorial System(tm) for Cancer Cell
Manuscript Draft

Manuscript Number: CANCER-CELL-D-09-00213R1

Title: Nuclear Receptor Expression Defines a Set of Prognostic Biomarkers for Lung Cancer

Article Type: Research Article

Keywords: nuclear receptors; expression profiling; lung cancer; NURSA; biomarkers

Corresponding Author: David Mangelsdorf,

Corresponding Author's Institution: UT Southwestern

First Author: Yangsik Jeong

Order of Authors: Yangsik Jeong; Yang Xie; Guanghua Xiao; Xian-Jin Xie; Carmen Behrens; Luc Girard; Edward F Patz, Jr.; Ignacio I Wistuba; John D Minna; David J Mangelsdorf, PhD

Abstract: Utilizing quantitative real-time PCR expression data from 30 microdissected non-small cell lung cancers (NSCLCs) and their pair-matched normal lung epithelium, we identified the nuclear receptor (NR) superfamily as a biomarker that predicts patient survival and disease progression in both tissues. The NR signature from the NSCLC samples was validated in an independent microarray dataset from 442 resected lung adenocarcinomas. Remarkably, the prognostic signature in tumors could be distilled to expression of progesterone receptor and short heterodimer partner as single gene predictors of survival and high-risk stage 1 disease, respectively. Identification of prognostic NR expression patterns in tumor and normal lung epithelium from individual patients not only provides validated therapeutic targets but also may reveal the pathways involved lung tumorigenesis.

Suggested Reviewers: Charles Sawyers
Memorial Sloan-Kettering Cancer Center
sawyersc@mskcc.org

Expert in the field of hormone responsive cancers and genomics.

Myles Brown

Dana-Farber Cancer Institute

Myles_Brown@dfci.harvard.edu

Expert in the field of high-throughput data analysis and genomics in both the fields of cancer and nuclear receptors.

Opposed Reviewers:



David J. Mangelsdorf, Ph.D.
Professor and Chairman
Beatrice and Miguel Elias Distinguished Chair
in Biomedical Science

Department of Pharmacology
Howard Hughes Medical Institute

June 12, 2009

Xiaohong Helena Yang, Ph.D.
Scientific Editor, *Cancer Cell*

Dear Dr. Yang,

We are re-submitting the manuscript "Nuclear Receptor Expression Profiling Defines a Set of Prognostic Biomarkers for Lung Cancer" by Jeong et al., which we would like considered for publication as an article in *Cancer Cell*. Based on our email correspondence with you, we have revised the manuscript to clarify some of the key points and conclusions regarding significance of the nuclear receptor gene signature as a predictive (rather than retrospective correlative) biomarker for lung cancer. A new table reporting the Cox regression multivariate analysis is now also included to show that in addition to being a predictive marker, the risk of death that correlates with the NR signature is highly significant and independent of any clinical variables. We believe our work breaks precedent with other biomarker studies by making the following important contributions to the field:

1. We demonstrate that expression of the nuclear receptor superfamily in both the tumor and normal tissue of patients with non-small cell lung cancer (NSCLC) provides a novel, robust prognostic indicator of patient survival and progression of disease.
2. We provide the first single gene signatures for both survival and identification of early-stage, high-risk patients, which is considered the most clinically meaningful stage for predicting outcome.
3. We show that the predictive power of the nuclear receptor signature requires only the mRNA expression data and is independent of any other clinical features.
4. We also show that the risk of death associated with nuclear receptor expression profiling is independent of other clinical features.
5. To our knowledge, this is the first prognostic biomarker set for lung cancer that identifies a class of validated drug targets that might be used therapeutically to treat individual patients. Since nuclear receptors are well-studied transcription factors, they also offer a testable set of genes that may lead to a deeper understanding of the genesis and progression of the disease.
6. We provide a Sweave document (a literate programming package that permits reproduction of high-throughput data analysis). A major problem with most gene signature studies in the cancer field has been the inability of others to reproduce the work (e.g., see Nat. Med. 13, 1276 [2007]). Sweave overcomes this problem and to our knowledge, our manuscript would be the first of its kind in the field to provide such a document.

We suggest the following as potential reviewers for this work: Charles Sawyers at Memorial Sloan-Kettering Cancer Center (sawyersc@mskcc.org), Myles Brown at Dana-Farber Cancer Institute (Myles_Brown@dfci.harvard.edu), David Carbone at Vanderbilt-Ingram Cancer Center

(d.carbone@vanderbilt.edu), and Bert O'Malley at Baylor College of Medicine (berto@bcm.tmc.edu).

Thank you for your consideration of our work for publication in *Cancer Cell*.

Sincerely,

David J. Mangelsdorf, Ph.D.
Professor and Chair, Department of
Pharmacology, UTSW;
Investigator, HHMI
Email: davo.mango@utsouthwestern.edu

John D. Minna, M.D.
Professor, Departments of Internal
Medicine and Pharmacology, UTSW
Email: john.minna@utsouthwestern.edu

A response to reviewers is not applicable for this submission, since this was an invited revision by the editor and was never sent out for peer review. Nevertheless, below I briefly have outlined the types of changes we made in consultation with the editor, Dr. Xiaohong Helena Yang.

1. We re-wrote large sections of the paper (including the Summary and Significance) to clarify the key points and conclusions that set this work apart as a paradigm shift for biomarker analysis. We also emphasized the differences between the predictive (prognostic) gene signature analysis we did versus other methods (e.g., retrospective studies).
2. We included a new table (Table 2) that provides a multivariate Cox regression analysis to show that the NR signature is independent of clinical variables (which further supports one of the key findings of the paper).
3. We removed supplemental figure S4, which was somewhat confusing and redundant to other data presented in the paper.

Nuclear Receptor Expression Defines a Set of Prognostic Biomarkers for Lung Cancer

Yangsik Jeong^{1,2,3,4}, Yang Xie^{4,5}, Guanghua Xiao⁵, Xian-Jin Xie^{4,5}, Carmen Behrens⁷, Luc Girard^{1,3,4}, Edward F. Patz, Jr.⁹, Ignacio I. Wistuba^{7,8}, John D. Minna^{1,3,4,6,*}, & David J. Mangelndorf^{1,2,3,*}

¹ Department of Pharmacology

² Howard Hughes Medical Institute

³ Hamon Center for Therapeutic Oncology Research

⁴ Simmons Cancer Center

⁵ Department of Clinical Sciences

⁶ Department of Internal Medicine

University of Texas Southwestern Medical Center

6001 Forest Park Rd., Room ND9.124, Dallas, TX 75390-9050, USA

⁷ Department of Thoracic/Head& Neck Medical Oncology

⁸ Department of Pathology

University of Texas M.D. Anderson Cancer Center, 1515 Holcombe Boulevard, Houston, TX 77030-4009, USA

⁹ Department of Radiology, Department of Pharmacology and Cancer Biology, P.O. Box 3808 Duke University Medical Center, Durham, NC 27710, USA

*Correspondence: john.minna@utsouthwestern.edu (J.D.M.),
davo.mango@utsouthwestern.edu (D.J.M.).

Contact: David J. Mangelndorf (davo.mango@utsouthwestern.edu; 214-645-5957 [phone]; 214-645-5969 [fax].

Running title: Nuclear receptors as biomarkers for lung cancer

Keywords: nuclear receptors; expression profiling; lung cancer; NURSA; biomarkers

SUMMARY

Utilizing quantitative real-time PCR expression data from 30 microdissected non-small cell lung cancers (NSCLCs) and their pair-matched normal lung epithelium, we identified the nuclear receptor (NR) superfamily as a biomarker that predicts patient survival and disease progression in both tissues. The NR signature from the NSCLC samples was validated in an independent microarray dataset from 442 resected lung adenocarcinomas. Remarkably, the prognostic signature in tumors could be distilled to expression of progesterone receptor and short heterodimer partner as single gene predictors of survival and high-risk stage 1 disease, respectively. Identification of prognostic NR expression patterns in tumor and normal lung epithelium from individual patients not only provides validated therapeutic targets but also may reveal the pathways involved lung tumorigenesis.

SIGNIFICANCE

Despite numerous attempts, little progress has been made to identify biomarkers that can be used in lung cancer patients to predict outcome and guide therapy. In this study, we analyzed expression of the NR superfamily to provide a unique prognostic signature that can both predict patient survival and identify early stage high-risk patients. Importantly, NR expression in either the lung tumor or the adjacent normal tissue of patients has prognostic power. Because NRs are ligand-dependent transcription factors and targets of proven drugs, receptors identified in these profiles should provide promising targets for

mechanistic studies of lung cancer oncogenesis and therapeutics to treat individual patients. This study highlights the potential of using a rationally designed set of genes as theragnostic biomarkers.

INTRODUCTION

The prevalence of lung cancer as the primary cause of cancer death in the U.S. has led to renewed efforts to obtain biomarker signatures that provide prognostic information to guide therapy for individual patients (i.e., “personalized medicine”) (Jemal et al., 2008; Sun et al., 2007; Xie and Minna, 2008). A key strategy toward this goal has been to identify tumor biomarkers using gene expression profiling, combined with standard clinical data (e.g., age, gender, smoking history, histology and clinical pathologic stage) (Shedden et al., 2008; Xie and Minna, 2008). Such data would be particularly useful for choosing the appropriate therapeutic options for early stage patients (e.g., stage I non-small cell lung cancers, [NSCLCs]), where surgical resection (with or without adjuvant chemotherapy) is still the standard treatment (Minna and Schiller, 2008). However, even under favorable circumstances, a substantial fraction of patients relapse and die (Minna and Schiller, 2008). These statistics have led to multiple genome-wide expression studies to develop signatures that also predict patient outcomes (Chen et al., 2007; Potti et al., 2006; Shedden et al., 2008). While these approaches have identified potential biomarkers, nearly all of the gene signatures have been different and they have not provided a basis for understanding lung cancer pathogenesis (Beer et al., 2002; Chen et al., 2007; Endoh et al., 2004; Lu et al., 2006; Potti et al., 2006; Shedden et al., 2008). Perhaps more importantly, to date these studies have failed to yield new therapeutic targets. Clearly, identification of biomarkers that also provide

hypotheses for mechanism-based studies of carcinogenesis, and offer new therapeutic targets, would be of tremendous benefit.

Nuclear receptors (NRs) are a large family of ligand-dependent transcription factors that respond to a number of hormonal and dietary-derived lipids, including endocrine steroids, fat-soluble vitamins, fatty acids, and cholesterol metabolites (Chawla et al., 2001). NRs are also among the most successful targets of drugs approved to treat numerous diseases, including cancer (Gronemeyer et al., 2004; Shulman and Mangelsdorf, 2005). Previously, we have shown that NR expression profiling can be used to reveal the mechanistic basis of the hierarchical transcriptional networks that govern a number of physiological processes, including development, differentiation, reproduction, circadian rhythm, and metabolism (Barish et al., 2005; Bookout et al., 2006; Fu et al., 2005; Xie et al., 2009; Yang et al., 2006). In the present study, we investigated the potential role of the 48 members of the NR superfamily as theragnostic indicators in lung cancer. Our strategy of examining expression of NRs, which are known therapeutic targets with defined mechanisms of action, differs from previous, open-ended genome-wide microarray studies that have yet to yield useful clinical targets. Our goal was to use both normal and tumor NR expression signatures as clinical tools to classify patients with different survival outcomes, characterize the NR transcriptional networks that govern lung cancer pathobiology, and eventually develop NR-selective therapies targeted at hormonal manipulation of lung cancer. Utilizing quantitative, real-time PCR (QPCR), we evaluated the expression of the NR

superfamily in normal lung and pair-matched NSCLC tumor lesions microdissected from 30 individuals. The prediction model built from these 30 resected NSCLCs was then validated in a recent NCI-sponsored, multi-institutional, genome-wide microarray dataset taken from 442 resected lung adenocarcinomas (Shedden et al., 2008). We found that NR expression profiles can both predict patient survival and identify early stage high-risk patients. Of particular interest, this prediction model was dependent solely on the expression signature for the NR superfamily and did not require inclusion of clinical features. Furthermore, we found that expression of progesterone receptor (PR, NR3C3) and short heterodimer partner (SHP, NR0B2) are the principle components that describe the predictive power of the NR signature, and thereby represent the first single gene predictors for overall patient survival and high-risk, early stage disease, respectively. Finally, we provide a Sweave document (Coombes et al., 2007; Gentleman, 2005) as Supplemental Data online that contains a literate programming package to permit the full reproduction of our analysis.

RESULTS

Identification of the NR superfamily as a prognostic biomarker for lung cancer

QPCR was used to analyze the mRNA expression of all 48 members of the NR superfamily in a cohort of 30 NSCLC tumors and their pair-matched, histologically normal lung epithelium obtained by microdissection from the MD Anderson Cancer Center (MDACC). Prior studies have used macrodissected

lung tumor samples that included variable fractions of tumor cells (ranging from 20-80%). Our analysis of microdissected material permitted an unprecedented, quantitative comparison of NR expression in tumor cells to adjacent normal lung epithelium. The inclusion of normal tissue from the same patient also provided an internal control for systemic (e.g., hormonal) and local (e.g., microenvironmental) factors, and it allowed us to investigate whether NR expression from normal lung epithelium contained prognostic information. Detailed clinical data on the 30 patient cohort are given in supplemental data (Tables S1 and S2), and the QPCR datasets of NR expression are shown and summarized in supplemental data (Figure S1 and Table S3) (raw datasets are available at www.NURSA.org). Inspection of these data showed that there was considerable variation in NR expression between patients. Therefore, we investigated whether any prognostic association existed between NR expression and patient clinical features including disease progression and death. Unsupervised cluster analysis of NR expression in lung tumors revealed two distinct clusters of tissue samples (Figure 1A). Note that one tissue sample (857-SCC) did not fall into either cluster and was treated as an outlier. To our surprise, the two major branches of the dendrogram (cluster 1 and cluster 2) were associated with both overall survival rates ($P=0.001$) and disease progression rates ($P=0.062$), but no other clinical features (Table 1). In this study, disease progression was defined as either recurrence of lung cancer or patient death. Indeed, Kaplan-Meier plots for survival and disease progression showed that cluster 1 and cluster 2 segregated patients into those with poor and good prognostic outcomes, respectively ($P=0.000048$ for survival; $P=0.0018$ for

disease progression) (Figure 1B and C). These findings suggest that the NR signature defines an independent prognostic biomarker for survival and disease progression.

Analysis of the NR expression profiles in the histologically normal lung epithelium showed that the patterns in the normal tissues were also predictive for both survival and time to progression (Figure S2). Although 18 out of 48 NRs showed a statistically significant correlation in expression between normal and tumor tissue, the NRs that correlated with prognosis were different when comparing normal lung epithelium to tumor cells (see below).

It is of interest that the unsupervised cluster analysis also revealed two major clusters of NR genes that exhibited relatively high or low expression in the majority of the tumor samples (Figure 1A), suggesting that these receptors may be of mechanistic importance to lung cancer pathology.

Validation of the NR gene signature as a predictor of patient survival

To validate the use of NR expression as an independent prognostic marker, we used the NR gene signature to build a predictive model from the tumor samples of the 30 patient cohort by using recursive-partitioning tree analysis (RPART); and we further tested the prediction performance by the leave one-out cross-validation (LOOCV) method. The hazard ratio (HR), i.e., risk of death, for the predicted high-risk vs. the low-risk signatures using tumor samples was 7.03; 95% confidence interval [CI], 2.22 to 22.3; $P=0.00015$ (Figure 2A).

Because the majority of gene expression data now available from lung cancer samples comes from microarray expression studies, we investigated whether the NR expression profile could be validated within one of these previously acquired datasets. One of the largest independent lung cancer microarray datasets available is the recently published NCI Director's Consortium for study of lung cancer involving 442 resected NSCLCs (Shedden et al., 2008). From that study, the Affymetrix U133A microarray data for the 48 NR gene expression signatures were excerpted and used in three different ways to validate the prognostic value of NR expression. We first validated the 30-sample QPCR dataset on the 442-sample microarray dataset; and then we developed an NR signature from the microarray dataset and validated it on the QPCR data. Both directions of training and testing provided statistically significant predictive power for patient survival (Figure 2B and C), with validation of the QPCR data within the microarray data being the most significant (Figure 2B). The higher significance value for the QPCR dataset likely reflects the greater dynamic range and quantitative nature of the QPCR assay, and the greater homogeneity of the microdissected samples. Finally we divided the microarray data into training and testing sets for validation (Figure 2B–D). For this analysis the 442-sample dataset was divided into training and testing sets, and analyzed using the predictive RPART model. We used the same training and testing strategy as in the genome-wide analyses of these data (Shedden et al., 2008). The training set (n=256) included samples from University of Michigan Cancer Center (UM, n=177) and Moffitt Cancer Center (HLM, n=79), and the testing set (n=186)

included the Memorial Sloan-Kettering Cancer Center (MSK, n=104) and Dana-Farber Cancer Institute (CAN/DF, n=82) samples. Using just the NR expression profile from training data to build a predictive model yielded a hazard ratio of 2.04 (95% CI, 1.12 to 3.71; $P=0.018$) for the predicted high-risk vs. the predicted low-risk signature in testing data (Figure 2D). Interestingly, the NR signature was no longer predictive of patient survival when other clinical variables were included in the analysis (Figure S3). This latter finding suggests that all of the predictive power of the NR signature is contained within the expression data and is independent of knowing any of the other demographic features. Taken together, these results strongly support the utility of the NR gene signature as prognostic marker, even when applied and cross-validated independently by two different gene expression platforms (QPCR and microarray).

Although the clinical variables did not improve the predictive power of the NR signature, it was of interest to examine whether the risk of death (i.e., hazard ratio [HR]) that is associated with the NR signature was independent of the clinical variables. Therefore, we performed a retrospective multivariate Cox proportional-hazard analysis that included NR signature, gender, age at diagnosis, use of adjuvant chemotherapy, use of adjuvant radiation therapy, and stage as the co-variables. We first analyzed the Consortium testing dataset, which included samples from Memorial Sloan-Kettering Cancer Center and Dana-Farber Cancer Institute. The NR signatures that were used in this analysis were derived from the prediction model built from the Consortium training dataset (from the University of Michigan Cancer Center and Moffitt Cancer Center). This

multivariate analysis revealed that the association between NR signatures and survival was independent of other clinical variables (HR=1.98, $P=0.037$) (Table 2, left-column). Next, we analyzed the association between NR signatures and survival in the combined Consortium training and testing datasets using the NR signatures derived from the prediction model built from the MDACC dataset. Again, the association between NR signatures and survival was independent of other clinical variables (HR=1.89, $P=0.000099$), consistent with the results in Table 1. Thus, the data in Table 2 reveal a significant correlation exists between a patient's NR profile and survival when adjusted for other clinical variables. As expected, the correlation between tumor stage and patient survival was also highly significant, confirming this clinical feature as a well-recognized prognostic marker used in the clinic. It is interesting to note that gender also was significantly correlated to patient survival in our analysis (males had a higher risk than females).

Refinement of the NR signature into single gene predictors

We next explored the roles of specific NRs in the prediction models. To address this question, we further interrogated the RPART model (see experimental procedure for details) and found the progesterone receptor (PR, NR3C3) and the orphan receptor, short heterodimeric partner (SHP, NR0B2), performed remarkably well as single gene markers. Surprisingly, PR expression was identified as the only co-variable left in the final RPART prediction model built from the 30-patient MDACC dataset. PR was strongly associated with patient survival by LOOCV analysis ($P=0.00015$) (Figure 3A), and was highly predictive

($P=0.0048$) for lung cancer patient prognosis when independently validated in the microarray dataset (Figure 3B). Thus, the prediction of survival by PR expression alone was identical to that of the entire 48 NR gene set (compare Figure 3A and 3B to Figure 2A and 2B). The analysis also revealed that increased SHP expression was a novel biomarker of a good prognosis in the 30-patient LOOCV dataset (HR, 13.6; 95% CI, 3.01 to 61.4; $P=0.000019$) (Figure 3D), and this result was further validated in the testing cohort of the Consortium dataset (HR, 1.61; 95% CI, 1.13 to 2.3; $P=0.0078$) (Figure 3E). The protective effect based on PR and SHP expression was further strengthened by univariate Cox regression modeling, which consistently showed that expression of both NRs correlated with significantly low hazard ratios in the microarray dataset (Figure 3C and 3F).

NR expression in normal tissue predicts survival and disease progression

We also examined the potential prognostic value of NR expression in histologically normal lung tissue obtained from areas adjacent to the tumors of the MDACC cohort used in the above studies. When the normal tissue expression data were analyzed using the RPART model and validated by LOOCV, the NR signature provided statistically significant predictors of both disease progression (HR=10.2, $P=0.00003$) and overall patient survival (HR=2.5, $P=0.066$) (Figure S2). Interestingly, reiteration of the RPART model revealed two NRs, NR4A1 (also known as nerve growth factor induced gene B3 [NGFIB3]) and mineralocorticoid receptor (MR, or NR3C2), to be single-gene predictors for survival and disease progression that yield the same Kaplan-Meier plots as those observed when using the all 48 NRs (Figure S2). Although the prediction models

for normal tissue will require further validation in an independent dataset, this analysis indicates higher expression of NGFIB3 and MR correlates with a good prognosis. Given that most surgical biopsies include both normal and tumor tissue, these data suggest that analyzing NR expression profiles from tumor and corresponding normal lung epithelium will improve the clinical utility of this approach.

SHP expression predicts early stage, high-risk lung cancer patients

Since identification of early stage, high-risk patients is perhaps the most clinically useful classifier for guiding therapeutic strategy, we tested whether a specific NR gene signature has predictive power to classify stage I lung cancer patients into the high- and the low-risk groups. Importantly, expression of SHP was identified by RPART analysis to significantly differentiate high-risk from low-risk stage I patients in the Consortium samples (Figure 4A, $P=0.033$), whereas the PR signature was marginally predictive (Figure 4B, $P=0.069$). These results reveal SHP to be the first known single-gene predictor of high-risk patients with stage 1 lung cancer.

DISCUSSION

Several recent studies using microarray experiments have proposed various sets of genetic signatures for lung cancer prognosis (Beer et al., 2002; Chen et al., 2007; Endoh et al., 2004; Lu et al., 2006; Potti et al., 2006; Shedden et al., 2008). Although successfully validated in independent testing sets, the gene signatures from these studies share little if any overlap with one another (Beer et al., 2002;

Chen et al., 2007; Potti et al., 2006). Furthermore, because of the open-ended nature of genome-wide analyses, the signatures have provided little insight into the pathogenesis or pathophysiology of lung cancer. To date, these studies also have not identified any new therapeutic targets. Here, we report a rationally designed lung cancer gene expression study targeting the NRs, a class of transcription factors that are known to govern complex physiologic and pathophysiologic processes, and are themselves the targets of validated drugs for many diseases including cancer. This family also includes a number of orphan receptors, many of which are currently being evaluated as potential new therapeutic targets for a number of diseases (Shulman and Mangelsdorf, 2005).

Our analysis revealed several findings that should have important and practical implications for the use of the NR gene signature in a clinical setting. First, we demonstrated that the NR-superfamily gene-expression signature is an excellent predictor of both patient survival and progression of lung cancer. We used both unsupervised and supervised approaches to validate the prognostic potential of NRs in independent experiments. In addition to validating the predictive power of the entire NR superfamily signature as a whole, PR and SHP were identified as robust, single gene predictors. The demonstration of PR as a predictive marker is supported by a previous retrospective study where PR was shown to be associated with survival in patients with lung adenocarcinoma (Ishibashi et al., 2005). Expression of PR, together with estrogen receptor α ($ER\alpha$), is now well established as a clinical guide to both prognostic anticipation and therapeutic intervention of breast cancer. Indeed, in thinking about the next

step in our studies, the finding that certain lung cancers express specific, known therapeutic NR targets (e.g., PR, ER α and ER β , AR, RARs, PPARs), brings up the real possibility of treating these patients whose tumors express these receptors with drugs (agonists or antagonists) that target the receptors. In a prior preclinical study, treatment with progesterone inhibited lung tumor xenograft growth (Ishibashi et al., 2005). By contrast, anti-estrogen therapy is being tested as a lung cancer therapeutic (Siegfried, 2006; Stabile et al., 2002; Stabile et al., 2005; Traynor et al., 2008); and in a mouse lung cancer study, the use of a PPAR γ agonist had a synergistic effect at reducing tumor burden when used with cis-platinum (Girnun et al., 2007). Evaluation of the QPCR profiles from our study revealed a high degree of patient-to-patient variability in NR expression (Figure S1), and this observation provides a strong rationale for using this approach to guide individualized treatment in the future. A reasonable assumption based on our work here is that predicting sporadic responses to drugs like anti-estrogens might be accomplished by screening patients for NR expression using the methodology highlighted in this study. Similarly, our data suggest that NR profiling of individual tumors provides a clinical paradigm for identifying potential responders to NR drugs.

A second finding of considerable interest was that the orphan nuclear receptor SHP is also a prognostic lung cancer biomarker, particularly of early stage disease. To our knowledge this is the first single gene predictor for high-risk early-stage lung cancer patients. SHP has been extensively studied for its role in liver lipid metabolism (Goodwin et al., 2000; Lu et al., 2000), and as

transcriptional repressor of other NRs (Nishizawa et al., 2002). Intriguingly, a recent report found SHP expression was negatively associated with liver tumorigenesis in a mouse model (Zhang et al., 2008). These findings prompt further exploration into whether there is a connection between the known physiological role of SHP and lung tumorigenesis or whether SHP has a unique pathophysiologic function in the disease pathogenesis. To that end, we note that FXR agonists, a PPAR γ agonist (rosiglitazone), agents that inhibit HNF-1 α action, and a number of orphan drugs are all inducers of SHP expression (Chanda et al., 2008). These compounds might be tested in preclinical models to see if they inhibit lung tumorigenesis or malignant behavior. Also germline mutations in SHP or polymorphisms in FXR that regulate the level of SHP expression could play a role in SHP function.

A third noteworthy finding from our study was the ability to predict overall survival based on NR expression in normal tissue of patients with lung cancer. Whether this may be due to a “field effect” of the nearby cancer or to some pre-existing nature of normal lung epithelium is not yet known. However, this finding does suggest that interrogating the histologically normal tissue may yield insight into lung cancer oncogenesis. To that end we note that the prognostic NR signature in normal tissue is completely different than that of the adjacent tumor. In contrast to that observed in tumors, distillation of the NR signature using RPART analysis revealed that NGFIB3 (NR4A1) and MR are single gene biomarkers found in normal tissue for predicting disease progression and overall survival, respectively. NR4A family members have been shown to be tumor

suppressors in a mouse model of myeloid leukemogenesis (Mullican et al., 2007). Similarly, underexpression of MR has been shown to be correlated to colorectal carcinoma progression (Fabio et al., 2007). These studies support the notion that higher expression of NR4A1 and MR might play a protective role against lung tumor pathogenesis.

A fourth finding of our study was the independent demonstration that the NR gene signature could be tested and cross-validated using two different gene expression platforms, QPCR and microarray. Given that microarray data do not have the dynamic or quantitative properties of data generated by QPCR, the cross-validation of the NR gene signature between different platforms strongly supports the idea that the NR superfamily may be a powerful prognostic predictor that also is functionally involved in lung cancer pathophysiology. In any case it seems clear that a combination of a more robust collection process (microdissection vs. tissue mass) together with more quantitative measurements (QPCR vs. microarray) may reduce variability and strengthen the data. Indeed, the 95% confidence intervals of hazard ratios for both PR and SHP genes from the 30 patient dataset were smaller than that from Consortium data (with sample size 442) (Figure 3C and 3F). Hazard ratios of the high risk vs. low risk group, defined using unsupervised cluster results, were also higher for the 30 patient dataset (Figure 1B) compared to the consortium data (Figure S4). Thus, while labor intensive, improving sample homogeneity and the quality of the expression data is likely to provide more reliable prognostic information.

Finally, the NR expression profile provides specific, testable hypotheses on the role of the NRs in lung cancer pathogenesis. For example, blocking the function of a highly expressed tumor cell NR could inhibit tumor growth or development, while overexpressing a low abundance tumor cell NR could test its tumor suppressive capability. Surprisingly, interrogating the non-neoplastic tissue within the vicinity of the tumor also provided an NR gene signature that was predictive for survival. Thus, NR expression in normal lung epithelium provides the basis for testing NR function in the airway field where lung tumors develop. A goal of future studies will be to determine whether the NR signature is innate to the normal tissue or whether this expression signature has been affected by its proximity to the tumor. Perhaps one of the most surprising observations from this study is that an NR signature has not appeared in the prognostic signatures obtained in any of the previous global gene-expression studies. This is true in spite of the fact that, at least in the multi-site consortium database we analyzed, excerpting just the NR expression information yielded a predictive NR gene signature that was not discovered using global gene analysis (Shedden et al., 2008). Thus, our study provides a strategic rationale for using an informed, candidate gene profiling approach to identify prognostic markers, and interrogate specific gene families that may play roles in the cancer biology.

EXPERIMENTAL PROCEDURES

Collection of primary tissue samples

Thirty primary tumor and corresponding normal tissues (including 23 adenocarcinomas and 7 squamous cell carcinomas) were obtained by surgical resection under approval of the institutional review boards at MD Anderson Cancer center. Sixteen patients were diagnosed with stage I disease, five patients with stage II disease, five patients with stage III disease, and four patients with stage IV disease. The clinical data on each of the 30 patients are given in Table S3. All tissues were stored at -80°C after being snap frozen in liquid nitrogen. Serial sectioning of each sample was used to histologically evaluate tumor and normal tissue for subsequent microdissection (Maitra et al., 2001). RNAs were isolated from each sample using the Qiagen RNeasy Mini Kit (Quiagen Sciences, MD).

Reverse Transcription and Quantitative Real-time PCR assay

All cDNAs were prepared for quantitative real-time PCR (TaqMan[®] method) as described (Bookout et al., 2006). Briefly, 2 μg of total RNA was DNase-treated with 2 U of DNase I in final volume 20 μl containing 4.2 μM MgCl_2 . The reverse transcription reaction was performed in 100 μl final volume, followed by addition of 100 μl of DEPC-H₂O. Human universal cDNAs for broadly expressed NRs or tissue specific cDNAs for restricted expression NRs was used to construct a standard curve of the following concentrations: no template control (NTC), 0.008, 0.04, 0.2, 1, 5, 25 ng for 18S RNA; and NTC, 0.016, 0.08, 0.4, 2.0, 10, 50 ng for

each NR RNA. These quantities are based on the RNA concentration used for the reverse transcription reaction. A negative reverse transcription sample and a control for genomic DNA contamination were included for both 18S and NR. Per sample, 10 ng of cDNA was assayed in triplicate wells of a 384-well plate. The final forward and reverse primer concentrations used were 75 nM for 18S rRNA and 300 nM for all NRs. For this study the 48 NRs plus the two common splice variants for PPAR γ (i.e., PPAR γ 2) and PPAR δ (i.e., PPAR δ 2) were included in the analysis of all samples from the MDACC patient set. Primer sequences have been reported elsewhere (www.NURSA.org).

QPCR data analysis

Data were imported into Microsoft Excel[®] and evaluated for PCR efficiency (e), $e = 10^{[-1/\text{slope}]}$ where the slope was obtained from the standard curve calculated by the sequence detection system software of the ABI7900 instrument for the endogenous 18S reference and target NR. Relative mRNA amounts were calculated by $quantity = (e)^{-Ct}$. The calculated quantities were averaged (avg), and the standard deviations ($stdev$) and coefficients of variation ($CV=stdev/avg$) were determined for the 18S and NR of each sample. Data points that showed >17% CV were considered outliers and removed. Normalized values for expression of each NR were calculated using $normalized\ value = NR\ quantity\ avg / 18S\ quantity\ avg$. The standard deviation of the normalized value was calculated as $(normalized\ value) \times [(CV\ of\ reference)^2 + (CV\ of\ gene\ of\ interest)^2]^{1/2}$. Normalized values are represented as a bar graph. All these QPCR

data analysis procedures are predefined and the same as in previous publications. The entire QPCR dataset of NR expression in normal and tumor samples from the 30 patient cohort is available in Figure S1 and online at www.NURSA.org.

Microarray data preprocessing

Consortium microarray raw data (Shedden et al., 2008) were downloaded from National Cancer Institute's caArray database and preprocessed by RMA background correction and Quantile-Quantile normalization (Bolstad et al., 2003). All gene-expression values were log-transformed (on a base 2 scale).

Unsupervised clustering analysis

The hierarchical clustering algorithm (Garzotto et al., 2005) was used to group NR expression versus the 30 MDACC patient cohort based on the QPCR expression profile. Gene expression values were log-transformed (base 2 scale) in a manner similar to the transformation of the microarray data. Euclidian distance and average link were used in the hierarchical clustering algorithm.

Supervised classification using Recursive Partitioning

Supervised classification was performed using Recursive Partitioning and Regression Trees (Hess et al., 1999), a widely used classification method in biomedical research (Garzotto et al., 2005; Hess et al., 1999; Koziol et al., 2003; Valera et al., 2007). Recursive partitioning is a nonparametric method and does

not make distribution assumptions for the predictor variables. The algorithm itself is simple and intuitive. At each step, the recursive partitioning program determines for each variable (in this case for each of the NR genes) a cutoff point that best splits all of the individuals into low risk and high risk groups and selects the variable that performs best. Next, the process is repeated on each of the resulting subpopulations. The iteration will stop until either a subpopulation contains one class of individuals or the subpopulation is too small to subdivide. In this study, the response variable in the recursive partitioning model was the survival time, either overall survival or progression-free survival; the co-variables in the model are all NR genes. The program RPART, a freely available R package (RDC Team, 2008), was implemented to generate the decision tree. All parameters were used as the default values set in the package. The relative risk of each individual patient (relative to the overall population in the training data) was predicted from the tree model. The patients with predicted relative risk greater than one were considered as high-risk group, and otherwise as low-risk group. In our analysis, there was no gene selection step before model building and all the parameters used in the prediction model were predefined as the default value in R program; therefore, the testing data were not used for the model building procedure, similar to a blinded testing procedure. In order to explore the roles of individual NRs or subsets of NRs in prediction models, we looked into the tree structure of prediction models and found that PR was the only co-variable left in the prediction model built from the 30-patient MDACC data set. In order to see the prognosis ability of other NR genes, we removed PR from

the prediction model and identified that SHP as single gene signature also has prognosis ability. We further explored whether a subset of NR genes can have better prognosis than single gene signature in MDACC data set. We identified a three-NR gene signature by changing the parameter minsplit (the minimum number of observations that must exist in a node in order for a split to be attempted) to 10 in RPART function, and found that the prognosis results are similar to using PR one gene signature. Note, by default, minsplit parameter equals to 20, which is used in all rest of the study. All tree structure and parameters used in the prediction model can be found in the supplemental material.

Survival analysis

Overall survival time was calculated from the date of surgery until death or the last follow-up contact. Progression-free survival was defined as the time interval between the date of surgery and the date of disease recurrence or death from any cause, whichever came first, or date of last follow-up evaluation. Survival curves were estimated using the product-limit method of Kaplan-Meier (Kaplan, 1958) and were compared using the log-rank test. Univariate Cox proportional-hazards analysis (Collett, 2003) was also performed, with survival as the dependent variable. Two-sided *P* values of less than 0.05 were considered to indicate statistical significance.

Sweave report

A Sweave document is enclosed in the Supplemental Data online to permit others to reproduce any or all parts of our statistical analyses report. Sweave is a literate programming R package that combines the source code (in R) and documentation (in LaTeX) in one file and thereby permits reproduction of published high-throughput data analysis (Coombes et al., 2007; Gentleman, 2005; Lammport, 1994).

SUPPLEMENTAL DATA

The Supplementary Data include 4 tables, 4 figures, and one methods (Sweave) document and can be found with this article online.

ACKNOWLEDGEMENTS

The authors thank S. Kliewer, A. Bookout, B. Kim, and W. Lee for discussions and suggestions. J.D.M. is a director at Hamon Center for Therapeutic Oncology Research and D.J.M. is an investigator at Howard Hughes Medical Institute. This work was funded by the Howard Hughes Medical Institute, National Institutes of Health grants U19DK62434 (to D.J.M.), SPORE P50 CA70907 (to J.D.M), NIH UL1 RR024982 (to G.X.), the Robert A. Welch Foundation (D.J.M.), the Gillson Longenbaugh Foundation (J.D.M.), and DOD PROSPECT (J.D.M.).

REFERENCES

- Barish, G. D., Downes, M., Alaynick, W. A., Yu, R. T., Ocampo, C. B., Bookout, A. L., Mangelsdorf, D. J., and Evans, R. M. (2005). A Nuclear Receptor Atlas: macrophage activation. *Mol Endocrinol* *19*, 2466-2477.
- Beer, D. G., Kardia, S. L., Huang, C. C., Giordano, T. J., Levin, A. M., Misek, D. E., Lin, L., Chen, G., Gharib, T. G., Thomas, D. G., *et al.* (2002). Gene-expression profiles predict survival of patients with lung adenocarcinoma. *Nat Med* *8*, 816-824.
- Bolstad, B. M., Irizarry, R. A., Astrand, M., and Speed, T. P. (2003). A comparison of normalization methods for high density oligonucleotide array data based on variance and bias. *Bioinformatics* *19*, 185-193.
- Bookout, A. L., Jeong, Y., Downes, M., Yu, R. T., Evans, R. M., and Mangelsdorf, D. J. (2006). Anatomical profiling of nuclear receptor expression reveals a hierarchical transcriptional network. *Cell* *126*, 789-799.
- Chanda, D., Park, J. H., and Choi, H. S. (2008). Molecular basis of endocrine regulation by orphan nuclear receptor Small Heterodimer Partner. *Endocr J* *55*, 253-268.
- Chawla, A., Repa, J. J., Evans, R. M., and Mangelsdorf, D. J. (2001). Nuclear receptors and lipid physiology: opening the X-files. *Science* *294*, 1866-1870.
- Chen, H. Y., Yu, S. L., Chen, C. H., Chang, G. C., Chen, C. Y., Yuan, A., Cheng, C. L., Wang, C. H., Terng, H. J., Kao, S. F., *et al.* (2007). A five-gene signature and clinical outcome in non-small-cell lung cancer. *N Engl J Med* *356*, 11-20.
- Collett, D. (2003). Modelling survival data in medical research. Chapman & Hall/CRC.
- Coombes, K. R., Wang, J., and Baggerly, K. A. (2007). Microarrays: retracing steps. *Nat Med* *13*, 1276-1277; author reply 1277-1278.
- Di Fabio, F., Alvarado, C., Majdan, A., Gologan, A., Voda, L., Mitmaker, E., Beitel, L.K., Gordon, P.H., and Trifiro, M. (2007). Underexpression of mineralocorticoid receptor in colorectal carcinoma and association with VEGFR-2 overexpression. *J Gastrointest Surg* *11*, 1521-1528.
- Endoh, H., Tomida, S., Yatabe, Y., Konishi, H., Osada, H., Tajima, K., Kuwano, H., Takahashi, T., and Mitsudomi, T. (2004). Prognostic model of pulmonary adenocarcinoma by expression profiling of eight genes as determined by

quantitative real-time reverse transcriptase polymerase chain reaction. *J Clin Oncol* 22, 811-819.

Fu, M., Sun, T., Bookout, A. L., Downes, M., Yu, R. T., Evans, R. M., and Mangelsdorf, D. J. (2005). A Nuclear Receptor Atlas: 3T3-L1 adipogenesis. *Mol Endocrinol* 19, 2437-2450.

Garzotto, M., Beer, T. M., Hudson, R. G., Peters, L., Hsieh, Y. C., Barrera, E., Klein, T., and Mori, M. (2005). Improved detection of prostate cancer using classification and regression tree analysis. *J Clin Oncol* 23, 4322-4329.

Gentleman, R. (2005). Reproducible research: a bioinformatics case study. *Stat Appl Genet Mol Biol* 4, Article2.

Girnun, G. D., Naseri, E., Vafai, S. B., Qu, L., Szwaya, J. D., Bronson, R., Alberta, J. A., and Spiegelman, B. M. (2007). Synergy between PPARgamma ligands and platinum-based drugs in cancer. *Cancer Cell* 11, 395-406.

Goodwin, B., Jones, S. A., Price, R. R., Watson, M. A., McKee, D. D., Moore, L. B., Galardi, C., Wilson, J. G., Lewis, M. C., Roth, M. E., *et al.* (2000). A regulatory cascade of the nuclear receptors FXR, SHP-1, and LXR-1 represses bile acid biosynthesis. *Mol Cell* 6, 517-526.

Gronemeyer, H., Gustafsson, J.A., and Laudet, V. (2004). Principles for modulation of the nuclear receptor superfamily. *Nat. Rev. Drug Discov.* 3, 950–964.

Hess, K. R., Abbruzzese, M. C., Lenzi, R., Raber, M. N., and Abbruzzese, J. L. (1999). Classification and regression tree analysis of 1000 consecutive patients with unknown primary carcinoma. *Clin Cancer Res* 5, 3403-3410.

Ishibashi, H., Suzuki, T., Suzuki, S., Niikawa, H., Lu, L., Miki, Y., Moriya, T., Hayashi, S., Handa, M., Kondo, T., and Sasano, H. (2005). Progesterone receptor in non-small cell lung cancer--a potent prognostic factor and possible target for endocrine therapy. *Cancer Res* 65, 6450-6458.

Jemal, A., Siegel, R., Ward, E., Hao, Y., Xu, J., Murray, T., and Thun, M. J. (2008). Cancer statistics, 2008. *CA Cancer J Clin* 58, 71-96.

Kaplan, E., and Meier, P. (1958). Nonparametric Estimation from Incomplete Observations. *Journal of the American Statistical Association* 53, 457-481.

Koziol, J. A., Zhang, J. Y., Casiano, C. A., Peng, X. X., Shi, F. D., Feng, A. C., Chan, E. K., and Tan, E. M. (2003). Recursive partitioning as an approach to selection of immune markers for tumor diagnosis. *Clin Cancer Res* 9, 5120-5126.

- Lamport, L. (1994). *LaTeX: A Document Preparation System*: Addison Wesley, Boston).
- Lu, T. T., Makishima, M., Repa, J. J., Schoonjans, K., Kerr, T. A., Auwerx, J., and Mangelsdorf, D. J. (2000). Molecular basis for feedback regulation of bile acid synthesis by nuclear receptors. *Mol Cell* 6, 507-515.
- Lu, Y., Lemon, W., Liu, P. Y., Yi, Y., Morrison, C., Yang, P., Sun, Z., Szoke, J., Gerald, W. L., Watson, M., *et al.* (2006). A gene expression signature predicts survival of patients with stage I non-small cell lung cancer. *PLoS Med* 3, e467.
- Maitra, A., Wistuba, II, and Gazdar, A. F. (2001). Microdissection and the study of cancer pathways. *Curr Mol Med* 1, 153-162.
- Minna, J. D., and Schiller, J. (2008). Neoplasms of the Lung. In *Harrison's Principles of Internal Medicine*, D. Kasper, A. Fauci, D.L. Longo, E. Braunwald, S. Hauser, and J. Jameson, eds. (New York: McGraw-Hill), pp. 551-562.
- Mullican, S.E., Zhang, S., Konopleva, M., Ruvolo, V., Andreeff, M., Milbrandt, J., and Conneely, O.M. (2007). Abrogation of nuclear receptor Nr4a3 and Nr4a1 leads to development of acute myeloid leukemia. *Nat Med* 13, 730-735.
- Nishizawa, H., Yamagata, K., Shimomura, I., Takahashi, M., Kuriyama, H., Kishida, K., Hotta, K., Nagaretani, H., Maeda, N., Matsuda, M., *et al.* (2002). Small heterodimer partner, an orphan nuclear receptor, augments peroxisome proliferator-activated receptor gamma transactivation. *J Biol Chem* 277, 1586-1592.
- Potti, A., Mukherjee, S., Petersen, R., Dressman, H. K., Bild, A., Koontz, J., Kratzke, R., Watson, M. A., Kelley, M., Ginsburg, G. S., *et al.* (2006). A genomic strategy to refine prognosis in early-stage non-small-cell lung cancer. *N Engl J Med* 355, 570-580.
- RDC Team (2008). *R: A language and Environment for Statistical Computing*. Version 2.8.1. <http://cran.r-project.org/doc/manuals/refman.pdf>.
- Shedden, K., Taylor, J. M., Enkemann, S. A., Tsao, M. S., Yeatman, T. J., Gerald, W. L., Eschrich, S., Jurisica, I., Giordano, T. J., Misek, D. E., *et al.* (2008). Gene expression-based survival prediction in lung adenocarcinoma: a multi-site, blinded validation study. *Nat Med* 14, 822-827.
- Shulman, A. I., and Mangelsdorf, D. J. (2005). Retinoid x receptor heterodimers in the metabolic syndrome. *N Engl J Med* 353, 604-615.

- Siegfried, J. M. (2006). Hormone replacement therapy and decreased lung cancer survival. *J Clin Oncol* 24, 9-10.
- Stabile, L. P., Davis, A. L., Gubish, C. T., Hopkins, T. M., Luketich, J. D., Christie, N., Finkelstein, S., and Siegfried, J. M. (2002). Human non-small cell lung tumors and cells derived from normal lung express both estrogen receptor alpha and beta and show biological responses to estrogen. *Cancer Res* 62, 2141-2150.
- Stabile, L. P., Lyker, J. S., Gubish, C. T., Zhang, W., Grandis, J. R., and Siegfried, J. M. (2005). Combined targeting of the estrogen receptor and the epidermal growth factor receptor in non-small cell lung cancer shows enhanced antiproliferative effects. *Cancer Res* 65, 1459-1470.
- Sun, S., Schiller, J. H., Spinola, M., and Minna, J. D. (2007). New molecularly targeted therapies for lung cancer. *J Clin Invest* 117, 2740-2750.
- Traynor, A. M., Schiller, J. H., Stabile, L. P., Kolesar, J. M., Eickhoff, J. C., Dacic, S., Hoang, T., Dubey, S., Marcotte, S. M., and Siegfried, J. M. (2008). Pilot study of gefitinib and fulvestrant in the treatment of post-menopausal women with advanced non-small cell lung cancer. *Lung Cancer*.
- Valera, V. A., Walter, B. A., Yokoyama, N., Koyama, Y., Iiai, T., Okamoto, H., and Hatakeyama, K. (2007). Prognostic groups in colorectal carcinoma patients based on tumor cell proliferation and classification and regression tree (CART) survival analysis. *Ann Surg Oncol* 14, 34-40.
- Xie, C. Q., Jeong, Y., Fu, M., Bookout, A. L., Garcia-Barrio, M. T., Sun, T., Kim, B. H., Xie, Y., Root, S., Zhang, J., *et al.* (2009). Expression Profiling of Nuclear Receptors in Human and Mouse Embryonic Stem Cells. *Mol Endocrinol* 23, 724-733.
- Xie, Y., and Minna, J. D. (2008). Predicting the future for people with lung cancer. *Nat Med* 14, 812-813.
- Yang, X., Downes, M., Yu, R. T., Bookout, A. L., He, W., Straume, M., Mangelsdorf, D. J., and Evans, R. M. (2006). Nuclear receptor expression links the circadian clock to metabolism. *Cell* 126, 801-810.
- Zhang, Y., Xu, P., Park, K., Choi, Y., Moore, D. D., and Wang, L. (2008). Orphan receptor small heterodimer partner suppresses tumorigenesis by modulating cyclin D1 expression and cellular proliferation. *Hepatology* 48, 289-298.

FIGURE LEGENDS

Figure 1. QPCR analysis of the NR gene-expression signature in lung cancer patients

(A) Unsupervised cluster analysis of the 30 MDACC lung cancer patient cohort using the QPCR profile of the NR superfamily. Vertical and horizontal axes represent NR and lung cancer patient clusters, respectively.

(B and C) Kaplan-Meier plots showing the association of the NR gene signature with overall patient survival (B) and disease progression (C). *P*-values were obtained using the log-rank test. Red color represents sample Cluster I and blue color represents Cluster II defined by an unsupervised clustering algorithm using NR gene profiling data. ○ indicates censored samples. ADC, adenocarcinoma; SCC, squamous cell carcinoma.

Figure 2. Kaplan-Meier plots showing the predictive power of the NR gene signature in training and testing sets from multiple institutions

(A) LOOCV of the recursive-partitioning tree model (RPART) for the 30-sample MDACC QPCR dataset. The hazard ratio (HR) for the predicted high-risk vs. the predicted low-risk signatures was 7.03; 95% CI, 2.22 to 22.3; *P*=0.00015.

(B and C) Independent validation of the NR gene-expression signature between the MDACC cohort and consortium cohort. The MDACC cohort (n=30) training set was tested in the consortium cohort (n=442) (B), and vice versa (C).

(D) Independent validation of the NR gene signature in the 442-sample cohort multi-institute consortium using RPART analysis. The microarray datasets were divided into two groups, one for the training and the other for the testing cohort. *P*-values were obtained by the log-rank test. Red and black lines represent predicted high- and low-risk groups, respectively. ○ indicates censored samples.

Figure 3. Identification of single-NR gene biomarkers for lung cancer prognosis

(A and B, D and E) Kaplan-Meier survival plots using single gene prediction model of PR (A and B) and SHP (D and E). The MDACC cohort was tested using LOOCV (A and D), or used as a training set and independently tested in the multi-site consortium cohort (B and E). *P*-values were obtained using log-rank test. Red and black lines represent high- and low-risk groups, respectively. ○ indicates censored samples.

(C and F) Hazard ratios from univariate Cox regression model for PR and SHP expression, respectively, in the MDACC and multi-site consortium data sets.

Figure 4. Kaplan-Meier survival plots showing single NR gene predictors in stage I lung cancer patients

(A and B) Predictive models for SHP (A) and PR (B) were trained in the MDACC samples and tested in the stage I lung cancer patients of the consortium cohort. *P*-values were obtained by log-rank test. Red and black lines represent predicted high- and the low-risk groups, respectively. ○ indicates censored samples.

Table 1. Patient demographics summarized by unsupervised cluster analysis of lung tumors

	Cluster 1	Cluster 2	<i>P</i> -value†
Sample size	13	16	
Age (mean ± s.e.)	62.6±2.4	63±2.1	0.902
Gender (% female)	38%	56%	0.340
Race (% non-white)	0%	13%	0.187
Histology (ADC/SCC)	8/5	13/3	0.238
Stage I	62%	56%	0.730
Stage II	8%	19%	
Stage III	15%	19%	
Stage IV	15%	6%	
Death rate	85%	25%	0.001
Disease progression rate	92%	63%	0.062
Smokers	15%	13%	0.823
Adjuvant Therapy	15%	6%	0.422

†indicates *P*-values by t-test for Age and by Fisher's exact test for other variables comparing cluster 1 and 2.

ADC, adenocarcinoma; SCC, squamous cell carcinoma.

Table 2. Death hazard ratios (HR) from multivariate Cox regression analysis from two independent datasets

Variable	MSK and CAN/DF Dataset		Total Consortium Dataset	
	HR	<i>P</i> -value	HR	<i>P</i> -value
Gender	1.88	0.019	1.34	0.07
Age at diagnosis	1.02	0.22	1.04	2.4e-07
Adjuvant chemotherapy	2.02	0.016	1.22	0.34
Adjuvant radiation therapy	1.48	0.210	1.50	0.059
Stage	2.76	0.00046	3.05	8.5e-11
NR signature*	1.98	0.037	1.89	9.9e-05

*The NR signature for the MSK and CAN/DF dataset (n=186) was derived based on the prediction model built from the University of Michigan Cancer Center and Moffitt Cancer Center Consortium training dataset. The NR signature for the total Consortium dataset (n=442) was derived based on the prediction model built from the MDACC dataset.

MSK, Memorial Sloan-Kettering Cancer Center; CAN/DF, Dana-Farber Cancer Institute.

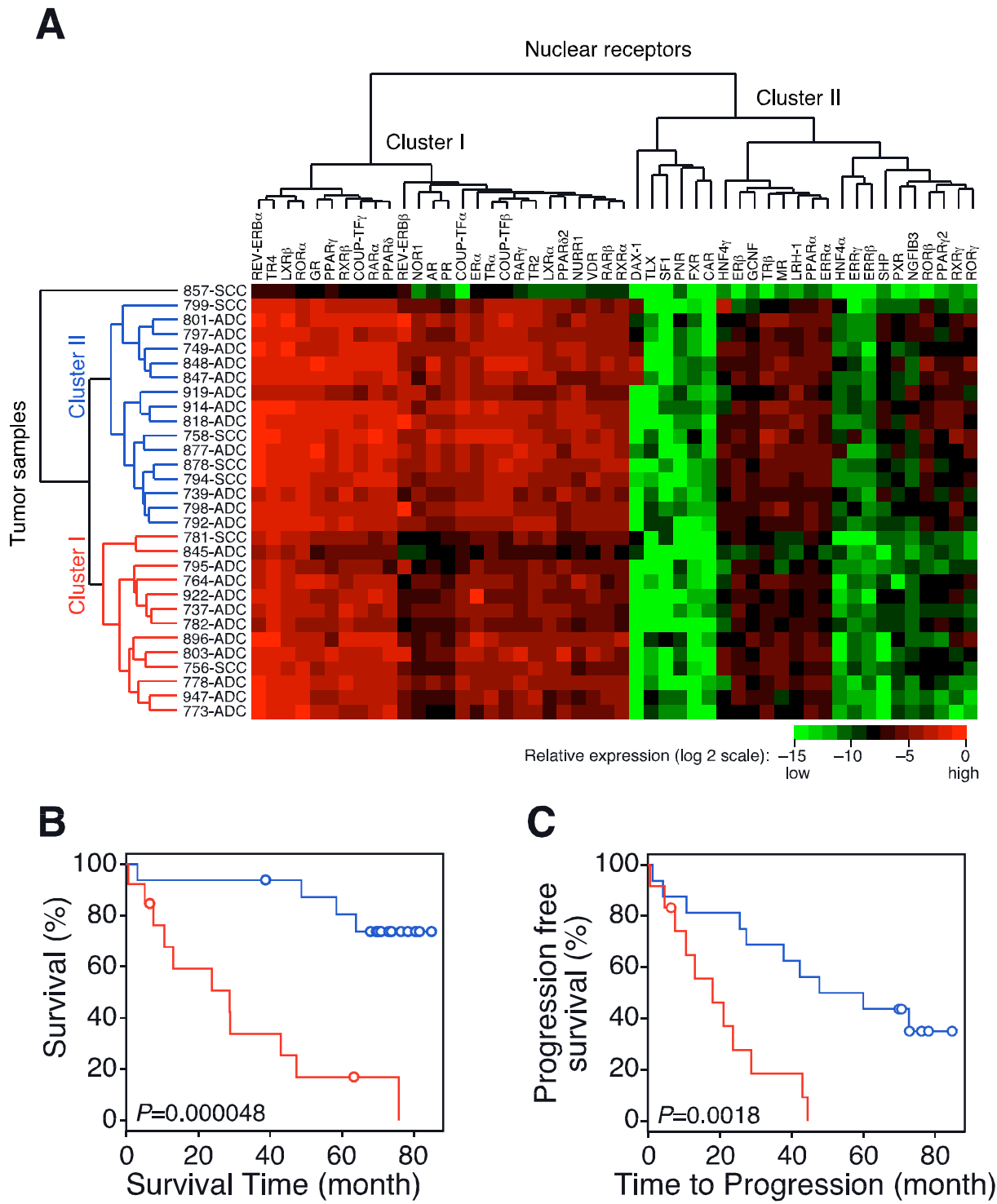


Figure 1
Jeong et al.

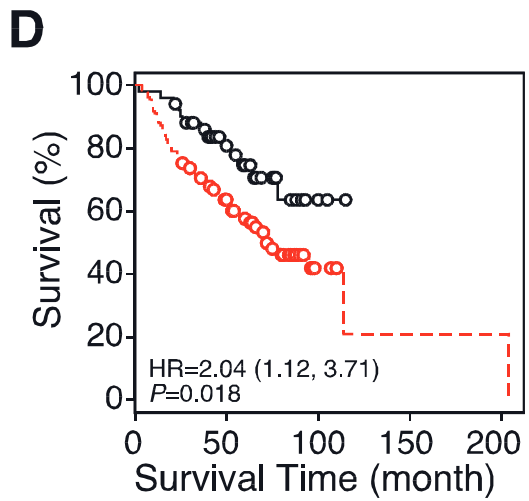
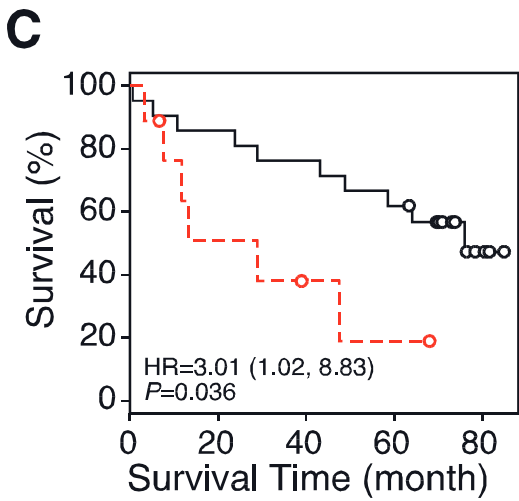
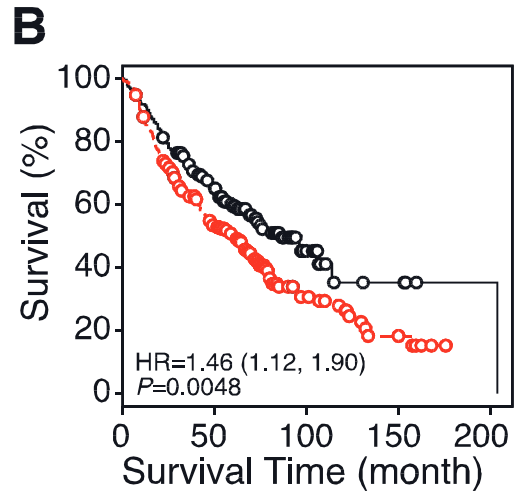
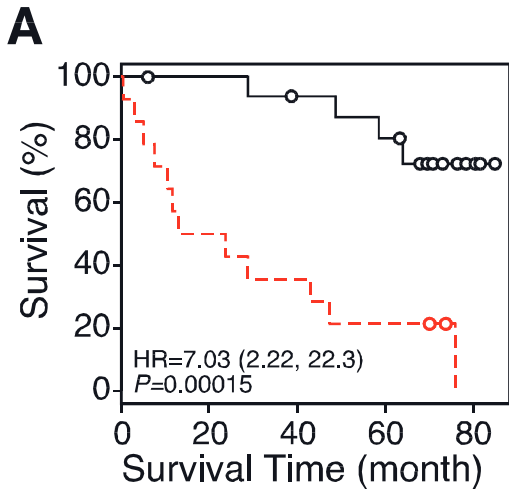


Figure 2
Jeong et al.

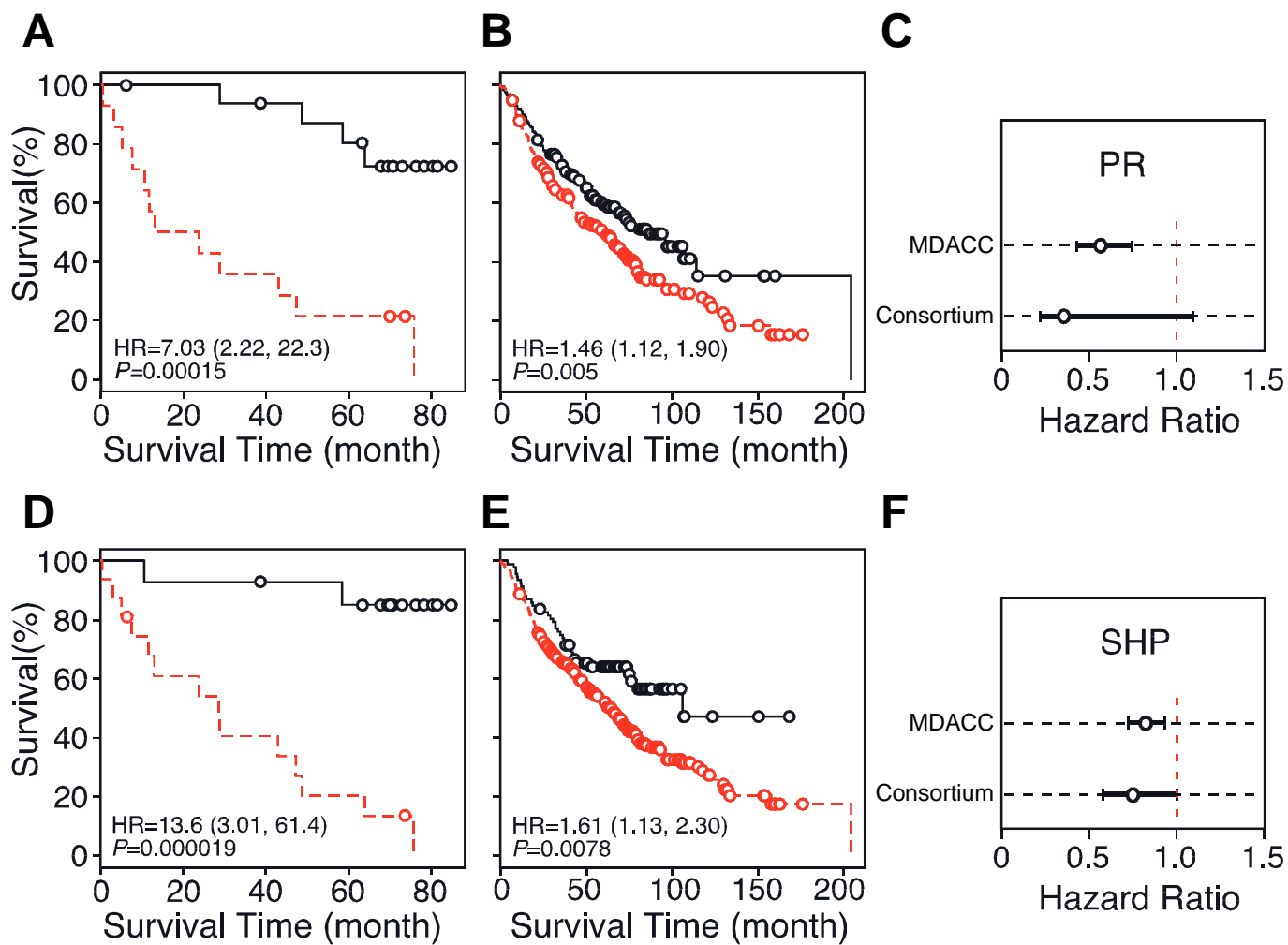


Figure 3
Jeong et al.

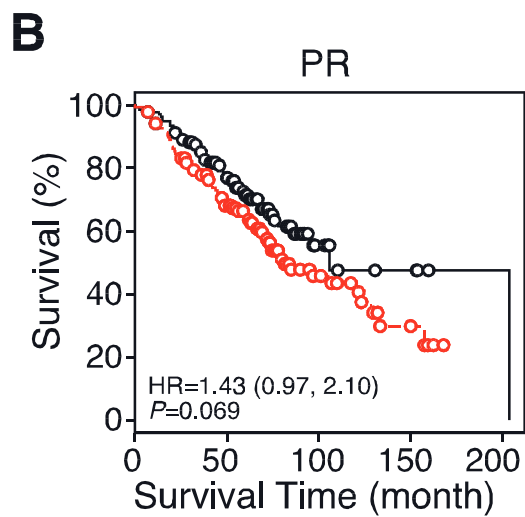
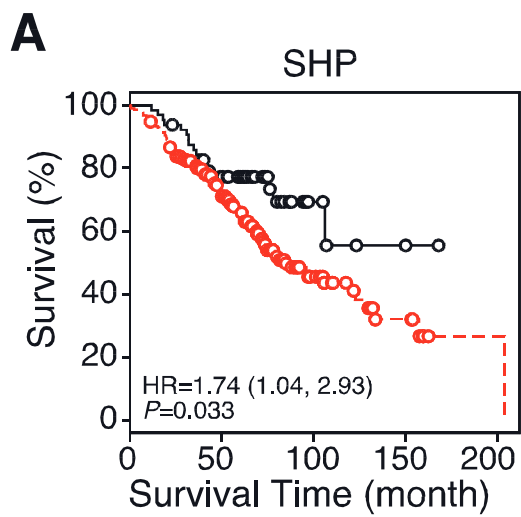


Figure 4
Jeong et al.

Supplemental Figures

Nuclear Receptor Expression Defines a Set of Prognostic Biomarkers for Lung Cancer

Yangsik Jeong^{1,2,3,4}, Yang Xie^{4,5}, Guanghua Xiao⁵, Xian-Jin Xie^{4,5}, Carmen Behrens⁷, Luc Girard^{1,3,4}, Edward F. Patz, Jr.⁹, Ignacio I. Wistuba^{7,8}, John D. Minna^{1,3,4,6,*}, & David J. Mangelndorf^{1,2,3,*}

¹ Department of Pharmacology

² Howard Hughes Medical Institute

³ Hamon Center for Therapeutic Oncology Research

⁴ Simmons Cancer Center

⁵ Department of Clinical Sciences

⁶ Department of Internal Medicine

University of Texas Southwestern Medical Center 6001 Forest Park Rd., Room ND9.124, Dallas, TX 75390-9050, USA

⁷ Department of Thoracic/Head& Neck Medical Oncology

⁸ Department of Pathology

University of Texas M.D. Anderson Cancer Center, 1515 Holcombe Boulevard, Houston, TX 77030-4009, USA

⁹ Department of Radiology, Department of Pharmacology and Cancer Biology, P.O. Box 3808 Duke University Medical Center, Durham, NC 27710, USA

*Correspondence: john.minna@utsouthwestern.edu (J.D.M.),
davo.mango@utsouthwestern.edu (D.J.M.).

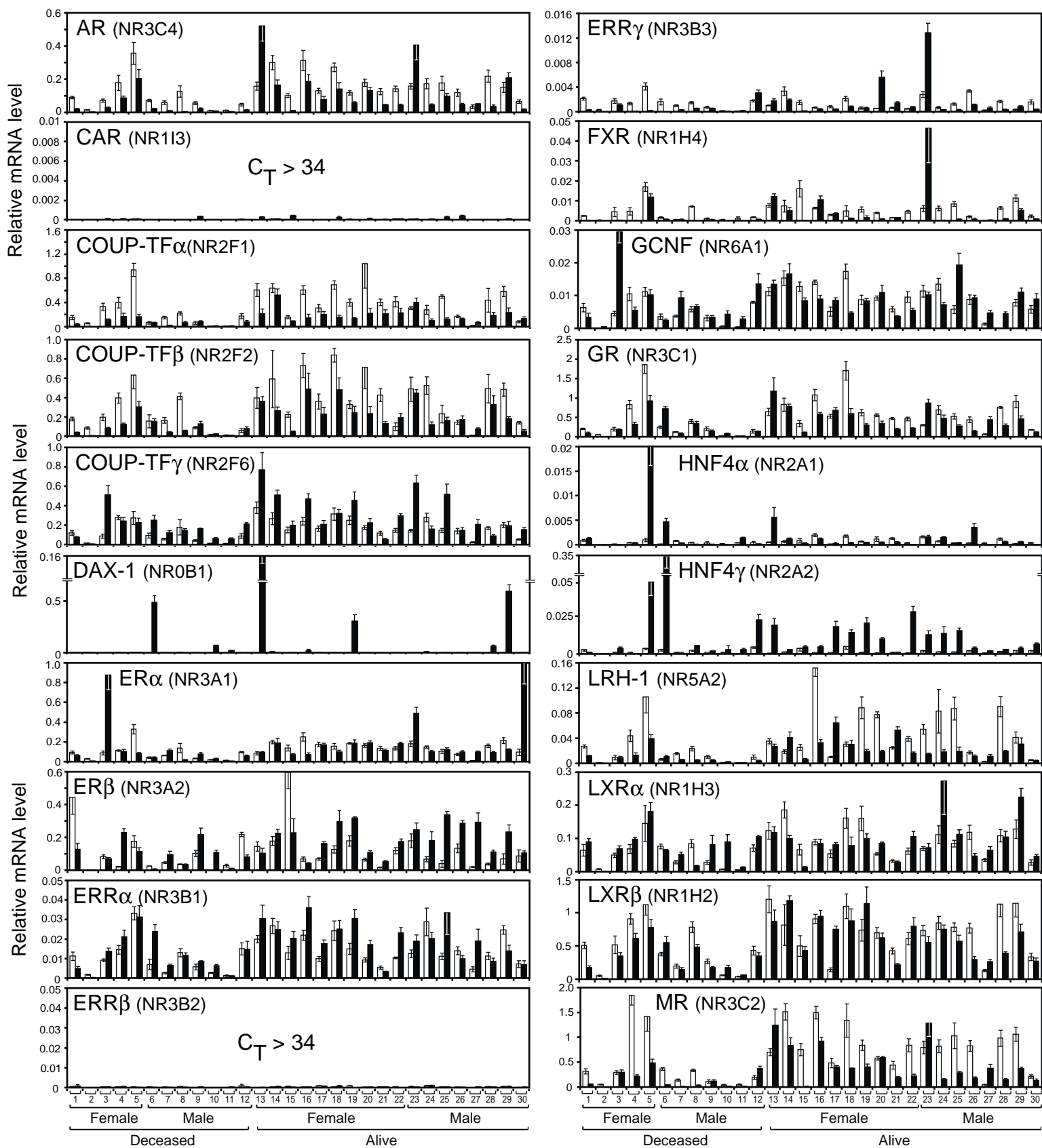


Figure S1. Expression profiles of the NR superfamily in lung tissues.

Quantitative real-time PCR analysis was performed for 48 NRs (including 2 common splice variants each for PPAR γ and PPAR δ) in 30 pair-matched tissues (normal and tumor) from lung cancer patients. Relative expression values were obtained as described in Methods. Ct > 34 was scored as below detection. Open and filled bars represent normal and pair-matched tumor tissues from each patient, respectively. The patients are numbered from 1–30 (see Table S2) and grouped according to gender and survival status with each patient being in the same position for each NR dataset.

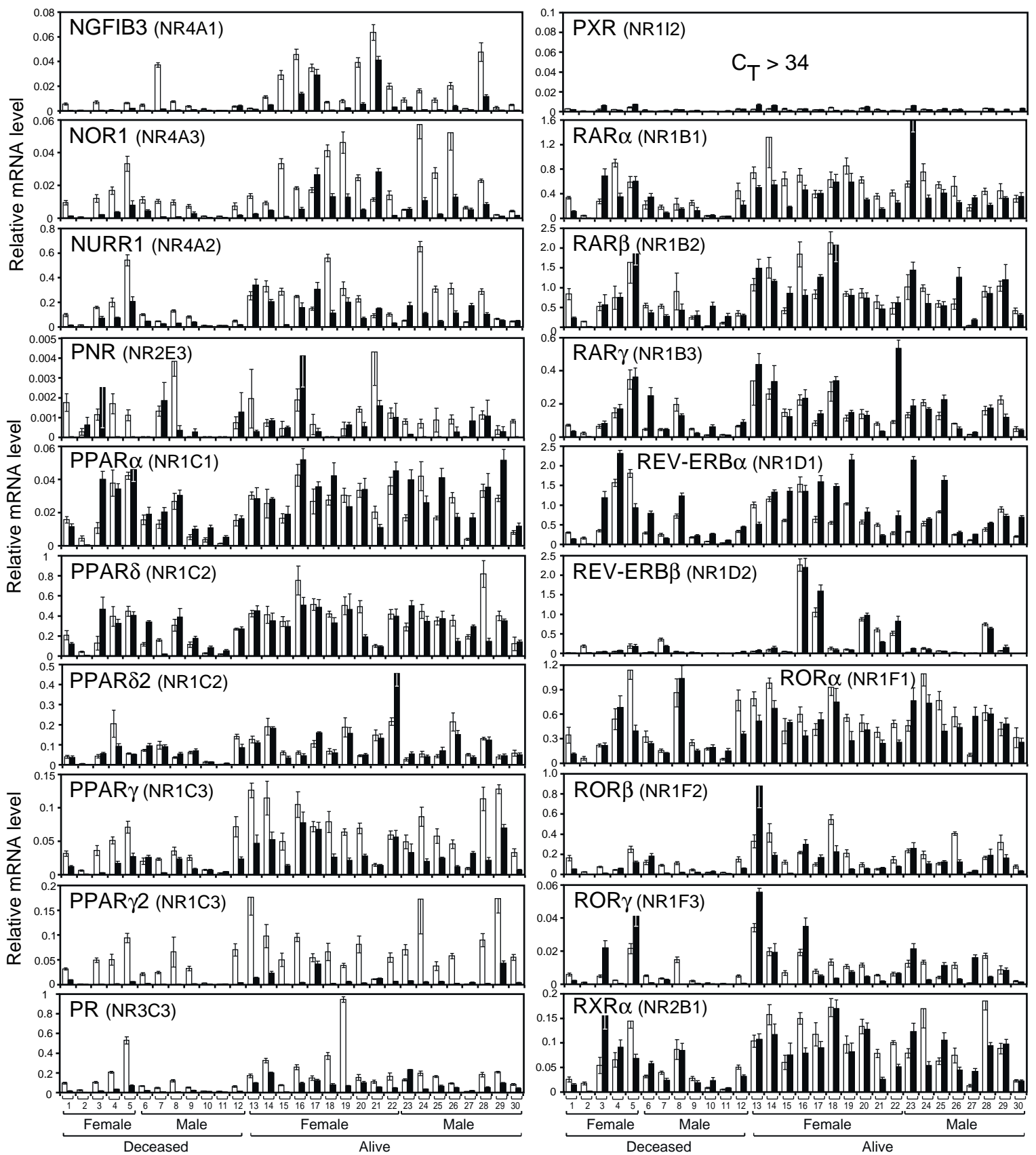


Figure S1 (continued). Expression profiles of the NR superfamily in lung tissues.

Quantitative real-time PCR analysis was performed for 48 NRs (including 2 common splice variants each for $PPAR\gamma$ and $PPAR\delta$) in 30 pair-matched tissues (normal and tumor) from lung cancer patients. Relative expression values were obtained as described in Methods. $C_t > 34$ was scored as below detection. Open and filled bars represent normal and pair-matched tumor tissues from each patient, respectively. The patients are numbered from 1–30 (see Table S2) and grouped according to gender and survival status with each patient being in the same position for each NR dataset.

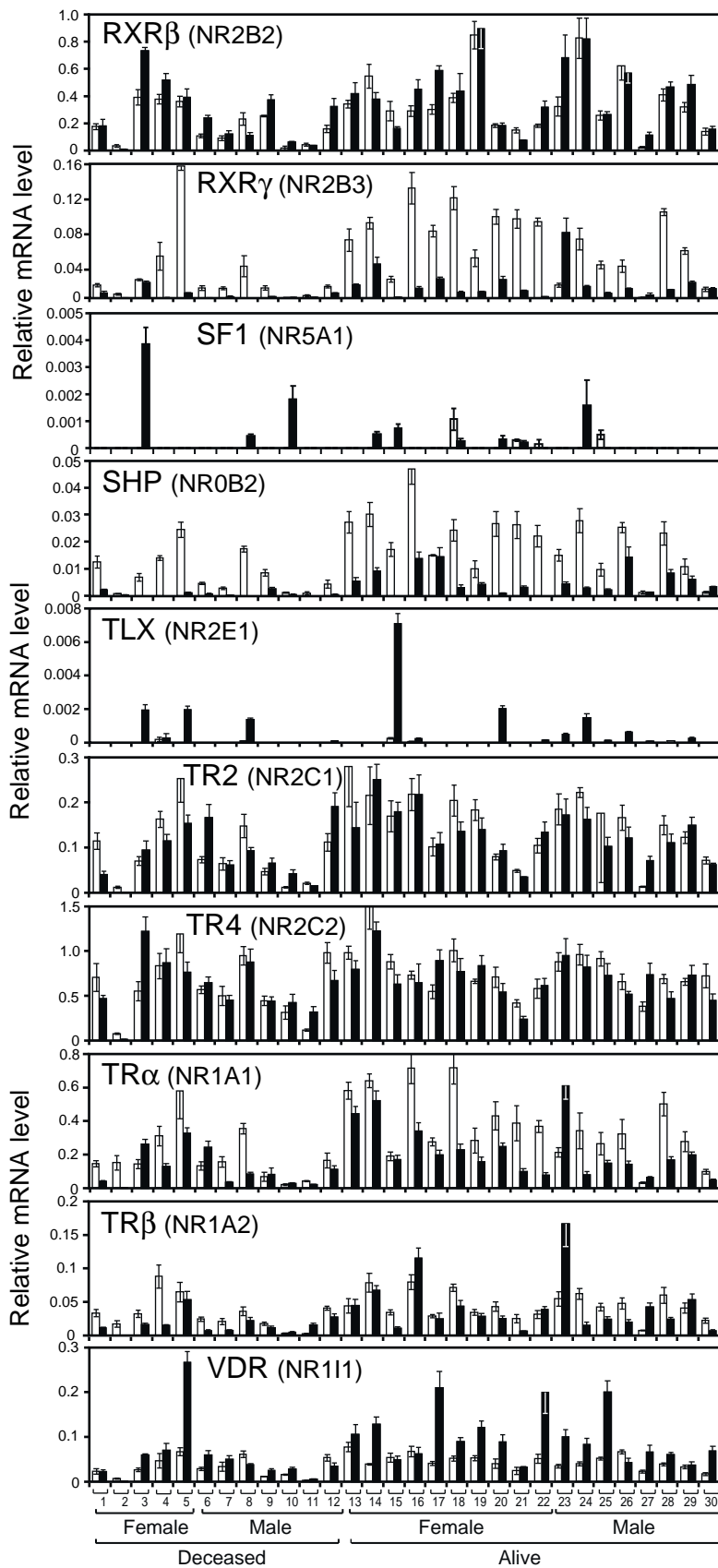


Figure S1 (continued). Expression profiles of the NR superfamily in lung tissues.

Quantitative real-time PCR analysis was performed for 48 NRs (including 2 common splice variants each for PPAR γ and PPAR δ) in 30 pair-matched tissues (normal and tumor) from lung cancer patients. Relative expression values were obtained as described in Methods. Ct > 34 was scored as below detection. Open and filled bars represent normal and pair-matched tumor tissues from each patient, respectively. The patients are numbered from 1–30 (see Table S2) and grouped according to gender and survival status with each patient being in the same position for each NR dataset.

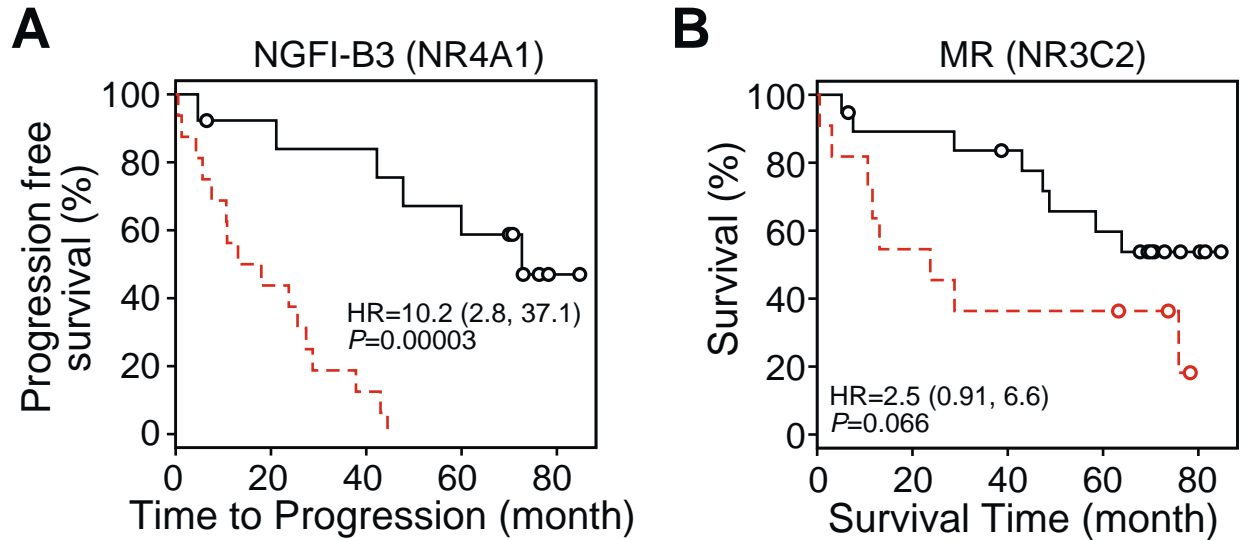


Figure S2. Identification of NRs as prognostic biomarkers in normal lung tissue from lung cancer patients.

(A and B) Kaplan-Meier plots of time to progression and survival are shown for NGFI-B and MR, respectively. Note that these two plots are identical to those obtained when using the entire 48 NR gene set. (A) LOOCV of recursive-partitioning tree model of the MDACC QPCR data in normal tissues shows that NGFI-B is the single gene left in the predictive model for disease progression (HR=10.2, 95% CI 2.8 to 37.1; $P=0.00003$). (B) Similar LOOCV analysis shows MR is a single-gene predictor of the entire 48 NR gene set as associated with patient survival (HR=2.5, 95% CI 0.91 to 6.6; $P=0.066$). Red and black lines represent high- and low-risk groups, respectively. Open circles indicate censored samples.

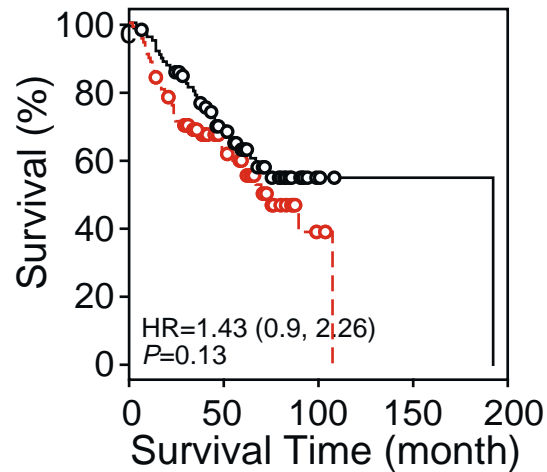


Figure S3. Kaplan-Meier estimates of survival time based on NR expression when clinical variables are included in the analysis.

The microarray dataset from the four institute Consortium was divided into two groups, one for the training cohort and the other for the testing cohort. We included 48 NR expression variables and clinical variables including gender, age, stage, treatments (i.e., those receiving adjuvant chemo-therapy or not, and those receiving adjuvant radiation therapy or not) as co-variables in RPART predictive model. The final predictive tree structure can be seen in the Sweave report (Supplemental Data online). The predictive model was built in the training cohort and then validated in the testing cohort. In the testing cohort, patients in the predicted high risk group live significantly shorter than patients in the predicted low risk group, (HR = 1.43; 95% CI, 0.9 to 2.26; $P=0.13$). P -values were obtained by log-rank test. Red and black lines represent predicted high- and low-risk groups, respectively. Open circles indicate censored samples.

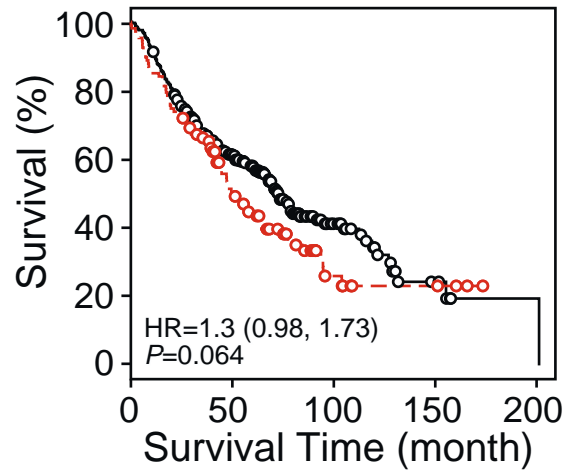


Figure S4. Kaplan-Meier plots of survival time of the Consortium cohort based on the 48 NR expression signatures.

Unsupervised hierarchical cluster analysis of the microarray signature of the 48 NRs divides the 442 Consortium samples into two clusters. The patients in these two clusters have significantly different survival times. *P*-values were obtained using the log-rank test. Red and black colors were defined by unsupervised clustering algorithm using NR gene signature. Open circles indicate censored samples.

Table S1. Summary of patient clinical information.

Feature	Cohort (n=30)
Age (y)	
Median	67
Range	44.0-77.7
Mean	63.3
Gender	
Female	15
Male	15
Race	
White	28
Black	1
Asian	1
TNM Stage	
I	17
II	4
III	5
IV	4
Tumor type	
ADC	22
SCC	8
Survival	
Dead	16
Female	7
Male	9
Alive	14
Female	8
Male	6
Smoking history†	
No	4
Yes	26
Adjuvant therapy	
No	27
Yes	3

Abbreviations: ADC, adenocarcinoma; SCC, squamous cell carcinoma; TNM, tumor size, node involvement, metastasis status.

†, Patients who had smoked at least 100 cigarettes in their lifetime were defined as smokers.

Table S2. Clinical information on individual patients.

Sample ID	Date of surgery	Sex	Race	DOB	Tobacco history	Pack-years	Pathology (TNM)	Stage	Last contact/vital status	Date of recurrence	N.A. therapy	
1	847-ADC	9/22/01	F	W	9/2/41	Yes/current	35	T2,N0,M0	IB	10/8/01 (D)	None	No
2	773-ADC	5/21/01	F	W	9/30/23	Yes/current	50	T4,N2,M1	IV	5/10/02 (D)	11/9/01	No
3	848-ADC	9/27/01	F	W	7/2/53	Yes/current	45	T2,N0,M0	IB	9/21/03 (D)	None	No
4	801-SCC	8/3/01	F	W	3/6/38	Yes/current	60	T4,N1,M1	IV	12/28/03 (D)	None	No
5	845-ADC	9/19/01	F	W	4/18/43	Yes/former	35	T2,N1,M0	IIB	10/14/05 (D)	1/2/04	No
6	947-ADC	8/30/02	M	W	5/13/34	Yes/current	75	T4,N0,M0	IIIB	12/2/02 (D)	10/7/02	No
7	758-SCC	4/28/01	M	W	10/15/31	Yes/former	8	T2,N2,M0	IIIA	10/1/01 (D)	9/17/01	No
8	857-SCC	10/24/01	M	W	9/19/30	Yes/current	80	T2,N0,M0	IB	6/11/02 (D)	None	No
9	919-ADC	6/27/02	M	W	12/6/32	Yes/current	70	T2,N0,M0	IB	5/17/03 (D)	None	No
10	878-SCC	11/19/01	M	W	2/13/39	Yes/former	43	T4,N2,M0	IIIB	12/23/02 (D)	Unknown	Yes
11	877-ADC	12/12/01	M	W	9/23/44	Yes/current	75	T2,N1,M0	IIB	5/9/04 (D)	6/13/03	No
12	797-ADC	7/26/01	M	W	5/25/32	Yes/current	77	T2,N0,M0	IB	2/26/05 (D)	None	No
13	896-ADC	2/11/02	F	W	12/23/52	Yes/current	30	T1,N0,M0	IA	5/5/05 (A)	4/1/04	No
14	922-ADC	7/18/02	F	As	12/4/56	No	0	T1,N0,M0	IA	5/6/08 (A)	1/26/06	No
15	799-SCC	7/30/01	F	W	1/4/40	Yes/current	100	T2,N0,M0	IB	7/13/05 (D)	5/5/03	No
16	778-ADC	6/7/01	F	W	4/18/43	Yes/former	20	T2,N0,M0	IB	3/27/08 (A)	6/9/06	No
17	764-ADC	5/15/01	F	W	5/16/43	Yes/current	105	T2,N0,M0	IB	4/12/07 (A)	None	No
18	781-SCC	6/18/01	F	W	10/20/25	Yes/current	56	T1,N0,M0	IA	2/16/07 (A)	8/15/04	No
19	803-ADC	8/7/01	F	B	5/14/36	Yes/current	50	T2,N1,M0	IIB	4/24/08 (A)	7/2/02	No
20	739-ADC	3/2/01	F	W	1/14/28	Yes/former	60	T2,N2,M0	IIIA	7/3/06 (D)	2/25/05	No
21	737-ADC	3/1/01	F	W	9/9/27	Yes/current	40	T1,N0,M0	IA	3/31/08 (A)	None	No
22	749-ADC	8/22/05	F	W	5/3/35	No	0	T2,N0,M0	IB	3/20/08 (A)	None	No
23	795-ADC	6/29/01	M	W	5/8/37	No	0	T1,N0,M0	IA	1/11/08 (A)	None	No
24	794-SCC	7/18/01	M	W	9/13/34	Yes/current	100	T2,N1,M0	IIB	5/23/07 (A)	None	No
25	792-ADC	7/12/01	M	W	1/11/34	Yes/current	100	T1,N0,M0	IA	4/8/08 (D)	1/11/05	No
26	798-ADC	7/30/01	M	W	10/9/42	Yes/current	84	T2,N0,M1	IV	6/19/08 (A)	None	No
27	818-ADC	7/10/01	M	W	8/8/57	No	0	T4,N1,M1	IV	11/10/07 (D)	8/13/02	Yes
28	756-SCC	4/19/01	M	W	6/2/45	Yes/current	85	T1,N2,M0	IIIA	5/23/07 (A)	None	No
29	782-ADC	6/21/01	M	W	10/21/32	Yes/current	150	T1,N0,M0	IA	5/9/06 (D)	10/29/01	No
30	914-ADC	7/11/02	M	W	5/22/36	Yes/former	80	T2,N0,M0	IB	10/22/07 (A)	3/28/06	No

Abbreviations: ADC, adenocarcinoma; SCC, squamous cell carcinoma; W, white; B, black; As, asian; TNM, tumor size, node involvement, metastasis status; A, alive; D, dead.

Table S3. Summary of NR expression data in normal and tumor lung tissue taken from lung cancer patients.

Broadly expressed in both normal and tumor (n=22)		Selectively expressed in either tumor or normal tissue			Low to undetectable* expression in normal and tumor (n=3)
		Tumor (n=7)	Normal (n=18)		
ER α	RAR γ	COUP-TF γ	AR	PPAR γ	CAR
ERR α	REV-ERB α	DAX-1	COUP-TF α	PPAR γ 2	ERR β
GCNF	REV-ERB β	ER β	COUP-TF β	PR	PXR
GR	ROR α	HNF4 α	ERR γ	ROR β	
LXR α	RXR α	HNF4 γ	FXR	ROR γ	
LXR β	RXR β	TLX	LRH-1	RXR γ	
PPAR α	TR2	SF1	MR	SHP	
PPAR δ	TR4		NGFIB3		
PPAR δ 2	TR α		NOR1		
RAR α	TR β		NURR1		
RAR β	VDR		PNR		

* Ct > 34.

Raw primary data can be found at www.NURSA.org.

Table S4. Correlation of NR expression between tumor and normal tissue.

Nuclear Receptors	Pearson Correlation	<i>P</i> value
REV-ERB β *	0.96	5.47E-17
RXR β *	0.85	2.42E-09
COUP-TF β *	0.76	9.15E-07
PPAR δ 2*	0.76	1.15E-06
NGFI-B3*	0.76	1.33E-06
RAR β *	0.76	1.39E-06
ROR γ *	0.74	2.81E-06
TR2*	0.73	4.51E-06
PPAR α *	0.70	1.97E-05
PPAR γ *	0.69	2.05E-05
TLX*	0.69	2.25E-05
RAR γ *	0.68	3.08E-05
LXR β *	0.67	5.39E-05
TR4*	0.67	5.72E-05
ERR α *	0.64	0.000162
ROR α *	0.63	0.000192
RXR α *	0.62	0.000291
REV-ERB α *	0.58	0.000838
GR	0.57	0.001004
COUP-TF α	0.57	0.001103
TR α	0.56	0.001409
COUP-TF γ	0.54	0.001869
SHP	0.54	0.002036
PPAR δ	0.52	0.003233
ROR β	0.52	0.003413
LXR α	0.51	0.004302
PXR	0.49	0.006065
AR	0.49	0.006387
VDR	0.48	0.00667
TR β	0.48	0.007836
PPAR γ 2	0.43	0.017747
MR	0.43	0.018366
RAR α	0.43	0.018471
NOR1	0.40	0.029223
ERR β	0.39	0.032868
NURR1	0.37	0.045347
LRH-1	0.33	0.077539
PR	0.33	0.078355
PNR	0.31	0.092401

FXR	0.26	0.169483
GCNF	0.26	0.172028
ERR γ	0.25	0.188439
ER β	0.24	0.208889
HNF4 γ	0.23	0.214435
HNF4 α	0.11	0.557613
RXR γ	0.11	0.567836
ER α	0.04	0.821723
SF-1	-0.06	0.748715
DAX-1	-0.14	0.473384
CAR	-0.15	0.437427

QPCR expression levels for NRs from the 30 pairs of normal and tumor lung samples were determined and a Pearson correlation coefficient calculated with an associated *P* value. Statistical significant values ($P < 0.001$ after multiple testing correction) are noted with an asterisk.

Supplementary Data

Nuclear Receptor Expression Profiling Defines a Set of Prognostic Biomarkers for Lung Cancer

Yangsik Jeong, Yang Xie, Guanghai Xiao, Xian-Jin Xie, Carmen Behrens, Luc Girard, Edward F. Patz, Jr., Ignacio I Wistuba, John D Minna & David J Mangelsdorf

Sweave Report

Include R library

```
> library(survival)
> library(rpart)

function for showing p values in figures

> pv.expr <- function(x, digits = 1) {
+   if (!x)
+     return(0)
+   exponent <- floor(log10(x))
+   base <- round(x/10^exponent, digits)
+   ifelse(x > 1e-04, paste("pv = ", base * (10^exponent), sep = ""),
+     paste("pv = ", base, "E", exponent, sep = ""))
+ }

Generate heatmap for MDACC PCR data. If the PCR value is 0, then
replace it with the minimum non-zero value. Take log2 transformation of PCR
values.

> mda <- read.csv("MDA_data.csv", row.names = 1)
> mda.pcr <- mda[, -(1:4)]
> mda.pcr[mda.pcr == 0] <- min(mda.pcr[mda.pcr != 0])
> mda[, -(1:4)] <- mda.pcr <- log2(mda.pcr)

> rgb.palette <- colorRampPalette(c("green", "black", "red"), space = "rgb")
> heatmap(t(mda.pcr), scale = "none", col = rgb.palette(13), margins = c(4,
+   4), cex.axis = 1)
```

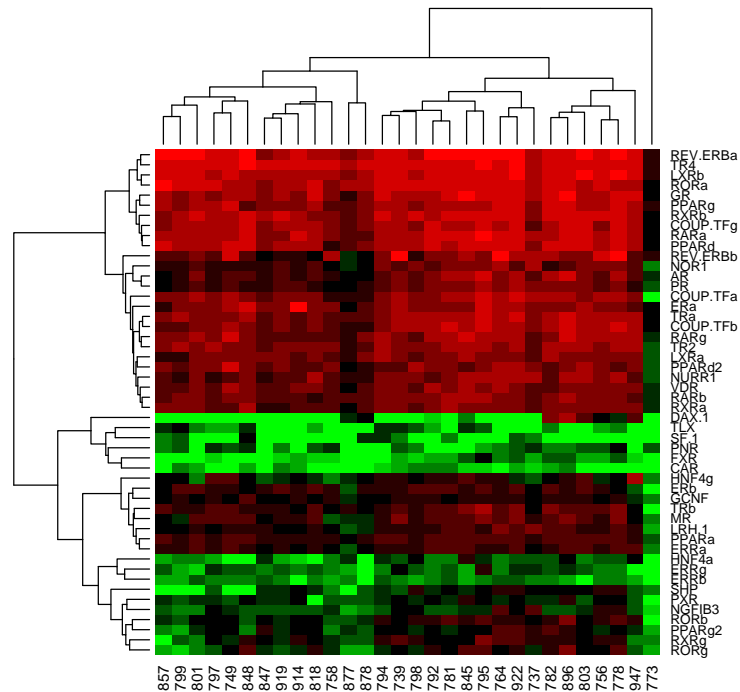


Figure 1a heatmap for MDACC PCR data

Characterize MDACC patients using unsupervised clustering algorithm.

```
> cluster <- cutree(hclust(dist(mda.pcr)), k = 3)
> mda.clust <- data.frame(cluster, mda[, 1:4])[cluster != 3, ]
```

Cluster 3 includes only one patient and is regarded as an outlier based on NR expression profile. Then we looked at that patient's clinical data and found the patient has very short survival time.

```
> sf <- survfit(Surv(Survival_Time, Dead) ~ cluster, data = mda.clust)
> logrank <- survdiff(Surv(Survival_Time, Dead) ~ cluster, data = mda.clust)
> logrank
```

Call:

```
survdiff(formula = Surv(Survival_Time, Dead) ~ cluster, data = mda.clust)
```

	N	Observed	Expected	(O-E) ² /E	(O-E) ² /V
cluster=1	16	4	10.8	4.28	16.5
cluster=2	13	11	4.2	11.02	16.5

Chisq= 16.5 on 1 degrees of freedom, p= 4.84e-05

```

> pv <- pchisq(logrank$chisq, 1, lower.tail = F)
> summary(coxph(Surv(Survival_Time, Dead) ~ cluster, data = mda.clust))

Call:
coxph(formula = Surv(Survival_Time, Dead) ~ cluster, data = mda.clust)

n= 29
      coef exp(coef) se(coef)      z      p
cluster 2.16      8.7      0.613 3.53 0.00042

      exp(coef) exp(-coef) lower .95 upper .95
cluster      8.7      0.115      2.62      28.9

Rsquare= 0.395 (max possible= 0.953 )
Likelihood ratio test= 14.6 on 1 df, p=0.000134
Wald test              = 12.4 on 1 df, p=0.000417
Score (logrank) test = 16.5 on 1 df, p=4.84e-05

> plot(sf, main = "", xlab = "Survival Time (month)", ylab = "Survival",
+       cex.lab = 1.5, mark = c(1, 19), cex = 1.2)
> text(60, 0.5, pv.expr(pv), cex = 1.5)

```

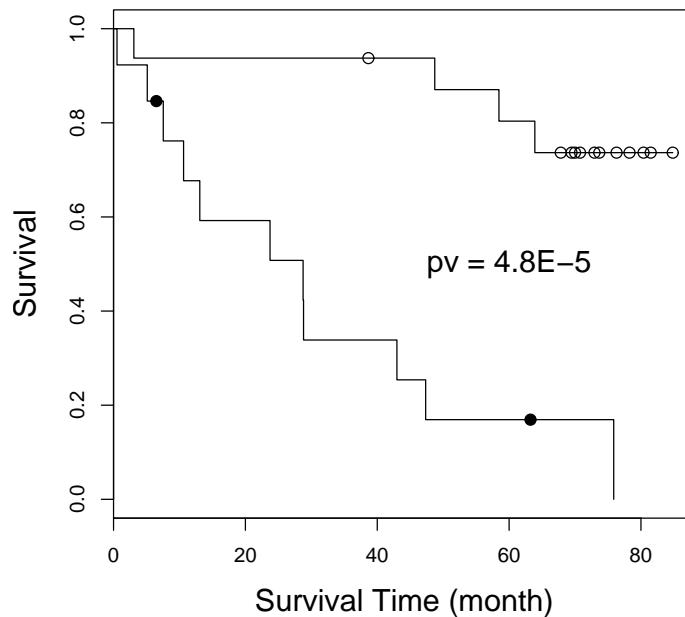


Figure 1b. KM plot for overall survival


```

> sf <- survfit(Surv(TOE, Progression) ~ cluster, data = mda.clust)
> logrank <- survdiff(Surv(TOE, Progression) ~ cluster, data = mda.clust)
> logrank

```

Call:

```
survdiff(formula = Surv(TOE, Progression) ~ cluster, data = mda.clust)
```

n=28, 1 observation deleted due to missingness.

	N	Observed	Expected	(O-E) ² /E	(O-E) ² /V
cluster=1	16	10	15.83	2.15	9.76
cluster=2	12	11	5.17	6.57	9.76

Chisq= 9.8 on 1 degrees of freedom, p= 0.00178

```

> pv <- pchisq(logrank$chisq, 1, lower.tail = F)
> summary(coxph(Surv(TOE, Progression) ~ cluster, data = mda.clust))

```

Call:

```
coxph(formula = Surv(TOE, Progression) ~ cluster, data = mda.clust)
```

n=28 (1 observation deleted due to missingness)

	coef	exp(coef)	se(coef)	z	p
cluster	1.46	4.31	0.502	2.91	0.0036

	exp(coef)	exp(-coef)	lower .95	upper .95
cluster	4.31	0.232	1.61	11.5

Rsquare= 0.267 (max possible= 0.984)

Likelihood ratio test= 8.69 on 1 df, p=0.00319

Wald test = 8.46 on 1 df, p=0.00362

Score (logrank) test = 9.76 on 1 df, p=0.00178

```

> {
+   plot(sf, main = "", xlab = "Time to Progression (month)",
+        ylab = "Progression free survival", cex.lab = 1.5, mark = c(1,
+        19), cex = 1.2)
+   text(50, 0.9, pv.expr(pv), cex = 1.5)
+ }

```

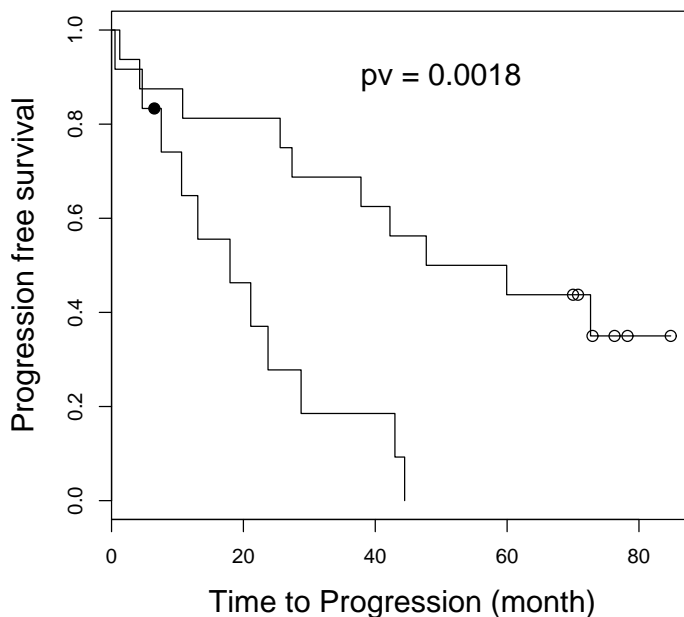


Figure 1c. KM plot for progression free survival

Predicting MDACC patients' survival using recursive-partitioning tree analysis (RPART) and then use leave one out cross validation (LOOCV) to check the performance.

```

> mda.surv <- mda[, -(3:4)]
> fit <- rpart(Surv(Survival_Time, Dead) ~ ., data = mda.surv)
> print(fit)

n= 30

node), split, n, deviance, yval
  * denotes terminal node

1) root 30 41.707190 1.0000000
  2) PR>=-4.899576 17 11.093620 0.3051777 *
  3) PR< -4.899576 13 8.068598 2.8613000 *

> res <- rep(0, 30)
> for (i in 1:30) {
+   fit <- rpart(Surv(Survival_Time, Dead) ~ ., data = mda.surv[-i,
+   ])
+   res[i] <- (predict(fit, newdat = mda.surv[i, ]) > 1)

```

```

+ }
> sf <- survfit(Surv(Survival_Time, Dead) ~ res, data = mda.surv)
> summary(coxph(Surv(Survival_Time, Dead) ~ res, data = mda.surv))

Call:
coxph(formula = Surv(Survival_Time, Dead) ~ res, data = mda.surv)

n= 30
  coef exp(coef) se(coef)      z      p
res 1.95      7.03   0.589 3.31 0.00092

      exp(coef) exp(-coef) lower .95 upper .95
res      7.03      0.142      2.22      22.3

Rsquare= 0.355 (max possible= 0.958 )
Likelihood ratio test= 13.2 on 1 df, p=0.000285
Wald test              = 11.0 on 1 df, p=0.000925
Score (logrank) test = 14.3 on 1 df, p=0.000152

> logrank <- survdiff(Surv(Survival_Time, Dead) ~ res, data = mda.surv)
> logrank

Call:
survdiff(formula = Surv(Survival_Time, Dead) ~ res, data = mda.surv)

      N Observed Expected (O-E)^2/E (O-E)^2/V
res=0 16         4   10.91      4.38    14.3
res=1 14        12    5.09      9.37    14.3

Chisq= 14.3 on 1 degrees of freedom, p= 0.000152

> pv <- pchisq(logrank$chisq, 1, lower.tail = F)

Use Kaplan-Meier plot to show the predictive power of NR gene signature
in MDACC LOOCC analysis.

> plot(sf, conf.int = F, main = "MDACC LOOCC", xlab = "Survival Time (month)",
+      ylab = "Survival", cex.lab = 1.2, mark = c(1, 19), cex = 1.5)
> text(50, 0.6, pv.expr(pv), cex = 1.5)

```

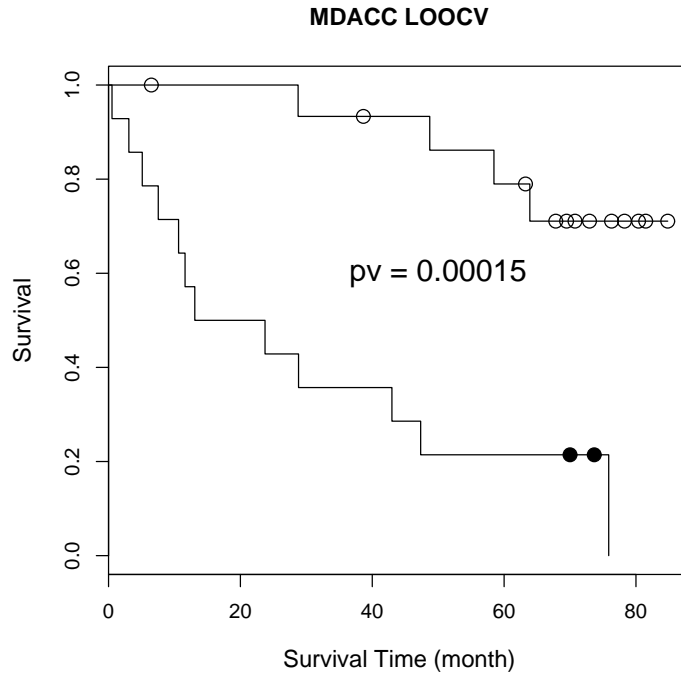


Figure 2a. LOOCV of the recursive-partitioning tree model for the 30-sample MDACC QPCR data set.

Read Consortium data

```
> Consortium <- read.csv("Consortium_data.csv", row.names = 1)
```

Divide Consortium data into training and testing sets, using the same arrangement as Shedden et al. paper

```
> dat.train <- Consortium[Consortium$TESTTYPE == "Train", c(1,
+ 2, 10:57)]
> dat.test <- Consortium[Consortium$TESTTYPE == "Test", c(1, 2,
+ 10:57)]
> fit <- rpart(Surv(month, death) ~ ., data = dat.train)
> print(fit)
```

n=254 (1 observation deleted due to missingness)

```
node), split, n, deviance, yval
* denotes terminal node
```

- 1) root 254 383.721300 1.0000000
- 2) SF.1>=5.035 238 355.235900 0.9321384

```

4) COUP.TFb>=6.17875 202 291.440300 0.8316414
8) PPARd< 6.396667 190 264.976500 0.7728499
16) COUP.TFb< 7.47875 178 244.205400 0.7107610
32) PPARd< 5.698333 7 1.733478 0.1332612 *
33) PPARd>=5.698333 171 234.749600 0.7479395
66) DAX.1< 4.6775 62 71.571530 0.4847427
132) TRb< 6.335 9 1.758713 0.1206434 *
133) TRb>=6.335 53 64.098200 0.5645271
266) ERRa< 7.2075 46 48.769070 0.4704948
532) COUP.TFg>=6.725 13 11.104640 0.1410123 *
533) COUP.TFg< 6.725 33 29.811300 0.6617683
1066) RXRg>=5.255 10 5.824201 0.2138250 *
1067) RXRg< 5.255 23 17.427060 0.9020286 *
267) ERRa>=7.2075 7 10.083650 1.4280350 *
67) DAX.1>=4.6775 109 154.239700 0.9353668
134) NOR1< 5.808333 41 64.483780 0.5934419
268) NURR1< 5.873333 15 11.672550 0.2041338 *
269) NURR1>=5.873333 26 43.908780 0.8997544
538) PR>=4.275 17 26.493760 0.5361375 *
539) PR< 4.275 9 6.248823 2.3703860 *
135) NOR1>=5.808333 68 81.456440 1.2175480
270) MR>=5.945 58 68.849110 1.0750540
540) ERa>=5.621667 7 4.285743 0.3296640 *
541) ERa< 5.621667 51 58.806370 1.2095250
1082) PNR< 4.7225 16 26.455710 0.6444469 *
1083) PNR>=4.7225 35 26.466970 1.5237510
2166) COUP.TFb< 6.83625 26 12.252950 1.2556770 *
2167) COUP.TFb>=6.83625 9 8.916298 2.8217610 *
271) MR< 5.945 10 6.484173 2.5454740 *
17) COUP.TFb>=7.47875 12 9.302349 2.1612190 *
9) PPARd>=6.396667 12 13.595450 2.5960540 *
5) COUP.TFb< 6.17875 36 52.937150 1.6650440
10) ERRa< 7.0875 23 32.112400 1.2075800
20) COUP.TFg>=6.63 12 12.389740 0.7048566 *
21) COUP.TFg< 6.63 11 12.325520 2.2287740 *
11) ERRa>=7.0875 13 12.719170 3.1216850 *
3) SF.1< 5.035 16 13.967780 2.6992260 *

```

```

> group <- ifelse(predict(fit, newdat = dat.test) > 1, "High",
+ " Low")
> sf <- survfit(Surv(month, death) ~ group, data = dat.test)
> summary(coxph(Surv(month, death) ~ group, data = dat.test))

```

```

Call:
coxph(formula = Surv(month, death) ~ group, data = dat.test)

```

```

n=186 (1 observation deleted due to missingness)
      coef exp(coef) se(coef)      z      p
groupHigh 0.712      2.04    0.306 2.33 0.02

      exp(coef) exp(-coef) lower .95 upper .95
groupHigh      2.04      0.49      1.12      3.71

```

```

Rsquare= 0.033 (max possible= 0.975 )
Likelihood ratio test= 6.25 on 1 df, p=0.0124
Wald test              = 5.42 on 1 df, p=0.0200
Score (logrank) test = 5.65 on 1 df, p=0.0175

```

```

> logrank <- survdiff(Surv(month, death) ~ group, data = dat.test)
> logrank

```

Call:

```
survdiff(formula = Surv(month, death) ~ group, data = dat.test)
```

n=186, 1 observation deleted due to missingness.

	N	Observed	Expected	(O-E) ² /E	(O-E) ² /V
group= Low	51	13	22.3	3.89	5.64
group=High	135	61	51.7	1.68	5.64

Chisq= 5.6 on 1 degrees of freedom, p= 0.0175

```

> pv <- pchisq(logrank$chisq, 1, lower.tail = F)

```

Figure2B. Independent validation of the NR gene signature in the 442-sample cohort multi-institute consortium using RPART analysis. The microarray data sets were divided into two groups, one for the training and the other for the testing cohort.

```

> plot(sf, conf.int = F, main = "Consortium Train to Test without clinical variable",
+      xlab = "Time to Dead (Month)", ylab = "Survival", cex.lab = 1.2,
+      mark = c(1, 19), cex = 1.5, lty = 1, lwd = 2)
> text(100, 0.9, pv.expr(pv), cex = 1.5)

```

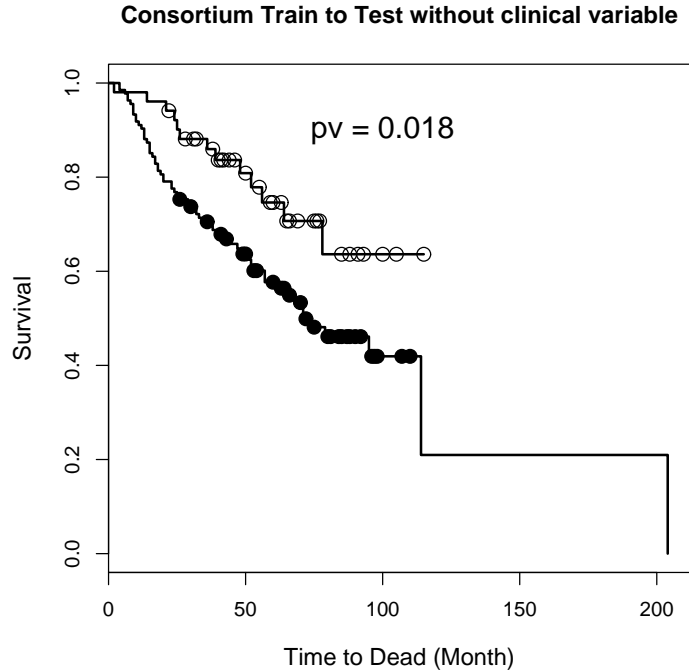


Figure 2b. Independent validation of the NR gene signature in the 442-sample cohort multi-institute consortium using RPART analysis.

Normalize and combine MDACC data and Consortium data

```
> Consortium.expr <- Consortium[, 10:57]
> Consortium.expr <- scale(Consortium.expr)
> mda.surv <- mda[, -(3:4)]
> mda.surv[, -(1:2)] <- scale(mda.surv[, -(1:2)])
> common.gene <- intersect(colnames(mda.surv)[-(1:2)], colnames(Consortium.expr))
> mda.data <- data.frame(type = "mda", Stage = NA, mda.surv[, 1:2],
+   mda.surv[, common.gene])
> Consortium.data <- data.frame(type = "Consortium", Stage = Consortium$stage,
+   Dead = Consortium$death, Survival_Time = Consortium$month,
+   Consortium.expr[, common.gene])
> combined <- data.frame(rbind(mda.data, Consortium.data))
```

Use MDACC as training data and Consortium as testing data

```
> data.train <- combined[combined$type == "mda", ]
> data.test <- combined[combined$type == "Consortium", ]
> fit <- rpart(Surv(Survival_Time, Dead) ~ ., data = data.train)
> print(fit)
```



```

n= 30

node), split, n, deviance, yval
  * denotes terminal node

1) root 30 41.707190 1.0000000
  2) PR>=0.04657526 17 11.093620 0.3051777 *
  3) PR< 0.04657526 13 8.068598 2.8613000 *

> group <- ifelse(predict(fit, newdat = data.test) > 1, "High",
+   " Low")
> sf <- survfit(Surv(Survival_Time, Dead) ~ group, data = data.test)
> summary(coxph(Surv(Survival_Time, Dead) ~ group, data = data.test))

Call:
coxph(formula = Surv(Survival_Time, Dead) ~ group, data = data.test)

n=440 (2 observations deleted due to missingness)
      coef exp(coef) se(coef)  z      p
groupHigh 0.377      1.46   0.135 2.8 0.0051

      exp(coef) exp(-coef) lower .95 upper .95
groupHigh      1.46      0.686   1.12   1.9

Rsquare= 0.018 (max possible= 0.997 )
Likelihood ratio test= 8.03 on 1 df,  p=0.00460
Wald test              = 7.85 on 1 df,  p=0.00509
Score (logrank) test = 7.94 on 1 df,  p=0.00484

> logrank <- survdiff(Surv(Survival_Time, Dead) ~ group, data = data.test)
> logrank

Call:
survdiff(formula = Surv(Survival_Time, Dead) ~ group, data = data.test)

n=440, 2 observations deleted due to missingness.

      N Observed Expected (O-E)^2/E (O-E)^2/V
group= Low 209      91      112      4.11      7.97
group=High 231     145      124      3.74      7.97

Chisq= 8 on 1 degrees of freedom, p= 0.00476

> pv <- pchisq(logrank$chisq, 1, lower.tail = F)

```

Figure2C. MDACC to consortium. The MDACC cohort (n=30) was used as training set and the predictive model was tested in the consortium cohort (n=442)

```

> plot(sf, conf.int = F, main = "MDACC to consortium", xlab = "Time to Dead (Month)",
+      ylab = "Survival", cex.lab = 1.2, mark = c(1, 19), cex = 1.5,
+      lwd = 2)
> text(140, 0.9, pv.expr(pv), cex = 1.5)

```

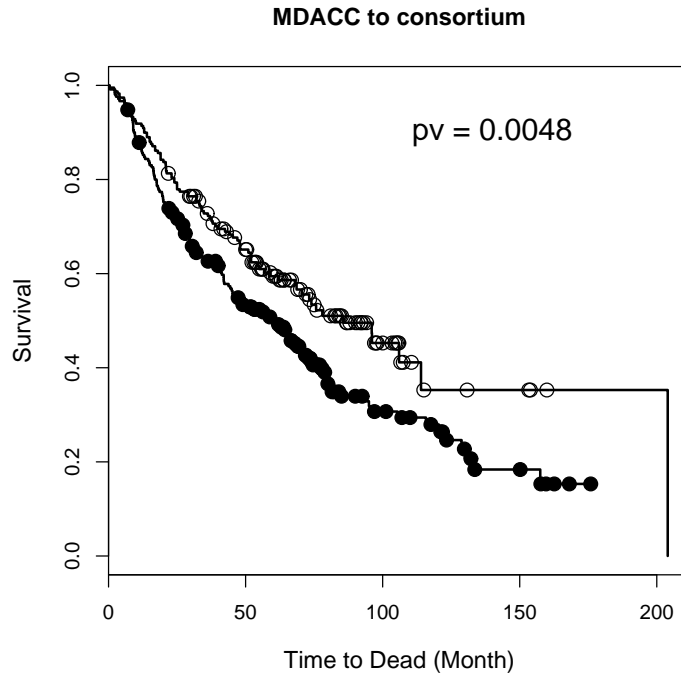


Figure 2c. MDACC to consortium

Use consortium as the training data and MDACC as the testing data

```

> data.test <- combined[combined$type == "mda", -2]
> data.train <- combined[combined$type == "Consortium", -2]
> fit <- rpart(Surv(Survival_Time, Dead) ~ ., data = data.train)
> print(fit)

```

n=440 (2 observations deleted due to missingness)

```

node), split, n, deviance, yval
* denotes terminal node

```

```

1) root 440 650.960700 1.0000000
2) SF.1>=-1.600797 422 612.349500 0.9473605
4) PPARd< 1.546829 393 557.598200 0.8889341
8) RORa>=-1.110901 353 488.590600 0.8127724

```

```

16) RARa>=-0.8263496 282 357.962100 0.7005085
32) RARg< 0.7062089 206 236.112100 0.5957128
64) NURR1< -1.126548 22 7.912262 0.1177802 *
65) NURR1>=-1.126548 184 215.220500 0.6709268
130) PXR>=1.269161 9 1.729126 0.1354368 *
131) PXR< 1.269161 175 206.439800 0.7109939
262) TR2>=1.257944 11 4.844043 0.1918291 *
263) TR2< 1.257944 164 194.013000 0.7694938
526) LXRa>=-0.8594324 134 144.483400 0.6588147 *
527) LXRa< -0.8594324 30 42.461040 1.3332290
1054) ERa>=0.1125855 13 13.110410 0.6988573 *
1055) ERa< 0.1125855 17 21.932320 2.1376250 *
33) RARg>=0.7062089 76 113.805200 1.0449810
66) GR>=0.1164013 21 28.988230 0.4769354
132) NGFIB3>=0.2269965 9 1.775888 0.1120559 *
133) NGFIB3< 0.2269965 12 18.553220 1.0365880 *
67) GR< 0.1164013 55 76.323680 1.3577180
134) ERa>=1.44486 7 3.714183 0.2946938 *
135) ERa< 1.44486 48 61.587110 1.6885060
270) FXR>=1.1885 7 7.610207 0.3961379 *
271) FXR< 1.1885 41 44.954860 2.0384140 *
17) RARa< -0.8263496 71 118.121600 1.2993340
34) SHP>=0.9231351 12 15.193210 0.4609037 *
35) SHP< 0.9231351 59 95.018530 1.5203210
70) DAX.1< -0.4961372 17 22.775660 0.6645850 *
71) DAX.1>=-0.4961372 42 59.723230 2.1019450
142) LXRb>=-0.3823468 15 17.205720 1.1617770 *
143) LXRb< -0.3823468 27 32.151590 3.1673350 *
9) RORa< -1.110901 40 54.464440 1.8193850
18) AR>=-0.4973712 24 24.203220 1.1693540 *
19) AR< -0.4973712 16 18.400040 3.6731330 *
5) PPARd>=1.546829 29 40.620470 2.1935050
10) PPARg< 0.3242693 19 22.356910 1.4967360 *
11) PPARg>=0.3242693 10 11.316950 3.9286630 *
3) SF.1< -1.600797 18 19.521260 3.1164310 *

```

```

> group <- ifelse(predict(fit, newdat = data.test) > 1, "High",
+ " Low")
> table(group)

```

```

group
Low High
21 9

```

```

> sf <- survfit(Surv(Survival_Time, Dead) ~ group, data = data.test)
> summary(coxph(Surv(Survival_Time, Dead) ~ group, data = data.test))

```

```

Call:
coxph(formula = Surv(Survival_Time, Dead) ~ group, data = data.test)

n= 30
      coef exp(coef) se(coef)      z      p
groupHigh 1.1      3.01    0.55 2.00 0.045

      exp(coef) exp(-coef) lower .95 upper .95
groupHigh    3.01    0.333    1.02    8.83

Rsquare= 0.115 (max possible= 0.958 )
Likelihood ratio test= 3.66 on 1 df, p=0.0557
Wald test              = 4.01 on 1 df, p=0.0452
Score (logrank) test = 4.38 on 1 df, p=0.0363

> logrank <- survdiff(Surv(Survival_Time, Dead) ~ group, data = data.test)
> logrank

```

```

Call:
survdiff(formula = Surv(Survival_Time, Dead) ~ group, data = data.test)

```

	N	Observed	Expected	(O-E) ² /E	(O-E) ² /V
group= Low	21	10	13.12	0.742	4.38
group=High	9	6	2.88	3.381	4.38

Chisq= 4.4 on 1 degrees of freedom, p= 0.0363

```
> pv <- pchisq(logrank$chisq, 1, lower.tail = F)
```

Figure2D Cross-validation of the NR gene-expression signature. The consortium cohort (n=442) training set was tested in the MDACC cohort (n=30)

```

> plot(sf, conf.int = F, main = "Consortium to MDACC", xlab = "Time to Dead (Month)",
+      ylab = "Survival", cex.lab = 1.2, mark = c(1, 19), cex = 1.5,
+      lwd = 2)
> text(20, 0.2, pv.expr(pv), cex = 1.5)

```

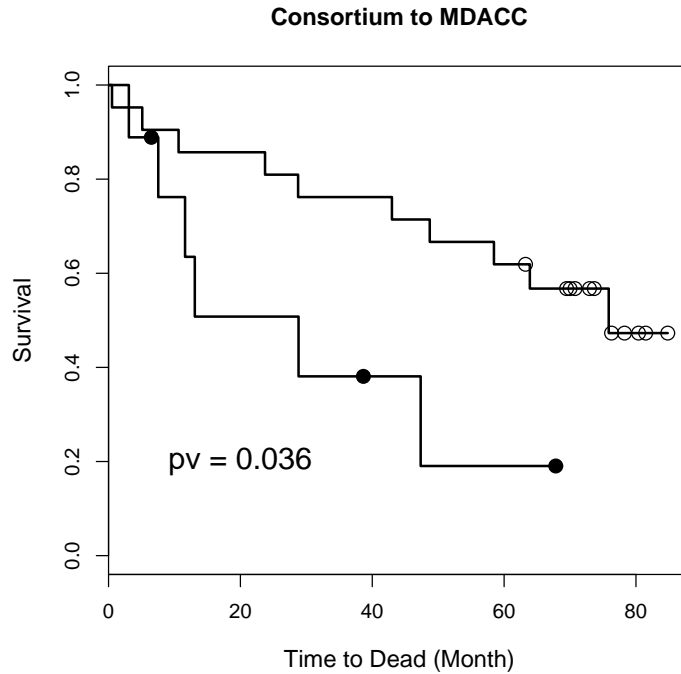


Figure 2d. Consortium to MDACC

Figure 3A is same as Figure 2A

Figure 3B is same as Figure 2C

```

> ind.PR <- which(colnames(mda.surv) == "PR")
> fit <- rpart(Surv(Survival_Time, Dead) ~ ., data = mda.surv[,
+   -ind.PR])
> print(fit)

n= 30

node), split, n, deviance, yval
  * denotes terminal node

1) root 30 41.707190 1.0000000
 2) SHP>=0.4814448 13 5.878756 0.1838269 *
 3) SHP< 0.4814448 17 14.064460 2.2471280 *

> res <- rep(0, 30)
> for (i in 1:30) {
+   fit <- rpart(Surv(Survival_Time, Dead) ~ ., data = mda.surv[-i,
+     -ind.PR])
+   res[i] <- (predict(fit, newdat = mda.surv[i, ]) > 1)

```

```

+ }
> summary(coxph(Surv(Survival_Time, Dead) ~ res, data = mda.surv))

Call:
coxph(formula = Surv(Survival_Time, Dead) ~ res, data = mda.surv)

n= 30
  coef exp(coef) se(coef)      z      p
res 2.61      13.6   0.769 3.39 0.00069

      exp(coef) exp(-coef) lower .95 upper .95
res      13.6      0.0735      3.01      61.4

Rsquare= 0.461 (max possible= 0.958 )
Likelihood ratio test= 18.6 on 1 df,  p=1.65e-05
Wald test              = 11.5 on 1 df,  p=0.00069
Score (logrank) test = 18.3 on 1 df,  p=1.91e-05

> sf <- survfit(Surv(Survival_Time, Dead) ~ res, data = mda.surv)
> logrank <- survdiff(Surv(Survival_Time, Dead) ~ res, data = mda.surv)
> logrank

Call:
survdiff(formula = Surv(Survival_Time, Dead) ~ res, data = mda.surv)

      N Observed Expected (O-E)^2/E (O-E)^2/V
res=0 14         2    10.04      6.44    18.3
res=1 16        14     5.96     10.85    18.3

Chisq= 18.3 on 1 degrees of freedom, p= 1.91e-05

> pv <- pchisq(logrank$chisq, 1, lower.tail = F)

> plot(sf, conf.int = F, main = "MDACC LOOCV SHP", xlab = "Survival Time (month)",
+       ylab = "Survival", cex.lab = 1.2, mark = c(1, 19), cex = 1.5)
> text(60, 0.6, pv.expr(pv), cex = 1.5)

```

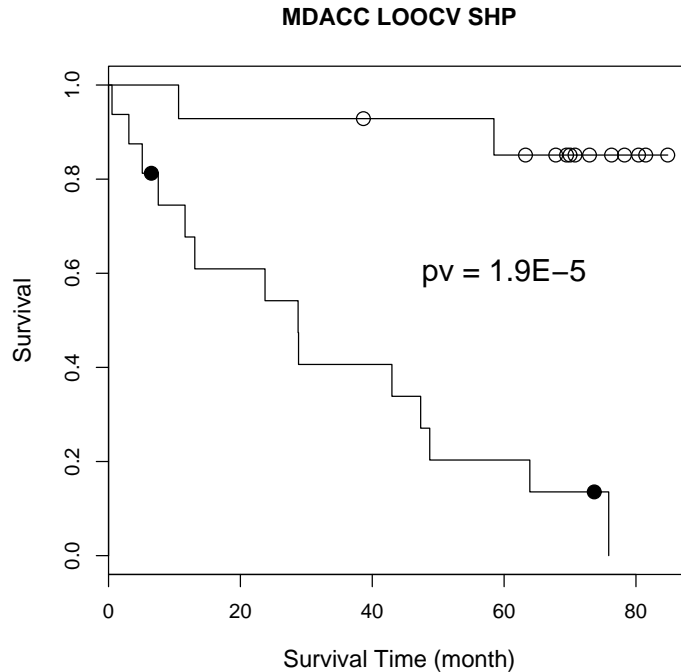


Figure 3d. The MDACC LOOCV without PR gene

```

> data.train <- combined[combined$type == "mda", colnames(combined) !=
+   "PR"]
> data.test <- combined[combined$type == "Consortium", ]
> fit <- rpart(Surv(Survival_Time, Dead) ~ ., data = data.train)
> print(fit)

n= 30

node), split, n, deviance, yval
  * denotes terminal node

1) root 30 41.707190 1.0000000
  2) SHP>=0.4814448 13  5.878756 0.1838269 *
  3) SHP< 0.4814448 17 14.064460 2.2471280 *

> group <- ifelse(predict(fit, newdat = data.test) > 1, "High",
+   " Low")
> sf <- survfit(Surv(Survival_Time, Dead) ~ group, data = data.test)
> summary(coxph(Surv(Survival_Time, Dead) ~ group, data = data.test))

Call:
coxph(formula = Surv(Survival_Time, Dead) ~ group, data = data.test)

```



```

n=440 (2 observations deleted due to missingness)
      coef exp(coef) se(coef)      z      p
groupHigh 0.478      1.61    0.181 2.63 0.0084

      exp(coef) exp(-coef) lower .95 upper .95
groupHigh      1.61      0.62      1.13      2.3

Rsquare= 0.017 (max possible= 0.997 )
Likelihood ratio test= 7.73 on 1 df, p=0.00544
Wald test              = 6.94 on 1 df, p=0.00843
Score (logrank) test = 7.07 on 1 df, p=0.00782

> logrank <- survdiff(Surv(Survival_Time, Dead) ~ group, data = data.test)
> logrank

Call:
survdiff(formula = Surv(Survival_Time, Dead) ~ group, data = data.test)

n=440, 2 observations deleted due to missingness.

      N Observed Expected (O-E)^2/E (O-E)^2/V
group= Low  92      36      53      5.46      7.08
group=High 348     200     183      1.58      7.08

Chisq= 7.1 on 1 degrees of freedom, p= 0.00779

> pv <- pchisq(logrank$chisq, 1, lower.tail = F)

> {
+   plot(sf, conf.int = F, main = "MDACC to consortium, SHP",
+        xlab = "Time to Dead (Month)", ylab = "Survival", cex.lab = 1.2,
+        mark = c(1, 19), cex = 1.5, lwd = 2)
+   text(140, 0.9, pv.expr(pv), cex = 1.5)
+ }

```

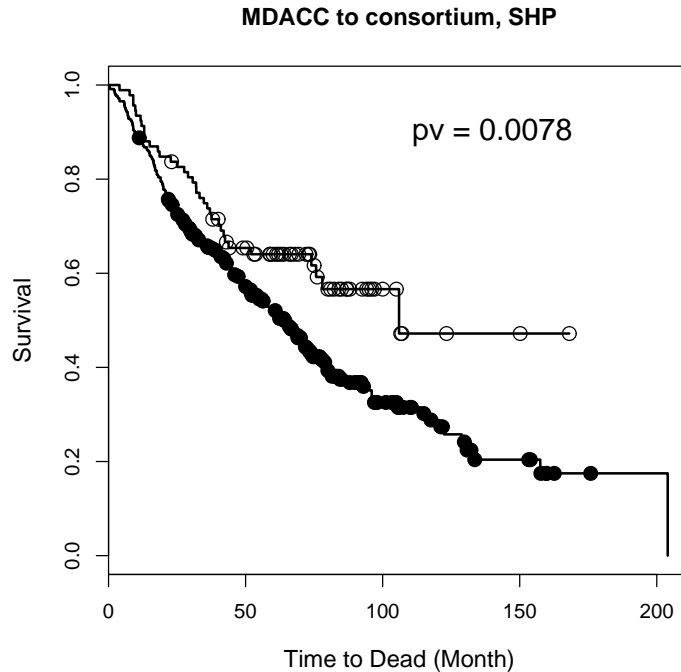


Figure 3e. MDACC to consortium without PR gene

Kaplan-Meier survival plots showing the performance of using single NR gene predictors, SHP and PR separately, in stage I lung cancer patients.

Figure 4A

predicting stage I lung cancer patients survival using SHP alone

```
> data.test <- combined[combined$type == "Consortium" & combined$Stage ==
+   1, colnames(combined) != "PR"]
> group <- ifelse(predict(fit, newdat = data.test) > 1, "High",
+   " Low")
> sf <- survfit(Surv(Survival_Time, Dead) ~ group, data = data.test)
> summary(coxph(Surv(Survival_Time, Dead) ~ group, data = data.test))
```

Call:

```
coxph(formula = Surv(Survival_Time, Dead) ~ group, data = data.test)
```

```
n= 275
      coef exp(coef) se(coef)      z      p
groupHigh 0.557      1.74   0.264  2.11 0.035

      exp(coef) exp(-coef) lower .95 upper .95
```

```
groupHigh      1.74      0.573      1.04      2.93
```

```
Rsquare= 0.018 (max possible= 0.982 )
```

```
Likelihood ratio test= 5.03 on 1 df, p=0.0249
```

```
Wald test          = 4.44 on 1 df, p=0.0350
```

```
Score (logrank) test = 4.56 on 1 df, p=0.0327
```

```
> logrank <- survdiff(Surv(Survival_Time, Dead) ~ group, data = data.test)
```

```
> logrank
```

```
Call:
```

```
survdiff(formula = Surv(Survival_Time, Dead) ~ group, data = data.test)
```

	N	Observed	Expected	(O-E) ² /E	(O-E) ² /V
group= Low	64	17	26.6	3.44	4.55
group=High	211	94	84.4	1.08	4.55

```
Chisq= 4.6 on 1 degrees of freedom, p= 0.0328
```

```
> pv <- pchisq(logrank$chisq, 1, lower.tail = F)
```

```
> {
```

```
+   plot(sf, conf.int = F, main = "MDACC to consortium, SHP, stageI only",
```

```
+       xlab = "Time to Dead (Month)", ylab = "Survival", cex.lab = 1.2,
```

```
+       mark = c(1, 19), cex = 1.5, lwd = 2)
```

```
+   text(140, 0.9, pv.expr(pv), cex = 1.5)
```

```
+ }
```

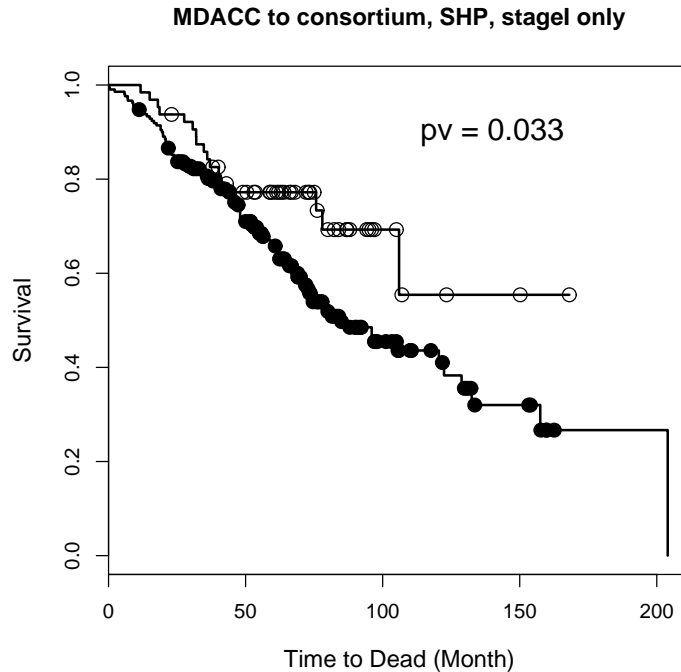


Figure 4a. predicting stage I lung cancer patients survival using SHP alone

predicting stage I lung cancer patients survival using PR alone

```

> data.train <- combined[combined$type == "mda", ]
> fit <- rpart(Surv(Survival_Time, Dead) ~ ., data = data.train)
> print(fit)

n= 30

node), split, n, deviance, yval
  * denotes terminal node

1) root 30 41.707190 1.0000000
  2) PR>=0.04657526 17 11.093620 0.3051777 *
  3) PR< 0.04657526 13 8.068598 2.8613000 *

> data.test <- combined[combined$type == "Consortium" & combined$Stage ==
+ 1, ]
> group <- ifelse(predict(fit, newdat = data.test) > 1, "High",
+ " Low")
> sf <- survfit(Surv(Survival_Time, Dead) ~ group, data = data.test)
> summary(coxph(Surv(Survival_Time, Dead) ~ group, data = data.test))

```

```

Call:
coxph(formula = Surv(Survival_Time, Dead) ~ group, data = data.test)

n= 275
      coef exp(coef) se(coef)      z      p
groupHigh 0.355      1.43    0.197  1.80 0.071

      exp(coef) exp(-coef) lower .95 upper .95
groupHigh      1.43      0.701    0.97    2.10

Rsquare= 0.012 (max possible= 0.982 )
Likelihood ratio test= 3.32 on 1 df, p=0.0683
Wald test              = 3.26 on 1 df, p=0.0711
Score (logrank) test = 3.29 on 1 df, p=0.0697

> logrank <- survdiff(Surv(Survival_Time, Dead) ~ group, data = data.test)
> logrank

Call:
survdiff(formula = Surv(Survival_Time, Dead) ~ group, data = data.test)

      N Observed Expected (O-E)^2/E (O-E)^2/V
group= Low 137      44    53.5      1.67      3.3
group=High 138      67    57.5      1.55      3.3

Chisq= 3.3 on 1 degrees of freedom, p= 0.0692

> pv <- pchisq(logrank$chisq, 1, lower.tail = F)

> {
+   plot(sf, conf.int = F, main = "MDACC to consortium, stageI only",
+        xlab = "Time to Dead (Month)", ylab = "Survival", cex.lab = 1.2,
+        mark = c(1, 19), cex = 1.5, lwd = 2)
+   text(140, 0.9, pv.expr(pv), cex = 1.5)
+ }

```

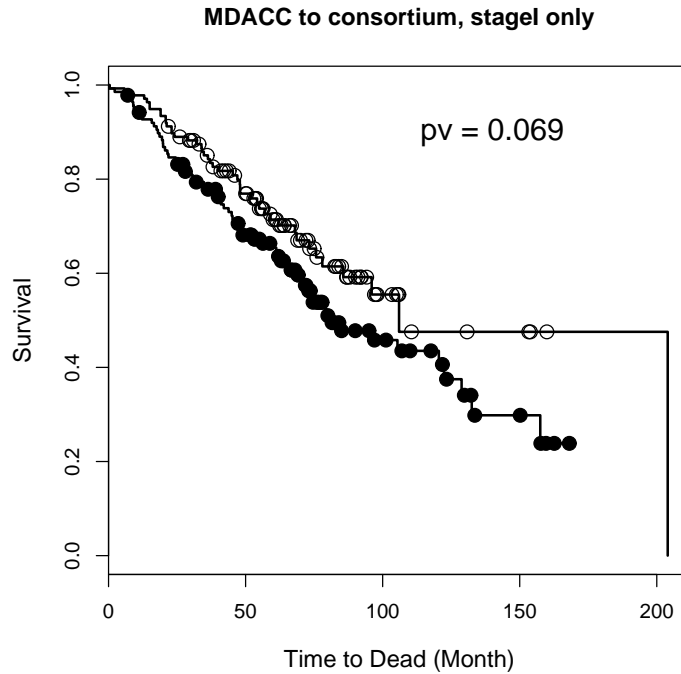


Figure4b. predicting stage I lung cancer patients survival using PR alone.

read normal tissue data

```
> mda.normal <- read.csv("MDA_data_normal.csv", row.names = 1)
> dim(mda.normal)
```

```
[1] 30 54
```

```
> mda.normal[1:4, 1:16]
```

	Dead	Survival_Time	Progression	TOE	COUP.TFb	TR4	DAX.1
737	0	84.819672	0	84.819672	0.42587400	0.4170522	0
739	1	63.901639	1	47.737705	0.71241461	0.7078501	0
749	0	6.491803	0	6.491803	0.09914638	0.5795992	0
756	0	72.950820	0	72.950820	0.49208097	0.6910128	0
	LXRb	RARa	RXRb	REV.ERBa	REV.ERBb	COUP.TFg	RORa
737	0.4245388	0.3603237	0.1484563	0.4978787	0.5986191	0.1063993	0.3778851
739	0.6956200	0.6239872	0.1837411	0.5680166	0.8705468	0.1573902	0.4897771
749	0.6110015	0.4097818	0.1818671	0.2851873	0.5119912	0.1322197	0.4820626
756	1.1302375	0.4390864	0.4070447	0.3802573	0.7447870	0.1530503	0.6154929
	GR	PPARg					
737	0.4709204	0.1468401					
739	0.5554739	0.6925421					

```
749 0.4594592 0.5910218
756 0.7583135 1.1323468
```

Identification of NR expression as prognostic biomarkers in normal lung tissues from lung cancer patients.

```
> fit <- rpart(Surv(TOE, Progression) ~ ., data = mda.normal[,
+   -(1:2)])
> print(fit)
```

```
n=29 (1 observation deleted due to missingness)
```

```
node), split, n, deviance, yval
      * denotes terminal node
```

```
1) root 29 39.18022 1.0000000
   2) NGFIB3>=0.008300668 13 14.53515 0.4504191 *
   3) NGFIB3< 0.008300668 16 10.95998 2.0097130 *
```

```
> res <- rep(0, 30)
> for (i in 1:30) {
+   fit <- rpart(Surv(TOE, Progression) ~ ., data = mda.normal[-i,
+   -(1:2)])
+   res[i] <- (predict(fit, newdat = mda.normal[i, -(1:2)]) >
+   1)
+ }
> sf <- survfit(Surv(TOE, Progression) ~ res, data = mda.normal)
> logrank <- survdiff(Surv(TOE, Progression) ~ res, data = mda.normal)
> logrank
```

Call:

```
survdiff(formula = Surv(TOE, Progression) ~ res, data = mda.normal)
```

```
n=29, 1 observation deleted due to missingness.
```

	N	Observed	Expected	(O-E) ² /E	(O-E) ² /V
res=0	13	6	14.53	5.01	17.4
res=1	16	16	7.47	9.74	17.4

```
Chisq= 17.4 on 1 degrees of freedom, p= 3.02e-05
```

```
> pv <- pchisq(logrank$chisq, 1, lower.tail = F)
> summary(coxph(Surv(TOE, Progression) ~ res, data = mda.normal))
```

Call:

```
coxph(formula = Surv(TOE, Progression) ~ res, data = mda.normal)
```



```

n=29 (1 observation deleted due to missingness)
  coef exp(coef) se(coef)    z    p
res 2.33      10.2    0.656 3.54 0.00039

```

```

  exp(coef) exp(-coef) lower .95 upper .95
res      10.2    0.0976    2.83    37.1

```

```

Rsquare= 0.462 (max possible= 0.985 )
Likelihood ratio test= 18.0 on 1 df, p=2.25e-05
Wald test              = 12.6 on 1 df, p=0.000393
Score (logrank) test = 17.4 on 1 df, p=3.02e-05

```

```

> plot(sf, main = "MDACC Normal Tissue LOOCV", xlab = "Time to Progression (month)",
+      ylab = "Progression free survival", cex.lab = 1.5, mark = c(1,
+      19), cex = 1.2, lwd = 1)
> text(60, 0.2, pv.expr(pv), cex = 1.5)

```

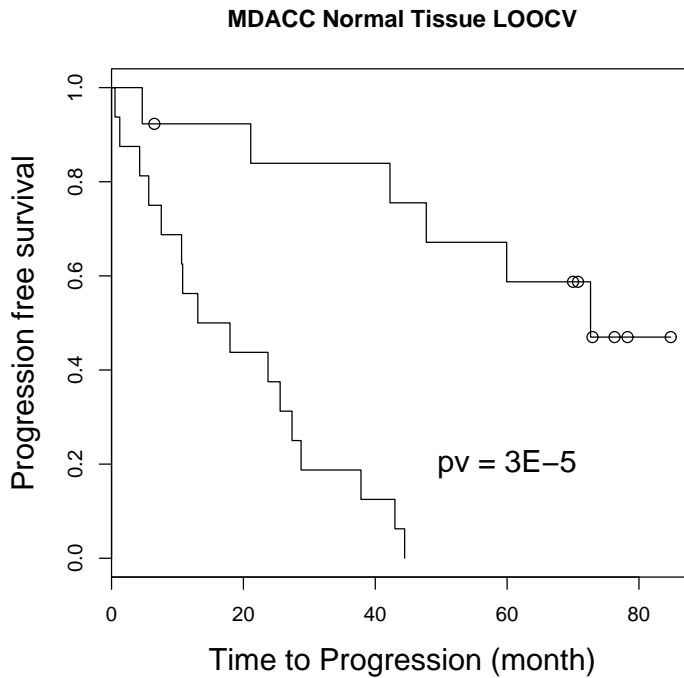


Figure S2a. Kaplan-Meier plots of time to progression, LOOCV of recursive-partitioning tree model of the MDACC

Kaplan-Meier plots of overall survival time, LOOCV of recursive-partitioning tree model of the MDACC

```

> fit <- rpart(Surv(Survival_Time, Dead) ~ ., data = mda.normal[,
+   -(3:4)])
> print(fit)

n= 30

node), split, n, deviance, yval
      * denotes terminal node

1) root 30 41.70719 1.0000000
  2) MR>=0.04008524 18 14.96726 0.4520124 *
  3) MR< 0.04008524 12 12.19802 2.5391310 *

> res <- rep(0, 30)
> for (i in 1:30) {
+   fit <- rpart(Surv(Survival_Time, Dead) ~ ., data = mda.normal[-i,
+   -(3:4)])
+   res[i] <- (predict(fit, newdat = mda.normal[i, -(3:4)]) >
+   1)
+ }
> sf <- survfit(Surv(Survival_Time, Dead) ~ res, data = mda.normal)
> logrank <- survdiff(Surv(Survival_Time, Dead) ~ res, data = mda.normal)
> logrank

Call:
survdiff(formula = Surv(Survival_Time, Dead) ~ res, data = mda.normal)

      N Observed Expected (O-E)^2/E (O-E)^2/V
res=0 19         8    11.32     0.976     3.38
res=1 11         8     4.68     2.363     3.38

Chisq= 3.4  on 1 degrees of freedom, p= 0.066

> pv <- pchisq(logrank$chisq, 1, lower.tail = F)
> summary(coxph(Surv(Survival_Time, Dead) ~ res, data = mda.normal))

Call:
coxph(formula = Surv(Survival_Time, Dead) ~ res, data = mda.normal)

n= 30
  coef exp(coef) se(coef)      z      p
res 0.897      2.45    0.504  1.78 0.075

      exp(coef) exp(-coef) lower .95 upper .95
res      2.45      0.408    0.914    6.58

Rsquare= 0.097  (max possible= 0.958 )

```

```

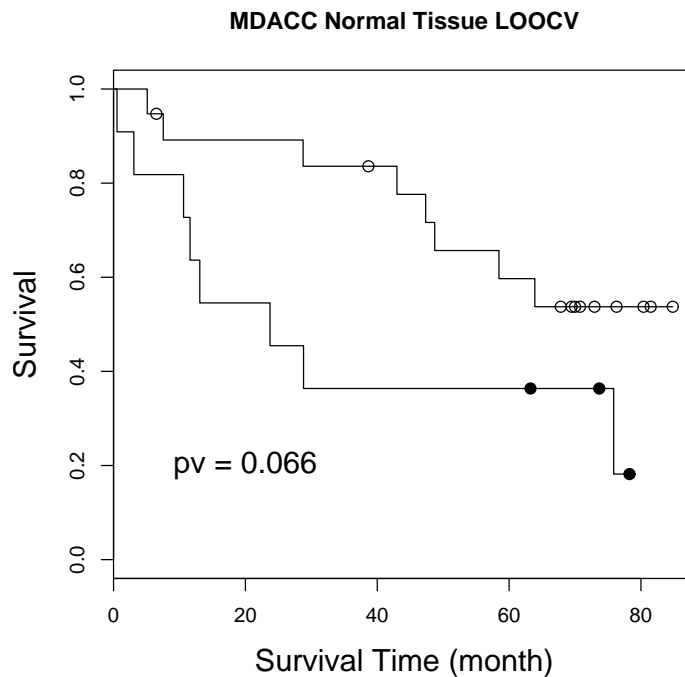
Likelihood ratio test= 3.07 on 1 df, p=0.0796
Wald test              = 3.17 on 1 df, p=0.075
Score (logrank) test = 3.38 on 1 df, p=0.066

```

```

> plot(sf, main = "MDACC Normal Tissue LOOCV", xlab = "Survival Time (month)",
+      ylab = "Survival", cex.lab = 1.5, mark = c(1, 19), cex = 1.2,
+      lwd = 1)
> text(20, 0.2, pv.expr(pv), cex = 1.5)

```



FigureS2b Kaplan-Meier plots of overall survival time, LOOCV of recursive-partitioning tree model of the MDACC

Kaplan-Meier estimates of survival time for NR expression when clinical variables are included in the analysis. The microarray data set from four the 4 institute consortium were divided into two groups, one for the training and the other for the testing cohort.

```

> dat.train <- Consortium[Consortium$TESTTYPE == "Train", ]
> dat.test <- Consortium[Consortium$TESTTYPE == "Test", ]
> fit <- rpart(Surv(month, death) ~ ., data = dat.train)
> print(fit)

```

n=254 (1 observation deleted due to missingness)

```
node), split, n, deviance, yval
* denotes terminal node
```

```
1) root 254 383.721300 1.00000000
2) stage< 1.5 156 202.737700 0.66829300
4) RORb< 4.665 120 155.062600 0.53791530
8) RXRg< 4.93 11 1.864147 0.06792644 *
9) RXRg>=4.93 109 139.269700 0.62690120
18) LXRb>=7.065 39 37.405480 0.32035740
36) REV.ERBa< 9.42 22 7.552179 0.08865569 *
37) REV.ERBa>=9.42 17 17.242840 0.78262790 *
19) LXRb< 7.065 70 91.576500 0.84658590
38) RARg< 7.225 48 57.767080 0.64300480
76) PNR>=4.6575 41 33.436310 0.51160520
152) DAX.1< 4.6175 7 1.691907 0.15404630 *
153) DAX.1>=4.6175 34 27.498220 0.60038320
306) HNF4g>=4.08 23 18.245680 0.42965100
612) NGFIB3< 7.581667 10 4.337518 0.17020370 *
613) NGFIB3>=7.581667 13 8.612122 0.71861550 *
307) HNF4g< 4.08 11 5.131342 1.06703600 *
77) PNR< 4.6575 7 13.171150 2.55292800 *
39) RARg>=7.225 22 26.131730 1.53438700 *
5) RORb>=4.665 36 36.582160 1.20639900
10) SHP>=7.47 7 7.459030 0.49655790 *
11) SHP< 7.47 29 22.895000 1.53094000
22) PNR>=4.8675 12 8.933589 0.95225090 *
23) PNR< 4.8675 17 9.592501 2.10976900 *
3) stage>=1.5 98 137.290600 1.89650400
6) ERa>=5.505556 34 42.218900 1.16462800
12) RARg< 7.3275 22 27.016830 0.77837040
24) RARa>=6.36125 11 10.078790 0.42791790 *
25) RARa< 6.36125 11 11.515790 1.36952300 *
13) RARg>=7.3275 12 5.878286 2.43517100 *
7) ERa< 5.505556 64 82.577530 2.56887000
14) LRH.1< 4.295 23 33.859350 1.49440000
28) PPARa< 4.495 15 15.370270 1.07328000 *
29) PPARa>=4.495 8 13.913090 2.59727300 *
15) LRH.1>=4.295 41 37.126450 3.64341900
30) ERb< 5.58875 33 25.841990 3.12878300
60) ERRb< 5.38 19 12.265540 2.28985200 *
61) ERRb>=5.38 14 8.373323 4.61573700 *
31) ERb>=5.58875 8 7.585137 5.27569700 *
```

```
> group <- ifelse(predict(fit, newdat = dat.test) > 1, "High",
+ " Low")
> sf <- survfit(Surv(month, death) ~ group, data = dat.test)
```

```

> summary(coxph(Surv(month, death) ~ group, data = dat.test))

Call:
coxph(formula = Surv(month, death) ~ group, data = dat.test)

n=186 (1 observation deleted due to missingness)
      coef exp(coef) se(coef)      z      p
groupHigh 0.355      1.43    0.235 1.51 0.13

      exp(coef) exp(-coef) lower .95 upper .95
groupHigh      1.43      0.701      0.9      2.26

Rsquare= 0.012 (max possible= 0.975 )
Likelihood ratio test= 2.29 on 1 df,  p=0.13
Wald test              = 2.29 on 1 df,  p=0.131
Score (logrank) test = 2.31 on 1 df,  p=0.129

> logrank <- survdiff(Surv(month, death) ~ group, data = dat.test)
> logrank

Call:
survdiff(formula = Surv(month, death) ~ group, data = dat.test)

n=186, 1 observation deleted due to missingness.

      N Observed Expected (O-E)^2/E (O-E)^2/V
group= Low 98      35     41.4    0.992    2.30
group=High 88      39     32.6    1.261    2.30

Chisq= 2.3 on 1 degrees of freedom, p= 0.13

> pv <- pchisq(logrank$chisq, 1, lower.tail = F)

> plot(sf, conf.int = F, main = "Consortium Train to Test with clinical variable",
+      xlab = "Time to Dead (Month)", ylab = "Survival", cex.lab = 1.2,
+      mark = c(1, 19), cex = 1.5, lty = 1, lwd = 2)
> text(100, 0.9, pv.expr(pv), cex = 1.5)

```

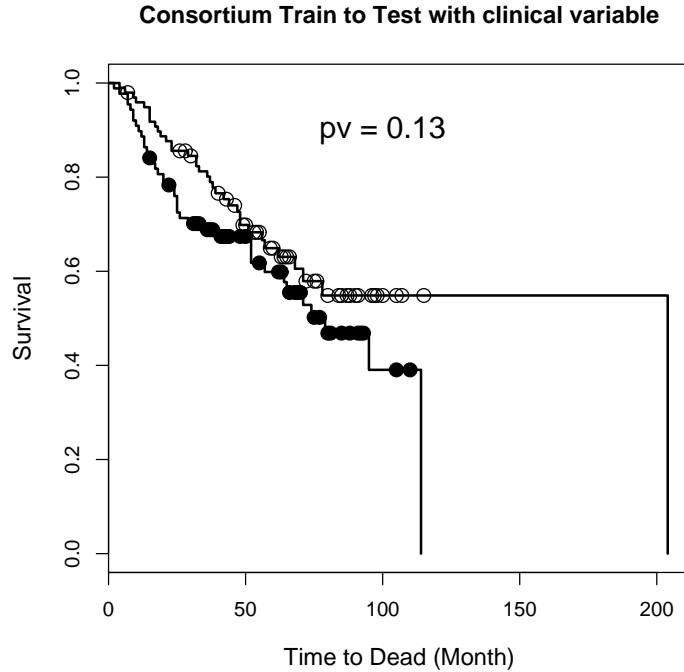


Figure S3. Kaplan-Meier estimates of survival time for NR expression when clinical variables are included in the analysis.

Consortium unsupervised clustering

```
> Consortium <- read.csv("Consortium_data.csv", row.names = 1)
> hc <- hclust(dist(Consortium[, 10:57]))
> plot(hc)
> cluster <- cutree(hc, k = 2)
> sf <- survfit(Surv(month, death) ~ cluster, data = Consortium)
> summary(coxph(Surv(month, death) ~ cluster, data = Consortium))
```

Call:

```
coxph(formula = Surv(month, death) ~ cluster, data = Consortium)
```

```

n=440 (2 observations deleted due to missingness)
      coef exp(coef) se(coef)  z    p
cluster 0.266      1.30   0.144 1.85 0.065
```

```

      exp(coef) exp(-coef) lower .95 upper .95
cluster      1.30      0.766   0.984   1.73
```

```
Rsquare= 0.007 (max possible= 0.997 )
```

```
Likelihood ratio test= 3.29 on 1 df, p=0.0699
```

```

Wald test          = 3.42  on 1 df,  p=0.0645
Score (logrank) test = 3.44  on 1 df,  p=0.0637

> logrank <- survdiff(Surv(month, death) ~ cluster, data = Consortium)
> logrank

Call:
survdiff(formula = Surv(month, death) ~ cluster, data = Consortium)

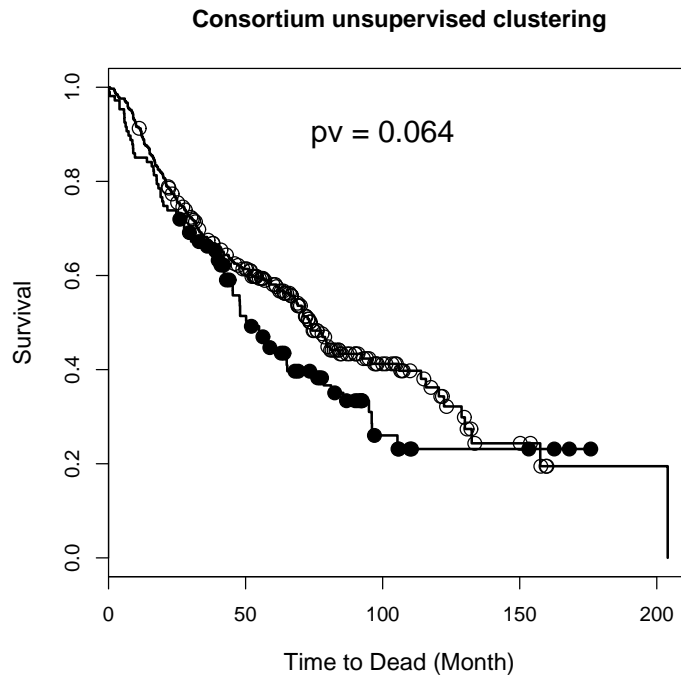
n=440, 2 observations deleted due to missingness.

      N Observed Expected (O-E)^2/E (O-E)^2/V
cluster=1 333      168   180.1      0.81     3.43
cluster=2 107       68    55.9      2.61     3.43

Chisq= 3.4  on 1 degrees of freedom, p= 0.0638

> pv <- pchisq(logrank$chisq, 1, lower.tail = F)
> plot(sf, conf.int = F, main = "Consortium unsupervised clustering",
+      xlab = "Time to Dead (Month)", ylab = "Survival", cex.lab = 1.2,
+      mark = c(1, 19), cex = 1.5, lty = 1, lwd = 2)
> text(100, 0.9, pv.expr(pv), cex = 1.5)

```



FigureS5. Consortium unsupervised clustering

Applying E_{max} Model and Bivariate Thin Plate Splines to Assess Drug Interactions

Maiying Kong¹ & J. Jack Lee²

¹Department of Bioinformatics and Biostatistics, School of Public Health and Information Sciences, University of Louisville, Louisville, Kentucky 40292, U.S.A.

²Department of Biostatistics, University of Texas, M. D. Anderson Cancer Center, Unit 1411, 1515 Holcombe Boulevard, Houston, Texas 77030, U.S.A.

TABLE OF CONTENTS

1. Abstract
2. Introduction
3. Statistical Method
 - 3.1. Estimating dose-effect curves
 - 3.2. Predicting additive effects
 - 3.3. Assessing drug interactions using bivariate thin plate splines
4. Case Studies
 - Case study 1: cells grown in the medium with 2.3 μM folic acid (Low FA experiment)
 - Case study 2: cells grown in the medium with 78 μM folic acid (High FA experiment)
5. Discussion
6. Acknowledgement
7. References

1. ABSTRACT

In this paper, we extend the semiparametric approach proposed by Kong and Lee (2008, Biometric) to the case where dose effect curves follow the E_{max} model instead of the median effect equation. When the maximum effects for the investigated drugs are different, we give a procedure to obtain the additive effect based on the Loewe additivity model. Then, a bivariate thin plate spline approach is applied to estimate the effect beyond additivity along with its 95% point-wise confidence interval as well as its 95% simultaneous confidence band for any combination dose. Thus, synergy, additivity, and antagonism can be identified. The advantages of the method are that it not only provides an overall assessment of the combination effect on the entire two-dimensional dose space spanned by the experimental doses, but also enables one to identify complex patterns of drug interaction in combination studies. In addition, this approach is robust to outliers. To illustrate this procedure, two case studies provided by Dr. William R. Greco at Roswell Park Cancer Institute were analyzed.

2. INTRODUCTION

Studies of interactions among biologically active agents, such as drugs, carcinogens, or environmental pollutants have become increasingly important in many branches of biomedical research. For example, in cancer chemotherapy, the therapeutic effect of many anticancer drugs is limited when they are used as single drugs. Finding combination therapies with increased treatment effect and decreased toxicity effect is an active and promising research area (1). An effective and accurate evaluation of drug interaction for *in vitro* and/or *in vivo* studies can help to determine whether a combination therapy should be further investigated.

The literature supports the view that the Loewe additivity model should be considered as the gold standard to define drug interaction (2-5). The Loewe additivity model defines an additive effect based on the following equation

$$\frac{d_{y,1}}{D_{y,1}} + \frac{d_{y,2}}{D_{y,2}} = 1. \quad (E 1)$$

Here y is the predicted additive effect, which is produced by the combination dose (d_1, d_2) when the two drugs do not interact, $D_{y,1}$ and $D_{y,2}$ are the respective doses of drug 1 and drug 2 required to produce the same effect y when applied alone. If we know the dose-effect relationship for each single agent, say $E(d)=f_i(d)$ for agent i ($i=1,2$), we are able to obtain the dose $D_{y,i}$ by using the inverse function of f_i , denoted as $f_i^{-1}(y)$. By replacing $D_{y,1}$ and $D_{y,2}$ in equation (E 1) with $f_1^{-1}(y)$ and $f_2^{-1}(y)$, respectively, we can obtain an equation including the single variable y , i.e.,

$$\frac{d_1}{f_1^{-1}(y)} + \frac{d_2}{f_2^{-1}(y)} = 1. \quad (E 2)$$

By solving equation (E 2), we can obtain the predicted additive effect y . If the observed effect at (d_1, d_2) is more than (equal to, or less than) the predicted effect, we say that the combination dose (d_1, d_2) is synergistic (additive, or

antagonistic). When the dose-effect curve is decreasing, for example, plotting percent cell survival versus dose, the effect is more than the predicted effect means that the measurement for the observed effect is smaller than that of the predicted effect.

In our previous studies (6-8), we found that Chou and Talalay's (9) median effect equation was appropriate to describe the dose-effect relationships. Chou and Talalay's median effect equation, in its nonlinear form, can be written as follows:

$$E = \frac{(d / ED_{50})^m}{1 + (d / ED_{50})^m} \quad (E 3)$$

where ED_{50} is the dose required to produce 50% of the maximum effect, and m is the slope factor (Hill coefficient), measuring the sensitivity of the effect to the dose range of the drug. For data in the case studies provided by Dr. Greco (see Section 4 for details), we found that the median effect equation (E 3) can not describe the marginal dose effect relationship adequately, since the plateau of the effect does not go to zero when a large dose level of a drug is applied. Instead, the following E_{max} model (E 4) presented by Ting (10) describes the dose-effect relationship very well:

$$E = E_0 - \frac{(d / ED_{50})^m E_{max}}{1 + (d / ED_{50})^m} \quad (E 4)$$

In the E_{max} model (E 4), E_0 is the base effect, corresponding to the measurement of response when no drug is applied; E_{max} is the maximum effect attributable to the drug; ED_{50} is the dose level producing half of E_{max} , i.e., ED_{50} is the dose level required to produce the effect at a value of $E_0 - 0.5E_{max}$ (Figure 1, Panel A); d is the dose level, which produces the effect E . Thus, $E_0 - E_{max}$ will be the asymptotic net effect when a large dose of the drug is applied. Different maximum effects for agents may reflect different mechanism of action for these drugs (11). In *in-vitro* studies, one of the commonly used endpoints is cell growth, which is used to measure the effects of inhibitors. When no drugs (or, no inhibitors) are applied, the cell proliferation obtains its largest value. In this case, the dose effect curve is similar to the one shown in Figure 1 Panel A, where $E_{max} > 0$. The effect range determined by the dose effect curve lies between ($E_0 - E_{max}$, E_0), and the asymptotic measurement for the maximum drug effect is $E_0 - E_{max}$.

To investigate drug interaction, theoretically, we expect the measurements for the endpoints to be similar when no drug is applied. The measurements without any drug applied are used as controls. Due to certain environmental factors other than experimental conditions, the measurements for the controls under different environmental conditions may be different. Thus, one may need to standardize the observed effects by the mean of the control for each environmental condition (2, 3), and then take $E_0 = 1$. In this paper, we will consider the following dose effect curve for each drug:

$$E = 1 - \frac{(d / ED_{50})^m E_{max}}{1 + (d / ED_{50})^m} \quad (E 5)$$

which assumes an effect at value 1 when no drug is applied. Once we obtain the dose-effect curve for each single drug, we can use the Loewe additivity model (E 1) to obtain the additive effect for any combination dose, particularly, for the combination dose with observed effects. Thus, we may obtain the differences of observed effects and the predicted additive effect at each observed combination dose. We use the bivariate thin plate splines approach (12) to estimate the relationship between these differences and the combination doses. Consequently, a response surface of the differences over the combination doses is obtained, and 95% confidence surfaces of the response surface can be constructed. When the dose response curves decrease with increasing dose, the observed effect is less than the predicted additive effect implies that the observed effect is stronger than the predicted effect, thus indicating that the combination dose is synergistic. Conversely, when the observed effect is larger than the predicted additive effect, it implies that the observed effect is weaker than the predicted effect, thus indicating that the combination dose is antagonistic. However, these inferences should be made based on sound statistical considerations. Based on the fitted response surface and its upper and lower confidence surfaces, whether the difference is significantly less than zero, not different from zero, or greater than zero can be judged. Thus, the patterns of drug interaction in terms of synergy, additivity, and antagonism can be obtained. We organize our presentation as follows. In Section 3.1, we describe the underlying stochastic assumption for the dose effect curve and the procedure to estimate the parameters in each marginal dose effect curve. In Section 3.2, we present how to obtain the additive response surface based on the Loewe additivity model, especially in the case when the maximum effects of the drugs are different. In Section 3.3, we present how to assess the effect surface beyond the additivity surface and how to construct its 95% confidence surfaces. Thus, drug interactions in terms of synergy, additivity, or antagonism can be identified for all combination doses in the region containing the combination design points. In section 4, we illustrate how to use the procedure in Section 3 by analyzing the two case studies provided by Dr. Greco. The last section is devoted to a short discussion.

3. STATISTICAL METHOD

Assume that the observed data are (d_{1i}, d_{2i}, E_i) for $i=1, \dots, n$. For each i , (d_{1i}, d_{2i}) is the observed combination dose and E_i is the corresponding observed effect. We call the observations with only drug 1 or drug 2 applied alone as marginal observations. That is, the marginal observations for drug 1 are the observations (d_{1i}, d_{2i}, E_i) with $d_{2i}=0$ ($i=1, \dots, n$), and the marginal observations for drug 2 are the observations (d_{1i}, d_{2i}, E_i) with $d_{1i}=0$ ($i=1, \dots, n$). The marginal dose-effect curves will be estimated based on the marginal observations, which are presented in Section 3.1. It is commonly accepted that the additive effect should be obtained based on the dose-effect relationships for each individual drug. In Section 3.2, we present how to obtain the predicted effect at combination dose (d_1, d_2) based on the Loewe additivity model (E 1) and the marginal dose-effect curves (E 5). We denote the predicted effect as $\hat{F}_p(d_1, d_2)$. By definition, there is no drug interaction when only single drug is applied. Therefore, the term for drug interaction is meaningful only for the combination dose (d_1, d_2) with nonzero d_1 and d_2 . In Section 3.3, we develop a procedure to estimate the effect beyond additivity for any combination dose (d_1, d_2) with nonzero d_1 and d_2 , denoted by $\hat{f}(d_1, d_2)$.

3.1. Estimating dose effect curves

Chou and Talalay (9), Chou (4), and Kong and Lee (6) estimate the parameters in the median effect equation (E 3) by using the transformation $\log E/(1-E) = m \log(d/ED_{50}) = \alpha + m \log(d)$ and applying the least squares method in the linear regression setting, where $\alpha = -m \log(ED_{50})$. However, in our case studies (see Section 4), the experiments include many low doses, whose measurements for effects are larger than 1 after adjusting the effect at control to be 1. Thus, a similar transformation for models (E 3) and (E 5) can not be carried out. Since the measurements are continuous, we propose to apply nonlinear least squares regression to estimate the parameters in models (E 3) and (E 5) with the assumption that a stochastic error with $N(0, \sigma^2)$ exists on the right hand side of the two models. One should be clear that estimating the dose effect curve for drug i only requires the marginal observations for drug i with $i=1, 2$. The least squares method to nonlinear regression was applied to estimate the parameters in the marginal dose effect curves in the two case studies in Section 4.

3.2. Predicting additive effects

In this subsection, we present how to obtain the predicted effect based on the Loewe additivity model (E 1) when model (E 5) is applied as the marginal dose-effect curve for each drug. When model (E 5) is applied, the dose required to produce effect E is given by

$$d = ED_{50} \left(\frac{1-E}{E - (1-E_{max})} \right)^{1/m}$$

However, the maximum effects for the two drugs may be different. Without loss of generality, we assume that the maximum effect of drug 1 is larger than the maximum effect of drug 2, i.e., $E_{max,1} > E_{max,2}$. For this case, when the dose effect curves are decreasing, neither drug when applied alone can produce an effect in $(0, 1 - E_{max,1})$ (Figure 1, Panel B). In the following, we develop the procedure to obtain the predicted additive effect based on the Loewe additivity model (E 1), where we can see that the predicted effect will be in the interval of $(1 - E_{max,1}, 1)$ for any combination dose (d_1, d_2) .

Recall that the Loewe additivity model (E 1) can be rewritten as $d_1 + (D_{y,1}/D_{y,2})d_2 = D_{y,1}$, and the ratio $D_{y,1}/D_{y,2}$ (denoted as $\rho(y)$), is often called the relative potency of drug 2 versus drug 1 at effect level y , which means that the effect of 1 unit of drug 2 will produce the same effect as $\rho(y)$ units of drug 1. Generally speaking, the relative potency $\rho(y)$ is dose-dependent (7). When there is no drug interaction, the effect of the combination dose (d_1, d_2) will produce the same effect as drug 1 alone at dose level $D_{y,1}$, which equals to $d_1 + \rho(y)d_2$, or drug 2 alone at dose $D_{y,2}$, which equals to $\rho(y)^{-1}d_1 + d_2$ (Figure 2, Panel A). All these combination doses (d_1, d_2) on the line \overline{PQ} will have the predicted effect y , where \overline{PQ} is the line connecting the points $P=(D_{y,1}, 0)$ and $Q=(0, D_{y,2})$ (Figure 2, Panel A). This line \overline{PQ} is often called an additive isobole (2, 3).

When $E_{max,1} > E_{max,2}$, as illustrated in Figure 1 Panel B, we can calculate the dose of drug 1 required to produce the maximum effect of drug 2, i.e., $D_{1-E_{max,2},1} = ED_{50,1} \left(\frac{E_{max,2}}{E_{max,1} - E_{max,2}} \right)^{1/m_1}$. Note that the range of the effect for drug 2 is $(1 - E_{max,2}, 1)$, which could be produced by drug 1 alone at a dose level between 0 and $D_{1-E_{max,2},1}$. Based on the Loewe additivity model, for any level of effect y in $(1 - E_{max,2}, 1)$, the associated additive isobole is the line connecting $(D_{y,1}, 0)$ and $(0, D_{y,2})$. Since when y varies from $1 - E_{max,2}$ to 1, the dose of drug 1 required to produce effect y

varies from $D_{1-E_{max,2}}$ to 0, while the dose of drug 2 required to produce effect y varies from infinitely large to 0. Particularly, when y is close to $1-E_{max,2}$, the dose of drug 1 required to produce such an effect y will be close to $D_{1-E_{max,2}}$, and the dose of drug 2 required to produce such an effect y will go to infinity. Figure 2 Panel B shows four typical additive isoboles (dashed lines), which connect equally effective doses of drug 1 and drug 2 at different effect levels. From left to right, the effect level decreases in magnitude. The additive isoboles may not be parallel since the relative potency may not be constant. When y varies in $(1-E_{max,2}, 1)$, all these additive isoboles will cover the region between the two solid vertical lines (Figure 2 Panel B). Meanwhile, any combination dose (d_1, d_2) with $d_1 < D_{1-E_{max,2}}$ must lie on one of these isoboles. Therefore, for any combination dose (d_1, d_2) with $d_1 < D_{1-E_{max,2}}$, the predicted additive effect, say y , can be obtained by solving the following nonlinear equation for E :

$$\frac{d_1}{ED_{50,1} \left(\frac{1-E}{E-(1-E_{max,1})} \right)^{1/m_1}} + \frac{d_2}{ED_{50,2} \left(\frac{1-E}{E-(1-E_{max,2})} \right)^{1/m_2}} = 1.$$

Now we examine the predicted effect for the combination dose (d_1, d_2) with $d_1 \geq D_{1-E_{max,2}}$. When $d_1 \geq D_{1-E_{max,2}}$, drug 1 alone at dose d_1 produces an effect

$$E = 1 - \frac{(d_1 / ED_{50,1})^{m_1} E_{max,1}}{1 + (d_1 / ED_{50,1})^{m_1}},$$

an effect beyond $1-E_{max,2}$, which can not be produced by drug 2 alone at any dose level. In this case, if the effect at the combination dose is more than the effect produced by drug 1 alone, then drug 2 potentiates the effect of drug 1. In this case, synergy occurs because the predicted additive effect will be the effect produced by drug 1 alone at dose level d_1 . Alternatively, since drug 2 alone can not produce such an effect, we could consider $D_{y,2}$ being infinitely large. Thus, the Loewe additivity model is reduced to $d_1/D_{y,1}=1$. No matter which approach we take, the predicted effect y will be the same, which can be obtained by the following equation:

$$y = f_1(D_{y,1}) = f_1(d_1) = 1 - \frac{(d_1 / ED_{50,1})^{m_1} E_{max,1}}{1 + (d_1 / ED_{50,1})^{m_1}}.$$

Thus, we can obtain the predicted effect for any combination dose (d_1, d_2) . Similar to the notation in Kong and Lee (6), we denote the predicted effect as $\hat{F}_p(d_1, d_2)$ at the combination dose (d_1, d_2) . In the following subsection, we develop the procedure to estimate the effect beyond the additivity, denoted by $\hat{f}(d_1, d_2)$, and to construct its 95% confidence interval and confidence band. We will assess drug interaction based on the estimated $\hat{f}(d_1, d_2)$ and its confidence band.

3.3. Assessing drug interactions using bivariate thin plate splines

In section 3.2, we present how to obtain the predicted additive effect for any combination dose (d_1, d_2) , particularly, for any combination dose (d_1, d_2) with observed effect. Thus, we can calculate the differences of observed effects and predicted effect for any observed combination dose (d_1, d_2) . By definition, there is no drug interaction when a single drug is used alone. Therefore, we set the differences to zero for the marginal observations, that is, the combination doses (d_1, d_2) with only one nonzero component. A bivariate thin plate spline is applied to estimate the differences as a function of the combination dose, say, $f(d_1, d_2)$. When the dose-effect curves are decreasing, $f(d_1, d_2) < 0$ indicates that the effect is more than the predicted effect at (d_1, d_2) , thus the combination dose (d_1, d_2) is synergistic. Inversely, $f(d_1, d_2) > 0$ indicates that the combination dose (d_1, d_2) is antagonistic. Kong and Lee (6) used the different observed combination doses as the knots for the bivariate thin plate splines (12). The choice of knots is easier if the number of combination doses is not large and the combination doses are not so close, such as the ones from factorial designs or uniform design (13). However, when ray designs are applied, the combination doses at low doses are very close to each other, and some columns of the design matrix (i.e., Ω and Z_1 in the following notations) may be highly correlated, which result in a nearly singular matrix for estimating the parameters in the function f . If that happens, a low rank smoothing thin plate spline (14), such as the knots formed by selecting the observed combination doses with the distance being larger than some pre-specified small number, should be applied to avoid the singularity of the involved matrix due to the low rank of the design matrix. Alternatively, one may take an appropriate transformation to the dose, such as the log-transformation, to make the experimental combination doses under the transformation evenly distributed in certain region, so that the effect beyond additivity can be estimated by using bivariate thin plate splines without such a difficulty.

Suppose the selected knots are $(\kappa_{1k}, \kappa_{2k})$ ($k=1, \dots, K$), then the bivariate thin plate spline can be expressed by the following form:

$f(d_1, d_2) = \gamma_0 + \gamma_1 d_1 + \gamma_2 d_2 + \sum_{k=1}^K v_k \eta \left(\| (d_1, d_2)^T - (\kappa_{1k}, \kappa_{2k})^T \| \right)$,
 where $\gamma = (\gamma_0, \gamma_1, \gamma_2)'$ and $v = (v_1, \dots, v_K)'$ are the parameters in the thin plate spline function f , and
 $\eta(r) = \frac{1}{16\pi} r^2 \log r^2$ for $r > 0$ and $\eta(r) = 0$ for $r = 0$. The distance in the expression is the Euclidean distance. Let us
 denote

$$\Omega = \left[\eta \left(\| (\kappa_{1k}, \kappa_{2k})^T - (\kappa_{1k'}, \kappa_{2k'})^T \| \right) \right]_{1 \leq k, k' \leq K},$$

$$Y_R = \left[\left(E_1 - \hat{F}_p(d_{11}, d_{21}) \right) 1_{\{d_{11} \neq 0 \ \& \ d_{21} \neq 0\}}, \dots, \left(E_n - \hat{F}_p(d_{1n}, d_{2n}) \right) 1_{\{d_{1n} \neq 0 \ \& \ d_{2n} \neq 0\}} \right]^T$$

$$X = [1, d_{1i}, d_{2i}]_{1 \leq i \leq n}, \quad Z_1 = \left[\eta \left(\| (d_{1i}, d_{2i})^T - (\kappa_{1k}, \kappa_{2k})^T \| \right) \right]_{1 \leq k \leq K, 1 \leq i \leq n},$$

and $T^T = [1, \kappa_{1k}, \kappa_{2k}]_{1 \leq k \leq K}$.

Following the notation by Kong and Lee (6) and Green and Silverman (12), consider a QR decomposition of T^T , say $T^T = FG$, where F is a $K \times K$ orthogonal matrix and G is a $K \times 3$ upper triangular matrix. Let F_2 be the last $K-3$ columns of F . Set $u = (F_2^T \Omega F_2)^{-\frac{1}{2}} v$ and $Z = Z_1 F_2 (F_2^T \Omega F_2)^{-\frac{1}{2}}$, where $(F_2^T \Omega F_2)^{-\frac{1}{2}}$ is the matrix square root of $F_2^T \Omega F_2$. Based on the approach proposed by Ruppert, Wand, and Carroll (15) and Wang (16), detailed by Kong and Lee (6) in this setting, the parameters in terms of γ and u can be obtained by solving the following mixed effect model:

$$Y_R = X\gamma + Zu + \varepsilon \quad \text{with} \quad \begin{pmatrix} u \\ \varepsilon \end{pmatrix} \sim N \left(\begin{pmatrix} 0 \\ 0 \end{pmatrix}, \begin{pmatrix} \sigma_u^2 I_{K-3} & 0 \\ 0 & \sigma_\varepsilon^2 I_n \end{pmatrix} \right). \quad (E6)$$

Thus, the parameters can be estimated by $\begin{pmatrix} \hat{\gamma} \\ \hat{u} \end{pmatrix} = (C^T C + \hat{\lambda} D)^{-1} C^T Y_R$ with $\hat{\lambda} = \hat{\sigma}_\varepsilon^2 / \hat{\sigma}_u^2$, $C = [X \ Z]$, and
 $D = \text{diag}(0, 0, 0, 1, \dots, 1)$, where the number of zeros in the matrix D corresponds to the number of γ_i 's ($i=0,1,2$) and
 the number of ones corresponds to the number of u_i 's ($i=1, \dots, K-3$). Under these notations, for any
 combination dose (d_1, d_2) , $f(d_1, d_2)$ can be predicted by $\hat{f}(d_1, d_2) = \hat{\gamma}_0 + \hat{\gamma}_1 d_1 + \hat{\gamma}_2 d_2 + Z_0 \hat{u}$ with
 $Z_0 = \left[\eta \left(\| (d_1, d_2)^T - (\kappa_{1k}, \kappa_{2k})^T \| \right) \right]_{1 \leq k \leq K} F_2 (F_2^T \Omega F_2)^{-1/2}$, and an approximate $100(1-\alpha)\%$ point-wise confidence interval for $f(d_1, d_2)$ can be constructed by

$$\hat{f}(d_1, d_2) \pm z_{\alpha/2} \hat{\sigma}_\varepsilon \sqrt{C_d (C^T C + \hat{\lambda} D)^{-1} C_d^T}, \quad (E7)$$

where $C_d = (1, d_1, d_2, Z_0)$ and $z_{\alpha/2}$ is the upper $\frac{\alpha}{2} \times 100\%$ percentile of the standard normal distribution. Thus, we
 can construct 95% point-wise lower and upper confidence surfaces for $f=0$ by taking the intercept lines of the
 confidence surfaces with the dose plane. The combination doses in the area outside the bound with $f < 0$ are claimed to
 be synergistic, the combination doses inside the bound are claimed to be additive, and the combination doses in the area
 outside the bound with $f > 0$ are claimed to be antagonistic.

Note that based on the 95% point-wise confidence surface (E7), some combination doses which are additive may
 be claimed as synergistic or antagonistic based on a single surface. To be conservative and to control the family-wise
 error rate, we also construct a simultaneous confidence band, which shares a similar format to equation (E7) except
 that $z_{\alpha/2}$ is replaced by $\sqrt{EDF \times F_{EDF, n-EDF}^\alpha}$ (17), where EDF is the effective degrees of freedom from the
 resulting bivariate smoothing splines (12) and is defined as the trace of the matrix $C (C^T C + \hat{\lambda} D)^{-1} C^T$, and

$F_{EDF, n-EDF}^\alpha$ is the upper $100 \times \alpha$ percentile of the F distribution with EDF and $n-EDF$ degrees of freedom. Here n is
 the total number of observations except controls. In each of the two case studies presented in next section, we reported
 the plots of different patterns of drug interaction based on the 95% point-wise confidence intervals (CI) and the 95%
 simultaneous confidence band (SCB), respectively (see Figure 4 and 6).

4. CASE STUDIES

The following two data sets were provided by Dr. Greco. The two data sets resulted from examining the joint
 effect of trimetrexate (TMQ) and AG2034 with cells grown in medium with different level of folic acid: 2.3 μM in the
 first experiment (called Low FA experiment), and 78 μM in the second experiment (called High FA experiment). Here

TMQ is a lipophilic inhibitor of the enzyme, dihydrofolate reductase, and AG2034 is an inhibitor of the enzyme, glycinamide ribonucleotide formyltransferase. All drug concentrations are in μM . The endpoint was the growth of HCT-8 human ileocecal adenocarcinoma cells, in 96-well plates, as measured by the SRB protein stain. Treatments of cells in wells by drugs were randomized across the plates. Each 96-well plate included 8 wells as instrumental blanks (no cells); thus 88 wells were used for drug treatments. Five replicate plates were used for each set of 88 treated wells. Each of these two large data sets came from two 5-plate stacks with a maximum of 880 treated wells per experiment. There were 110 control wells per experiment with no drugs applied to the cells. Ray designs were used for these two experiments, and the experimental doses were distributed in 14 rays, including two rays for TMQ and AG2034 when used alone. Complete experimental details and mechanistic implications are included in Faessel *et al* (18). Assuming that the first observation recorded in each dose or combination dose from the first 5-plate stack was from the same plate, say 1st plate, the second observation from the 2nd plate, and so on, and also assuming that the first observation recorded in each dose or combination dose from the second 5-plate stack was from the same plate, say 6th plate, the second observation from the 7th plate, and so on, we have total 10 plates for each of the two data sets.

To examine whether there is a significant difference among the plates for control groups. We applied one-way analysis of variance (ANOVA) to the controls in each individual data set. The p-values were 0.001 for the Low FA experimental data and 0.005 for the High FA experimental data. The results indicate a significant plate effect among the 10 plates for each experiment, that is, the inter-plate variability is high. To attenuate the effect from the inter-plate variability, a standardization procedure, where the effect readings were divided by the mean of the controls in each associated plate, was applied for each data set. Thus, the mean for controls within each plate is standardized to 1, and we will treat the effect for controls as 1. In addition to 110 controls for each experiment, we have 761 observations for the Low FA experiment and 769 observations for the High FA experiment. The statistical method described in Section 3 was applied to each one of the two standardized data sets, and the results for each experiment are presented in the following two subsections.

Lee *et al.* (19) performed extensively exploratory data analyses and identified 129 outliers out of 871 (14.8%) effect readings in the Low FA experiment and 126 outliers out of 879 (14.3%) effect readings in the High FA experiment. To compare with the results obtained by Lee *et al.* (19), we also applied the statistical method described in Section 3 to the data sets with outliers removed. For each experiment, we report the detailed analyses for the original data set and the final result for the data set excluding outliers.

4.1. Case study 1: cells grown in the medium with 2.3 μM folic acid (Low FA experiment)

In the first experiment, called the Low FA experiment, the cells were grown in medium with 2.3 μM folic acid. We fitted marginal dose effect curves for TMQ and AG2034 by using both the median effect equation (E 3) and the E_{max} model (E 5). The dose levels for TMQ when applied alone were 5.47×10^{-6} , 4.38×10^{-5} , 1.38×10^{-4} , 4.38×10^{-4} , 8.75×10^{-4} , 1.75×10^{-3} , 3.5×10^{-3} , 7×10^{-3} , 2.21×10^{-2} , 7×10^{-2} , and 0.56 μM , and the dose levels for AG2034 when applied alone were 2.71×10^{-5} , 2.71×10^{-4} , 6.87×10^{-4} , 2.17×10^{-3} , 4.3×10^{-3} , 8.7×10^{-3} , 1.74×10^{-2} , 3.48×10^{-2} , 0.11, 0.3475, and 2.78 μM . Note that some effect readings at low doses or combination doses are greater than 1, thus, the logit transformation can not be carried out. Nonlinear least squares regression was applied to estimate the parameters in models (E 3) and (E 5). Figure 3 Panel A and Panel B show the fitted respective marginal dose effect curves for TMQ and AG2034 with the dose levels shown on a log scale, where the dotted-dashed lines are the curves based on the median effect model (E 3), and the solid lines are the dose-effect curves based on the E_{max} model (E 5). From the fitted dose effect curves, we found that the E_{max} model provided a much better fit than the median effect equation for the marginal data. Therefore, we chose the E_{max} model to describe the dose effect relationship in this case study. The parameters estimated for TMQ and AG2034 are shown in the three columns under the title “Low FA” in Table 1. Here the estimate of $E_{max, TMQ}$ is slightly larger than the estimate of $E_{max, AG2034}$. We plotted the distribution of the combination doses using the original scale (not shown) and found that most of the combination doses were crowded in the low dose level region, which could cause a singularity of the involved matrices due to the low rank of Ω and Z_1 used for estimating the effect beyond additivity when using bivariate thin plate splines in Section 3.3. Hence, we applied a log transformation of the form $\log(\text{dose} + \delta)$ for each dose level, where δ is a small number, say 2.74×10^{-6} , half of the smallest dose level for the two drugs when applied alone. We plotted the distribution of the combination doses on the $\log(\text{dose} + \delta)$ scale, which is shown in Figure 3, Panel C. In Panel C, the points on the horizontal line are the doses of TMQ on the $\log(\text{dose} + \delta)$ scale, the points on the vertical line are the doses of AG2034 on the $\log(\text{dose} + \delta)$ scale, and the points on each of the remaining 12 design rays are the combination doses at each ray with each dose component on the $\log(\text{dose} + \delta)$ scale. The 12 design rays for combination doses from left to right in Panel C correspond to the combination doses at 12 ratios of TMQ to AG2034, i.e., 1:250, 1:50, 1:20, 1:10, 1:5, 1:5, 2:5, 4:5, 2:1, 5:1, 10:1. The 12 rays from left to right in Panel C are denoted by the letters E, F, G, H, I, J, K, L, M, N, O, P, representing the curves 15, 13, 11, 7, 5, 3, 9, 4, 6, 10, 12, 14 in the original data set for the Low FA experiment. Note that the rays 3 and 9, denoted by J and K, are indeed the same fixed dose ratio. To obtain the predicted additive effects, the procedure described in Section 3.2 was applied, where the dose levels were kept on the original scale. The contour plot of the

predicted additive effect is shown in Figure 3 Panel D. Note that the effect levels for TMQ applied alone are in $(1 - E_{max, TMQ}, 1)$, which is $(0.1190, 1)$, and the effect levels for AG2034 applied alone are in $(1 - E_{max, AG2034}, 1)$, which is $(0.1312, 1)$. The vertical line with contour level 0.13 is the predicted effect produced by TMQ alone at such a dose level. The plot of the differences of observed effects and predicted effects versus the dose levels of AG2034 on $\log(\text{dose} + \delta)$ scale is shown in Figure 3 Panel E. From Panel E, the differences are not distributed around zero, specifically, the differences are significantly less than zero for some observations with AG2034 in the range of $(-7, -4)$ on the $\log(\text{dose} + \delta)$ scale with $\delta = 2.74 \times 10^{-6}$, i.e., in the range of $0.001 \mu\text{M}$ to $0.018 \mu\text{M}$ on the original dose scale. Therefore, the pure additive effect model could not describe the data well. At all single or combination doses, we used bivariate thin plate splines to fit the differences versus the transformed doses with the knots at all the distinct dose levels. The transformation is taken as $\log(\text{dose} + \delta)$ where dose is a single or a combination dose. By convention, there is no drug interaction when a single drug is applied. Therefore the differences were set as zeroes for the marginal doses. By applying the bivariate thin plate splines in Section 3.3, we obtain $\hat{\sigma}_e^2 = 0.0041$, $\hat{\sigma}_u^2 = 0.2318$, and $\hat{\lambda} = \hat{\sigma}_e^2 / \hat{\sigma}_u^2 = 0.0178$. Next, 95% point-wise upper and lower confidence surfaces were constructed based on equation (E 7). Figure 3 Panel F shows the contour plot of the fitted spline function $f(d_1, d_2)$ at the levels of $-0.1, 0$, and 0.1 as thin solid lines, the intercept lines of its corresponding 95% point-wise upper confidence surface with the dose plane as thick dashed lines, and the intercept lines of its corresponding 95% point-wise lower confidence surface with the dose plane as thick solid lines. The combination doses inside the thick dashed curves, painted as light blue, are synergistic since the effects beyond additivity at these combination doses are significantly smaller than zero; the combination doses inside the thick solid curves, painted as light pink, are antagonistic since the effects beyond additivity at these combinations were significantly larger than zero. The combination doses in the uncolored region, which lie between the thick solid curves and the thick dashed curves, are additive since the effects beyond additivity are not significantly different from zero. Specifically, the combination doses with AG2034 in the transformed scale in the range of $(-7, -4)$ inside the thick dashed line are synergistic, which is consistent with the residual plot in Panel E. The fitted response surface was obtained by adding the fitted spline function f (i.e., the effect beyond additivity) to the predicted additive surface, and the contour plot of the fitted response surface at the contour levels of $0.2, 0.5$, and 0.9 is shown in Figure 3, Panel I. The final residuals were obtained by subtracting the fitted effects from the observed effects. The plots of final residuals versus the dose levels of TMQ and AG2034 on the $\log(\text{dose} + \delta)$ scale are shown in Figure 3 Panel G and H, respectively. From these two panels, we see that the residuals are centered around zero along the experimental dose range. We conclude that the model fits the data reasonably well.

To examine the patterns of drug interactions in different rays and different experimental combination doses, we combined Panels F and I in Figure 3, that is, we plotted the contour curves of the fitted response surface at the levels of $0.2, 0.5$, and 0.9 in Panel F, along with the representative design rays and experimental combination doses as dots on these rays, shown in Figure 4, Panel A. From Figure 4, Panel A, the combination doses on the rays E through K (Curve 15, 13, 11, 7, 5, 3, 9 in the original data set) are synergistic when the effect levels are between 0.9 to a number smaller than 0.2 . The combination doses on these rays are additive when the effect level is less than this small number, and the combination doses at low level on these lines are either additive or antagonistic. The combination doses on the rays N, O, and P (Curves 10, 12, and 14 in the original data set) are additive when the effects are less than 0.9 , and the combination doses at low dose levels are antagonistic.

In addition to the 95% point-wise confidence surface, we also constructed the 95% simultaneous confidence band with $\hat{\lambda} = 0.0178$, and $\sqrt{EDF \times F_{EDF, n-EDF}^\alpha} = 12.20$, where $n=761$, $EDF=119$, and $\alpha = 0.05$. The resulting patterns of drug interactions are shown in Figure 4, Panel B, where the thick dashed line is the intercept line of the 95% upper simultaneous confidence surface with the dose plane. Based on Figure 4, Panel B, we conclude that the combination doses inside the thick dashed curves, painted as light blue, are synergistic. The combination doses outside the thick dashed curves are additive. As it can be seen, the synergistic area shrinks using the simultaneous confidence band method compared to the point-wise confidence interval approach and the antagonistic area disappears. A point-wise confidence interval is appropriate for making inferences for each observed design ray. The simultaneous confidence band is suitable for making a global assessment. However, it can be overly conservative.

In addition, we fitted the data set with outliers removed (19) for the Low FA experiment, the results for assessing drug interactions are presented in Figure 4, Panel C and Panel D. The information in Panel C is parallel to that in Panel A, and the information in Panel D is parallel to that in Panel B. By comparing the plots across panels, we conclude that the results from fitting the original data set and those from fitting the data set excluding outliers are very similar. Therefore, the semiparametric method presented in Section 3 is robust to outliers in this example.

It should be noticed that extrapolations based on spline estimations have to be considered with caution. The fitted response surface for the differences between the observed effects and predicted effects gives an overall picture of drug interaction (see Figure 4, Panel A or Panel B). However, the fitted results on the two larger areas outside the experiment rays E and P should not be over-interpreted since there is no experimental data in such areas and we forced the differences of the observed effects and predicted additive effects to be zero at the marginal observed dose levels.

4.2. Case study 2: cells grown in the medium with 78 μM folic acid (High FA experiment)

In the High FA experiment, the dose levels for TMQ when applied alone were 5.47×10^{-6} , 4.38×10^{-5} , 1.38×10^{-4} , 4.38×10^{-4} , 8.75×10^{-4} , 1.75×10^{-3} , 3.5×10^{-3} , 7×10^{-3} , 2.21×10^{-2} , 7×10^{-2} , and $0.56 \mu\text{M}$, and the dose levels for AG2034 when applied alone were 2.71×10^{-4} , 2.17×10^{-3} , 6.87×10^{-3} , 2.17×10^{-2} , 4.34×10^{-2} , 8.68×10^{-2} , 1.74×10^{-1} , 3.47×10^{-1} , 1.1, 3.47, and $27.8 \mu\text{M}$. The procedure to analyze this data set was the same as in case study 1. By applying nonlinear least squares regression, we estimated the marginal dose effect curves using the median effect equation (E 3) (dotted-dashed lines) and the E_{max} model (E 5) (solid lines), shown in Figure 5, Panel A and B. It is clear that the E_{max} model fitted the data better than the median effect equation, thus, we chose the E_{max} model as the dose effect curve for this data set. The estimated parameters for the marginal dose effect curves for the E_{max} model are shown in the three columns under the title “High FA” in Table 1. The combination doses on the original scale (not shown) are crowded in low dose level region, thus we applied the transformation in the form of $\log(\text{dose}+\delta)$ to each dose level, where δ is a small number, say 2.74×10^{-6} , one half of the lowest dose level for TMQ and AG2034 when applied alone. The distribution of the experimental dose levels on the $\log(\text{dose}+\delta)$ scale is shown in Figure 5 Panel C. The 12 design rays for the combination doses correspond to the 12 dose ratios of TMQ versus AG2034 at 1:2500, 1:1250, 1:500, 1:200, 1:100, 1:50, 1:50, 1:25, 1:12.5, 1:5, 1:2, 1:1, which are denoted by the letters E, F, G, H, I, J, K, L, M, N, O, and P, representing the curves 15, 13, 11, 7, 5, 3, 9, 4, 6, 10, 12, 14 in the original data set for the High FA experiment. By applying the procedure described in Section 3.2, we obtained the contour plot of the predicted additive effect shown in Figure 5, Panel D. Particularly, the contour line at level 0.15 is the predicted effect produced by TMQ alone since AG2034 could not produce such an effect when applied alone, and the effect levels for AG2034 applied alone ranged from 0.1816 to 1. Figure 5, Panel E shows the differences of observed effects and predicted effects versus the dose levels of AG2034 on the $\log(\text{dose}+\delta)$ scale. From Panel E, the differences are not centered around zero, specifically, they are significantly less than zero for some observations with AG2034 in the range of $(-5, 0)$ on the $\log(\text{dose}+\delta)$ scale, i.e., in the range of $6.7 \times 10^{-3} \mu\text{M}$ to $1.0 \mu\text{M}$ on the original dose scale, indicating that some combination doses were synergistic and the pure additive effect model could not describe the data well. We used bivariate thin plate splines to fit these differences versus the transformed doses or combination doses with the knots at all distinct dose levels. The transformation is taken as $\log(\text{dose}+\delta)$ where dose is a single dose or a combination dose. We constructed its 95% point-wise confidence surfaces based on equation (E 7). The estimated $\hat{\sigma}_\epsilon^2 = 0.0066$, $\hat{\sigma}_u^2 = 0.0779$, and $\hat{\lambda} = \hat{\sigma}_\epsilon^2 / \hat{\sigma}_u^2 = 0.0842$. Figure 5, Panel F shows the contour plot of the fitted spline function f at levels of $-0.1, 0$, and 0.1 as thin solid lines, the intercept lines of its corresponding 95% point-wise upper confidence surface with the dose plane as thick dashed lines, and the intercept lines of its corresponding 95% point-wise lower confidence surface with the dose plane as thick solid lines. The combination doses inside the thick dashed curves, painted as light blue, are synergistic; the combination doses inside the thick solid curves, painted as light pink, are antagonistic, while the combination doses in the uncolored area are additive. The fitted response surface was obtained by adding the fitted spline function f to the predicted additive surface, which is shown in Figure 5, Panel I. The plots of the final residuals versus the dose levels of TMQ and AG2034 on the $\log(\text{dose}+\delta)$ scale are shown in Figure 5, Panels G and H, respectively. From these two panels, the residuals are centered around zero along the experimental dose range indicating that the model describes the data reasonably well.

To examine the patterns of drug interactions in different rays and different experimental combination doses, we combined Panels F and I in Figure 5 to form Figure 6, Panel A, as we did for analyzing the Low FA experiment data. From Figure 6, Panel A, the combination doses on all 12 rays are synergistic when the effect levels are between 0.9 and 0.15. The combination doses at high dose levels are additive, and most the combination doses at low dose levels are additive. In addition, we constructed a 95% simultaneous confidence band based on equation (E 7) with $z_{\alpha/2}$ replaced by $\sqrt{EDF \times F_{EDF, n-EDF}^\alpha}$. Here $EDF=91$, $n=769$, and $\sqrt{EDF \times F_{EDF, n-EDF}^\alpha} = 10.77$. The results are presented in Figure 6, Panel B, where the thick dashed line is the intercept line of the upper 95% simultaneous confidence surface with the dose plane. Based on Figure 6, Panel B, we conclude that the combination doses inside the thick dashed curves, painted as light blue, are synergistic. The combination doses outside the thick dashed curves are additive. Again, the simultaneous confidence band yields more conservative results and is more suitable for the global assessment. In addition, we fitted the data set with outliers removed for the High FA experiment. The results for assessing drug interactions are presented in Figure 6, Panel C and Panel D. By comparing Panel C to Panel A, and Panel D to Panel B, we conclude that the results from fitting the original data set and those from fitting the data set excluding outliers are very similar. Thus, the results indicate that the semiparametric method is robust to outliers.

5. DISCUSSION

We extended the approach proposed by Kong and Lee (6) to the case where the E_{max} model is more appropriate to describe the marginal dose effect relationship. It may not be unusual that some effect readings at low doses to be beyond the mean of the controls. In this case, the standardized effect is greater than 1 and a logit

transformation to a linear model (4, 8, 9) cannot be carried out. Hence, other models such as the E_{max} model are needed and nonlinear regression methods can be applied for estimating parameters for the dose-effect curves. In the case studies in Section 4, nonlinear least squares regression was applied to estimate the parameters for the dose-effect curves specified by the median effect equation and the E_{max} model.

Another extension of the approach by Kong and Lee (6) in this paper is a solution to the problem arising when the experimental points are very close, when the low rank of the design matrix may cause computational problems in matrix inversion. In this case, one may consider a low-rank thin plate spline (14) to estimate the surface beyond additivity, or alternatively, one may apply an appropriate transformation to the doses so that the combination doses on the transformed scale are more evenly distributed. In our case studies, we first applied the transformation $\log(\text{dose}+\delta)$ to each component of the combination doses and then applied bivariate thin plate splines with knots being all the different observed doses on the $\log(\text{dose}+\delta)$ scale. In both case studies, we chose δ as half of the smallest non-zero dose among TMQ and AG2034 when applied alone, that is, $\delta=2.74 \times 10^{-6}$ for both experiments. The δ should not be selected too small or too large compared with the magnitude of the dose levels. An extremely small δ will result in a relatively large distance between the marginal doses and combination doses. Conversely, a large δ will dominate in the transformation $\log(\text{dose}+\delta)$ when the dose levels are low. From the final residual plots, it is evident that the current transformation works well.

It is well known that the smoothing parameter λ governs the trade-off between the goodness-of-fit and the smoothness of the function f . When λ becomes larger, the fitted function f tends to be smoother and the residuals tend to be larger. The selection of the smoothing parameter plays a key role in the fitted results. In our case studies, the smoothing parameter, $\hat{\lambda}$, was selected as $\hat{\sigma}_\epsilon^2 / \hat{\sigma}_u^2$, which is almost identical to the selected smoothing parameter based on the generalized cross validation (GCV) criterion and "leave-out-one" cross validation (CV) criterion. For example, for the Low FA experimental data, the selected parameters based on the mixed model approach, CV, and GCV were 0.0178, 0.0112, 0.0071, respectively, while for the High FA experimental data, the corresponding selected parameters were 0.0842, 0.0842, 0.0531, respectively. Indeed, Kohn, Ansley, and Tharm (20) showed that the estimation of the smoothing parameter based on a mixed model approach is comparable with the standard method of GCV. By applying a mixed effects model, the smoothing parameter can be automatically determined by $\hat{\sigma}_\epsilon^2 / \hat{\sigma}_u^2$. This method has been implemented in S-PLUS by Ruppert *et al.* (15) by using the function `lme` (21). In our previous study (6), based on extensive simulations, we showed that the selection of the smoothing parameter provides a good estimate to the underlying function in general.

In the two case studies, we also performed the same analyses for the two reduced data sets analyzed by Lee *et al.* (19), and the results were almost identical, which indicates that the semiparametric method developed here is robust to outliers. The semiparametric method can also assess drug interactions for the combination doses not on the design rays, and identify complex patterns of drug interaction in combination studies. In addition, the semiparametric method gives an overall assessment of the combination effect in the entire two-dimensional dose space spanned by the experimental doses with a caveat that extrapolation beyond data points can be risky.

Last but not the least, we would like to point out that the estimated function $f(d_1, d_2)$ and its 95% confidence surfaces can guide the exploration of whether some parametric models are sufficient to describe the data. In the literature, many parametric models have been proposed. Greco, Bravo, and Parsons (22) gave an excellent review on the response surface approach. However, when one has no prior knowledge on the response surface model, or when the data cannot be adequately represented by a parametric model, most parametric approaches will fail. Blindly using any parametric model can be dangerous and may lead to the wrong conclusions of drug interactions. In our proposed approach, there is no need to assume any parametric models for $f(d_1, d_2)$. We provide a promising approach by modeling the mixture effect data with spline techniques via a mixed-effect model. We advocate the use of the semiparametric method for model building because we typically do not know the true patterns of drug interactions. The conclusions of drug interactions are based on the estimated f and its confidence surfaces, which are determined by the underlying data. The S-PLUS code for the current case studies can be obtained from the first author.

6. ACKNOWLEDGEMENT

We thank Dr. William R. Greco for supplying these data sets and his invitation for this manuscript, and thank two referees for their constructive comments. JJL is supported in part by the Department of Defense grants W81XWH-05-2-0027 and W81XWH-07-1-0306 and a National Cancer Institute grant CA16672.

7. REFERENCES

1. F. Kanzawa, K. Nishio, K. Fukuoka, T. Sunami, and N. Saijo: In vitro interactions of a new derivative of spicamycin, KRN5500, and other anticancer drugs using a three-dimensional model. *Cancer Chemother. Pharmacol.* 43, 353-363 (1999).
2. M.C. Berenbaum: What is synergy?. *Pharmacological Reviews* 41, 93-141 (1989).
3. W.R. Greco, G. Bravo, J. C. Parsons: The search of synergy: A critical review from a response surface perspective. *Pharmacological Reviews* 47(2), 331-385 (1995).
4. T. C. Chou: Theoretical basis, experimental design, and computerized simulation of synergism and antagonism in drug combination studies. *Pharmacological Reviews* 58, 621-681 (2006).
5. J. J. Lee, M. Kong, G. D. Ayers, R. Lotan: Interaction index and different methods for determining drug interaction in Combination Therapy. *Journal of Biopharmaceutical Statistics* 17, 461-480 (2007).
6. M. Kong, J. J. Lee: A semiparametric response surface model for assessing drug interactions. *Biometrics* 64, 396-405 (2008).
7. M. Kong, J. J. Lee: A general response surface model with varying relative potency for assessing drug interactions. *Biometrics* 62 (4), 986-995 (2006).
8. J. J. Lee, M. Kong: A confidence interval for interaction index for assessing multiple drug interaction. *Statistics in Biopharmaceutical Research* (in press, 2008).
9. T. C. Chou, P. Talalay: Quantitative analysis of dose effect relationships: the combined effects of multiple drugs or enzyme inhibitors. *Advances in Enzyme Regulation* 22, 27-55 (1984).
10. N. Ting: *Dose Finding in Drug Development*. Springer, New York, USA, 127-145 (2006).
11. D. M. Jonker, S. A. G. Visser, P. H. van der Graaf, R. A. Voskuyl, and M. Danhof: Towards a mechanism based analysis of pharmacodynamic drug-drug interaction in vivo. *Pharmacology and Therapeutics* 106, 1-18 (2005).
12. P. J. Green, B. W. Silverman: *Nonparametric Regression and Generalized Linear Models*. Chapman & Hall, London (1994).
13. M. Tan, H. Fang, G. Tian, and P. J. Houghton: Experimental design and sample size determination for testing synergism in drug combination studies based on uniform measures. *Statistics in Medicine* 22, 2091-2100 (2003).
14. H. Wang, and M. G. Ranalli: Low-rank smoothing splines on complicated domains. *Biometrics* 63, 209-217 (2007).
15. D. Ruppert, M. P. Wand, and R. J. Carroll: *Semiparametric Regression*. Cambridge University Press, UK (2003).
16. Y. Wang: Mixed effect smoothing spline analysis of variance. *Journal of the Royal Statistical Society B* 60, 159-174 (1998).
17. H. Scheffe: *The Analysis of Variance*. New York : John Wiley & Sons (1959)
18. H. M. Faessel, H. K. Slocum, R.C. Jackson, T.J. Boritzki, Y.M. Rustum, M. G. Nair, and W.R. Greco: Super in vitro synergy between inhibitors of dihydrofolate reductase and inhibitors of other folate-requiring enzymes: The critical role of polyglutamylolation. *Cancer Res.* 58, 3036-3050 (1998).
19. J. J. Lee, H. Y. Lin, D. D. Liu, and M. Kong: Applying E_{max} model and Interaction Index for Assessing Drug Interaction in Combination Studies. Submitted to *Frontiers in Biosciences*.
20. R. Kohn, C.F. Ansley, D. Tharm: The performance of cross validation and maximum likelihood estimators of spline smoothing parameters. *Journal of the American Statistical Association* 86, 1042-1050 (1991).
21. J. C. Pinheiro, D. M. Bates: *Mixed-Effects Models in S and S-PLUS*. New York: Springer-Verlag (2000).
22. W.R. Greco, G. Bravo, and J. C. Parsons: The search of synergy: A critical review from a response surface perspective. *Pharmacological Reviews* 47(2), 331-385 (1995).

Running Title: E_{max} Model and Bivariate Splines for Drug Interaction

Key Words Additivity, Antagonism, Synergy, Bivariate splines, E_{max} model, the Loewe additivity model

Send correspondence to: Maiying Kong, Department of Bioinformatics and Biostatistics, School of Public Health and Information Sciences, University of Louisville, Louisville, Kentucky 40292, U.S.A. Tel: 502-852-3988, Fax: 502-852-3294, E-mail: maiying.kong@louisville.edu

Table 1: The estimated parameters for the E_{max} models in the two case studies: the first three columns are the estimated parameters for the marginal dose effect curves in the Low FA experiment, and the last three columns are the estimated parameters for the marginal dose effect curves in the High FA experiment

Drug name	Low FA			High FA		
	E_{max}	ED_{50}	Slope m	E_{max}	ED_{50}	Slope m
TMQ	0.8810 (0.0161)	0.0013 (0.0001)	2.2496 (0.2330)	0.8847 (0.0326)	0.0134 (0.0015)	3.7230 (0.7323)
AG2034	0.8688 (0.0154)	0.0060 (0.0003)	3.1644 (0.3703)	0.8184 (0.0311)	0.4700 (0.0540)	1.6869 (0.2400)

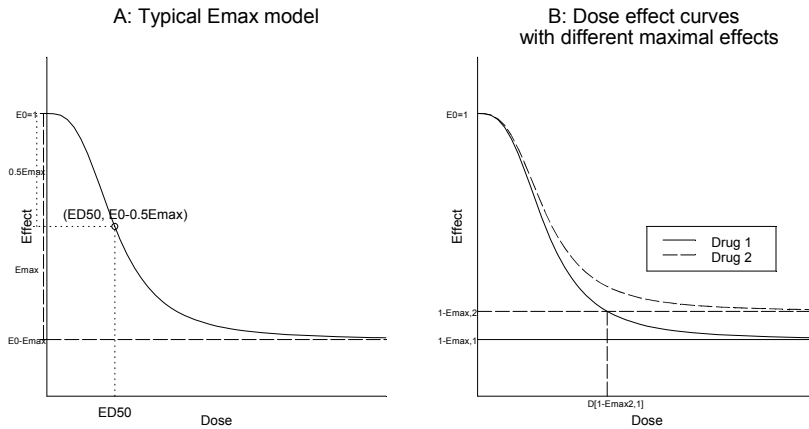


Figure 1: Panel A shows a typical dose effect curve with the maximum effect, i.e., E_{max} being less than 1. ED_{50} in Panel A is the dose required to produce half of the maximum effect, i.e., $E_0-0.5E_{max}$. Panel B shows two dose effect curves with different maximum effects, say, $E_{max,1} > E_{max,2}$. In Panel B, drug 1 at dose level $D_{1-E_{max,2},1}$ produces the maximum effect produced by drug 2 alone.

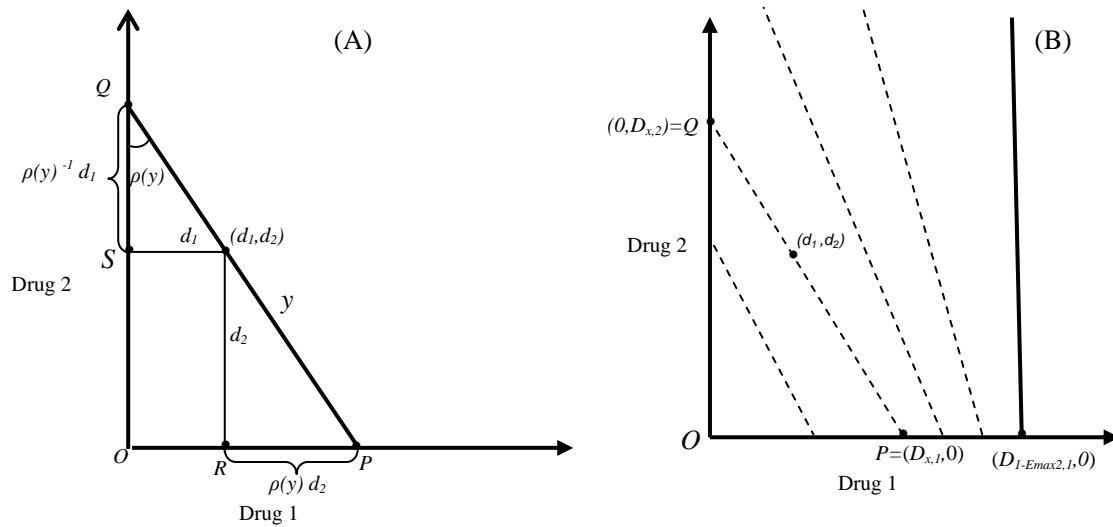


Figure 2: Panel A shows an additive isobole under the Loewe additivity model. Any combination dose (d_1, d_2) on the line \overline{PQ} produces the same effect as drug 1 alone at dose $D_{y,1}$ (i.e., $d_1 + \rho(y)d_2$), or drug 2 alone at dose $D_{y,2}$ (i.e., $\rho(y)^{-1}d_1 + d_2$), y is the predicted effect for any combination dose at the line \overline{PQ} , and $\rho(y)$ is the relative potency at the effect level y . Panel B shows that the additive isoboles associated with the effect level in $(1 - E_{max,2}, 1)$ cover the bound between the two solid vertical lines under the assumption $E_{max,1} > E_{max,2}$. Each dashed line corresponds to an isobole.

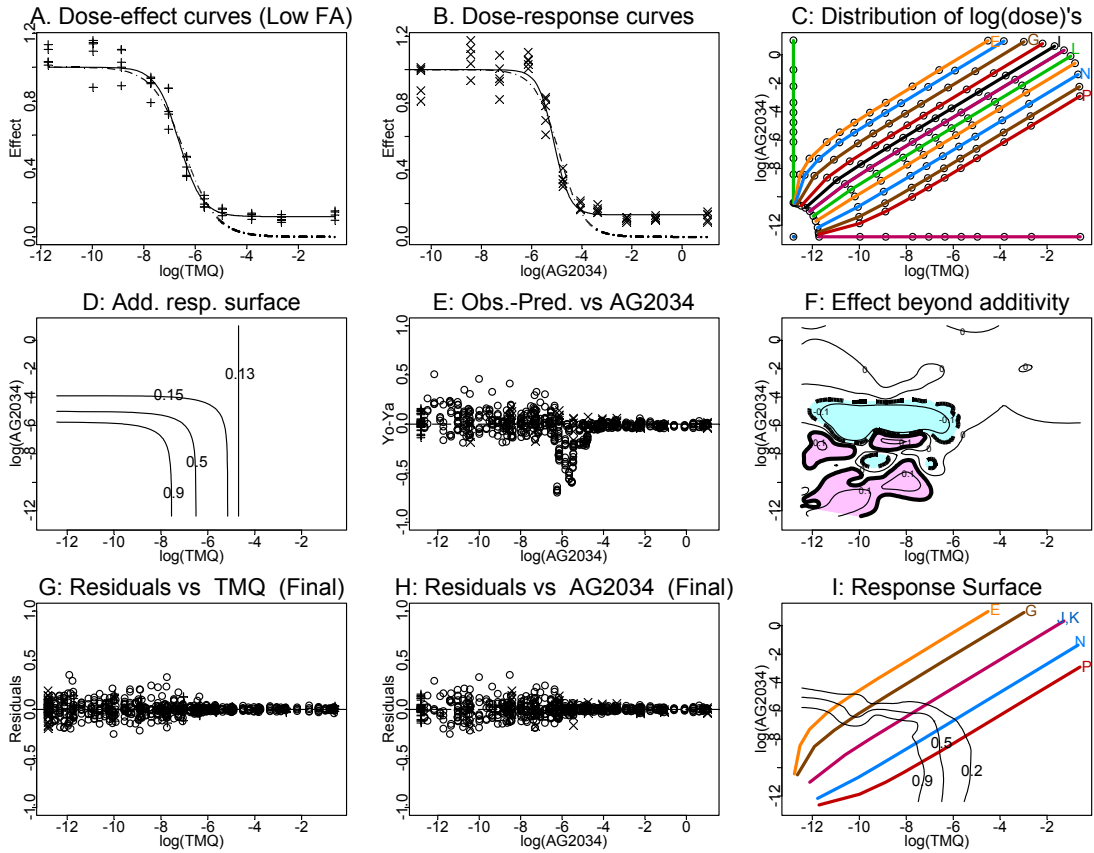


Figure 3: Results from analyzing the Low FA experimental data. Panels A and B show the fitted marginal dose effect curves for TMQ and AG2034 respectively, where the dotted-dashed line in each panel is the fitted dose effect curve based on the median effect equation (E 3), while the solid line in each panel is the fitted dose effect curve based on the E_{max} model (E 5). Panel C shows the distribution of the experimental doses and combination doses on the $\log(\text{dose}+\delta)$ scale with $\delta=2.74 \times 10^{-6}$, along with the 12 rays from left to right with dose ratios of TMQ versus AG2034 at 1:250, 1:125, 1:50, 1:20, 1:10, 1:5, 1:5, 2:5, 4:5, 2:1, 5:1, 10:1, denoted by the letters E, F, G, H, I, J, K, L, M, N, O, and P, representing the curves 15, 13, 11, 7, 5, 3, 9, 4, 6, 10, 12, and 14 in the original data set. Panel D shows the contour plot of the predicted additive effect, while Panel E shows the plot of the differences between the observed effects and the predicted effects versus the dose level of AG2034 on the $\log(\text{dose}+\delta)$ scale. Panel F shows the contour plot of the fitted effect beyond the additivity effect at levels -0.1, 0, and 0.1 as thin solid lines, along with the intercept line of the upper 95% point-wise confidence surface with the dose plane as thick dashed lines and the intercept line of the lower 95% point-wise confidence surface with the dose plane as thick solid lines. In Panel F, the combination doses in the light blue area are synergistic, the combination doses in the light pink area are antagonistic, and the combination doses in the uncolored area are additive. The colored lines in Panels C and I are the design rays. Panels G and H are the plots of the final residuals versus TMQ and AG2034 on the $\log(\text{dose}+\delta)$ scale, respectively, and Panel I is the contour plot of the fitted response surface at the levels of 0.9, 0.5, and 0.2, along with some representative design rays.

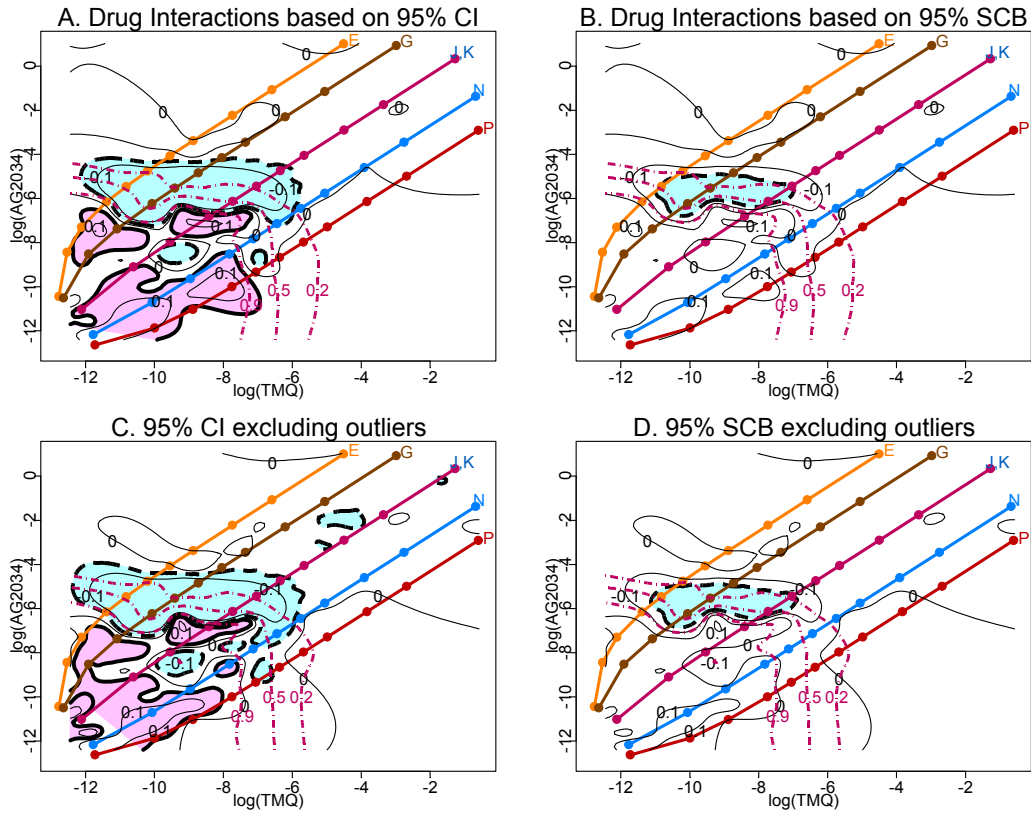


Figure 4: Different patterns of drug interactions for the Low FA experimental data based on 95% point-wise confidence intervals (Panel A) and 95% simultaneous confidence bands (Panel B). Panel A is the combination of Figure 3 Panel F and Panel I, along with the design points shown as dots on each ray. The thin solid lines are the contour lines of the fitted effect surface beyond the additivity surface at the levels of -0.1, 0, and 0.1, the thick dashed lines are the intercept lines of the upper 95% point-wise confidence surface with the dose plane, and the thick solid lines are the intercept lines of the lower 95% point-wise confidence surface with the dose plane. The colored lines with the letters “E”, “G”, “J, K”, “N”, and “P” are the representatives of the design rays. The red dotted-dashed lines are the contour lines of the fitted response surface at the levels of 0.9, 0.5, and 0.2. Based on Panel A, the combination doses in the light blue area are synergistic, the combination doses in the light pink area are antagonistic, and the combination doses on the uncolored area are additive. Panel B presents the same information as Panel A except that the thick dashed lines are the intercept lines of the upper 95% simultaneous confidence surface with the dose plane and there are no intercept lines for the lower 95% simultaneous confidence surface with the dose plane. Based on Panel B, the combination doses inside the dashed lines are synergistic, otherwise additive. Panel B gives more conservative results for assessing drug interactions. Panel C and Panel D are the results from fitting the data set excluding outliers for the Low FA experiment, where the information in Panel C is parallel to that in Panel A, and the information in Panel D is parallel to that in Panel B.

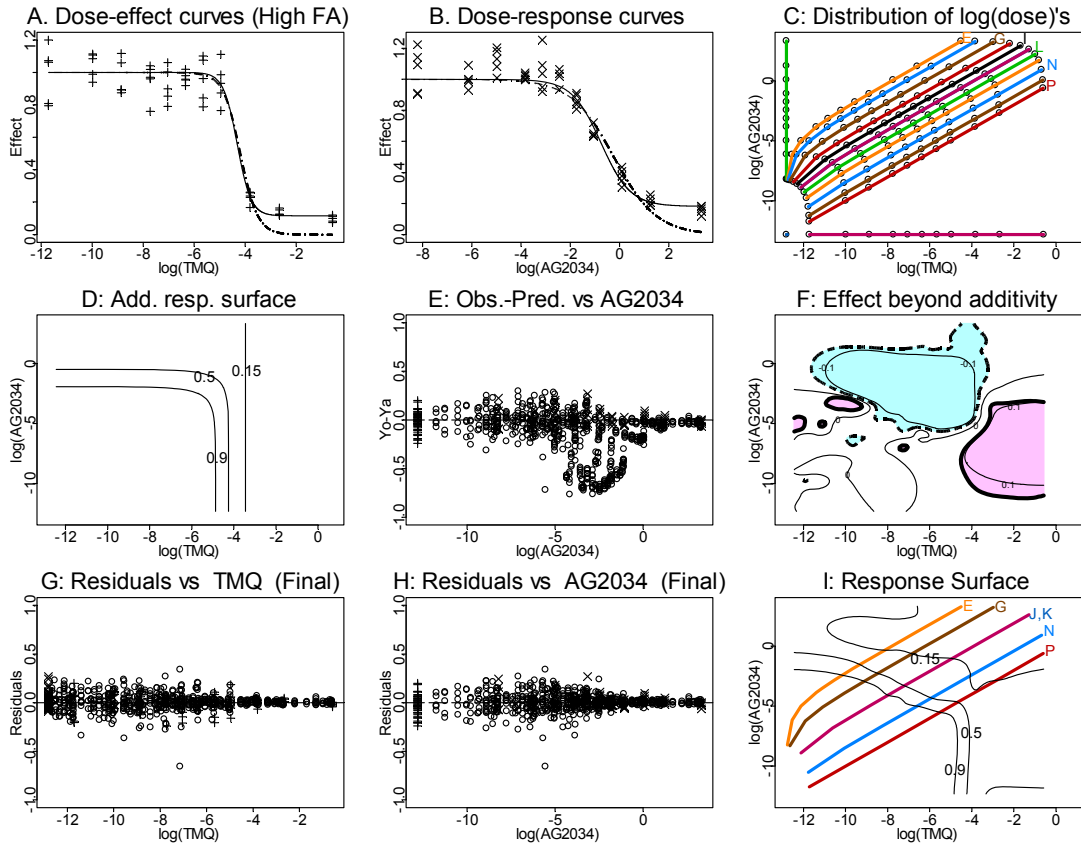


Figure 5: Results from analyzing the High FA experimental data. Panels A and B show the fitted marginal dose effect curves for TMQ and AG2034 respectively, where the dotted-dashed line in each panel is the fitted dose effect curve based on the median effect equation (E 3), while the solid line in each panel is the fitted dose effect curve based on the E_{max} model (E 5). Panel C shows the distribution of the experimental doses and combination doses on the $\log(\text{dose}+\delta)$ scale with $\delta=2.74 \times 10^{-6}$, along with the 12 rays from left to right with dose ratios of TMQ versus AG2034 at 1:2500, 1:1250, 1:500, 1:200, 1:100, 1:50, 1:50, 1:25, 1:12.5, 1:5, 1:2, 1:1, denoted by the letters E, F, G, H, I, J, K, L, M, N, O, P, representing the curves 15, 13, 11, 7, 5, 3, 9, 4, 6, 10, 12, 14 in the original data set. Panel D shows the contour plot of the predicted additive effect, while Panel E shows the plot of the differences between the observed effects and the predicted effects versus the dose level of AG2034 on the $\log(\text{dose}+\delta)$ scale. Panel F shows the contour plot of the fitted effect beyond the additivity effect at levels -0.1, 0, and 0.1, along with the intercept line of the upper confidence surface with the dose plane as thick dashed lines. In Panel F, the combination doses in the light blue area are synergistic, the combination doses in the light pink area are antagonistic, and the combination doses in the uncolored area are additive. The colored lines in Panel C and I are the representatives of the design rays. Panel G and H are the plots of the final residuals versus TMQ and AG2034 on the $\log(\text{dose}+\delta)$ scale, respectively, and Panel I is the contour plot of the fitted response surface at the levels of 0.9, 0.5, and 0.15, along with some representative design rays.

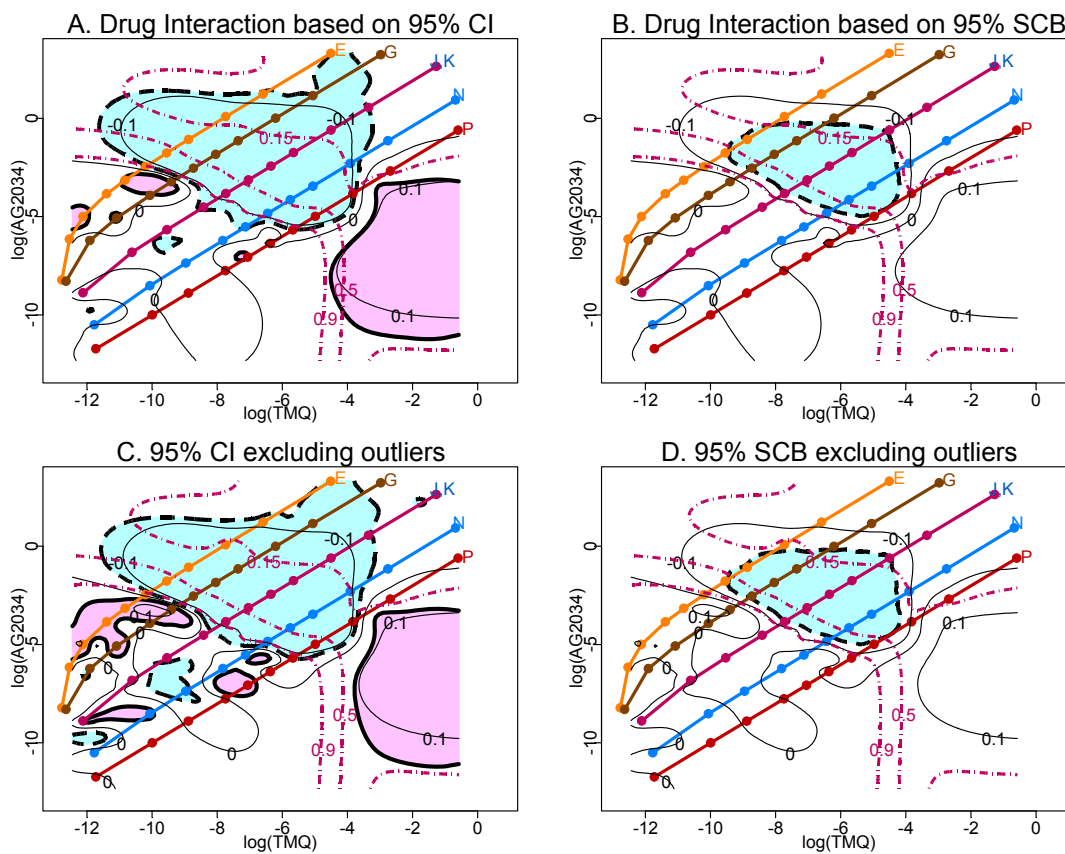


Figure 6: Different patterns of drug interactions for the High FA experiment based on 95% point-wise confidence intervals (Panel A) and 95% simultaneous confidence bands (Panel B). Panel A is the combination of Figure 5 Panels F and I, along with the design points shown as dots on each ray. The thin solid lines are the contour lines of the fitted effect surface beyond the additivity surface at the levels of -0.1, 0, and 0.1, the thick dashed lines are the intercept lines of the upper 95% point-wise confidence surface with the dose plane, and the thick solid lines are the intercept lines of the lower 95% point-wise confidence surface with the dose plane. The colored lines with the letter “E”, “G”, “J, K”, “N”, and “P” are the representatives of the design rays. The red dotted-dashed lines are the contour lines of the fitted response surface at the levels of 0.9, 0.5, and 0.15. In Panel A, the combination doses in the light blue area are synergistic, the combination doses in the light pink area are antagonistic, and the combination doses in the uncolored area are additive. Panel B gives the same information as Panel A except that the thick dashed lines are the intercept lines of the upper 95% simultaneous confidence surface with the dose plane. Based on Panel B, the combination doses inside the dashed lines are synergistic, otherwise additive. Panel B gives more conservative results for assessing drug interactions. Panel C and Panel D are the results from fitting the data set excluding outliers for the High FA experiment, where the information in Panel C is parallel to that in Panel A, and the information in Panel D is parallel to that in Panel B.

Table 1. Summary of parameter estimates (Standard Error) for the Low FA case

Curve	Dose ratio (TMQ/AG)	E _{max}	ED ₅₀	m	Residual sum of squares
A (8)					
B (16)					
C (1)		0.877 (0.007)	0.00133 (0.00006)	2.345 (0.190)	0.0779
D (2)		0.872 (0.007)	0.00621 (0.00024)	3.045 (0.269)	0.0749
E (15)	0.004	0.869 (0.008)	0.00359 (0.00017)	3.250 (0.437)	0.0969
F (13)	0.008	0.863 (0.008)	0.00294 (0.00014)	2.621 (0.276)	0.0897
G (11*)	0.02	0.865 (0.006)	0.00151 (0.00005)	5.0	0.0817
H (7*)	0.05	0.889 (0.007)	0.00274 (0.00011)	4.5	0.1025
I (5)	0.1	0.885 (0.005)	0.00253 (0.00009)	3.449 (0.306)	0.0689
J (3)	0.2	0.882 (0.005)	0.00244 (0.00007)	4.019 (0.402)	0.0655
K (9*)	0.2	0.872 (0.007)	0.00233 (0.00007)	5.0	0.0843
L (4)	0.4	0.889 (0.006)	0.00278 (0.00011)	5.473 (0.583)	0.0855
M (6)	0.8	0.890 (0.005)	0.00200 (0.00007)	3.208 (0.263)	0.0738
N (10)	2	0.887 (0.008)	0.00169 (0.00009)	2.544 (0.258)	0.0984
O (12)	5	0.878 (0.008)	0.00145 (0.00007)	2.206 (0.206)	0.0837
P (14)	10	0.874 (0.006)	0.00134 (0.00006)	1.971 (0.128)	0.0599

* m is fixed at a certain value

Table 2. Estimated interaction index and its 95% confidence interval at each dose combination for the Low FA case

Curve	TMQ dose	AG2034 dose	Dose Ratio (TMQ/AG)	Dilution	Predicted Effect	II	95% CI for II	
							Lower limit	Upper limit
A (8)								
B (16)								
C (1)								
D (2)								
E (15)	1.07E-07	2.66E-05	0.004	1	1	0.87	0.18	4.29
	8.58E-07	0.000213		2	0.9999	0.73	0.28	1.89
	2.71E-06	0.000673		3	0.9962	0.67	0.37	1.20
	8.58E-06	0.002129		4	0.864	0.61	0.48	0.78
	1.72E-05	0.004259		5	0.4454	0.58	0.52	0.65
	3.43E-05	0.008517		6	0.1802	0.56	0.45	0.71
	6.86E-05	0.017000		7	0.1368	0.61	0.24	1.55
	0.000137	0.034100		8	0.1319	0.91	0	4.35E+03
	0.000434	0.107700		9	0.1314	2.71	0	1.30E+157
	0.001373	0.340700		10	0.1314	8.58	0	NA
	0.011000	2.725500		11	0.1314	68.6	0	NA
F (13)	2.10E-07	2.61E-05	0.008	1	1	0.28	0.08	0.91
	1.68E-06	0.000209		2	0.9991	0.35	0.17	0.71
	5.32E-06	0.000660		3	0.9828	0.4	0.26	0.62
	1.68E-05	0.002088		4	0.746	0.47	0.4	0.55
	3.37E-05	0.004177		5	0.3788	0.52	0.46	0.58
	6.73E-05	0.008353		6	0.188	0.59	0.47	0.74
	0.000135	0.016700		7	0.1454	0.76	0.4	1.47
	0.000269	0.033400		8	0.138	1.26	0.02	67.11
	0.000851	0.105700		9	0.1366	3.79	0	1.72E+37
	0.002692	0.334100		10	0.1366	11.95	0	NA
	0.021500	2.673100		11	0.1366	95.63	0	NA
G (11)	4.97E-07	2.47E-05	0.02	1	1.0000	5.60	1.90	16.45
	3.98E-06	0.000197		2	1.0000	1.09	0.60	1.96
	1.26E-05	0.000624		3	0.9885	0.47	0.36	0.63
	3.98E-05	0.001974		4	0.2987	0.22	0.19	0.25
	7.95E-05	0.003949		5	0.1410	0.17	0.09	0.32
	0.000159	0.007898		6	0.1350	0.27	0.00	3.09E+04
	0.000318	0.015800		7	0.1348	0.54	0.00	1.62E+161
	0.000636	0.031600		8	0.1348	1.09	0.00	NA
	0.002012	0.099900		9	0.1348	3.44	0.00	NA
	0.006364	0.315900		10	0.1348	10.87	0.00	NA
	0.050900	2.527300		11	0.1348	86.95	0.00	NA
H (7)	1.09E-06	2.17E-05	0.05	1	1.0000	12.11	3.53	41.51
	8.75E-06	0.000174		2	1.0000	2.71	1.42	5.15
	2.77E-05	0.000549		3	0.9992	1.29	0.88	1.90
	8.75E-05	0.001738		4	0.8773	0.65	0.57	0.74

	0.000175	0.003475		5	0.3035	0.43	0.38	0.48
	>=0.000350	>=0.006950		6 - 11	<= 0.1219	NA	NA	NA
I (5)	1.82E-06	1.81E-05	0.1	1	1.0000	2.39	0.70	8.17
	1.46E-05	0.000145		2	0.9999	1.17	0.59	2.30
	4.61E-05	0.000458		3	0.9966	0.83	0.55	1.24
	0.000146	0.001448		4	0.8509	0.61	0.52	0.71
	0.000292	0.002896		5	0.3906	0.51	0.47	0.55
	0.000583	0.005792		6	0.1506	0.38	0.31	0.47
	>=0.001167	>=0.011600		7 - 11	<= 0.1188	NA	NA	NA
J (3)	2.73E-06	1.36E-05	0.2	1	1.0000	12.56	2.59	60.87
	2.19E-05	0.000109		2	1.0000	3.31	1.38	7.95
	6.92E-05	0.000343		3	0.9993	1.67	0.99	2.81
	0.000219	0.001086		4	0.9344	0.88	0.71	1.08
	0.000438	0.002172		5	0.5008	0.61	0.57	0.65
	0.000875	0.004344		6	0.1577	0.40	0.33	0.48
	>=0.001750	>=0.008688		7 - 11	<= 0.1204	NA	NA	NA
K (9)	2.73E-06	1.36E-05	0.2	1	1.0000	88.77	14.80	532.45
	2.19E-05	0.000109		2	1.0000	9.70	3.84	24.48
	6.92E-05	0.000343		3	0.9998	3.04	1.83	5.06
	0.000219	0.001086		4	0.9550	1.02	0.86	1.21
	0.000438	0.002172		5	0.4457	0.55	0.51	0.60
	0.000875	0.004344		6	0.1429	0.32	0.21	0.47
	>=0.001750	>=0.008688		7 - 11	<= 0.1280	NA	NA	NA
L (4)	3.65E-06	9.05E-06	0.4	1	1.0000	812.88	82.77	7.98E+03
	2.92E-05	7.24E-05		2	1.0000	53.71	13.70	210.53
	9.22E-05	0.000229		3	1.0000	12.38	5.18	29.56
	0.000292	0.000724		4	0.9964	2.99	1.98	4.51
	0.000583	0.001448		5	0.8651	1.31	1.10	1.56
	0.001167	0.002896		6	0.2103	0.56	0.50	0.63
	>=0.002333	>=0.005792		7 - 11	<= 0.1134	NA	NA	NA
M (6)	4.38E-06	5.43E-06	0.8	1	1.0000	4.95	1.18	20.69
	3.50E-05	4.34E-05		2	1.0000	2.40	1.01	5.71
	0.000111	0.000137		3	0.9989	1.63	0.93	2.87
	0.000350	0.000434		4	0.9580	1.12	0.85	1.48
	0.000700	0.000869		5	0.7206	0.90	0.80	1.03
	0.001400	0.001738		6	0.2804	0.72	0.64	0.80
	0.002800	0.003475		7	0.1325	0.41	0.25	0.67
	>=0.005600	>=0.006950		8 - 11	<= 0.1128	NA	NA	NA
N (10)	4.97E-06	2.47E-06	2	1	1.0000	1.37	0.32	5.84
	3.98E-05	1.97E-05		2	0.9998	1.17	0.47	2.89
	0.000126	0.000062		3	0.9967	1.08	0.59	1.98
	0.000398	0.000197		4	0.9417	0.99	0.72	1.37

	0.000795	0.000395		5	0.7418	0.95	0.80	1.13
	0.001591	0.000790		6	0.3742	0.90	0.79	1.02
	0.003182	0.001580		7	0.1721	0.81	0.64	1.03
	>=0.006364	>=0.003159		8 - 11	<= 0.1236	NA	NA	NA
O (12)	5.26E-06	1.04E-06	5	1	1.0000	0.67	0.18	2.52
	4.21E-05	8.35E-06		2	0.9995	0.76	0.33	1.76
	0.000133	2.64E-05		3	0.9934	0.82	0.46	1.45
	0.000421	8.35E-05		4	0.9227	0.88	0.65	1.21
	0.000841	0.000167		5	0.7294	0.92	0.78	1.10
	0.001683	0.000334		6	0.4094	0.97	0.87	1.08
	0.003365	0.000668		7	0.2060	1.01	0.83	1.24
	0.006731	0.001337		8	0.1420	1.05	0.67	1.65
	>=0.021300	>=0.004227		9 - 11	<= 0.1239	NA	NA	NA
P (14)	5.36E-06	5.32E-07	10	1	1.0000	0.39	0.14	1.09
	4.29E-05	4.26E-06		2	0.9988	0.54	0.28	1.05
	0.000136	1.35E-05		3	0.9887	0.65	0.42	1.02
	0.000429	4.26E-05		4	0.9015	0.79	0.62	1.01
	0.000858	8.52E-05		5	0.7095	0.88	0.76	1.02
	0.001716	0.000170		6	0.4221	0.99	0.89	1.10
	0.003431	0.000341		7	0.2272	1.12	0.95	1.32
	0.006863	0.000681		8	0.1544	1.30	0.98	1.74
	>=0.021700	>=0.002155		9 - 11	<= 0.1292	NA	NA	NA

Table 3. Summary of parameter estimates (Standard Error) for the High FA case

Curve	Dose ratio (TMQ/AG)	E _{max}	ED ₅₀	m	Residual sum of squares
A (8)					
B (16)					
C (1)		0.883 (0.012)	0.0137 (0.0012)	3.625 (0.650)	0.1074
D (2)		0.831 (0.015)	0.5224 (0.0439)	1.468 (0.137)	0.0770
E (15)	0.0004	0.867 (0.014)	0.1943 (0.0122)	2.558 (0.405)	0.1134
F (13)	0.0008	0.863 (0.010)	0.1447 (0.0068)	2.643 (0.258)	0.0852
G (11)	0.002	0.859 (0.010)	0.0912 (0.0045)	2.996 (0.355)	0.0999
H (7)	0.005	0.881 (0.006)	0.0699 (0.0027)	2.887 (0.253)	0.0746
I (5)	0.01	0.881 (0.009)	0.0484 (0.0026)	2.528 (0.251)	0.0977
J (3)	0.02	0.884 (0.006)	0.0331 (0.0011)	2.114 (0.136)	0.0615
K (9)	0.02	0.885 (0.008)	0.0369 (0.0019)	2.160 (0.195)	0.0861
L (4)	0.04	0.886 (0.008)	0.0288 (0.0014)	2.504 (0.255)	0.0959
M (6)	0.08	0.885 (0.009)	0.0197 (0.0010)	2.242 (0.214)	0.0881
N (10)	0.2	0.862 (0.010)	0.0154 (0.0007)	3.309 (0.415)	0.0909
O (12)	0.5	0.878 (0.009)	0.0139 (0.0006)	3.491 (0.405)	0.0933
P (14)	1	0.893 (0.008)	0.0183 (0.0009)	2.735 (0.213)	0.0669

Table 4. Estimated interaction index and its 95% confidence interval at each dose combination for the High FA case

Curve	TMQ dose	AG2034 dose	Dose Ratio (TMQ/AG)	Dilution	Predicted Effect	II	95% CI for II	
							Lower limit	Upper limit
A (8)								
B (16)								
C (1)								
D (2)								
E (15)	1.07E-07	0.000266	0.0004	1	1.0000	48.28	2.53	922.71
	8.58E-07	0.002128		2	1.0000	10.31	1.36	78.32
	2.71E-06	0.006729		3	0.9998	4.39	0.96	20.02
	8.58E-06	0.021278		4	0.9970	1.87	0.68	5.14
	1.72E-05	0.042555		5	0.9825	1.12	0.55	2.28
	3.43E-05	0.085110		6	0.9063	0.67	0.44	1.02
	6.86E-05	0.170221		7	0.6388	0.40	0.32	0.48
	0.000137	0.340441		8	0.2994	0.21	0.16	0.28
	>=0.000434	>=1.076570		9 - 11	<= 0.1433	NA	NA	NA
F (13)	2.10E-07	0.000261	0.0008	1	1.0000	42.38	3.74	479.71
	1.68E-06	0.002087		2	1.0000	8.02	1.56	41.25
	5.32E-06	0.006599		3	0.9998	3.20	0.96	10.63
	1.68E-05	0.020868		4	0.9949	1.27	0.59	2.75
	3.37E-05	0.041737		5	0.9688	0.73	0.44	1.23
	6.73E-05	0.083474		6	0.8363	0.42	0.32	0.56
	0.000135	0.166947		7	0.4876	0.24	0.20	0.28
	0.000269	0.333894		8	0.2224	0.11	0.08	0.16
	>=0.000851	>=1.055866		9 - 11	<= 0.1418	NA	NA	NA
G (11)	4.97E-07	0.000247	0.002	1	1.0000	80.07	5.84	1097.54
	3.98E-06	0.001973		2	1.0000	9.20	1.67	50.66
	1.26E-05	0.006239		3	0.9997	2.78	0.84	9.26
	3.98E-05	0.019730		4	0.9913	0.85	0.42	1.71
	7.95E-05	0.039460		5	0.9351	0.42	0.28	0.63
	0.000159	0.078920		6	0.6609	0.21	0.17	0.25
	0.000318	0.157841		7	0.2796	0.10	0.08	0.12
	>=0.000636	>=0.315682		8 - 11	<= 0.1614	NA	NA	NA
H (7)	1.09E-06	0.000217	0.005	1	1.0000	33.80	3.34	342.20
	8.75E-06	0.001736		2	1.0000	4.54	1.03	20.08
	2.77E-05	0.005491		3	0.9994	1.50	0.54	4.20
	8.75E-05	0.017363		4	0.9843	0.51	0.29	0.90
	0.000175	0.034725		5	0.8955	0.27	0.20	0.37
	0.000350	0.069450		6	0.5603	0.15	0.13	0.17
	0.000700	0.138900		7	0.2239	0.07	0.06	0.09
	>=0.001400	>=0.277800		8 - 11	<= 0.1344	NA	NA	NA
I (5)	1.82E-06	0.000181	0.01	1	1.0000	4.94	0.61	39.76

	1.46E-05	0.001447		2	0.9999	1.11	0.30	4.13
	4.61E-05	0.004575		3	0.9977	0.50	0.21	1.20
	0.000146	0.014469		4	0.9592	0.23	0.15	0.37
	0.000292	0.028938		5	0.8071	0.16	0.12	0.20
	0.000583	0.057875		6	0.4556	0.11	0.09	0.13
	0.001167	0.115750		7	0.2041	0.07	0.06	0.09
	>=0.002333	>=0.231500		8 - 11	<= 0.1347	NA	NA	NA
J (3)	2.73E-06	0.000136	0.02	1	1.0000	0.67	0.13	3.34
	2.19E-05	0.001085		2	0.9993	0.28	0.10	0.74
	6.92E-05	0.003432		3	0.9924	0.18	0.09	0.34
	0.000219	0.010852		4	0.9206	0.13	0.09	0.17
	0.000438	0.021703		5	0.7354	0.11	0.09	0.13
	0.000875	0.043406		6	0.4261	0.10	0.09	0.12
	0.001750	0.086813		7	0.2139	0.10	0.08	0.11
	>=0.003500	>=0.173625		8 - 11	<= 0.1405	NA	NA	NA
K (9)	2.73E-06	0.000136	0.02	1	1.0000	0.93	0.15	5.72
	2.19E-05	0.001085		2	0.9995	0.36	0.12	1.12
	6.92E-05	0.003432		3	0.9946	0.22	0.11	0.47
	0.000219	0.010852		4	0.9390	0.15	0.10	0.22
	0.000438	0.021703		5	0.7800	0.13	0.10	0.16
	0.000875	0.043406		6	0.4722	0.11	0.10	0.13
	0.001750	0.086813		7	0.2316	0.11	0.09	0.13
	>=0.003500	>=0.173625		8 - 11	<= 0.1443	NA	NA	NA
L (4)	3.65E-06	0.000090	0.04	1	1.0000	2.89	0.34	24.37
	2.92E-05	0.000723		2	0.9999	0.69	0.18	2.62
	9.22E-05	0.002288		3	0.9983	0.33	0.14	0.80
	0.000292	0.007234		4	0.9702	0.18	0.12	0.29
	0.000583	0.014469		5	0.8538	0.15	0.11	0.19
	0.001167	0.028938		6	0.5312	0.13	0.11	0.15
	0.002333	0.057875		7	0.2326	0.12	0.10	0.15
	>=0.004667	>=0.115750		8 - 11	<= 0.1355	NA	NA	NA
M (6)	4.38E-06	5.43E-05	0.08	1	1.0000	0.73	0.10	5.17
	3.50E-05	0.000434		2	0.9998	0.27	0.08	0.89
	0.000111	0.001373		3	0.9973	0.17	0.08	0.37
	0.000350	0.004341		4	0.9660	0.13	0.09	0.21
	0.000700	0.008681		5	0.8594	0.13	0.10	0.17
	0.001400	0.017363		6	0.5823	0.14	0.12	0.16
	0.002800	0.034725		7	0.2842	0.16	0.13	0.18
	>=0.005600	>=0.069450		8 - 11	<= 0.1571	NA	NA	NA
N (10)	4.97E-06	2.47E-05	0.2	1	1.0000	61.54	3.00	1262.99
	3.98E-05	0.000197		2	1.0000	4.66	0.64	34.02
	0.000126	0.000624		3	1.0000	1.21	0.31	4.73
	0.000398	0.001973		4	0.9983	0.41	0.20	0.87

	0.000795	0.003946		5	0.9830	0.28	0.17	0.46
	0.001591	0.007892		6	0.8570	0.23	0.17	0.31
	0.003182	0.015784		7	0.4280	0.21	0.18	0.25
	0.006364	0.031568		8	0.1800	0.23	0.18	0.30
	>=0.020124	>=0.099827		9 - 11	<= 0.1390	NA	NA	NA
O (12)	5.26E-06	1.04E-05	0.5	1	1.0000	194.98	6.90	5509.68
	4.21E-05	8.35E-05		2	1.0000	11.38	1.16	111.41
	0.000133	0.000264		3	1.0000	2.57	0.51	12.90
	0.000421	0.000835		4	0.9998	0.78	0.30	1.97
	0.000841	0.001669		5	0.9978	0.50	0.25	0.98
	0.001683	0.003339		6	0.9754	0.40	0.24	0.64
	0.003365	0.006678		7	0.7849	0.36	0.27	0.48
	0.006731	0.013356		8	0.3109	0.35	0.30	0.41
	>=0.021285	>=0.042235		9 - 11	<= 0.1263	NA	NA	NA
P (14)	5.36E-06	5.32E-06	1	1	1.0000	10.38	0.65	165.28
	4.29E-05	4.26E-05		2	1.0000	1.89	0.29	12.19
	0.000136	0.000135		3	1.0000	0.87	0.24	3.15
	0.000429	0.000426		4	0.9998	0.55	0.23	1.29
	0.000858	0.000851		5	0.9986	0.50	0.25	1.03
	0.001716	0.001702		6	0.9910	0.51	0.29	0.92
	0.003431	0.003404		7	0.9436	0.56	0.37	0.86
	0.006863	0.006809		8	0.7232	0.64	0.50	0.83
	0.021702	0.021531		9	0.1851	0.80	0.65	0.99
	>=0.068627	>=0.068088		10, 11	<= 0.1109	NA	NA	NA

A simulation study for comparing testing statistics in response-adaptive randomization

Xuemin Gu¹ and J. Jack Lee^{2,§}

¹Department of Biostatistics, Division of Quantitative Sciences, The University of Texas M. D. Anderson Cancer Center, P O Box 301402, Unit 1409, Houston, Texas 77230-1402, USA

²Department of Biostatistics, Division of Quantitative Sciences, The University of Texas M. D. Anderson Cancer Center, P O Box 301402, Unit 1411, Houston, Texas 77230-1402, USA

§Corresponding author

Email addresses:

XMG: xuegu@mdanderson.org

JJL: jjlee@mdanderson.org

Abstract

Background

Response-adaptive randomizations are able to assign more patients in a comparative clinical trial to the tentatively better treatment. However, due to the adaptation in patient allocation, the samples to be compared are no longer independent. At large sample sizes, many asymptotic properties of test statistics derived for independent sample comparison are still applicable in adaptive randomization provided that the patient allocation ratio converges asymptotically. However, the small sample properties of commonly used test statistics in response-adaptive randomization are not fully studied.

Methods

Simulations are systematically conducted to characterize the statistical properties of 8 test statistics in 6 response-adaptive randomization methods at 6 allocation targets with sample sizes ranging from 20 to 200. Since adaptive randomization is usually not recommended for sample size less than 30, the present paper focuses on the case with a sample of 30 to give general recommendations with regard to test statistics for contingency table in response-adaptive randomization at small sample sizes.

Results

Among all asymptotic test statistics, the Cook's correction to Chi-square test (T_{MC}) is the best in attaining the nominal size of hypothesis test. The William's correction to log-likelihood ratio test (T_{ML}) gives slightly inflated type I error and higher power as compared with T_{MC} , but it is more robust against the unbalance in patient allocation. T_{MC} and T_{ML} are usually the two test statistics

with the highest power in different simulation scenarios. When focusing on T_{MC} and T_{ML} , the generalized drop-the-loser urn (GDL) has the best ability to attain the correct size of hypothesis test. Among all sequential methods that can target different allocation ratios, GDL has the lowest variation and the highest overall power at all allocation ratios. The performance of different adaptive randomization methods and test statistics also depends on allocation targets. At the limiting allocation ratio of drop-the-loser (DL) and play-the-winner (RPW) urn, DL outperforms all other methods including GDL. When comparing the power of test statistics in the same randomization method but at different allocation targets, the powers of log-likelihood-ratio, log-relative-risk, log-odds-ratio, Wald-type Z, and Chi-square test statistics are maximized at their corresponding optimal allocation ratios for power. Except for the optimal allocation target for log-relative-risk, the other 4 optimal targets could assign more patients to the worse arm in some simulation scenarios. Another optimal allocation target, R_{RSIHR} , proposed by Rosenberger and Sriram (*Journal of Statistical Planning and Inference*, 1997) is aimed at minimizing the number of failures at fixed power using Wald-type Z test statistics. Among allocation ratios that always assign more patients to the better treatment, R_{RSIHR} usually has less variation in patient allocation, and value of variation is consistent across all simulation scenarios. Additionally, the patient allocation at R_{RSIHR} is not that extreme. Therefore, R_{RSIHR} provides a good balance between assigning more patients to the better treatment and maintaining the overall power.

Conclusions

The Cook's correction to Chi-square test and Williams' correction to log-likelihood-ratio test are generally recommended for hypothesis test in response-adaptive randomization, especially when sample sizes are small. The generalized drop-the-loser urn design is the recommended method for its good overall properties. Also recommended is the use of the R_{RSIHR} allocation target.

Background

The response-adaptive randomization (RAR) in clinical trials is a class of flexible ways of assigning treatment to new patients sequentially based on available data. The RAR adjusts the allocation probabilities to reflect the interim results of the trial, thereby allowing patients to benefit from the interim knowledge as it accumulates in the trial. In practice, unequal allocation probabilities are generated based on the current assessment of treatment efficacy, which results in more patients being assigned to the treatment that is putatively superior.

Many RAR designs have been proposed over the years [1-13]. The two key issues extensively investigated are the evaluations of parameter estimations and hypothesis testing. Due to the dependency of assigning new patients based on observed data at that time, conventional estimates of a treatment effect are often biased; therefore, efforts have been made to quantify and correct estimation bias [14, 15]. Recent theoretical works have been focused on solving problems encountered in practice, which includes delayed response, implementation for multi-arm trials, and incorporating covariates [1, 3, 11, 16-18]. Many recent theoretical developments are summarized in [19]. Additionally, in order to compare treatment efficacies through hypothesis testing, studies have been conducted on power comparisons and sample size calculations under the framework of adaptive randomization [20-24]. However, most of the works focusing on asymptotic properties are based on large sample sizes [4, 12, 22, 25, 26], thus these properties have not been fully studied with small sample sizes. The mathematical challenge imposed by the correlation of data makes it extremely difficult to derive exact solutions for finite samples. Up to now, only limited results on exact solutions have been available [15, 27], and computer simulation

has to be relied upon when sample size is small [23, 24], which is often the case in early phase II trials.

Each RAR design has its own objective, and there are both advantages and disadvantages associated with that objective. It is not our purpose to give a comprehensive assessment of different designs by comparing their advantages and disadvantages. Instead, the primary objective of the present study is to characterize the small sample properties of RAR based on a frequentist approach. In particular, we focus on comparing the performance of commonly used test statistics in RAR of two-arm comparative trials with a binary outcome. Due to the departure from normality caused by data correlation and the discrete nature of a binary outcome, hypothesis tests usually can not be controlled at the level of nominal significance. Thus, to make our simulation comparison more relevant, our assessment of hypothesis testing methods and RAR procedures is based on the calculation of both statistical power and the comparison to the nominal type I error rate. Several RAR methods studied in our simulations can assign patients according to a given allocation target, which may be optimal in terms of maximizing the power or minimizing the expected treatment failure. Therefore, we also compare the properties of test statistics at different optimal allocation targets.

The remaining parts of this paper are organized into 4 sections. In the Method Section, we introduce the adaptive randomization procedures, the optimal allocation rates, and the test statistics used in the simulation. In the Results Section, we present the simulation results. We provide a discussion and final recommendations regarding the RAR methods and hypothesis tests in the Discussions and Conclusion Sections.

Methods

In the present section, we briefly describe the randomization methods, asymptotic hypothesis test statistics, and optimal patient allocation targets that are relevant to our simulations. More detailed information can be found in the corresponding references.

Response-based Adaptive Randomization (RAR)

The RAR procedures investigated in the present study are randomized play-the-winner urn (RPW) [8] [10], and drop-the-loser urn (DL) [28], sequential maximum likelihood estimation design (SMLE) [12], doubly-adaptive biased coin design (DBCD) [2, 3], sequential estimation-adjusted urn designs (SEU) [13], and generalized drop-the-loser urn (GDL) [11]. RPW, DL, SEU and GDL are all urn models in the sense that the treatment for each patient is selected by sampling balls from an urn. In the usual clinical trial setting, an urn model consists of one urn with different types of balls that represent the different treatments under study. Patients are assigned to treatments by randomly selecting balls from the urn. Initially, the urn contains an equal number of balls for each of the treatment offered in the trial. With the progress of a clinical trial, certain rules are applied to update the contents of the urn in such a way that favors the selection of balls corresponding to the better treatment. For example, under the RPW design, the observation of a successful treatment response leads to the addition of a (>0) balls of the same type to the urn; a lack of success leads to the addition of b (>0) balls of the other type to the urn ($a=b=1$ in our simulation). The limiting allocation rate of patients on treatment 1 is $q_2/(q_1+q_2)$, where $q_1=1-p_1$ and $q_2=1-p_2$ are failure rates, and p_1 and p_2 are success rates (or response rates) for treatments 1 and 2. In the DL model, patients are assigned to a treatment based on the type of ball that is drawn; however a treatment failure results in the removal of a treatment ball from the

urn, and treatment successes are ignored. Due to the finite probabilities of extinction, immigration balls are added to the urn. If an immigration ball is drawn, an additional ball of each type is added. The sampling process is repeated until a treatment ball is drawn. The DL urn design has the same limiting allocation as the RPW urn, but less variability in patient allocation. Both SEU and GDL are urn models allowing fraction number of balls, and can target any allocation rate. For SEU method [13], if the limiting allocation of RPW urn is the target in a two-arm trial, then $\hat{q}_1(i) / (\hat{q}_1(i) + \hat{q}_2(i))$ balls of type 2 and $\hat{q}_2(i) / (\hat{q}_1(i) + \hat{q}_2(i))$ balls of type 1 are added to the urn following the allocation of the i th patient. Obviously, the response status of the i th patient is related to the contents of SEU urn only through the calculation of $\hat{q}_1(i)$ and $\hat{q}_2(i)$. For a two-arm GDL urn model [11], when a treatment ball is drawn, a new patient is assigned accordingly, but the ball will not be returned to the urn. Depending on the response of the patient, the conditional average numbers of balls being added back to the urn are b_1 and b_2 , respectively, for treatments 1 and 2. Therefore, the conditional average numbers of type 1 and type 2 balls being taken out of the urn can be defined as d_1 and d_2 , where $d_1=1-b_1$ and $d_2=1-b_2$. Immigration balls are also present in a GDL urn. Whenever an immigration ball is drawn, a_1 and a_2 balls, respectively, are added for treatments 1 and 2. Zhang et al [11] have shown that the limiting allocation rate of patients on treatment 1 is

$$\frac{n_1}{n} \rightarrow \frac{\frac{a_1}{d_1}}{\frac{a_1}{d_1} + \frac{a_2}{d_2}}. \quad (1)$$

The GDL urn becomes a DL urn when $a_1=1$, $a_2=1$, $b_1=p_1$, and $b_2=p_2$. Although GDL is a general method with different ways of implementation, a convenient approach is taken in our simulation. When a treatment ball is drawn, the ball is not returned, and no ball is added regardless of the

response of the patient. When an immigration ball is drawn, $C\rho_1$ and $C\rho_2$ balls of type 1 and 2 are added, where C is a constant, and ρ_1 and ρ_2 are allocation targets on treatments 1 and 2, which are estimated sequentially using the maximum likelihood estimates (MLE) [11].

The SMLE and DBCD methods can also target any allocation ratios, and SMLE can be implemented as a special case of DBCD method. In DBCD method, the probability of the $(i+1)$ th patient being assigned to treatment 1 is calculated by

$$\Pr \left[\text{The } (i+1)\text{th patient is assigned to treatment 1} \right] = g \left(\frac{n_1(i)}{i}, \rho_1(i) \right), \quad (2)$$

where $n_1(i)/i$ and $\rho_1(i)$ are the current allocation rate and estimated allocation rate on treatment 1 [2, 3]. The properties of the DBCD depend largely on the selection of g , which can be considered as a measuring function for the deviation from the allocation target. In the present study, we use the following function suggested by Hu and Zhang [3]:

$$g(r, \rho) = \frac{\rho(\rho/r)^\gamma}{\rho(\rho/r)^\gamma + (1-\rho)((1-\rho)/(1-r))^\gamma}$$

$$g(0, \rho) = 1$$

$$g(1, \rho) = 0$$
(3)

where γ is a tuning parameter. When γ approaches infinity, the DBCD becomes deterministic and the patients are assigned to the putatively better treatment with probability 1. When γ is equal to 0, the MLE of ρ becomes the allocation target, and the DBCD method is essentially the same as the SMLE design proposed by Melfi et al [12].

Hypothesis Tests for Two-Arm Comparative Trials

In two-arm comparative trials, the results of a binary outcome variable can be summarized by a 2×2 contingency table (Table 1). The following hypothesis test is often conducted to compare treatment efficacies:

$$\begin{aligned} H_0 : & \quad p_1 = p_2 \\ H_1 : & \quad p_1 \neq p_2 \end{aligned} \quad (4)$$

Nine test statistics for the hypothesis test in (4) are given in Table 2. When relative risk (q_1/q_2) and odds ratio (p_1q_2/q_1p_2) are used to quantify the differences between 2 treatment arms, the test statistics are log-relative-risk and log-odds-ratio, T_{Risk} and T_{Odds} , which are asymptotically distributed as Chi-squared distribution with one degree of freedom (χ_1^2). When simple difference is used to measure the treatment effect, the applicable test statistics are the Wald-type test statistic T_{Wald} and the score-type test statistics T_{Chisq} , where the variance of simple difference in response rates is evaluated at H_1 or H_0 respectively. Additionally, the test statistics based on the log of likelihood ratio (T_{LLR}) can also be constructed. Besides the 5 commonly used test statistics mentioned above, 4 modified test statistics are also included in Table 2. T_{MO} is a modified log-odds-ratio test proposed by Gart using the approximation of discrete distributions by their continuous analogues [29]. As shown in Table 2, T_{MO} is essentially a modification to T_{Odds} by adding 0.5 to each cell of a 2×2 table. Similarly, Agresti and Caffo proposed a modification to T_{Wald} by adding 1 to each cell of a contingency table [30], which results in the test statistic T_{MW} in Table 2. T_{MC} is the Cook's continuity correction to Chi-square test statistics T_{Chisq} . Willimas provided a modification to log-likelihood-ratio test T_{LLR} [31]. The original test statistic T_{LLR} is improved by multiplying a scale factor such that the null distribution of the new test statistic T_{ML} has the same moments as the Chi-square distribution.

Since all test statistics in Table 2 are based on χ_1^2 , they are asymptotically equivalent and any one of them can be used for large sample sizes. Meanwhile at small sample sizes, an exact test can be conducted if a model is specified for the data given in Table 1. For example, depending on the

number of fixed margins predetermined for the design, one of the following 3 models can be applied [32]:

$$\Pr(r_1 | n, n_1, r) = h(r_1 | n, n_1, r), \quad (5)$$

$$\Pr(r_1, r | n, n_1, p) = h(r_1 | n, n_1, r)b(r | n, p), \quad (6)$$

and

$$\Pr(r_1, r, n_1 | n, p, \rho) = h(r_1 | n, n_1, r)b(r | n, p)b(n_1 | n, \rho), \quad (7)$$

where $h(r_1 | n, n_1, r)$ represents the hypergeometric distribution of r_1 , $b(r | n, p)$ gives the binomial distribution of r under the null hypothesis of equal response rates ($H_0: p_1 = p_2 = p$), and $b(n_1 | n, \rho)$ denotes the binomial distributions of patients on arm 1 with an allocation ratio of ρ ($\rho = 0.5$ for equal randomization). The p-value of exact test can be calculated by maximizing the probability in (5), (6), or (7) over the 2 nuisance parameters, p and ρ . However, due to data dependency, none of the above 3 models are applicable in adaptive randomization. For example, the allocation ratio ρ in adaptive randomization is a random variable with unknown distribution, and the binomial distribution of n_1 assumed in model (7) is not valid even when the null hypothesis is true. Therefore, unconditional exact tests are not available in adaptive randomization, and asymptotic test statistics such as the ones in Table 2 are needed to test the hypothesis in (4) for adaptive randomization.

Optimal Allocation Ratios

The SMLE, DBCD, SEU, and GDL methods can be utilized to allocate patients based on different allocation targets. The allocation targets simulated in the present study are summarized in Table 3, where R_{Risk} , R_{Odds} , R_{Wald} , R_{Chisq} , and R_{LLR} are optimal allocation ratios maximizing the power of T_{Risk} , T_{Odds} , T_{Wald} , T_{Chisq} , and T_{LLR} respectively, at fixed sample size. The derivation of T_{Risk} , T_{Odds} , T_{Wald} , T_{Chisq} , and T_{LLR} can be found in [33, 34]. The method used is equivalent to

minimizing the variance of corresponding test statistic at a fixed total sample size, and consequently the power of that test statistic is maximized. R_{RSIHR} is a recently proposed allocation target that is optimal in minimizing the expected total number of failures among all trials with the same power [15, 33]. The general theoretical framework and the practical implementation of optimal allocation in k -arm trials with binary outcomes are discussed and demonstrated by Tymofyeyev et al [35], where the optimization can be conducted over different goals. In practice, the performance of the methodology depends on the chosen RAR procedure. The present simulation study only focuses on two-arm trials, where straightforward implementation can be achieved for maximizing the power or minimizing the total number of failures.

Results

Simulations are conducted at different total numbers of patients ranging from 20 to 200. To simplify the presentation, the results for trials with 30 patients are shown here. When patients are less than 30, adaptive randomization is generally not recommended. For sample size of 100 or larger, all methods yield similar properties in general. For all of the urn models, one ball for each treatment is consistently used as the initial contents of the urn. The number of immigration balls is 1 for both the DL and GDL urns. The tuning parameter of DBCD, γ , is fixed at 0 or 2. When γ is 0, it results in the SMLE method. The value of the constant C in GDL is 2, which is equivalent to adding 2 treatment balls on average when an immigration ball is drawn. All simulation results are calculated based on 10,000 simulation runs.

The simulation results for allocation rates on arm 1 are shown in Table 5. For the purpose of comparison, the true allocation rates are shown in Table 4. Among all RAR methods, DBCD has

the best ability to attain the true allocation target. The comparison between SMLE and DBCD shows that, the allocation becomes more unbalanced and the variation of DBCD decreases with increasing value of γ . On the other hand, the patient allocation of SEU results in more balanced allocation between two arms with a much larger variation compared with other RAR methods. The GDL has the lowest variation among the 4 sequential RAR methods. When R_{RPW} (the same as R_{DL}) is the allocation target, DL urn method has the lowest variation in patient allocation, which is consistent with the fact that the lower bound of the estimate of $\text{Var}(R_{RPW})$ is attained by DL urn [4]. The comparison among allocation targets shows that R_{LLR} has the lowest variation in patient allocation, and the highest variation is usually found at R_{Risk} or R_{RPW} . However, R_{RPW} and R_{Risk} are usually the top two allocation targets that assign more patients to the better treatment. R_{Wald} , R_{Odds} , and R_{LLR} will assign more patients to the worse arm in some simulation cases. Among the 3 allocation targets that assign more patients to the better treatment (R_{RSIHR} , R_{Risk} and R_{RPW}), R_{RSIHR} has a stable and often the lowest variation in patient allocation.

The simulation results for 5 null cases and 10 alternative cases are shown in Tables 6-11 with one table for each of the six allocation targets. To simplify the presentation, the results are shown only for the 4 modified test statistics T_{MW} , T_{MO} , T_{MC} , T_{ML} , and the log-relative-risk test statistic T_{Risk} because they tend to have better performance than the four corresponding unmodified tests. Additionally, Table 12 summarizes the results of each test statistic in Tables 6-11 by averaging the results over the 5 null cases and the 10 alternative cases for a given RAR methods and at a given allocation target. The qualitative comparisons among test statistics, RAR methods, and allocation targets can be made based on the results in Table 12. Detailed comparison at a given scenario can be found in Tables 6-11.

As shown in Table 12, the worst performance can be found in the results of log-relative-risk test statistic T_{Risk} , which is often conservative, but can have much inflated type I error at R_{Risk} . T_{MW} , the Agresti's correction to T_{Wald} , is always slightly conservative across all simulation cases. Meanwhile, T_{MO} the test using log-odds-ratio is very conservative, especially when response rate is low (also see Tables 6-11). Overall, the Cook's correction to Chi-square test statistic, T_{MC} , is the best in attaining the correct type I error rate. The Williams' correction to log-likelihood-ratio test, T_{ML} , is slightly inflated as compared with chi-square test T_{MC} . The simulation results not shown here indicate that T_{ML} is very robust against the unbalance in patient allocation even when sample size is 20. The comparison between different RAR methods shows that the mean type I error of GDL can usually match the correct size of tests better than other methods. The type I error of DBCD is usually the most inflated one, except at R_{Odds} . The type I error of SEU is comparable with GDL, but more conservative.

The power comparison of different test statistics indicates that T_{Risk} is the statistic with the highest power at R_{Risk} and R_{RPW} , but with a much inflated type I error. Except at R_{Risk} and R_{RPW} , Cook's correction to Chi-square test T_{MC} or Williams' correction to log-likelihood-ratio test T_{ML} is the one with the highest power. Usually, GDL has the highest power and SEU has the lowest power among all RAR methods. DBCD and SMLE have similar power, but DBCD is more powerful in most cases. At target R_{RPW} , DL urn has the best statistical properties. On average, the target with the lowest power achieved by test statistics is R_{Risks} . The highest overall power can usually be achieved by test statistics at R_{RSIHR} and R_{LLR} , but R_{LLR} has the disadvantage of assigning more patients to the worse treatment in some cases.

Discussion

In response-adaptive randomization, the assignment of a new patient depends on the treatment outcomes of patients previously enrolled in the trial. Delayed responses are often encountered in practice. Recently, the problem of delayed response in multi-arm generalized drop-the-loser urn and generalized Friedman's urn design is studied for both continuous and discontinuous outcomes [11, 16, 17, 36]. It is shown that, under reasonable assumption about the delay, the asymptotic properties of adaptive design are not affected by the delay. In the present study, the primary focus is the comparison between commonly used test statistics for 2×2 table. Based on results not shown here, a less extreme allocation with higher variation would be expected when a random delay is assumed. For the sake of simplicity, it is assumed that the response status of each of the patients already in the trial is available before the allocation of a new patient in our simulations.

One goal of adaptive randomization is to assign more patients to the superior treatment, which is meaningful only if the treatment identified as better during the trial will not cause serious health problems in the future. Ethical concerns could arise should patients experience unforeseeable, serious, long-term side effects from the treatment when adaptive randomization is based only on short-term benefits. Thus, RAR is only suitable under the assumptions that the treatments putatively considered to be superior do not have serious long-term adverse effects. This point holds regardless of which randomization method is used.

The RAR methods simulated in the present study are aimed at assigning patients to the better treatment with probabilities higher than what otherwise would be allowed by equal randomization. The price being paid is that the sample sizes on the two comparing arms are no

longer fixed, and the adaptation in patient allocation can complicate the statistical inference at the end of the trial. The properties of test statistics will change when the patient allocation ratio changes in adaptive randomization. The power of test statistics shown in the present simulation is obtained by averaging over trials with an unknown distribution of allocation ratios. As shown in our simulation results, a large deviation from the nominal significance level of the hypothesis test can be found under the null hypothesis. Therefore, the practice of comparing asymptotic hypothesis testing methods based solely on statistical power under the alternative hypothesis is not recommended. It is important to compare adaptive randomization methods based on both the type I error rate and the statistical power, especially when the sample size is small.

General recommendations given in the result section are based on the aggregated results across different settings. Because the performance of test statistics, RAR methods, and allocation target are closely related to each other, recommendations under a specific scenario can be found based on the detailed simulation results in Tables 6-11.

Based on simulation results, the Cook's correction to Chi-square test statistic T_{MC} and Williams' correction to log-likelihood-ratio test T_{ML} is recommended to be used for hypothesis testing at the end of adaptive randomization. T_{MC} has good ability to attain the correct significance level, and is relatively robust against the change of RAR method or allocation target. T_{ML} has more robust performance than T_{MC} and has higher power, but its type I error is slightly inflated as compared with T_{MC} . When the sample size is small, T_{ML} attains more accurate type I error than T_{MC} . The original Wald-type Z test statistic T_{Wald} , which is very sensitive to patient allocation and has inflated type I error, should be avoided at small sample sizes. On the other hand, T_{MW} , the

Argresti's correction to T_{Wald} , and T_{MO} the modified log-odds-ratio test are too conservative and under powered at small sample sizes.

The primary objective of current study is to compare test statistics. Since the recommended test statistics are T_{MC} and T_{ML} , the comparison between RAR methods and allocation targets are mainly based on these two selected test statistics. Among SMLE, DBCD, SEU, and GDL methods, GDL has the best ability to attain the correct size of hypothesis test, and has comparatively higher overall power at most allocation targets due to its low variation in patient allocation. Therefore, GDL is the recommended RAR method. The sequential estimation-adjusted urn (SEU) method is comparable with GDL in controlling the type I error. However, SEU is often under powered, and the high variation makes it less useful in practice. The DBCD method with γ equal to 2 is the best in targeting the true allocation ratio. When T_{MC} is the test statistic, DBCD has slightly inflated type I error and lower power as compared with GDL. Therefore, the balance between controlling the type I error, obtaining higher power, and targeting a given allocation ratio can be reached when γ is equal to 2. The simulation comparison of statistical power for different RAR methods also indicates that DL urn has the best statistical properties at R_{RPW} , mainly due to its low variation in patient allocation.

The statistical characteristics of hypothesis tests and RAR methods also depend on allocation targets. At R_{Wald} , R_{Odds} , and R_{LLR} targets, more patients could be assigned to the inferior treatment in certain parameter spaces. In contrast, R_{Risk} , R_{RPW} , and R_{RSIHR} always assign more patients to the better treatment. However, due to the more extreme allocation of R_{Risk} and R_{RPW} , both power and type I error of R_{Risk} and R_{RPW} will suffer as compared with R_{RSIHR} . On the other hand, the variation of patient allocation at R_{RSIHR} is relatively small with a stable value across all

simulation scenarios. Additionally, among all designs with similar power using Wald-type test statistic, R_{RSIHR} allocation ratio can achieve fewer failures in the whole trial. Therefore, R_{RSIHR} is recommended among all the allocation targets in the present study.

Although the simulation results are not shown here, for comparison purpose, adaptive randomization is also simulated using Optimal Design (OD) [37] and Thompson's traditional Bayesian method [38]. The Optimal Design (OD) is developed based on Bayesian decision theoretic analysis. A well defined utility will be optimized over not only for the n patients in the trial but also considering additional N future patients, referred to as patient horizon. The commonly used utility is the total number of success in all $(n+N)$ patients. The N patients outside the trial will be assigned to one treatment based on the decision made from the n patients in the trial. If a large patient horizon is used, the potential loss due to wrong decision at the end of trial will also be large. Therefore, the OD method will emphasize on collecting information during the trial such that the probability of making the right decision will be improved, which is equivalent to increasing the frequentist's power in hypothesis testing. If a small patient horizon is used, the OD method will focus on assigning more patients to the better arm, and resulted in a more unbalanced patient allocation. An efficient implementation of OD has to rely on backward induction through dynamic programming, which is computationally expensive for large sample sizes [39]. In Bayesian adaptive randomization of two-arm comparative trials with binary outcomes, it is often assumed that the prior distributions of response rates follow a Beta distribution: $p_1 \sim \text{Beta}(a_1, b_1)$ and $p_2 \sim \text{Beta}(a_2, b_2)$. Therefore, the posterior distribution of response rate also follows a Beta distribution, and the probability of a new patient being assigned to arm 1 is calculated by $\Pr(p_1 > p_2 | \text{Data})$, which converges to 0 or 1 with increasing sample size. When the patient

horizon is zero and $Beta(1,1)$ is used for both p_1 and p_2 , the performances of all test statistics are poor in OD and Bayesian method, primarily due to the more extreme allocation and higher variation as compared with other RAR methods. However, the poor performance of OD and Bayesian method is caused by the way chosen for implementation rather than their intrinsic properties. There are many new methods that can be used to achieve better frequentist's characteristics in Optimal Design [40] or Bayesian method. For example, a lower limit and a higher limit can be set for the randomization probability to avoid the extreme allocation probabilities close to 0 or 1. The primary objective of present study is to compare the commonly used test statistics. The simulation of OD and Bayesian method enable us to investigate the properties of test statistics at allocation ratios that are more extreme than the ones found in RAR methods. The simulation results indicate that the Williams' correction to log-likelihood ratio test is very robust against extreme patient allocation. For example, when sample size is only 20, the type I error of T_{ML} can still be controlled at a reasonable level in OD and Bayesian methods. The performance of Cook's correction to Chi-square test is inferior to T_{ML} with larger inflated type I error. On the other hand, the Wald type test statistic T_{Wald} and T_{MW} are extremely sensitive to unbalanced allocation ratios.

Conclusion

The Cook's correction to Chi-square test and Williams' correction to log-likelihood-ratio test are recommended for hypothesis test of RAR at small sample sizes. Among all the RAR methods compared, GDL method has better statistical properties in controlling type one error and maintaining high statistical power. The RSIHR allocation target provides a good balance between assigning more patients to the better treatment and maintaining a high overall power.

Abbreviations

RAR: Response-adaptive randomization

RPW: Randomized play-the-winner

DL: Drop-the-loser

DBCD: Doubly-adaptive biased coin design

SMLE: Sequential maximum likelihood estimation design

SEU: Sequential estimation-adjusted urn

GDL: Generalized drop-the-loser urn

RSIHR: Optimal allocation target minimizing total numbers of failure for Wald-type test statistics at fixed power

MLE: Maximum likelihood estimate

OD: Optimal design

Competing interests

The authors declare that they have no competing interests.

Authors' contribution

XMG conducted the simulation part of the study. Both XMG and JJJ participated in designing the study and writing the manuscript. All authors read and approved the final manuscript.

Acknowledgements

This work was supported in part by grants CA16672 from the National Cancer Institute and W81XWH-06-1-0303 and W81XWH-07-1-0306 from the Department of Defense. The authors also thank the editorial assistance from Ms. Lee Ann Chastain.

References

1. Andersen J, Faries D, Tamura R: **A randomized play-the-winner design for multi-arm clinical trials.** *Communications in Statistics-Theory and Methods* 1994, **23**:309-323.
2. Eisele JR: **The doubly adaptive biased coin design for sequential clinical trials.** *Journal of Statistical Planning and Inference* 1994, **38**:249-262.
3. Hu FF, Zhang LX: **Asymptotic properties of doubly adaptive biased coin designs for multi-treatment clinical trials.** *Annals of Statistics* 2004, **32**(1):268-301.
4. Ivanova S, Rosenberger WF, Durham S, Flournoy N: **A birth and death urn for randomized clinical trials: asymptotic methods.** *Sankhya: The Indian Journals of Statistics* 2000, **62** (B):104-118.
5. Li W, Durham SD, Flournoy N: **Randomized Pôlya urn.** In: *1996 Proceedings of the Biopharmaceutical Section of the American Statistical Association: 1997; Alexandria: American Statistical Association; 1997*: 166-170.
6. Rosenberger WF, Stallard N, Ivanova A, Harper CN, Ricks ML: **Optimal adaptive designs for binary response trials.** *Biometrics* 2001, **57**:909-913.
7. Wei LJ: **The generalized Polya's urn design for sequential medical trials.** *Annals of Statistics* 1979, **7**:291-296.
8. Wei LJ, Durham SD: **The randomized play-the-winner rule in medical trials.** *Journal of American Statistical Association* 1978, **85**:156-162.
9. Yang Y, Zhu D: **Randomized allocation with nonparametric estimation for a multi-armed bandit problem with covariates.** *Annals of Statistics* 2002, **30**:100-121.
10. Zelen M: **Play the winner rule and the controlled clinical trial.** *Journal of the American Statistical Association* 1969, **64**:131-146.

11. Zhang LX, Chan WS, Cheung SH, Hu FF: **A generalized drop-the-loser urn for clinical trials with delayed responses.** *Statistica Sinica* 2007, **17**(1):387-409.
12. Melfi VF, Page C, Geraldes M: **An adaptive randomized design with application to estimation.** *Canadian Journal of Statistics* 2001, **29**(1):107-116.
13. Zhang LX, Hu FF, Cheung SH: **Asymptotic theorems of sequential estimation-adjusted urn models.** *Annals of Applied Probability* 2006, **16**(1):340-369.
14. Coad DS, Ivanova A: **Bias calculations for adaptive urn designs.** *Sequential Analysis* 2001, **20**(3):91-116.
15. Rosenberger WF, Sriram TN: **Estimation for an adaptive allocation design.** *Journal of Statistical Planning and Inference* 1997, **59**:309-319.
16. Bai ZD, Hu FF, Rosenberger WF: **Asymptotic properties of adaptive designs for clinical trials with delayed response.** *Annals of Statistics* 2002, **30**(1):122-139.
17. Hu FF, Zhang LJ: **Asymptotic normality of urn models for clinical trials with delayed response.** *Bernoulli* 2004, **10**:447-463.
18. Rosenberger WF, Vidyashankar AN, Agarwal DK: **Covariate-adjusted response-adaptive designs for binary response.** *Journal of Biopharmaceutical Statistics* 2001, **11**:227-236.
19. Hu FF, Rosenberger WF: **The Theory of Response-Adaptive Randomization in Clinical Trials.** Hoboken, New Jersey: John Wiley & Sons, Inc.; 2006.
20. Hu FF, Rosenberger WF: **Optimality, variability, power: evaluating response-adaptive randomization procedures for treatment comparisons.** *Journal of the American Statistical Association* 2003, **98**(463):671-678.
21. Zhang LJ, Rosenberger WF: **Response-adaptive randomization for clinical trials with continuous outcomes.** *Biometrics* 2006, **62**(2):562-569.
22. Hu FF, Rosenberger WF, Zhang LX: **Asymptotically best response-adaptive randomization procedures.** *Journal of Statistical Planning and Inference* 2006, **136**(6):1911-1922.
23. Morgan CC, Coad DS: **A comparison of adaptive allocation rules for group-sequential binary response clinical trials.** *Statistics in Medicine* 2007, **26**(9):1937-1954.
24. Guimaraes P, Palesch Y: **Power and sample size simulations for Randomized Play-the-Winner rules.** *Contemporary Clinical Trials* 2007, **28**(4):487-499.

25. Matthews PC, Rosenberger WF: **Variance in randomized play-the-winner clinical trials.** *Statistics & Probability Letters* 1997, **35**:233-240.
26. Bai ZD, Hu FF: **Asymptotics in randomized urn models.** *Annals of Applied Probability* 2005, **15** (1B):914-940.
27. Matthews PC, Rosenberger WF: **Variance in randomized play-the-winner clinical trials.** *Statistics & Probability Letters* 1997, **35**(3):233-240.
28. Ivanova A: **A play-the-winner-type urn design with reduced variability.** *Metrika* 2003, **58**:1-13.
29. Gart JJ: **Alternative analyses of contingency tables.** *Journal of Royal Statistical Society B* 1966, **28**:164-179.
30. Agresti A, Caffo B: **Simple and effective confidence intervals for proportions and differences of proportions results from adding two successes and two failures.** *The American Statistician* 2000, **54**(4):280-288.
31. Williams SS: **Improved likelihood ratio tests for complete contingency tables.** *Biometrika* 1976, **63**:33-37.
32. Upton GJG: **A comparison of alternative tests for the 2×2 table comparative trial.** *Journal of Royal Statistical Society A* 1982, **145**:86-105.
33. Rosenberger WF, Lachin JM: **Randomization in Clinical Trials: Theory and Practice.** New York: Wiley; 2002.
34. Jennison C, Turnbull BW: **Group Sequential Methods with Applications to Clinical Trials.** Boca Raton: Chapman & Hall/CRC; 2000.
35. Tymofeyev Y, Rosenberger WF, Hu FF: **Implementing optimal allocation in sequential binary response experiments.** *Journal of American Statistical Association* 2007, **102**(477):224-234.
36. Sun RB, Cheung SH, Zhang LX: **A generalized drop-the-loser rule for multi-treatment clinical trials.** *Journal of Statistical Planning and Inference* 2007, **137**(6):2011-2023.
37. Berry DA, Fristedt B: **Bandit Problems.** New York: Chapman and Hall; 1985.
38. Thompson WR: **On the likelihood that one unknown probability exceeds another in the view of the evidence of the two samples.** *Biometrika* 1933, **25**:275-294.
39. Berry DA, Eick SG: **Adaptive assignment versus balanced randomization in clinical trials: a decision**

- analysis.** *Statistics in Medicine* 1995, **14**:231-246.
40. Cheng Y, Berry DA: **Optimal adaptive randomized designs for clinical trials.** *Biometrika* 2007, **94**(4):673-689.

Figure and Table Captions

Table 1. Summary of data from a two-arm comparative clinical trial

Table 2. Test statistics

Table 3. Allocation targets

Table 4. Asymptotic allocation rates on arm 1 calculated from true p_1 and p_2

Table 5. Mean and standard deviation (in parenthesis) of allocation rate on arm 1 for $n = 30$. The 2 Urn modes, RPW and DL, have exactly the same limiting allocation rate R_{RPW} . The 4 sequential methods, SMLE, DBCD, SEU, and GDL, can target the following 6 allocation targets: R_{Wald} , R_{Risk} , R_{Odds} , R_{LLR} , R_{RSIHR} , and R_{RPW} .

Table 6. Power and type I error at R_{Wald} (alpha = 0.05, $n = 30$). For each RAR methods, the results of the following 5 test statistics are shown: Agresti's correction to Wald-type Z test T_{MW} , log-relative-risk test T_{Risk} , Gart's correction to log-odds-ratio test T_{MO} , Cook's correction to Chi-square test T_{MC} , and Williams' correction log-likelihood-ratio test T_{ML} .

Table 7. Power and type I error at R_{Risk} (alpha = 0.05, $n = 30$). For each RAR methods, the results of the following 5 test statistics are shown: Agresti's correction to Wald-type Z test T_{MW} , log-relative-risk test T_{Risk} , Gart's correction to log-odds-ratio test T_{MO} , Cook's correction to Chi-square test T_{MC} , and Williams' correction log-likelihood-ratio test T_{ML} .

Table 8. Power and type I error at R_{Odds} (alpha = 0.05, $n = 30$). For each RAR methods, the results of the following 5 test statistics are shown: Agresti's correction to Wald-type Z test T_{MW} , log-relative-risk test T_{Risk} , Gart's correction to log-odds-ratio test T_{MO} , Cook's correction to Chi-square test T_{MC} , and Williams' correction log-likelihood-ratio test T_{ML} .

Table 9. Power and type I error at R_{LLR} (alpha = 0.05, $n = 30$). For each RAR methods, the results of the following 5 test statistics are shown: Agresti's correction to Wald-type Z test T_{MW} , log-relative-risk test T_{Risk} , Gart's correction to log-odds-ratio test T_{MO} , Cook's correction to Chi-square test T_{MC} , and Williams' correction log-likelihood-ratio test T_{ML} .

Table 10. Power and type I error at R_{RSIHR} (alpha = 0.05, $n = 30$). For each RAR methods, the results of the following 5 test statistics are shown: Agresti's correction to Wald-type Z test T_{MW} , log-relative-risk test T_{Risk} , Gart's correction to log-odds-ratio test T_{MO} , Cook's correction to Chi-square test T_{MC} , and Williams' correction log-likelihood-ratio test T_{ML} .

Table 11. Power and type I error at R_{RPW} (alpha = 0.05, $n = 30$). For each RAR methods, the results of the following 5 test statistics are shown: Agresti's correction to Wald-type Z test T_{MW} , log-relative-risk test T_{Risk} , Gart's correction to log-odds-ratio test T_{MO} , Cook's correction to Chi-square test T_{MC} , and Williams' correction log-likelihood-ratio test T_{ML} .

Table 12. The mean and standard deviation (in parenthesis) of type I error and power calculated by averaging simulation results over the 5 null cases and the 10 alternative cases of simulation scenarios. All results have been multiplied by 100% (alpha = 0.05, $n = 30$).

Figures and Tables

Table 1. Summary of data from a two-arm comparative clinical trial

	Response	Failure	Margins
Treatment 1	r_1	f_1	n_1
Treatment 2	r_2	f_2	$n - n_1 = n_2$
Margins	$r_1 + r_2 = r$	$n - r = f_1 + f_2 = f$	n

n : total number of patients; n_1, n_2 : patients on treatment 1 and 2; r : total number of treatment successes; r_1, r_2 : number of successes on treatment 1 and 2.

Table 2. Test statistics

Log-Relative-Risk	$T_{Risk} = (\log(f_2 n_1 / f_1 n_2))^2 / (r_1 / n_1 f_1 + r_2 / n_2 f_2)$
Log-odds-ratio	$T_{Odds} = (\log(f_2 r_1 / f_1 r_2))^2 / (1/f_1 + 1/f_2 + 1/r_1 + 1/r_2)$
Wald-type Z	$T_{Wald} = (r_1 / n_1 - r_2 / n_2)^2 / (f_2 r_1 / n_1^3 + f_1 r_2 / n_2^3)$
Chi-Square	$T_{Chisq} = (n - 1)(r_1 f_2 - r_2 f_1)^2 / r f n_1 n_2$
Log-likelihood-ratio	$T_{LLR} = 2 \cdot (r_1 \log r_1 + r_2 \log r_2 + f_1 \log f_1 + f_2 \log f_2 - r \log r - f \log f - n_1 \log n_1 - n_2 \log n_2 + n \log n)$
Gart's Correction to T_{Odds} [29]	$T_{MO} = (\log(f_2' n_1' / f_1' n_2'))^2 / (r_1' / n_1' f_1' + r_2' / n_2' f_2')$
Agresti's Correction to T_{Wald}	$T_{MW} = (r_1'' / n_1'' - r_2'' / n_2'')^2 / (f_2'' r_1'' / n_1''^3 + f_1'' r_2'' / n_2''^3)$
Cook's Correction to T_{Chisq}	$T_{MC} = (n - 1)(r_1 f_2 - r_2 f_1 - 0.5)^2 / r f n_1 n_2$
William's Correction to T_{LLR} [31]	$T_{ML} = [1 + (n_2 - r f)(n_2 - n_1 n_2) / 6 r f n_1 n_2 n]^{-1} \cdot T_{LLR}$

$$r'_1 = r_1 + 0.5, r'_2 = r_2 + 0.5, f'_1 = f_1 + 0.5, f'_2 = f_2 + 0.5, r'' = r + 1, f'' = f + 1, n'_1 = n_1 + 1, n'_2 = n_2 + 1, n'' = n + 2$$

$$r''_1 = r_1 + 1, r''_2 = r_2 + 1, f''_1 = f_1 + 1, f''_2 = f_2 + 1, r''' = r + 2, f''' = f + 2, n''_1 = n_1 + 2, n''_2 = n_2 + 2, n''' = n + 4$$

Table 3. Allocation targets

Optimal allocation ratio (n_1/n_2) for maximizing powers	
R_{Risk}	$\sqrt{p_1 q_2 / p_2 q_1}$
$R_{Odds} /$	$\sqrt{p_2 q_2 / p_1 q_1}$
R_{Chisq}	$\sqrt{p_1 q_1 / p_2 q_2}$
$R_{Wald} /$	$\sqrt{p_1 q_1 / p_2 q_2}$
R_{Neyman}	$\sqrt{p_1 q_1 / p_2 q_2}$
R_{LLR}	$\{q_2 - p_2 \exp[I_1 - I_2 / (p_2 - p_1)]\} / \{-q_1 + p_1 \exp[I_1 - I_2 / (p_2 - p_1)]\}$
Other allocation targets	
$R_{RPW} /$	q_2 / q_1
R_{DL}	q_2 / q_1
R_{RSIHR}	$\sqrt{p_1 / p_2}$ (Minimize the number of failure at fixed power of T_{Wald})

$$I_1 = p_1 \log(p_1) + q_1 \log(q_1), \quad I_2 = p_2 \log(p_2) + q_2 \log(q_2)$$

Table 4. Asymptotic allocation rates on arm 1 calculated from true p_1 and p_2

p_1	0.100	0.100	0.100	0.100	0.300	0.300	0.300	0.500	0.500	0.700
p_2	0.300	0.500	0.700	0.900	0.500	0.700	0.900	0.700	0.900	0.900
R_{Wald} / R_{Neyman}	0.396	0.375	0.396	0.500	0.478	0.500	0.604	0.522	0.625	0.604
R_{Risk}	0.337	0.250	0.179	0.100	0.396	0.300	0.179	0.396	0.250	0.337
R_{Odds} / R_{Chisq}	0.604	0.625	0.604	0.500	0.522	0.500	0.396	0.478	0.375	0.396
R_{LLR}	0.534	0.538	0.528	0.500	0.507	0.500	0.472	0.493	0.462	0.466
R_{RSIHR}	0.366	0.309	0.274	0.250	0.436	0.396	0.366	0.458	0.427	0.469
R_{RPW} / R_{DL}	0.438	0.357	0.250	0.100	0.417	0.300	0.125	0.375	0.167	0.250

Table 5. Mean and standard deviation (in parenthesis) of allocation rate on arm 1 for $n = 30$. The 2 Urn modes, RPW and DL, have exactly the same limiting allocation rate R_{RPW} . The 4 sequential methods, SMLE, DBCD, SEU, and GDL, can target the following 6 allocation targets: R_{Wald} , R_{Risk} , R_{Odds} , R_{LLR} , R_{RSIHR} , and R_{RPW} .

		p_1	0.2	0.3	0.5	0.7	0.8	0.1	0.1	0.1	0.1	0.3	0.3	0.3	0.5	0.5	0.7
		p_2	0.2	0.3	0.5	0.7	0.8	0.3	0.5	0.7	0.9	0.5	0.7	0.9	0.7	0.9	0.9
Urn	RPW		0.500(0.081)	0.500(0.095)	0.500(0.129)	0.500(0.179)	0.500(0.209)	0.444(0.080)	0.375(0.092)	0.287(0.096)	0.181(0.088)	0.430(0.109)	0.341(0.120)	0.227(0.123)	0.411(0.147)	0.288(0.160)	0.375(0.202)
	DL		0.500(0.048)	0.500(0.058)	0.500(0.078)	0.500(0.092)	0.500(0.097)	0.447(0.046)	0.383(0.055)	0.316(0.056)	0.249(0.053)	0.437(0.067)	0.363(0.071)	0.290(0.066)	0.424(0.082)	0.343(0.082)	0.416(0.092)
SMLE	R_{Wald}		0.500(0.106)	0.500(0.103)	0.500(0.098)	0.500(0.103)	0.500(0.106)	0.440(0.100)	0.424(0.098)	0.441(0.100)	0.501(0.102)	0.483(0.101)	0.500(0.104)	0.559(0.100)	0.517(0.100)	0.576(0.099)	0.558(0.101)
	R_{Risk}		0.500(0.130)	0.500(0.134)	0.500(0.140)	0.500(0.151)	0.500(0.158)	0.397(0.117)	0.325(0.107)	0.259(0.095)	0.186(0.079)	0.415(0.133)	0.334(0.124)	0.238(0.109)	0.411(0.139)	0.298(0.131)	0.375(0.149)
	R_{Odds}		0.500(0.109)	0.500(0.098)	0.500(0.091)	0.500(0.099)	0.500(0.109)	0.562(0.110)	0.577(0.107)	0.561(0.110)	0.499(0.126)	0.517(0.095)	0.500(0.098)	0.438(0.109)	0.485(0.095)	0.423(0.107)	0.438(0.109)
	R_{LLR}		0.500(0.093)	0.500(0.092)	0.500(0.091)	0.500(0.093)	0.500(0.094)	0.519(0.094)	0.522(0.094)	0.515(0.094)	0.499(0.095)	0.506(0.092)	0.499(0.091)	0.483(0.093)	0.495(0.092)	0.477(0.094)	0.481(0.094)
	R_{RSIHR}		0.500(0.117)	0.500(0.116)	0.500(0.109)	0.500(0.106)	0.500(0.102)	0.417(0.108)	0.369(0.100)	0.335(0.093)	0.312(0.087)	0.447(0.112)	0.408(0.107)	0.378(0.103)	0.459(0.106)	0.429(0.105)	0.468(0.101)
	R_{RPW}		0.500(0.100)	0.500(0.109)	0.500(0.131)	0.500(0.166)	0.500(0.192)	0.447(0.099)	0.384(0.105)	0.297(0.106)	0.179(0.091)	0.434(0.117)	0.343(0.122)	0.209(0.110)	0.405(0.141)	0.255(0.136)	0.332(0.174)
DBCD	R_{Wald}		0.500(0.090)	0.500(0.075)	0.500(0.055)	0.500(0.075)	0.500(0.090)	0.417(0.081)	0.393(0.073)	0.416(0.081)	0.499(0.095)	0.475(0.065)	0.500(0.075)	0.585(0.081)	0.525(0.065)	0.607(0.073)	0.584(0.081)
	R_{Risk}		0.500(0.126)	0.500(0.124)	0.500(0.123)	0.500(0.127)	0.500(0.140)	0.371(0.106)	0.285(0.086)	0.216(0.071)	0.138(0.054)	0.394(0.116)	0.300(0.104)	0.187(0.083)	0.391(0.118)	0.250(0.108)	0.337(0.130)
	R_{Odds}		0.500(0.082)	0.500(0.061)	0.500(0.047)	0.500(0.061)	0.500(0.082)	0.585(0.085)	0.607(0.078)	0.586(0.086)	0.499(0.110)	0.520(0.053)	0.501(0.061)	0.413(0.086)	0.480(0.054)	0.394(0.079)	0.414(0.084)
	R_{LLR}		0.500(0.049)	0.500(0.046)	0.500(0.044)	0.500(0.047)	0.500(0.049)	0.474(0.048)	0.468(0.046)	0.477(0.047)	0.500(0.047)	0.493(0.045)	0.500(0.046)	0.524(0.047)	0.508(0.045)	0.532(0.046)	0.527(0.048)
	R_{RSIHR}		0.500(0.107)	0.500(0.099)	0.500(0.078)	0.500(0.060)	0.500(0.054)	0.392(0.093)	0.332(0.077)	0.297(0.069)	0.273(0.063)	0.431(0.088)	0.387(0.080)	0.353(0.075)	0.453(0.069)	0.417(0.066)	0.464(0.055)
	R_{RPW}		0.500(0.064)	0.500(0.074)	0.500(0.104)	0.500(0.148)	0.500(0.185)	0.440(0.063)	0.366(0.072)	0.266(0.078)	0.129(0.064)	0.422(0.087)	0.317(0.095)	0.157(0.082)	0.386(0.118)	0.201(0.112)	0.284(0.158)
SEU	R_{Wald}		0.500(0.113)	0.500(0.106)	0.500(0.098)	0.500(0.106)	0.500(0.114)	0.476(0.113)	0.464(0.110)	0.473(0.113)	0.505(0.117)	0.493(0.104)	0.502(0.106)	0.535(0.108)	0.509(0.102)	0.540(0.102)	0.532(0.108)
	R_{Risk}		0.500(0.155)	0.500(0.168)	0.500(0.195)	0.500(0.223)	0.500(0.237)	0.433(0.143)	0.361(0.130)	0.296(0.115)	0.234(0.091)	0.440(0.166)	0.365(0.154)	0.280(0.126)	0.437(0.197)	0.337(0.171)	0.411(0.212)
	R_{Odds}		0.500(0.101)	0.500(0.104)	0.500(0.130)	0.500(0.176)	0.500(0.196)	0.514(0.108)	0.497(0.124)	0.462(0.143)	0.388(0.137)	0.489(0.119)	0.453(0.134)	0.384(0.131)	0.469(0.150)	0.399(0.146)	0.438(0.177)
	R_{LLR}		0.500(0.093)	0.500(0.091)	0.500(0.091)	0.500(0.093)	0.500(0.092)	0.510(0.093)	0.512(0.094)	0.508(0.093)	0.501(0.094)	0.503(0.092)	0.500(0.091)	0.493(0.094)	0.498(0.093)	0.490(0.094)	0.490(0.092)
	R_{RSIHR}		0.500(0.149)	0.500(0.146)	0.500(0.131)	0.500(0.116)	0.500(0.106)	0.461(0.143)	0.425(0.130)	0.402(0.122)	0.383(0.113)	0.475(0.136)	0.449(0.126)	0.429(0.121)	0.479(0.124)	0.460(0.117)	0.481(0.109)
	R_{RPW}		0.500(0.135)	0.500(0.155)	0.500(0.192)	0.500(0.222)	0.500(0.233)	0.469(0.129)	0.424(0.136)	0.367(0.135)	0.294(0.113)	0.462(0.164)	0.408(0.162)	0.326(0.141)	0.456(0.197)	0.366(0.173)	0.423(0.208)
GDL	R_{Wald}		0.500(0.056)	0.500(0.046)	0.500(0.033)	0.500(0.047)	0.500(0.056)	0.450(0.051)	0.437(0.046)	0.452(0.051)	0.500(0.058)	0.486(0.040)	0.499(0.047)	0.548(0.052)	0.514(0.041)	0.562(0.046)	0.548(0.051)
	R_{Risk}		0.500(0.106)	0.500(0.114)	0.500(0.128)	0.500(0.144)	0.500(0.154)	0.397(0.093)	0.320(0.085)	0.251(0.071)	0.181(0.055)	0.407(0.114)	0.319(0.104)	0.220(0.078)	0.397(0.128)	0.274(0.104)	0.356(0.138)
	R_{Odds}		0.500(0.040)	0.500(0.035)	0.500(0.055)	0.500(0.090)	0.500(0.112)	0.527(0.043)	0.508(0.053)	0.454(0.072)	0.341(0.080)	0.484(0.045)	0.431(0.064)	0.327(0.072)	0.447(0.071)	0.342(0.080)	0.390(0.102)
	R_{LLR}		0.500(0.029)	0.500(0.026)	0.500(0.024)	0.500(0.026)	0.500(0.029)	0.517(0.027)	0.521(0.026)	0.515(0.027)	0.500(0.028)	0.505(0.024)	0.500(0.026)	0.485(0.027)	0.495(0.025)	0.479(0.026)	0.483(0.028)
	R_{RSIHR}		0.500(0.073)	0.500(0.070)	0.500(0.058)	0.500(0.045)	0.500(0.039)	0.431(0.065)	0.389(0.057)	0.362(0.051)	0.342(0.047)	0.454(0.062)	0.423(0.056)	0.398(0.052)	0.466(0.052)	0.440(0.046)	0.472(0.038)
	R_{RPW}		0.500(0.053)	0.500(0.065)	0.500(0.088)	0.500(0.116)	0.500(0.133)	0.454(0.052)	0.399(0.063)	0.329(0.067)	0.236(0.059)	0.444(0.075)	0.367(0.082)	0.263(0.073)	0.420(0.098)	0.303(0.092)	0.370(0.121)

Table 6. Power and type I error at R_{Wald} ($\alpha = 0.05, n = 30$). For each RAR methods, the results of the following 5 test statistics are shown: Agresti's correction to Wald-type Z test T_{MW} , log-relative-risk test T_{Risk} , Gart's correction to log-odds-ratio test T_{MO} , Cook's correction to Chi-square test T_{MC} , and Williams' correction log-likelihood-ratio test T_{ML} .

p_1		0.200	0.300	0.500	0.700	0.800	0.100	0.100	0.100	0.100	0.300	0.300	0.300	0.500	0.500	0.700
p_2		0.200	0.300	0.500	0.700	0.800	0.300	0.500	0.700	0.900	0.500	0.700	0.900	0.700	0.900	0.900
SMLE	T_{MW}	0.031	0.048	0.056	0.050	0.033	0.196	0.674	0.953	0.999	0.201	0.600	0.950	0.203	0.680	0.202
	T_{Risk}	0.102	0.072	0.039	0.014	0.003	0.326	0.693	0.940	0.996	0.181	0.501	0.798	0.113	0.288	0.024
	T_{MO}	0.007	0.022	0.041	0.024	0.007	0.063	0.492	0.928	0.999	0.162	0.563	0.923	0.161	0.495	0.069
	T_{MC}	0.044	0.052	0.056	0.055	0.044	0.231	0.689	0.954	0.999	0.203	0.601	0.952	0.205	0.693	0.235
	T_{ML}	0.074	0.066	0.055	0.067	0.079	0.308	0.709	0.954	0.999	0.203	0.595	0.951	0.205	0.711	0.309
DBCD	T_{MW}	0.029	0.050	0.057	0.052	0.026	0.186	0.685	0.957	0.999	0.212	0.607	0.958	0.206	0.696	0.191
	T_{Risk}	0.120	0.085	0.041	0.008	0.001	0.361	0.721	0.954	0.998	0.204	0.524	0.811	0.109	0.257	0.010
	T_{MO}	0.004	0.017	0.045	0.017	0.003	0.041	0.462	0.933	0.999	0.169	0.587	0.934	0.164	0.475	0.042
	T_{MC}	0.037	0.056	0.058	0.056	0.034	0.211	0.696	0.958	0.999	0.215	0.607	0.959	0.208	0.706	0.215
	T_{ML}	0.077	0.074	0.059	0.073	0.077	0.311	0.718	0.958	0.999	0.217	0.607	0.959	0.210	0.727	0.315
SEU	T_{MW}	0.031	0.045	0.048	0.044	0.030	0.200	0.655	0.946	0.999	0.190	0.583	0.948	0.191	0.675	0.213
	T_{Risk}	0.067	0.048	0.033	0.016	0.006	0.259	0.646	0.922	0.991	0.154	0.486	0.812	0.114	0.342	0.046
	T_{MO}	0.013	0.026	0.039	0.027	0.011	0.094	0.522	0.921	0.999	0.158	0.553	0.926	0.157	0.533	0.095
	T_{MC}	0.046	0.051	0.049	0.050	0.046	0.248	0.675	0.949	0.999	0.195	0.585	0.950	0.195	0.698	0.258
	T_{ML}	0.062	0.055	0.047	0.055	0.062	0.285	0.683	0.947	0.999	0.190	0.577	0.949	0.193	0.710	0.305
GDL	T_{MW}	0.036	0.051	0.051	0.049	0.034	0.223	0.696	0.954	1.000	0.195	0.601	0.958	0.200	0.692	0.214
	T_{Risk}	0.075	0.060	0.040	0.010	0.001	0.309	0.703	0.949	0.999	0.184	0.543	0.868	0.124	0.304	0.015
	T_{MO}	0.007	0.022	0.046	0.023	0.006	0.077	0.549	0.937	0.999	0.167	0.588	0.945	0.169	0.547	0.077
	T_{MC}	0.048	0.057	0.051	0.055	0.047	0.260	0.708	0.955	1.000	0.198	0.602	0.960	0.204	0.705	0.253
	T_{ML}	0.074	0.064	0.052	0.063	0.076	0.319	0.721	0.956	1.000	0.200	0.602	0.960	0.205	0.720	0.314

Table 7. Power and type I error at R_{Risk} ($\alpha = 0.05, n = 30$). For each RAR methods, the results of the following 5 test statistics are shown: Agresti's correction to Wald-type Z test T_{MW} , log-relative-risk test T_{Risk} , Gart's correction to log-odds-ratio test T_{MO} , Cook's correction to Chi-square test T_{MC} , and Williams' correction log-likelihood-ratio test T_{ML} .

p_1		0.200	0.300	0.500	0.700	0.800	0.100	0.100	0.100	0.100	0.300	0.300	0.300	0.500	0.500	0.700
p_2		0.200	0.300	0.500	0.700	0.800	0.300	0.500	0.700	0.900	0.500	0.700	0.900	0.700	0.900	0.900
SMLE	T_{MW}	0.024	0.045	0.061	0.051	0.041	0.156	0.615	0.923	0.990	0.185	0.560	0.898	0.189	0.611	0.214
	T_{Risk}	0.136	0.105	0.078	0.061	0.050	0.363	0.716	0.945	0.997	0.230	0.588	0.923	0.206	0.612	0.210
	T_{MO}	0.002	0.008	0.032	0.039	0.040	0.022	0.278	0.792	0.988	0.096	0.466	0.903	0.157	0.615	0.220
	T_{MC}	0.033	0.047	0.060	0.064	0.068	0.177	0.615	0.923	0.996	0.183	0.570	0.939	0.202	0.701	0.316
	T_{ML}	0.069	0.071	0.061	0.049	0.051	0.278	0.659	0.921	0.975	0.195	0.543	0.883	0.179	0.621	0.253
DBCD	T_{MW}	0.018	0.046	0.072	0.054	0.042	0.134	0.617	0.931	0.993	0.198	0.565	0.896	0.199	0.586	0.207
	T_{Risk}	0.166	0.123	0.091	0.066	0.062	0.402	0.744	0.951	0.998	0.253	0.606	0.926	0.225	0.649	0.243
	T_{MO}	0.001	0.003	0.030	0.046	0.049	0.004	0.164	0.746	0.994	0.074	0.457	0.904	0.158	0.623	0.248
	T_{MC}	0.023	0.047	0.070	0.068	0.077	0.148	0.612	0.928	0.998	0.193	0.575	0.940	0.218	0.707	0.327
	T_{ML}	0.071	0.083	0.071	0.050	0.050	0.278	0.665	0.928	0.979	0.207	0.549	0.880	0.184	0.596	0.240
SEU	T_{MW}	0.026	0.039	0.045	0.043	0.032	0.172	0.598	0.903	0.988	0.178	0.537	0.888	0.183	0.606	0.198
	T_{Risk}	0.105	0.092	0.075	0.059	0.049	0.307	0.686	0.935	0.996	0.201	0.546	0.903	0.186	0.581	0.193
	T_{MO}	0.009	0.018	0.029	0.027	0.023	0.062	0.372	0.794	0.986	0.121	0.468	0.887	0.146	0.582	0.176
	T_{MC}	0.041	0.044	0.050	0.064	0.070	0.209	0.605	0.903	0.994	0.178	0.542	0.922	0.194	0.681	0.289
	T_{ML}	0.057	0.052	0.047	0.049	0.048	0.266	0.640	0.900	0.981	0.183	0.526	0.879	0.178	0.624	0.245
GDL	T_{MW}	0.023	0.043	0.059	0.047	0.038	0.168	0.617	0.929	0.993	0.182	0.558	0.902	0.196	0.580	0.195
	T_{Risk}	0.113	0.092	0.076	0.062	0.053	0.347	0.720	0.950	0.998	0.227	0.593	0.928	0.220	0.617	0.213
	T_{MO}	0.001	0.006	0.031	0.040	0.042	0.016	0.283	0.831	0.994	0.094	0.473	0.908	0.161	0.604	0.220
	T_{MC}	0.030	0.047	0.058	0.064	0.070	0.194	0.618	0.928	0.998	0.180	0.567	0.943	0.214	0.696	0.311
	T_{ML}	0.077	0.068	0.058	0.044	0.045	0.292	0.653	0.927	0.990	0.189	0.540	0.901	0.182	0.606	0.236

Table 8. Power and type I error at R_{Odds} ($\alpha = 0.05, n = 30$). For each RAR methods, the results of the following 5 test statistics are shown: Agresti's correction to Wald-type Z test T_{MW} , log-relative-risk test T_{Risk} , Gart's correction to log-odds-ratio test T_{MO} , Cook's correction to Chi-square test T_{MC} , and Williams' correction log-likelihood-ratio test T_{ML} .

p_1		0.200	0.300	0.500	0.700	0.800	0.100	0.100	0.100	0.100	0.300	0.300	0.300	0.500	0.500	0.700
p_2		0.200	0.300	0.500	0.700	0.800	0.300	0.500	0.700	0.900	0.500	0.700	0.900	0.700	0.900	0.900
SMLE	T_{MW}	0.030	0.040	0.042	0.040	0.031	0.202	0.630	0.935	0.998	0.178	0.562	0.939	0.174	0.637	0.205
	T_{Risk}	0.022	0.023	0.030	0.026	0.017	0.143	0.502	0.857	0.984	0.128	0.475	0.884	0.129	0.497	0.112
	T_{MO}	0.024	0.031	0.036	0.031	0.023	0.163	0.587	0.926	0.999	0.154	0.536	0.929	0.151	0.598	0.167
	T_{MC}	0.053	0.048	0.043	0.047	0.052	0.283	0.682	0.946	0.999	0.184	0.566	0.947	0.180	0.690	0.285
	T_{ML}	0.048	0.045	0.040	0.044	0.049	0.266	0.662	0.938	0.998	0.174	0.551	0.941	0.171	0.672	0.270
DBCD	T_{MW}	0.029	0.040	0.044	0.040	0.028	0.191	0.632	0.940	0.999	0.180	0.572	0.941	0.178	0.644	0.198
	T_{Risk}	0.011	0.018	0.032	0.026	0.018	0.085	0.448	0.864	0.994	0.120	0.490	0.906	0.141	0.547	0.134
	T_{MO}	0.026	0.033	0.042	0.031	0.024	0.178	0.609	0.934	0.999	0.165	0.555	0.933	0.161	0.619	0.185
	T_{MC}	0.052	0.046	0.045	0.046	0.048	0.280	0.688	0.948	0.999	0.185	0.573	0.949	0.181	0.696	0.284
	T_{ML}	0.040	0.043	0.043	0.043	0.038	0.244	0.667	0.945	0.999	0.178	0.565	0.944	0.174	0.680	0.252
SEU	T_{MW}	0.032	0.041	0.043	0.037	0.030	0.207	0.647	0.935	0.996	0.183	0.562	0.924	0.186	0.636	0.204
	T_{Risk}	0.047	0.040	0.035	0.032	0.028	0.214	0.605	0.903	0.993	0.152	0.503	0.894	0.140	0.528	0.146
	T_{MO}	0.014	0.026	0.032	0.023	0.020	0.127	0.540	0.900	0.995	0.148	0.520	0.914	0.150	0.587	0.159
	T_{MC}	0.049	0.047	0.043	0.047	0.052	0.268	0.676	0.938	0.998	0.187	0.564	0.945	0.191	0.695	0.284
	T_{ML}	0.059	0.049	0.042	0.044	0.049	0.285	0.677	0.935	0.995	0.182	0.551	0.922	0.183	0.665	0.268
GDL	T_{MW}	0.029	0.037	0.049	0.041	0.030	0.203	0.657	0.943	0.999	0.167	0.573	0.929	0.178	0.617	0.192
	T_{Risk}	0.024	0.032	0.046	0.035	0.031	0.183	0.625	0.936	0.999	0.158	0.560	0.922	0.165	0.583	0.166
	T_{MO}	0.013	0.026	0.043	0.034	0.033	0.124	0.587	0.930	0.999	0.150	0.552	0.928	0.161	0.619	0.204
	T_{MC}	0.051	0.047	0.050	0.050	0.058	0.281	0.700	0.948	0.999	0.177	0.579	0.949	0.187	0.695	0.298
	T_{ML}	0.050	0.047	0.046	0.039	0.043	0.282	0.700	0.947	0.999	0.176	0.563	0.933	0.169	0.652	0.258

Table 9. Power and type I error at R_{LLR} ($\alpha = 0.05, n = 30$). For each RAR methods, the results of the following 5 test statistics are shown: Agresti's correction to Wald-type Z test T_{MW} , log-relative-risk test T_{Risk} , Gart's correction to log-odds-ratio test T_{MO} , Cook's correction to Chi-square test T_{MC} , and Williams' correction log-likelihood-ratio test T_{ML} .

p_1		0.200	0.300	0.500	0.700	0.800	0.100	0.100	0.100	0.100	0.300	0.300	0.300	0.500	0.500	0.700
p_2		0.200	0.300	0.500	0.700	0.800	0.300	0.500	0.700	0.900	0.500	0.700	0.900	0.700	0.900	0.900
SMLE	T_{MW}	0.034	0.043	0.046	0.044	0.031	0.212	0.659	0.946	0.999	0.187	0.575	0.948	0.182	0.667	0.218
	T_{Risk}	0.039	0.034	0.033	0.022	0.008	0.203	0.597	0.911	0.995	0.146	0.490	0.869	0.124	0.432	0.072
	T_{MO}	0.018	0.029	0.040	0.031	0.017	0.129	0.577	0.931	0.999	0.162	0.549	0.934	0.156	0.587	0.133
	T_{MC}	0.052	0.050	0.046	0.052	0.051	0.274	0.692	0.951	0.999	0.192	0.578	0.953	0.185	0.700	0.278
	T_{ML}	0.060	0.050	0.044	0.051	0.057	0.289	0.691	0.948	0.999	0.186	0.567	0.950	0.181	0.698	0.289
DBCD	T_{MW}	0.036	0.047	0.050	0.045	0.031	0.223	0.688	0.957	0.999	0.192	0.591	0.956	0.192	0.697	0.225
	T_{Risk}	0.063	0.049	0.037	0.012	0.001	0.278	0.686	0.947	0.998	0.171	0.528	0.872	0.129	0.356	0.026
	T_{MO}	0.010	0.028	0.046	0.026	0.009	0.094	0.569	0.946	0.999	0.169	0.579	0.942	0.171	0.580	0.094
	T_{MC}	0.050	0.055	0.051	0.052	0.044	0.265	0.710	0.959	0.999	0.197	0.592	0.959	0.197	0.715	0.267
	T_{ML}	0.071	0.062	0.051	0.057	0.066	0.315	0.727	0.960	0.999	0.198	0.591	0.959	0.199	0.733	0.316
SEU	T_{MW}	0.034	0.043	0.046	0.043	0.033	0.215	0.665	0.947	0.999	0.187	0.581	0.947	0.186	0.671	0.214
	T_{Risk}	0.047	0.038	0.031	0.018	0.007	0.226	0.617	0.915	0.995	0.148	0.492	0.854	0.125	0.414	0.063
	T_{MO}	0.016	0.027	0.038	0.028	0.013	0.124	0.573	0.931	0.999	0.161	0.553	0.929	0.157	0.574	0.123
	T_{MC}	0.052	0.049	0.047	0.050	0.050	0.276	0.696	0.952	0.999	0.191	0.583	0.951	0.191	0.701	0.270
	T_{ML}	0.063	0.051	0.044	0.052	0.061	0.294	0.696	0.949	0.999	0.186	0.573	0.948	0.186	0.701	0.292
GDL	T_{MW}	0.033	0.037	0.043	0.038	0.032	0.230	0.670	0.950	1.000	0.178	0.585	0.956	0.177	0.675	0.215
	T_{Risk}	0.035	0.032	0.036	0.018	0.005	0.230	0.645	0.937	0.999	0.151	0.537	0.905	0.139	0.449	0.049
	T_{MO}	0.016	0.030	0.043	0.031	0.014	0.139	0.614	0.945	1.000	0.172	0.582	0.951	0.172	0.612	0.127
	T_{MC}	0.052	0.050	0.044	0.048	0.053	0.293	0.719	0.955	1.000	0.189	0.588	0.960	0.186	0.722	0.275
	T_{ML}	0.063	0.051	0.044	0.049	0.064	0.322	0.722	0.955	1.000	0.189	0.587	0.960	0.187	0.728	0.302

Table 10. Power and type I error at R_{RSIHR} ($\alpha = 0.05$, $n = 30$). For each RAR methods, the results of the following 5 test statistics are shown: Agresti's correction to Wald-type Z test T_{MW} , log-relative-risk test T_{Risk} , Gart's correction to log-odds-ratio test T_{MO} , Cook's correction to Chi-square test T_{MC} , and Williams' correction log-likelihood-ratio test T_{ML} .

p_1		0.200	0.300	0.500	0.700	0.800	0.100	0.100	0.100	0.100	0.300	0.300	0.300	0.500	0.500	0.700
p_2		0.200	0.300	0.500	0.700	0.800	0.300	0.500	0.700	0.900	0.500	0.700	0.900	0.700	0.900	0.900
SMLE	T_{MW}	0.028	0.045	0.056	0.048	0.035	0.174	0.648	0.944	0.999	0.192	0.588	0.946	0.202	0.678	0.228
	T_{Risk}	0.118	0.085	0.058	0.034	0.018	0.343	0.712	0.950	0.999	0.207	0.568	0.910	0.172	0.515	0.102
	T_{MO}	0.004	0.012	0.040	0.034	0.023	0.037	0.397	0.890	0.998	0.130	0.538	0.936	0.170	0.616	0.156
	T_{MC}	0.038	0.049	0.056	0.057	0.057	0.200	0.657	0.945	0.999	0.192	0.591	0.953	0.208	0.718	0.290
	T_{ML}	0.070	0.065	0.056	0.054	0.062	0.291	0.685	0.945	0.998	0.196	0.579	0.946	0.197	0.705	0.301
DBCD	T_{MW}	0.020	0.050	0.057	0.050	0.038	0.157	0.654	0.948	0.999	0.201	0.605	0.956	0.217	0.700	0.242
	T_{Risk}	0.138	0.103	0.062	0.030	0.013	0.383	0.732	0.953	0.999	0.227	0.594	0.922	0.186	0.534	0.097
	T_{MO}	0.001	0.007	0.038	0.034	0.020	0.017	0.323	0.887	0.999	0.123	0.554	0.942	0.185	0.628	0.159
	T_{MC}	0.028	0.056	0.057	0.057	0.060	0.183	0.662	0.948	0.999	0.202	0.607	0.959	0.221	0.733	0.304
	T_{ML}	0.074	0.079	0.057	0.052	0.064	0.293	0.693	0.948	0.999	0.208	0.593	0.954	0.207	0.726	0.317
SEU	T_{MW}	0.029	0.039	0.050	0.044	0.033	0.181	0.626	0.930	0.998	0.178	0.559	0.932	0.182	0.653	0.214
	T_{Risk}	0.095	0.070	0.044	0.024	0.010	0.275	0.650	0.926	0.996	0.163	0.512	0.875	0.137	0.449	0.071
	T_{MO}	0.014	0.021	0.037	0.028	0.016	0.075	0.466	0.892	0.997	0.137	0.521	0.921	0.152	0.574	0.128
	T_{MC}	0.044	0.045	0.050	0.053	0.049	0.225	0.642	0.932	0.998	0.181	0.562	0.945	0.189	0.696	0.271
	T_{ML}	0.058	0.053	0.050	0.052	0.062	0.268	0.657	0.929	0.997	0.178	0.548	0.934	0.179	0.684	0.289
GDL	T_{MW}	0.031	0.048	0.052	0.050	0.036	0.206	0.682	0.951	1.000	0.197	0.610	0.961	0.212	0.690	0.235
	T_{Risk}	0.084	0.065	0.050	0.026	0.009	0.321	0.715	0.952	1.000	0.201	0.591	0.919	0.173	0.495	0.076
	T_{MO}	0.002	0.016	0.042	0.034	0.017	0.047	0.476	0.923	1.000	0.147	0.577	0.947	0.186	0.613	0.142
	T_{MC}	0.040	0.052	0.052	0.056	0.053	0.228	0.689	0.952	1.000	0.198	0.611	0.964	0.216	0.721	0.289
	T_{ML}	0.074	0.062	0.051	0.055	0.063	0.301	0.707	0.952	1.000	0.199	0.602	0.962	0.207	0.722	0.316

Table 11. Power and type I error at R_{RPW} ($\alpha = 0.05$, $n = 30$). For each RAR methods, the results of the following 5 test statistics are shown: Agresti's correction to Wald-type Z test T_{MW} , log-relative-risk test T_{Risk} , Gart's correction to log-odds-ratio test T_{MO} , Cook's correction to Chi-square test T_{MC} , and Williams' correction log-likelihood-ratio test T_{ML} .

p_1		0.200	0.300	0.500	0.700	0.800	0.100	0.100	0.100	0.100	0.300	0.300	0.300	0.500	0.500	0.700
p_2		0.200	0.300	0.500	0.700	0.800	0.300	0.500	0.700	0.900	0.500	0.700	0.900	0.700	0.900	0.900
RPW	T_{MW}	0.031	0.039	0.050	0.050	0.042	0.191	0.631	0.918	0.966	0.166	0.538	0.859	0.183	0.585	0.204
	T_{Risk}	0.071	0.058	0.059	0.061	0.060	0.287	0.683	0.939	0.993	0.193	0.565	0.905	0.197	0.607	0.216
	T_{MO}	0.004	0.012	0.032	0.038	0.039	0.047	0.410	0.840	0.967	0.105	0.467	0.867	0.151	0.584	0.196
	T_{MC}	0.045	0.042	0.050	0.063	0.075	0.227	0.640	0.921	0.988	0.167	0.546	0.914	0.196	0.680	0.301
	T_{ML}	0.067	0.050	0.049	0.049	0.053	0.288	0.661	0.916	0.931	0.172	0.523	0.820	0.173	0.573	0.235
DL	T_{MW}	0.032	0.043	0.052	0.050	0.040	0.208	0.658	0.944	0.998	0.183	0.586	0.939	0.204	0.658	0.219
	T_{Risk}	0.057	0.051	0.055	0.048	0.032	0.273	0.679	0.947	0.998	0.192	0.588	0.935	0.199	0.612	0.164
	T_{MO}	0.003	0.013	0.038	0.041	0.033	0.047	0.464	0.906	0.998	0.123	0.527	0.934	0.172	0.641	0.193
	T_{MC}	0.043	0.045	0.052	0.062	0.064	0.237	0.662	0.944	0.999	0.184	0.592	0.956	0.216	0.723	0.307
	T_{ML}	0.058	0.050	0.050	0.049	0.056	0.275	0.672	0.943	0.998	0.183	0.567	0.940	0.188	0.688	0.283
SMLE	T_{MW}	0.027	0.040	0.048	0.049	0.044	0.188	0.626	0.921	0.968	0.167	0.537	0.848	0.175	0.550	0.195
	T_{Risk}	0.073	0.062	0.058	0.063	0.072	0.283	0.678	0.936	0.993	0.193	0.563	0.910	0.196	0.617	0.247
	T_{MO}	0.006	0.012	0.031	0.040	0.049	0.054	0.409	0.840	0.969	0.108	0.463	0.864	0.148	0.584	0.229
	T_{MC}	0.039	0.044	0.049	0.061	0.079	0.226	0.636	0.922	0.989	0.168	0.547	0.911	0.190	0.671	0.315
	T_{ML}	0.064	0.054	0.046	0.046	0.047	0.287	0.659	0.917	0.925	0.171	0.519	0.794	0.165	0.528	0.200
DBCD	T_{MW}	0.031	0.037	0.053	0.049	0.044	0.202	0.635	0.929	0.969	0.181	0.529	0.813	0.173	0.503	0.192
	T_{Risk}	0.063	0.054	0.065	0.072	0.081	0.290	0.685	0.942	0.994	0.202	0.572	0.911	0.209	0.640	0.285
	T_{MO}	0.003	0.010	0.033	0.043	0.054	0.041	0.407	0.866	0.981	0.110	0.460	0.856	0.146	0.573	0.257
	T_{MC}	0.041	0.040	0.054	0.067	0.083	0.236	0.640	0.930	0.990	0.181	0.543	0.905	0.195	0.660	0.325
	T_{ML}	0.061	0.048	0.052	0.042	0.036	0.289	0.661	0.925	0.857	0.183	0.511	0.696	0.160	0.407	0.144
SEU	T_{MW}	0.033	0.040	0.047	0.041	0.032	0.204	0.633	0.924	0.994	0.183	0.553	0.908	0.185	0.618	0.199
	T_{Risk}	0.076	0.059	0.058	0.048	0.043	0.278	0.664	0.929	0.996	0.183	0.529	0.899	0.170	0.564	0.182
	T_{MO}	0.012	0.021	0.028	0.027	0.024	0.100	0.467	0.855	0.993	0.130	0.493	0.900	0.143	0.578	0.169
	T_{MC}	0.051	0.047	0.050	0.059	0.065	0.251	0.652	0.925	0.997	0.186	0.556	0.933	0.197	0.686	0.286
	T_{ML}	0.062	0.051	0.048	0.047	0.049	0.293	0.671	0.923	0.992	0.185	0.541	0.904	0.183	0.642	0.251
GDL	T_{MW}	0.032	0.045	0.049	0.045	0.032	0.216	0.658	0.937	0.998	0.171	0.576	0.916	0.192	0.602	0.196
	T_{Risk}	0.056	0.053	0.053	0.050	0.042	0.281	0.681	0.942	0.998	0.180	0.586	0.927	0.196	0.615	0.197
	T_{MO}	0.004	0.017	0.036	0.040	0.037	0.066	0.480	0.900	0.998	0.122	0.525	0.918	0.165	0.622	0.219
	T_{MC}	0.044	0.049	0.050	0.058	0.061	0.250	0.666	0.939	0.999	0.173	0.584	0.948	0.206	0.700	0.314
	T_{ML}	0.061	0.054	0.047	0.044	0.043	0.294	0.681	0.937	0.998	0.175	0.560	0.920	0.179	0.639	0.256

Table 12. The mean and standard deviation (in parenthesis) of type I error and power calculated by averaging simulation results over the 5 null cases and the 10 alternative cases of simulation scenarios. All results have been multiplied by 100% ($\alpha = 0.05, n = 30$).

		Type I error						Power					
		T_{MW}	T_{RISK}	T_{MO}	T_{MC}	T_{ML}	Row Mean	T_{MW}	T_{RISK}	T_{MO}	T_{MC}	T_{ML}	Row Mean
R_{Wald}	<i>SMLE</i>	4.4(1.1)	4.6(4.1)	2.0(1.4)	5.0(0.6)	6.8(0.9)	4.6(2.4)	56.6(34.1)	48.6(35.2)	48.5(36.8)	57.6(33.4)	59.4(31.9)	54.2(33.2)
	<i>DBCD</i>	4.3(1.4)	5.1(5.1)	1.7(1.7)	4.8(1.2)	7.2(0.8)	4.6(2.9)	56.9(34.4)	49.5(35.9)	48.0(37.6)	57.7(33.9)	60.2(31.8)	54.5(33.7)
	<i>SEU</i>	4.0(0.9)	3.4(2.4)	2.3(1.2)	4.8(0.2)	5.6(0.6)	4.0(1.7)	56.0(34.0)	47.7(34.8)	49.6(36.1)	57.5(33.0)	58.4(32.3)	53.8(32.9)
	<i>GDL</i>	4.4(0.8)	3.7(3.1)	2.1(1.6)	5.2(0.4)	6.6(1.0)	4.4(2.2)	57.3(34.0)	50.0(36.2)	50.6(36.9)	58.4(33.2)	60.0(32.0)	55.3(33.3)
	Mean	4.3(1.0)	4.2(3.6)	2.0(1.4)	5.0(0.7)	6.5(1.0)	4.4(2.3)	56.7(32.8)	49.0(34.2)	49.2(35.4)	57.8(32.1)	59.5(30.7)	54.4(33.0)
R_{Risk}	<i>SMLE</i>	4.4(1.4)	8.6(3.5)	2.4(1.8)	5.5(1.4)	6.0(1.0)	5.4(2.8)	53.4(33.2)	57.9(31.5)	45.4(35.2)	56.2(32.7)	55.1(31.1)	53.6(31.7)
	<i>DBCD</i>	4.6(2.0)	10.2(4.4)	2.6(2.3)	5.7(2.2)	6.5(1.4)	5.9(3.5)	53.3(33.4)	60.0(30.5)	43.7(36.0)	56.5(32.9)	55.0(31.1)	53.7(31.9)
	<i>SEU</i>	3.7(0.8)	7.6(2.3)	2.1(0.8)	5.4(1.3)	5.1(0.4)	4.8(2.2)	52.5(32.8)	55.3(32.2)	45.9(34.1)	55.2(32.1)	54.2(31.2)	52.6(31.3)
	<i>GDL</i>	4.2(1.3)	7.9(2.4)	2.4(1.9)	5.4(1.6)	5.8(1.4)	5.1(2.5)	53.2(33.3)	58.1(31.6)	45.8(35.8)	56.5(32.6)	55.2(31.7)	53.8(31.9)
	Mean	4.2(1.3)	8.6(3.1)	2.4(1.7)	5.5(1.5)	5.9(1.2)	5.3(2.8)	53.1(31.9)	57.8(30.3)	45.2(33.9)	56.1(31.3)	54.9(30.1)	53.4(31.5)
R_{Odds}	<i>SMLE</i>	3.7(0.6)	2.4(0.5)	2.9(0.5)	4.8(0.4)	4.5(0.4)	3.7(1.0)	54.6(33.9)	47.1(34.3)	52.1(34.9)	57.6(32.6)	56.4(32.9)	53.6(32.5)
	<i>DBCD</i>	3.6(0.7)	2.1(0.8)	3.1(0.7)	4.7(0.3)	4.1(0.2)	3.5(1.1)	54.8(34.2)	47.3(35.2)	53.4(34.5)	57.8(32.7)	56.5(33.4)	53.9(32.8)
	<i>SEU</i>	3.6(0.5)	3.6(0.8)	2.3(0.7)	4.7(0.3)	4.9(0.7)	3.8(1.1)	54.8(33.5)	50.8(33.8)	50.4(34.8)	57.5(32.5)	56.6(32.2)	54.0(32.1)
	<i>GDL</i>	3.7(0.8)	3.4(0.8)	3.0(1.1)	5.1(0.4)	4.5(0.4)	3.9(1.0)	54.6(34.2)	53.0(34.6)	52.5(35.0)	58.1(32.7)	56.8(33.0)	55.0(32.5)
	Mean	3.7(0.6)	2.9(0.9)	2.8(0.8)	4.9(0.4)	4.5(0.5)	3.7(1.1)	54.7(32.6)	49.5(33.2)	52.1(33.4)	57.8(31.4)	56.6(31.6)	54.1(32.3)
R_{LLR}	<i>SMLE</i>	4.0(0.6)	2.7(1.2)	2.7(1.0)	5.0(0.2)	5.2(0.6)	3.9(1.3)	55.9(33.9)	48.4(35.0)	51.6(35.6)	58.0(32.8)	58.0(32.6)	54.4(32.8)
	<i>DBCD</i>	4.2(0.8)	3.3(2.6)	2.4(1.5)	5.0(0.4)	6.1(0.8)	4.2(1.9)	57.2(34.0)	49.9(35.9)	51.4(36.6)	58.6(33.1)	60.0(32.2)	55.4(33.2)
	<i>SEU</i>	4.0(0.6)	2.8(1.6)	2.4(1.0)	4.9(0.2)	5.4(0.8)	3.9(1.5)	56.1(33.9)	48.5(34.8)	51.2(35.7)	58.1(32.8)	58.2(32.5)	54.4(32.8)
	<i>GDL</i>	3.7(0.5)	2.5(1.3)	2.7(1.2)	4.9(0.4)	5.4(0.9)	3.8(1.5)	56.4(34.1)	50.4(35.8)	53.1(35.9)	58.9(33.1)	59.5(32.5)	55.7(33.1)
	Mean	3.9(0.6)	2.8(1.6)	2.5(1.1)	5.0(0.3)	5.6(0.8)	4.0(1.5)	56.4(32.6)	49.3(34.0)	51.8(34.6)	58.4(31.7)	58.9(31.2)	55.0(32.7)
R_{RSIHR}	<i>SMLE</i>	4.2(1.1)	6.2(4.0)	2.3(1.5)	5.2(0.8)	6.1(0.7)	4.8(2.4)	56.0(33.9)	54.8(33.7)	48.7(36.4)	57.5(33.2)	58.4(32.0)	55.1(32.6)
	<i>DBCD</i>	4.3(1.5)	6.9(5.2)	2.0(1.6)	5.2(1.3)	6.5(1.1)	5.0(3.0)	56.8(34.0)	56.3(33.4)	48.2(37.0)	58.2(33.2)	59.4(31.8)	55.7(32.8)
	<i>SEU</i>	3.9(0.8)	4.8(3.4)	2.3(1.0)	4.8(0.4)	5.5(0.5)	4.3(1.9)	54.5(33.8)	50.5(34.5)	48.6(35.8)	56.4(33.0)	56.6(32.4)	53.3(32.7)
	<i>GDL</i>	4.3(0.9)	4.7(3.0)	2.2(1.6)	5.1(0.6)	6.1(0.9)	4.5(2.0)	57.4(33.7)	54.4(34.5)	50.6(36.6)	58.7(33.0)	59.7(32.1)	56.2(32.8)
	Mean	4.2(1.0)	5.7(3.8)	2.2(1.3)	5.1(0.8)	6.1(0.8)	4.6(2.3)	56.2(32.6)	54.0(32.8)	49.0(35.0)	57.7(31.8)	58.5(30.8)	55.1(32.5)
R_{RPW}	<i>RPW</i>	4.2(0.8)	6.2(0.5)	2.5(1.6)	5.5(1.4)	5.4(0.8)	4.8(1.7)	52.4(32.3)	55.9(32.1)	46.3(34.1)	55.8(32.1)	52.9(30.1)	52.7(31.0)
	<i>DL</i>	4.3(0.8)	4.8(1.0)	2.6(1.7)	5.3(0.9)	5.3(0.4)	4.5(1.4)	56.0(33.5)	55.9(33.4)	50.0(36.1)	58.2(32.6)	57.4(32.5)	55.5(32.4)
	<i>SMLE</i>	4.2(0.9)	6.5(0.6)	2.8(1.8)	5.4(1.6)	5.1(0.8)	4.8(1.7)	51.7(32.3)	56.2(31.8)	46.7(33.7)	55.7(31.9)	51.7(30.2)	52.4(30.9)
	<i>DBCD</i>	4.3(0.9)	6.7(1.0)	2.9(2.1)	5.7(1.8)	4.8(1.0)	4.9(1.9)	51.2(31.8)	57.3(31.2)	47.0(34.1)	56.0(31.5)	48.3(29.2)	52.0(30.6)
	<i>SEU</i>	3.8(0.6)	5.7(1.3)	2.2(0.6)	5.4(0.8)	5.1(0.6)	4.5(1.5)	54.0(33.1)	54.0(32.7)	48.3(34.4)	56.7(32.1)	55.9(31.7)	53.8(31.6)
	<i>GDL</i>	4.0(0.8)	5.1(0.6)	2.7(1.6)	5.2(0.7)	5.0(0.8)	4.4(1.3)	54.6(33.5)	56.0(33.0)	50.2(35.3)	57.8(32.4)	56.4(32.3)	55.0(32.0)
	Mean	4.1(0.8)	5.8(1.1)	2.6(1.5)	5.4(1.2)	5.1(0.7)	4.6(1.6)	53.3(31.4)	55.9(31.0)	48.1(33.2)	56.7(30.7)	53.8(29.8)	53.5(31.2)
Equal Allocation		4.0(0.5)	2.9(1.7)	2.4(1.0)	5.0(0.2)	5.6(0.8)	4.0(1.5)	56.2(33.9)	48.5(35.0)	50.9(35.9)	58.1(32.9)	58.4(32.4)	54.4(32.9)

Applying E_{max} model and interaction index for assessing drug interaction in combination studies

J. Jack Lee¹, Heather Y. Lin¹, Diane D. Liu¹, and Maiying Kong²

¹Department of Biostatistics, University of Texas, M. D. Anderson Cancer Center, Unit 1411, 1515 Holcombe Boulevard, Houston, Texas 77030, U.S.A.

²Department of Bioinformatics and Biostatistics, School of Public Health and Information Sciences, University of Louisville, Louisville, Kentucky 40292, U.S.A.

TABLE OF CONTENTS

1. Abstract
2. Introduction
3. Material and Method
 - 3.1 Data Sets
 - 3.2 Statistical Methods
 - 3.2.1: E_{max} Model
 - 3.2.2: Interaction Index under the E_{max} Model
 - 3.2.3: Confidence Interval for the Interaction Index
 - 3.3 Data Analysis Plan
4. Exploratory Data Analysis
5. Data Preprocessing: Outlier Rejection and Data Standardization
 - 5.1 Outlier Rejection
 - 5.2 Data Standardization
6. Results
 - 6.1 Results for the Low Folic Acid Experiment
 - 6.2 Results for the High Folic Acid Experiment
7. Summary
8. Discussion
9. Acknowledgement
10. References

1. ABSTRACT

Applying the E_{max} model in the context of the Loewe additivity model, we analyze the data from the combination drug study of trimetrexate (TMQ) and AG2034 (AG) in low and high folic acid (FA) media. The E_{max} model provides a sufficient fit to the data. TMQ is more potent than AG in both Low FA and High FA experiments. At low TMQ:AG ratios when a smaller amount of the more potent drug (TMQ) is added to a larger amount of the less potent drug (AG), it results in synergy. However, when the TMQ:AG ratio reaches 0.4 or larger in the low FA medium, or when the TMQ:AG ratio reaches 1 or larger in the high FA medium, synergy tends to be weakened and the mode of drug interaction becomes additive. In general, synergistic effect is stronger at higher doses which produce stronger effects (effect closer to $1-E_{max}$) than at the lower dose levels which produce weaker effects (effect closer to 1) in the same dilution series. The two drugs are more potent in the low FA medium compared to the high FA medium. The drug synergy, however, is stronger in the high FA medium.

2. INTRODUCTION

Due to complex disease pathways, combination treatments can be more effective and less toxic than treatments with a single regimen. Successful applications of combination therapy have improved the effectiveness in treating many diseases. For example, the combination of a non-nucleoside reverse transcriptase inhibitor or protease inhibitor with two nucleosides is considered a standard front-line therapy in AIDS. Typically, a combination of three to four drugs is required to provide durable response and immune reconstitution (1). Another example is that platinum-based doublet chemotherapy regimens are now considered to be the standard of care in patients with advanced stage non-small cell lung cancer (2). Combination treatments have also been shown to prevent and to overcome drug resistance in infectious diseases such as malaria, and in complex diseases such as cancer (3, 4). The advent of the development of targeted agents has also spurred much development in seeking effective therapies for cancer by combining multiple targeted agents with or without chemotherapy, or combining multiple treatment modalities such as the combination of drug treatment, surgery, and/or radiation therapy (5, 6).

“How does one assess the effect of a combination therapy?” It is a simple question. Yet, the complexity of the answer increases as one analyzes it further. This first answer may be that if a combination therapy shows an effect that is greater than the effect produced by each single component given alone, the combination therapy is working. The notion of classifying drug interaction as additive, synergistic, or antagonistic is logical and easily understandable in a general sense, but can be confusing without a specific and agreeable definition. Excellent reviews of drug synergisms can be found in Berenbaum (7), Greco et al. (8), Suhnel (9), Chou (10), and Tallarida (11), to name a few. In essence, to quantify the effect of combination therapy, one must first define what “additivity” is. If the combination effect is more (or less) than the additive effect of the single agents, then it is considered synergistic (or antagonistic), accordingly. Furthermore, due to the stochastic error in producing the effect in all experiments, drug interaction should also be assessed in a statistical sense. A more rigorous definition requires synergy to be defined only when the combined drug effect is statistically significantly higher than the additive effect. Conversely, antagonism is observed when the combination effect is statistically lower than the additive effect.

Despite controversies and multiple definitions of additivity or no drug interaction, the Loewe additivity model is commonly accepted as the gold standard for quantifying drug interaction (7-11). The Loewe additivity model is defined as:

$$\frac{d_1}{D_{y,1}} + \frac{d_2}{D_{y,2}} = 1. \quad (E 1)$$

Here y is the predicted additive effect at the combination dose (d_1, d_2) when the two drugs do not interact. $D_{y,1}$ and $D_{y,2}$ are the respective doses of drug 1 and drug 2 required to produce the same effect y when used alone. Note that the Loewe additivity can be easily demonstrated in a “sham combination” (i.e., a drug is combined with itself or its diluted form). For example, suppose drug 2 is a 50% diluted form of drug 1. The combination of one unit of drug 1 and one unit of drug 2 will produce the same effect as 1.5 units of drug 1 or 3 units of drug 2. Plugging the respective values in equation (E 1), we have $1/1.5 + 1/3 = 1$. Given the dose-effect relationship for each single agent, say $E_i(d) = f_i(d)$ for agent i ($i=1,2$), $D_{y,i}$ can be obtained by using the inverse function of f_i , say, $f_i^{-1}(y)$. Replacing $D_{y,1}$ and $D_{y,2}$ in equation (E 1) with $f_1^{-1}(y)$ and $f_2^{-1}(y)$, respectively, we can rewrite equation (E 1) as

$$\frac{d_1}{f_1^{-1}(y)} + \frac{d_2}{f_2^{-1}(y)} = 1. \quad (E 2)$$

Note that (E 2) involves an unknown variable y . By solving equation (E 2), the predicted additive effect y_{add} can be obtained under the Loewe additivity model. Denote that the observed mean effect is y_{obs} at the combination dose (d_1, d_2). The drug combination at that dose is considered synergistic, additive, or antagonistic when the effect y_{obs} is greater than, equal to, or less than y_{add} , respectively. When the dose-effect curve is decreasing (or increasing), a synergistic effect corresponds to a smaller (or larger) value than the predicted quantity.

Alternatively, to measure and quantify the magnitude of drug interaction, the interaction index (II) can be defined as:

$$II = \frac{d_1}{D_{y_{obs},1}} + \frac{d_2}{D_{y_{obs},2}} \quad (E 3)$$

Note that $II < 1$, $II = 1$, and $II > 1$ correspond to the drug interaction being synergistic, additive, and antagonistic, respectively. Chou and Talalay’s (12) proposed the median effect equation (E 4) to characterize the dose-effect relationship in combination studies:

$$E(d) = \frac{(d / ED_{50})^m}{1 + (d / ED_{50})^m}, \quad (E 4)$$

where ED_{50} is the dose required to produce 50% of the maximum effect. Although the median effect equation can be applied in many settings, it assumes that, when m is positive, $E(d)=0$ for $d=0$ and $E(d)=1$ for $d=\infty$, respectively. On the other hand, when m is negative, $E(d)=1$ for $d=0$ and $E(d)=0$ for $d=\infty$, respectively. If we assume that the data follow the median effect equation, a linear relationship can be found by plotting the logit transformation of the effect versus the logarithm transformed dose. A more detailed account of the interpretation and use of the interaction index can be found in a number of references (13-16). Several methods for constructing the confidence interval estimation of the interaction index were proposed in Lee and Kong (17).

To help advance the research for developing and comparing methods for analyzing data for combination studies, Dr. William R. Greco at the Roswell Park Cancer Institute has organized an effort and invited several groups to participate in an exercise to compare rival modern approaches to model data from two-agent concentration-effect studies. We describe the data and the statistical methods including the E_{max} model and the calculation of the interaction index under the E_{max} model in Section 3. Exploratory data analysis is shown in Section 4. Data preprocessing for outlier rejection and standardization are described in Section 5. The main result of the data analysis is presented in Section 6 with a summary given in Section 7. Discussion is provided in Section 8.

3. MATERIAL AND METHOD

3.1 Data Sets

Two data sets provided by Dr. Greco are used to examine the effect of the combination treatment of trimetrexate (TMQ) and AG2034 (AG) in HCT-8 human ileocecal adenocarcinoma cells. The cells were grown in medium with two levels of folic acid: 2.3 μ M (the first data set, called Low FA) and 78 μ M (the second data set, called High FA). Trimetrexate is a lipophilic inhibitor of the enzyme, dihydrofolate reductase; and AG2034 is an inhibitor of the enzyme, glycinamide ribonucleotide formyltransferase. The experiment was conducted on 96-well plates. The endpoint was the cell growth measured by an absorbance measurement (ranges from 0 to 2), recorded in an automated 96-well plate reader. Each 96-well plate included 8 wells as instrumental blanks (no cells) and the remaining 88 wells were used for drug treatments. The experiments were performed using the “ray design,” which maintains a fixed dose ratio between TMQ and AG in a serial of 11 dose dilutions. With 88 wells in each plate, each 5-plate stack studied the combination doses at 7 curves (i.e., design rays) plus a “curve” with all controls. Two stacks were used for studying 14 design rays and they are: TMQ only, AG only, and twelve other design rays with a fixed dose ratio (TMQ:AG) for each ray. The fixed dose ratios in the Low FA experiment are: 1:250, 1:125, 1:50, 1:20, 1:10, 1:5 (2 sets), 2:5, 4:5, 2:1, 5:1, and 10:1. Similarly, the fixed dose ratios in the High FA experiment are: 1:2500, 1:1250, 1:500, 1:200, 1:100, 1:50 (2 sets), 1:25, 2:25, 1:5, 1:2, and 1:1. Data from each of the 16 curves (2 for controls, 2 for single agents, and 12 for combinations) are grouped together. Curves 1-8 were performed on the first stack with Curve 8 serving as the “control” experiment while Curve 9-16 were performed on the second stack with Curve 16 serving as the “control” experiment. Treatments of cells in wells by different drug combinations were randomized across the plates. Five replicate plates were used for each set of two stacks. Therefore, a total of 10 plates were used for each of the two medium conditions (Low FA and High FA). The maximum number of treated wells per medium condition is 880 (16 curves x 11 dilutions x 5 replicates). Complete experimental details and mechanistic implications were reported in Faessel et al. (18).

3.2 Statistical Methods

3.2.1: E_{max} model

Due to the fact that the measure of cell growth plateaus and does not reach zero at the maximum dose levels used in the experiments, the median effect equation (E 4) does not fit the data. Instead, we take the E_{max} model (19) to fit the data at hand.

$$E(d) = E_0 - E_{max} + \frac{E_{max}}{1 + (d / ED_{50})^m}, \quad (E 5)$$

where E_0 is the base effect, corresponding to the measurement of the cell growth when no drug is applied; E_{max} is the maximum effect attributable to the drug; ED_{50} is the dose level producing half of E_{max} ; d is the dose level, which produces the effect $E(d)$, and m is a slope factor (Hill coefficient), measuring the sensitivity of the effect within a dose range of the drug. Thus, $E_0 - E_{max}$ is the asymptotic effect when a very large dose of the drug is applied. Figure 1 shows a few examples of the E_{max} model where E_0 is assumed to be 1. The parameter m governs how quickly the curve drops. For the three cases in the first row in Figure 1, ED_{50} is fixed at 2 and E_{max} is at 0.8, while the slope varies. When $m=1$ (Panel A), the dose response curve drops slowly; when $m=5$ (Panels B and E), a sigmoid shape curve is formed, and when $m=20$ (Panels C and F), the drop of the sigmoid curve becomes very steep. In the three curves in the first row, as the dose increases, the curves drop, and the effect asymptotes to $1 - E_{max} = 0.2$. In the second row, the three plots are set at $E_{max} = 1$, which means that as the dose increases, the treatment will reach the theoretical full effect. For example, if the effect measure is cell count, all the cells will be killed at very high doses of the

treatment when $E_{max} = 1$. The figures also show that, as ED_{50} increases, the curves are shifted to the right indicating that the treatment is less potent. In all cases when m increases, the effect drops more rapidly. We apply the non-linear weighted least squares method to estimate the parameters in the E_{max} model. Due to the heteroscedascity observed in the data, that the variance increases as the observed response increases, we use the reciprocal of the fitted response as the weight function (20). Estimation is carried out using S-PLUS, R (21), and SAS (22).

3.2.2: Interaction Index under the E_{max} Model

Similarly to using the median effect model, the E_{max} model can be applied to fit the single-drug and combination dose response curves, and then, the interaction index can be calculated accordingly. Although equation (E 5) allows different values of E_0 and E_{max} for different curves, for calculating the interaction index, we need to assume all curves have the same E_0 so that the "base measure" of no drug effect is the same in all curves. This can be achieved by dividing all effect measures with the mean of the controls. Note that E_{max} can remain different in different curves to signify different drug potencies. However, the calculation of the interaction index will be a little more complicated when different drugs or combinations produce different E_{max} 's as will be shown later.

From this point on, we assume the dose response curve follows the following E_{max} model

$$E(d) = 1 - E_{max} + \frac{E_{max}}{1 + (d / ED_{50})^m}. \quad (E 6)$$

Our experiments study the effect of treatments in inhibiting cell growth. The effect measure is cell growth corresponding to the amount of cells observed. Hence, the height of the dose effect curve decreases when the dose increases. In this case, we have $m > 0$. In addition, as d goes to infinity, the effect plateaus at $1 - E_{max}$. Hence, E_{max} must be between 0 and 1.

In the study of two drug combinations, we need to fit three curves using the E_{max} model: curve 1 for drug 1 alone, curve 2 for drug 2 along, and curve c for drug combinations. Denote $E_{max, i}$, $ED_{50, i}$, and m_i as the three parameters for drug i ($i=1,2, c$). Given an effect e ($e > 1 - E_{max}$), the corresponding dose $d(e)$ can be calculated as

$$d(e) = ED_{50} \left(\frac{1 - e}{e - 1 + E_{max}} \right)^{1/m} \quad (E 7)$$

Note that the dose for the combination treatment can be obtained simply as the sum of the doses of the single agents. This approach works well for the ray design with constant or varying relative potency between the two drugs (12, 17). Without loss of generality, we can assume that $E_{max, 1} > E_{max, 2}$. In addition, we assume that the dose ratio for the two drugs in the combination treatment ($d_c = d_1 + d_2$) is fixed with $d_1 / d_2 = p$. Upon fitting the three dose response curves, the interaction index at a fixed effect e where $e \in (1 - \hat{E}_{max, c}, 1)$ can be calculated as the following:

$$\hat{II} = \frac{\hat{d}_c(e) \times p / (1 + p)}{\hat{D}_{y,1}(e)} + \frac{\hat{d}_c(e) / (1 + p)}{\hat{D}_{y,2}(e)} \text{ for } 1 - \hat{E}_{max, 2} < e < 1, \text{ and} \quad (E 8)$$

$$\hat{II} = \frac{\hat{d}_c(e) \times p / (1 + p)}{\hat{D}_{y,1}(e)} \text{ for } 1 - \hat{E}_{max, 1} < e \leq 1 - \hat{E}_{max, 2}.$$

For $e \leq 1 - \hat{E}_{max, 1}$, the interaction index cannot be calculated. However, the combination effect in this range is more than additive because it reaches to the effect level that no single agent alone can achieve. If $E_{max, 1} = E_{max, 2}$, the interaction index can be calculated using the first formula in (E 8).

3.2.3: Confidence Interval for the Interaction Index

We can apply the delta method to calculate the (large sample) variance of the interaction index (23). From our previous work (17), we found that better estimation of the confidence interval for the interaction index can be achieved by working on the

logarithmic transformation of the interaction index.

By applying the delta method, $Var(\log(\hat{\Pi})) = \frac{1}{\hat{\Pi}^2} Var(\hat{\Pi})$.

When $1 - \hat{E}_{max,2} < e < 1$, the variance of $\hat{\Pi}$ can be calculated by

$$Var(\hat{\Pi}) = \left(\frac{\hat{d}_c(e) \times p / (1+p)}{\hat{D}_{y,1}(e)} \right)^2 V_1 + \left(\frac{\hat{d}_c(e) / (1+p)}{\hat{D}_{y,2}(e)} \right)^2 V_2 + \left(\frac{\hat{d}_c(e) \times p / (1+p)}{\hat{D}_{y,1}(e)} + \frac{\hat{d}_c(e) / (1+p)}{\hat{D}_{y,2}(e)} \right)^2 V_c; \quad (E 9)$$

if $1 - \hat{E}_{max,1} < e \leq 1 - \hat{E}_{max,2}$, then

$$Var(\hat{\Pi}) = \left(\frac{\hat{d}_c(e) \times p / (1+p)}{\hat{D}_{y,1}(e)} \right)^2 V_1 + \left(\frac{\hat{d}_c(e) \times p / (1+p)}{\hat{D}_{y,1}(e)} \right)^2 V_c. \quad (E 10)$$

where

$$V_i = \begin{pmatrix} \frac{-1}{\hat{m}_i(e-1+\hat{E}_{max,i})} & \frac{1}{\hat{ED}_{50,i}} & -\frac{1}{\hat{m}_i^2} \log \frac{1-e}{e-1+\hat{E}_{max,i}} \end{pmatrix} Var \left(\hat{E}_{max,i}, \hat{ED}_{50,i}, \hat{m}_i \right) \begin{pmatrix} \frac{-1}{\hat{m}_i(e-1+\hat{E}_{max,i})} \\ \frac{1}{\hat{ED}_{50,i}} \\ -\frac{1}{\hat{m}_i^2} \log \frac{1-e}{e-1+\hat{E}_{max,i}} \end{pmatrix}$$

for $i=1, 2, c$.

Upon the calculation of the variance for $\log(\hat{\Pi})$, the point-wise $(1-\alpha)100\%$ confidence interval for Π for a specified effect can be constructed as

$$\left(\hat{\Pi} \exp(-z_{\alpha/2} \sqrt{Var(\log(\hat{\Pi}))}), \hat{\Pi} \exp(z_{\alpha/2} \sqrt{Var(\log(\hat{\Pi}))}) \right), \quad (E 11)$$

where $z_{\alpha/2}$ is the upper $\alpha/2$ upper percentile of the standard normal distribution. We also construct the simultaneous confidence band for the interaction index over the range of estimated responses. Because the estimation process involves estimating nine parameters from three curves, to construct a Scheffé type of simultaneous confidence band, we simply replace $z_{\alpha/2}$ in equation (E 11) by $(\chi_p^2(\alpha))^{1/2}$ where $p=9$ (24).

3.3 Data Analysis Plan

The overall objective of the data analysis is to assess synergistic effect of the combination of TMQ and AG in both low and high FA media. We apply the exploratory data analysis first followed by estimating the dose-response relationship using the E_{max} model. The drug interaction is evaluated by calculating the interaction index under the Loewe additivity model. Exploratory data analysis is performed to understand the data structure, patterns, and to determine whether preprocessing of the data in terms of outlier rejection and standardization is required before the data modeling. The Low FA and High FA experiments are analyzed separately then compared. For each experiment, the E_{max} model is applied to fit the two marginal and twelve combination dose response curves. The interaction index and its 95% confidence intervals are computed for each of the twelve combinations. The overall pattern of the drug interaction is assessed by examining the interaction index from the 12 fixed-ratio combinations together. A one-dimensional distribution plot via the BLiP plot (25) is applied to display the data. A two-dimensional scatter plot, a contour plot, and an image plot as well as a three-dimensional perspective plot are used to show the dose response relationship. A Trellis plot (26) is also applied to assemble the individual plots together into consecutive panels conditioning on different values of fixed dose ratios.

4. EXPLORATORY DATA ANALYSIS

As in all data analyses, we begin with exploratory data analysis. For the Low and High FA experiments, there are 871 and 879 readings, respectively. Only 9 and 1 observations are missing out of the maximum of 880 readings in each experiment, respectively. The data also comes with designated curve numbers ranging from 1 to 16 and data point numbers ranging from 1 to 176. Each curve number indicates a specific dose combination. We re-label the curves as A-P where A and B correspond to the control (no drug) curves; C and D correspond to the TMQ and AG alone curves, and curves E through P correspond to the combination curves with fixed dose ratios in ascending order. Each point number indicates the readings at each specific dilution of each curve. Since five duplicated experiments were performed, there are up to five readings for each specific point number. There is, however, no designation of the plate number in the data received. Figure 2 shows the variable percentile plot of the distribution of the effect from the Low FA and High FA experiments using the BLiP plot with each segment corresponding to a

five percent increment (25). The plot gives an overall assessment on the distribution of the outcome variable of cell growth without conditioning on experimental settings. The middle 20% of the data (40th to 60th percentiles) are shaded in a light orange color. This figure indicates that the data have a bimodal distribution with most data cluttered either around a low value of 0.2 or at a high value of 1.2. For the Low FA experiment, the distribution of the effect ranges from 0.072 to 1.506 with the lower, middle, and upper quartiles being 0.149, 0.449, and 1.150, respectively. Similarly, for the High FA experiments, the effect range is between 0.070 and 1.545. The three quartiles are 0.213, 0.990, and 1.1495, respectively. The median of Low FA data is smaller than the median of the High FA data. The bimodal distributions could result from steep dose response curves. As a consequence, the slope may not be able to be estimated well in certain cases.

To help understand the pattern of the fixed ratio dose assignment in a ray design and the relationship between the fixed ratio doses and curve number, we plot the logarithm transformed dose of TMQ and AG in Figure 3 for both the Low FA and High FA experiments. As can be seen, Curves A and B are the controls with no drugs. Curves C and D correspond to the single drug study of TMQ and AG, respectively. Curves E through P are the various fixed ratio combination doses of TMQ and AG. Note that Curves J and K have the same dose ratios. Within each curve, the 11 dilutions are marked by 11 circles. For the combination studies, the curves for different dose ratios are parallel to each other on the log dose scale. If the same plot is shown in the original scale, these lines will form “rays,” radiating out from the origin like sun rays. Hence, the term “ray design” is used to describe this type of experiment. The corresponding dose ranges used for each drug alone are: 5.47×10^{-6} to $0.56 \mu\text{M}$ for TMQ in both the Low FA and High FA experiments, and 2.71×10^{-5} to $2.78 \mu\text{M}$ for AG2034 in the Low FA experiment and 2.71×10^{-4} to $27.78 \mu\text{M}$ in the High FA experiment.

Figures 4 and 5 show the raw data of the effect versus dose level by curve for the Low FA and High FA experiments, respectively. Instead of using the actual dose, we plot the data using a sequentially assigned dose level to indicate each dilution within each curve such that the data can be shown clearly. In addition, the data points at each dilution for each curve are coded from 1 to 5 according to the order of the appearance in the data set. We assume that these numbers correspond to the replicate number for each design point (well position in the stack of 5 plates). Because the plate number was not listed in the data, we are not certain if this is the case. From the plot, one can see that there are outliers in several dilution series. Notably, in Figure 4, the effects from plate (replicate) #1 in Curves B, E, F, and K tend to be lower than all other replicates. There are also some unusually large values seen, for example, replicate 2 in Curve A, dose level (dilution series) 6; replicate 3 in Curve L, dose level 4; and replicate 2 in Curve M dose level 1. Similarly, for the High FA experiments, plate #1 seems to have some low values in Curves B, C, H, I, and J, and plate #4 seems to have some low values in Curves E, K, N, O, and P. These findings indicate that certain procedures need to be performed to remove the obvious outliers in order to improve the data quality before the data analysis.

Figure 6 shows the perspective plot, contour plot, and image plot for the Low FA experiment. From the perspective plots in Panels A (back view), B (front view), and C (side view), we can see that the effect starts at a high plane plateau at an effect level of about 1.2 when the doses of TMQ or AG are small. As the dose of each drug increases, the effect remains about constant for a while, then, a sudden drop occurs. This steep downward slope can be found by taking the trajectory of any combination of the TMQ and AG doses, which is evident in the dose response curves shown in Figures 4 and 5 as well. The steep drop of the effect can also be found in the contour plot and the image plot. Similar patterns of the dose response relationship are shown in Figure 7 for the High FA experiment as well. The drop of the effect occurs at smaller doses in the Low FA experiment and at larger doses in the High FA experiment.

5. DATA PREPROCESSING: OUTLIER REJECTION AND DATA STANDARDIZATION

5.1 Outlier Rejection

To address the concern that outliers may adversely affect the analysis outcome, we devised the following simple plan. For each of the 176 point numbers (16 curves x 11 dilutions), the five effect readings should be close to each other because they are from the replicated experiments. However, since the plate number was not in the data set, we cannot assess the plate effect. Neither can we reject a certain replicate plate entirely should there be an outlying plate nor apply a mixed effect model treating the plate effect as a random effect. For the four or five effect readings in each point number (only 9 point numbers in the Low FA and 1 in the High FA experiments have 4 readings), we compute the median and the interquartile range. An effect reading is considered as an outlier if the value is beyond median ± 1.4529 times the interquartile range. If the data are normally distributed (i.e., follow a Gaussian distribution), the range expands to cover the middle 95% of the data. Hence, only about 5% of the data points (2.5% at each extreme) are considered as outliers. The number 1.4529 is obtained by $qnorm(.975)/(qnorm(.75) - qnorm(.25))$ where $qnorm(x)$ is a quantile function which returns the x^{th} percentiles from a normal distribution. Upon applying the above rule, 129 out of 871 (14.8%) effect readings in the Low FA experiment and 126 out of 879 (14.3%) of the High FA experiment are considered outliers and are removed before proceeding to further analysis. The numbers of outliers in replicates 1 to 5 are 60, 28, 19, 14, and 8 for the Low FA experiment and 35, 18, 21, 34, and 18 for the High FA experiment indicating that there is a non-random pattern of outliers which could be attributed to experimental conditions. Note that the outlier rejection algorithm is only applied “locally.” In other words, it only applies to the up to five replicated readings in each of the 176 experimental conditions.

5.2 Data Standardization

After outliers are removed from the data, we compute the mean of the control curves. The means for Curve 8 and 16 are 1.1668 and 1.1534 for the Low FA experiments and 1.1483 and 1.1477 for the High FA experiments, respectively. To apply the E_{max} model in equation (E 6) with $E_0 = 1$, we standardize the data by dividing the effect readings of Curves 1-7 by the mean of Curve 8 and Curves 9-15 by the mean of Curve 16, respectively.

6. RESULTS

6.1 Results for the Low Folic Acid Experiment

The E_{max} model in equation (E 6) was applied to fit all dose response curves. For the Low FA experiments, the parameter estimates, their corresponding standard errors, and the residual sum of squares are given in Table 1. The dose response relationships showing the data and the fitted curves are displayed in Figure 8. Note that although model fitting was performed on the original dose scale, dose is plotted on the logarithmically transformed scale to better show the dose response relationship. The fitted marginal dose response curves for TMQ (Curve C) and AG (Curve D) are shown in a blue dashed line and a red dotted line, respectively. Table 1 shows that \hat{ED}_{50} is 0.00133 for TMQ and 0.00621 for AG, indicating that TMQ is about 4.7 times more potent than AG at the \hat{ED}_{50} level. For Curves E through P, the fitted dose response curve for the combination treatment is shown as a solid black line superimposed on the marginal dose response curves. The proposed E_{max} model fits all curves well except for Curves G, H and K. For Curve G, although the model estimates converge in an initial attempt, the parameter m is estimated with a standard error of 30.3. The large standard error essentially indicates that the estimate \hat{m} is not reliable. For Curve K, the model does not converge on the original dose scale but converges on the logarithmically transformed dose scale. However, the standard error of the estimate \hat{m} is still very large, which leads us to believe that the model is not very stable as well. For Curve H, as can be seen in Figure 8, there are no observed effects between 0.3 and 1 from the second to the fifth dilutions. The parameter m cannot be estimated and the model fails to converge on both the original scale and the logarithmic scale. To address these problems, we conclude that the data do not provide us sufficient information to yield a reasonable estimate of the parameter m . Therefore, we take a remedial approach by fixing m , then, proceed to estimate the other two parameters. Upon checking the data, we set the parameter m as 5, 4.5, and 5 for Curves G, H, and K, respectively. The choice of m is somewhat arbitrary with the goals to yield a good fit to the data and produce a small residual sum of squares. The resulting "reduced" models fit the data reasonably well but with a consequence that there is no standard error estimate for \hat{m} , which affects the variance estimation of the interaction index (to be shown later). Based on limited sensitivity analysis, the estimation of the interaction index remains reasonably robust.

In all dose response curves, the standardized effect level starts to drop between dose levels (dilutions) 3 to 6. Once the effect starts to drop, it drops quickly and plateaus to the $1 - \hat{E}_{max}$ level. There are ample data points at the effect levels around 1 (dose levels 1-4) and $1 - \hat{E}_{max}$ (dose levels 8-11). However, due to the sharp drop in the dose response curves, less data points can be found in the middle of the effect range. When the number of data points becomes too few or does not spread out to cover enough range, it becomes harder for the model to converge, as seen in Curves G, H, and K. The overall results for the curve fitting of the Low FA experiments are that \hat{E}_{max} are between 0.863 to 0.890; \hat{ED}_{50} are between 0.00133 to 0.00621; and \hat{m} are between 1.971 to 5.473. The residual sums of squares are between 0.0599 to 0.1025 and without large values, suggesting that the model fits the data reasonably well.

Based on the fitted dose response curve, interaction index (II) can be calculated over the entire effect range and at specific dose combinations. Table 2 gives a detailed result of the estimated interaction index and its 95% point-wise confidence interval at each dose combination for each combination curve. The II is calculated at the predicted effect level from the combination curve and not at the observed effect level. The results are shown in a trellis plot in Figure 9 where red lines represent the point-wise confidence intervals at each specific effect level and black dashed lines indicate the simultaneous confidence bands of II for the entire range. From the figure we find that the interaction index can be estimated with very good precision in all curves except at the two extremes when the effect is close to 1 or $1 - \hat{E}_{max}$. The trend and the pattern of the interaction index are clearly shown in these figures. For Curves E through K, i.e., with a TMQ:AG dose ratio ranging from 0.004 to 0.2, synergy is observed in the effect range between 0.2 to 0.9. For Curves L and M which have TMQ:AG ratios of 0.4 and 0.8, we see that synergy is observed at the low effect level from 0.2 to about 0.5. Beyond 0.5 the combinations are generally additive. For Curves N, O, and P with TMQ:AG ratios of 2, 5, and 10, the synergistic effect is lost and we see additivity in all dose ranges.

6.2 Results for the High Folic Acid Experiment

Similarly, Table 3 gives the parameter estimates, the corresponding standard errors, and sums of squares for all the curves in the High FA experiment. Unlike in the Low FA cases, the model fitting for all curves in the High FA experiment converge using the E_{max} model. The estimated \hat{E}_{max} ranges from 0.831 to 0.893; \hat{ED}_{50} ranges from 0.0137 to 0.1943 except for Curve D (AG alone with $\hat{ED}_{50} = 0.5224$); and \hat{m} ranges between 1.468 and 3.625. The residuals sums of squares are between

0.0615 to 0.1134. Compared to the Low FA experiments, \hat{ED}_{50} are higher in the High FA experiments, indicating that the drugs are less potent with the high FA medium. Note that doses for the TMQ are the same between the two experiments but the doses for AG are actually 10 times higher in the high FA experiments. In addition, $\hat{ED}_{50} = 0.0137$ and 0.00133 for TMQ alone in the high and low FA experiments, respectively, which indicates that the drug is 10 times less potent in the high FA medium compared to the low FA medium. The potency of AG is even more dramatically reduced. Figure 10 shows that the E_{max} model provides an excellent fit to all the curves. Table 4 gives the detailed account of the interaction index in all dilutions for all combination curves. The results are summarized in a trellis plot in Figure 11. Again, the red lines represent the point-wise confidence intervals at each specific effect level and black dashed lines correspond to the simultaneous confidence bands of Π for the whole range. With the high FA medium, synergy can be achieved for most of the drug combinations in all the effect range except at the very low or very high effects. The confidence intervals are still very tight although they are a little wider than the Low FA counterparts. As the TMQ:AG ratio increases from 0.0004 to 0.5, synergy is observed across all dilution series. In addition, higher synergy is observed at the lower effect levels particularly when the TMQ:AG is at 0.01 or lower (Curves E, F, G, H, and I). In the middle effect levels (effect between 0.2 to 0.8), Π ranges from about 0.1 in Curves J and K, to 0.12 in Curve L, to 0.15 in Curve M, to 0.25 in Curve N, and to 0.35 in Curve O. The higher the TMQ:AG ratio is, the less the synergy it produces. In Curve P when the TMQ:AG ratio reaches 1, synergy is lost.

7. SUMMARY

In both the Low FA and High FA experiments, TMQ is more potent than AG. At low TMQ:AG ratios, i.e., when a small amount of the more potent drug (TMQ) is added to a larger amount of the less potent drug (AG), it results in synergy. However, when the TMQ:AG ratio reaches to 0.4 or larger for the low FA medium, or when the TMQ:AG ratio reaches to 1 or larger for the high FA medium, synergy tends to become less, or the interaction becomes additive. In general, synergistic effect is stronger at higher doses which produce stronger effects (effect closer to $1 - E_{max}$) than at the lower dose levels which produce weaker effects (effect closer to 1) in the same dilution series.

The two drugs are more potent in the low FA medium compared to the high FA medium. The drug synergy, however, is stronger in the high FA medium.

8. DISCUSSION

The data supplied by Dr. Greco provide an excellent opportunity to apply and compare various approaches for studying combination drug effects. For the median effect model, a linear relationship between the logit transformed effect and the log-dose makes the model fitting straightforward and easy. However, when measuring cell growth as in the data we received, if the maximum drug effect reaches a plateau and does not kill all the cells even at the highest experimental doses, the median effect model (12) does not apply. We take the E_{max} model (19), which provides an adequate fit for most data. For the E_{max} model, parameter estimation has to be obtained via iterative procedures, for example, the non-linear weighted least squares method which can address the heteroscedascity problem. The model convergence is not guaranteed and whether the model converges or not depends on the data and the choice of the initial values. We find that PROC NLIN in SAS provides a more comprehensive and robust environment for estimating parameters with nonlinear regression compared to the `nls()` function in S-PLUS/R. It can be useful to apply SAS first to estimate the parameters, then, feed the results into S-PLUS/R for further data analysis and graphics. Unlike fitting the linearly-transformed median effect model via linear regression, for which a solution can always be found, fitting the E_{max} model via nonlinear regression, however, may not converge in some cases. The nonconvergence of the model may indicate pathological conditions in the data such that the data do not provide adequate information for model fitting. We had convergence problems for the Curves G, H, and K in the Low FA experiment. In these cases, there is not sufficient data in the middle of the effect range; hence, the parameters cannot be estimated reliably. We had to fix the m parameter before we could estimate the other two parameters. From the dose response curves, we find that TMQ is more potent than AG and the drugs are more potent in the low FA medium than in the high FA medium.

Upon the construction of the marginal and combination dose response curves, we applied the Loewe additivity model to compute the interaction index. Note that the definition of drug interaction, such as the interaction index, is model dependent. In addition, based on the definition of the interaction index (7, 8), the scale of the dose level should be in the original physical scale. No matter which models one uses, the dose levels in calculating the interaction index must be translated back to the original dose scale. Under the given model, we find that the drug interaction between TMQ and AG is largely synergistic. Synergy is more clear and evident in the high FA experiment than in the low FA experiment. In addition, synergy is more likely to be observed when a small dose of more potent drug (TMQ) is added to the large dose of the less potent drug (AG). When a large amount of more potent drug is present, adding the less potent drug does not show synergy because the effect is largely achieved by the more potent drug already. In addition, the interval estimation shows that the 95% confidence intervals are wider at the two extremes of the effect which are closer to 1 or $1 - E_{max}$. The result is consistent with many regression settings where estimation achieves higher precision in the center of the data but lower precision at the extremes.

We have provided a simple, yet useful approach for analyzing the drug interaction for combination studies. The interaction index for each fixed dose ratio is computed, then, displayed together using the trellis plot. The method works well for the ray design. Other methods have been proposed to model the entire response surface using the parametric approach (27) or the semiparametric approach (28). The results from applying the semiparametric model are reported in a companion article (29).

9. ACKNOWLEDGEMENT

We thank Dr. William R. Greco for organizing this project for comparing rival modern approaches to analyzing the combination studies, supplying the data sets, and invitation for presenting this manuscript. The authors also thank Ms. Vicky Cervantes for her editorial assistance. This work is supported in part by grants W81XWH-05-2-0027, W81XWH-07-1-0306 from the Department of Defense, and the grant CA16672 from the National Cancer Institute.

10. REFERENCES

1. R. C. Rathbun, S. M. Lockhart, R. J. Stephens: Current HIV treatment guidelines - An overview. *Curr Pharm Des* 12(9), 1045-1063 (2006)
2. J. R. Molina, A. A. Adjei, J. R. Jett: Advances in chemotherapy of non-small cell lung cancer. *Chest* 130(4), 1211-1219 (2006)
3. M. M. Nyunt, C. V. Plowe: Pharmacologic advances in the global control and treatment of malaria: Combination therapy and resistance. *Clin Pharmacol and Ther* 82(5), 601-605 (2007)
4. K. K. Sankhala, K. P. Papadopoulos: Future options for imatinib mesilate-resistant tumors. *Expert Opinion on Investigational Drugs* 16(10), 1549-1560 (2007)
5. R. Bianco, V. Damiano, T. Gelardi, G. Daniele, F. Ciardiello, G. Tortora: Rational combination of targeted therapies as a strategy to overcome the mechanisms of resistance to inhibitors of EGFR signaling. *Curr Pharm Des* 13(33), 3358-3367 (2007)
6. S. Sathornsumetee, D. A. Reardon, A. Desjardins, J. A. Quinn, J. J. Vredenburgh, J. N. Rich: Molecularly targeted therapy for malignant glioma. *Cancer* 110(1), 12-24 (2007)
7. M. C. Berenbaum: What is synergy? *Pharmacol Rev* 41, 93-141 (1989)
8. W. R. Greco, G. Bravo, J. C. Parsons: The search of synergy: A critical review from a response surface perspective. *Pharmacol Rev* 47(2), 331-385 (1995)
9. J. Suhnel: Parallel dose-response curves in combination experiments. *Bull of Math Biol* 60(2), 197-213 (1998)
10. T. C. Chou: Theoretical basis, experimental design, and computerized simulation of synergism and antagonism in drug combination studies. *Pharmacol Rev* 58, 621-681 (2006)
11. R. J. Tallarida: An overview of drug combination analysis with isobolograms. *J Pharmacol Exp Ther* 319(1), 1-7 (2006)
12. T. C. Chou, P. Talalay: Quantitative analysis of dose effect relationships: the combined effects of multiple drugs or enzyme inhibitors. *Adv in Enzyme Reg* 22, 27-55 (1984)
13. S. G. Machado, S.G. A. Robinson: A direct, general approach based on isobolograms for assessing the joint action of drugs in pre-clinical experiments. *Statistics in Medicine*, 13:2289-2309 (1994).
14. C. Gennings: On testing for drug/chemical interactions: Definitions and inference. *Journal of Biopharmaceutical Statistics*, 10, 457-467 (2000)
15. K.S. Dawson, W.H. Carter Jr., C. Gennings: A statistical test for detecting and characterizing departures from additivity in drug/chemical combinations. *Journal of Agricultural, Biological, and Environmental Statistics*, 5, 342-359 (2000)
16. J. J. Lee, M. Kong, G. D. Ayers, R. Lotan: Interaction index and different methods for determining drug interaction in combination therapy. *J Biopharm Stats* 17, 461-480 (2007)
17. J. J. Lee, M. Kong: A confidence interval for interaction index for assessing multiple drug interaction. *Stats Biopharm Res* (In-press, 2008)
18. H. M. Faessel, H. K. Slocum, R.C. Jackson, T.J. Boritzki, Y.M. Rustum, M. G. Nair, and W.R. Greco: Super in vitro synergy between inhibitors of dihydrofolate reductase and inhibitors of other folate-requiring enzymes: The critical role of polyglutamylolation. *Cancer Res.* 58, 3036-3050 (1998)
19. N. Ting: *Dose Finding in Drug Development*. Springer, NY, 127-145 (2006)
20. J.M. Chambers, T.J. Hastie: Statistical Models in S. *Chapman & Hall Computer Science Series*, 450 – 452 (1992)
21. S. Huet, A. Bouvier, M.-A. Poursat, E. Jolivet: *Statistical Tools for Nonlinear Regression: A Practical Guide with S-PLUS and R Examples*. (2nd ed.) Springer, NY (2003)
22. *SAS/STAT 9.1 User's Guide*, SAS Institute, Cary, NC (2007)

23. P.J. Bickel, K.A. Doksum: *Mathematical Statistics: Basic Ideas and Selected Topics*. New Jersey: Prentice Hall, pp. 306-314 (2001)
24. C. Cox, G. Ma: Asymptotic confidence bands for generalized nonlinear regression models. *Biometrics* 51, 142-150 (1995)
25. J. J. Lee, Z. N. Tu: A Versatile One-Dimensional Distribution Plot: The BLiP Plot. *Amer Statistician* 51(4), 353-358 (1997)
26. M. J. Crawley: *The R Book*, NY, Wiley (2007)
27. M. Kong, J. J. Lee: A general response surface model with varying relative potency for assessing drug interactions. *Biometrics* 62(4), 986-995 (2006)
28. M. Kong, J. J. Lee: A semiparametric response surface model for assessing drug interactions. *Biometrics* (in press, 2008)
29. M. Kong, J. J. Lee: Applying E_{max} model and bivariate thin plate splines to assess drug interactions. Submitted to *Frontiers in Biosciences*.

Abbreviations: AG: AG2034, an inhibitor of the enzyme glycinamide ribonucleotide formyltransferase; FA: folic acid; II: interaction index; TMQ: Trimetrexate, a lipophilic inhibitor of the enzyme dihydrofolate reductase;

Key Words: additivity, antagonism, confidence interval estimation, E_{max} model, Loewe additivity model, nonlinear regression, synergy, trellis plot.

Send correspondence to: J. Jack Lee, Department of Biostatistics, University of Texas, M. D. Anderson Cancer Center, Unit 447, 1515 Holcombe Boulevard, Houston, Texas 77030, U.S.A.
Tel: 713-794-4158, Fax: 713-563-4242, E-mail: jjlee@mdanderson.org.

Running Title: E_{max} model and interaction index for drug interaction

Figure Legend:

Figure 1: Dose response curves under the E_{max} model by varying the parameters E_{max} , $ED50$, and m .

Figure 2: Variable width percentile plot for the observed effect in experiments with low and high folic acid media. Each vertical bar indicates a five percent increment. The middle 20% of the data are shaded in a light orange color.

Figure 3: Experimental design showing the logarithmically transformed AG2034 (AG) dose versus the logarithmically transformed trimetrexate (TMQ) dose in the fixed ratio experiments. A total of 16 curves are shown. Curves A and B are the controls with no drugs. Curves C and D are single drug studies for TMQ and AG, respectively. Curves E through P are the combination drug studies. Each curve has 11 dilutions shown in circles. Panels A: low folic acid medium. Panel B: high folic acid medium.

Figure 4: Distribution of the effect versus dose level for Curves A through P for the experiment with low folic acid medium.

Figure 5: Distribution of the effect versus dose level for Curves A through P for the experiment with high folic acid medium.

Figure 6: Perspective plots (Panels A, B, and C), contour plots (Panels D and E), and image plot (Panel F) for the effect versus logarithm transformed doses of trimetrexate and AG2034 for the experiment with low folic acid medium.

Figure 7: Perspective plots (Panels A, B, and C), contour plots (Panels D and E), and image plot (Panel F) for the effect versus logarithmically transformed doses of trimetrexate and AG2034 for the experiment with high folic acid medium.

Figure 8: Effect versus logarithmically transformed dose plot for the combination study of trimetrexate and AG2034 with low folic acid medium. Raw data are shown in open circles. The blue dashed line and the red dotted line indicate the fitted marginal dose response curves for trimetrexate and AG2034, respectively. The black solid line indicates the fitted dose response curve for the combination study of trimetrexate and AG2034.

Figure 9: Trellis plot of the estimated interaction index (solid line) and its point-wise 95% confidence interval (red solid lines) and the 95% simultaneous confidence band (dashed lines) for the low folic acid experiment. The estimates at the design points where experiments were conducted are shown in red. The interaction index is plotted on the logarithmically transformed scale but labeled on the original scale.

Figure 10: Effect versus logarithmically transformed dose plot for the combination study of trimetrexate and AG2034 with high folic acid medium. Raw data are shown in open circles. The blue dashed line and the red dotted line indicate the fitted marginal dose response curves for trimetrexate and AG2034, respectively. The black solid line indicates the fitted dose response curve for the combination study of trimetrexate and AG2034.

Figure 11: Trellis plot of the estimated interaction index (solid line) and its point-wise 95% confidence interval (red solid lines) and the 95% simultaneous confidence band (dashed lines) for the high folic acid experiment. The estimates at the design points where experiments were conducted are shown in red. The interaction index is plotted on the logarithmically transformed scale but labeled on the original scale.

Amplification of *PDGFRA* and *KIT* in Non-small Cell Lung Cancer

Alex H. Ramos^{1,2,3,*}, Amit Dutt^{1,2,*}, Craig Mermel^{1,2,3}, Sven Perner⁴, Jeonghee Cho¹, Christopher J. Lafargue⁵, Laura A. Johnson^{1,2}, Kumiko E. Tanaka^{1,2}, Adam J. Bass^{1,2}, Jordi Barretina^{1,2}, Barbara A. Weir^{1,2}, Rameen Beroukhi^{1,2}, Roman K. Thomas^{6,7}, John D. Minna^{8,9,10}, Lucian R. Chirieac^{3,11}, Neal I. Lindeman^{3,11}, David G. Beer¹², Patrick Wagner⁵, Ignacio I. Wistuba^{13,14}, Mark A. Rubin⁵, Matthew Meyerson^{1,2,3}

¹ Department of Medical Oncology and Center for Cancer Genome Discovery, Dana-Farber Cancer Institute, Boston, MA 02115, USA

² Cancer Program, Broad Institute of Harvard and MIT, Cambridge, MA 02142, USA

³ Department of Pathology, Harvard Medical School, Boston, MA 02115, USA

⁴ Department of Pathology, University Hospital of Tübingen, Tübingen, Germany 72076

⁵ Department of Pathology, Weill Medical College of Cornell University, New York, NY 10021, USA

⁶ Max Planck Institute for Neurological Research with Klaus-Joachim-Zülch Laboratories of the Max-Planck Society and the Medical Faculty of the University of Cologne, Cologne, Germany 50931

⁷ Center for Integrated Oncology and Department I for Internal Medicine, University of Cologne, Cologne, Germany 50931

⁸ Hamon Center for Therapeutic Oncology Research-Simmons Cancer Center and Departments of ⁹ Internal Medicine and ¹⁰ Pharmacology, University of Texas Southwestern Medical Center, Dallas, TX 75390, USA

¹¹ Department of Pathology, Brigham and Women's Hospital, Boston, MA 02115, USA

¹² Section of Thoracic Surgery, Department of Surgery, University of Michigan, Ann Arbor, MI 48109, USA

¹³ Departments of Epidemiology and ¹⁴ Pathology, The University of Texas M. D. Anderson Cancer Center, Houston, TX 77030, USA

*These authors contributed equally to this work

Correspondence should be addressed to:

Matthew Meyerson
 Department of Medical Oncology
 Dana-Farber Cancer Institute
 44 Binney Street, Dana1537
 Boston, MA 02115
Matthew.Meyerson@dfci.harvard.edu

Running Title: Amplification of *PDGFRA* and *KIT* in NSCLC

Abstract

In cancer, proto-oncogenes are often activated by genomic amplification. Here we report recurrent focal amplifications of chromosome segment 4q12 overlapping the oncogenes *PDGFRA* and *KIT* in non-small cell lung cancer (NSCLC). Single nucleotide polymorphism (SNP) array and fluorescent *in situ* hybridization (FISH) analysis indicate that 4q12 is amplified in 9% of lung squamous cell carcinomas and 3% of lung adenocarcinomas. We further demonstrate that the lung squamous cell carcinoma cell line NCI-H1703 exhibits focal amplification of *PDGFRA* and is dependent on PDGFRA activity for cell growth. Treatment of NCI-H1703 cells with *PDGFRA*-specific shRNAs or with the *PDGFRA*/*KIT* small molecule inhibitors imatinib and sunitinib leads to cell growth inhibition. Together these observations implicate *PDGFRA* and *KIT* as potential oncogenes in NSCLC and present a novel opportunity for targeted therapy.

Introduction

Lung cancer is the leading cause of cancer mortality in the United States and worldwide. The majority of lung cancer cases are non-small cell lung cancers (NSCLC), the most common forms of which are the two histological subtypes, adenocarcinoma and squamous cell carcinoma. Despite advances in systemic therapies and surgical techniques, 5-year survival rates for all types and stages of lung cancer remain low (16%) (1).

Like other solid tumors, NSCLC cases are subject to large scale rearrangements leading to copy number gains and losses across the genome (2-4). Systematic analyses of copy number alterations in lung adenocarcinoma have identified genes such as *EGFR*, *MYC*, *MDM2*, *TERT*, *NKX2-1*, *PIK3CA*, and *MET* to be selectively amplified (5-8). Other studies focusing on oncogenic point mutations have identified recurrent mutations leading to aberrant activation of *EGFR*, *KRAS*, *PIK3CA*, *ERBB2*, and *BRAF* among other genes (9-12). Furthermore, inactivating point mutations and deletions in *TP53*, *STK11*, *NF1*, *CDKN2A*, and *PTEN* have been reported (13-17). Most recently, mutations in several tyrosine kinase genes including *PDGFRA* and *KDR* have also been reported (15). Unlike lung adenocarcinoma, the range of genetic alterations in lung squamous cell carcinoma is less understood. Activating deletions in the extracellular domain of *EGFR* (*EGFRvIII* mutation) have been identified in 5% of lung squamous cell carcinoma samples examined (18). In addition, chromosome 3q amplifications encompassing *PIK3CA* and other genes have been found in 18% of lung squamous cell carcinoma samples (19). Nonetheless, despite these efforts to characterize the NSCLC genome, further work is needed to identify the complete spectrum of genetic lesions involved in NSCLC pathogenesis.

Importantly, a recent study using a proteomic rather than genomic approach to discover kinases activated in lung cancer identified phosphorylation of the receptor tyrosine kinase *PDGFRA* in 5% (8/150) of primary NSCLC cases and in the lung squamous cell carcinoma cell line, NCI-H1703 (20). Treatment of NCI-H1703 with imatinib, an FDA-approved *PDGFRA* and *KIT* inhibitor, resulted in apoptotic cell death. Aberrant *PDGFRA* activation has been shown to play a tumorigenic role in

gastrointestinal stromal tumors (GIST) and several brain tumor types (21, 22). Constitutively activating point mutations in *PDGFRA* are found in 5% of GIST cases. Additionally, *PDGFRA* is amplified in glioblastoma multiforme and other malignant brain tumors. However, in NSCLC the genetic basis for PDGFRA dependency is unclear.

We have therefore investigated the role of PDGFRA in NSCLC etiology using a combination of copy number analyses in primary samples and *in vitro* experiments in cell line models. Here, we demonstrate that *PDGFRA*, as well as the neighboring kinase *KIT*, are recurrently amplified in NSCLC at a frequency of 9% in squamous cell carcinoma and 3% in adenocarcinomas. The role of *KIT* in NSCLC tumorigenesis remains unclear due to the absence of cell line models that harbor endogenous *KIT* amplification in which to perform functional testing. However, using the cell line NCI-H1703, we highlight the role of *PDGFRA* as a novel prospective oncogene in NSCLC and its potential as a target for novel therapeutic modalities in lung cancer.

Materials and Methods

NSCLC primary samples and cell lines

Genomic DNA was extracted from 74 fresh frozen primary tumors and 84 cell lines. Primary samples were collected from six different sites: Memorial-Sloan Kettering Cancer Center (2 tumors), University of Michigan (1 tumor), Washington University in St. Louis (3 tumors), Dana-Farber Cancer Institute/The Broad Institute (8 tumors), Brigham and Women's Hospital tissue bank (25 tumors), and from the University Health Network in Toronto (35 tumors). Cell lines were obtained from ATCC (26 cell lines),

DSMZ (5 cell lines), Dana-Farber Cancer Institute/The Broad Institute (1 cell line), NCI Developmental Therapeutics Program (3 cell lines), and from J.D. Minna at University of Texas Southwestern Medical Center (49 cell lines). Additionally, raw Affymetrix 250K SNP array data from 554 primary adenocarcinomas as published in Weir et al. (5) and 22 NSCLC cell lines from the NCI caArray open-source database were utilized

SNP array experiments and analysis

SNP array experiments were performed on 734 NSCLC tumor and cell line samples as described in Weir et al (5). Data was analyzed using GISTIC as described in Beroukhi et al (23). Briefly, genomic DNA was genotyped using the Sty I chip of the 500K Human Mapping Array set (Affymetrix Inc) at the Broad Institute. Raw probe intensities were processed using the GenePattern software package; copy number was computed by dividing the intensity of each probeset by the mean value of that probeset in the five closest normals by Euclidean distance (see Beroukhi et al). Normalized data was segmented with GenePattern modules based on the GLAD algorithm. G-scores derived from GISTIC were obtained for each SNP probe across chromosome 4. Only amplifications exceeding log₂ ratio of 0.3 were included. G-scores were compared against a null model generated by random permutations to determine a false discovery rate (q-value). Peaks with q-values below 0.25 were considered significant. Both the peak region determined by minimal common overlap (chr4:54781155-54868471, probes 57234:57238) and the wide peak determined by a leave-one-out approach (chr4:54758116-55357275, probes 57231:57300) are reported.

Tissue microarray Fluorescent in-situ hybridization (TMA-FISH)

To assess for *PDGFRA* amplification, a probe spanning *PDGFRA* (chr4q12, 99.3 kb) and a reference probe spanning a stable region identified by SNP data in NSCLC (chr4q22.3-q23, 193 kb) were used. For the *PDGFRA* target probe, the Biotin-14-dCTP labeled BAC clone CTD-2054G 11 (conjugated to produce a red signal) was applied. For the reference probe, the Digoxigenin 11-dUTP labeled BAC clone RP11-799A1 2 (conjugated to produce a green signal) was applied. Correct chromosomal probe localization was confirmed on normal lymphocyte metaphase preparations. BAC clones were obtained from the BACPAC Resource Center, Children's Hospital Oakland Research Institute (CHORI) (Oakland, CA) and Invitrogen (Carlsbad, CA). Tissue hybridization, washing, and color detection were performed as described previously (39). *PDGFRA* amplification by FISH was assessed in 171 samples (represented by 497 tissue microarray cores). At least one TMA core could be evaluated per case. The samples were analyzed under a 60x oil immersion objective using an Olympus BX-511 fluorescence microscope, a CCD (charge-coupled device) camera and the CytoVision FISH imaging and capturing software (Applied Imaging, San Jose, CA). Semi-quantitative evaluation of the tests was independently performed by two evaluators (A.R., S.P.). For each case, we attempted to analyze at least 100 nuclei.

Cell culture and reagents

The NSCLC cell lines, NCI-H1703 and HCC15 were obtained from ATCC (Manassas, Virginia, United States) and DSMZ (Braunschweig, Germany), respectively. Cells were maintained in RPMI 1640 complete media supplemented with 10% calf

serum (Gibco/Invitrogen, Carlsbad, California, United States) and penicillin/streptomycin (Gibco/Invitrogen). Unless otherwise noted, cells were placed in media containing 0.5% calf serum 24 h prior to 100ng/mL PDGF (#9909, Cell Signaling Technologies, Danvers, MA, United States) stimulation for 20 minutes at 37 °C. Imatinib and Sunitinib were purchased from LC Laboratories (Woburn, Massachusetts, United States) and diluted in DMSO to the indicated concentrations.

shRNA mediated PDGFRA knockdown

shRNA vectors targeted against *PDGFRA* and *GFP* were obtained from TRC (The RNAi Consortium). The target sequences of the PDGFRA shRNA constructs are:

PDGFRA#1 (TRCN0000001422): 5'- CCCAACTTTCTTATCCAACTT-3'.

PDGFRA #2 (TRCN0000001423): 5'- CCAGCCTCATATAAGAAGAAA-3'.

PDGFRA #3 (TRCN0000001424): 5'- CCAGCTTTCATTACCCTCTAT-3'.

PDGFRA #4 (TRCN0000001425): 5'- CGGTGAAAGACAGTGGAGATT-3'.

PDGFRA #5 (TRCN0000001426): 5'- CAATGGACTTACCCTGGAGAA-3'.

The sequence targeted by the GFP shRNA is 5'-GCAAGCTGACCCTGAAGTTCAT-3'.

Lentiviruses were made by transfection of 293T packaging cells with these constructs using a three plasmid system as previously described (41). Target cells were incubated with lentiviruses for 6 hours in the presence of 8 µg/ml polybrene and left in fresh media. Two days after infection, puromycin (2 µg/ml for NCI-H1703 and HCC15) was added. Cells were grown in the presence of puromycin for four days. Fifty micrograms of total cell lysates prepared from the puromycin selected cell lines was analyzed by Western blotting using anti-PDGFRA monoclonal antibody (# sc-31166, Santa Cruz Biotechnology), anti-

phospho PDGFRA monoclonal antibody (# sc- 12910, Santa Cruz Biotechnology) and anti-Actin monoclonal antibody (# sc-1615, Santa Cruz Biotechnology).

Cell survival assays with tumor cell lines expressing shPDGFRA and shGFP constructs.

800 cells for each tumor cell line expressing shRNAs targeting *PDGFRA* or *GFP* along with uninfected cells were seeded in 6 wells on a 96 well plate. Cell viability was determined at 24 hour time points for 4 consecutive days using the WST-1 assay (Roche Applied Science). The percentage of cell viability is plotted for each cell line of readings obtained on Day 3 relative to Day 1.

Soft agar anchorage-independent growth assay with tumor cell lines expressing shPDGFRA and shGFP constructs.

NCI-H1703 and HCC15 cells expressing shPDGFRA and shGFP were suspended in a top layer of RPMI1640 containing 10% calf serum and 0.4% Select agar (Gibco/Invitrogen, Carlsbad, California, United States) and plated on a bottom layer of RPMI1640 containing 10% calf serum and 0.5% Select agar. Imatinib or Sunitinib were added as described to the top agar. After 3 weeks incubation for HCC15 cells and 5 weeks for NCI-H1703 cells, colonies were counted in triplicate. IC50s were determined by nonlinear regression using the Prism Graphpad software.

Cytotoxicity assays

Lung cancer cell lines were treated with Imatinib or Sunitinib one day after plating and cell survival was assessed 4 days later using the WST-1 assay (Roche, <http://www.roche.com>). Each data point represents the median of six replicate wells for each tumor cell line and inhibitor concentration. IC50s were determined by nonlinear regression using the Prism Graphpad software.

Immunoblotting

Cells were lysed in a buffer containing 50 mM Tris-HCl (pH 7.4), 150 mM NaCl, 2.5 mM EDTA, 1% Triton X-100, and 0.25% IPEGAL. Protease inhibitors (Roche, <http://www.roche.com>) and phosphatase inhibitors (Calbiochem, La Jolla, CA, United States) were added prior to use. Samples were normalized for total protein content. Lysates were boiled in sample buffer, separated by SDS-PAGE on 8% polyacrylamide gels, transferred to PVDF membrane, and probed as described. Antibodies used for immunoblotting were: anti-PDGFR α monoclonal antibody (# sc-31166, Santa Cruz Biotechnology), anti-phospho PDGFR α monoclonal antibody (# sc-12910, Santa Cruz Biotechnology) and anti-Ac-tin monoclonal antibody (# sc-1615, Santa Cruz Biotechnology).

Results

***PDGFRA* and *KIT* are amplified in non-small cell lung cancer**

To determine if *PDGFRA* is recurrently amplified in NSCLC, 734 NSCLC samples (628 primary samples, 106 cell lines) were evaluated for copy number aberrations with Affymetrix 250K SNP arrays (Fig. 1A, Supplementary Table S1). Using the GISTIC (Genomic Identification of Significant Targets in Cancer) algorithm (23), a 600 Kb region on 4q12 (54.76 to 55.36 Mb) was found to be significantly amplified. The sole genes within this region are *PDGFRA* and the closely related receptor tyrosine kinase *KIT*.

Visual inspection revealed amplifications at 4q12 overlapping the *PDGFRA/KIT* locus in 31 (4.2%) NSCLC samples (Figure 1B, Supplementary Table S2). The majority (93%; 29/31) of these amplifications were relatively focal events (<50% of the length of chromosome 4q) suggesting that selective amplification of target genes is occurring. Comparing NSCLC subtypes, 8.7% (5/57) of squamous cell carcinomas and 3.5% (21/588) of adenocarcinomas showed amplifications, suggesting that 4q12 is amplified at appreciable frequencies across both major NSCLC subtypes. The inferred copy number and length of focal amplifications ranged from 2.47 to 10.24 copies (median = 2.8 copies) and from 0.45 to 48.4 Mb (median = 7.55 Mb), respectively. Here, non-integer copy number values are the result of smoothing across multiple SNP probes using the GLAD (Gain and Loss Analysis of DNA) segmentation algorithm (24). The only previously described oncogenes in these focally amplified regions are *PDGFRA* and *KIT*. Interestingly, our group has found recurrent point mutations in *KDR*, a

receptor tyrosine kinase located adjacent to *KIT*, as well as *PDGFRA* and rarely in *KIT* (15). In our data, *KDR* is often amplified with *PDGFRA* and *KIT* (28/31 samples) but it does not fall within the GISTIC region of statistical significance.

Most of the samples (26/29) with focal amplification at 4q12 had amplicons spanning both *PDGFRA* and *KIT*. However, three samples had amplicon breakpoints between *PDGFRA* and *KIT* and only amplify one of the two genes, suggesting that only one of these genes is necessary for NSCLC tumorigenesis. Two primary adenocarcinoma samples, S M-11SU and SM-11U9, are *PDGFRA*^{WT}/*KIT*^{AMPLIFIED} while the lung squamous cell carcinoma cell line NCI-H1703 is *PDGFRA*^{AMPLIFIED}/*KIT*^{WT} (Supplementary Fig. S1). Importantly, the lung squamous cell carcinoma cell line NCI-H1703 has recently been shown to over express phosphorylated PDGFRA protein and to exhibit activated MAP kinase pathway signaling (20). To identify any possible activating point mutations or insertion/deletions in NCI-H1703, the coding region of *PDGFRA* cDNA was sequenced but no somatic alterations were detected (data not shown).

To validate our initial findings, we performed fluorescence *in situ* hybridization (FISH) in an independent set of 171 primary NSCLC tumor samples using a bacterial artificial chromosome (BAC) probe overlapping *PDGFRA* (Fig. 1 C). A BAC probe overlapping a non-amplified genomic region (4q21), as indicated by SNP array analysis, was used as a control. Of the 171 NSCLC samples evaluated, 11 (6%) were found to have amplification of the *PDGFRA* locus. Within subtypes, *PDGFRA* amplification was observed in 3.0% (2/66) of adenocarcinoma and 9.3% (9/96) of squamous cell carcinoma samples, closely mirroring the results observed by SNP array analysis

(Supplementary Table S3). Interestingly, two different amplification phenotypes were observed. Seven samples exhibited high-level amplification (CN >10) of *PDGFRA* in ~5% of tumor cells within the sample. Conversely, four samples with *PDGFR* gain showed lower levels of amplification (CN 4-8) present in the majority (>50%) of a sample's tumor cells.

***PDGFRA* is essential for tumor cell survival**

Unregulated expression of oncogenes has been shown to be necessary for tumor cell proliferation or viability. Given this dependency upon continued oncogenic signaling, termed oncogene addiction, tumor cells with genetically altered oncogenes can often be effectively treated with targeted agents (25). Six cell lines harboring 4q12 copy number gain, whether broad or focal, were tested for *PDGFRA* expression (Supplementary Fig. S2). Of these, NCI-H1703 cells highly expressed *PDGFRA* and were studied further. In order to demonstrate a role for *PDGFRA* in the survival of NSCLC with *PDGFRA* amplification, we tested a series of shRNA constructs in NCI-H1703 cells and control HCC15 cells without 4q12 amplification. As shown in Fig. 2 A, three out of five short hairpin RNAs were found to significantly knock down the *PDGFRA* expression in NCI-H1703 cells. This knock down of *PDGFRA* inhibited cell survival and anchorage-independent growth in NCI-H1703 cells, but not in the HCC15 cells (Fig. 2 B and Supplementary Fig. S3 A). Together, these observations implicate *PDGFRA* as an essential gene in a subset of NSCLC samples; similar to other known

oncogenes, such as *EGFR* and *FGFR2*, that can render oncogene-expressing cells dependent upon their activation (26, 27).

Effect of PDGFRA kinase inhibitors on *PDGFRA* over expressing cells

We then investigated whether inhibition of PDGFRA kinase activity with small molecule inhibitors could be effective against NCI-H1703 cells. To this end, we examined the effect of two small molecule tyrosine kinase inhibitors, imatinib and sunitinib, that are approved for the treatment of leukemia, GIST, and advanced renal cell carcinoma (28-30). While imatinib specifically inhibits tyrosine kinase activity of ABL, KIT, and PDGFRA; sunitinib is a multi-targeted tyrosine kinase inhibitor of VEGFR-family receptors, PDGFR-family receptors, KIT, RET, FLT3, and CSF-1R (31, 32). Treatment with 2 μ M imatinib or sunitinib for 40 minutes at 37°C inhibited the constitutive phosphorylation of *PDGFRA* in NCI-H1703 cells harboring amplification of *PDGFRA* (Fig 3 A) suggesting that both inhibitors inhibited *PDGFRA* kinase activity. Consistent with this *in vitro* effect, treatment with imatinib or sunitinib also resulted in marked decrease of cell survival in culture as determined by WST-based cell proliferation assays, with an IC₅₀ of 20nM and 74nM, respectively (Fig 3 B & 3 C). Furthermore, imatinib inhibited anchorage independent colony formation in soft agar at an IC₅₀ of 80 nM while sunitinib inhibited colony formation at an IC₅₀ of 200 nM. Notably, treatment of HCC15 cells with imatinib or sunitinib had little to no effect on cell survival or colony formation ability (Supplementary Fig. S4A & S4B).

Discussion

The advent of targeted cancer therapeutics emphasizes the significance of identifying genetic alterations that lead to oncogene dependency in tumors. Notably, discovery of tumorigenic NSCLC somatic alterations in proto-oncogenes with existing targeted therapeutic approaches in other cancer types could provide opportunities for immediate adoption of clinically approved treatments.

We have identified recurrent focal amplifications of 4q12 NSCLC. To our knowledge, this is the first description of 4q12 amplification in NSCLC. Systematic statistical analysis suggests that the oncogenes *PDGFRA* and *KIT* are the target of these copy number gains. *KDR*, a VEGFR-family receptor involved in tumor angiogenesis, is adjacent to *KIT* and is also often amplified. Even though it does not lie within the genomic region of statistical significance, it is possible that *KDR* is also a target of 4q12 gain. *PDGFRA*, *KIT*, and *KDR* are often amplified together in brain tumors (33, 34). In GISTs, *PDGFRA* and *KIT* are activated by point mutations (21, 35) and therapies targeting these kinases have proved highly efficacious. Point mutations have also been found in *PDGFRA*, *KIT*, and *KDR* in lung adenocarcinomas however the oncogenicity of these mutations are not known (15).

We further demonstrate that the lung squamous carcinoma cell line NCI-H1703 focally amplifies *PDGFRA* and is dependent on PDGFRA signaling for cell growth. This observation indicates that focal amplifications at 4q12 can lead to aberrant PDGFRA activation and subsequent oncogenic signaling. The role of *KIT* in samples with 4q12 amplification remains unclear due to a lack of appropriate cell line models. Importantly,

amplification of *PDGFRA* and *KIT* presents a potential opportunity for targeted therapy in a subset of NSCLC patients. Treatment of NCI-H1703 cells with *PDGFRA*-specific shRNAs and the small molecule inhibitors imatinib or sunitinib leads to cell death. Interestingly, a phase II clinical trial of sunitinib in previously treated NSCLC patients demonstrated an objective response rate of 11% (7/63 patients) (36). It remains to be seen whether NSCLC patients responsive to sunitinib harbor 4q12 amplification.

The use of a single therapeutic agent to target multiple kinases within a tumor has been previously suggested (37, 38). It is not known whether 4q12 amplification in NSCLC samples leads to simultaneous activation of both *PDGFRA* and *KIT* or only one of the two. Nonetheless, both kinases are known targets of imatinib and sunitinib and it could be presumed that both kinases could be inhibited with one small molecule inhibitor. Thus it is possible that 4q12 amplification in NSCLC combined with immunohistochemistry for *PDGFRA* and/or *KIT* could be sufficient as a marker for sensitivity to imatinib and sunitinib regardless of which oncogenes are activated. This data argues that further testing of these agents in NSCLC patients with 4q12 gain may lead to important advances in the care of these patients.

Acknowledgements

We thank Shantanu Banerji for critical reading of the manuscript. A.D. is supported by the Swiss National Science Foundation Fellowship #PBZHB-106297. This work was supported by National Cancer Institute grants 5R01CA109038 and 5P20CA90578 (M.M.).

References

1. Jemal A, Siegel R, Ward E , *et al.* Cancer statistics, 2008. *CA Cancer J Clin* 2008;58(2):71-96.
2. Weir B, Zhao X, Meyerson M. Somatic alterations in the human cancer genome. *Cancer Cell* 2004;6(5):433-8.
3. Tonon G, Brennan C, Protopopov A , *et al.* Common and contrasting genomic profiles among the major human lung cancer subtypes. *Cold Spring Harb Symp Quant Biol* 2005;70:11-24.
4. Lockwood WW, Chari R, Coe BP , *et al.* DNA amplification is a ubiquitous mechanism of oncogene activation in lung and other cancers. *Oncogene* 2008;27(33):4615-24.
5. Weir BA, Woo MS, Getz G , *et al.* Characterizing the cancer genome in lung adenocarcinoma. *Nature* 2007;450(7171):893-8.
6. Kwei KA, Kim YH, Girard L, *et al.* Genomic profiling identifies TITF1 as a lineage-specific oncogene amplified in lung cancer. *Oncogene* 2008;27(25):3635-40.
7. Yamamoto H, Shigematsu H, Nomura M , *et al.* PIK3CA mutations and copy number gains in human lung cancers. *Cancer Res* 2008;68(17):6913-21.
8. Engelman JA, Zejnullahu K, Mitsudomi T , *et al.* MET amplification leads to gefitinib resistance in lung cancer by activating ERBB3 signaling. *Science* 2007;316(5827):1039-43.
9. Davies H, Hunter C, Smith R, *et al.* Somatic mutations of the protein kinase gene family in human lung cancer. *Cancer Res* 2005;65(17):7591-5.

10. Samuels Y, Wang Z, Bardelli A, *et al.* High frequency of mutations of the PIK3CA gene in human cancers. *Science* 2004;304(5670):554.
11. Stephens P, Hunter C, Bignell G, *et al.* Lung cancer: intragenic ERBB2 kinase mutations in tumours. *Nature* 2004;431(7008):525-6.
12. Naoki K, Chen TH, Richards WG, Sugarbaker DJ, Meyerson M. Missense mutations of the BRAF gene in human lung adenocarcinoma. *Cancer Res* 2002;62(23):7001-3.
13. Takahashi T, Nau MM, Chiba I, *et al.* p53: a frequent target for genetic abnormalities in lung cancer. *Science* 1989;246(4929):491-4.
14. Sanchez-Cespedes M, Parrella P, Esteller M, *et al.* Inactivation of LKB1/STK11 is a common event in adenocarcinomas of the lung. *Cancer Res* 2002;62(13):3659-62.
15. Ding L, Getz G, Wheeler DA, *et al.* Somatic mutations affect key pathways in lung adenocarcinoma. *Nature* 2008;455(7216):1069-75.
16. Packenham JP, Taylor JA, White CM, Anna CH, Barrett JC, Devereux TR. Homozygous deletions at chromosome 9p21 and mutation analysis of p16 and p15 in microdissected primary non-small cell lung cancers. *Clin Cancer Res* 1995;1(7):687-90.
17. Forgacs E, Biesterfeld EJ, Sekido Y, *et al.* Mutation analysis of the PTEN/MMAC1 gene in lung cancer. *Oncogene* 1998;17(12):1557-65.
18. Ji H, Zhao X, Yuza Y, *et al.* Epidermal growth factor receptor variant III mutations in lung tumorigenesis and sensitivity to tyrosine kinase inhibitors. *Proc Natl Acad Sci U S A* 2006;103(20):7817-22.
19. Okudela K, Suzuki M, Kageyama S, *et al.* PIK3CA mutation and amplification in human lung cancer. *Pathol Int* 2007;57(10):664-71.

20. Rikova K, Guo A, Zeng Q , *et al.* Global survey of phosphotyrosine signaling identifies oncogenic kinases in lung cancer. *Cell* 2007;131(6):1190-203.
21. Hirota S, Ohashi A, Nishida T , *et al.* Gain-of-function mutations of platelet-derived growth factor receptor alpha gene in gastrointestinal stromal tumors . *Gastroenterology* 2003;125(3):660-7.
22. Fleming TP, Saxena A, Clark WC , *et al.* Amplification and/or overexpression of platelet-derived growth factor receptors and epidermal growth factor receptor in human glial tumors. *Cancer Res* 1992;52(16):4550-3.
23. Beroukhi R, Getz G, Nghiemphu L , *et al.* Assessing the significance of chromosomal aberrations in cancer: methodology and application to glioma. *Proc Natl Acad Sci U S A* 2007;104(50):20007-12.
24. Hupe P, Stransky N, Thiery JP, Radvanyi F, Barillot E. Analysis of array CGH data: from signal ratio to gain and loss of DNA regions. *Bioinformatics* 2004;20(18):3413-22.
25. Sharma SV, Settleman J. Oncogene addition: setting the stage for molecularly targeted cancer therapy. *Genes Dev* 2007;21(24):3214-31.
26. Greulich H, Chen TH, Feng W , *et al.* Oncogenic transformation by inhibitor-sensitive and -resistant EGFR mutants. *PLoS Med* 2005;2(11):e313.
27. Dutt A, Salvesen HB, Chen TH , *et al.* Drug-sensitive FGF R2 mutations in endometrial carcinoma. *Proc Natl Acad Sci U S A* 2008;105(25):8713-7.
28. Wardelmann E, Merkelbach-Bruse S, Pauls K , *et al.* Polyclonal evolution of multiple secondary K1 T mutations in gastrointestinal stromal tumors under treatment with imatinib mesylate. *Clin Cancer Res* 2006;12(6):1743-9.

29. van Oosterom AT, Judson I, Verweij J , *et al.* Safety and efficacy of imatinib (STI571) in metastatic gastrointestinal stromal tumours: a phase I study. *Lancet* 2001;358(9291):1421-3.
30. Motzer RJ, Hutson TE, Tomczak P , *et al.* Sunitinib versus interferon alfa in metastatic renal-cell carcinoma. *N Engl J Med* 2007;356(2):115-24.
31. Christensen JG. A preclinical review of sunitinib, a multitargeted receptor tyrosine kinase inhibitor with anti-angiogenic and antitumour activities. *Ann Oncol* 2007;18 Suppl 10:x3-10.
32. Karaman MW, Herrgard S, Treiber DK , *et al.* A quantitative analysis of kinase inhibitor selectivity. *Nat Biotechnol* 2008;26(1):127-32.
33. Joensuu H, Pupa M, Sihto H, Tynninen O, Nupponen NN. Amplification of genes encoding KIT, PDGFRA and VEGFR2 receptor tyrosine kinases is frequent in glioblastoma multiforme. *J Pathol* 2005;207(2):224-31.
34. Pupa M, Tynninen O, Sihto H , *et al.* Amplification of KIT, PDGFRA, VEGFR2, and EGFR in gliomas. *Mol Cancer Res* 2006;4(12):927-34.
35. Singer S, Rubin BP, Lux ML , *et al.* Prognostic value of KIT mutation type, mitotic activity, and histologic subtype in gastrointestinal stromal tumors. *J Clin Oncol* 2002;20(18):3898-905.
36. Socinski MA, Novello S, Brahmer JR , *et al.* Multicenter, phase II trial of sunitinib in previously treated, advanced non-small-cell lung cancer. *J Clin Oncol* 2008;26(4):650-6.

37. Sartore-Bianchi A, Ricotta R, Cerea G, Maugeri MR, Siena S. Rationale and clinical results of multi-target treatments in oncology. *Int J Biol Markers* 2007;22(1 Suppl 4):S77-87.
38. Petrelli A, Giordano S. From single- to multi-target drugs in cancer therapy: when aspecificity becomes an advantage. *Curr Med Chem* 2008;15(5):422-32.
39. Perner S, Wagner P, Soltermann A, *et al.* TTF1 expression in non-small cell lung carcinoma: association with TTF 1 gene amplification and improved survival. *J Pathol* 2008.

Figure Legends

Figure 1. Recurrent genomic amplifications of *PDGFRA* and *KIT* in NSCLC samples. *A*, smoothed copy number estimates within chromosome arm 4q in top 200 NSCLC samples (columns; ordered by amplification of 4q12). The color scale ranges from blue (deletion) to red (amplification) with estimated copy numbers shown. Grey regions represent the centromere or absence of SNP copy number data. Plotted GISTIC G-scores on the right are from all available samples. The green line on the GISTIC plot represents a significance threshold of 0.25 false discovery rate q-value. *B*, magnified view of smoothed copy number estimates from the centromere to 61 Mb on chromosome 4 from 31 NSCLC samples having amplification greater than 2.46 copies (log₂ ratio of 0.3) at 4q12. Samples are sorted according to the maximum copy number estimate for *PDGFRA* and *KIT*. Solid and dashed lines indicate positions of *PDGFRA* and *KIT*, respectively. Color scale as in panel *A*. *C*, FISH for *PDGFRA* (red) and chromosome 4 reference probe (green) displaying high-level and low-level gain of *PDGFRA* in the lung squamous cell carcinoma samples CTMA4 and TMA148, respectively. A lung adenocarcinoma sample, CTMA11, with no amplification at *PDGFRA* is shown on the right for reference. Nuclei are stained with 4,6-diamidino-2-phenylindole (DAPI; blue).

Figure 2. *PDGFRA*-amplified NSCLC cells are addicted to PDGFRA activity. *A*, PDGFRA expression in NCI-H1703 and HCC15 was confirmed by immunoblotting using actin as a loading control (left panel). shRNA constructs used to knockdown *PDGFRA*

expression were packaged into lentiviruses and used to infect NCI-H1703 and HCC15 cells. Anti-PDGFR α immunoblot shows that hairpins #1, #3 and #5 efficiently knock down endogenous PDGFR α expression in NCI-H1703 cells. Actin is included as a loading control. NI, no infection. shGFP, control hairpin specific for green fluorescent protein used as a negative control (right panel). *B* and *C*, infection with three independent hairpins (#1, #3 and #5) did not inhibit cell survival of HCC15 cells as assessed by WST assay (*B*) but did inhibit survival of NCI-H1703 cells over expressing wild type PDGFR α (*C*). All results normalized to survival of cells infected with shGFP.

Figure 3. PDGFR α tyrosine kinase activity is essential in NSCLC cells. *A*, PDGFR α is constitutively phosphorylated, with or without PDGF ligand, in NCI-H1703 cells, as compared with HCC15 cells. Stimulation with PDGF was carried out for 20 minutes at 37°C with 100 ng/ml of PDGF. Treatment of these cell lines for 40 minutes with 2 μ M PDGFR kinase inhibitor imatinib and sunitinib inhibits basal phosphorylation, as evidenced by immunoblotting with anti-phospho-PDGFR α (upper panel). Similar levels of expression of PDGFR α are confirmed by immunoblotting with anti-PDGFR α (middle panel) using actin as a loading control (lower panel). *B* and *C*, treatment with the indicated concentrations of imatinib and sunitinib inhibited survival of NCI-H1703 cells, but not of HCC15 cells, as determined by WST assay performed after 4 days treatment. IC₅₀s are indicated.

Supplementary Materials

Figure S1. Raw (black) and smoothed (red) copy number data for NCI-H1703 defining a 4q12 amplification of *PDGFRA*. Estimated copy number values (y axis) are plotted according to position on chromosome 4 (x axis). Genomic positions of *SCFD2*, *FIP1L1*, *LNX1*, *CHIC2*, *PDGFRA*, and *KIT* are shown along the x axis.

Figure S2. Western blot analysis of *PDGFRA* in six different 4q12 amplified (NCI-H1703, NCI-H661, NCI-H1819, NCI-H1838, NCI-H23 and HCC366) and one non-amplified (HCC15) NSCLC cell lines. NCI-H1703 cells show increased *PDGFRA* expression as compared to other NSCLC cell lines.

Figure S3. Anchorage independent growth of NCI-H1703 cells is dependent on *PDGFRA* activity. *A* and *B*, infection with three independent hairpins (#1, #3 and #5) inhibited colony formation in soft agar in NCI-H1703 cells over expressing wild type *PDGFRA*, but not HCC15 cells. All results are normalized to survival or colony formation by cells infected with shGFP.

Figure S4. Treatment of NCI-H1703 cells with kinase inhibitors decreases colony formation ability. *A* and *B*, treatment of NCI-H1703 cells with imatinib and sunitinib resulted in a marked decrease in colony formation in soft agar with IC50s in the 20 nM and 81 nM range, respectively, whereas similar treatment of the HCC 15 cell line without *PDGFRA* amplification had no significant effect.

Figure 1.

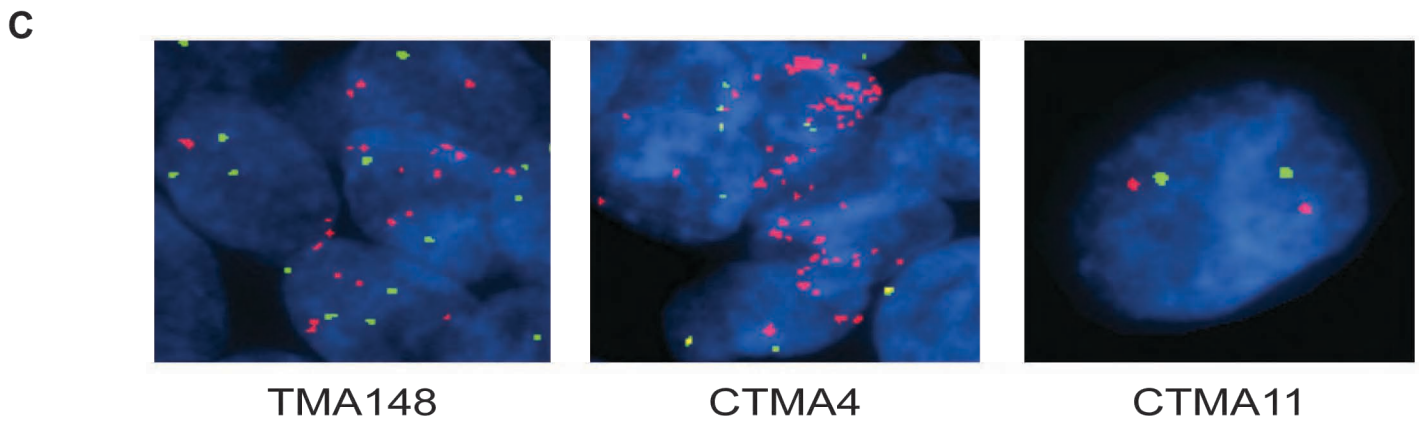
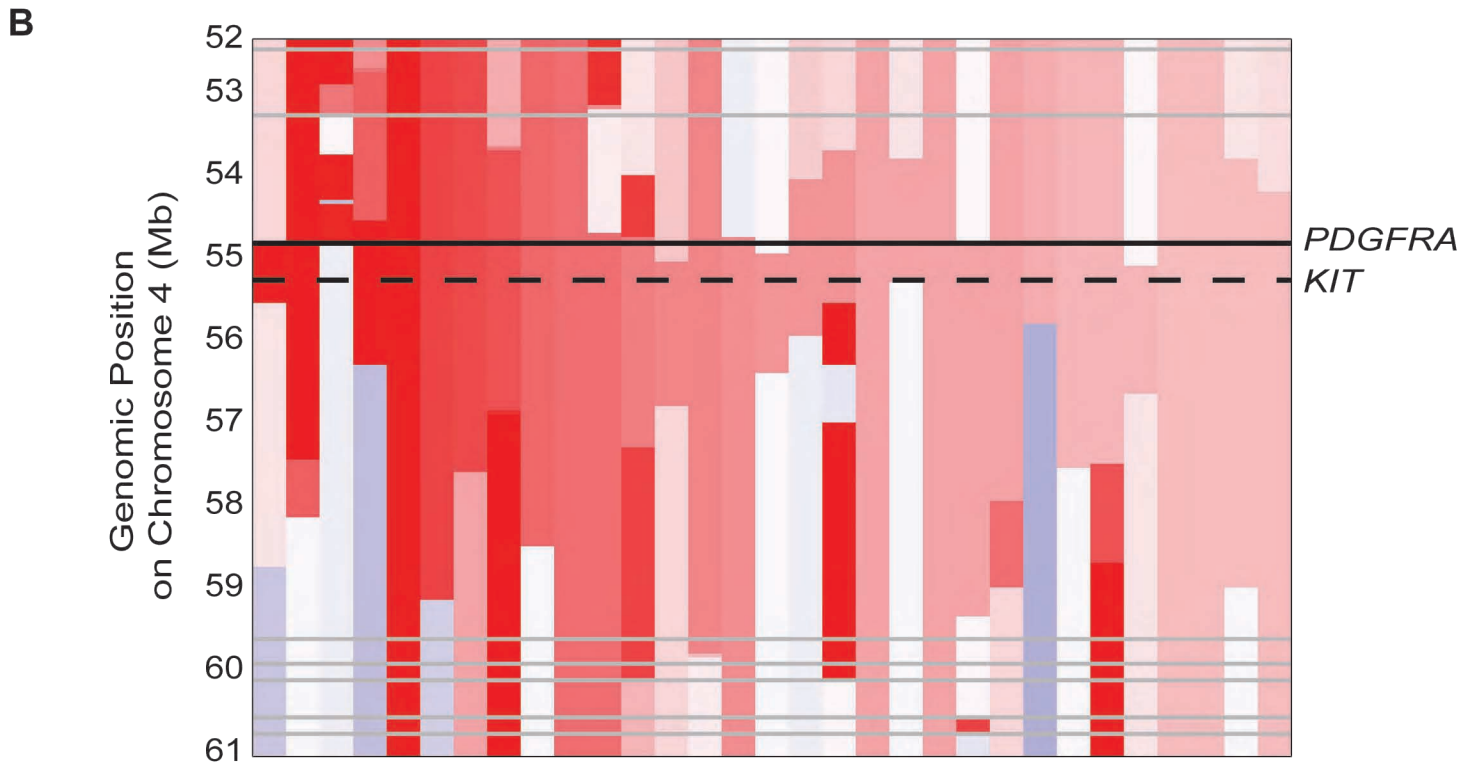
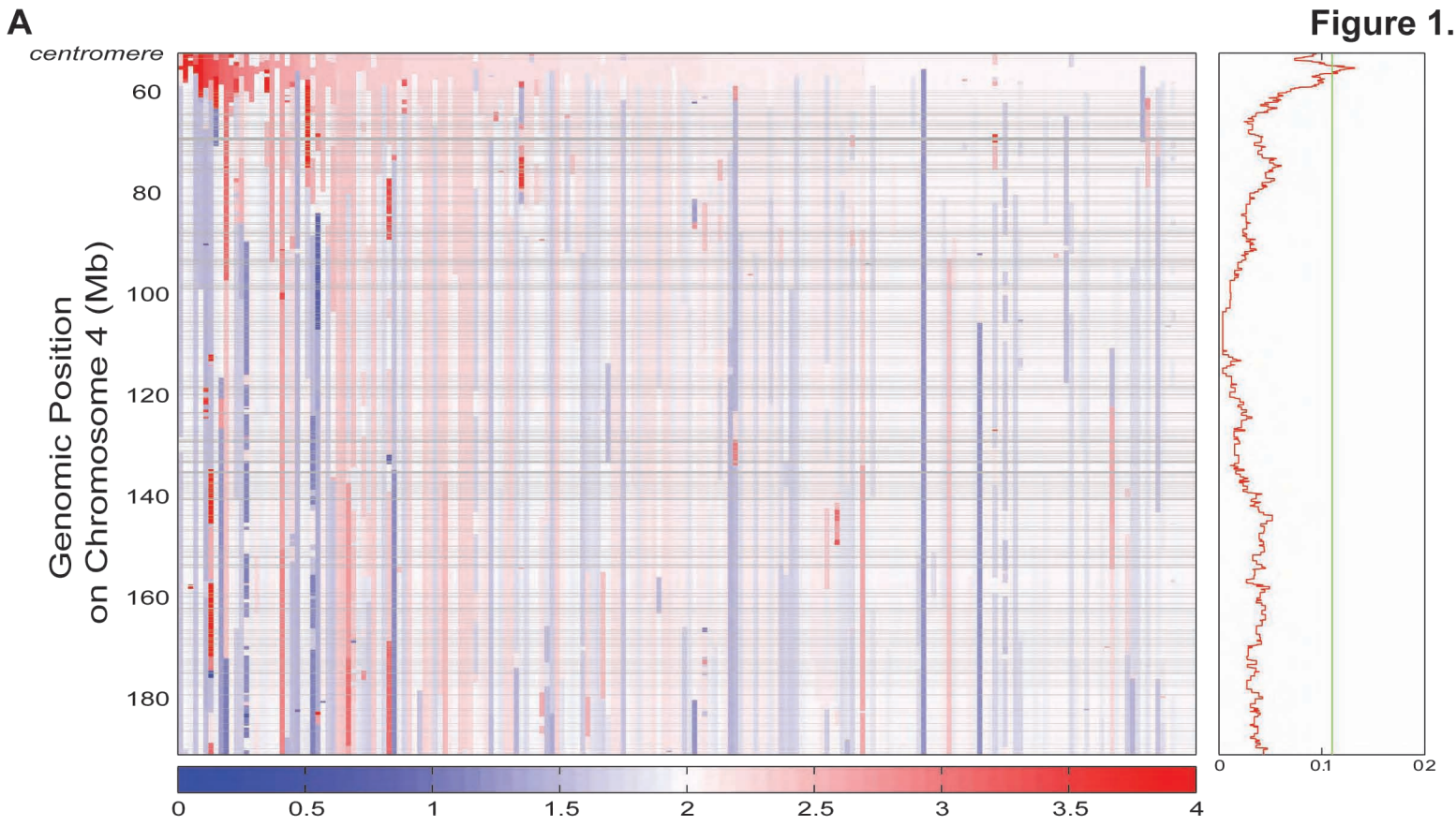
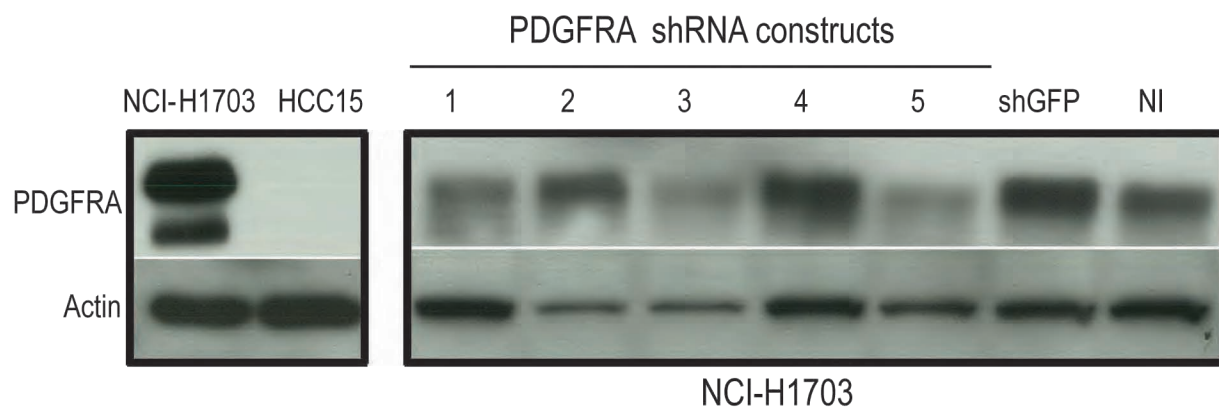
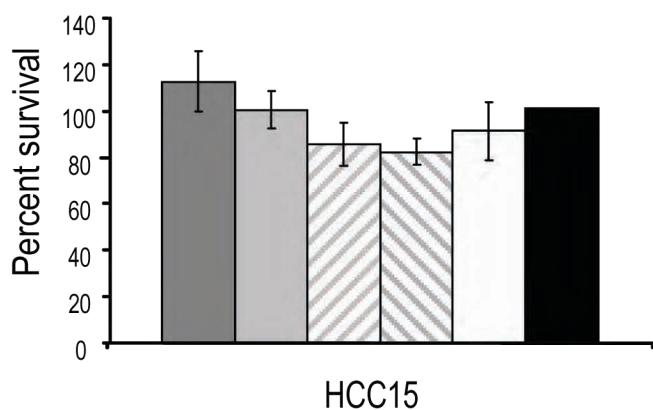


Figure 2.

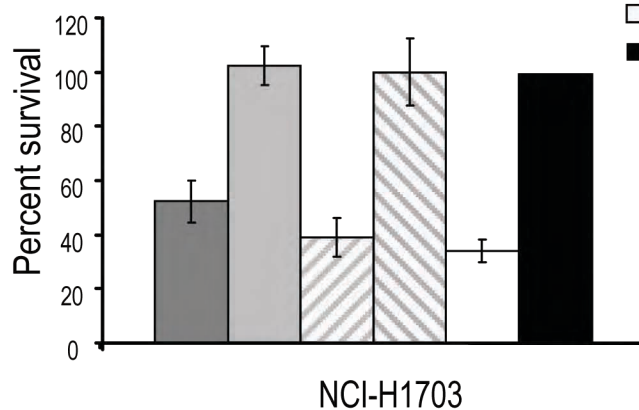
A



B

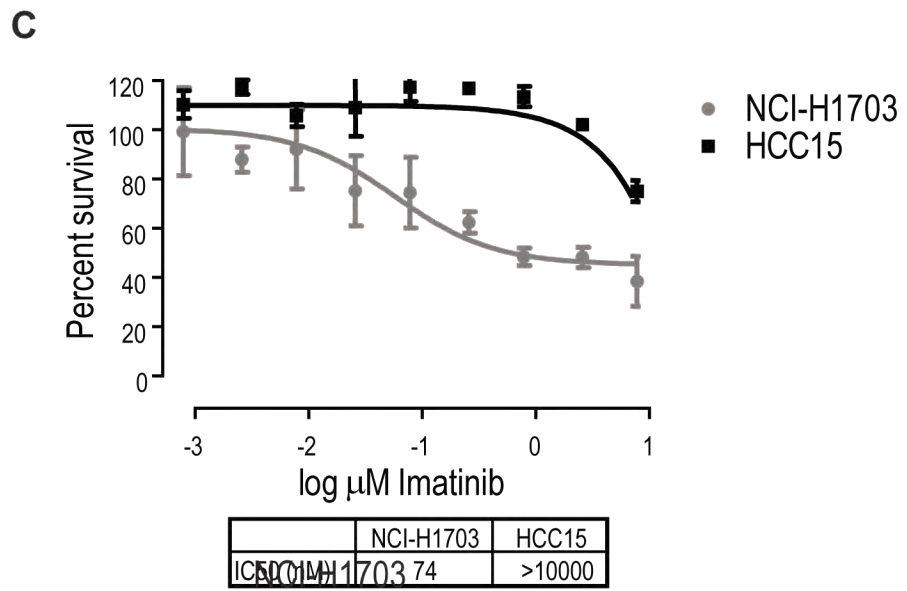
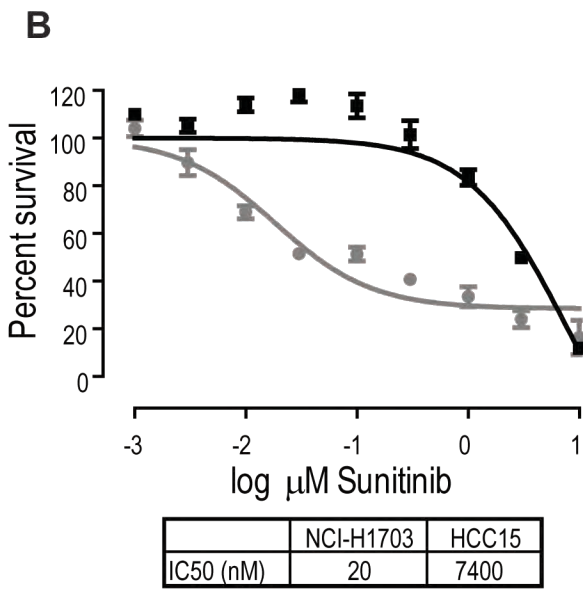
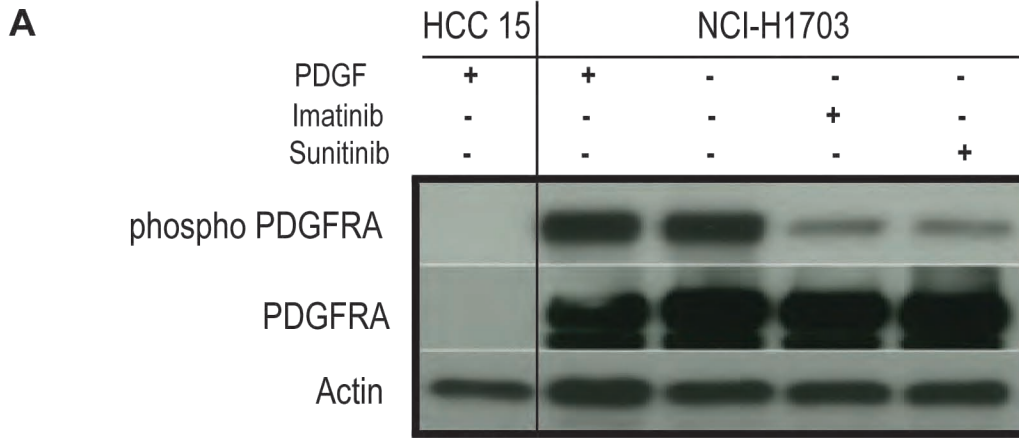


C



- shPDGFRA # 1
- shPDGFRA # 2
- ▨ shPDGFRA # 3
- ▨ shPDGFRA # 4
- shPDGFRA # 5
- shGFP

Figure 3.



**NON-SMALL CELL LUNG CANCER PATIENT SURVIVAL WHEN ASSESSED AS A FIRST ORDER
NONLINEAR PROCESS: EFFECT OF THERAPY AND STAGE**

David J. Stewart

University of Texas MD Anderson Cancer Center

Send reprint requests to:

David J. Stewart, MD, FRCPC

Professor of Medicine

Deputy Chair, Department of Thoracic/Head & Neck Medical Oncology

University of Texas MD Anderson Cancer Center

1515 Holcombe Blvd, Unit 432

Houston, TX 77030

Telephone: (713) 692-6363

Fax: (713) 796-8655

E-mail: dstewart@mdanderson.org

Key words: log-linear plots, nonlinear regression analysis, non-small cell lung cancer

Running Title: NSCLC survival as a first-order process

Acknowledgements: This work was conducted under the auspices of the Lung Cancer Program of MD Anderson Cancer Center, and was supported in part by Cancer Center Support Grant number 5-P30 CA16672-32 and by Department of Defense grant number W81XWH-07-1-0306

ABSTRACT

Background: With first order kinetics, inflection points on semilog plots imply different limiting processes.

Methods: Kaplan-Meier overall and progression-free survival curve heights from selected NSCLC publications were measured manually. Nonlinear exponential decay was assessed using GraphPad Prism.

Results: Our preliminary observations, if confirmed, would suggest the following: Palliative front-line

chemotherapy: Twelve of 15 curves for untreated controls and single agents were fit by 2-3-phase decay models while 42 of 48 curves for multidrug regimens were fit only by one-phase models. Rapid-decay-phase curves were convex in 0% vs 54%, respectively ($p < 0.001$). The paucity of inflection points suggests outcome is driven primarily by continuous variables. Hence, individual patient outcome might be predicted better using continuous variables than by dichotomizing variables. Curve convexities suggest discontinuation of combination chemotherapy after 4-6 cycles “synchronizes” patient death. Characterizing patients dying along the leading convex edge might identify subgroups that would benefit from maintenance therapy. Adjuvant

Chemotherapy: Overall half-life was longer with adjuvant chemotherapy than with matched controls ($p = 0.03$), apparently more from a shift of rapid-phase patients into the potentially-cured slow-decay-phase fraction than from prolongation of survival of patients who die despite therapy. Stage: Two-phase-decay curves predominated for stage II-IV populations. Rapid-decay-phase half-life shortened while rapid-phase size increased with increasing stage ($p < 0.04$), suggesting molecular characteristics that drive tumor cell growth rates determine not only patient survival time but also stage at presentation.

Conclusions: Future studies will explore adaptations of mixture distribution or nonlinear mixed effects modelling using individual patient data for multivariate nonlinear exponential decay survival analyses.

INTRODUCTION:

Survival analyses in cancer clinical trials generally use Kaplan-Meier plots in reporting survival. Differences between groups are generally assessed by comparing median overall survival time (OS), progression-free survival time (PFS), proportion of patients alive at a particular time (eg, 1 year) or by calculating hazard ratios, etc.

Biological processes such as drug disappearance¹ and enzymatic reactions² may follow first order kinetics, with disappearance of a given proportion of remaining drug, substance, etc, in a given time, rather than there being disappearance of a given quantity of substance per unit time. For processes such as drug disappearance that follow first order kinetics, plotting linear effect vs time will give a curved line, while plotting log effect vs time will give a straight line, and the slope of the line can be used to calculate the half-life¹. In pharmacokinetic (PK) analyses, presence of an inflection point in the log-linear curve indicates a distinct process driving the rate of drug disappearance. For example, the rate of drug disappearance during the initial portion of the curve (the “distribution phase”) is driven by drug uptake into tissues, the second portion (following the first inflection point) may be driven by metabolism/excretion, and the third portion (following a second inflection point) may be driven by saturation of metabolism/excretion processes, by redistribution of drug from tissues to blood, etc¹. Additional inflection points and curve segments may also occur with some biological processes.

We hypothesized that patient survival variables may in many instances also follow first order kinetics, and in these instances, plotting log % OS, PFS, etc vs time should give a straight line. We hypothesized that dichotomous variables that drive prognosis (eg, variables that are present vs absent or that are above vs below a threshold) would give an inflection point on a plot of log % OS or PFS, etc, vs time in the same manner that different processes give inflection points on a PK curve, while continuous variables that affect prognosis would alter the slope of the survival curve without giving an inflection point. If these hypotheses were correct, then inflection points on semilog plots of survival variables could give insight into the minimum number of dichotomous variables that are driving prognosis, and nonlinear regression analyses analogous to

compartmental PK analyses might permit one to define the proportion of the initial population accounted for by each subgroup and the half-life of each distinct subgroup.

With respect to standard analyses that use similar approaches, proportional hazards models generally average the entire curve, without deriving specific information from curve inflection points. Nonlinear mixed effects modelling³ and mixture distribution analyses⁴⁻⁶ have been used to estimate proportion of patients cured of a malignancy, and there is at least a limited experience using them to assess impact of therapy or prognostic variables^{5, 7, 8}.

In this manuscript, we used nonlinear regression exponential decay analyses of Kaplan-Meier OS and PFS curves from published non-small cell lung cancer (NSCLC) clinical trials as a preliminary feasibility assessment of the potential utility of such approaches in assessment of impact of treatment and prognostic variables on patient outcome. In embarking on the exercise, we anticipated that we would detect multiple inflection points on most curves, in keeping with there being several dichotomous variables driving prognosis.

METHODS:

In this preliminary feasibility assessment, we used OS and PFS curves from selected NSCLC published trials involving front-line chemotherapy in advanced disease⁹⁻²⁶, adjuvant chemotherapy in resected stage I-III disease^{12, 27-37} and survival as a function of stage^{10, 12, 20, 26-30, 32-44}, and also used curves from best supportive care arms from 2 second line therapy trials^{45, 46}. From printouts of these survival curves, height of curve above baseline was measured in mm for different time points from initiation of therapy. Height for each time point was converted to a percent of the curve height at time 0. We then used one-phase, 2-phase and 3-phase exponential decay programs in GraphPad Prism version 5.0 to model the data. The value of Y at time = 0 was set as a constant at 100% and the plateau phase (ie, the value of Y at time = infinity) was set as a constant at 0%. Curves were considered to conform to a one-phase model rather than a two-phase model (or to a two-phase model rather than a three-phase model) if one of the phases accounted for <1% of the patient population, or if half-lives for two phases differed by <10%.

Across studies, the median percent of patients in each decay phase and the median half-life of the rapid-decay phase were calculated for different groups. Groups were compared using Wilcoxon signed rank tests for matched groups (patients treated with adjuvant therapy vs control groups from the same study), and Kruskal-Wallis testing was used for comparisons of non-matched groups. Chi-square testing with Yates correction was used to compare groups with respect to proportion of curves fit by 2-3 phase decay models vs proportion fit by only one phase decay models, and with respect to proportion of curves with major convexities.

RESULTS:

Some typical curve shapes are outlined in Figure 1. Of 172 OS or PFS curves analyzed, 72 (42%) were fit by one-phase exponential decay models, 92 (53%) were fit by two-phase exponential decay models (single inflection point) and 8 (5%) were fit by three-phase exponential decay models (two inflection points). In Table 1 are characteristics of exponential decay curves for different patient groups. The total number in the table exceeds 172 since some curves were included both in assessments of effect of stage as well as assessment of effect of therapy.

Many of the curves had small shoulders at early follow-up time points. For OS, these small shoulders were probably related in part to selection of patients with relatively good performance status. For PFS, the small shoulders may have been related primarily to the fact that first re-evaluation of tumor status generally didn't occur until 6-8 weeks after therapy initiation. Refitting the data after omitting points on the early shoulder in most cases did not alter conclusions about number of curve inflection points (data not shown).

Overall, 41 of the curves (24%) had substantially more than just an initial shoulder, and appeared to be convex over much of the rapid decay phase. Examples are presented in Figure 2. Curve characteristics varied with therapy (Table 2). In patients on front-line chemotherapy trials for advanced disease, 12 of 15 (80%) OS or PFS curves from patients receiving best supportive care or single agent chemotherapy could be fit by 2-3 phase decay models, compared to only 6 of 48 (12.5%) curves from patients treated with regimens involving 2 or more agents ($p < 0.001$). The proportion of curves fit by only a single phase decay model increased with the number of agents used in therapy. In addition, 54% of curves from patients treated with regimens involving ≥ 2

agents appeared to have convex rapid decay phases, compared to none of 15 curves for patients treated with best supportive care or single agent therapy ($p < 0.001$).

Proportion of patients in the rapid-decay phase and rapid-decay phase half-lives for different patient groups are presented in Table 3. For 2- and 3-phase decay curves, the models frequently hit constraints with respect to the half-life of the slow-decay phase, and the slow-decay phase half-lives were generally very long with very wide 95% confidence intervals, and hence are not presented in this preliminary analysis. For curves that could be fit by either a 2- or 3-phase-decay model, data from the 2-phase-decay model were used for Table 3 and for the accompanying analyses. In therapy of advanced disease, the rapid-decay phase was larger, but the alpha half-life was longer with regimens involving ≥ 2 agents than with best supportive care or with single agent therapy, in keeping with the high proportion of curves from patients treated with multi-agent regimens that could be fit with only one-phase decay models.

With adjuvant chemotherapy, there was a smaller PFS rapid-decay phase with adjuvant chemotherapy than in control groups and a trend towards a smaller OS rapid-decay phase. Median alpha half-life (ie, half-life of the rapid-decay phase) was slightly longer with adjuvant chemotherapy for both OS and PFS, although this was not statistically significant. When one-phase exponential decay half-lives were calculated for OS and PFS from curves in studies of adjuvant chemotherapy vs matched controls, both OS and PFS half-lives were significantly longer in the adjuvant groups than in the matched control groups (Table 4).

With respect to stage, 6 of 10 (60%) OS curves from stage I untreated patients were best fit by one-phase decay models, compared to 4 of 22 (18%) OS curves from stage II-IV untreated patients (Table 1). Hence, stage I curves tended to be characterized by one-phase decay with very long half-life. For stages II-IV, the proportion of patients in the rapid decay phase increased and the half-life of the rapid decay phase decreased with increasing stage (Table 4).

DISCUSSION:

This preliminary assessment suggests that it may be feasible to use nonlinear exponential decay analysis to assess patient survival variables, and it also suggests that specific hypotheses may be generated by this approach, such as the ones outlined below. It is stressed that substantially more work will be needed to determine whether or not our observations were driven solely by methodology-related artefact, but the results suggest that adaptations of procedures such as mixture distribution analyses and nonlinear mixed effects modelling to permit nonlinear exponential decay analysis of censored individual patient data could potentially provide useful insights that might not be as apparent with more usual survival analysis approaches.

We had expected that we would routinely detect multiple inflection points on the curves, and we found substantially fewer inflection points than anticipated. The sparseness of curve inflection points suggests to us that most prognostic variables function as continuous variables affecting curve slope, rather than functioning as dichotomous variables that slot a patient into a specific patient subgroup. Hence, apparently dichotomous prognostic variables like gender may simply be surrogates for various continuous variables. Even with prognostic variables that are known to be continuous, it is common practice to dichotomize them around a cut-point. While this dichotomization may be useful in helping identify factors with prognostic significance, the paucity of survival curve inflection points would lead us to hypothesize that models that use continuous variables would do a better job of predicting outcome of individual patients than would models that dichotomize prognostic variables. For example, in NSCLC, it may be useful to consider actual tumor size rather than whether it is T1 (<3 cm diameter) or T2 (> 3cm), to consider number and bulk of nodes involved rather than just grouping them as N0 to N3, and to explore use of some measure of hormonal status rather than simply grouping patients as male vs female. Clinicians generally prefer to have simple “yes-no” rules in deciding management approaches, but it may be time to consider moving beyond this.

The higher proportion of advanced disease studies with curves conforming to one-phase decay curves when ≥ 2 drugs are used compared to when 0-1 drugs are used and when compared to assessments of impact of stage or effect of adjuvant chemotherapy for early stage disease could have arisen by chance, by inclusion of more than one curve from some studies, or through observer bias. However, one biologically plausible

hypothesis that could explain it is that the routine practice of discontinuing chemotherapy after 3-6 cycles may be synchronizing patient death. Randomized trials have generally failed to identify a benefit of continuing chemotherapy beyond this point⁴⁷⁻⁵⁰, but it is possible that there may be specific subpopulations that would benefit, and some studies of maintenance chemotherapy have suggested that it may be of benefit in some patients⁵¹. It would be of interest to assess tumor molecular characteristics and clinical features for patients dying along the leading edge of the convexity to determine if one might identify such a specific subpopulation that would benefit from maintenance chemotherapy.

Adjuvant chemotherapy was associated with longer OS and PFS half-lives compared to controls when only one-phase exponential decay models were used, in keeping with randomized trials^{27, 37} and meta-analyses⁵² that indicate a benefit of adjuvant chemotherapy in resected NSCLC. When we used for each study the model with the largest number of phases that could be fit successfully, adjuvant therapy (compared to untreated matched controls) was associated with a significant reduction in the proportion of patients in the rapid decay phase for PFS and a similar trend for OS. This suggests that the adjuvant chemotherapy is actually shifting patients into the cured fraction and not just prolonging survival. The slight trend towards prolongation of the alpha half-life would suggest that it also may be somewhat prolonging survival of patients who are not cured.

While proportion of patients in the rapid-decay phase decreased from stage II to stage IV, it was high in stage I patients. This is probably due to insufficient follow up time in several of the stage I studies to permit detection of a slower decay phase. The shortening of the alpha half-life as one goes from stage I to stage IV disease and the increase in proportion of patients in the rapid decay phase as one goes from stages II through IV suggests that molecular characteristics associated with rapid tumor cell growth increase the proportion of patients who are destined to die of disease while at the same time decreasing survival time of those who eventually die of NSCLC. Hence, one might hypothesize that a patient with recurrent stage I NSCLC would have more indolent disease than would a patient with equal bulk disease that was stage IV at presentation, and that the two would tend to have different molecular characteristics and possibly different treatment susceptibilities. In addition, this would suggest that molecular characteristics drive both prognosis and stage-*i.e.*, a patient with relatively indolent disease might tend to have it discovered when it was still in an early stage

since it would stay at an early stage longer, while patients with more rapidly growing disease would be less likely to have the disease discovered by chance while it was still early stage. Hence, this is in keeping with the concept that stage at presentation is a surrogate for tumor cell growth rate in addition to being a surrogate for presence of micrometastatic disease, and that tumor cell molecular characteristics will eventually supplant stage as the important determinant of tumor management strategies.

Adaptations of methods such as mixture distribution or nonlinear mixed effects modelling to assess exponential survival decay using individual patient data could prove useful in a variety of ways. Instead of just assessing the impact of a prognostic or treatment variable on outcomes such as median survival or percent survival at a specific time, these approaches could potentially be used to assess impact of the variables on a variety of individual outcome components such as proportion of patients shifted from a poor outcome groups to better outcome groups, half-life of each subgroup, etc. It could also be used to estimate maximum achievable survival time for members of each subgroup, proportion of the total population accounted for by each subgroup at different time points along the survival curve, and time beyond which one may have a relatively homogeneous population of good prognosis patients. This ability to predict the point at which the population becomes homogeneous could be particularly useful in helping identify molecular factors associated with good prognosis. We plan to explore this further using individual patient data.

Table 1. Characteristics of exponential decay curves for different patient groups					
	No. Curves				
	1 phase decay	2 phase decay	3 phase decay	Rapid Phase Curve Convexity ^a	
				Yes	No
Front Line Chemotherapy for Advanced Disease:					
Overall survival:					
Best supportive care ^b	1	4	1	0	6
Single agent	2	3	0	0	5
Two-drug regimen	22	4	2	13	15
≥ Three-drug regimen	7	0	0	5	2
Progression-free survival:					
Best supportive care ^c	0	2	0	0	2
Single agent	0	1	0	0	1
Two-drug regimen	11	0	0	6	5
≥ Three-drug regimen	2	0	0	2	0
Adjuvant Chemotherapy for Stage I-III Resected Disease:					
Overall survival:					
Adjuvant chemotherapy	6	17	1	5	19
Control	8	12	1	3	18
Progression-free survival:					
Adjuvant chemotherapy	1	11	2	1	13
Control	1	11	0	0	12
Stage^d:					
Overall survival:					
Stage I	6	5	0	1	10
Stage I-II ^e	0	1	0	0	1
Stage I-III ^e	1	8	0	0	9
Stage II	1	6	1	2	6
Stage III	2	6	2	2	8
Localized, incomplete resection	0	1	0	0	1
Stage IV	1	4	1	1	5
Progression-free survival:					
Stage I	1	1	0	0	2
Stage I-II ^e	0	1	0	0	1
Stage I-III ^e	0	2	0	0	2
Stage II	0	1	0	0	1
Stage III	0	2	0	0	2
Localized, incomplete resection	0	5	0	0	5
Stage IV	0	2	0	0	2
Other subgroup analyses:					
Overall survival	10	10	1	3	18
Progression-free survival	0	2	0	0	2
<ul style="list-style-type: none"> a. Convexity that is more than simply a shoulder on the initial part of the curve b. Includes 2 curves from best supportive care arms of studies of second line therapies c. Includes 1 curve from best supportive care arm of a study of second line therapy d. From publications on survival vs stage and from control arms of adjuvant studies and best supportive care arms of studies of chemotherapy for advanced disease e. Not broken down by individual stage 					

Table 2. Effect of therapy details on curve characteristics			
No. drugs	No. curves	No. with 2-3 phase decay ^a	No. with convexity ^a
0	8	7	0
1	7	5	0
2	39	6	19
≥ 3	9	0	7
a. $p < 0.001$ for 0-1 drugs vs ≥ 2 drugs (Chi-square with Yates correction)			

Table 3. Comparison of proportion of patients in rapid-decay phase and rapid-decay-phase half-lives across groups.

Group	No. studies	% Rapid Decay		p	Alpha half-life		p
		Median	Range		median	range	
First line chemotherapy for advanced NSCLC:							
OS: Best supportive care	6	96.7	82.6-100	0.006 ^{a,b}	4.4	3.8-4.7	0.0008 ^{a,b}
OS: Single Agent	5	94.8	66.4-100		4.9	1.5-7.1	
OS: Two Drugs	28	100	12.9-100		7.5	2.5-11.5	
OS: \geq Three drugs	7	100	100-100		6.8	4.6-12.2	
PFS: Best supportive care	2	94.5	91.9-97.1	0.0019 ^{a,b}	2.7	2.4-3.0	0.06 ^{a,b}
PFS: Single Agent	1	14.6	-		2.2	-	
PFS: Two Drugs	11	100	100-100		3.9	3.2-5.2	
PFS: \geq Three drugs	2	100	100-100		4.5	3.6-5.4	
Adjuvant chemotherapy vs control ^e :							
OS adjuvant chemo	24	89.3	1.3-100	0.12 ^{c,d}	63.7	4.4-245.0	0.47 ^{c,d}
OS controls	24	94.4	43.9-100		45.1	7.0-339.0	
PFS adjuvant chemo	13	68.2	29.9-100	0.02 ^{c,d}	12.6	5.0-58.2	0.54 ^{c,d}
PFS controls	13	85.0	44.0-100		10.9	5.1-98.6	
Survival by Stage ^f :							
OS: Stage I	11	100	40.6-100	0.23 ^{a,b} (0.04 ^{a,h})	105.6	15.3-339	0.0001 ^{a,b} (0.0004 ^{a,h})
OS: Stage I-II ^g	1	65.6	-		34.8	-	
OS: Stage I-III ^g	9	80.8	4.3-100		12.6	6.6-59.3	
OS: Stage II	8	79.1	49.4-100		19.1	12.7-58.5	
OS: Stage III	10	92.5	62.8-100		11.5	6.6-33.6	
OS: Stage IV	6	96.9	82.9-100		4.3	3.1-5.9	
PFS: Stage I	2	87.3	74.6-100	0.19 ^{a,b}	69.4	40.1-98.6	0.13 ^{a,b}
PFS: Stage I-II ^g	1	53.5	-		11.0	-	
PFS: Stage I-III ^g	2	33.7	23.3-44.0		8.5	6.1-10.9	
PFS: Stage II	1	72.0	-		13.2	-	
PFS: Stage III	2	77.5	77.5-85.0		8.0	6.0-10.0	
PFS: Stage IV	2	94.5	91.9-97.1		2.7	2.4-3.0	

a. Kruskal-Wallis

b. comparison across groups

c. Wilcoxon signed rank test

d. vs matched control group

e. Total numbers differ from Table 1 since control arms were included more than once here if compared to more than one chemotherapy arm from the same trial, while being included only once in Table 1. Total numbers differ from Table 3 since Table 3 included only single OS or PFS curves from each trial, while Table 4 also includes curves from subgroup analyses.

- f. From studies on effect of stage or on untreated control arms from adjuvant therapy studies and studies of therapy for advanced disease
- g. from studies for which data were not broken down by individual stages
- h. comparison across stages II to IV

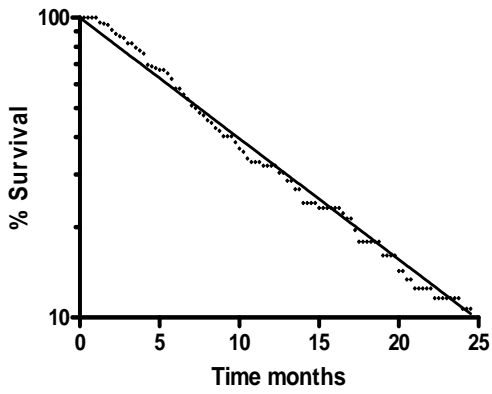
Table 4. Overall and progression-free survival half-lives with adjuvant chemotherapy for stage I-III disease ^a				
Group	No. Studies	Overall half-life		P
		Median	Range	
Overall survival:				
Adjuvant chemotherapy	13	61.9	20.2-299.0	0.0002 ^b
Matched control	13	48.6	7.0-226.0	
Progression-free survival:				
Adjuvant chemotherapy	6	69.4	17.0-221.0	0.03 ^b
Matched control	6	54.7	8.8-98.6	
a. Curves for adjuvant therapy compared to matched control curves, using half-lives derived from one-phase exponential decay models b. Wilcoxon signed rank test comparing adjuvant therapy curve to matched control curve				

Figure 1. Typical one-three phase decay survival curves showing both semilog plots and the corresponding linear plots

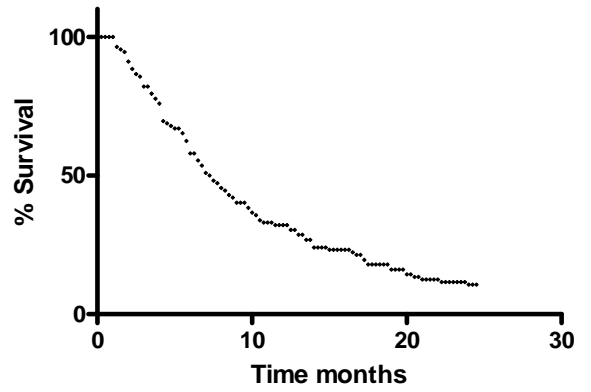
Figure 2. Examples of semilog plots with convex rapid phases (with and without a possible second phase), and corresponding linear plots

Figure 1. Representative curve types (linear vs semilog plots)

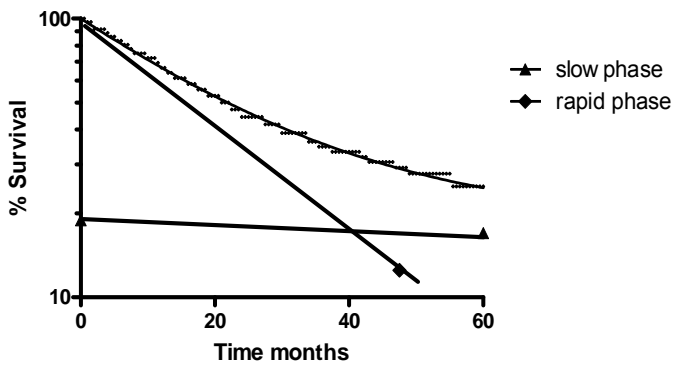
1 phase (semilog)



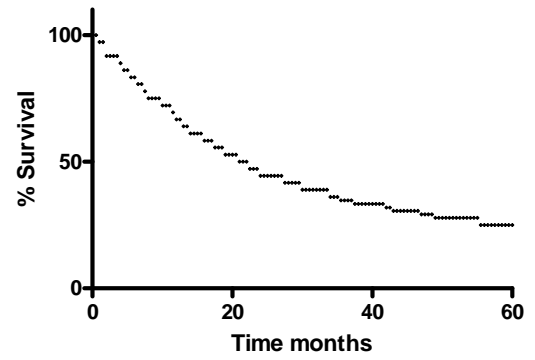
1 phase (linear)



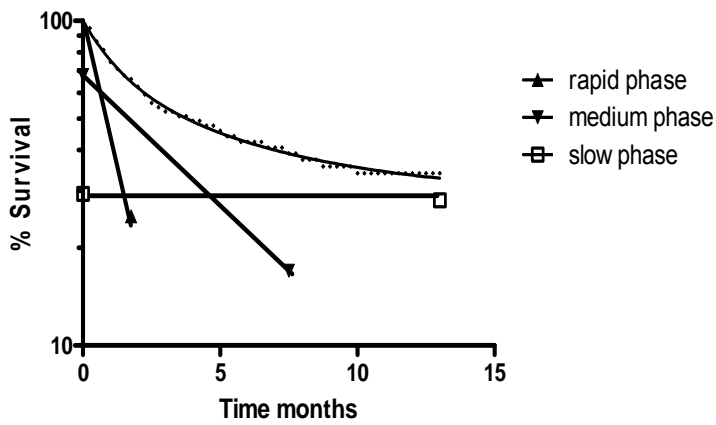
2 phase (semilog)



2 phase (linear)



3 phase (semilog)



3 phase (linear)

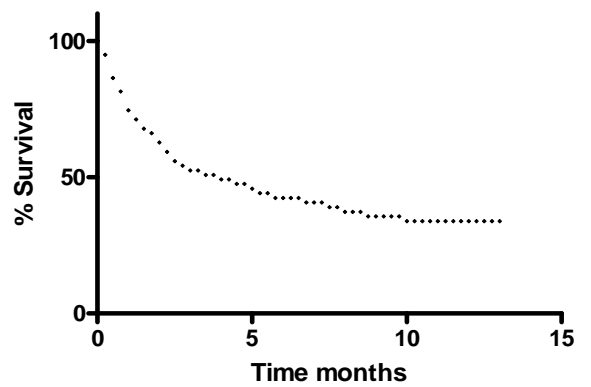
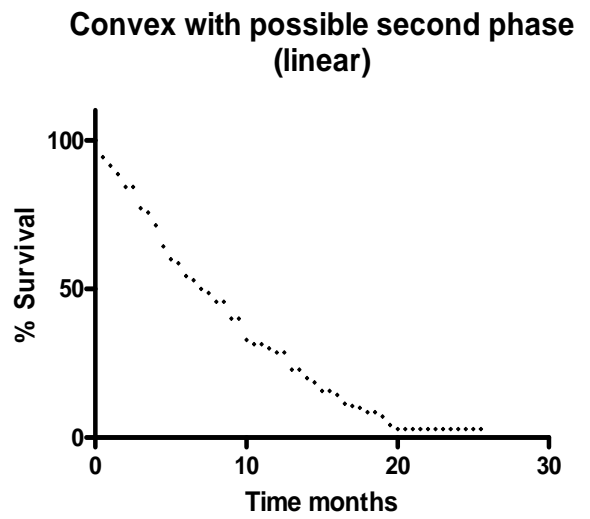
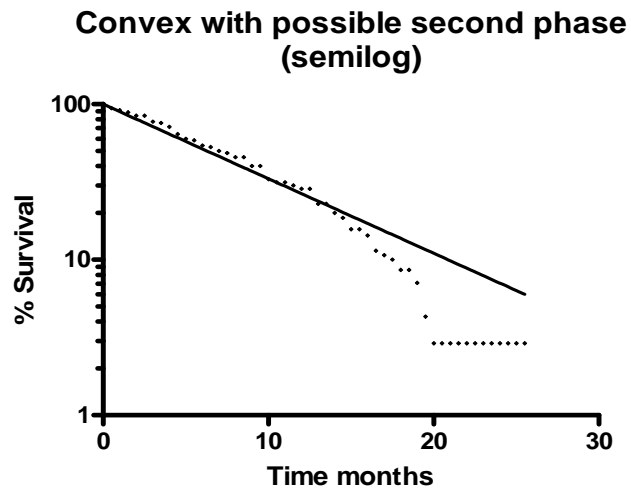
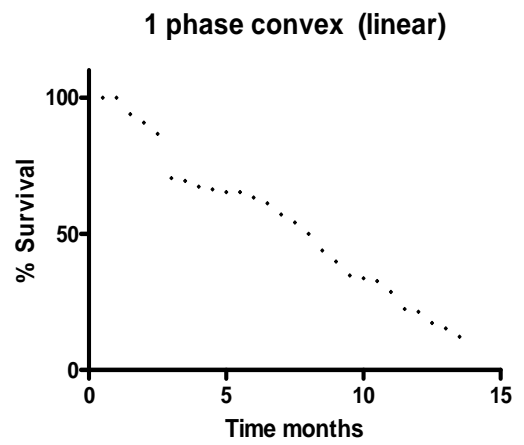
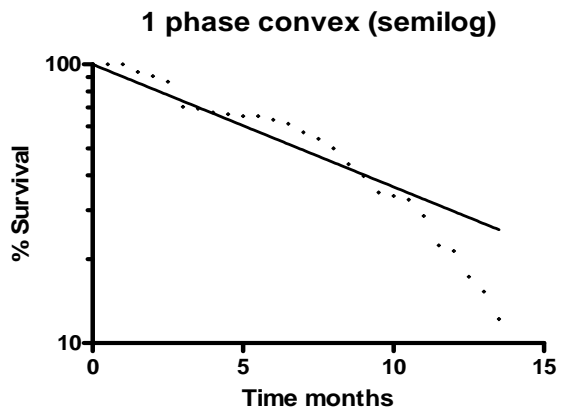


Figure 2. Examples of curves with convex rapid phase



REFERENCES:

1. Benet L, Mitchell J, Sheiner L. Pharmacokinetics: The Dynamics of Drug Absorption, Distribution, and Elimination. In: Goodman Gilman A, Rall T, Nies A, Taylor P, eds. Goodman and Gilman's The Pharmacological Basis of Therapeutics. Eighth ed. New York, NY: Pergamon Press; 1990:3-32.
2. White A, Handler P, Smith E. Enzymes. II Kinetics, Inhibition, Metabolic Inhibitors, Control of Enzymatic Activity. In: White A, Handler P, Smith E, eds. Principles of Biochemistry. New York, NY: McGraw-Hill; 1968:223-46.
3. Law NJ, Taylor JM, Sandler H. The joint modeling of a longitudinal disease progression marker and the failure time process in the presence of cure. *Biostatistics* 2002;3(4):547-63.
4. Peng Y, Dear KB, Carriere KC. Testing for the presence of cured patients: a simulation study. *Stat Med* 2001;20(12):1783-96.
5. De Angelis R, Capocaccia R, Hakulinen T, Soderman B, Verdecchia A. Mixture models for cancer survival analysis: application to population-based data with covariates. *Stat Med* 1999;18(4):441-54.
6. Gordon NH. Application of the theory of finite mixtures for the estimation of 'cure' rates of treated cancer patients. *Stat Med* 1990;9(4):397-407.
7. McLean IW, Foster WD, Zimmerman LE. Uveal melanoma: location, size, cell type, and enucleation as risk factors in metastasis. *Hum Pathol* 1982;13(2):123-32.
8. Nie L, Chu H, Cole SR. A general approach for sample size and statistical power calculations assessing of interventions using a mixture model in the presence of detection limits. *Contemp Clin Trials* 2006;27(5):483-91.
9. Bonomi P, Kim K, Fairclough D, et al. Comparison of survival and quality of life in advanced non-small-cell lung cancer patients treated with two dose levels of paclitaxel combined with cisplatin versus etoposide with cisplatin: results of an Eastern Cooperative Oncology Group trial. *J Clin Oncol* 2000;18(3):623-31.
10. Buccheri G, Ferrigno D, Rosso A, Vola F. Further evidence in favour of chemotherapy for inoperable non-small cell lung cancer. *Lung Cancer* 1990;6:87-98.
11. Lilenbaum RC, Herndon JE, 2nd, List MA, et al. Single-agent versus combination chemotherapy in advanced non-small-cell lung cancer: the cancer and leukemia group B (study 9730). *J Clin Oncol* 2005;23(1):190-6.
12. Chemotherapy in non-small cell lung cancer: a meta-analysis using updated data on individual patients from 52 randomised clinical trials. Non-small Cell Lung Cancer Collaborative Group. *Bmj* 1995;311(7010):899-909.
13. Fossella F, Pereira JR, von Pawel J, et al. Randomized, multinational, phase III study of docetaxel plus platinum combinations versus vinorelbine plus cisplatin for advanced non-small-cell lung cancer: the TAX 326 study group. *J Clin Oncol* 2003;21(16):3016-24.
14. Fukuoka M, Masuda N, Furuse K, et al. A randomized trial in inoperable non-small-cell lung cancer: vindesine and cisplatin versus mitomycin, vindesine, and cisplatin versus etoposide and cisplatin alternating with vindesine and mitomycin. *J Clin Oncol* 1991;9(4):606-13.
15. Kelly K, Crowley J, Bunn PA, Jr., et al. Randomized phase III trial of paclitaxel plus carboplatin versus vinorelbine plus cisplatin in the treatment of patients with advanced non--small-cell lung cancer: a Southwest Oncology Group trial. *J Clin Oncol* 2001;19(13):3210-8.
16. Klastersky J, Sculier JP, Ravez P, et al. A randomized study comparing a high and a standard dose of cisplatin in combination with etoposide in the treatment of advanced non-small-cell lung carcinoma. *J Clin Oncol* 1986;4(12):1780-6.
17. Klastersky J, Sculier JP, Bureau G, et al. Cisplatin versus cisplatin plus etoposide in the treatment of advanced non-small-cell lung cancer. Lung Cancer Working Party, Belgium. *J Clin Oncol* 1989;7(8):1087-92.

18. Le Chevalier T, Brisgand D, Douillard JY, et al. Randomized study of vinorelbine and cisplatin versus vindesine and cisplatin versus vinorelbine alone in advanced non-small-cell lung cancer: results of a European multicenter trial including 612 patients. *J Clin Oncol* 1994;12(2):360-7.
19. Mylonakis N, Tsavaris N, Bacoyiannis C, et al. A randomized prospective study of cisplatin and vinblastine versus cisplatin, vinblastine and mitomycin in advanced non-small cell lung cancer. *Ann Oncol* 1992;3(2):127-30.
20. Rapp E, Pater JL, Willan A, et al. Chemotherapy can prolong survival in patients with advanced non-small-cell lung cancer--report of a Canadian multicenter randomized trial. *J Clin Oncol* 1988;6(4):633-41.
21. Rosso R, Ardizzoni A, Salvati F, et al. Etoposide v etoposide and cisplatin in the treatment of advanced non-small cell lung cancer: a FONICAP randomized study. *Semin Oncol* 1988;15(6 Suppl 7):49-51.
22. Sandler A, Gray R, Perry MC, et al. Paclitaxel-carboplatin alone or with bevacizumab for non-small-cell lung cancer. *N Engl J Med* 2006;355(24):2542-50.
23. Schiller JH, Harrington D, Belani CP, et al. Comparison of four chemotherapy regimens for advanced non-small-cell lung cancer. *N Engl J Med* 2002;346(2):92-8.
24. Shinkai T, Saijo N, Eguchi K, et al. Cisplatin and vindesine combination chemotherapy for non-small cell lung cancer: a randomized trial comparing two dosages of cisplatin. *Jpn J Cancer Res* 1986;77(8):782-9.
25. Veeder MH, Jett JR, Su JQ, et al. A phase III trial of mitomycin C alone versus mitomycin C, vinblastine, and cisplatin for metastatic squamous cell lung carcinoma. *Cancer* 1992;70(9):2281-7.
26. Woods RL, Williams CJ, Levi J, et al. A randomised trial of cisplatin and vindesine versus supportive care only in advanced non-small cell lung cancer. *Br J Cancer* 1990;61(4):608-11.
27. Arriagada R, Bergman B, Dunant A, Le Chevalier T, Pignon JP, Vansteenkiste J. Cisplatin-based adjuvant chemotherapy in patients with completely resected non-small-cell lung cancer. *N Engl J Med* 2004;350(4):351-60.
28. Douillard JY, Rosell R, De Lena M, et al. Adjuvant vinorelbine plus cisplatin versus observation in patients with completely resected stage IB-IIIa non-small-cell lung cancer (Adjuvant Navelbine International Trialist Association [ANITA]): a randomised controlled trial. *Lancet Oncol* 2006;7(9):719-27.
29. Imaizumi M. Postoperative adjuvant cisplatin, vindesine, plus uracil-tegafur chemotherapy increased survival of patients with completely resected p-stage I non-small cell lung cancer. *Lung Cancer* 2005;49(1):85-94.
30. Kato H, Ichinose Y, Ohta M, et al. A randomized trial of adjuvant chemotherapy with uracil-tegafur for adenocarcinoma of the lung. *N Engl J Med* 2004;350(17):1713-21.
31. The benefit of adjuvant treatment for resected locally advanced non-small-cell lung cancer. The Lung Cancer Study Group. *J Clin Oncol* 1988;6(1):9-17.
32. Nakagawa M, Tanaka F, Tsubota N, Ohta M, Takao M, Wada H. A randomized phase III trial of adjuvant chemotherapy with UFT for completely resected pathological stage I non-small-cell lung cancer: the West Japan Study Group for Lung Cancer Surgery (WJSG)--the 4th study. *Ann Oncol* 2005;16(1):75-80.
33. Olaussen KA, Dunant A, Fouret P, et al. DNA repair by ERCC1 in non-small-cell lung cancer and cisplatin-based adjuvant chemotherapy. *N Engl J Med* 2006;355(10):983-91.
34. Rosell R, Gomez-Codina J, Camps C, et al. A randomized trial comparing preoperative chemotherapy plus surgery with surgery alone in patients with non-small-cell lung cancer. *N Engl J Med* 1994;330(3):153-8.
35. Roth JA, Fossella F, Komaki R, et al. A randomized trial comparing perioperative chemotherapy and surgery with surgery alone in resectable stage IIIa non-small-cell lung cancer. *J Natl Cancer Inst* 1994;86(9):673-80.
36. Scagliotti GV, Fossati R, Torri V, et al. Randomized study of adjuvant chemotherapy for completely resected stage I, II, or IIIa non-small-cell Lung cancer. *J Natl Cancer Inst* 2003;95(19):1453-61.
37. Winton T, Livingston R, Johnson D, et al. Vinorelbine plus cisplatin vs. observation in resected non-small-cell lung cancer. *N Engl J Med* 2005;352(25):2589-97.
38. Betticher DC, Hsu Schmitz SF, Totsch M, et al. Prognostic factors affecting long-term outcomes in patients with resected stage IIIa pN2 non-small-cell lung cancer: 5-year follow-up of a phase II study. *Br J Cancer* 2006;94(8):1099-106.

39. Bonomi P, Faber L. Neoadjuvant chemoradiation therapy in non-small cell lung cancer: the Rush University experience. *Lung Cancer* 1993;9:383-90.
40. Gralla RJ. Preoperative and adjuvant chemotherapy in non-small cell lung cancer. *Semin Oncol* 1988;15(6 Suppl 7):8-12.
41. Lin E, Karp D. Color-matrix cancer staging and chemotherapy handbook. 2 ed. Houston, TX: The University of Texas M.D. Anderson Cancer Center; 2003.
42. Mountain CF. A new international staging system for lung cancer. *Chest* 1986;89(4 Suppl):225S-33S.
43. Wisnivesky JP, Yankelevitz D, Henschke CI. The effect of tumor size on curability of stage I non-small cell lung cancers. *Chest* 2004;126(3):761-5.
44. Wisnivesky JP, Henschke C, McGinn T, Iannuzzi MC. Prognosis of Stage II non-small cell lung cancer according to tumor and nodal status at diagnosis. *Lung Cancer* 2005;49(2):181-6.
45. Shepherd FA, Rodrigues Pereira J, Ciuleanu T, et al. Erlotinib in previously treated non-small-cell lung cancer. *N Engl J Med* 2005;353(2):123-32.
46. Thatcher N, Chang A, Parikh P, et al. Gefitinib plus best supportive care in previously treated patients with refractory advanced non-small-cell lung cancer: results from a randomised, placebo-controlled, multicentre study (Iressa Survival Evaluation in Lung Cancer). *Lancet* 2005;366(9496):1527-37.
47. von Plessen C, Bergman B, Andresen O, et al. Palliative chemotherapy beyond three courses conveys no survival or consistent quality-of-life benefits in advanced non-small-cell lung cancer. *Br J Cancer* 2006;95(8):966-73.
48. Westeel V, Quoix E, Moro-Sibilot D, et al. Randomized study of maintenance vinorelbine in responders with advanced non-small-cell lung cancer. *J Natl Cancer Inst* 2005;97(7):499-506.
49. Smith IE, O'Brien ME, Talbot DC, et al. Duration of chemotherapy in advanced non-small-cell lung cancer: a randomized trial of three versus six courses of mitomycin, vinblastine, and cisplatin. *J Clin Oncol* 2001;19(5):1336-43.
50. Buccheri GF, Ferrigno D, Curcio A, Vola F, Rosso A. Continuation of chemotherapy versus supportive care alone in patients with inoperable non-small cell lung cancer and stable disease after two or three cycles of MACC. Results of a randomized prospective study. *Cancer* 1989;63(3):428-32.
51. Rinaldi M, Belvedere O, Cauchi C, Defferrari C, Viola G, Grossi F. Maintenance chemotherapy in non-small cell lung cancer. *Ann Oncol* 2006;17 Suppl 2:ii67-70.
52. Berghmans T, Paesmans M, Meert AP, et al. Survival improvement in resectable non-small cell lung cancer with (neo)adjuvant chemotherapy: results of a meta-analysis of the literature. *Lung Cancer* 2005;49(1):13-23.

Use of cytokine and angiogenic factor (CAF) profiling of non-small cell lung cancer cell lines to identify secreted proteins associated with response to chemotherapy and targeted agents

Sub-category:

Proteomics/Immunohistochemistry

Category:

All

Meeting:

2008 Molecular Markers

Abstract No:

67

Author(s):

L. A. Byers, H. T. Tran, P. K. Tumula, S. Yan, Z. Du, M. Herynk, J. D. Minna, J. V. Heymach

Abstract:

Background: Non-small cell lung cancer (NSCLC) is a heterogeneous disease, with a variety of signaling pathways driving disease progression and therapeutic resistance. To better understand the role of cytokines and angiogenic factors in these pathways, we performed in vitro profiling of proteins secreted by NSCLC tumor cells.

Methods: Using multiplex bead assay, 43 cytokines and angiogenic factors (CAF) were measured in conditioned media from forty, subconfluent NSCLC cell lines. Unsupervised clustering of all the factors was performed to identify CAF signatures among the cell lines. Individual CAF levels were then correlated with the cell lines' mutation status (EGFR and K-Ras mutated versus wild type) and sensitivity to various chemotherapies and targeted agents (as determined by the concentration required to inhibit growth by 50%) using two-sample t-test.

Results: Unsupervised clustering of the 43 CAF levels for the NSCLC cell lines revealed at least two distinct CAF signatures among the cell lines. Individual CAFs (ex., FGF, IL-10, MIP-1b) were significantly correlated with EGFR and K-Ras mutational status, with p-values < 0.05 by t-test comparing mutated to wild type cell lines. Additionally, certain factors were associated with sensitivity to specific drugs. For example, sensitivity to the EGFR inhibitors, erlotinib and gefitinib, was associated with elevated Gro-alpha and low IL-12; while docetaxel sensitivity was associated with higher TNF-beta. **Conclusions:** This exploratory analysis demonstrates that NSCLC cell lines have distinct patterns of protein secretion and are associated with response to treatment. These results are being further investigated in clinical samples from patients treated with these agents as potential predictive markers of treatment response. (Supported by P50 CA70907, W81XWH-07-1-0306 01, and W81XWH-06-1-0303)

Abstract Disclosures

Abstracts that were granted an exception in accordance with ASCO's Conflict of Interest Policy and are designated with a caret symbol (^) here and in the print version.

► Associated Presentation(s):

1. Use of cytokine and angiogenic factor (CAF) profiling of non-small cell lung cancer cell lines to identify secreted proteins associated with response to chemotherapy and targeted agents

Meeting: 2008 Molecular Markers
Presenter: Lauren A Byers, MD
Session: General Poster Session B (General Poster Session)

► **Other Abstracts in this Sub-Category:**

1. Relationship of expression of S100A2 calcium-binding protein and response to pancreatectomy for pancreatic cancer

Meeting: 2008 Molecular Markers Abstract No: 59 First Author: A. V. Biankin
Category: All - Proteomics/Immunohistochemistry

2. Survivin as a prognostic marker for urothelial carcinoma of the bladder: A multi-institutional study

Meeting: 2008 Molecular Markers Abstract No: 60 First Author: J. A. Karam
Category: All - Proteomics/Immunohistochemistry

3. Multi-institutional external validation of the predictive value of KI-67 labeling index in patients treated with radical cystectomy

Meeting: 2008 Molecular Markers Abstract No: 61 First Author: S. Shariat
Category: All - Proteomics/Immunohistochemistry

[More...](#)

► **Abstracts by L. A. Byers:**

1. Association between human papillomavirus (HPV) status with serum cytokine and angiogenic factor (CAF) profile after induction chemotherapy in head and neck squamous cell carcinoma (HNSCC).

Meeting: 2009 ASCO Annual Meeting Abstract No: 6081 First Author: L. A. Byers
Category: Head and Neck Cancer

2. Use of cytokine and angiogenic factor (CAF) profiling of non-small cell lung cancer cell lines to identify secreted proteins associated with response to chemotherapy and targeted agents

Meeting: 2008 Molecular Markers Abstract No: 67 First Author: L. A. Byers
Category: All - Proteomics/Immunohistochemistry

3. Use of protein expression profiling to identify markers of radiation sensitivity and resistance in the NCI 60 cell lines

Meeting: 2008 Molecular Markers Abstract No: 70 First Author: J. S. Yordy
Category: All - Proteomics/Immunohistochemistry

[More...](#)

► **Presentations by L. A. Byers:**

1. Association between human papillomavirus (HPV) status with serum cytokine and angiogenic factor (CAF) profile after induction chemotherapy in head and neck squamous cell carcinoma (HNSCC).

Meeting: 2009 ASCO Annual Meeting

Presenter: [Lauren A Byers, MD](#)

Session: [Head and Neck Cancer](#) (General Poster Session)

2. Use of cytokine and angiogenic factor (CAF) profiling of non-small cell lung cancer cell lines to identify secreted proteins associated with response to chemotherapy and targeted agents

Meeting: [2008 Molecular Markers](#)

Presenter: [Lauren A Byers, MD](#)

Session: [General Poster Session B](#) (General Poster Session)

3. Profiling of cytokines and angiogenic factors (C/AF) in head and neck (HN) cancer correlates circulating biomarkers with clinical outcomes following induction chemotherapy.

Meeting: [2008 ASCO Annual Meeting](#)

Presenter: [Lauren A Byers, MD](#)

Session: [Head and Neck Cancer](#) (Oral Presentation)

[More...](#)

► ***Educational Book Manuscripts by L. A. Byers:***

No items found.



Phase II pilot study of neoadjuvant docetaxel and cisplatin followed by adjuvant erlotinib in patients with stage I-III non-small cell lung cancer (NSCLC).

Sub-category:

Adjuvant Therapy

Category:

Lung Cancer--Local-Regional and Adjuvant Therapy

Meeting:

2009 ASCO Annual Meeting

Abstract No:

7566

Citation:

J Clin Oncol 27:15s, 2009 (suppl; abstr 7566)

Author(s):

K. A. Gold, J. J. Lee, D. Rice, W. Tse, D. Stewart, I. Wistuba, R. S. Herbst, S. M. Lippman, W. K. Hong, E. S. Kim; M. D. Anderson Cancer Center, Houston, TX

Abstract:

Background: Pts with early stage NSCLC, especially with nodal disease, have a poor prognosis despite curative intent therapy. It is unclear which pts may derive the benefit of chemotherapy. The primary endpoint of the study was to assess the tolerability of the regimen. In addition, the clinical response of the chemotherapy regimen as well as tumor biomarkers modulation will be examined. **Methods:** Pts had previously untreated, potentially surgically resectable, stage I-III NSCLC with ECOG performance status (PS) 0-1 and adequate laboratory parameters. After baseline tissue was obtained, chemotherapy was administered (docetaxel [T] 75 mg/m² and cisplatin [P] 80 mg/m² every 3 wks) for 3 cycles. Subsequently, pts underwent restaging, then planned definitive therapy with surgical resection. Pts were then offered treatment for 1 year with erlotinib (E) 150 mg PO daily. Bronchoscopic biopsies were performed at 6 months and 1 year post-surgery. **Results:** 41 pts were enrolled between 2/07 and 11/08. 3 were not eligible and did not receive treatment. Of the 38 eligible pts: median age was 65 years (42-80); 24 (63.2%) were male; 26 (68%) were PS 1. Stage IB 18% (7), IIB 37% (14), IIIA 39% (15), IIIB 5% (2). 31 pts completed all 3 cycles (35 pts completed at least 2 cycles). 32 pts underwent definitive surgical resection with 1 pt pending for surgery. 5 others did not undergo surgery: pneumonia (1), progressive disease (1), definitive chemo-radiation (3). For pts completing at least 2 cycles of chemotherapy, the radiographic response rate was 57% (20) by RECIST criteria with 40% (14) having stable disease. 1 pt had a complete pathologic response. 16 pts have started adjuvant E, 4 have completed 1 yr of treatment. Grade 3/4 toxicities included neutropenia (6 pts) and hypokalemia (4 pts). Blood and tissue specimens will be analyzed to assess sensitivity to chemotherapy. **Conclusions:** Neoadjuvant T and P is a tolerable and active regimen with an encouraging response rate in stage I-III resectable NSCLC. In addition to clinical characteristics, determining which patients will benefit from chemotherapy by analyzing their tumor biomarkers may help improve overall outcomes of curative lung cancer pts. Supported by grant DoD# W81XWH-07-1-0306.

Abstract Disclosures**Faculty and Discussant Disclosures****Annual Meeting Planning Committee Disclosures****2009 Annual Meeting Proceedings Part I Errata**

Abstracts that were granted an exception in accordance with ASCO's Conflict of Interest Policy and are designated with a caret symbol (^) here and in the print version.

► **Associated Presentation(s):**

1. Phase II pilot study of neoadjuvant docetaxel and cisplatin followed by adjuvant erlotinib in patients with stage I-III non-small cell lung cancer (NSCLC).

Meeting: [2009 ASCO Annual Meeting](#)

Presenter: [Kathryn A Gold, MD](#)

Session: [Lung Cancer - Local-Regional and Adjuvant Therapy \(General Poster Session\)](#)

► **Other Abstracts in this Sub-Category:**

1. Surgery (S) alone, preoperative (preop) paclitaxel/carboplatin (PC) chemotherapy followed by S, or S followed by adjuvant (adj) PC chemotherapy in early-stage non-small cell lung cancer (NSCLC): Results of the NATCH multicenter, randomized phase III trial.

Meeting: [2009 ASCO Annual Meeting](#) Abstract No: 7500 First Author: [E. Felip](#)
Category: [Lung Cancer--Local-Regional and Adjuvant Therapy - Adjuvant Therapy](#)

2. Updated survival analysis of JBR.10: A randomized phase III trial of vinorelbine/cisplatin versus observation in completely resected stage IB and II non-small cell lung cancer (NSCLC).

Meeting: [2009 ASCO Annual Meeting](#) Abstract No: 7501 First Author: [M. D. Vincent](#)

Category: [Lung Cancer--Local-Regional and Adjuvant Therapy - Adjuvant Therapy](#)

3. MSH2 and adjuvant cisplatin-based chemotherapy in non-small cell lung cancer.

Meeting: [2009 ASCO Annual Meeting](#) Abstract No: CRA7502 First Author: [P. Fouret](#)

Category: [Lung Cancer--Local-Regional and Adjuvant Therapy - Adjuvant Therapy](#)

[More...](#)

► **Abstracts by K. A. Gold:**

1. Phase II pilot study of neoadjuvant docetaxel and cisplatin followed by adjuvant erlotinib in patients with stage I-III non-small cell lung cancer (NSCLC).

Meeting: [2009 ASCO Annual Meeting](#) Abstract No: 7566 First Author: [K. A. Gold](#)

Category: [Lung Cancer--Local-Regional and Adjuvant Therapy - Adjuvant Therapy](#)

[More...](#)

► **Presentations by K. A. Gold:**

1. Phase II pilot study of neoadjuvant docetaxel and cisplatin followed by adjuvant erlotinib in patients with stage I-III non-small cell lung cancer (NSCLC).

Meeting: [2009 ASCO Annual Meeting](#)

Presenter: [Kathryn A Gold, MD](#)

Session: [Lung Cancer - Local-Regional and Adjuvant Therapy \(General Poster Session\)](#)

[More...](#)

► ***Educational Book Manuscripts by K. A. Gold:***

No items found.

©Copyright 2008 American Society of Clinical Oncology All rights reserved worldwide.

Secreted Cytokine and Angiogenic Factor (CAF) profiles associated with age and sex in NSCLC.

Matthew H. Herynk¹, Emer Hanrahan¹, Heather Yan Lin², Tina Cascone¹, Shaoyu Yan³, Lauren Byers⁴, John Yordy⁵, J. Jack Lee², Hai T. Tran¹, and John V Heymach¹.

Departments of Thoracic/Head and Neck Medical Oncology¹, Biostatistics and Mathematics², Pharmacy Pharmacology Research³, Cancer Medicine⁴, and Radiation Oncology⁵.

Background: Subgroup analyses from recent clinical trials in non-small cell lung cancer (NSCLC) suggest therapeutic efficacy in a sex-specific manner from drugs such as bevacizumab and vandetanib. These differences suggest that factors inherent in the basic male/female biology may impact growth and survival mechanisms in NSCLC tumors. We sought to identify if there are sex-specific differences in secreted cytokine and angiogenic factors (CAFs) in NSCLC cell lines and patient samples.

Methods: Thirty-five CAFs were measured by multiplex bead suspension arrays (MBSA) and ELISAs from pre-treatment plasma (N=123) and serum (N=151) collected from patients with stage IIIB/IV NSCLC participating in a randomized phase 2 trials of vandetanib alone or in combination with chemotherapy. MBSA were used to measure the levels of 48 secreted CAFs in conditioned media from 36 NSCLC cell lines (female N=17, male N=19). Subconfluent cells were serum-starved overnight and the media was changed, 24 hours later, conditioned media was collected and the cells were lysed. Measured CAF levels were normalized to total protein from whole cell lysates.

Results: Univariate analysis of serum and plasma samples revealed statistically significant differences in the concentrations of 18 CAFs between male and female patients with most being higher in females including; plasma IL-15 (mean 1193 vs. 291 pg/ml; P =0.0009), sIL-2R (mean 1413 vs. 577 pg/ml; P =0.004), MIG (CXCL-9) (mean 184 vs. 67 pg/ml; P =0.0007), and macrophage inflammatory protein-1 (MIP-1alpha, CCL3) (mean 319 vs. 108 pg/ml; P =0.0067). Conditioned media from 36 NSCLC cell lines was analyzed for levels of secreted CAFs. Nine CAFs determined to be statistically significant in patient samples were also present in the cell line analyses and two factors, MIP-1alpha and intracellular adhesion molecule-1 (ICAM-1) also demonstrated increased levels in female versus male cell lines, but these differences did not reach statistical significance. While 18 CAFs were statistically significant in patient samples, no individual factors were statistically significant in conditioned media from cell lines. Subgroup analysis of female cell lines revealed an age association with 26 secreted CAFs in NSCLC cell lines. The majority were upregulated in cell lines originally derived from patients >50 y/o (N=10) vs <50 (N=5) including IL-15 (2.05 vs.1.27 pg/ml, P=0.011), MIG (0.12 vs. 0.095 pg/ml,

P=0.033), EGF (14.21 vs. 11.25 pg/ml, P=0.034), and ICAM-1 (11.08 vs. 7.66 pg/ml P=0.057).

Conclusions: Significant CAF differences were observed when male and female patient samples and conditioned media from cell lines were analyzed, thus suggesting an important role for age and sex in the secreted CAF profiles of NSCLC. Because EGFR inhibitors have shown preferential efficacy for females, and hormone signaling varies between male vs. female populations as well as between younger vs. older women, the contributions of EGFR and hormone signaling on the sex-different secreted factors is being further investigated. These secreted factors are involved in a number of signaling networks and thus may contribute to a broad range of effects on tumor growth, metastases, and therapeutic efficacy of angiogenesis inhibitors and other targeted agents.

Development of a Quantum Dots (QDs)-based Quantification Method for Multiplexed Biomarkers in Prediction of Metastasis

Dong-hai Huang¹, Clifford C. Hoyt², Xiang-hong Peng¹, Dongsheng Wang¹, Hongzheng Zhang¹, Fadlo R. Khuri¹, Dong M. Shin¹, Zhuo (Georgia) Chen¹

1. Department of Hematology/Oncology, Winship Cancer Institute, Emory University, Atlanta, GA
2. Cambridge Research & Instrumentation (CRi), Inc., Woburn, MA

Quantum dots (QDs) are semiconductor nanoscale particles with novel optical properties well-suited to multiplexed immunostaining of formalin-fixed paraffin embedded (FFPE) tissues. In this study, we report development of a novel quantification method that utilizes QDs, multispectral imaging and advanced image analysis based on “machine learning”, to provide per-cell, flow cytometry-like quantification of protein expression levels in cancer cells in intact tissue sections. We look at three proteins, EGFR, E-cadherin (E-cad) and β -catenin (β -cat), in lung and head and neck cancers. QD secondary antibody conjugates (emitting at 605, 705, and 655 nm) were used to detect protein expression levels, which were evaluated for correlation with clinical characteristics. Method development and validation included: (1) the comparison of single biomarker detection using conventional immunohistochemistry (IHC) with the same except using QD-based immunohistofluorescence (IHF); and (2) the comparison of biomarker signals from samples stained with single QD IHF in serial sections with biomarker signals from the same proteins but from samples stained simultaneously with multiple QD IHF. FFPE tissue sections from 30 head and neck cancer cases and 20 lung cancer cases were used for the validation. Both Pearson's and Spearman's tests show significant correlation between IHC and QD-IHF for the single marker staining tests (EGFR: correlation coefficient $r^2=0.8-0.9$, $p < 0.00001$; E-cad: $r^2=0.9$, $p < 0.00001$; β -cat: $r^2=0.7-0.8$, $p < 0.00001$), and for the single-plex versus multiplex tests (EGFR: $r^2=0.8-0.9$, $p < 0.00001$; E-cad: $r^2=0.8$, $p < 0.00001$; β -cat: $r^2=0.7-0.8$, $p < 0.00001$). Images of the 30 head and neck FFPE samples, (which consisted of ten non-metastatic primary tumors (Tu^{Met-}), ten metastatic primary tumors (Tu^{Met+}), and ten matched lymph node metastasis (LNM)) were acquired with a CRi multispectral

camera and analyzed with CRi advanced machine learning-based software for multiplexed quantification. A weighted index, defined as a result that at least two of the three biomarkers express above or below defined thresholds in Tu^{Met+} samples, was tested for predictive power of LNM. Cut-off thresholds of E-cad < 53, EGFR < 65 and β -cat >40 were used. In the current study, the positive predictive value (PPV) of the weighted index is 77.8%, the negative predictive value (NPV) is 72.7%, the sensitivity is 70% and the specificity is 80%. In summary, a quantification system of multiplexed biomarkers using QD-IHF has potential applications in prediction of LNM and validation and monitoring of the outcome of anticancer therapies. (Supported by grants from NIH R21 CA125062, DOD W81XWH-07-1-0306 Project 5, and GCC Distinguished Scholar Award to ZC).

Immunohistochemical Expression of Membrane Transporters Correlates with Histology of Non-Small Cell Lung Carcinoma. Maria Nunez, Carmen Behrens, Heather Lin, Ludmila Prudkin, Milind Suraokar, Denise M. Woods, Luc Girard, John Minna, Jack Lee, Wayne Hofstetter, Wilbur Franklin, Cesar A. Moran, Wilbur Franklin, Waun Ki Hong, David Stewart, Ignacio I. Wistuba.

Membrane transporters Folate receptor alpha (FOLR1), Reduced folate carrier 1 (RFC1), Copper transporter receptor 1 (CTR1), Glucose 4 (GLUT4) and RHOA regulate uptake of molecules and drugs inside the cell. FOLR1 and RFC1 are over expressed in epithelial tumors and are potential therapeutic targets and tumor biomarkers; however there is limited information on the expression of these receptors in non-small cell lung carcinoma (NSCLC).

Immunohistochemical (IHC) protein expression of FOLR1, RFC1, CTR1, GLUT4 and RHOA was examined in 320 surgically resected NSCLCs placed in tissue microarrays, including 202 adenocarcinomas and 110 squamous carcinomas, and correlated with patients' clinico-pathological characteristics. A semiquantitative IHC score was obtained assessing intensity of immunostaining and percentage of positive tumor cells.

The pattern of IHC expression varied in malignant cells, with FOLR1, RFC1 and GLUT4 expressed in the membrane and cytoplasm, CTR1 expressed in the cytoplasm and nucleus, and RHOA expressed only in the cytoplasm. In all cases expression in tumor cells was higher than in non-malignant lung epithelial cells. Tumor stroma IHC expression was frequently detected, especially in endothelial cells, lymphocytes, macrophages and fibroblasts. Adenocarcinomas showed significantly higher expression compared with squamous cell carcinoma for most markers, including membrane ($P<0.001$) and cytoplasmic ($P<0.001$) FOLR1, cytoplasmic ($P<0.001$) and nuclear ($P<0.004$) CTR1, and cytoplasmic RHOA ($P<0.001$). Female NSCLC patients had significantly higher expression of membrane and cytoplasmic FOLR1 ($P=0.01$) compared with male patients. Ever smoker patients demonstrated significantly lower expression of membrane ($P<0.001$) and cytoplasmic FOLR1 ($P<0.002$), and higher expression of membrane ($P=0.04$) and cytoplasmic ($P=0.03$) GLUT4, and membrane RFC1 ($P=0.01$), compared with never smokers. In adenocarcinomas, the presence of *EGFR* mutations correlated with higher expression of membrane FOLR1 ($P<0.002$), and *KRAS* mutation with higher expression of membrane GLUT4 ($P<0.004$) and lower expression of nuclear CTR1 ($P=0.02$). Finally, squamous carcinomas showed higher positive endothelial cell expression of FOLR1 ($P=0.00001$) than adenocarcinomas.

We conclude: 1. membrane transporters proteins are over expressed in NSCLC compared to normal lung epithelium; 2. significant differences were found between adenocarcinomas and squamous lung cancer in both tumor cells and the tumor microenvironment; 3. differences were found in tumors of males and females, between tumors from never and ever smokers, and tumors with *EGFR* or *KRAS* mutations. The different patterns of transporter expression may explain the superior response of NSCLC patients with adenocarcinoma histology to pemetrexed. Supported by grants US DoD W81XWH-07-1-0306, and UT-Lung SPORE P50CA70907

Phase I trial of neoadjuvant dasatinib in patients with resectable malignant pleural mesothelioma.

Sub-category:

Local-Regional Therapy

Category:

Lung Cancer--Local-Regional and Adjuvant Therapy

Meeting:

2009 ASCO Annual Meeting

Abstract No:

7580

Citation:

J Clin Oncol 27:15s, 2009 (suppl; abstr 7580)

Author(s):

R. Mehran, J. Gil, D. Rice, S. Swisher, J. J. Lee, S. Lippman, K. Pisters, G. Blumenschein, W. K. Hong, A. S. Tsao; M. D. Anderson Cancer Center, Houston, TX

Abstract:

Background: The optimal multi-modality treatment for resectable malignant pleural mesothelioma (MPM) remains unknown. We designed a biomarker-based neoadjuvant trial from our preclinical studies showing that dasatinib, a multi-targeted Src kinase inhibitor, has activity against MPM and target specificity to Src Tyr419.

Methods: Untreated MPM patients underwent extended surgical staging (ESS) with multiple biopsies to account for tumor heterogeneity, lymph node status and to rule out sarcomatoid features. If deemed a surgical candidate for either pleurectomy/decortication (P/D) or extrapleural pneumonectomy (EPP), patients received 4 weeks of oral dasatinib (70 mg BID) followed by P/D or EPP. If either a radiographic or molecular response (dephosphorylation of Src Tyr419 in tumor) is achieved, an additional 2 years of dasatinib maintenance after adjuvant radiotherapy and systemic chemotherapy is given. The primary endpoint of this trial was biomarker modulation of Src Tyr419. Secondary endpoints included response, survival, safety/toxicity, and biomarker modulation in tumor/serum/platelets/pleural effusion. The total planned sample size is 24 to detect a 50% reduction in positive p-Src Tyr419 expression with 80% power, one-sided 10% type I error rate, and 10% inevaluable rate. **Results:** To date, ten patients have registered on the trial (4/08 - 12/08); six have successfully completed the ESS, neoadjuvant dasatinib, and P/D (n=3) or EPP (n=3). Two patients are still receiving neoadjuvant dasatinib; and 2 patients were deemed to not be surgical candidates due to a rapid decline in PS and one was found to have bilateral mesothelioma. The main side effects to dasatinib were grade 1-2: anemia, nausea, vomiting, anorexia, electrolyte abnormalities, fatigue, and anxiety. Grade 3 toxicities included hyperkalemia (1), infection - pneumonia (1), and hypoxia (1). There were no grade 4-5 toxicities. Post-surgical grade 3 toxicity included anemia, electrolyte abnormalities, arrhythmia, HTN, and pleural effusion; one grade 4 episode of hyperglycemia was seen. **Conclusions:** This study demonstrates that biomarker-based neoadjuvant MPM trials with novel agents are feasible. Updated clinical and translational correlative results will be presented.

Abstract Disclosures**Faculty and Discussant Disclosures****Annual Meeting Planning Committee Disclosures****2009 Annual Meeting Proceedings Part I Errata**

Abstracts that were granted an exception in accordance with ASCO's Conflict of Interest Policy and are

designated with a caret symbol (^) here and in the print version.

► **Associated Presentation(s):**

1. Phase I trial of neoadjuvant dasatinib in patients with resectable malignant pleural mesothelioma.

Meeting: [2009 ASCO Annual Meeting](#)

Presenter: [Reza Mehran, MD](#)

Session: [Lung Cancer - Local-Regional and Adjuvant Therapy \(General Poster Session\)](#)

► **Other Abstracts in this Sub-Category:**

1. A phase III trial of carboplatin, paclitaxel, and thoracic radiation therapy with or without thalidomide in patients with stage III non-small cell carcinoma of the lung (NSCLC): E3598.

Meeting: [2009 ASCO Annual Meeting](#) Abstract No: 7503 First Author: [J. H. Schiller](#)

Category: [Lung Cancer--Local-Regional and Adjuvant Therapy - Local-Regional Therapy](#)

2. Randomized, phase III study of mitomycin/vindesine/cisplatin (MVP) versus weekly irinotecan/carboplatin (IC) or weekly paclitaxel/carboplatin (PC) with concurrent thoracic radiotherapy (TRT) for unresectable stage III non-small cell lung cancer (NSCLC): WJTOG0105.

Meeting: [2009 ASCO Annual Meeting](#) Abstract No: 7504 First Author: [M. Satouchi](#)

Category: [Lung Cancer--Local-Regional and Adjuvant Therapy - Local-Regional Therapy](#)

3. Phase II study of pemetrexed, carboplatin, and thoracic radiation with or without cetuximab in patients with locally advanced unresectable non-small cell lung cancer: CALGB 30407.

Meeting: [2009 ASCO Annual Meeting](#) Abstract No: 7505 First Author: [R. Govindan](#)

Category: [Lung Cancer--Local-Regional and Adjuvant Therapy - Local-Regional Therapy](#)

[More...](#)

► **Abstracts by R. Mehran:**

1. Integrating microRNA and mRNA expression profiling using a novel algorithm identified a small set of unique genes upregulated in malignant pleural mesothelioma (MPM).

Meeting: [2009 ASCO Annual Meeting](#) Abstract No: e22111 First Author: [M. Suraokar](#)

Category: [Tumor Biology and Human Genetics - Molecular Targets](#)

2. Phase I trial of neoadjuvant dasatinib in patients with resectable malignant pleural mesothelioma.

Meeting: [2009 ASCO Annual Meeting](#) Abstract No: 7580 First Author: [R. Mehran](#)

Category: Lung Cancer--Local-Regional and Adjuvant Therapy - [Local-Regional Therapy](#)

3. [Correlation of endoscopic tumor length with lymph node involvement and poor long-term survival in esophageal cancer patients.](#)

Meeting: [2009 Gastrointestinal Cancers Symposium](#) Abstract No: 14 First Author: [P. Gaur](#)

Category: [Esophagus and Stomach - Prevention, diagnosis, and screening](#)

[More...](#)

► **Presentations by R. Mehran:**

1. Phase I trial of neoadjuvant dasatinib in patients with resectable malignant pleural mesothelioma.

Meeting: [2009 ASCO Annual Meeting](#)

Presenter: [Reza Mehran, MD](#)

Session: [Lung Cancer - Local-Regional and Adjuvant Therapy \(General Poster Session\)](#)

[More...](#)

► **Educational Book Manuscripts by R. Mehran:**

No items found.

Keap1 and Nrf2 Expression in Non-Small Cell Lung Carcinomas Correlates with Clinicopathological Features

Solis LM, Behrens C, Bekele BN, Suraokar M, Ozburn N, Moran CA, Minna J, Stewart D, Swisher S, Corvalan AH, Wistuba I.

UT-M.D. Anderson Cancer Center, Houston TX, Hamon Center for Therapeutic Oncology Research-Simmons Cancer Center, UT Southwestern Medical Center, Dallas

Most non-small cell lung carcinomas (NSCLC) demonstrate resistance to chemotherapy. Nuclear factor erythroid-2 related factor 2 (Nrf2) is a transcription factor associated with in vitro resistance to chemotherapy. Kelch-like ECH-associated protein 1 (Keap1) is a cytoplasmic repressor of Nrf2. *KEAP1* inactivation is a relatively frequent genetic alteration in NSCLC, and leads to Nrf2 activation (Singh et al, PloS Med 3:e240, 2006). We investigated the immunohistochemical (IHC) expression of nuclear Nrf2 and cytoplasmic Keap1 proteins in 304 surgically resected NSCLC tissues in tissue microarrays (adenocarcinomas, n=190; squamous cell carcinomas, n=114). We correlated those findings with patients' clinicopathological features, and in adenocarcinomas with *EGFR* and *KRAS* mutations. We also examined the expression of Nrf2 and Keap1 using whole tissue sections in 79 NSCLC tumors (36 chemo naïve and 43 treated with neoadjuvant chemotherapy). We detected Nrf2 expression in 26% (77/299) of NSCLCs being significantly higher in squamous cell carcinoma (43/112, 38%) compared with adenocarcinoma (34/188, 18%; $P=0.0001$). In adenocarcinomas, Nrf2 was not expressed in *EGFR* mutant (0/23) compared with wild-type tumors (31/145, 21%; $P=0.009$). Keap1 expression score was significantly higher in squamous cell carcinoma compared with adenocarcinoma ($P<0.0001$). In patients with NSCLC stage I/II, who did not receive adjuvant or neoadjuvant treatment, Nrf2 overexpression significantly correlated with poor overall survival in multivariate analysis (HR=2.468; 95%CI 1.468, 4.151; $P=0.0007$). In patients with squamous cell carcinoma histology, low Keap1 expression correlated with poor overall survival (HR=0.479; 95%CI 0.260, 0.882; $P=0.018$). We found that Nrf2 expression in tumor tissue sections is heterogeneous and ranges from 5-80% (mean=27%) of tumor cells. NSCLC resected from patients treated with neoadjuvant chemotherapy showed Nrf2 expression in 28% (12/43) of NSCLC tumors, being higher in squamous cell carcinoma (5/11, 45%). *KEAP1* mutation (exons 2-5) was detected in 1/20 tumors examined. Normal bronchial epithelia adjacent to NSCLC tumors did not show Nrf2 expression, suggesting that no field effect phenomenon on Nrf2 expression is present. We conclude that: 1. increased expression of Nrf2 and decreased expression of Keap1 are relatively frequent abnormalities in NSCLC, especially in squamous cell carcinoma histology; and, 2. altered IHC expression of these markers correlates with NSCLC patients' outcome. The identification of the subset of patients with abnormal expression of Nrf2 may be important for better selection of treatment in NSCLC. (Supported by grants US DoD W81XWH-07-1-0306, and UT-Lung SPORE P50CA70907).

Overexpression of *epiregulin* is associated with *KRAS* mutations, aggressive phenotypes and regulates the growth of non-small cell lung cancer

Noriaki Sunaga¹, Hisao Imai¹, Kimihiro Shimizu², Seiichi Kakegawa², David S Shames³, Luc Girard³, John D Minna³ and Masatomo Mori¹

¹Department of Medicine and Molecular Science, ²Thoracic and Visceral Organ Surgery, Gunma University School of Medicine; ³Hamon Center for Therapeutic Oncology Research, University of Texas Southwestern Medical Center at Dallas.

Abstract

Epiregulin (EREG) is a growth factor that belongs to the epidermal growth factor (EGF) family. Although recent studies have reported the overexpression of EREG in several types of cancers including pancreas, colon and bladder cancers, its biological and clinicopathological significance in lung cancer development still remains unknown leading us to study the expression, molecular genetic and clinical correlations and functional consequences of EREG in lung cancers. We first examined the expression of EREG mRNA by quantitative RT-PCR and correlated this with clinical parameters, *KRAS*, and *EGFR* mutation status in 63 lung cancer cell lines including 26 small cell lung cancer (SCLC) cell lines and 37 non-small cell lung cancer (NSCLC) cell lines, and 89 primary NSCLC tumor specimens. EREG expression was significantly higher in NSCLC compared to SCLC lines ($P < 0.001$) and was significantly higher in NSCLC lines with *KRAS* mutations than NSCLC lines with wild-type *KRAS* ($P = 0.018$). In primary NSCLC tumors, EREG expression was significantly higher in *KRAS* mutation-positive tumors ($P = 0.032$) but lower in *EGFR* mutation-positive tumors ($P = 0.002$). EREG was abundantly expressed in tumors with pleural involvement ($P = 0.002$), lymphatic permeation ($P = 0.026$) or vascular invasion ($P = 0.004$) compared to those without such characteristics. **We performed combined microarray expression profiling on 4 NSCLC lines with or without short hairpin RNA (shRNA)-mediated stable *KRAS* knockdown and immortalized human bronchial epithelial cells (HBECs) with and without oncogenic *KRAS*, and found that EREG was significantly upregulated by oncogenic *KRAS*.** Small interfering RNAs (siRNAs)-mediated knockdown of EREG expression inhibited *in vitro* cell growth of *KRAS* mutant/EREG overexpressing NSCLC cells, while siRNAs targeted at EREG did not affect the growth of EREG-nonexpressing NSCLC cells. These results indicate that oncogenic activation of *KRAS* positively regulates EREG expression, which contributes to aggressive phenotypes of NSCLC tumors, and identifying EREG as a therapeutic target for *KRAS* mutant NSCLCs.

2009 AACR Annual Meeting**April 18-22, 2009****Denver, CO** [Print this Page for Your Records](#)[Close Window](#)**Abstract Number:** 5 56**Session Title:** MicroRNA/Noncoding RNA Expression in Cancer 1**Presentation Title:** Integrating microRNA and mRNA expression profiles identified a small set of unique genes up-regulated in malignant pleural mesothelioma (MPM)**Presentation Start/End Time:** Sunday, Apr 19, 2009, 8:00 AM -12:00 PM**Location:** Hall B-F, Poster Section 23**Poster Section:** 23**Poster Board Number:** 14**Author Block:** *Milind Suraokar, Alejandro Corvalan, Chi-wan Chow, Adi Gazdar, Cesar Moran, Gabriela Raso, Reza Mehran, Anne Tsao, Ignacio Wistuba.* U.T.M.D. Anderson Cancer Center, Houston, TX, U.T. Southwestern Medical Center, Dallas, TX

MPM is a highly aggressive neoplasm with poor prognosis and needs discovery of newer and critical therapeutic targets. MicroRNA's (miRNA's) play an important role in many different types of cancer but there is lack of published reports detailing their role in MPM. We decided to employ a global profiling strategy using miRNA microarrays to search for miRNA's involved in the pathogenesis of MPM. We analyzed miRNA profiles, using Agilent human miRNA microarray v1 slides, to find an up regulation of 44 versus down regulation of 29 miRNA's in mesothelioma MSTO-211H cancer cells compared to HCT-4012 - a pleural telomerase-transformed control cell line. Whereas profiling of 16 MPM tissues (8 normal versus 8 tumor) revealed down regulation of 11 miRNA's in tumor tissue. Along with addressing the discrepancy between cells and tissue with respect to miRNA profiles we needed to devise a method to screen the possible candidates in order to focus on the most relevant miRNA's. One alternative is to choose miRNA's that regulate genes known to be involved in the cause or progression of MPM. However search of miRNA targets using the online targetscan 4.2 program (<http://www.targetscan.org>) resulted in >1000 unique genes. This is expected since miRNA's are thought to regulate hundreds of genes and multiple miRNA's could regulate a common message. Therefore we decided to explore a novel screening strategy, which integrates miRNA with messenger RNA (cDNA) expression profiles to narrow down our list of miRNA's. We obtained cDNA profiles on same cell lines and tissue samples using Affymetrix U133 plus 2.0 chips. Bioinformatic analysis using the MultiExperiment Viewer software (www.tm4.org/mev.html), involving data reduction techniques (Correspondance Analysis), hierarchical clustering methods and Serial Analysis for Microarray (SAM), proposed up regulation of ~300 genes in MPM compared to normal tissues. Next using a custom-designed search algorithm we computed the number of miRNA's regulating a common or different set of genes. Of the ~300 mRNA's up regulated in MPM only 32 are recognized by the 11 down regulated miRNA's. Moreover most of the miRNA's regulate single messages while ~20 % of the messages are regulated by more than 1 miRNA's. Interestingly some of these targets include Ets variant 1 (ETV1) and Protein kinase C - epsilon (PRKCE), which has not been evaluated in MPM but implicated in other cancers. Our next step is to validate our profiling studies using real-time PCR and protein analysis methods. Therefore aside from selecting highly relevant miRNA's our innovative approach will also enable discovery of novel genes based on their ability to be bound by single or multiple miRNA's. Supported by Grant: DoD W81XWH-07-1-0306.

2009 AACR Annual Meeting**April 18-22, 2009****Denver, CO**

Citation Format: {Authors}. {Abstract title} [abstract]. In: Proceedings of the 100th Annual Meeting of the American Association for Cancer Research; 2009 Apr 18-22; Denver, CO. Philadelphia (PA): AACR; 2009. Abstract nr {Abstract number}

[Disclosure Information for CME-Designated Sessions](#)

OASIS - Online Abstract Submission and Invitation System™ ©1996-2009, Coe-Truman Technologies, Inc.

Use of protein expression profiling to identify markers of radiation sensitivity and resistance in the NCI 60 cell lines

Sub-category:

Proteomics/Immunohistochemistry

Category:

All

Meeting:

2008 Molecular Markers

Abstract No:

70

Author(s):

J. S. Yordy, L. A. Byers, M. Davies, G. B. Mills, Z. Ju, U. Raju, K. Ang, J. V. Heymach

Abstract:

Background: Radiation therapy plays an important role in achieving local control of many solid tumors and prospective clinical trials have shown enhanced local control and survival when radiation is combined with chemotherapy and/or targeted agents. However, there are currently no validated biomarkers that predict tumor response to radiation. Therefore, there is a need to identify predictive biomarkers to refine clinical practice.

Methods: Reverse phase protein arrays (RPPA) were performed to measure over 100 proteins and post-translational modifications in the NCI 60 cell lines under serum-starved and serum-stimulated conditions to represent the chronic hypoxia and reperfusion taking place within virtually all solid tumors. Protein levels were correlated with publicly available radiation sensitivity data for the NCI 60. T tests comparing protein expression and activation between groups of radiosensitive and radioresistant cells as defined by the surviving fraction at 2 Gy (SF2) and the dose of radiation producing 37% cell survival (D_{0}), as well as p53 mutational status, were done to identify candidate protein biomarkers and signaling pathways involved in cellular responses to radiation.

Continuous variable correlation analyses comparing radiation sensitivity to protein expression confirmed statistically significant correlations. **Results:** The basal expression of more than 10 proteins, including EGFR, Src and IGFR, demonstrated a statistically significant correlation with radiation resistance (p -value ≤ 0.05). Src and Akt, among other proteins, also had statistically significant changes in protein expression between serum-starved-then-stimulated conditions that correlated with radiation resistance. These identified proteins represent canonical signaling pathways with multiple protein effectors, some of which have the additional potential to be therapeutically targeted. **Conclusions:** This work identifies candidate proteins and signaling pathways associated with the modulation of radiation sensitivity that may serve as biomarkers for tumor response to radiation therapy as well as targets for therapeutic intervention. (Supported by P50 CA70907, W81XWH-07-1-0306 01)

Abstract Disclosures

Abstracts that were granted an exception in accordance with ASCO's Conflict of Interest Policy and are designated with a caret symbol (^) here and in the print version.

► Associated Presentation(s):

1. Use of protein expression profiling to identify markers of radiation sensitivity and resistance in the NCI 60 cell lines

Meeting: [2008 Molecular Markers](#)

Presenter: John S Yordy, MD, PhD

Session: General Poster Session B (General Poster Session)

► **Other Abstracts in this Sub-Category:**

1. Relationship of expression of S100A2 calcium-binding protein and response to pancreatectomy for pancreatic cancer

Meeting: 2008 Molecular Markers Abstract No: 59 First Author: A. V. Biankin
Category: All - Proteomics/Immunohistochemistry

2. Survivin as a prognostic marker for urothelial carcinoma of the bladder: A multi-institutional study

Meeting: 2008 Molecular Markers Abstract No: 60 First Author: J. A. Karam
Category: All - Proteomics/Immunohistochemistry

3. Multi-institutional external validation of the predictive value of KI-67 labeling index in patients treated with radical cystectomy

Meeting: 2008 Molecular Markers Abstract No: 61 First Author: S. Shariat
Category: All - Proteomics/Immunohistochemistry

[More...](#)

► **Abstracts by J. S. Yordy:**

1. Use of protein expression profiling to identify markers of radiation sensitivity and resistance in the NCI 60 cell lines

Meeting: 2008 Molecular Markers Abstract No: 70 First Author: J. S. Yordy
Category: All - Proteomics/Immunohistochemistry

[More...](#)

► **Presentations by J. S. Yordy:**

1. Use of protein expression profiling to identify markers of radiation sensitivity and resistance in the NCI 60 cell lines

Meeting: 2008 Molecular Markers
Presenter: John S Yordy, MD, PhD
Session: General Poster Session B (General Poster Session)

[More...](#)

► **Educational Book Manuscripts by J. S. Yordy:**

No items found.

Reverse Phase Protein Arrays Reveal Biomarkers of Radiation Resistance in Head and Neck and Lung Cancer Cell Lines

John S Yordy, Byers LA, Davies M, Molkentine D, Raju U, Mills G, Minna J, Coombes K, Ang KK, Heymach JV

Background: Radiation therapy is used to improve local control for many solid tumors. Prospective clinical trials have shown enhanced local control and survival when chemotherapy and/or targeted agents is combined with radiation. However, there are currently no validated biomarkers predicting tumor response to radiation or combined therapy and these are essential to improve clinical practice.

Methods: Reverse phase protein arrays were performed to measure 120 proteins and post-translational modifications in 9 head and neck (HN) and 20 lung cancer cell lines. Subsets of radiation-sensitive and radiation-resistant cell lines were identified based on the surviving fraction at 2 Gy. Protein levels were correlated with radiation sensitivity data using t-tests to identify proteins or phosphoproteins differentially expressed between groups of radiosensitive and radioresistant cells to identify candidate protein biomarkers and signaling pathways involved in cellular responses to radiation. Continuous variable correlation analyses comparing radiation sensitivity to protein expression confirmed statistically significant correlations.

Results: The expression of more than 10 proteins was significantly correlated with radiation resistance in the HN and lung cancer cell lines, including Src, EGFR, IGFR and receptor tyrosine kinase downstream signaling effectors such as phosphorylated PI3K, STAT family members and MEK1 (p -value ≤ 0.05). These identified proteins are part of known signaling pathways consisting of multiple protein effectors. Some of these identified proteins, as well other proteins within the same signaling cascade, have the additional potential to be therapeutically targeted.

Conclusion: These findings suggest receptor tyrosine kinases and their dependent downstream signaling pathways are associated with radiotherapy resistance. This work identifies candidate proteins and signaling pathways associated with the modulation of radiation sensitivity that may serve as biomarkers for tumor response to radiation therapy as well as targets for therapeutic intervention in HN and lung cancers. (Supported by P50 CA70907, P50 CA97007, W81XWH-07-1-0306 01)

Profiling in pharmacologically re-expressed microRNAs by 5-azacytidine and SAHA identified a metastasis associated miR-148b in malignant pleural mesothelioma cell lines

Corvalan A, Suraokar M, Gazdar A, Moran C, Raso G, Mehran R, Tsao A, Wistuba I.

Background. MicroRNAs (miRNAs) have emerged as key players in human carcinogenesis. Recently it has been shown that some miRNAs can be epigenetically up-regulated by aberrant hypermethylation in human cancer. Malignant pleural mesothelioma (MPM) is a highly malignant neoplasm with different histological subtypes. To explore the role of epigenetically mediated up-regulation of miRNAs in MPM we performed pharmacological unmasking of miRNA expression in cell lines.

Methods. Five mesothelioma cell lines, including one normal mesothelial (Met5A) and five MPMs (epithelioid H2452, biphasic H211 and unclassified H28 and H2052) were treated *in vitro* with the demethylating agent 5-aza-cytidine (5-Aza; 1 μ M) and SAHA (2.5 μ M) for 96 hrs. After RNA extraction (Trizol), miRNA profiling was performed by Agilent human microRNA kit v2.

Results. Total miRNA up-regulated (two-fold) after the treatment were 299 (51%) in normal mesothelial Met5A cell line, and lower in the malignant cell lines: 171 (29%) in H2452, 79 (13.5%) in H211, 55 (9.4%) in H28, and 56 (9.6%) in H2052. We detected that 167 (55.9%) miRNAs were exclusively up-regulated in Met5A, 56 (32.7%) in H2452, 21 (26.6%) in H211, 16 (29.1%), in H28, and 18 (32.1%) in H2052. Among all unique miRNA, only 17 (let-7b, let-7c, let-7f-2, miR-302c, miR-328, miR-510, miR-125b-1, miR-16-1, miR-223, miR-302b, miR-383, miR-551b, miR-922, miR-148a, miR-18b, miR-302d, miR-326) have been previously associated to human carcinogenesis. Interestingly, one of these miRNA (miR-148a) has been associated with microRNA tumor metastasis signature.

Discussion. The number of total and unique miRNA upregulated after 5-Aza and SAHA was lower in MPM cell lines compared with normal Met5A cell line. Up-regulation of unique miRNAs was found associated with cell lines obtained from some specific subtypes of MPM. The identification of metastasis associated miR-148a suggests a potential biomarker for metastasis in this highly malignant neoplasm. Further studies, including the analysis of tissue specimens are needed to validate these results.

Grant support: PROSPECT DoD W81XWH-07-1-0306.

Secreted Cytokine and Angiogenic Factor (CAF) profiles associated with age and sex in NSCLC.

Matthew H. Herynk¹, Emer Hanrahan¹, Heather Yan Lin², Tina Cascone¹, Shaoyu Yan³, Lauren Byers⁴, John Yordy⁵, J. Jack Lee², Hai T. Tran¹, and John V Heymach¹.

Departments of Thoracic/Head and Neck Medical Oncology¹, Biostatistics and Mathematics², Pharmacy Pharmacology Research³, Cancer Medicine⁴, and Radiation Oncology⁵.

Background: Subgroup analyses from recent clinical trials in non-small cell lung cancer (NSCLC) suggest therapeutic efficacy in a sex-specific manner from drugs such as bevacizumab and vandetanib. These differences suggest that factors inherent in the basic male/female biology may impact growth and survival mechanisms in NSCLC tumors. We sought to identify if there are sex-specific differences in secreted cytokine and angiogenic factors (CAFs) in NSCLC cell lines and patient samples.

Methods: Thirty-five CAFs were measured by multiplex bead suspension arrays (MBSA) and ELISAs from pre-treatment plasma (N=123) and serum (N=151) collected from patients with stage IIIB/IV NSCLC participating in a randomized phase 2 trials of vandetanib alone or in combination with chemotherapy. MBSA were used to measure the levels of 48 secreted CAFs in conditioned media from 36 NSCLC cell lines (female N=17, male N=19). Subconfluent cells were serum-starved overnight and the media was changed, 24 hours later, conditioned media was collected and the cells were lysed. Measured CAF levels were normalized to total protein from whole cell lysates.

Results: Univariate analysis of serum and plasma samples revealed statistically significant differences in the concentrations of 18 CAFs between male and female patients with most being higher in females including; plasma IL-15 (mean 1193 vs. 291 pg/ml; P =0.0009), sIL-2R (mean 1413 vs. 577 pg/ml; P =0.004), MIG (CXCL-9) (mean 184 vs. 67 pg/ml; P =0.0007), and macrophage inflammatory protein-1 (MIP-1alpha, CCL3) (mean 319 vs. 108 pg/ml; P =0.0067). Conditioned media from 36 NSCLC cell lines was analyzed for levels of secreted CAFs. Nine CAFs determined to be statistically significant in patient samples were also present in the cell line analyses and two factors, MIP-1alpha and intracellular adhesion molecule-1 (ICAM-1) also demonstrated increased levels in female versus male cell lines, but these differences did not reach statistical significance. While 18 CAFs were statistically significant in patient samples, no individual factors were statistically significant in conditioned media from cell lines. Subgroup analysis of female cell lines revealed an age association with 26 secreted CAFs in NSCLC cell lines. The majority were upregulated in cell lines originally derived from patients >50 y/o (N=10) vs <50 (N=5) including IL-15 (2.05 vs.1.27 pg/ml, P=0.011), MIG (0.12 vs. 0.095 pg/ml,

P=0.033), EGF (14.21 vs. 11.25 pg/ml, P=0.034), and ICAM-1 (11.08 vs. 7.66 pg/ml P=0.057).

Conclusions: Significant CAF differences were observed when male and female patient samples and conditioned media from cell lines were analyzed, thus suggesting an important role for age and sex in the secreted CAF profiles of NSCLC. Because EGFR inhibitors have shown preferential efficacy for females, and hormone signaling varies between male vs. female populations as well as between younger vs. older women, the contributions of EGFR and hormone signaling on the sex-different secreted factors is being further investigated. These secreted factors are involved in a number of signaling networks and thus may contribute to a broad range of effects on tumor growth, metastases, and therapeutic efficacy of angiogenesis inhibitors and other targeted agents.

Immunohistochemical Expression of Membrane Transporters Correlates with Histology of Non-Small Cell Lung Carcinoma. Maria Nunez, Carmen Behrens, Heather Lin, Ludmila Prudkin, Milind Suraokar, Denise M. Woods, Luc Girard, John Minna, Jack Lee, Wayne Hofstetter, Wilbur Franklin, Cesar A. Moran, Wilbur Franklin, Waun Ki Hong, David Stewart, Ignacio I. Wistuba.

Membrane transporters Folate receptor alpha (FOLR1), Reduced folate carrier 1 (RFC1), Copper transporter receptor 1 (CTR1), Glucose 4 (GLUT4) and RHOA regulate uptake of molecules and drugs inside the cell. FOLR1 and RFC1 are over expressed in epithelial tumors and are potential therapeutic targets and tumor biomarkers; however there is limited information on the expression of these receptors in non-small cell lung carcinoma (NSCLC).

Immunohistochemical (IHC) protein expression of FOLR1, RFC1, CTR1, GLUT4 and RHOA was examined in 320 surgically resected NSCLCs placed in tissue microarrays, including 202 adenocarcinomas and 110 squamous carcinomas, and correlated with patients' clinico-pathological characteristics. A semiquantitative IHC score was obtained assessing intensity of immunostaining and percentage of positive tumor cells.

The pattern of IHC expression varied in malignant cells, with FOLR1, RFC1 and GLUT4 expressed in the membrane and cytoplasm, CTR1 expressed in the cytoplasm and nucleus, and RHOA expressed only in the cytoplasm. In all cases expression in tumor cells was higher than in non-malignant lung epithelial cells. Tumor stroma IHC expression was frequently detected, especially in endothelial cells, lymphocytes, macrophages and fibroblasts. Adenocarcinomas showed significantly higher expression compared with squamous cell carcinoma for most markers, including membrane ($P<0.001$) and cytoplasmic ($P<0.001$) FOLR1, cytoplasmic ($P<0.001$) and nuclear ($P<0.004$) CTR1, and cytoplasmic RHOA ($P<0.001$). Female NSCLC patients had significantly higher expression of membrane and cytoplasmic FOLR1 ($P=0.01$) compared with male patients. Ever smoker patients demonstrated significantly lower expression of membrane ($P<0.001$) and cytoplasmic FOLR1 ($P<0.002$), and higher expression of membrane ($P=0.04$) and cytoplasmic ($P=0.03$) GLUT4, and membrane RFC1 ($P=0.01$), compared with never smokers. In adenocarcinomas, the presence of *EGFR* mutations correlated with higher expression of membrane FOLR1 ($P<0.002$), and *KRAS* mutation with higher expression of membrane GLUT4 ($P<0.004$) and lower expression of nuclear CTR1 ($P=0.02$). Finally, squamous carcinomas showed higher positive endothelial cell expression of FOLR1 ($P=0.00001$) than adenocarcinomas.

We conclude: 1. membrane transporters proteins are over expressed in NSCLC compared to normal lung epithelium; 2. significant differences were found between adenocarcinomas and squamous lung cancer in both tumor cells and the tumor microenvironment; 3. differences were found in tumors of males and females, between tumors from never and ever smokers, and tumors with *EGFR* or *KRAS* mutations. The different patterns of transporter expression may explain the superior response of NSCLC patients with adenocarcinoma histology to pemetrexed. Supported by grants US DoD W81XWH-07-1-0306, and UT-Lung SPORE P50CA70907

Enriched Tumor Expression of Folate Transporters Correlates With Adenocarcinoma Histology Type, Female Gender and Presence of *EGFR* Mutation in Non-Small Cell Lung Carcinoma

Author Block: *Maria Ines Nunez, Carmen Behrens, Denise M. Woods, Heather Lin, Milind Suraakar, Luc Girard, John Minna, Jack Lee, W Hofstetter, Wilbur Franklin, Cesar A. Moran, Waun K. Hong, David J. Stewart, Ignacio I. Wistuba.*

Pathology Department - UT M.D. Anderson Cancer Center, Houston, TX, Biostatistics Department - UT M.D. Anderson Cancer Center, Houston, TX, Hamon Center - UT Southwestern Medical Center, Dallas, TX, Thoracic Surgery Department - UT M.D. Anderson Cancer Center, Houston, TX, University of Colorado Cancer center, Denver, CO, Thoracic/Head and Neck Medical Oncology Department - UT M.D. Anderson Cancer Center, Houston, TX

Background: Membrane bound folate receptor alpha (FOLR1) and transmembrane Reduced folate carrier 1 (RFC1) regulate uptake of folate as well as folate linked conjugates inside the cell. FOLR1 and RFC1 are over expressed in epithelial primary and metastatic tumors and are promising therapeutic targets and tumor biomarkers. Due to limited information on the expression of these receptors in non-small cell lung carcinoma (NSCLC) we studied the protein immunohistochemical (IHC) expression of these receptors in a large set of tumors and correlate our findings with patients' clinicopathologic features.

Methods: IHC protein expression of FOLR1, RFC1, was examined in 320 surgically resected NSCLCs placed in tissue microarrays, including 202 adenocarcinomas and 110 squamous carcinomas, and correlated with patients' clinico-pathological characteristics. A semiquantitative IHC score was obtained assessing intensity of immunostaining and percentage of positive tumor cells.

Results: The pattern of IHC expression varied in malignant cells, with FOLR1 and RFC1 expressed in the membrane and cytoplasm. In all cases expression in tumor cells was higher than in non-malignant lung epithelial cells. Tumor stroma IHC expression was frequently detected, especially in endothelial cells, lymphocytes, macrophages and fibroblasts. Adenocarcinomas showed significantly higher expression compared with squamous cell carcinoma for membrane ($P<0.001$) and cytoplasmic ($P<0.001$) FOLR1. Interestingly, these protein expression findings are supported by 4 published gene expression datasets, collectively profiling about 400 tumor samples, which show that FOLR1 mRNA is expressed at higher levels in adenocarcinomas compared to squamous cell carcinomas. Female NSCLC patients had significantly higher expression of membrane and cytoplasmic FOLR1 ($P=0.01$) compared with male patients. Ever smoker patients demonstrated significantly lower expression of membrane ($P<0.001$) and cytoplasmic FOLR1 ($P<0.002$), and higher expression of membrane RFC1 ($P=0.01$), compared with never smokers. In adenocarcinomas, the presence of *EGFR* mutations correlated with higher expression of membrane FOLR1 ($P<0.002$). Finally, squamous carcinomas showed higher positive endothelial cell expression of FOLR1 ($P=0.00001$) than adenocarcinomas

Conclusion: 1. FOLR1 and RFC1 membrane transporters proteins are over expressed in NSCLC compared to normal lung epithelium; 2. significant differences were found between adenocarcinomas and squamous lung cancer in both tumor cells and the tumor microenvironment; 3. differences were found in tumors of males and females, between tumors from never and ever smokers, and tumors with *EGFR*

mutations. The different patterns of transporter expression may explain the superior response of NSCLC patients with adenocarcinoma histology to pemetrexed.

Supported by grants US DoD W81XWH-07-1-0306, and UT-Lung SPORE P50CA70907.

Importance of Histopathology Quality Control of Non-Small Cell Lung Cancer Tissue Specimens for DNA/RNA Extraction and Profiling Analysis. G. Raso, A. Corvalan, C. Behrens, A. Basey, G. Mendoza, J. Roth, C. Moran, I. Wistuba.

Introduction: High throughput molecular profiling technologies require good quality tumor tissue samples and nucleic acids products. To achieve these high standards in our tissue bank we have in place a series of quality control activities, including detailed pathology analysis in frozen tissue specimens.

Methods: From more than 1,500 primary NSCLC tumor frozen samples collected from 1997 to 2007 we selected a subset of 492 cases stored in liquid nitrogen vapor phase. DNA and RNA were extracted and quantitated using a bioanalyzer system (Agilent). Before DNA/RNA extraction, we performed a detailed histopathology quality control of the frozen tissues to assess percentage of tumor tissue, tumor cells, normal tissue, necrosis, fibrosis and inflammation.

Results: Tumor >70% was present in 82% of the NSCLC specimens. Tumor cell content >50% was present in 64% (n=284 cases) of NSCLCs, being 68% in adenocarcinomas (n=211 cases) and 54% (n=73 cases) in squamous cell carcinomas. Thirty-eight percent of adenocarcinomas and 48% of squamous cell carcinomas showed 100% tumor tissue content. Ten to 30% of normal parenchyma was present in 43% of both histologies. From 311 tumor samples in which RNA integrity number (RIN) was obtained, RIN>8 was found in 26% and RIN>5 in 51%.

Conclusions: The required minimum standard for tumor content (>70%) was achieved in most of our NSCLC cases. However, tumor cell content was lower, especially in squamous cell carcinoma histology. The difference found in tumor cell content between squamous cell carcinoma and adenocarcinoma reflects the morphological heterogeneity of NSCLC. This work has been supported by the US Department of Defense PROSPECT and UT-Lung SPORE grants.

Keap1 and Nrf2 Expression in Non-Small Cell Lung Carcinomas Correlates with Clinicopathological Features

Solis LM, Behrens C, Bekele BN, Suraokar M, Ozburn N, Moran CA, Minna J, Stewart D, Swisher S, Corvalan AH, Wistuba I.

UT-M.D. Anderson Cancer Center, Houston TX, Hamon Center for Therapeutic Oncology Research-Simmons Cancer Center, UT Southwestern Medical Center, Dallas

Most non-small cell lung carcinomas (NSCLC) demonstrate resistance to chemotherapy. Nuclear factor erythroid-2 related factor 2 (Nrf2) is a transcription factor associated with in vitro resistance to chemotherapy. Kelch-like ECH-associated protein 1 (Keap1) is a cytoplasmic repressor of Nrf2. *KEAP1* inactivation is a relatively frequent genetic alteration in NSCLC, and leads to Nrf2 activation (Singh et al, PloS Med 3:e240, 2006). We investigated the immunohistochemical (IHC) expression of nuclear Nrf2 and cytoplasmic Keap1 proteins in 304 surgically resected NSCLC tissues in tissue microarrays (adenocarcinomas, n=190; squamous cell carcinomas, n=114). We correlated those findings with patients' clinicopathological features, and in adenocarcinomas with *EGFR* and *KRAS* mutations. We also examined the expression of Nrf2 and Keap1 using whole tissue sections in 79 NSCLC tumors (36 chemo naïve and 43 treated with neoadjuvant chemotherapy). We detected Nrf2 expression in 26% (77/299) of NSCLCs being significantly higher in squamous cell carcinoma (43/112, 38%) compared with adenocarcinoma (34/188, 18%; $P=0.0001$). In adenocarcinomas, Nrf2 was not expressed in *EGFR* mutant (0/23) compared with wild-type tumors (31/145, 21%; $P=0.009$). Keap1 expression score was significantly higher in squamous cell carcinoma compared with adenocarcinoma ($P<0.0001$). In patients with NSCLC stage I/II, who did not receive adjuvant or neoadjuvant treatment, Nrf2 overexpression significantly correlated with poor overall survival in multivariate analysis (HR=2.468; 95%CI 1.468, 4.151; $P=0.0007$). In patients with squamous cell carcinoma histology, low Keap1 expression correlated with poor overall survival (HR=0.479; 95%CI 0.260, 0.882; $P=0.018$). We found that Nrf2 expression in tumor tissue sections is heterogeneous and ranges from 5-80% (mean=27%) of tumor cells. NSCLC resected from patients treated with neoadjuvant chemotherapy showed Nrf2 expression in 28% (12/43) of NSCLC tumors, being higher in squamous cell carcinoma (5/11, 45%). *KEAP1* mutation (exons 2-5) was detected in 1/20 tumors examined. Normal bronchial epithelia adjacent to NSCLC tumors did not show Nrf2 expression, suggesting that no field effect phenomenon on Nrf2 expression is present. We conclude that: 1. increased expression of Nrf2 and decreased expression of Keap1 are relatively frequent abnormalities in NSCLC, especially in squamous cell carcinoma histology; and, 2. altered IHC expression of these markers correlates with NSCLC patients' outcome. The identification of the subset of patients with abnormal expression of Nrf2 may be important for better selection of treatment in NSCLC. (Supported by grants US DoD W81XWH-07-1-0306, and UT-Lung SPORE P50CA70907).

Phase I trial of neoadjuvant dasatinib in patients with resectable malignant pleural mesothelioma.

Sub-category:

Local-Regional Therapy

Category:

Lung Cancer--Local-Regional and Adjuvant Therapy

Meeting:

2009 ASCO Annual Meeting

Abstract No:

7580

Citation:

J Clin Oncol 27:15s, 2009 (suppl; abstr 7580)

Author(s):

R. Mehran, J. Gil, D. Rice, S. Swisher, J. J. Lee, S. Lippman, K. Pisters, G. Blumenschein, W. K. Hong, A. S. Tsao; M. D. Anderson Cancer Center, Houston, TX

Abstract:

Background: The optimal multi-modality treatment for resectable malignant pleural mesothelioma (MPM) remains unknown. We designed a biomarker-based neoadjuvant trial from our preclinical studies showing that dasatinib, a multi-targeted Src kinase inhibitor, has activity against MPM and target specificity to Src Tyr419.

Methods: Untreated MPM patients underwent extended surgical staging (ESS) with multiple biopsies to account for tumor heterogeneity, lymph node status and to rule out sarcomatoid features. If deemed a surgical candidate for either pleurectomy/decortication (P/D) or extrapleural pneumonectomy (EPP), patients received 4 weeks of oral dasatinib (70 mg BID) followed by P/D or EPP. If either a radiographic or molecular response (dephosphorylation of Src Tyr419 in tumor) is achieved, an additional 2 years of dasatinib maintenance after adjuvant radiotherapy and systemic chemotherapy is given. The primary endpoint of this trial was biomarker modulation of Src Tyr419. Secondary endpoints included response, survival, safety/toxicity, and biomarker modulation in tumor/serum/platelets/pleural effusion. The total planned sample size is 24 to detect a 50% reduction in positive p-Src Tyr419 expression with 80% power, one-sided 10% type I error rate, and 10% inevaluable rate. **Results:** To date, ten patients have registered on the trial (4/08 - 12/08); six have successfully completed the ESS, neoadjuvant dasatinib, and P/D (n=3) or EPP (n=3). Two patients are still receiving neoadjuvant dasatinib; and 2 patients were deemed to not be surgical candidates due to a rapid decline in PS and one was found to have bilateral mesothelioma. The main side effects to dasatinib were grade 1-2: anemia, nausea, vomiting, anorexia, electrolyte abnormalities, fatigue, and anxiety. Grade 3 toxicities included hyperkalemia (1), infection - pneumonia (1), and hypoxia (1). There were no grade 4-5 toxicities. Post-surgical grade 3 toxicity included anemia, electrolyte abnormalities, arrhythmia, HTN, and pleural effusion; one grade 4 episode of hyperglycemia was seen. **Conclusions:** This study demonstrates that biomarker-based neoadjuvant MPM trials with novel agents are feasible. Updated clinical and translational correlative results will be presented.

Abstract Disclosures**Faculty and Discussant Disclosures****Annual Meeting Planning Committee Disclosures****2009 Annual Meeting Proceedings Part I Errata**

Abstracts that were granted an exception in accordance with ASCO's Conflict of Interest Policy and are

designated with a caret symbol (^) here and in the print version.

► **Associated Presentation(s):**

1. Phase I trial of neoadjuvant dasatinib in patients with resectable malignant pleural mesothelioma.

Meeting: [2009 ASCO Annual Meeting](#)

Presenter: [Reza Mehran, MD](#)

Session: [Lung Cancer - Local-Regional and Adjuvant Therapy \(General Poster Session\)](#)

► **Other Abstracts in this Sub-Category:**

1. A phase III trial of carboplatin, paclitaxel, and thoracic radiation therapy with or without thalidomide in patients with stage III non-small cell carcinoma of the lung (NSCLC): E3598.

Meeting: [2009 ASCO Annual Meeting](#) Abstract No: 7503 First Author: [J. H. Schiller](#)

Category: [Lung Cancer--Local-Regional and Adjuvant Therapy - Local-Regional Therapy](#)

2. Randomized, phase III study of mitomycin/vindesine/cisplatin (MVP) versus weekly irinotecan/carboplatin (IC) or weekly paclitaxel/carboplatin (PC) with concurrent thoracic radiotherapy (TRT) for unresectable stage III non-small cell lung cancer (NSCLC): WJTOG0105.

Meeting: [2009 ASCO Annual Meeting](#) Abstract No: 7504 First Author: [M. Satouchi](#)

Category: [Lung Cancer--Local-Regional and Adjuvant Therapy - Local-Regional Therapy](#)

3. Phase II study of pemetrexed, carboplatin, and thoracic radiation with or without cetuximab in patients with locally advanced unresectable non-small cell lung cancer: CALGB 30407.

Meeting: [2009 ASCO Annual Meeting](#) Abstract No: 7505 First Author: [R. Govindan](#)

Category: [Lung Cancer--Local-Regional and Adjuvant Therapy - Local-Regional Therapy](#)

[More...](#)

► **Abstracts by R. Mehran:**

1. Integrating microRNA and mRNA expression profiling using a novel algorithm identified a small set of unique genes upregulated in malignant pleural mesothelioma (MPM).

Meeting: [2009 ASCO Annual Meeting](#) Abstract No: e22111 First Author: [M. Suraokar](#)

Category: [Tumor Biology and Human Genetics - Molecular Targets](#)

2. Phase I trial of neoadjuvant dasatinib in patients with resectable malignant pleural mesothelioma.

Meeting: [2009 ASCO Annual Meeting](#) Abstract No: 7580 First Author: [R. Mehran](#)

Category: Lung Cancer--Local-Regional and Adjuvant Therapy - [Local-Regional Therapy](#)

3. Correlation of endoscopic tumor length with lymph node involvement and poor long-term survival in esophageal cancer patients.

Meeting: [2009 Gastrointestinal Cancers Symposium](#) Abstract No: 14 First Author: [P. Gaur](#)

Category: Esophagus and Stomach - [Prevention, diagnosis, and screening](#)

[More...](#)

► **Presentations by R. Mehran:**

1. Phase I trial of neoadjuvant dasatinib in patients with resectable malignant pleural mesothelioma.

Meeting: [2009 ASCO Annual Meeting](#)

Presenter: [Reza Mehran, MD](#)

Session: [Lung Cancer - Local-Regional and Adjuvant Therapy \(General Poster Session\)](#)

[More...](#)

► **Educational Book Manuscripts by R. Mehran:**

No items found.

BIOGRAPHICAL SKETCH

Provide the following information for the key personnel and other significant contributors.
Follow this format for each person. **DO NOT EXCEED FOUR PAGES.**

NAME Mehran, Reza J.	POSITION TITLE Professor		
eRA COMMONS USER NAME (credential, e.g., agency login)			
EDUCATION/TRAINING <i>(Begin with baccalaureate or other initial professional education, such as nursing, and include postdoctoral training.)</i>			
INSTITUTION AND LOCATION	DEGREE <i>(if applicable)</i>	YEAR(s)	FIELD OF STUDY
McGill University, Montreal, Canada	MDCM	1986	Medicine Surgery
McGill University, Montreal, Canada	MSc.	1989	Experimental Surgery
McGill University, Montreal, Canada	Resident	1986 - 1991	General Surgery
University of Montreal, Montreal Canada	Fellow	1992 - 1995	Cardio/Thorac Surgery

A. Positions and Honors

Positions and Employment

- 1996 – 2001 Vice Head and Assistant Professor of Surgery, Division of Thoracic Surgery, Faculty of Medicine, University of Ottawa, Ottawa, Ontario, Canada
- 2001 – 2001 Associate Professor of Surgery, Faculty of Medicine, University of Ottawa, Ottawa, Ontario, Canada
- 2001 – 2004 Associate Professor, Division of Thoracic Surgery, University of New Mexico Albuquerque, NM
- 2004 – 2008 Associate Professor, Thoracic and Cardiovascular Surgery, The University of Texas M. D. Anderson Cancer Center, Houston, TX
- 2008 – pres Professor, Thoracic and Cardiovascular Surgery, The University of Texas M. D. Anderson Cancer Center, Houston, TX

Honors

- 1986 Lange Medical Publication Award
- 1989 Davis and Geck Research Award
- 1990 Research prize, Quebec Society of Plastic Surgery
- 1993 United Nation Protection Force Service Medal, former Yugoslavia
- 1994 Chief of Defense Staff Commendation Award
- 1996 Commander's Commendation Award
- 1996 NATO Service Medal, former Yugoslavia
- 1997 Chief of Defense Staff Commendation Award
- 1999 The Canadian Decoration
- 1997 – pres. Order of St. Lazarus of Jerusalem
- 1997 – pres. Serving Brother, Most Venerable Order of Saint John of Jerusalem
- 1998 – pres. Order of St. Francis d'Assisi
- 2000 The Canadian Peacekeeping Medal
- 2003 Resident Teaching Award, University of New Mexico
- 2006 The Surgery Chief Resident Surgical Teaching Award, The University of Texas – Houston Medical School

B. Selected peer-reviewed publications (in chronological order)

1. **Mehran RJ**, Ricci MA, Graham AM, Carter K, Symes JF. Porcine model for vascular graft studies. *J Invest Surg* 4:37-44, 1991.
2. Ricci MA, **Mehran R**, Christou NV, Mohamed F, Graham AM, Symes JF. Species differences in the clearance of Staphylococcus aureus bacteremia. *J Invest Surg* 4:53-8, 1991.
3. Ricci MA, **Mehran RJ**, Petsikas D, Mohamed F, Guidoin R, Marois Y, Christou NV, Graham A, Symes JF. Species differences in the infectability of vascular grafts. *J Invest Surg* 4:45-52, 1991.
4. **Mehran RJ**, Graham AM, Ricci MA, Symes JF. Evaluation of muscle flaps in the treatment of infected aortic grafts. *J Vasc Surg* 15:487-94, 3/1992.

Appendices:

Appendix B: PROSPECT Database Screenshots

Clinical module: Patient Information, Social History, Medical History

Admin ▾ Projects ▾ Histo-Pathology Lab ▾ Logout

MRN Name

Path# Patient Completed

Status: Ready...

Other Malignancy Treatment Staging Follow up Pathology **All Clinical TO EXCEL**

Patient Information EXPORT TO EXCEL

Last Middle First MDAH

Gender Race DOB

City State Enter Date

Zip Code Country Age

Last Visit Date Death or Alive

Lost To Follow up Chemotherapy

Radiotherapy Recurrence

Social History EXPORT TO EXCEL

Smoking History Yes No Pack Years

Are you currently smoking? Yes No

If no, date quit smoking

Age started smoking regularly

Average number of cigarettes smoked per day?

If there was a quit-smoking period, total time during the smoking years. yrs., mos.

Age Quit Smoking

Overall Smoking Years

Actual Smoking Years

Pack Years

Asbestos Exposure Yes No

Alcohol History Yes No No. of Drinks / Month

Medical History EXPORT TO EXCEL

Hypertension Yes No Heart Problem Yes No Thyroid Yes No




Diabetes Yes No Renal Insufficiency Yes No Asthma Yes No

DVT Yes No Pulmonary Embolism Yes No Mild hemoptysis Yes No

Radiation Fibrosis Yes No Hepatic Problem Yes No COPD Yes No

Other Date COPD Dx

Clinical module: Other Malignancy

OtherMalignancy: 499975			Status: Ready...		
Click here to add <input type="text" value="1"/> more row(s).			Save it	Cancel it	
			Open it	Save and Close	
EXPORT TO EXCEL					
Malig. ID	Patient ID	Dx Date	Malig. Detail		Treatment
 45	113	1/1/1900	Period: Synchronous to lung cancer (within a year) Organ: Lung Histology: Adenocarcinoma Comments: NED: <input type="checkbox"/> NED Date: 1/1/1900	Surgery: <input type="checkbox"/> Date: 3/12/2003 Chemo: <input type="checkbox"/> Date: 1/1/1900 Radio: <input type="checkbox"/> Date: 1/1/1900	
 46	113	1/1/1900	Period: n/a Organ: Skin Histology: Melanoma Comments: NED: <input type="checkbox"/> NED Date: 1/1/1900	Surgery: <input type="checkbox"/> Date: 4/20/2004 Chemo: <input type="checkbox"/> Date: 1/1/1900 Radio: <input type="checkbox"/> Date: 1/1/1900	
 49	113	1/1/1900	Period: After lung cancer Organ: Skin Histology: Squamous Cell Carcinoma Comments: NED: <input type="checkbox"/> NED Date: 1/1/1900	Surgery: <input checked="" type="checkbox"/> Date: 2/9/2005 Chemo: <input type="checkbox"/> Date: 1/1/1900 Radio: <input type="checkbox"/> Date: 1/1/1900	

Clinical module: Treatment: Surgery, Chemotherapy, Radiotherapy and Other Treatments.

Status: Ready...

Surgery: 523912

[Click here](#) to add 1 more row(s). [Save It](#) [Cancel It](#) [Open It](#) [Save and Close](#) EXPORT TO EXCEL

Surgery ID	Patient ID	Surgery Date	Is MDA	Surgery Procedure	Comments	Margin Left
29	142	3/24/2003	<input type="checkbox"/>	n/a		<input type="checkbox"/>

Chemotherapy

[Click here](#) to add 1 more row(s). [Save It](#) [Cancel It](#) [Open It](#) [Save and Close](#) EXPORT TO EXCEL

Chemo ID	Chemo Type	Chemo Date	Drug	Tumor Size	Response	Comments
29	Is MDA: <input type="checkbox"/> Chemo. Type: Neoadjuvant	Start: 1/1/1900 Stop: 1/1/1900	A: Carboplatin B: Paclitaxel C: n/a #crs: 0	Before(CT) 0 After(CT) 0 % Reduction NaN Before(Patho) 0 After(Patho) 0 % Reduction NaN	Clin.: n/a CT: n/a Patho: n/a	
143	Is MDA: <input type="checkbox"/> Chemo. Type: 1st Line	Start: 7/29/2006 Stop: 9/16/2003	A: Cisplatin B: Etoposide C: n/a #crs: 0	Before(CT) 0 After(CT) 0 % Reduction NaN Before(Patho) 0 After(Patho) 0 % Reduction NaN	Clin.: n/a CT: n/a Patho: n/a	

Radiotherapy

[Click here](#) to add 1 more row(s). [Save It](#) [Cancel It](#) [Open It](#) [Save and Close](#) EXPORT TO EXCEL


Radio ID	Treatment Option	Radio Date	Tumor Size	Response	Comments
37	Is MDA: <input type="checkbox"/> Site1: L-lung Site2: n/a Site3: n/a Treatment Option: 1st Line	Start: 7/29/2003 Stop: 9/16/2003	Before(CT) 0 After(CT) 0 % Reduction NaN Before(Patho) 0 After(Patho) 0 % Reduction NaN	Clin.: n/a CT: n/a Patho: n/a	

Other Treatment



[Click here](#) to add 1 more row(s). [Save It](#) [Cancel It](#) [Open It](#) [Save and Close](#) EXPORT TO EXCEL

Treatment ID	Patient ID	Surgery Date	Other Treatment	Comments
8	142	5/5/2004	Craniotomy	

Clinical module: Staging

Staging:			Status: Ready...									
Click here to add <input type="text" value="1"/> more row(s). Save it Cancel it Open it Save and Close <input type="button" value="Excel Report"/>												
Stage ID	Patient ID	Staging Date	Current Situation				Clin. T	Clin. N	Clin. M	Clin. Stage	Pleu Eff	Malign PI Eff
 1	44	1/1/1900	Multiple primary tumor different histology				T2	NO	M1	IB	<input checked="" type="checkbox"/>	<input checked="" type="checkbox"/>
Pathology												
Tumor Specimens												
Patient ID	Accession	Surgical Date	Single Wedge	Multiple Wedge	Single Segmentectomy	Multiple Segmentectomy	Lobectomy	Bilobectomy	Pneumonectomy	# Nodules	Tumor ID	
44	s-04-23495	05/11/2005	False	False	False	False	True	False	False	2	23	
44	s-04-23495	05/11/2005	False	False	False	False	True	False	False	2	26	
44	s-04-23495	05/11/2005	False	False	False	False	True	False	False	2	27	
<input type="text" value=""/>												
Dx Specimens												
Patient_ID	AccessionNo	Path Type	Event	Dx Specimen Date	Specimen Type	Tumor Site	Specimen Avail					
44	SB-1111	Primary	Dx Specimen	01/19/2007	CORE BIOPSY	LLL						
Metastasis Specimens												
Patient_ID	AccessionNo	Path Type	Event	Met Date	Specimen Type	Tumor Site	Specimen Avail					
<input type="text" value=""/>												

Clinical module: Follow up

Follow up: 127855			Status: Ready...
Click here to add <input type="text" value="1"/> more row(s). Save it Cancel it Open it Save and Close EXPORT TO EXCEL			
Person Review		<input type="text" value="n/a"/>	Date Updated <input type="text"/>
Fu ID	Patient ID	Fu Date	Fu Detail
	422	55	2/4/2004
Status recurrence			
If "no change or no recurrence": Form of contact: <input type="text"/>			
If "recurrence": Form of contact: visit to clinic Date of recurr: 1/1/1900			
<input type="text" value="Thoracic Lymph"/>			
Site of Recur: n/a If Lung: n/a			
<input type="text" value="n/a"/>			
Recur Biopsy: <input type="checkbox"/> Image Date: 1/1/1900			
If "death": Death Date: <input type="text"/> Cause of Death: <input type="text"/>			
Info by: <input type="text"/>			
Comments:			
<input type="text"/>			
	298	55	1/4/2006
Status no change			
If "no change or no recurrence": Form of contact: visit to clinic			
If "recurrence": Form of contact: <input type="text"/> Date of recurr: <input type="text"/>			
<input type="text"/>			
Site of Recur: <input type="text"/> If Lung: <input type="text"/>			
<input type="text"/>			
Recur Biopsy: <input type="checkbox"/> Image Date: <input type="text"/>			
If "death": Death Date: <input type="text"/> Cause of Death: <input type="text"/>			
Info by: <input type="text"/>			
Comments:			
<input type="text"/>			

Pathological module: Tissue Pathological Data

- Primary Diagnosis Specimen
- Primary Surgical Specimen
- Metastasis Diagnosis Specimen
- Metastasis Surgical Specimen

Admin Projects Histo-Pathology Lab Logout

Select a participant Status: Ready...

Hist Dx TO EXCEL All Pathology TO EXCEL

[Click here](#) to add more row(s). [Save it](#) [Cancel it](#) [Open it](#) [Save and Close](#) EXPORT TO EXCEL

				Accession	Biopsy	Event
				563 SB-1111	Primary	Surgical Specimen
				564 SB-2222	Primary	Dx Specimen
				566 SS-1112	Metastasis	Surgical Specimen
				567 S-04-23495	Primary	Surgical Specimen
				568 SB-01-1234	Metastasis	Dx Specimen

Dx Specimen

[Click here](#) to add more row(s). [Save it](#) [Cancel it](#) [Open it](#) [Save and Close](#) EXPORT TO EXCEL

	Dx Specimen ID	Obtained Date	Accession ID	Accession No	Specimen Type	Tumor Site	Specimen Avail

Surgical Specimen

[Click here](#) to add more row(s). [Save it](#) [Cancel it](#) [Open it](#) [Save and Close](#) EXPORT TO EXCEL

	Surg ID	Acc. ID	Accession No	Surgical Date	Single Wedge	Multi Wedge	Single Segmen tectomy	Multi Segmen tectomy	Lobec tomy	Bilo bectomy	Pneumo nectomy	No of Nodules	T	N	M
	6	567	S-04-23495	5/11/2005	<input type="checkbox"/>	<input type="checkbox"/>	<input type="checkbox"/>	<input type="checkbox"/>	<input checked="" type="checkbox"/>	<input type="checkbox"/>	<input type="checkbox"/>	2	n/a	n/a	n/a

Met Specimen

[Click here](#) to add more row(s). [Save it](#) [Cancel it](#) [Open it](#) [Save and Close](#) EXPORT TO EXCEL

	Met Specimen ID	Met Date	Accession ID	Accession No	Specimen Type	Tumor Site	Specimen Avail
	DX 6	1/1/1900	566	SS-1112	n/a	n/a	<input type="checkbox"/>

Pathological module: Histology

Histology		Status: Ready	
<input type="button" value="Update"/> <input type="button" value="Delete"/>			
Hist ID:	<input type="text" value="5"/>	Dx Specimen ID:	<input type="text" value="22"/>
Met Specimen ID:	<input type="text" value="0"/>	Tumor ID:	<input type="text" value="0"/>
Histology Dx:	<input type="text" value="Metastasis to lung"/>		
Metastasis (to the lung) Dx:	<input type="text" value="Carcinoma"/>	Other Tumoral Characteristics (Hist Dx)	
Carcinoma Met Site:	<input type="text" value="Breast"/>	Necrosis %	<input type="text" value="23"/>
		Fibrosis %	<input type="text" value="3"/>
		Inflammation	<input type="text" value="Severe"/>

Pathological module: Staging and Tumor Information

Tumor: s-04-23495 (6)		Status: Ready...		
Click here to add <input type="text" value="1"/> more row(s).		Save it	Cancel it	
		Open it	Save and Close	
<input type="button" value="Excel Report"/>				
Tumor ID	Surgical ID	Specimen Type	Tumor Site	Localization
23	6	n/a	n/a	n/a
26	6	Bilobectomy	n/a	n/a
27	6	Lobectomy	n/a	n/a

Type of Tissue Available <input type="checkbox"/> Bronchus Extrapulmonary <input type="checkbox"/> Principal <input type="checkbox"/> Lobar Intrapulmonary <input type="checkbox"/> with Cartilage <input type="checkbox"/> w/o Cartilage <input type="checkbox"/> Bronchiole <input type="checkbox"/> Alveoli	Tumor Size(cm) <input type="text" value="0"/> <input type="checkbox"/> Tumor Invasion <input type="checkbox"/> Pleural <input type="checkbox"/> Neural <input type="checkbox"/> Vascular <input type="checkbox"/> Other <input type="checkbox"/> Margin Positive <input type="checkbox"/> Bronchial <input type="checkbox"/> Parenchymal <input type="checkbox"/> Soft Tissue <input type="checkbox"/> Other	Pathological T Pathological T: <input type="text" value="n/a"/> <input type="checkbox"/> Tx T1: <= 3 cm. T2: > 3 cm or <= 3cm and/or attached to visceral pleura <input type="checkbox"/> Pleural Attached T3: T4: <input type="checkbox"/> Parietal Pleura <input type="checkbox"/> >1 Nodal <input type="checkbox"/> Mediastinal Pleura <input type="checkbox"/> Invades to Great Vessel <input type="checkbox"/> Chest Wall <input type="checkbox"/> Invades to Heart <input type="checkbox"/> Mediastinal Fat <input type="checkbox"/> Invades to Trachea <input type="checkbox"/> Pericardium <input type="checkbox"/> Invades to Carina <input type="checkbox"/> Phrenic Nerve <input type="checkbox"/> Invades to Esophagus <input type="checkbox"/> Vagus Nerve <input type="checkbox"/> Invades to Vertebral Bones <input type="checkbox"/> Sympathetic Chain <input type="checkbox"/> Associated with Malignant Pleural Effusion <input type="checkbox"/> Atelectasis Entire Lung <input type="checkbox"/> Satellite Tumor Nodule (size)
--	---	--

Field Study	Lymph Node Metastasis <input type="checkbox"/> Lymph Node Involvement																																																						
Normal bronchial epithelium and premalignant lesions	Analysis of Lymph Node Station																																																						
<input type="checkbox"/> Normal Bronchial Epithelium <input type="checkbox"/> Normal Lung Parenchyma <input type="checkbox"/> Hyperplastic Alveoli <input type="checkbox"/> Bronchial Hyperplasia <input type="checkbox"/> Squamous Metaplasia <input type="checkbox"/> Mild Squamous Dysplasia <input type="checkbox"/> Moderately Squamous Dysplasia <input type="checkbox"/> High Squamous Dysplasia <input type="checkbox"/> In Situ Squamous Carcinoma <input type="checkbox"/> Atypical Adenomatous Hyperplasia <input type="checkbox"/> Tumorlet	<table border="1"> <thead> <tr> <th></th> <th>+</th> <th>Total</th> <th>+</th> <th>Total</th> <th>+</th> <th>Total</th> <th>+</th> <th>Total</th> </tr> </thead> <tbody> <tr> <td>S1</td> <td>0</td> <td>0</td> <td>S2</td> <td>0</td> <td>0</td> <td>S3</td> <td>0</td> <td>0</td> </tr> <tr> <td>S5</td> <td>0</td> <td>0</td> <td>S6</td> <td>0</td> <td>0</td> <td>S7</td> <td>0</td> <td>0</td> </tr> <tr> <td>S9</td> <td>0</td> <td>0</td> <td>S10</td> <td>0</td> <td>0</td> <td>S11</td> <td>0</td> <td>0</td> </tr> <tr> <td>S13</td> <td>0</td> <td>0</td> <td>S14</td> <td>0</td> <td>0</td> <td>NS</td> <td>0</td> <td>0</td> </tr> <tr> <td colspan="2">Total</td> <td>0</td> <td colspan="2">Total</td> <td>0</td> <td colspan="2">Total</td> <td>0</td> </tr> </tbody> </table> <input type="checkbox"/> Positive Contralateral LN mtt Path N: <input type="text" value="n/a"/> Type of LN metastasis Size of Metastasis <input type="checkbox"/> Intranodal <input type="checkbox"/> Capsular <input type="checkbox"/> Subcapsular <input type="checkbox"/> Perinodal Min. Size: <input type="text" value="0"/> Max. Size: <input type="text" value="0"/>		+	Total	+	Total	+	Total	+	Total	S1	0	0	S2	0	0	S3	0	0	S5	0	0	S6	0	0	S7	0	0	S9	0	0	S10	0	0	S11	0	0	S13	0	0	S14	0	0	NS	0	0	Total		0	Total		0	Total		0
	+	Total	+	Total	+	Total	+	Total																																															
S1	0	0	S2	0	0	S3	0	0																																															
S5	0	0	S6	0	0	S7	0	0																																															
S9	0	0	S10	0	0	S11	0	0																																															
S13	0	0	S14	0	0	NS	0	0																																															
Total		0	Total		0	Total		0																																															

Pathological module: Tissue Bank (Frozen and Paraffin)

Tissue Bank: s-04-23495		Status: Ready...					
Click here to add <input type="text" value="1"/> more row(s). Save it Cancel it Open it Save and Close <input type="button" value="Excel Report"/>							
Frozen	FFPE	TBID	Collection Date	Frozen Avail	FFPE Avail		
		<input type="text" value="6"/>	<input type="text" value="4/12/2008"/>	<input checked="" type="checkbox"/>	<input type="checkbox"/>		
		<input type="text" value="8"/>	<input type="text" value="4/13/2008"/>	<input type="checkbox"/>	<input type="checkbox"/>		
		<input type="text" value="9"/>	<input type="text" value="4/12/2008"/>	<input type="checkbox"/>	<input type="checkbox"/>		
Frozen							
Click here to add <input type="text" value="1"/> more row(s). Save it Cancel it Open it Save and Close <input type="button" value="Excel Report"/>							
ID	Tissue	Blood	Pleural				
 Frozen ID: <input type="text" value="0"/> TB ID: <input type="text" value="6"/> SPORE No: <input type="text" value="0"/> TID No: <input type="text" value="0"/>	DNA Conc <input type="text" value="0"/> DNA Vol <input type="text" value="0"/> DNA Quality <input type="text" value="n/a"/>	DNA Conc <input type="text" value="0"/> DNA Vol <input type="text" value="0"/> DNA Quality <input type="text" value="n/a"/>	DNA Conc <input type="text" value="0"/> DNA Vol <input type="text" value="0"/> DNA Quality <input type="text" value="n/a"/>				
	Normal Lung <input type="checkbox"/> Tumor <input type="checkbox"/> Bronchus <input type="checkbox"/> LN <input type="checkbox"/> Serum <input type="checkbox"/> Lymphocyte <input type="checkbox"/> Pleural <input type="checkbox"/>	RNA Conc <input type="text" value="0"/> RNA Vol <input type="text" value="0"/> RNA Quality <input type="text" value="n/a"/>	RNA Conc <input type="text" value="0"/> RNA Vol <input type="text" value="0"/> RNA Quality <input type="text" value="n/a"/>	RNA Conc <input type="text" value="0"/> RNA Vol <input type="text" value="0"/> RNA Quality <input type="text" value="n/a"/>			
	Prot Conc <input type="text" value="0"/> Prot Vol <input type="text" value="0"/> Prot Quality <input type="text" value="n/a"/>	Prot Conc <input type="text" value="0"/> Prot Vol <input type="text" value="0"/> Prot Quality <input type="text" value="n/a"/>	Prot Conc <input type="text" value="0"/> Prot Vol <input type="text" value="0"/> Prot Quality <input type="text" value="n/a"/>	Prot Conc <input type="text" value="0"/> Prot Vol <input type="text" value="0"/> Prot Quality <input type="text" value="n/a"/>			
	FFPE						
	Click here to add <input type="text" value="1"/> more row(s). Save it Cancel it Open it Save and Close <input type="button" value="Excel Report"/>						
	FFPE ID	TB ID	Cabinet	Tray	Block	Slide	
			<input type="text" value="0"/>	<input type="text" value="6"/>	<input type="text" value="0"/>	<input type="text" value="0"/>	

One example of the Excel reports.

	K	L	M	N	O	P	Q
1	Specimen Avail	Surgical Date	Single Wedge	Multiple Wedge	Single Segmentectomy	Multiple Segmentectomy	Lobectomy
2							
3							
4			+				
5		5/11/2005 0:00	FALSE	FALSE	FALSE	FALSE	TRUE
6		5/11/2005 0:00	FALSE	FALSE	FALSE	FALSE	TRUE
7		5/11/2005 0:00	FALSE	FALSE	FALSE	FALSE	TRUE
8		5/11/2005 0:00	FALSE	FALSE	FALSE	FALSE	TRUE
9							
10							
11							
12							
13		1/1/1900 0:00	FALSE	TRUE	TRUE	FALSE	FALSE
14		1/1/1900 0:00	FALSE	TRUE	TRUE	FALSE	FALSE
15	FALSE						
16	TRUE						
17							
18							
19		1/1/1900 0:00	FALSE	FALSE	FALSE	FALSE	FALSE
20							
21							
22							
23							
24							
25							
26		1/1/1900 0:00	FALSE	FALSE	FALSE	FALSE	FALSE
27							
28							
29							
30							
31							
32							
33							
34							
35							





Dictionary module

Admin ▾ Projects ▾ Histo-Pathology Lab ▾ Logout

Dictionarys

Country ▾ [Update](#)

Page 1 [2] [3] [4] [5] [...]

	Dictionarys	Set Order
+		
	Afghanistan	1
	Albania	2
	Algeria	3
	American Samoa	4
	Andorra	5
	Angola	6
	Anguilla	7
	Antarctica	8
	Antigua and Barbuda	9
	Arctic Ocean	10
	Argentina	11
	Armenia	12
	Aruba	13
	Ashmore and Cartier Islands	14
	Atlantic Ocean	15
	Australia	16
	Austria	17
	Azerbaijan	18
	Bahamas	19

Page 1 [2] [3] [4] [5] [...]

Page 1 of 14

5. Lee C, **Mehran RJ**, Lessard ML, Kerrigan CL. Leeches: controlled trial in venous compromised rat epigastric flaps. *Br J Plast Surg* 45:235-8, 1992.
6. Deslauriers J, **Mehran RJ**. Role of thoracoscopy in the diagnosis and management of pleural diseases. *Semin Thorac Cardiovasc Surg* 5:284-93, 1993.
7. Deslauriers J, **Mehran RJ**, Guimont C, Brisson J. Staging and management of lung cancer: sleeve resection. *World J Surg* 17:712-8, 1993.
8. **Mehran RJ**, Deslauriers J, Piroux M, Beaulieu M, Guimont C, Brisson J. Survival related to nodal status after sleeve resection for lung cancer. *J Thorac Cardiovasc Surg* 107:576-82; discussion 582-3, 1994.
9. **Mehran RJ**, Duranceau A. The use of endoprosthesis in the palliation of esophageal carcinoma. *Chest Surg Clin N Am* 4:331-46, 1994.
10. **Mehran R**, Connelly P, Boucher P, Berthiaume E, Cote M. Modern war surgery: the experience of Bosnia. 1: Deployment. *Can J Surg* 38:266-74, 1995.
11. **Mehran R**, Connelly P, Boucher P, Cote M. Modern war surgery: the experience of Bosnia. 2: The clinical experience. *Can J Surg* 38:338-46, 1995.
12. **Mehran RJ**, Deslauriers J. Indications for surgery and patient work-up for bullectomy. *Chest Surg Clin N Am* 5:717-34, 1995.
13. Shamji FM, Deslauriers J, Daniel TM, Matzinger FR, **Mehran RJ**, Todd TR. Postpneumonectomy syndrome with an ipsilateral aortic arch after left pneumonectomy. *Ann Thorac Surg* 62:1627-31, 1996.
14. Devin B, McCarthy A, **Mehran R**, Auger C. Necrotizing fasciitis of the retroperitoneum: an unusual presentation of group A Streptococcus infection. *Can J Surg* 41:156-60, 1998.
15. **Mehran R**, Jonker D, Crepeau A, Maroon J. Cost effectiveness of neoadjuvant chemotherapy in the management of distal esophageal carcinoma. *Canadian J Gastroenterology* 12:137B, 1998.
16. Valestaqui R, **Mehran RJ**. Traumatic hernia of the pericardium. *J Trauma* 46:513-4, 1999.
17. Chopra P, Killorn P, **Mehran RJ**. Cholelithoptysis and pleural empyema. *Ann Thorac Surg* 68:254-5, 1999.
18. **Mehran RJ**, Deslauriers J. Late complications. Postpneumonectomy syndrome. *Chest Surg Clin N Am* 9:655-73, 1999.
19. Jonker D, **Mehran R**, Maroun J, Crepeau A. Neoadjuvant chemotherapy before surgery for resectable carcinoma of the lower esophagus. *Dis Esophagus* 12:144-8, 1999.
20. Rasuli P, **Mehran R**, French G, Turek M, Lalonde KA, Cardinal P. Percutaneous retrieval of a vena cava filter from the right atrium: case report. *Can Assoc Radiol J* 51:30-5, 2000.
21. Gowan RT, **Mehran RJ**, Cardinal P, Jones G. Thoracic complications of Lemierre syndrome. *Can Respir J* 7:481-5, 2000.
22. Jetty P, **Mehran RJ**. Inadvertent suture through the chest tube: a simple solution to a frustrating problem. *Ann Thorac Surg* 69:261-2, 2000.
23. **Mehran R**, Schneider R, Franchebois P. The minor hepatic veins: anatomy and classification. *Clin Anat* 13:416-21, 2000.
24. Hyland MJ, Ashrafi AS, Crepeau A, **Mehran RJ**. Is video-assisted thoracoscopic surgery superior to limited axillary thoracotomy in the management of spontaneous pneumothorax? *Can Respir J* 8:339-43, 2001.
25. **Mehran R**, Ghosh R, Maziak D, O'Rourke K, Shamji F. Surgical treatment of thymoma. *Can J Surg* 45:25-30, 2002.
26. Wherrett CG, **Mehran RJ**, Beaulieu MA. Cerebral arterial gas embolism following diagnostic bronchoscopy: delayed treatment with hyperbaric oxygen. *Can J Anaesth* 49:96-9, 2002.
27. Martin LW, Swisher SG, Hofstetter W, Correa AM, **Mehran RJ**, Rice DC, Vaporciyan AA, Walsh GL, Roth JA. Intrathoracic leaks following esophagectomy are no longer associated with increased mortality. *Ann Surg* 242:392-402, 2005.
28. Campen MJ, Babu NS, Helms GA, Pett S, Wernly J, **Mehran R**, McDonald JD. Nonparticulate components of diesel exhaust promote constriction in coronary arteries from ApoE^{-/-} mice. *Toxicol Sci* 88:95-102, 2005.
29. Gamm DM, Harris A, **Mehran RJ**, Wood M, Foster CS, Mootha VV. Mucous membrane pemphigoid with fatal bronchial involvement in a seventeen-year-old girl. *Cornea* 25:474-8, 2006.
30. Masten BJ, Olson GK, Tarleton CA, Rund C, Schuyler M, **Mehran R**, Archibeque T, Lipscomb MF. Characterization of myeloid and plasmacytoid dendritic cells in human lung. *J Exp Med* 11:7784-93, 2006.

31. Herrera LJ, Correa AM, Vaporciyan AA, Hofstetter WL, Rice DC, Swisher SG, Walsh GL, Roth JA, **Mehran RJ**. Increased risk of aspiration and pulmonary complications after lung resection in head and neck cancer patients. *Ann Thorac Surg* 82:1982-8, 2006.
32. Blackmon, SH, Martin, LW, Correa, AM, Wynn, B, Hofstetter W, **Mehran RJ**, Rice D, Swisher S, Walsh GL, Roth JA, Vaporciyan AA. Propensity matched analysis of three techniques for intrathoracic esophagogastric anastomosis. *Ann Thorac Surg* 83:1805-13, 2007.
33. Jackson TA, **Mehran RJ**, Thakar D, Riedel B, Nunnally ME, Slinger P. Case 5-2007 Postoperative complications after pneumonectomy. *J Cardiothorac Vas Anesth* 21:743-751, 2007.
34. Yendamuri S, Komaki RR, Correa AM, Allen P, Wynn B, Blackmon S, Hofstetter WL, Rice DC, Roth JA, Swisher SG, Vaporciyan AA, Walsh GL, **Mehran RJ**. Comparison of limited surgery and three-dimensional conformal radiation in high-risk patients with stage I non-small cell lung cancer. *J Thorac Oncol* 2.:1022-28, 2007.
35. Cavalcanti JL, Nunez RF, Yeung HW, **Mehran RJ**, Macapinlac HA. Incidental finding of prostate cancer and adenomatous colon polyp in a patient with lung cancer. *Clin Nucl Med* 32 :871-3, 2007.
36. Rice DC, Stevens CW, Correa AM, Vaporciyan AA, Tsao A, Forster KM, Walsh GL, Swisher SG, Hofstetter WL, **Mehran RJ**, Roth JA, Liao Z, Smythe WR. Outcomes after extrapleural pneumonectomy and intensity-modulated radiation therapy for malignant pleural mesothelioma. *Ann Thorac Surg* 84:1685-1693, 2007.
37. Hofstetter W, Correa AM, Bekele N, Ajani JA, Phan A, Komaki RR, Liao Z, Maru D, Wu TT, **Mehran RJ**, Rice DC, Roth JA, Vaporciyan AA, Walsh GL, Francis A, Blackmon S, Swisher SG. Proposed modification of nodal status in AJCC esophageal cancer staging system. *Ann Thorac Surg* 84:365-375, 2007.
38. Leung KK, Maru D, Abraham S, Hofstetter WL, **Mehran R**, Anandasabapathy S. Optical EMR: confocal endomicroscopy-targeted EMR of focal high-grade dysplasia in Barrett's esophagus. *Gastrointest Endosc*, 6/24/2008.
39. Yendamuri S, Vaporciyan AA, Zaidi T, Feng L, Fernandez R, Bekele NB, Hofstetter WL, Jiang F, **Mehran RJ**, Rice DC, Spitz MR, Swisher SG, Walsh GL, Roth JA, Katz RL. 3p22.1 and 10q22.3 deletions detected by fluorescence in situ hybridization (FISH): a potential new tool for early detection of non-small cell lung Cancer (NSCLC). *J Thorac Oncol* 3(9):979-84, 9/2008.
40. Chang JY, Balter PA, Dong L, Yang Q, Liao Z, Jeter M, Bucci MK, McAleer MF, **Mehran RJ**, Roth JA, Komaki R. Stereotactic body radiation therapy in centrally and superiorly located stage I or isolated recurrent non-small-cell lung cancer. *Int J Radiat Oncol Biol Phys* 15(75 (4)):967-71, 11/2008.
41. Tsao AS, Mehran R, Roth JA. Neoadjuvant and intrapleural therapies for malignant pleural mesothelioma. *Clin Lung Cancer* 10(1):36-41, 1/2009.
42. Blackmon SH, Rice DC, Correa AM, Mehran R, Putman JB, Smythe WR, Walkes JC, Walsh GL, Moran C, Singh H, Vaporciyan AA, Reardon M. Management of Primary Pulmonary Artery Sarcomas. *The Annals of Thoracic Surgery* 87(3):977-84, 3/2009.
43. Jackson TA, **Mehran RJ**, Riedel BJCJ. Postoperative complications following pneumonectomy: A stem case and literature review. *J Anesth*. In Press.
44. Rice DC, Stevens CW, Forster K, Vaporciyan AA, Walsh GL, Swisher SG, Hofstetter W, **Mehran RJ**, Roth JA, Liao Z, Smythe R. Survival and recurrence patterns following extrapleural pneumonectomy and intensity modulated radiation therapy for malignant pleural mesothelioma. *J Thorac Cardiovasc Surg*. In Press.
45. Yendamuri S, **Mehran R**. 3D conformal radiation therapy vs non anatomical lung resection, a propensity matched analysis. *J Thorac Oncol*, In Press

C. Research Support

Ongoing Research Support

None

Completed Research Support

International Anesthesia Research Society Clinical

Scholar Research Award (Riedel) 2007-2008

Perioperative Endothelial Kinetics - A Predictor of Outcome Following Major Surgery

Role: Co-Principal Investigator